

UNCLASSIFIED

AD 290 770

*Reproduced
by the*

ARMED SERVICES TECHNICAL INFORMATION AGENCY
ARLINGTON HALL STATION
ARLINGTON 12, VIRGINIA



UNCLASSIFIED

NOTICE: When government or other drawings, specifications or other data are used for any purpose other than in connection with a definitely related government procurement operation, the U. S. Government thereby incurs no responsibility, nor any obligation whatsoever; and the fact that the Government may have formulated, furnished, or in any way supplied the said drawings, specifications, or other data is not to be regarded by implication or otherwise as in any manner licensing the holder or any other person or corporation, or conveying any rights or permission to manufacture, use or sell any patented invention that may in any way be related thereto.

Strength, Efficiency, and Design Data For Beryllium Structures



A GOVERNMENT RESEARCH REPORT

U. S. DEPARTMENT OF COMMERCE Office of Technical Services

distributes this and thousands of similar reports in the interest of science, industry, and the public—for which research and new products mean better health, better living, and a stronger economy.

HOW TO GET OTHER REPORTS

The Office of Technical Services is the Nation's clearinghouse for reports of research supported by the Army, Navy, Air Force, Atomic Energy Commission, and other Government agencies.

Abstracts of new reports available are published twice a month in U. S. GOVERNMENT RESEARCH REPORTS (\$15 a year domestic).

Selected Reports of particular interest to small business are described monthly in TECHNICAL REPORTS NEWSLETTER (\$1 a year domestic).

Translations of foreign technical material are also available from the Office of Technical Services and other sources. These are listed or abstracted semimonthly in TECHNICAL TRANSLATIONS (\$12 a year domestic).

The above periodicals may be ordered from Superintendent of Documents, U. S. Government Printing Office, Washington 25, D. C. or through a U. S. Department of Commerce Field Office.

Inquiries about the availability of reports and translations on any particular subject may be directed to Office of Technical Services, U. S. Department of Commerce, Washington 25, D. C., or to any Commerce field office.

Reports and translations are published by the Office of Technical Services for use by the public. Thus, you may use the know-how or reprint the information therein except that where patent questions appear to be involved the usual preliminary search is advised, and where copyrighted material is used permission should be obtained for its further publication.

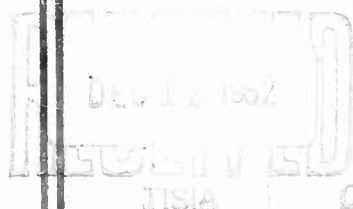
290 770

CATALOGED BY ASTIA

AD No. 29 0770

ASTIA

DEC 16 1962



NOTICE

When Government drawings, specifications, or other data are used for any purpose other than in connection with a definitely related Government procurement operation, the United States Government thereby incurs no responsibility nor any obligation whatsoever; and the fact that the Government may have formulated, furnished, or in any way supplied the said drawings, specifications, or other data, is not to be regarded by implication or otherwise as in any manner licensing the holder or any other person or corporation, or conveying any rights or permission to manufacture, use, or sell any patented invention that may in any way be related thereto.

ASD TECHNICAL REPORT 61-692

STRENGTH, EFFICIENCY, AND DESIGN DATA FOR
BERYLLIUM STRUCTURES

ROBERT F. CRAWFORD
A. BRUCE BURNS

LOCKHEED MISSILES & SPACE COMPANY
SUNNYVALE, CALIFORNIA

CONTRACT AF 33(616) 5905
PROJECT 1308
TASK 13028

February 1962

FLIGHT DYNAMICS LABORATORY

AERONAUTICAL SYSTEMS DIVISION
AIR FORCE SYSTEMS COMMAND
UNITED STATES AIR FORCE
WRIGHT-PATTERSON AIR FORCE BASE, OHIO

FOREWORD

This research report was prepared by the Structural Mechanics organization of Lockheed Missiles & Space Company. The work was done under USAF Contract AF 33(616)-6905, with Aeronautical Systems Division sponsorship. The research program was initiated by Project 1368, "Design Technologies and Structural Configuration Concepts for Aerospace Vehicles," Task 136806, "Beryllium Structural Development." The program was administered under the direction of the Structures Branch, Flight Dynamics Laboratory, with first Robert D. Guyton and then Norman P. Kempton as Project Engineer.

The Lockheed Project Leader for this program has been Robert F. Crawford. General supervision has been the responsibility of L. A. Riedinger, Manager of the Structural Mechanics organization. The testing was performed by A. M. C. Holmes and R. B. Clapper, who further contributed to this report by preparing Appendix A and Appendix B, respectively. R. L. Keeney assisted in the literature survey and in the compilation of data. The figures were prepared with the assistance of R. L. Keeney, C. E. Stuhlman, and L. K. Tilcens.

This report covers work conducted from February 1960 to December 1961.

This project and task are part of Air Force Systems Command's applied research program 750A "Mechanics of Flight."

ABSTRACT

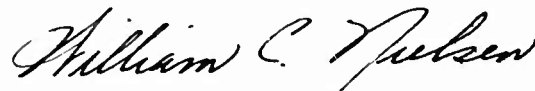
The purpose of this study program was to investigate the design capabilities of beryllium as a structural material and to derive and develop structural design curves and related data for efficient structural design with beryllium.

The metal beryllium is believed to have high potential for aerospace structures, but is not extensively considered in design applications at the present time because of uncertainties as to the proper design procedures. This report presents information based on studies and tests which clearly shows that beryllium now may be designed with confidence into many types of load-carrying structures, using well-known methods of structural analysis and appropriate margins of safety. The resulting beryllium structures are shown to be considerably lighter than identical structures fabricated from other metals, and these structures are attainable with currently available beryllium mill products.

PUBLICATION REVIEW

This report has been reviewed and is approved.

FOR THE COMMANDER:



WILLIAM C. NIELSEN
Colonel, USAF
Chief, Flight Dynamics Laboratory

CONTENTS

Section		Page
	FOREWORD	iii
	ABSTRACT	v
	ILLUSTRATIONS	xi
	TABLES	xxvi
	NOMENCLATURE	xxix
1	INTRODUCTION	1-1
2	PHYSICAL AND MECHANICAL PROPERTIES OF BERYLLIUM BLOCK, SHEET, AND EXTRUSION	2-1
	2.1 Introduction	2-1
	2.2 Physical Properties	2-3
	2.3 Mechanical Properties	2-10
	2.3.1 QMV Hot-Pressed Block	2-16
	2.3.2 Cross-Rolled Sheet	2-52
	2.3.3 Hot-Upset Sheet	2-68
	2.3.4 Extrusions	2-75
	2.4 Notch Sensitivity of Beryllium	2-80
	2.4.1 QMV Hot-Pressed Block	2-86
	2.4.2 Cross-Rolled Sheet	2-87
	2.5 The Biaxial Strength of Beryllium Block and Sheet	2-89
	2.5.1 General Metallurgical and Mechanical Properties of Beryllium	2-90
	2.5.2 Beryllium Block (Randomly Oriented)	2-93
	2.5.3 Beryllium Cross-Rolled Sheet	2-103
	2.6 References	2-114
	2.6.1 Cited References	2-114
	2.6.2 Uncited References	2-116

Section		Page
3	BERYLLIUM COMPONENT DESIGN DATA	3-1
	3.1 Introduction	3-1
	3.2 Buckling and Post-Buckling Design Charts for Flat Unstiffened Panels	3-12
	3.2.1 Compression Buckling	3-12
	3.2.2 Compression Post-Buckling	3-15
	3.2.3 Shear Buckling	3-18
	3.2.4 Shear Post-Buckling	3-21
	3.2.5 Column Buckling	3-25
	3.2.6 Interaction Formulas	3-28
	3.3 Buckling Design Charts for Monocoque Cylinders	3-29
	3.3.1 Buckling Due to Axial Compression	3-29
	3.3.2 Buckling Due to Torsion	3-39
	3.3.3 Buckling Due to Hydrostatic or Radial Pressure	3-42
	3.4 Crippling Design Charts	3-46
	3.5 Plastic Bending Design Charts	3-54
	3.6 Beryllium Joining	3-59
	3.6.1 Introduction	3-59
	3.6.2 Mechanical Joining	3-60
	3.6.3 Metallurgical Joining	3-87
	3.7 Application of Beryllium in Fail-Safe Design and in Fittings	3-97
	3.7.1 Fail-Safe Policy	3-97
	3.7.2 Tension-Type Fittings	3-97
	3.8 References	3-99
4	MINIMUM-WEIGHT DESIGN AND COMPARATIVE EFFICIENCY	4-1
	4.1 Introduction to Minimum-Weight Analysis	4-1
	4.2 Nondimensional Minimum-Weight Design Procedures	4-5
	4.2.1 Wide Columns	4-5
	4.2.2 Compression Panels	4-19
	4.2.3 Shear Panels	4-38

Section	Page
4.2.4 Multiweb Box Beams	4-44
4.2.5 Axially Loaded Cylinders	4-55
4.2.6 Cylinders in Torsion	4-62
4.2.7 Hydrostatically Compressed Cylinders	4-70
4.3 Example Minimum-Weight Design Charts for Beryllium Cross-Rolled Sheet	4-95
4.4 Comparative Efficiency Studies of Beryllium Cross-Rolled Sheet With Other Structural Materials	4-109
4.5 References	4-134
5 BERYLLIUM FABRICATION	5-1
5.1 Introduction	5-1
5.2 Hot-Pressed Block	5-2
5.3 Forging	5-3
5.4 Sheet	5-4
5.5 Extrusions	5-6
5.6 Machining - General	5-7
5.7 Turning	5-9
5.8 Milling	5-11
5.9 Drilling	5-12
5.10 Grinding	5-16
5.11 Parting	5-17
5.12 References	5-18
5.12.1 Cited Reference	5-18
5.12.2 Uncited References	5-18
6 CONCLUSIONS, RECOMMENDATIONS, AND APPLICATIONS	6-1
6.1 Conclusions	6-1
6.2 Recommendations	6-2
6.3 Applications	6-3
6.4 Reference	6-4

Appendix		Page
A	EXPERIMENTAL INVESTIGATION OF BERYLLIUM PANELS AND CYLINDERS	A-1
	A.1 Introduction	A-1
	A.2 Basic Testing Equipment and Procedures	A-2
	A.2.1 Loading	A-2
	A.2.2 Strain and Elongation Recording	A-4
	A.2.3 Heating of Specimens	A-8
	A.2.4 Strain Gages	A-9
	A.2.5 Temperature Measurement and Recording	A-10
	A.2.6 Measurement and Geometry of Specimens	A-13
	A.3 Details of Specific Tests	A-14
	A.3.1 Compression Panels	A-14
	A.3.2 Shear Panels	A-38
	A.3.3 Axially Loaded Monocoque Cylinders	A-59
	A.3.4 Externally Pressurized Monocoque Cylinder Test	A-77
B	EXPERIMENTAL INVESTIGATION OF THE BIAXIAL STRENGTH OF CROSS-ROLLED BERYLLIUM SHEET	B-1
	B.1 Introduction	B-1
	B.2 Apparatus and Procedure	B-1
	B.2.1 Specimens	B-1
	B.2.2 Loading Apparatus	B-2
	B.2.3 Strain and Deflection Measurements	B-6
	B.2.4 Heating of Specimens	B-9
	B.2.5 Temperature Measurements	B-10
	B.3 Summary of Test Results	B-11
	B.3.1 Room-Temperature Test Results	B-12
	B.3.2 Elevated-Temperature Test Results	B-15
C	FABRICATION AND TESTING OF BERYLLIUM STRUCTURAL SANDWICHES	C-1
	C.1 Introduction	C-1
	C.2 Fabrication	C-5
	C.3 Testing	C-7

ILLUSTRATIONS

Figure		Page
2-1	Effect of Temperature on the Specific Heat of Beryllium	2-5
2-2	Effect of Temperature on Thermal Conductivity of Beryllium	2-6
2-3	Effect of Temperature and BeO Content on Thermal Expansion of Beryllium	2-7
2-4	Effect of Temperature on Resistivity of Beryllium	2-8
2-5	Effect of Temperature on Magnetic Susceptibility of Beryllium	2-9
2-6	Tensile Stress-Strain Curves for Hot-Pressed Beryllium Block Having 1% BeO Content	2-11
2-7	Tensile Stress-Strain Curves for Hot-Pressed Beryllium Block Having 2% BeO Content	2-12
2-8	Tensile Stress-Strain Curves for Hot-Pressed Beryllium Block Having 3% BeO Content	2-13
2-9	Effect of Temperature and BeO Content on Young's Modulus of Hot-Pressed Beryllium Block	2-14
2-10	Effect of Temperature on the Longitudinal Ultimate Tensile Stress of Hot-Pressed Beryllium Block at Various Levels of Probability	2-18
2-11	Effect of Temperature on the Transverse Ultimate Tensile Stress of Hot-Pressed Beryllium Block at Various Probability Levels	2-19
2-12	Effect of Temperature on the Longitudinal Tensile Yield Stress of Hot-Pressed Beryllium Block at Various Probability Levels	2-20
2-13	Effect of Temperature on the Transverse Tensile Yield Stress of Hot-Pressed Beryllium Block at Various Probability Levels	2-21
2-14	Effect of Temperature on the Typical Compressive Yield Stress of Hot-Pressed Beryllium Block	2-22
2-15	Effect of Temperature on the Typical Ultimate Shear Stress of Hot-Pressed Beryllium Block	2-23
2-16	Effect of Temperature on the Typical Bearing Stress of Hot-Pressed Beryllium Block, $e/D = 2.67$	2-24

Figure		Page
2-17	Effect of Temperature on the Typical Bearing Stress of Hot-Pressed Beryllium Block, $e/D = 2.0$	2-25
2-18	Effect of Temperature on the Typical Bearing Stress of Hot-Pressed Beryllium Block, $e/D = 1.6$	2-26
2-19	Effect of Temperature on the Longitudinal Tensile Elongation of Hot-Pressed Beryllium Block	2-27
2-20	Effect of Temperature on Young's Modulus of Hot-Pressed Beryllium Block	2-28
2-21	Effect of Temperature on the Compressive Modulus of Hot-Pressed Beryllium Block	2-29
2-22	Typical Tensile Stress-Strain Curves at Room and Elevated Temperatures for Hot-Pressed Beryllium Block	2-30
2-23	Typical Compressive Stress-Strain Curves at Room and Elevated Temperature for Hot-Pressed Beryllium Block	2-31
2-24	Definition of Fatigue Terms	2-32
2-25	Axial S-N Curves for Hot-Pressed Beryllium Block at Room Temperature	2-34
2-26	Axial S-N Curves for Hot-Pressed Beryllium Block at 1100° F (1)	2-35
2-27	Axial S-N Curves for Hot-Pressed Beryllium Block at 1100° F (2)	2-36
2-28	Axial S-N Curves for Hot-Pressed Beryllium Block at Room Temperature (1)	2-37
2-29	Axial S-N Curves for Hot-Pressed Beryllium Block at Room Temperature (2)	2-38
2-30	Effect of Mean Stress on the Axial Fatigue Behavior of Unnotched Hot-Pressed Beryllium Block at Room Temperature	2-39
2-31	Axial S-N Curves for Hot-Pressed Beryllium Block at 800° F	2-41
2-32	Axial S-N Curves for Hot-Pressed Beryllium Block at 1200° F	2-42
2-33	Geometry for 2, 4, and 5 Fastener Joints	2-43
2-34	Arrangement for Beryllium Axial Fatigue Joint Tests	2-43
2-35	Axial S-N Curves for Hot-Pressed Beryllium Block Joints With 3/16-in. Steel Countersunk Screws at Room Temperature	2-44
2-36	Axial S-N Curves for Hot-Pressed Beryllium Block Joints With 1/4-in. Steel Countersunk Jo-Bolts at Room Temperature	2-45
2-37	Axial S-N Curves for Hot-Pressed Beryllium Block Joints With 1/4-in. Steel Countersunk Screws at Room Temperature	2-46

Figure		Page
2-38	Creep Curves for Hot-Pressed Beryllium Block at 1000°F	2-48
2-39	Creep Curves for Hot-Pressed Beryllium Block at 1250°F	2-49
2-40	Creep Curves for Hot-Pressed Beryllium Block at 1500°F	2-50
2-41	Stress-Rupture Curve for Hot-Pressed Beryllium Block at 1100°F	2-51
2-42	Effect of Temperature on the Typical Longitudinal Ultimate Tensile Stress of Cross-Rolled Beryllium Sheet	2-53
2-43	Effect of Temperature on the Typical Transverse Ultimate Tensile Stress of Cross-Rolled Beryllium Sheet	2-54
2-44	Effect of Temperature on the Typical Longitudinal Tensile Yield-Stress of Cross-Rolled Beryllium Sheet	2-55
2-45	Effect of Temperature on the Typical Transverse Tensile Yield-Stress of Cross-Rolled Beryllium Sheet	2-56
2-46	Effect of Temperature on the Typical Ultimate Shear Stress of Cross-Rolled Beryllium Sheet (Shearing Normal to Plane of Sheet)	2-57
2-47	Effect of Temperature on the Typical Bearing Stress of Cross-Rolled Beryllium Sheet	2-58
2-48	Effect of Temperature on Longitudinal Tensile Elongation of Cross-Rolled Beryllium Sheet	2-60
2-49	Effect of Temperature on Young's Modulus of Cross-Rolled Beryllium Sheet	2-61
2-50	Estimated Effect of Temperature on Compressive Modulus of Elasticity of Cross-Rolled Beryllium Sheet	2-62
2-51	Typical Tensile Stress-Strain Curves at Room and Elevated Temperatures for Cross-Rolled Beryllium Sheet	2-63
2-52	Typical Compressive Stress-Strain Curves at Room and Elevated Temperatures for Cross-Rolled Beryllium Sheet	2-64
2-53	Creep Curves for Cross-Rolled Beryllium Sheet at 1000°F	2-65
2-54	Creep Curves for Cross-Rolled Beryllium Sheet at 1250°F	2-66
2-55	Creep Curves for Cross-Rolled Beryllium Sheet at 1500°F	2-67
2-56	Effect of Temperature on the Typical Compressive Yield Strength of Hot-Upset Beryllium Sheet	2-69
2-57	Effect of Temperature on the Tensile Elongation of Hot-Upset Beryllium Sheet	2-70

Figure		Page
2-58	Effect of Temperature on Compressive Modulus of Elasticity of Hot-Upset Beryllium Sheet	2-71
2-59	Tensile Stress-Strain Curves for Hot-Upset Beryllium Sheet	2-72
2-60	Compressive Stress-Strain Curves for Hot-Upset Beryllium Sheet	2-73
2-61	Bending and Axial S-N Curves for Hot-Upset Beryllium Sheet at Room Temperature	2-74
2-62	Axial S-N Curves for Extruded Beryllium at Room Temperature	2-76
2-63	Axial S-N Curves for Extruded Beryllium at 1100°F (1)	2-77
2-64	Axial S-N Curves for Extruded Beryllium at 1100°F (2)	2-78
2-65	Stress-Rupture Curve for Extruded Beryllium at 1100°F	2-79
2-66	Notch Sensitivity of QMV Hot-Pressed Beryllium Block (1.55% BeO Content)	2-82
2-67	Notch Sensitivity of Cross-Rolled Beryllium Sheet (1.75% BeO Content)	2-83
2-68	Unnotched Ultimate Tensile Strength of Beryllium	2-84
2-69	Notch Specimen Geometry	2-85
2-70	Space Lattice of Beryllium	2-90
2-71	Composite Biaxial Yield and Fracture Criteria for Hot-Pressed Beryllium Block at Low Temperatures	2-94
2-72	High-Temperature Yield and Fracture Criteria	2-95
2-73	Intercrystalline Yield and Fracture Criteria	2-96
2-74	Yield Stress Versus Strain Rate of QMV-S-Y6826 Beryllium (2% BeO)	2-97
2-75	Modified Yield Criteria for Unequal Tensile and Compressive Yield Strengths	2-98
2-76	Biaxial Strength Criteria for Beryllium Block at Room Temperature	2-100
2-77	Biaxial Strength Criteria for Beryllium Block at 800°F	2-101
2-78	Biaxial Strength Criteria for Beryllium Block at 1000°F	2-102
2-79	Modified Maximum Shear-Stress Fracture Criterion for Beryllium Sheet	2-105
2-80	Modified Shear-Strain Energy Yield Criterion for Beryllium Sheet	2-106

Figure		Page
2-81	Yield and Fracture Criteria for Beryllium Having Preferred Grain Orientation With Basal Planes Parallel to σ_1 , σ_2 Plane	2-106
2-82	Wide-Sheet Bend Test Results for Cross-Rolled Beryllium Sheet at Room Temperature	2-108
2-83	Wide-Sheet Bend Test Results for Cross-Rolled Beryllium Sheet at 400°F	2-109
2-84	Wide-Sheet Bend Test Results for Cross-Rolled Beryllium Sheet at 600°F	2-110
3-1a	Typical Tensile Stress-Strain Curves for Beryllium Block Material (1.75% BeO Content)	3-3
3-1b	Typical Compressive Stress-Strain Curves for Beryllium Block Material (1.75% BeO Content)	3-4
3-2	Example Compressive Stress-Strain Curves for As-Received Beryllium Cross-Rolled Sheet (1.75% BeO Content)	3-5
3-3	Comparison of Typical Tensile and Compressive Stress-Strain Curves at Room Temperature for Beryllium As-Received Cross-Rolled Sheet	3-6
3-4	A Comparison of Typical Room-Temperature Compressive Stress-Strain Curves for Beryllium Cross-Rolled Sheet on the Basis of Grain Direction	3-7
3-5	Room-Temperature Plasticity Reduction Factors for As-Received Beryllium Cross-Rolled Sheet (1.75% BeO Content)	3-9
3-6	Plasticity Reduction Factors at 800°F for As-Received Beryllium Cross-Rolled Sheet (1.75% BeO Content)	3-10
3-7	Example Compression Buckling Curves at Room Temperature and 800°F for As-Received Beryllium Cross-Rolled Sheet (1.75% BeO Content)	3-13
3-8	Comparison of Various Post-Buckling Design Curves for Compression Panels With Beryllium Cross-Rolled Sheet Test Data	3-16
3-9	Example Shear Buckling Curves at Room Temperature and 800°F for As-Received Beryllium Cross-Rolled Sheet (1.75% BeO Content)	3-19
3-10	Example Post-Buckling Design Curves at Room Temperature and 800°F for Flat Shear Panels Fabricated From Beryllium Cross-Rolled Sheet	3-22
3-11a	Example Column Buckling Curves at Room Temperature and 800°F for As-Received Beryllium Cross-Rolled Sheet (1.75% BeO Content)	3-26

Figure		Page
3-11b	Typical Column Buckling Curves at Various Temperatures for Beryllium Block Material (1.75% BeO Content)	3-27
3-12	Buckling Coefficients for Long Monocoque Cylinders Subjected to a Uniform Axial Load	3-30
3-13	Example Buckling Curves at Room Temperature and 800°F for Long, Axially Loaded Monocoque Cylinders Fabricated From As-Received Beryllium Cross-Rolled Sheet (1.75% BeO Content)	3-31
3-14	Buckling Exponents for Short Monocoque Cylinders Subjected to a Uniform Axial Load	3-33
3-15a	Example Room-Temperature Buckling Curves for Short, Axially Loaded Monocoque Cylinders Fabricated From As-Received Beryllium Cross-Rolled Sheet (1.75% BeO Content)	3-34
3-15b	Example Buckling Curves at 800°F for Short, Axially Loaded Monocoque Cylinders Fabricated From As-Received Beryllium Cross-Rolled Sheet (1.75% BeO Content)	3-35
3-16	Example Buckling Curves at Room Temperature and 800°F for Long Monocoque Cylinders in Torsion Fabricated From As-Received Beryllium Cross-Rolled Sheet (1.75% BeO Content)	3-41
3-17	Design Chart for Monocoque Circular Cylinders Subjected to Uniform External Lateral or Hydrostatic Pressure	3-44
3-18a	Example Room-Temperature Crippling Curves for Beryllium Cross-Rolled Sheet (1.75% BeO Content)	3-48
3-18b	Example Crippling Curves at 800°F for Beryllium Cross-Rolled Sheet (1.75% BeO Content)	3-49
3-19a	Typical Crippling Curves at Room Temperature for Beryllium Block Material (1.75% BeO Content)	3-50
3-19b	Typical Crippling Curves at 400°F for Beryllium Block Material (1.75% BeO Content)	3-51
3-19c	Typical Crippling Curves at 800°F for Beryllium Block Material (1.75% BeO Content)	3-52
3-19d	Typical Crippling Curves at 1100°F for Beryllium Block Material (1.75% BeO Content)	3-53
3-20	Bending Modulus Curves for Beryllium Block at Room Temperature	3-55
3-21	Bending Modulus Curves for Beryllium QMV Block at 500°F	3-56
3-22	Bending Modulus Curves for Beryllium QMV Block at 800°F	3-57

Figure		Page
3-23	Bending Modulus Curves for Beryllium QMV Block at 1100° F	3-58
3-24	Effect of Temperature on 0.150 Thick Hot-Pressed Beryllium Block Double-Row Butt Joints Fastened With F200 and F260 Jo-Bolts	3-61
3-25	Effect of Temperature on 0.250 Thick Hot-Pressed Beryllium Block Double-Row Butt Joints Fastened With F200 and F260 Jo-Bolts	3-62
3-26	Effect of Temperature on 0.375 Thick Hot-Pressed Beryllium Block Double-Row Butt Joints Fastened With F200 and F260 Jo-Bolts	3-63
3-27	Effect of Temperature on 0.150 Thick Hot-Pressed Beryllium Block Single-Row Butt Joints Fastened With F200 and F260 Jo-Bolts	3-64
3-28	Effect of Temperature on 0.250 Thick Hot-Pressed Beryllium Block Single-Row Butt Joints Fastened With F200 and F260 Jo-Bolts	3-65
3-29	Effect of Temperature on 0.375 Thick Hot-Pressed Beryllium Block Single-Row Butt Joints Fastened With F200 and F260 Jo-Bolts	3-66
3-30	Effect of Temperature on 0.150 Thick Hot-Pressed Beryllium Block Double Row Butt Joints Fastened With NAS-560 HK Screws	3-67
3-31	Effect of Temperature on 0.250 Thick Hot-Pressed Beryllium Block Double-Row Butt Joints Fastened With NAS-560 HK Screws	3-68
3-32	Effect of Temperature on 0.375 Thick Hot-Pressed Beryllium Block Double-Row Butt Joints Fastened With NAS-560 HK Screws	3-69
3-33	Effect of Temperature on 0.150 Thick Hot-Pressed Beryllium Block Single-Row Butt Joints Fastened With NAS-560 HK Screws	3-70
3-34	Effect of Temperature on 0.250 Thick Hot-Pressed Beryllium Block Single-Row Butt Joints Fastened With NAS-560 HK Screws	3-71
3-35	Effect of Temperature on 0.375 Thick Hot-Pressed Beryllium Block Single-Row Butt Joints Fastened With NAS-560 HK Screws	3-72
3-36	Effect of Temperature on 0.150 Thick Hot-Pressed Beryllium Block Double-Row Butt Joints Fastened With NAS-517 Screws	3-74
3-37	Effect of Temperature on 0.250 Thick Hot-Pressed Beryllium Block Double-Row Butt Joints Fastened With NAS-517 Screws	3-75
3-38	Effect of Temperature on 0.150 Thick Hot-Pressed Beryllium Block Single-Row Butt Joints Fastened With NAS-517 Screws	3-76
3-39	Effect of Temperature on 0.250 Thick Hot-Pressed Beryllium Block Single-Row Butt Joints Fastened With NAS-517 Screws	3-77
3-40	Effect of Temperature on 0.250 Thick Hot-Pressed Beryllium Block Double-Row Butt Joints Fastened With SAL-100 Huckbolts	3-78
3-41	Effect of Temperature on 0.250 Thick Hot-Pressed Beryllium Block Single-Row Butt Joints Fastened With SAL-100 Huckbolts	3-79

Figure		Page
3-42	Effect of Temperature on 0.250 Thick Cross-Rolled Beryllium Sheet Butt Joints Fastened With 100-deg Head, Hollowend A-286 Rivets	3-80
3-43	Effect of Temperature on 0.133 Thick Cross-Rolled Beryllium Sheet Butt Joints Fastened With 100-deg Head, Hollowend A-286 Rivets	3-81
3-44	Geometry of Hollowend Rivets	3-82
3-45	Effect of Temperature and Edge Distance on 0.082-in., Cross-Rolled Beryllium Sheet Butt Joints Using 3/16-in., SAL-100 Huckbolts	3-84
3-46	Effect of Temperature and Edge Distance on 0.120-in., Hot-Pressed Beryllium Block Butt Joints Using 1/4-in., SAL-100 Huckbolts	3-86
3-47a	Beryllium Cross-Rolled Sheet to Beryllium Cross-Rolled Sheet Joint in a Truss-Core Sandwich Furnace-Brazed Specimen, Using 50 Ag-15.5 Cu-15.5 Zn-16.0 Cd-3.0 Ni Brazing Alloy. Magnified 60x, Unetched	3-92
3-47b	Beryllium Cross-Rolled Sheet to Beryllium Cross-Rolled Sheet Joint in a Truss-Core Sandwich Furnace-Brazed Specimen, Using 50 Ag-15.5 Cu-15.5 Zn-16.0 Cd-3.0 Ni Brazing Alloy. Magnified 240x, Unetched	3-93
3-48a	Beryllium Cross-Rolled Sheet to Titanium Core Joint in a Truss-Core Sandwich Furnace-Brazed Specimen, Using 50 Ag-15.5 Cu-15.5 Zn-16.0 Cd-3.0 Ni Brazing Alloy. Magnified 125x, Unetched	3-94
3-48b	Beryllium Cross-Rolled Sheet to Titanium Core Joint in a Truss-Core Sandwich Furnace-Brazed Specimen, Using 50 Ag-15.5 Cu-15.5 Zn-16.0 Cd-3.0 Ni Brazing Alloy. Magnified 500x, Unetched. This joint is adjacent to the joint shown in Fig. 3-48a	3-95
4-1	Cross-Sectional Geometry of an Unflanged, Integrally Stiffened Wide Column	4-6
4-2	Efficiency Chart for Unflanged, Integrally Stiffened Wide Columns	4-8
4-3	Cross-Sectional Geometry of Zee-Stiffened Wide Column	4-10
4-4	Efficiency Chart for Zee-Stiffened Wide Columns	4-11
4-5	Cross-Sectional Geometry of Truss-Core Sandwich Wide Column	4-12
4-6	Local Buckling Coefficients for Single-Truss-Core Sandwich and Semisandwich Plates Under Uniaxial Compression in the Direction of the Corrugations	4-14
4-7	Efficiency Chart for Truss-Core Sandwich Wide Columns	4-16

Figure		Page
4-8	Comparison of the Minimum-Weight Envelopes of Several Types of Stiffened, Wide-Column Construction When Subjected to a Compression Load in the Direction of the Stiffening Elements	4-18
4-9a	Efficiency Chart for Unflanged, Integrally Stiffened Flat Panels in Compression, Stiffeners Parallel to Load	4-21
4-9b	Efficiency Chart for Unflanged, Integrally Stiffened Flat Panels in Compression, Stiffeners Parallel to Load (Continuation of Fig. 4-9a)	4-22
4-10	Auxiliary Design Chart for Unflanged, Integrally Stiffened Flat Panels in Compression	4-23
4-11a	Efficiency Chart for Zee-Stiffened Flat Panels in Compression, Stiffeners Parallel to Load	4-26
4-11b	Efficiency Chart for Zee-Stiffened Flat Panels in Compression, Stiffeners Parallel to Load (Continuation of Fig. 4-11a)	4-27
4-12	Auxiliary Design Chart for Zee-Stiffened Flat Panels in Compression	4-28
4-13	Efficiency Chart for Truss-Core Sandwich Panels in Compression, Corrugations Parallel to Load	4-32
4-14	Efficiency Chart for Truss-Core Semisandwich Panels in Compression, Corrugations Parallel to Load	4-35
4-15	Comparison of the Minimum-Weight Envelopes of the Several Types of Stiffened Panel Construction When Subjected to a Compression Load in the Direction of the Stiffening Elements	4-37
4-16	Efficiency Chart for Truss-Core Sandwich Shear Panels	4-41
4-17	Comparison Between Minimum-Weight Truss-Core Sandwich Shear Panel and a Flat Unstiffened Panel	4-43
4-18	Schematic of Multiweb Box Beam in Bending	4-44
4-19	Values of A as a Function of m, n	4-50
4-20	Comparison of the Elastic Minimum-Solidity Equations for Several Multiweb Box Beams Composed of Different Combinations of Cover Plate and Web Construction (Two Combinations of Instability Modes Investigated)	4-51
4-21	Geometry of Truss-Core Sandwich Cylinder	4-56
4-22	Efficiency Factors for Truss-Core Sandwich Cylinders Under Uniform Axial Compression	4-59

Figure		Page
4-23	Comparative Efficiencies of Monocoque and Optimum Truss-Core Sandwich, Long Cylinders Subjected to Uniform Axial Compression	4-61
4-24	Efficiency Chart for Moderate-Length, Truss-Core Sandwich Cylinders Subjected to Torsion, $(L/R)^2 R/h > 35$; $(L/R)^2 h/R < 30$	4-65
4-25	Efficiency Chart for Long Truss-Core Sandwich Cylinders Subjected to Torsion, $(L/R)^2 h/R > 30$	4-67
4-26	Comparative Efficiencies of Monocoque and Optimum Truss-Core Sandwich Simply Supported Circular Cylinders of Moderate Length in Torsion, $L/R = 1$	4-69
4-27	Optimum Values of Truss Angle θ Versus p_{cr}/E and L/R for Moderate-Length, Truss-Core Sandwich Cylinders Subjected to a Uniform External Hydrostatic Pressure	4-74
4-28	Minimum Values of \bar{t}/R Versus p_{cr}/E and L/R for Truss-Core Sandwich Cylinders Subjected to a Uniform External Hydrostatic Pressure	4-75
4-29	Optimum Values of t_f/b_f for Truss-Core Sandwich Cylinders Subjected to a Uniform External Hydrostatic Pressure	4-76
4-30	Optimum Values of b_f/R for Truss-Core Sandwich Cylinders Subjected to a Uniform External Hydrostatic Pressure	4-77
4-31	Optimum Values of t_c/t_f for Truss-Core Sandwich Cylinders Subjected to a Uniform External Hydrostatic Pressure	4-78
4-32	Optimum Values of θ for Long Truss-Core Sandwich Cylinders Subjected to a Uniform External Hydrostatic Pressure	4-81
4-33	Cross Section Taken Longitudinally Through a Ring-Stiffened Cylinder	4-84
4-34	Optimum Design Chart (When n Is Specified) for Ring-Stiffened Cylinders Subjected to a Uniform External Hydrostatic Pressure, $L/R = 0.5$	4-87
4-35	Optimum Design Chart (When n Is Specified) for Ring-Stiffened Cylinders Subjected to a Uniform External Hydrostatic Pressure, $L/R = 1.0$	4-88
4-36	Optimum Design Chart (When n Is Specified) for Ring-Stiffened Cylinders Subjected to a Uniform External Hydrostatic Pressure, $L/R = 2.0$	4-89
4-37	Optimum Design chart (When n Is Specified) for Ring-Stiffened Cylinders Subjected to a Uniform External Hydrostatic Pressure, $L/R = 4.0$	4-90

Figure		Page
4-38	A Comparison Between Minimum-Weight Stiffened Cylinders Loaded Elastically in Hydrostatic Compression	4-94
4-39	Room-Temperature, Minimum-Weight Design Chart for Cross-Rolled Beryllium Sheet Wide Columns	4-96
4-40	800° F, Minimum-Weight Design Chart for Cross-Rolled Beryllium Sheet Wide Columns	4-98
4-41	Room-Temperature, Minimum-Weight Design Chart for Cross-Rolled Beryllium Sheet Compression Panels	4-99
4-42	800° F, Minimum-Weight Design Chart for Cross-Rolled Beryllium Sheet Compression Panels	4-100
4-43	Minimum-Weight Design Chart for Cross-Rolled Beryllium Sheet Shear Panels at Room Temperature and 800° F	4-101
4-44	Design Chart for Minimum-Weight Beryllium Cross-Rolled Sheet Multiweb Box Beams Loaded Elastically in Bending at Room Temperature	4-102
4-45	Design Chart for Minimum-Weight Beryllium Cross-Rolled Sheet Multiweb Box Beams Loaded Elastically in Bending at 800° F	4-103
4-46	Room Temperature, Minimum-Weight Design Chart for Beryllium Cross-Rolled Sheet Long Cylinders Subjected to a Uniform Axial Load	4-104
4-47	800° F, Minimum-Weight Design Chart for Beryllium Cross-Rolled Sheet Long Cylinders Subjected to a Uniform Axial Load	4-105
4-48	Minimum-Weight Design Chart for Cross-Rolled Beryllium Sheet Moderate-Length Cylinders in Torsion at Room Temperature and 800° F	4-106
4-49	Design Chart for Minimum-Weight Beryllium Cross-Rolled Sheet Cylinders Loaded Elastically in Hydrostatic Compression at Room Temperature and 800° F	4-107
4-50	Weight-Load Comparison at Room Temperature of Structural Materials Used in Monocoque Cylinders Elastically Loaded in Axial Compression	4-111
4-51	Weight-Load Comparison at 250° F of Structural Materials Used in Monocoque Cylinders Elastically Loaded in Axial Compression	4-112
4-52	Weight-Load Comparison at 500° F of Structural Materials Used in Monocoque Cylinders Elastically Loaded in Axial Compression	4-113
4-53	Weight-Load Comparison at 700° F of Structural Materials Used in Monocoque Cylinders Elastically Loaded in Axial Compression	4-114

Figure		Page
4-54	Weight-Load Comparison at 1000° F of Structural Materials Used in Monocoque Cylinders	4-115
4-55	Weight-Load Comparison at 1250° F of Structural Materials Used in Monocoque Cylinders Elastically Loaded in Axial Compression	4-116
4-56	Beryllium-Based Weight Ratios for Elastically Loaded Structures of Optimum Proportions Having a Minimum-Weight Equation Exponent of 2.54	4-117
4-57	Beryllium-Based Weight Ratios for Elastically Loaded Structures of Optimum Proportions Having a Minimum-Weight Equation Exponent of 3.0	4-120
4-58	Beryllium-Based Weight Ratios for Elastically Loaded Structures of Optimum Proportions Having a Minimum-Weight Equation Exponent of 2.36	4-121
4-59	Beryllium-Based Weight Ratios for Elastically Loaded Structures of Optimum Proportions Having a Minimum-Weight Equation Exponent of 2.25	4-122
4-60	Beryllium-Based Weight Ratios for Elastically Loaded Structures of Optimum Proportions Having a Minimum-Weight Equation Exponent of 2.0	4-123
4-61	Beryllium-Based Weight Ratios for Elastically Loaded Structures of Optimum Proportions Having a Minimum-Weight Equation Exponent of 1.858	4-124
4-62	Beryllium-Based Weight Ratios for Elastically Loaded Structures of Optimum Proportions Having a Minimum-Weight Equation Exponent of 1.77	4-125
4-63	Beryllium-Based Weight Ratios for Elastically Loaded Structures of Optimum Proportions Having a Minimum-Weight Equation Exponent of 1.667	4-126
4-64	Weight-Load Comparison at Room Temperature of Structural Material Used in Flat, Unstiffened Compression Panels	4-128
4-65	Weight-Load Comparison at 800°F of Structural Materials Used in Flat, Unstiffened Compression Panels	4-129
4-66	Weight-Load Comparison at Room Temperature of Structural Materials Used in Truss-Core Sandwich Compression Panels of Optimum Proportions	4-130
4-67	Weight-Load Comparison at 800°F of Structural Materials Used in Truss-Core Sandwich Compression Panels of Optimum Proportions	4-131

Figure		Page
4-68	Weight-Load Comparison at Room Temperature of Structural Materials Used in Zee-Stiffened Compression Panels of Optimum Proportions	4-132
4-69	Weight-Load Comparison at 800°F of Structural Materials Used in Zee-Stiffened Compression Panels of Optimum Proportions	4-133
5-1	Lathe Tool Geometry, Brazed Carbide	5-9
A-1	Universal Testing Machine, 50,000 lb	A-3
A-2	Cracking at a Resistance-Welded Thermocouple After Test	A-11
A-3	Geometry of Compression-Panel Tests	A-15
A-4	Detail of Knife-Edge Restraints	A-15
A-5	Compression-Panel Test Fixture	A-16
A-6	Specimen 1 Load Versus Strain Gages 3 and 4	A-24
A-7	Specimen 1 Load Versus Strain Averages of Gages 1 and 2, 3 and 4, and 5 and 6	A-25
A-8	Specimen 2 Load Versus Strain for Gages 3 and 4	A-26
A-9	Specimen 2 Load Versus Strain Averages of Gages 1 and 2, 3 and 4, and 5 and 6	A-27
A-10	Specimen 3 Load Versus Strain Gages 3 and 4	A-28
A-11	Specimen 3 Load Versus Strain Averages of Gages 1 and 2, 3 and 4, and 5 and 6	A-29
A-12	Specimen 4 Load Versus Strain Gages 7 and 8	A-30
A-13	Specimen 5 Load Versus Strain Gages 7 and 8	A-31
A-14	Thermocouple Locations on Compression-Panel Tests	A-32
A-15	Compression-Panel Test Fixture With Heat Lamps Installed	A-34
A-16	Room-Temperature Compression Panels After Test	A-36
A-17	Elevated-Temperature Compression Panels After Test	A-37
A-18	Shear Panel and Test Frame	A-40
A-19	Square Panel and Method of Loading	A-41
A-20	Shear Panel Specimen 6 After Test	A-42
A-21	Shear Panel Specimen 7 After Test	A-43
A-22	Shear Panel Specimen 6 Load Versus Elongation	A-45

Figure		Page
A-23	Load Elongation Curve, Shear Panel Specimen 7	A-46
A-24	Shear Panel Specimen 8 Load Versus Elongation	A-47
A-25	Load Elongation Curves, Shear Panel Specimen 9	A-48
A-26	Shear Panel Specimen 10 Load Versus Elongation	A-49
A-27	Shear Panel Specimen 8 After Test	A-50
A-28	Shear Panel Test With Heat Lamps Installed	A-52
A-29	Shear Panel Specimen 10 With Heat Shield	A-53
A-30	Average Temperatures (°F) at Midtest, Specimen 9	A-54
A-31	Average Temperatures (°F) at Midtest, Specimen 10	A-55
A-32	Shear Panel Specimen 10 After Test	A-57
A-33	Shear Panel Specimen 9 After Test	A-58
A-34	Cylinder-Loading Fixture and Specimen 14 After Test	A-61
A-35	Strain-Gage Locations, Specimen 11	A-63
A-36	Strain-Gage Locations, Specimen 14	A-63
A-37	Specimen 13 Strain Gages, Thermocouples, and Temperatures Recorded	A-64
A-38	Specimen 12 Strain-Gage and Thermocouple Locations; Temperatures Recorded	A-65
A-39	Strain-Gage and Thermocouple Locations, Specimen 15	A-66
A-40	Furnace for Cylinder Tests - Plan View	A-72
A-41	Specimens 11 (Right) and 12 (Left) After Test	A-74
A-42	Specimen 13 After Test	A-75
A-43	Specimen 15 After Test	A-76
A-44	Evacuated Cylinder (Specimen 16) After Test	A-78
B-1	General Arrangement of Biaxial Stress Test for Elevated-Temperature Testing	B-3
B-2	Details of Arrangement of Biaxial Stress Test Jig and Beam Deflectometer	B-4
B-3	Schematic of Specimen Load Jig Used for Biaxial Stress Tests	B-5
B-4	Biaxial Stress by Beam Bending of Cross-Rolled Beryllium Sheet at Room Temperature, 400°F, and 600°F	B-7

Figure		Page
B-5	Surface Strains Due to Biaxial Stress of Cross-Rolled Beryllium Sheet at Room Temperature	B-13
B-6	Beam Deflection for Biaxial Stress of Cross-Rolled Beryllium Sheet at Room Temperature	B-14
B-7	Surface Strains Due to Biaxial Stress of Cross-Rolled Beryllium Sheet at 400° F	B-16
B-8	Beam Deflection for Biaxial Stress of Cross-Rolled Beryllium Sheet at 400° F	B-17
C-1	Beryllium Truss-Core Sandwich (After Test)	C-2
C-2	Beryllium Facings on Titanium-Core Honeycomb Sandwich (After Test)	C-2
C-3	Cross Sections of Sandwiches	C-4
C-4	Tooling for Assuring That Panels Are Perpendicular to Bearing Plates	C-8
C-5	Failure of Truss-Core Sandwich Under Bending Loads	C-9
C-6	Beam Loading of Honeycomb Sandwich	C-10

TABLES

Table		Page
2-1	A Summary of Beryllium Physical Properties at Room Temperature	2-3
2-2	Typical Design Mechanical Properties of Beryllium	2-17
2-3	Ultimate Strength of Notched Beryllium Specimens	2-81
3-1	Summary of Pertinent Data and Test Results for Axially Loaded Monocoque Cylinders Fabricated From Beryllium Cross-Rolled Sheet	3-36
4-1	Minimum-Weight Efficiency Factors and Exponents for Wide Columns and Compression Panels	4-52
4-2	Maximum Values of t_w/b_w for Near-Optimum Design of Ring-Stiffened Cylinders Under Hydrostatic Pressure	4-91
4-3	Summary of Beryllium Ring-Stiffened Cylinder Tests From Ref. 4-14	4-92
4-4	Summary of Minimum-Weight Equation Exponents	4-119
5-1	Lathe Tool Geometry, Brazed Carbide	5-10
A-1	Summary of Compression Panel Tests	A-17
A-2	Specimen No. 1 Strain-Gage Readings at Various Loads	A-19
A-3	Specimen No. 2 Strain-Gage Readings at Various Loads	A-20
A-4	Specimen No. 3 Strain-Gage Readings at Various Loads	A-21
A-5	Specimen No. 4 Strain-Gage Readings at Various Loads	A-22
A-6	Specimen No. 5 Strain-Gage Readings at Various Loads	A-23
A-7	Specimen No. 4 Test Temperatures	A-33
A-8	Specimen No. 5 Test Temperatures	A-33
A-9	Shear Panel Tests: Basic Information	A-39
A-10	Axially Loaded Cylinders: Summary of Test Information	A-60
A-11	Specimen No. 11 Strain-Gage Readings at Various Loads	A-67
A-12	Specimen No. 12 Strain-Gage Readings at Various Loads	A-68
A-13	Specimen No. 13 Strain-Gage Readings at Various Loads	A-69

Table		Page
A-14	Specimen No. 14 Strain-Gage Readings at Various Loads	A-70
A-15	Specimen No. 15 Strain -Gage Readings at Various Loads	A-71
B-1	Strain and Deflection for Beryllium Biaxial Stress Tests	B-11

NOMENCLATURE

A	cross-sectional area; stress ratio, equal to alternating stress minus mean stress
a	length of a panel element
b	width of an element; width of a stiffened panel; the short dimension of a panel in shear; the length of the loaded edge of a panel in uniaxial compression
b_c	width of sandwich core element
b_f	width of sandwich or semisandwich facing sheet element; width of stiffener flange element
b_s	width of sheet element between ζ - ζ stiffeners
b_w	height of stiffener web element
C	circumference; a constant; compressive buckling coefficient for long cylinders; specific heat
c	restraint coefficient
D	diameter
D_f	flexural stiffness of sheet per unit width, $\frac{Et_s^3}{12(1 - \mu^2)}$
D_x	flexural stiffness of sandwich per unit width in x-direction, $D_x = (EI)_x$
D_{Q_x}	transverse shearing stiffness of sandwich on planes perpendicular to x-direction, per unit width
D_y	flexural stiffness of sandwich per unit width in y-direction, $D_y = (EI)_y$

D_{xy}	twisting stiffness of sandwich per unit width
d	depth of box beam, measured between centroids of the box-beam covers
E	Young's modulus; modulus of elasticity in tension, average ratio of stress to strain for stress below the proportional limit
E_c	modulus of elasticity in compression, average ratio of stress to strain for stress below the proportional limit
E_T	tangent modulus, local slope of the stress-strain curve
ϵ	efficiency factor
e	elongation in percent, a measure of the ductility of a material and based on a tension test; unit deformation or strain; the minimum distance from a hole ϕ to the edge of the sheet
F	allowable stress
F_b	allowable bending stress, modulus of rupture in bending
F_{bru}	ultimate bearing stress
F_{bry}	yield bearing stress
F_c	allowable compressive stress; column failing stress
F_{cc}	allowable crippling stress
$F_{c_{cr}}$	critical (or allowable) compressive stress in plates or panels
F_{cy}	compressive yield stress at which permanent strain equals 0.002 in./in.
F_s	allowable shearing stress
$F_{s_{cr}}$	critical (or allowable) shear stress in plates or panels
F_{su}	ultimate stress in pure shear (this value represents the average shearing stress over the cross section)
F_{tu}	ultimate tensile stress

F_{ty}	tensile yield stress at which permanent strain equals 0.002 in./in.
$F_{W_{cr}}$	critical (or allowable) compressive stress precipitating a wrinkling mode of instability
f_c	calculated compressive stress
f_s	calculated shearing stress
G	modulus of shearing rigidity
h	thickness of sandwich
I	bending moment of inertia of stiffener cross section taken about the stiffener centroidal axis
K	a constant, generally empirical; thermal conductivity; diagonal tension factor
K_F	buckling coefficient for compressive local buckling of a stiffener flange element
K_G	buckling coefficient for compressive general buckling of a stiffened panel
K_S	buckling coefficient for compressive local buckling of a sheet element of width b_s ; buckling coefficient for local shear buckling of an element
K_t	theoretical stress concentration factor for normal stress
K_W	buckling coefficient for compressive local buckling of a stiffener web element
K_X	buckling coefficient for compressive local buckling of truss-core sandwich or semisandwich
L	longitudinal (grain direction); length; length of cylinder
ℓ	length of a column, or wide column
M	applied moment or couple, usually a bending moment
M_a	allowable bending moment
M_i	bending moment per unit length of chord in multiweb box beams

m	reciprocal of the slope of the straight-line portion of a minimum-weight envelope when plotted on log-log paper
N	number of bays in a conventionally stiffened panel; number of cycles to failure in a fatigue test
N_x	compressive loading on an unstiffened or stiffened component in the direction of the stiffening elements, per unit width
N_{xy}	shear loading on an unstiffened or stiffened component in xy-plane, per unit width
n	number of rings in a ring-stiffened cylinder subjected to hydrostatic pressure; sometimes used interchangeably with small m defined above
P	applied load (total, not unit load)
p_{cr}	hydrostatic buckling pressure per unit area
q	shear flow
R	stress ratio, equal to minimum stress divided by maximum stress; radius
T	transverse (grain direction)
t	thickness of a flat, unstiffened plate
\bar{t}	equivalent flat-plate thickness of a stiffened component for weight purposes
t_c	thickness of core material in sandwich or semisandwich panels
t_f	thickness of facing sheet in sandwich or semisandwich panels; thickness of stiffener flange element
t_s	thickness of sheet or skin element between $\bar{C} - \bar{C}$ stiffeners
t_w	thickness of stiffener web element
W	weight of component per unit length
Z	nondimensional geometry parameter
Z_{nq}	a constant used in the general instability analysis of stiffened panels having either one or two stiffeners

\bar{z} distance from midsurface of skin to stiffener centroidal axis

Greek Symbols

α angle of diagonal tension; coefficient of thermal expansion; notch angle

η plasticity reduction factor

$\bar{\eta}$ effective plasticity reduction factor

η_G plasticity reduction factor for general instability

η_L plasticity reduction factor for local instability

η_T ratio of tangent modulus E_T to Young's modulus

θ angle between facing and core elements in truss-core sandwich and semi-sandwich panels

μ Poisson's ratio

ρ radius of gyration; density

σ used interchangeably with f_c ; stress

Σ solidity, fraction of the total enclosed area of cross section occupied by compression structure

τ used interchangeably with f_s

Subscripts

a allowable

avg average

b bending

br	bearing
c	compression; core
cc	crippling
cr	critical
e	Euler; endurance
f	facing; flange; fixed
G	general instability
L	local instability
max	maximum
min	minimum
net	based on net section
nom	nominal
o	outside; original; static;
opt	optimum value
p	compression cover
s	sheet or skin; shear
T	tangent; temperature
t	theoretical, tensile
u	ultimate
W	wrinkling
w	web
x	x-direction
y	yield, y-direction
1	direction of principal stress
2	direction of principal stress

Section 1

INTRODUCTION

All new metals which are proposed for structural applications must undergo a many-sided, detailed investigation before general acceptance by the aerospace industry. Mill products having standard quality and properties must be made available at a cost justifying use. Designers must be aware that either conventional methods of structural analysis are applicable or that new methods must be developed; and the fabricator must be able to turn out a quality component or part. Many members of the technical community have not been confident that beryllium has successfully attained these goals. This report, in summarizing past work and the results of the present program, shows clearly that beryllium can meet most of these requirements and is ready for acceptance as a structural material by industry.

Beryllium structural design information is presented in detail in this report. Physical and mechanical properties appear in Section 2. Section 3 gives data for designing beryllium structural components. Minimum-weight design information, together with efficiency comparisons of beryllium and other structural materials, is presented in Section 4. These sections are supplemented by a brief summary of beryllium fabrication state-of-the-art, presented in Section 5. Significant conclusions reached as a result of this program, recommendations for future work in areas as yet not clearly defined, and applications for structures appear in Section 6.

Each section in this report is presented in a manner to facilitate the use of information in the design of beryllium hardware. Sections 2 and 3 are principally of interest to the stress analyst, while Section 4 is intended for use in preliminary design. These sections logically develop a philosophy of beryllium design. In Section 2, the high modulus of elasticity, and high strength-to-weight ratio of beryllium are documented. These and other properties are used to develop component design charts in Section 3, many

Manuscript released by authors on 1 February 1962 for publication as an ASD Technical Report.

of which are substantiated by tests conducted under this program. Section 4 subsequently indicates the extent of possible weight savings by designing efficiently with beryllium. The impetus for preparing Section 4 arises from the fact that the highest structural efficiency is not obtained just by using beryllium; it is obtained by designing beryllium into the most efficient configuration for the particular structural application. If properties of beryllium are exploited without due consideration to design configuration, then other materials, designed into a more efficient configuration, may prove superior to beryllium when all design factors are evaluated, including cost. The designer is encouraged, therefore, to obtain maximum structural efficiency from beryllium wherever it is specified in design, particularly in view of its high cost per pound in comparison to other structural materials.

The types of tests conducted under this program and reported on herein are:

- Compression-panel tests
- Shear-panel tests
- Tests of cylinders in axial compression
- Tests of externally pressurized cylinders
- Notch-sensitivity tests
- Biaxiality tests

The panel and cylinder test results were generally predictable with good accuracy using conventional methods of structural analysis, and are discussed in Section 3. Tests were conducted at room temperature and at 800° F. In general, beryllium exhibits a catastrophic post-buckling failure mechanism at room temperature which should be recognized in design with appropriate margins of safety, the exact margin depending on the intended function of the component. This failure mechanism at room temperature is primarily caused by brittleness resulting from biaxial stress states developed in bending. The panel test components discussed in Section 3 developed considerable post-buckling strength at room temperature before failure, while the cylindrical test components developed little or no post-buckling strength.

At 800°F, beryllium used in panels and cylinders has post-buckling characteristics which are similar to those of the more common structural materials (such as steel or aluminum) when used in these applications. The actual temperature at which this change in the characteristics of beryllium takes place is below 800°F, and felt to be about 450°F. The notch-sensitivity test results are discussed in detail in Section 2. While beryllium is notch sensitive at room temperature, it is no more so than high-strength alloys of commonly used structural materials, such as steel. These alloys, like beryllium, require careful attention to the notch-sensitivity problem.

The biaxiality tests are also discussed in detail in Section 2, where the high biaxial strength of beryllium sheet as found in the tests is reported. Details of the experimental investigations of the panels and cylinders are described in Appendix A. Similar details for the biaxial strength tests are reported in Appendix B.

The results of several diversified studies conducted under this program are presented in the various sections of this report. Most of the information in Section 2 is derived from a survey of the literature and the substantial data in this field developed by Lockheed Missiles and Space Company. The information presented in Section 2 comprises selected data which is representative of currently available beryllium products. The minimum-weight analyses referenced in Section 4 are also the result of studies carried out in part under this program. Further studies, based on these minimum-weight analyses, were made to determine quantitatively the minimum weights attainable in beryllium and various other structural materials when used in various component-loading applications. These results are also shown in Section 4.

Section 2 presents physical and mechanical properties for the commercial beryllium products currently available, namely, QMV hot-pressed block, cross-rolled sheet, hot-upset sheet, and extrusion. However, in those portions of Section 3 dealing primarily with sheet products, the curves apply to cross-rolled sheet in preference to the hot-upset sheet. This decision was based largely on the greater amount of mechanical property data available on cross-rolled sheet, as well as the better commercial availability of this product to the user. For these same reasons, those

minimum-weight design curves appearing in Section 4 which apply to beryllium represent cross-rolled beryllium sheet only. Note, however, that sufficient information is given in Sections 3 and 4 to permit the individual to construct similar figures for other beryllium products.

Beryllium sandwiches were fabricated and tested late in this program. This work is reported in Appendix C.

In summary, the information in this report illustrates that beryllium may be designed into structural components with confidence provided that careful attention is given to the unusual failure mechanism at room temperature and to notch sensitivity.

Section 2

PHYSICAL AND MECHANICAL PROPERTIES OF BERYLLIUM BLOCK,
SHEET, AND EXTRUSION

2.1 INTRODUCTION

The current most reliable physical and mechanical properties of the several available forms of beryllium are presented in this Section, based on a thorough literature survey, letters and/or personal contacts made with all companies and agencies believed to have unpublished information on the subject, and tests conducted at Lockheed Missiles and Space Company as part of this study. The information gathered is quite complete for hot-pressed block, but diminishingly less complete respectively for cross-rolled sheet, hot-upset sheet, and extrusions. The order of completeness of the information for the various forms reflects, in general, the length of time the product has been available to the industry in amounts sufficient for testing purposes.

The properties presented are based on tests of material having BeO content of considerable variation. Early tests were probably made with material of relatively high BeO content since this was the grade of material available at the time. In many of these tests, the BeO content was not reported. Since then, the industry has gradually stabilized on a BeO content between 1 and 2 percent. Material currently produced commercially has a nominal BeO content of about 1.75 percent. Recently reported tests, therefore, have this nominal oxide content. In order to base the properties presented here on a comprehensive sample of test data, all available tests have been included, with those tests obviously unrepresentative of currently acceptable material being discarded. The resulting tables and charts are felt to be typical of currently produced beryllium, but because many of the data surveyed were incomplete, the oxide content is not defined unless it is definitely known to be a fixed percentage.

Most of the hot-pressed block properties have been developed by LMSC. Some of this information is sufficient to be presented on a probability basis, and nearly all of it represents a large enough sample to be very reliable. The cross-rolled sheet properties represent a best estimate of a reasonable amount of information from many sources. They may be considered typical of the current production material. Information on hot-upset sheet and extrusion properties is very limited. That information presented has been selectively extracted from the literature with emphasis on the current state-of-the-art.

The physical properties of beryllium are presented in subsection 2.2, while the mechanical properties are presented in subsection 2.3. Properties are given at elevated temperature as well as room temperature wherever possible. The format used is similar to that found in MIL-HDBK-5; that is, the room-temperature properties are presented in tabular form while the elevated-temperature properties are presented in graphical form.

Subsection 2.4 presents data on the notch sensitivity of beryllium hot-pressed block and cross-rolled sheet. Subsection 2.5 should be referred to for information on the biaxial strength of these same two beryllium products. The information in these two sections, while generally included under "mechanical properties," is treated in more detail in this report because of the peculiar nature of these properties which makes their presentation not a routine matter.

In summary, it should be noted that all beryllium products discussed in this report are from QMV, -200 mesh, hot-pressed, and sintered beryllium powder. The designation QMV refers to the type of beryllium powder and is often used in the literature as a prefix to the description of the material. It has been dropped in many places in the text of this report because only products of QMV powder are treated.

2.2 PHYSICAL PROPERTIES

The following physical characteristics of beryllium are generally applicable to all commercial forms, since they are influenced by differences in composition rather than differences in fabrication processes. BeO-content variations have been found to influence physical properties, and iron content is believed to cause variations, although published work in this area does not clearly indicate the magnitude of differences. Industry practice is to hold the impurities to a minimum, with BeO content being the principal variant. Some of the properties in this section are shown as functions of BeO content. The remaining properties are representative of material currently available; that is, with a nominal BeO content of 1.75 percent. A summary of room-temperature physical properties, taken from Ref. 2-1, is presented in Table 2-1.

Table 2-1

A SUMMARY OF BERYLLIUM PHYSICAL PROPERTIES AT ROOM TEMPERATURE

Density (lb/in. ³)	0.066
Specific Gravity	1.85
Atomic Number	4
Atomic Weight	9.02
Atomic Diameter (A)	2.221
Reflectivity, White Light (%)	55
Specific Heat, Room Temperature (BTU/lb/°F)	0.445
Latent Heat of Fusion (BTU/lb)	470
Melting Point (°F)	2340
Thermal Conductivity, Room Temperature (BTU/ft ² /ft/hr)	104
Thermal Expansion, Room Temperature (in./in./°F)	6×10^{-6}
Electrical Conductivity (% of copper)	35 to 45
Resistivity ($\mu\text{ohm-in.}^2/\text{in.}$)	1.6
Magnetic Susceptibility (CGS electromagnetic units)	-1.00

Figure 2-1 shows the variation of specific heat with temperature. The curve is in good agreement with a number of references and should be considered quite exact for BeO content of 1 percent. Reference 2-2 indicates that specific heat varies inversely with BeO content. Thermal conductivity is plotted against temperature in Fig. 2-2. The source, Ref. 2-1, presents a study of a wide variety of tests. Figure 2-3 shows the variation of thermal expansion with temperature and BeO content. Electrical resistivity and magnetic susceptibility versus temperature are shown in Figs. 2-4 and 2-5, respectively. There is no severe corrosion of beryllium in air at 400°C with 200-hr exposure. Reference 2-3 reports the time for onset of noticeable corrosion as 60 hr at 700°C and 1 hr at 900°C. The material tested was extruded vacuum-cast material.

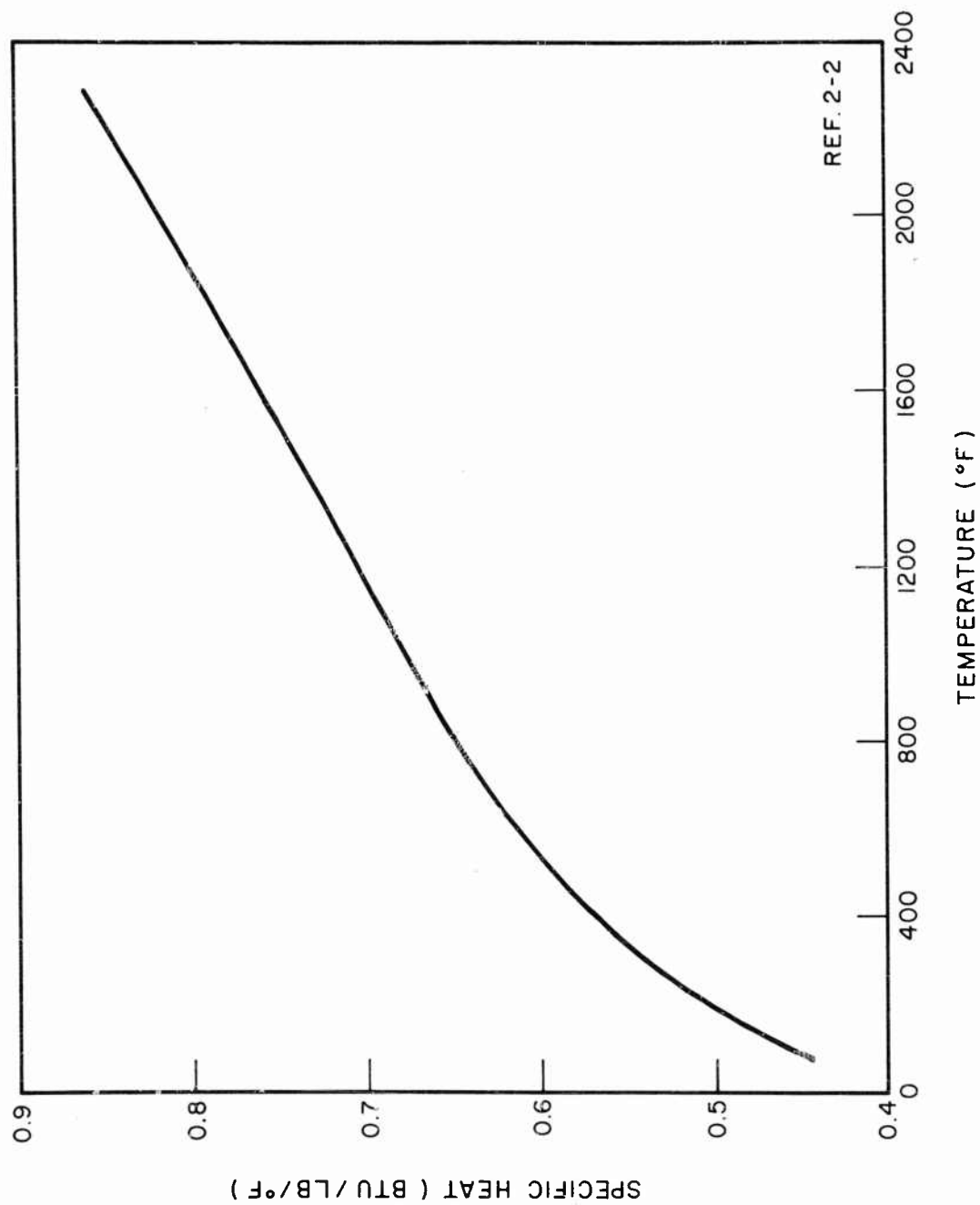


Fig. 2-1 Effect of Temperature on the Specific Heat of Beryllium

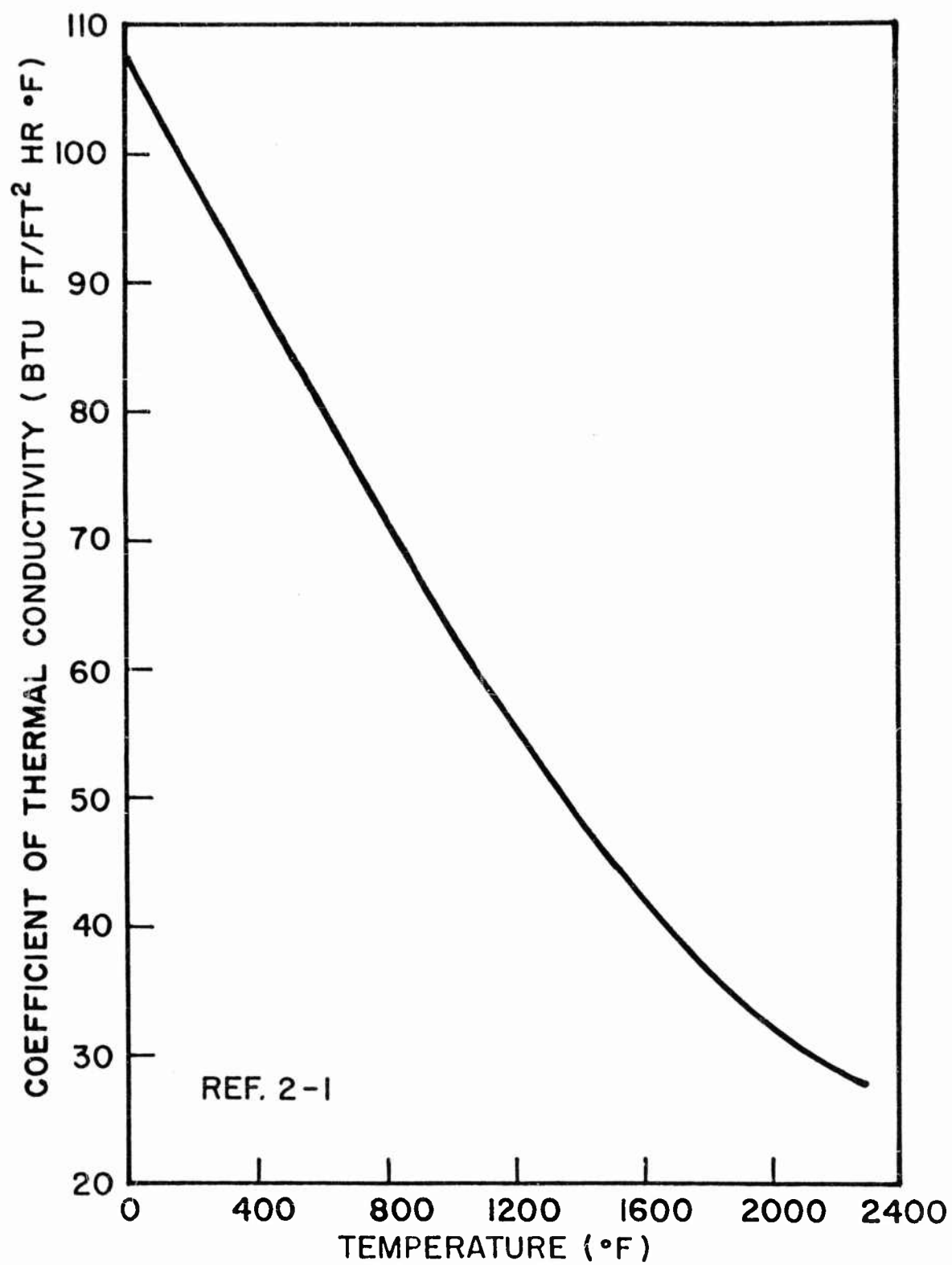


Fig. 2-2 Effect of Temperature on Thermal Conductivity of Beryllium

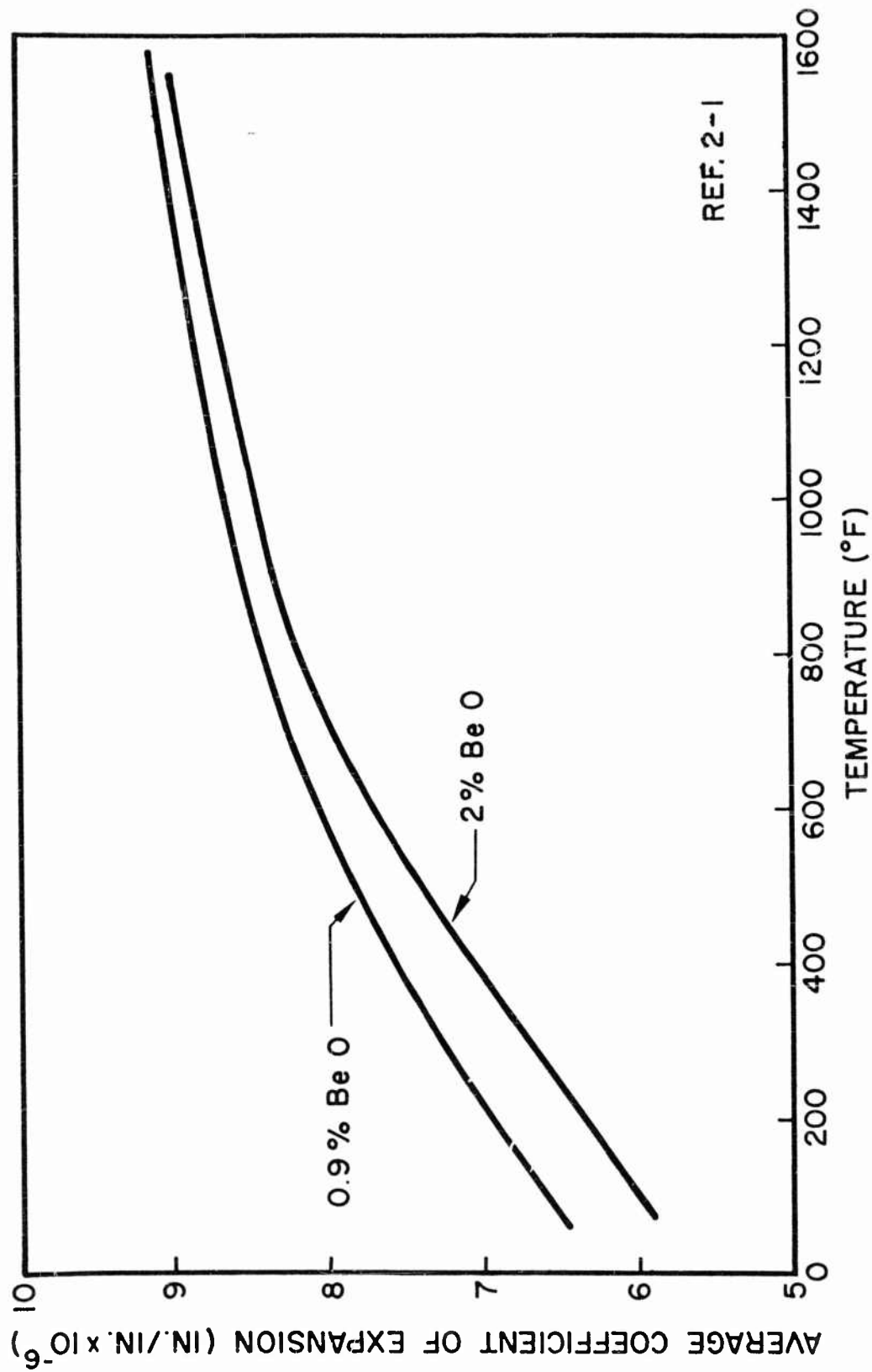


Fig. 2-3 Effect of Temperature and BeO Content on Thermal Expansion of Beryllium

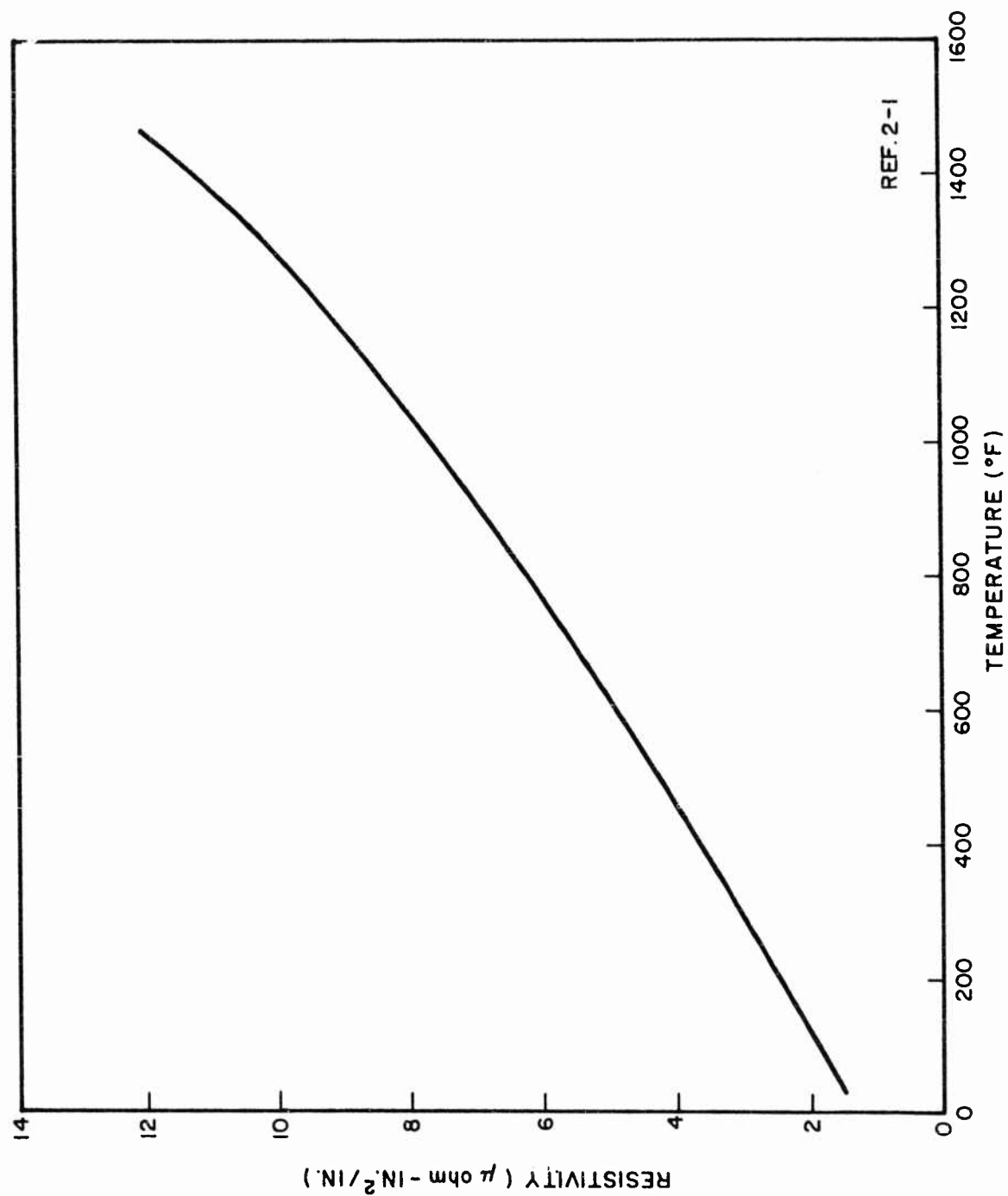


Fig. 2-4 Effect of Temperature on Resistivity of Beryllium

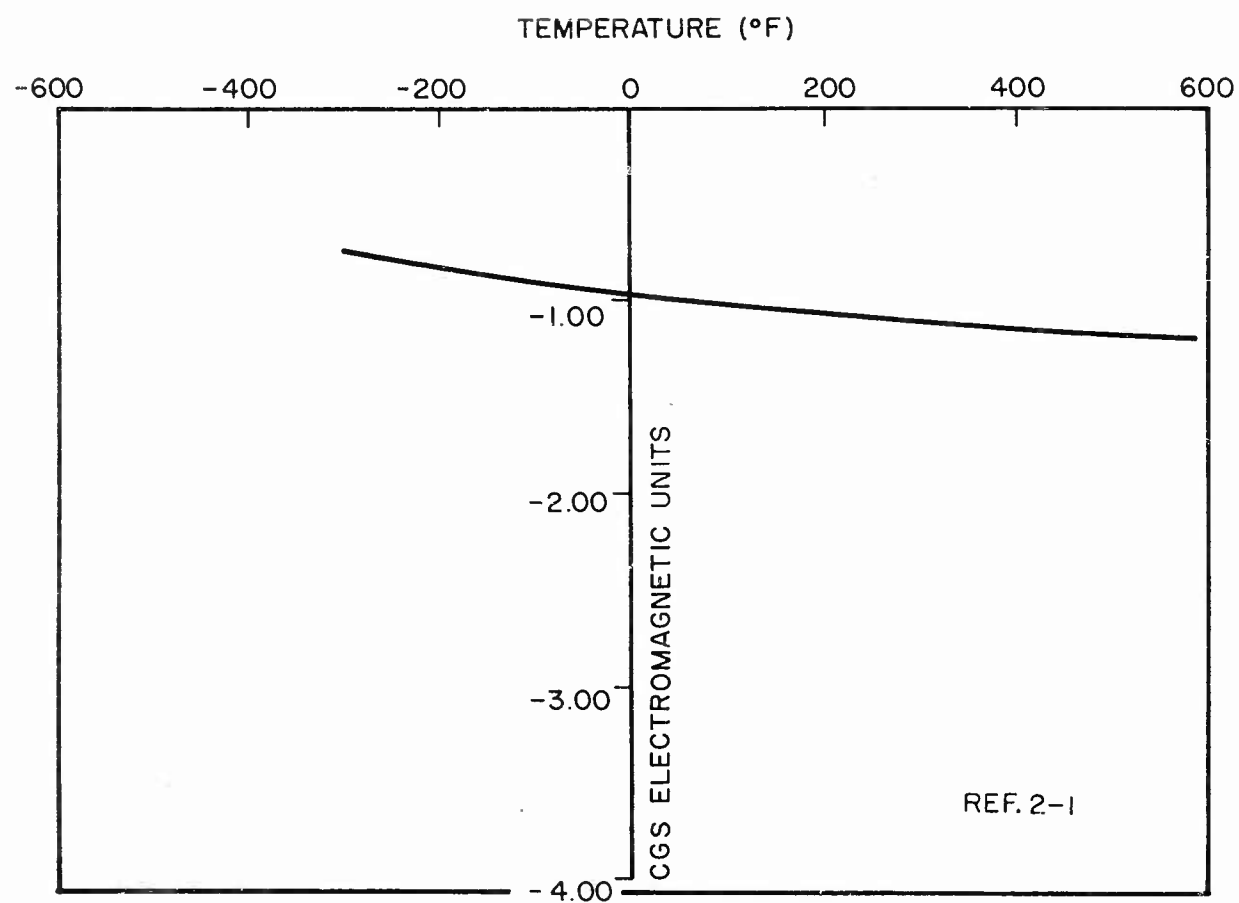


Fig. 2-5 Effect of Temperature on Magnetic Susceptibility of Beryllium

2.3 MECHANICAL PROPERTIES

Design mechanical properties are presented for the following forms of beryllium:

- Hot-pressed block
- Cross-rolled sheet
- Hot-upset sheet
- Extrusion

The properties shown are those commonly used in aerospace design, and closely pattern, insofar as is possible with the information currently available, the format for mechanical properties established in MIL-HDBK-5. The general order for presentation of properties is as follows: design mechanical properties at room and elevated temperature, ductility, stress-strain relationships, fatigue, and creep.

The mechanical properties of beryllium have been found to differ in the longitudinal and transverse grain directions. In this report, these terms have the normal connotation when applied to sheet or extrusion. However, in describing hot-pressed block, longitudinal refers to material tested parallel to the direction of pressing, and transverse refers to material tested normal to the direction of pressing.

The mechanical properties of all forms of beryllium vary with BeO content. Some typical variations are shown for hot-pressed block material in Figs. 2-6 through 2-9. The initial three figures present tensile stress-strain curves versus temperature for material having 1-, 2-, and 3-percent BeO content, respectively. Figure 2-9 shows the variation of Young's modulus with BeO content and temperature. These figures show that Young's modulus varies directly with BeO content but that variations in stress-strain properties with BeO content depend on temperature. These curves should not be used for design purposes. Figures presenting hot-pressed block stress-strain curves and mechanical properties for design are cited later in this section. As discussed in subsection 2.1, the design properties are generally based on a nominal BeO content of 1.75 percent unless otherwise stated.

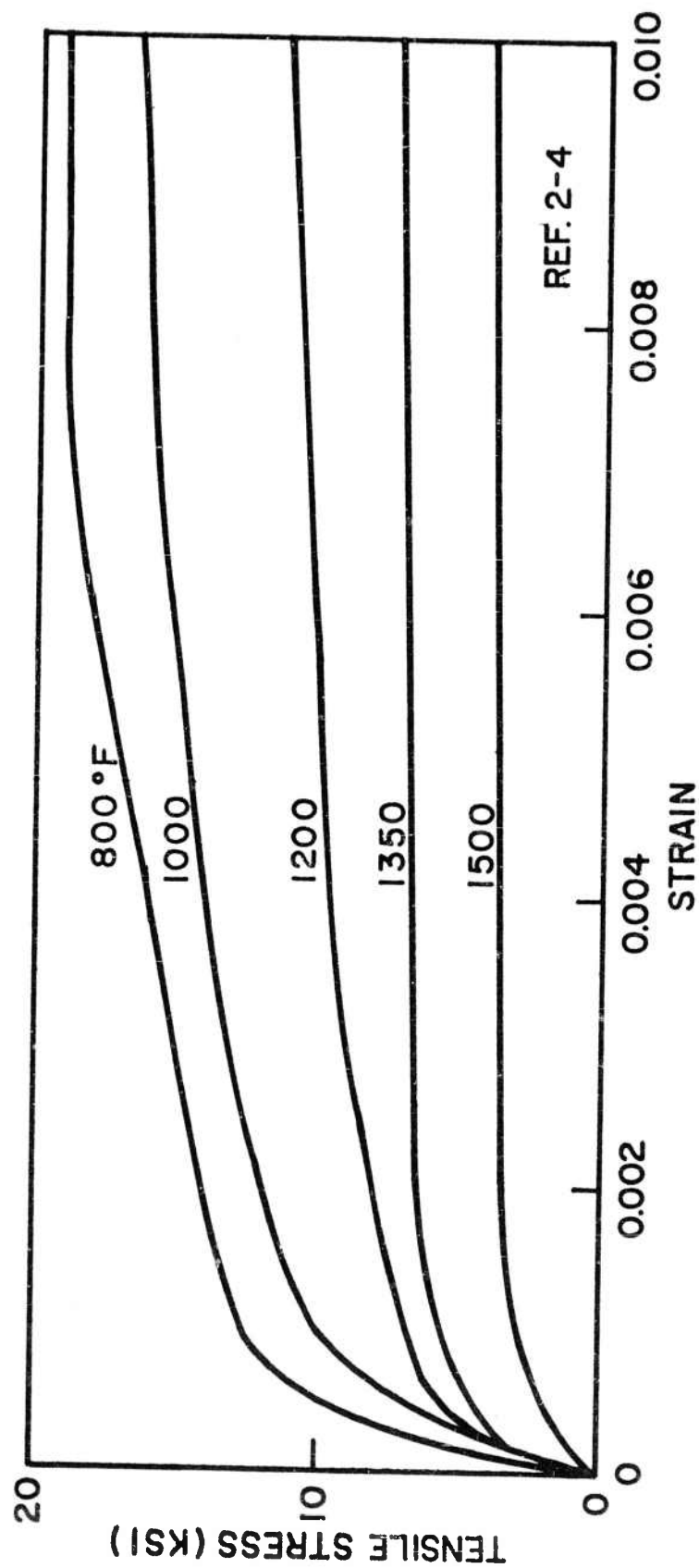
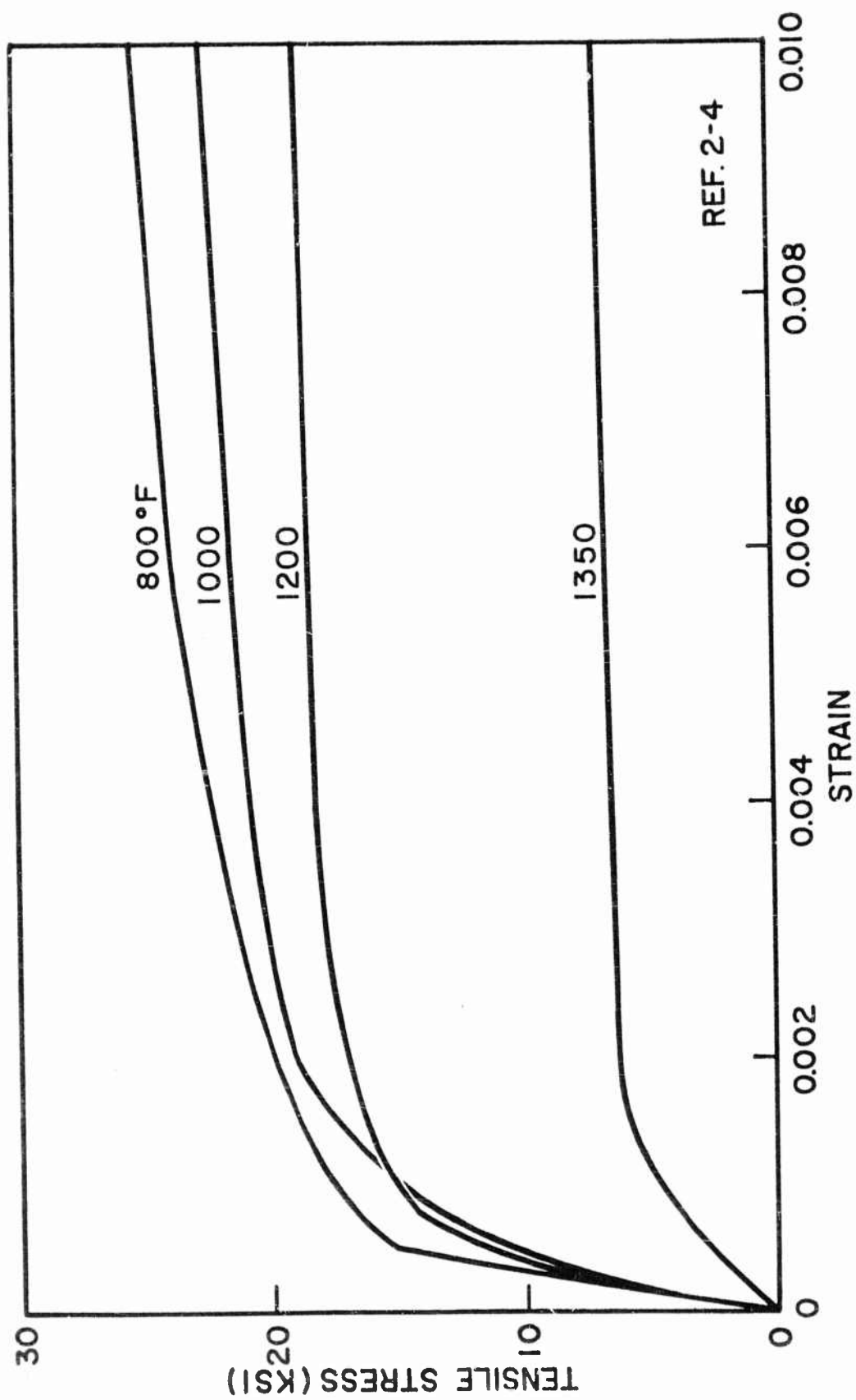


Fig. 2-6 Tensile Stress-Strain Curves for Hot-Pressed Beryllium Block Having 1% BeO Content



REF. 2-4

Fig. 2-7 Tensile Stress-Strain Curves for Hot-Pressed Beryllium Block Having 2% BeO Content

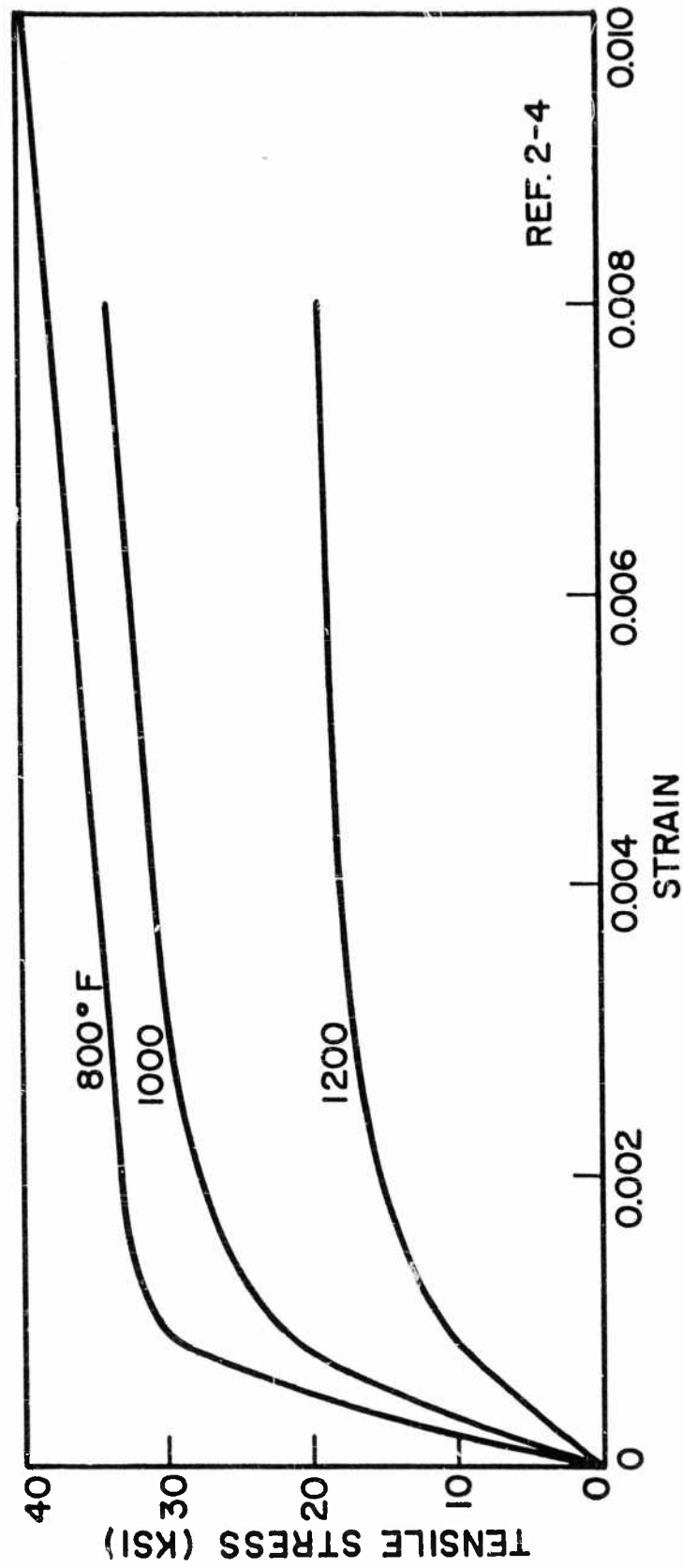


Fig. 2-8 Tensile Stress-Strain Curves for Hot-Pressed Beryllium Block Having 3% BeO Content

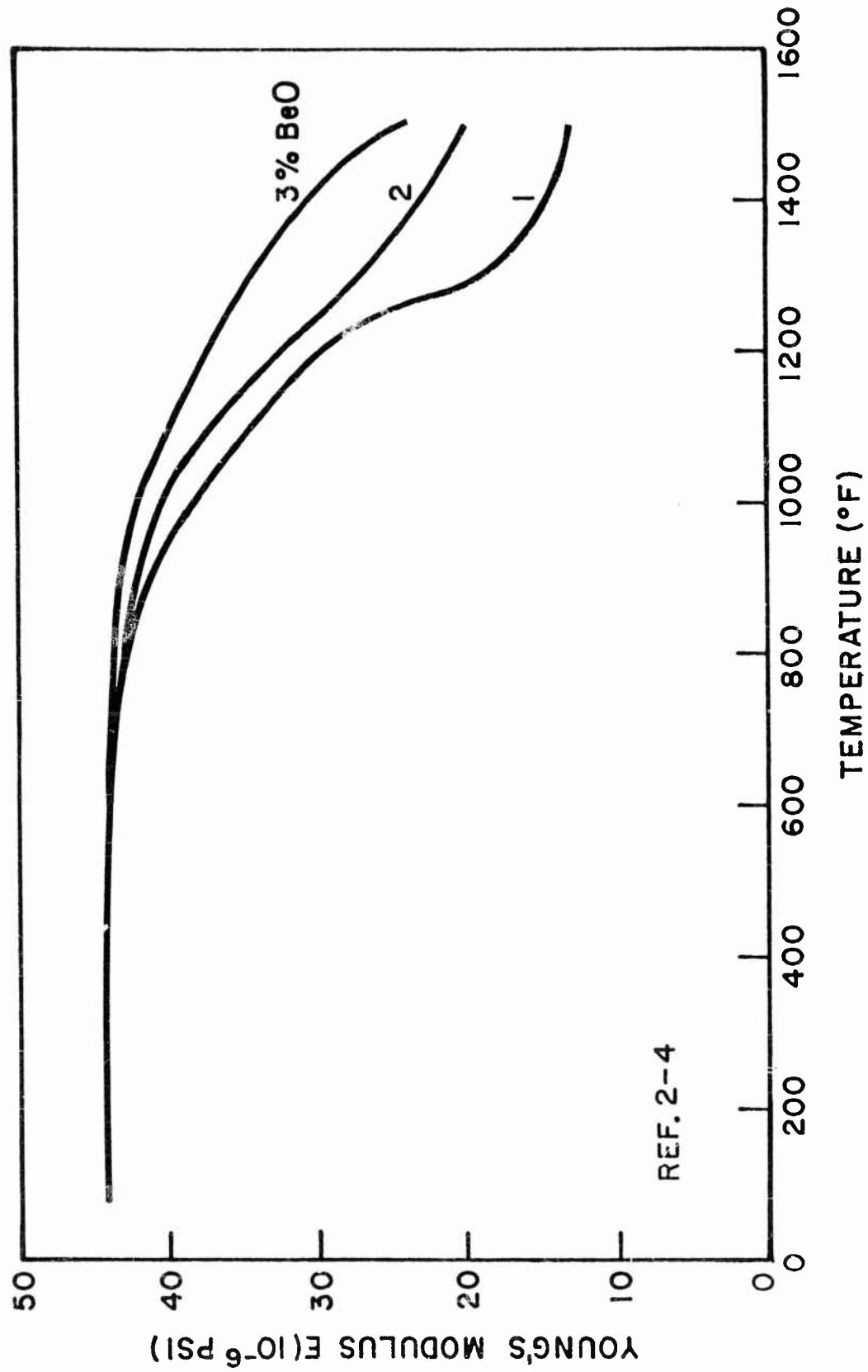


Fig. 2-9 Effect of Temperature and BeO Content on Young's Modulus of Hot-Pressed Beryllium Block

All forms of beryllium are insensitive to strain rate (excluding impact loading) until temperatures in excess of 800°F are reached. Consequently, strain rates are not specified for properties below 800°F. A nominal rate of 0.005 in./in./min applies to all data. All properties have been determined for uniaxial stressing conditions. Refer to subsections 2.4 and 2.5, respectively, for information on the notch sensitivity and biaxial strength of beryllium. Unless otherwise stated, the mechanical-property terms have the same definition as given in MIL-HDBK-5.

2.3.1 QMV Hot-Pressed Block

Design mechanical properties for hot-pressed block at room temperature are presented in Table 2-2. All properties are typical except the tensile ultimate, yield, and elongation values, which may be considered 90-percent probable on the basis of a statistical analysis of several hundred specimens tested by LMSC over the past several years. The remaining properties are based on quite extensive tests and have a good level of reliability. Figures 2-10 through 2-38 present elevated-temperature properties of hot-pressed block. All figures present typical properties except Figs. 2-10 through 2-13 which show 50-, 90-, and 99-percent probability properties. These figures present the variation of the tensile ultimate stress in the longitudinal and transverse directions with temperature (Figs. 2-10 and 2-11), and the variations of the tensile yield stress in the longitudinal and transverse directions with temperature (Figs. 2-12 and 2-13). The basis of these probability levels is identical to that noted above for the room-temperature tensile properties.

The variation of the compressive yield stress with temperature is presented in Fig. 2-14. The compressive yield stress is defined here as the stress corresponding to a permanent strain of 0.002. Ultimate shear stress versus temperature is given in Fig. 2-15. Figures 2-16 through 2-18 present ultimate and yield-bearing stresses versus temperature where pin diameter is varied, but edge distance e is held constant at 0.5 in. Data on pin diameters D of 3/16 in., 1/4 in., and 5/16 in., respectively, are presented. These curves are based on an evaluation by LMSC of Ref. 2-5 and associated unpublished data from Thermatest Laboratories. It should be noted that each figure represents a particular e/D value and gives bearing strengths significantly different from the other two e/D values. The variation of tensile elongation in the longitudinal direction with temperature is given in Fig. 2-19. This figure shows that hot-pressed block exhibits an increasing elongation up to 800°F followed by a rather steep reversal to 1400°F, at which point the elongation has decreased to 3.5 percent. The elongation has been reported to increase again above 1400°F.

Table 2-2
TYPICAL DESIGN MECHANICAL PROPERTIES OF BERYLLIUM^(a)

Form	Hot-Pressed Block		Cross-Rolled Sheet		Hot-Upset Sheet		Extrusions	
		Ref.		Ref.		Ref.		Ref.
F_{tu} (ksi)								
L	42 ^(b)	2-1	69 ^(c)		75.6	2-6	77.2	2-7
T	47 ^(b)	2-1	72 ^(c)					
F_{ty} (ksi)								
L	36 ^(b)	2-1	59 ^(c)		50.0	2-6	43.9	2-7
T	32 ^(b)	2-1	62 ^(c)					
F_{cy} (ksi)	40.5	2-1	58 ^(c)		50.0	2-8		
F_{su} (ksi)	50.8	2-1	70 ^(e)	2-5				
F_{bru} (ksi) ($e/D = 2.0$, 5/16-in. pin diam.)	128	2-5	144	2-5				
F_{bry} (ksi) ($e/D = 2.0$, 5/16-in. pin diam.)	120	2-5	130	2-5				
e_T (%)								
L	0.7 ^(b)	2-1	5.5 ^(c)		8.0	2-8		
T	1.5 ^(b)	2-1						
E (10^6 psi)	44	2-1	43.5	2-9	42.0	2-6		
E_c (10^6 psi)	42	2-1	42.5	2-10	≥ 45	2-6		
G (10^6 psi)	20	2-1	20.0	2-5			20.0	2-7
Poisson's ratio	0.025	2-11	0.09 ^(d)					

(a) All properties based on a nominal BeO content of 1.75%.

(b) These values are 90% probable.

(c) Value based on information of all references cited for this product.

(d) In plane of sheet; see subsection 2.5 for discussion.

(e) This value for shear ultimate taken normal to plane of sheet; $F_{su} \approx 40$ ksi in the plane of sheet (see Fig. 3-10)

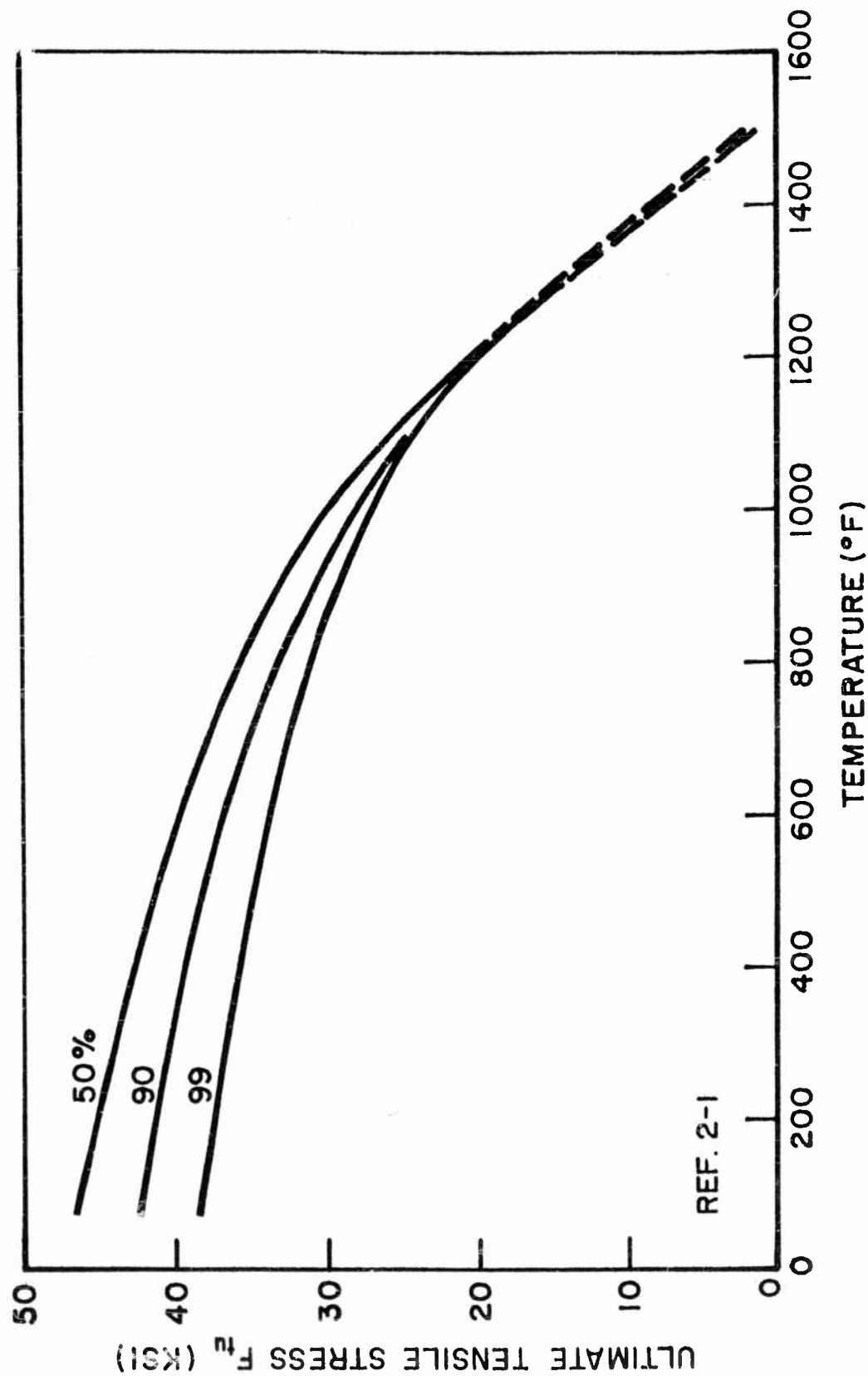


Fig. 2-10 Effect of Temperature on the Longitudinal Ultimate Tensile Stress of Hot-Pressed Beryllium Block at Various Levels of Probability

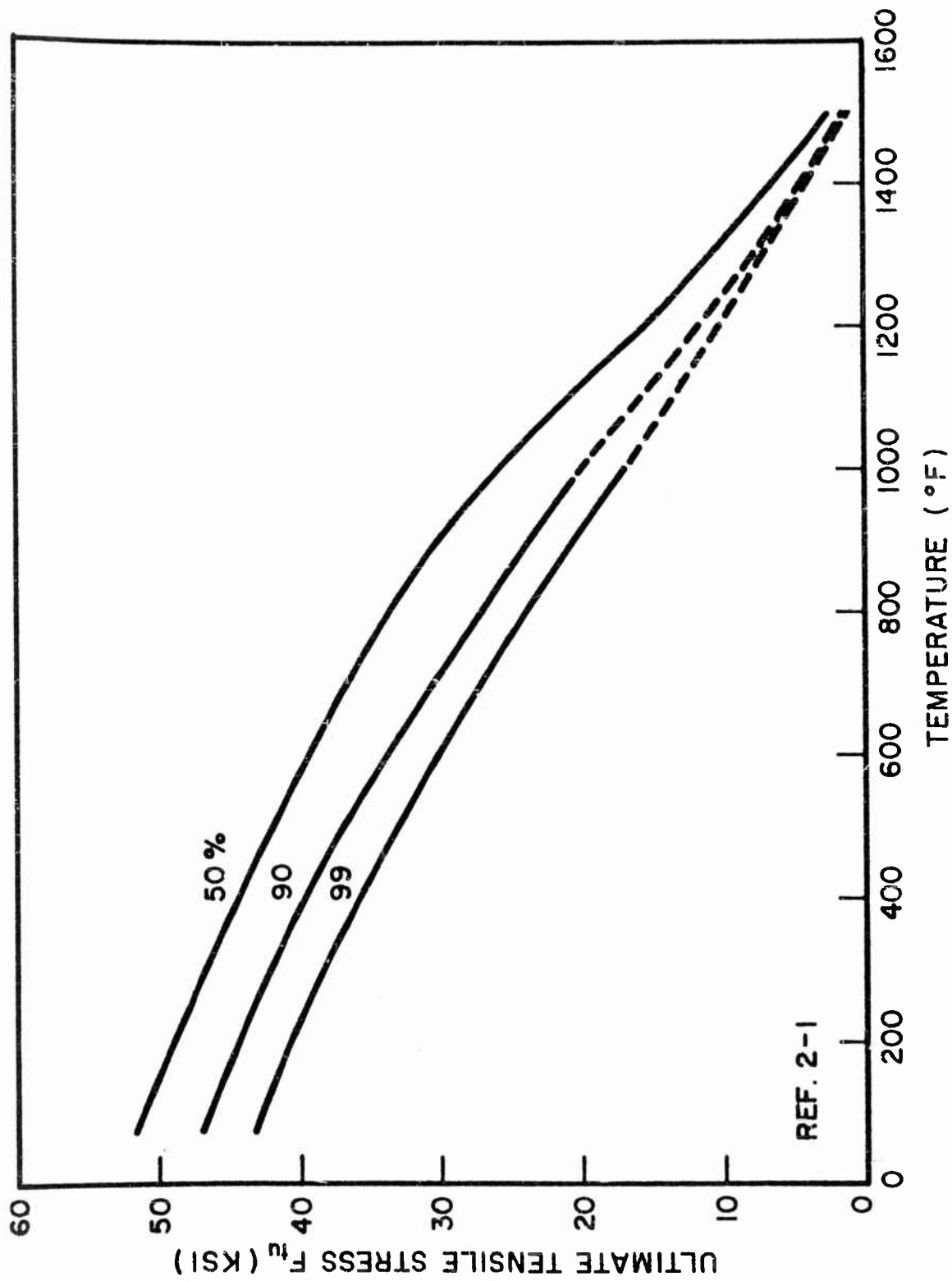


Fig. 2-11 Effect of Temperature on the Transverse Ultimate Tensile Stress of Hot-Pressed Beryllium Block at Various Probability Levels

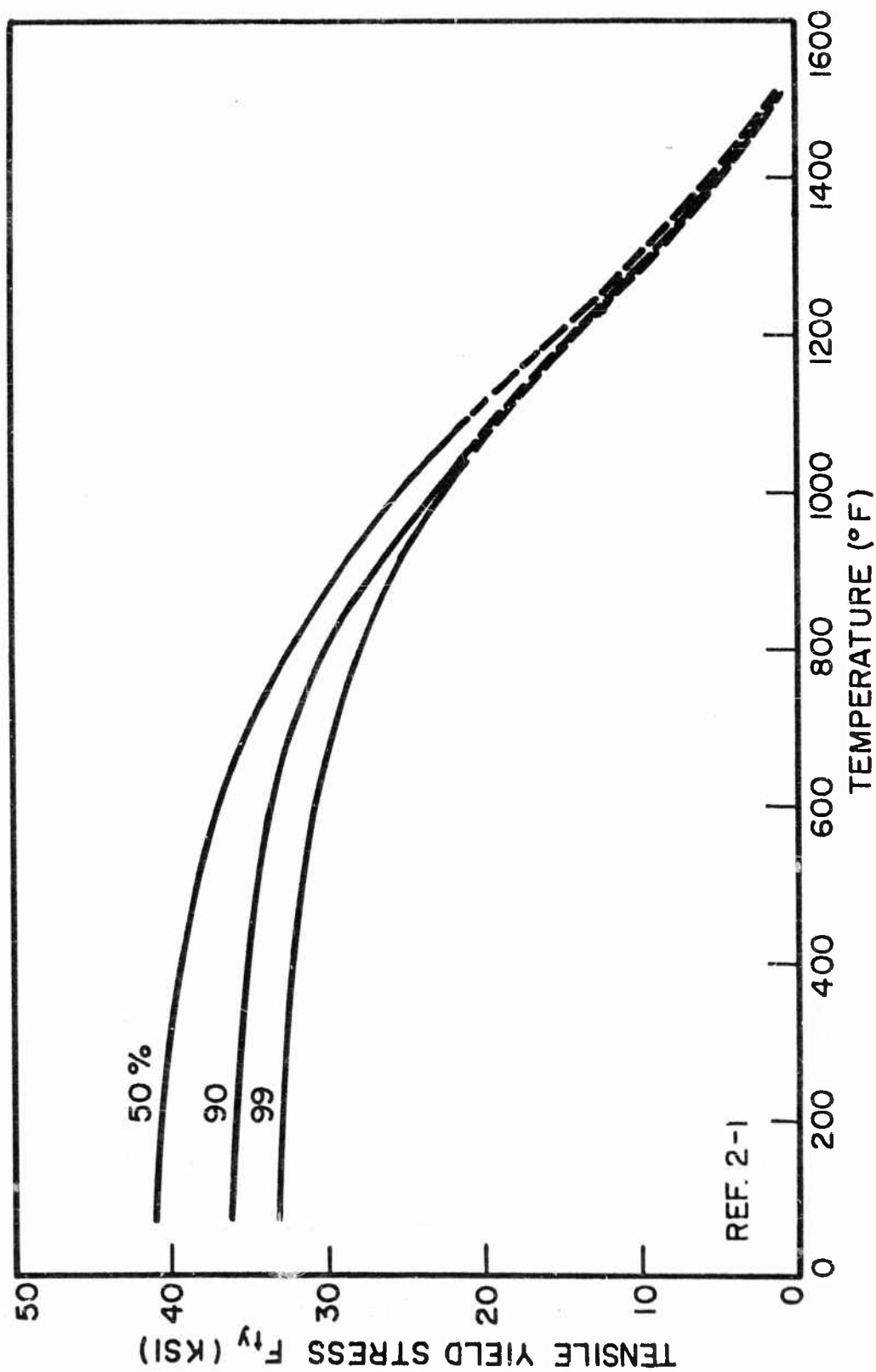


Fig. 2-12 Effect of Temperature on the Longitudinal Tensile Yield Stress of Hot-Pressed Beryllium Block at Various Probability Levels

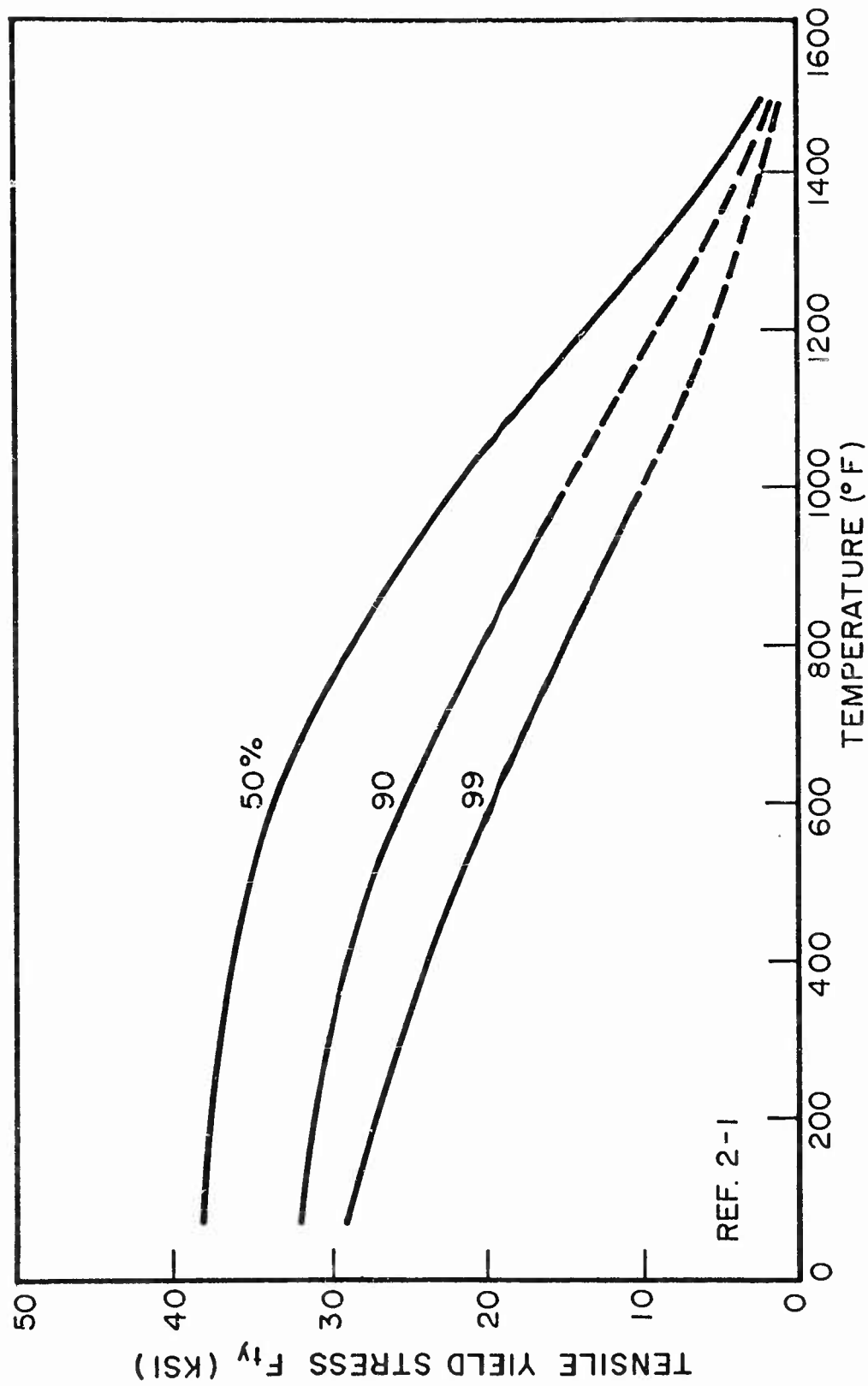


Fig. 2-13 Effect of Temperature on the Transverse Tensile Yield Stress of Hot-Pressed Beryllium Block at Various Probability Levels

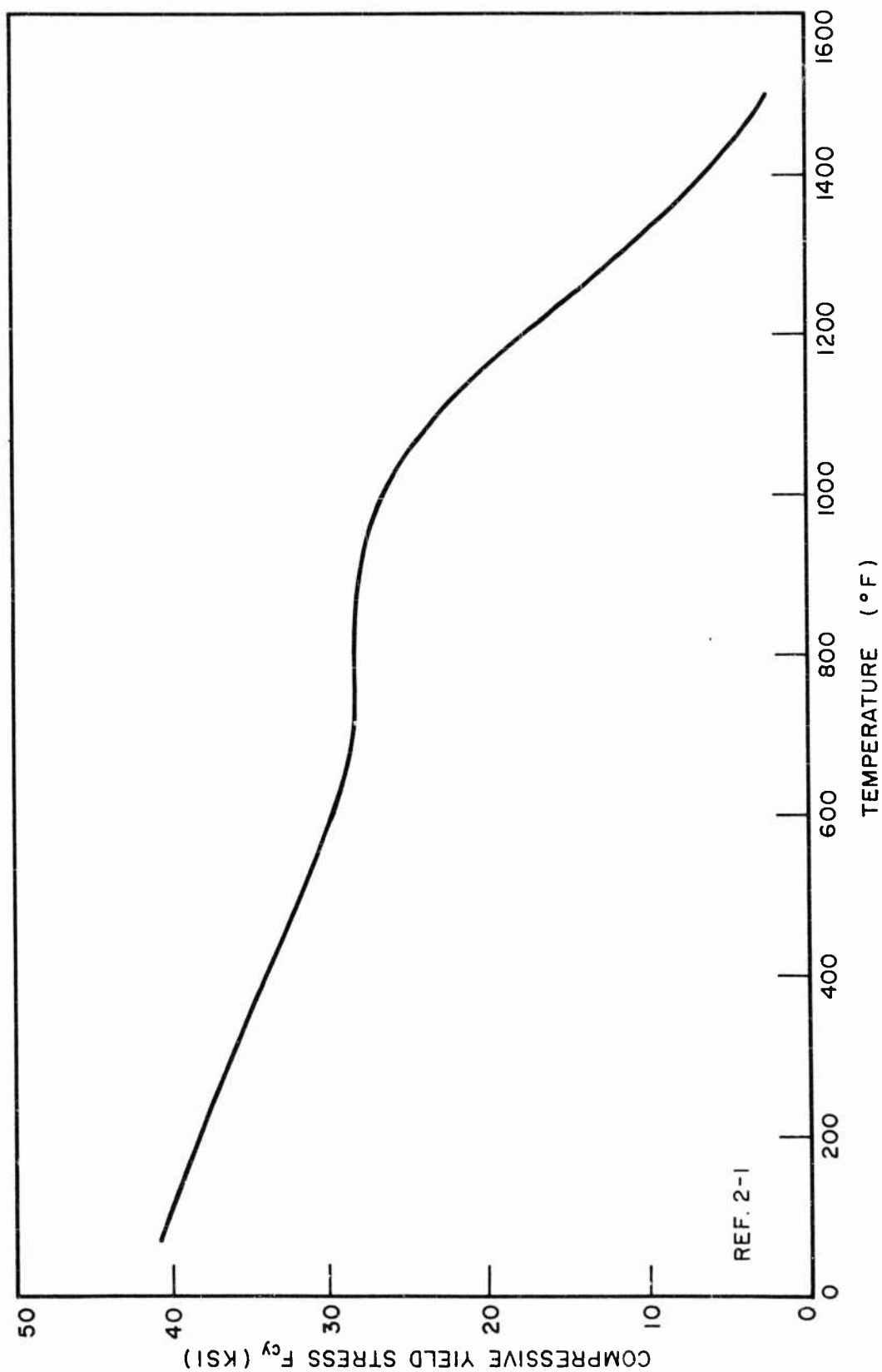


Fig. 2-14 Effect of Temperature on the Typical Compressive Yield Stress of Hot-Pressed Beryllium Block

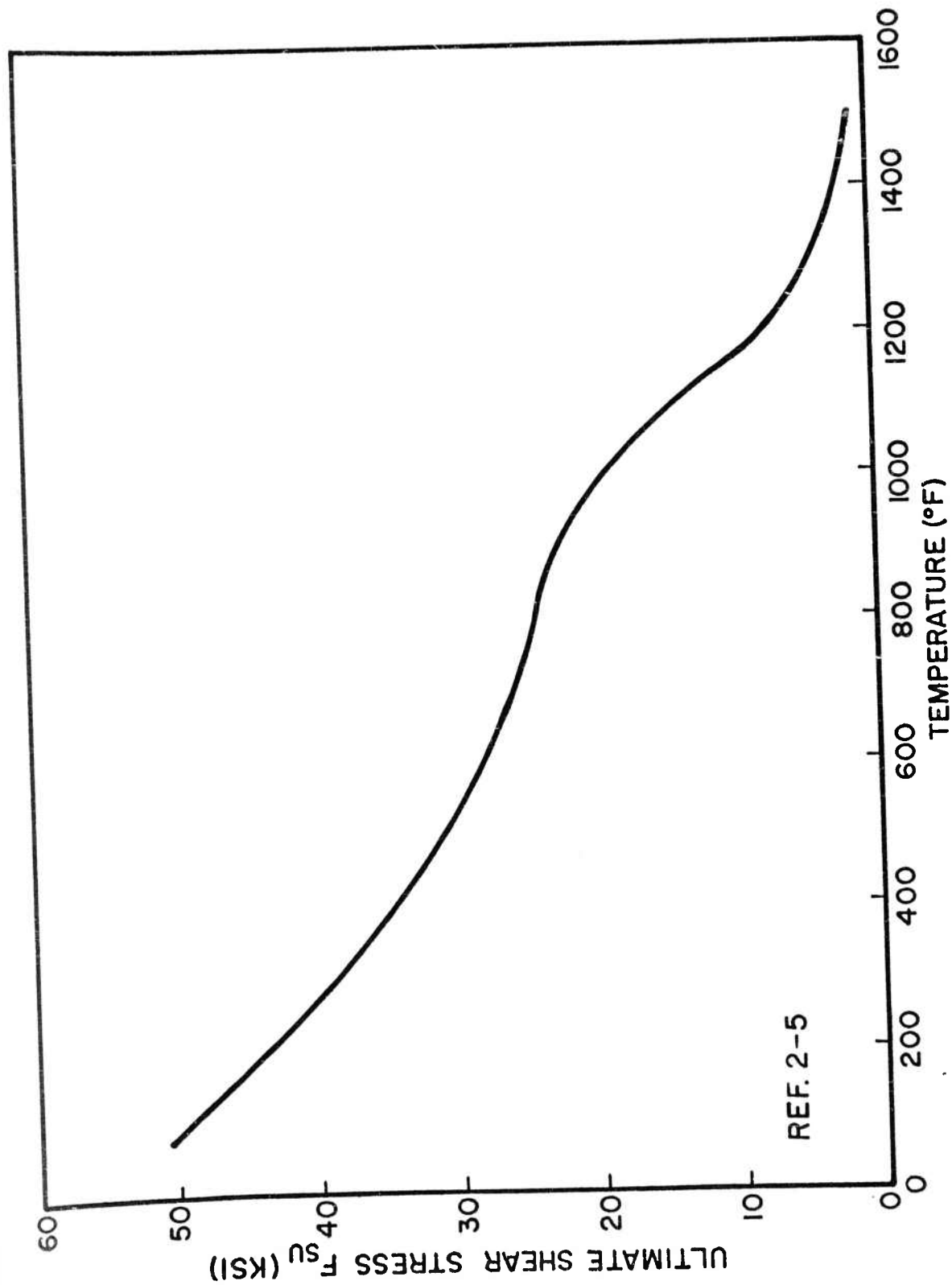


Fig. 2-15 Effect of Temperature on the Typical Ultimate Shear Stress of Hot-Pressed Beryllium Block

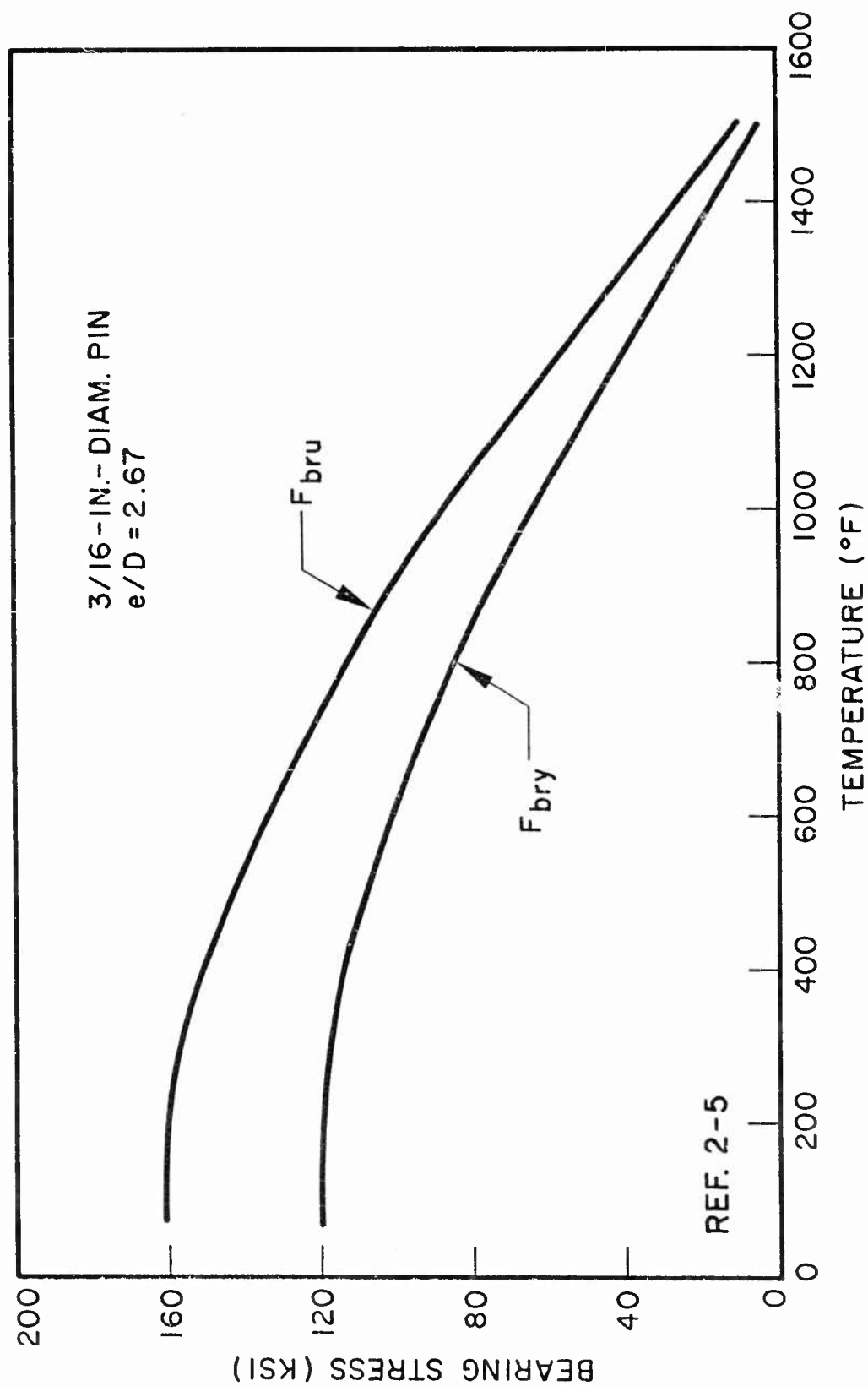


Fig. 2-16 Effect of Temperature on the Typical Bearing Stress of Hot-Pressed Beryllium Block,
 $e/D = 2.67$

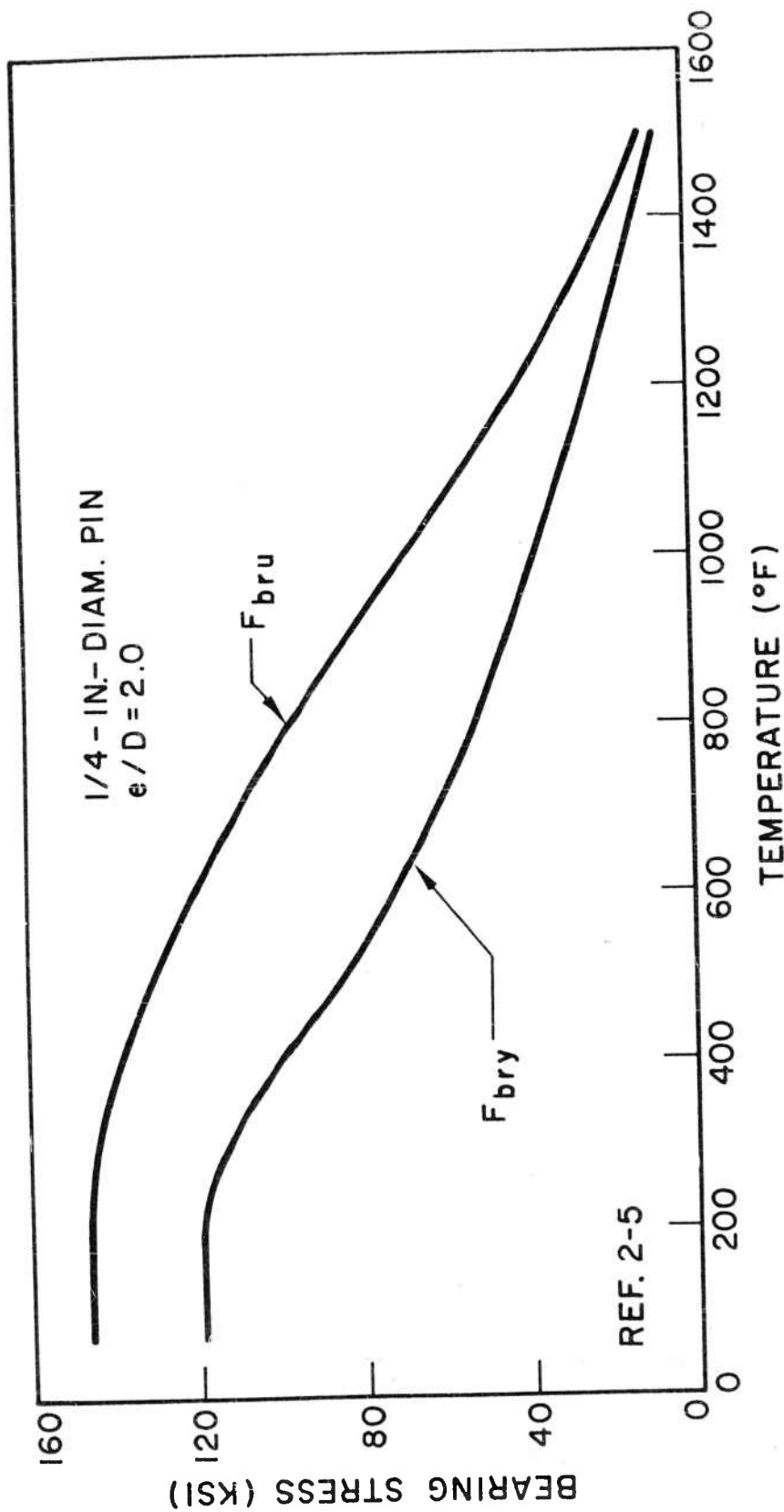


Fig. 2-17 Effect of Temperature on the Typical Bearing Stress of Hot-Pressed Beryllium Block,
e/D = 2.0

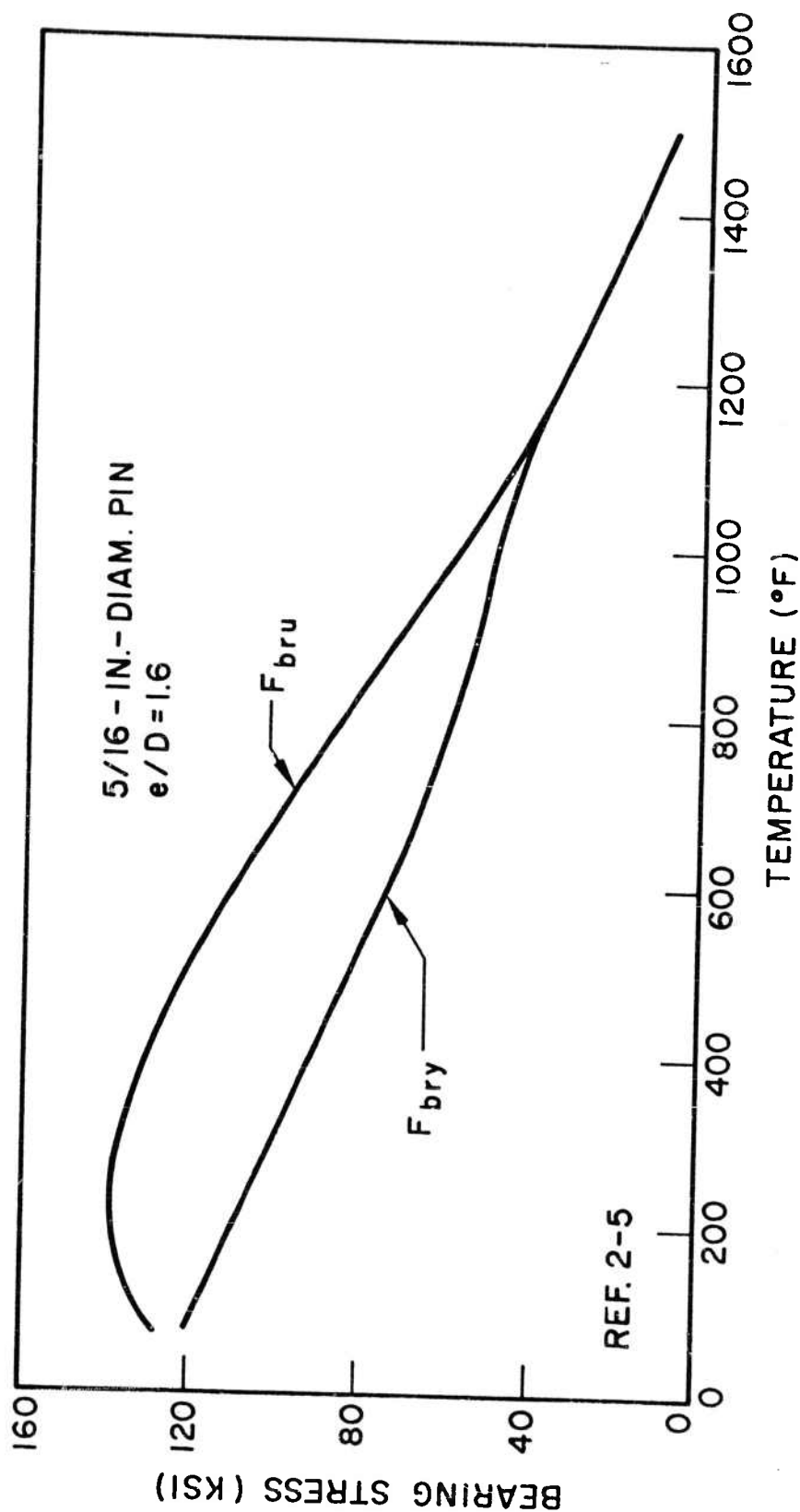


Fig. 2-18 Effect of Temperature on the Typical Bearing Stress of Hot-Pressed Beryllium Block,
e/D = 1.6

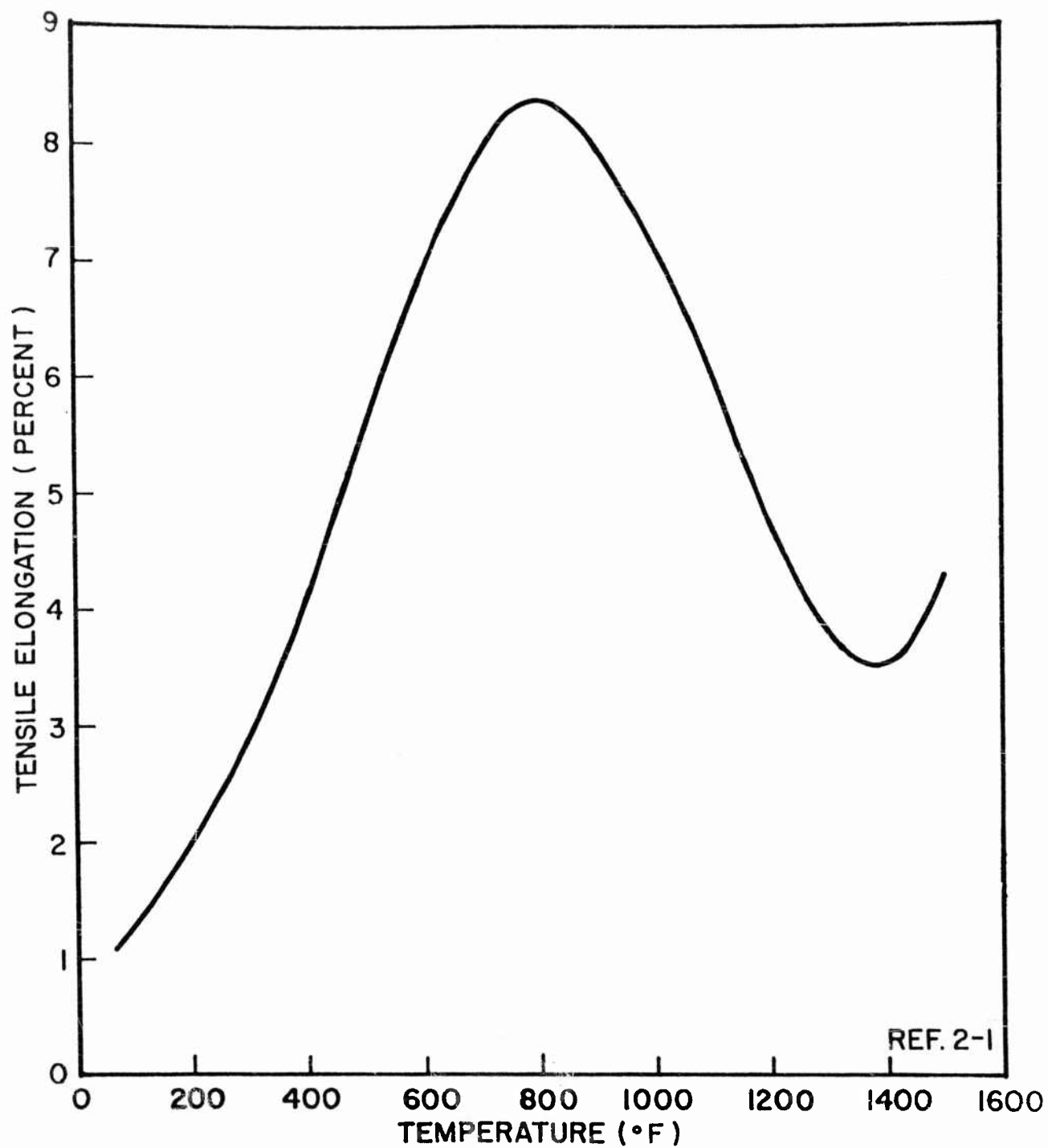


Fig. 2-19 Effect of Temperature on the Longitudinal Tensile Elongation of Hot-Pressed Beryllium Block

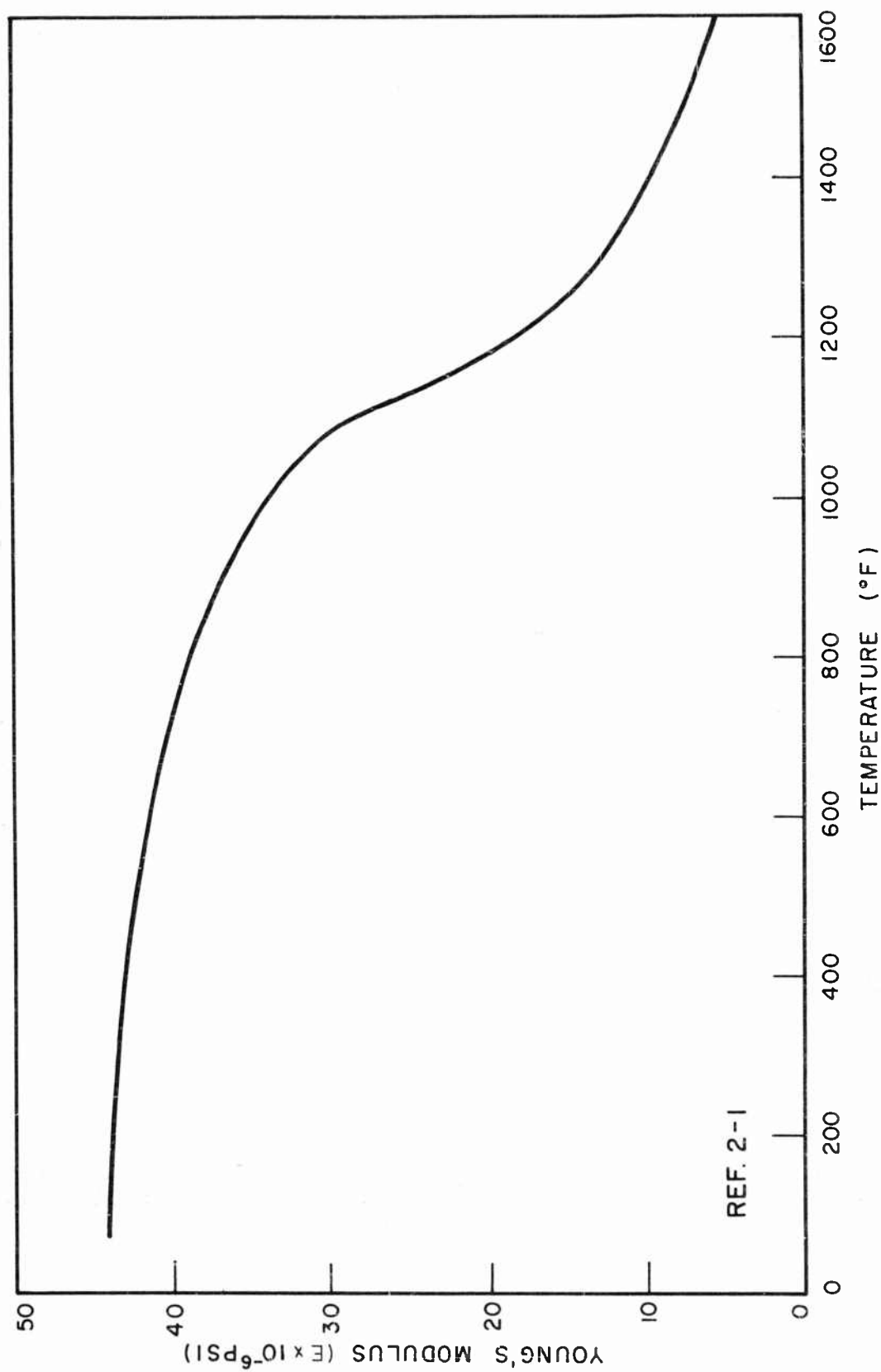


Fig. 2-20 Effect of Temperature on Young's Modulus of Hot-Pressed Beryllium Block

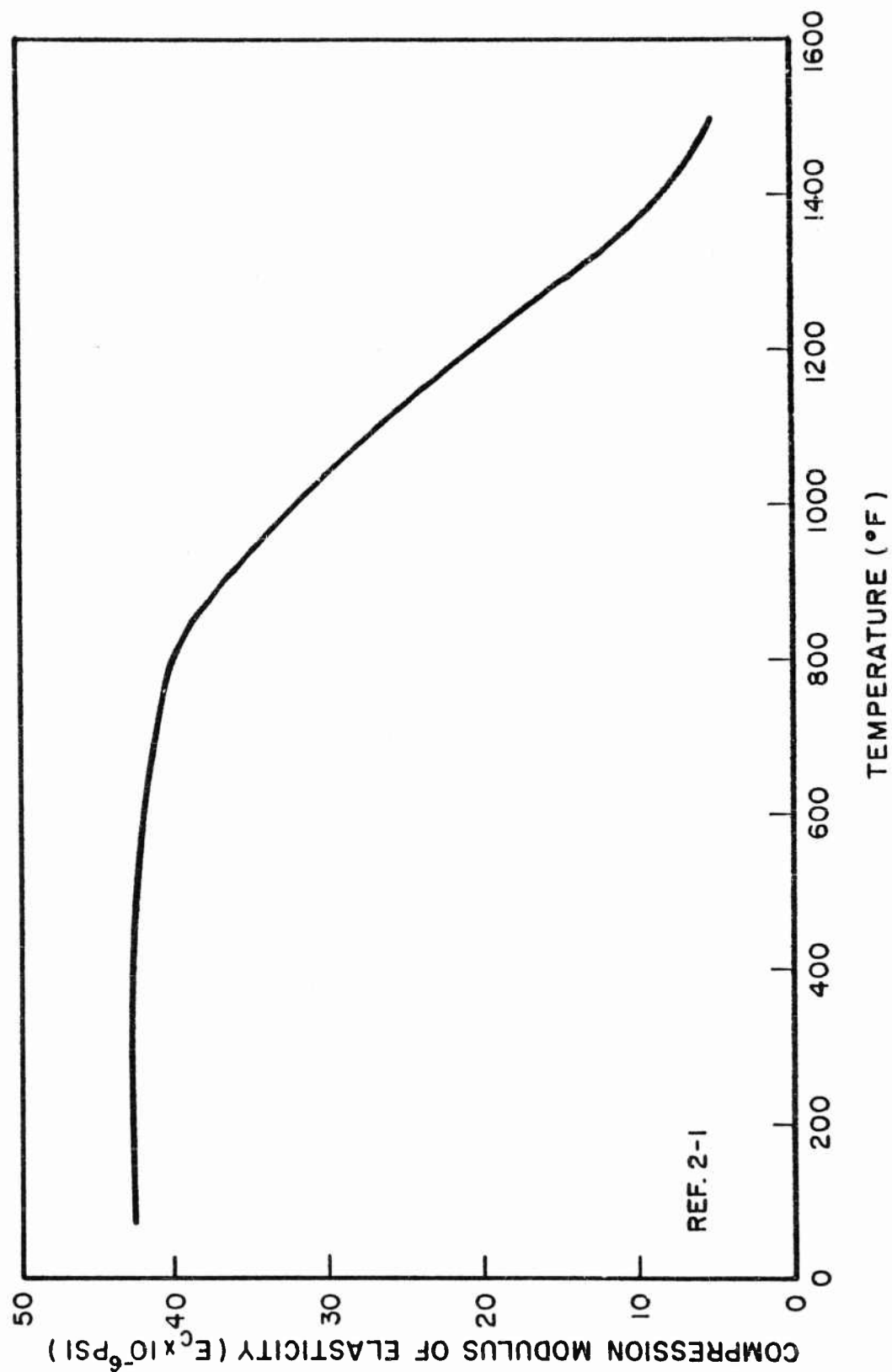


Fig. 2-21 Effect of Temperature on the Compressive Modulus of Hot-Pressed Beryllium Block

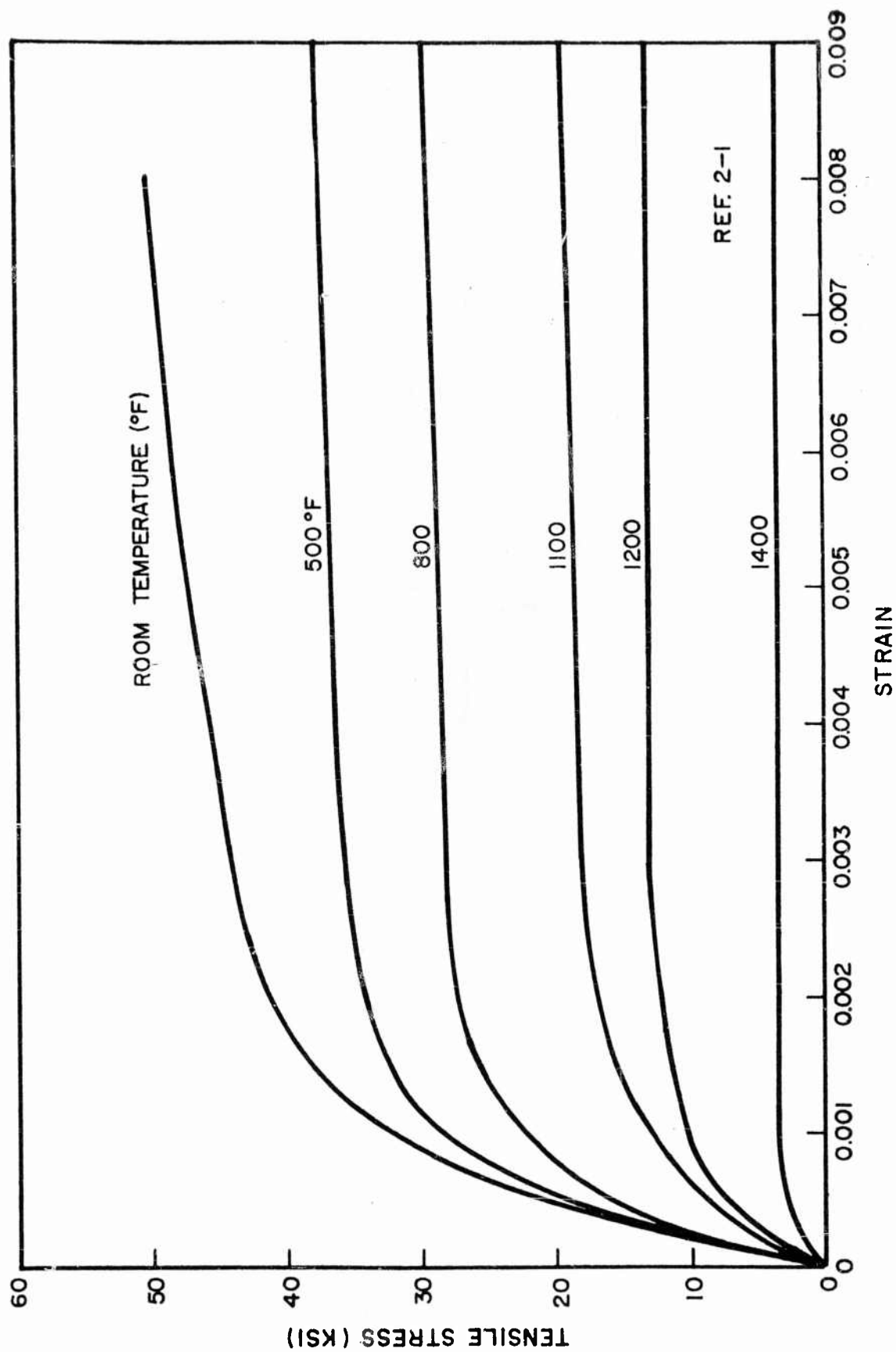


Fig. 2-22 Typical Tensile Stress-Strain Curves at Room and Elevated Temperatures for Hot-Pressed Beryllium Block

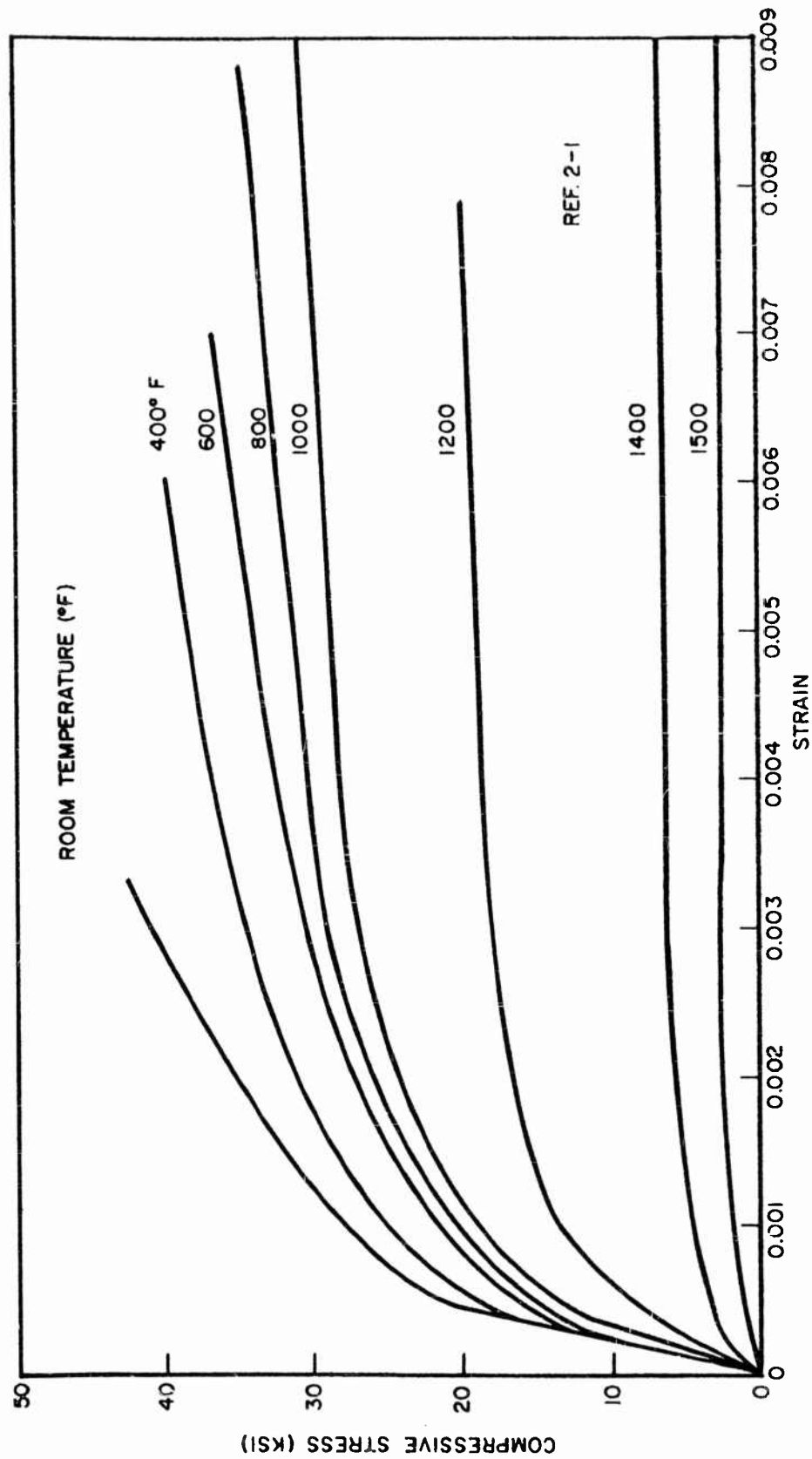


Fig. 2-23 Typical Compressive Stress-Strain Curves at Room and Elevated Temperatures for Hot-Pressed Beryllium Block

Young's modulus versus temperature is presented in Fig. 2-20, while the compressive modulus of elasticity is presented in Fig. 2-21. Typical stress-strain curves at room and elevated temperatures in tension and in compression are given in Figs. 2-22 and 2-23, respectively.

Axial fatigue information on hot-pressed beryllium block is presented in Figs. 2-24 through 2-37. The terminology is defined in Fig. 2-24.

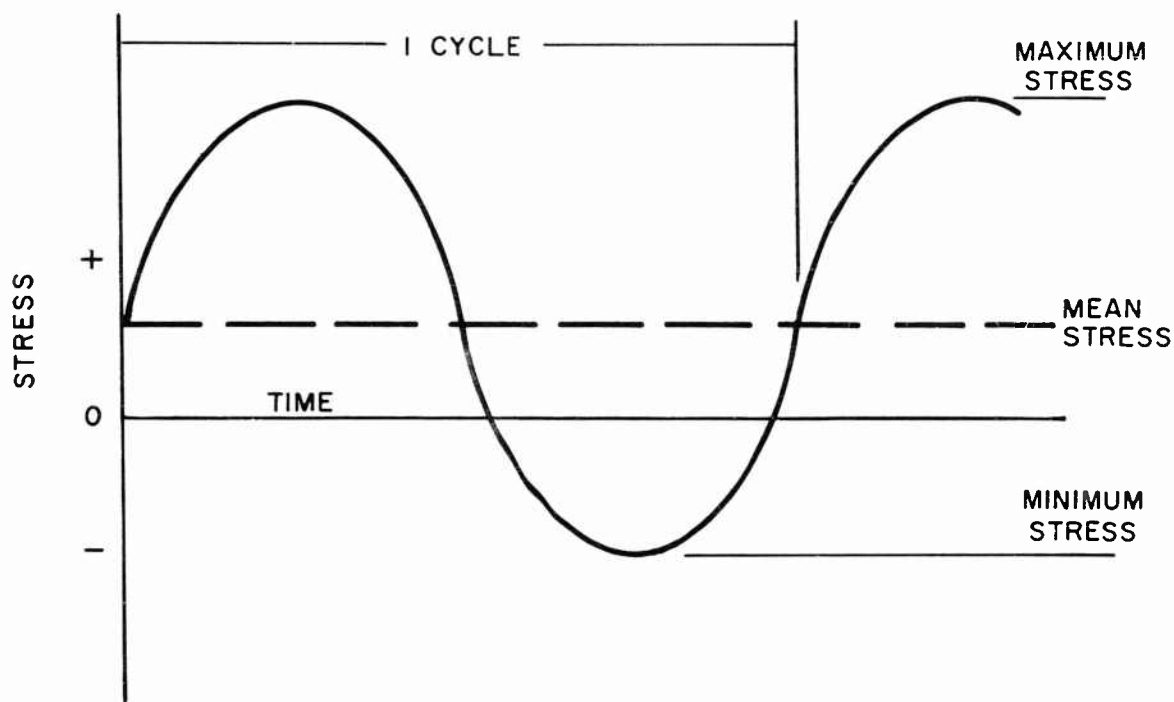


Fig. 2-24 Definition of Fatigue Terms

In addition:

$$\text{Alternating stress} = \text{maximum stress} - \text{mean stress}$$

$$\text{Stress range} = \text{maximum stress} - \text{minimum stress}$$

$$\text{Stress ratio} = R = \frac{\text{minimum stress}}{\text{maximum stress}}$$

$$\text{Stress ratio} = A = \frac{\text{alternating stress}}{\text{mean stress}}$$

The axial fatigue characteristics of hot-pressed block as a function of various combinations of stress concentration factor K_t and stress ratio R are given in Figs. 2-25 through 2-32. Figures 2-25 through 2-27 are taken from Ref. 2-7. The initial figure presents information at room temperature, while the other two present information at 1100°F. A testing frequency of approximately 350 cps was used to obtain data at both temperatures. The stress in these figures is given in terms of maximum stress. A comparison of Figs. 2-25 and 2-26 shows the effect of temperature on the fatigue characteristics of identical specimens. Similarly, Figs. 2-26 and 2-27 show the effect of a decreasing mean stress (presented in terms of R) on identical notched specimens at 1100°F. All three figures present information on unnotched specimens as well as notched specimens. Additional combinations of K_t and R at room temperature only are treated in Figs. 2-28 and 2-29. These figures are taken from Ref. 2-12 and are presented in terms of alternating stress, in contrast to maximum stress in the preceding three figures. However, by substituting the definitions presented above, it can be shown that:

$$\text{maximum stress} = \frac{2}{1 - R} [\text{alternating stress}]$$

These figures indicate, in the curves for the type I specimen, that the effect of a decreasing mean stress (R decreasing from 0 to -1) is to substantially increase the alternating stress for the range of cycles to failure shown. The stresses for the type II and type III specimens are based on net area. A more complete picture of the relationship between mean stress, alternating stress, and cycles to failure for the case of axial fatigue in unnotched hot-pressed block at room temperature is shown in Fig. 2-30.

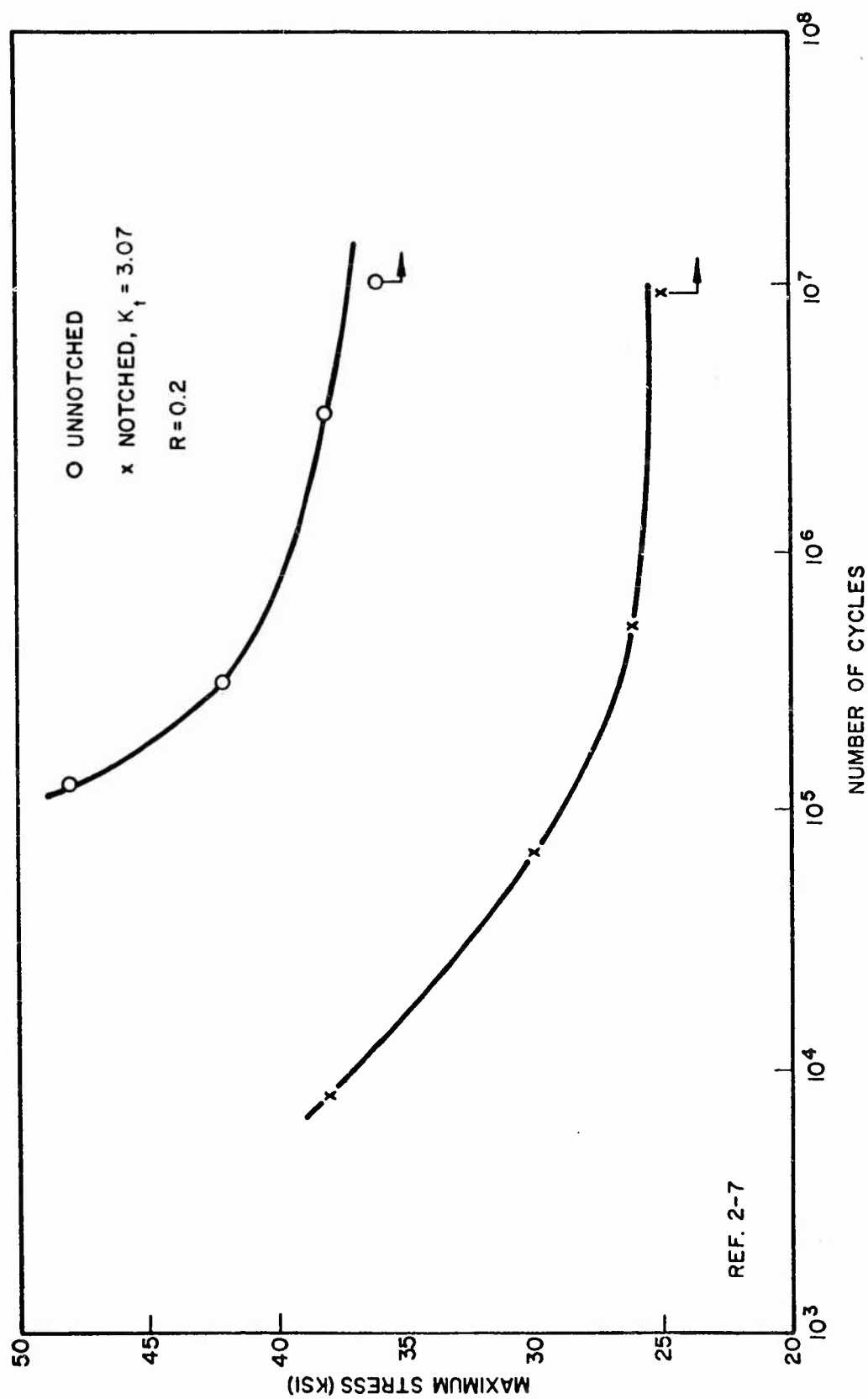


Fig. 2-25 Axial S-N Curves for Hot-Pressed Beryllium Block at Room Temperature

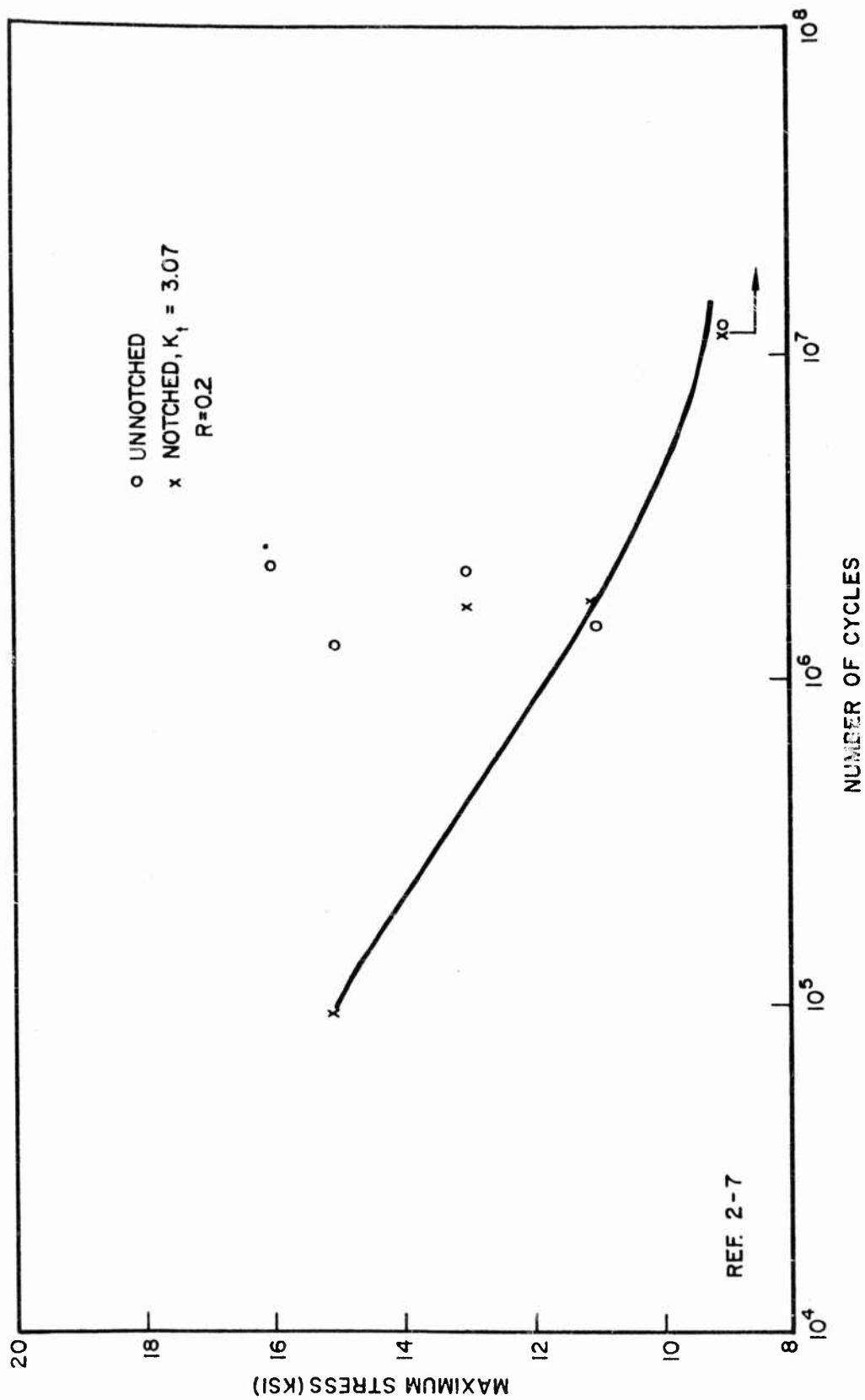


Fig. 2-26 Axial S-N Curves for Hot-Pressed Beryllium Block at 1100°F (1)

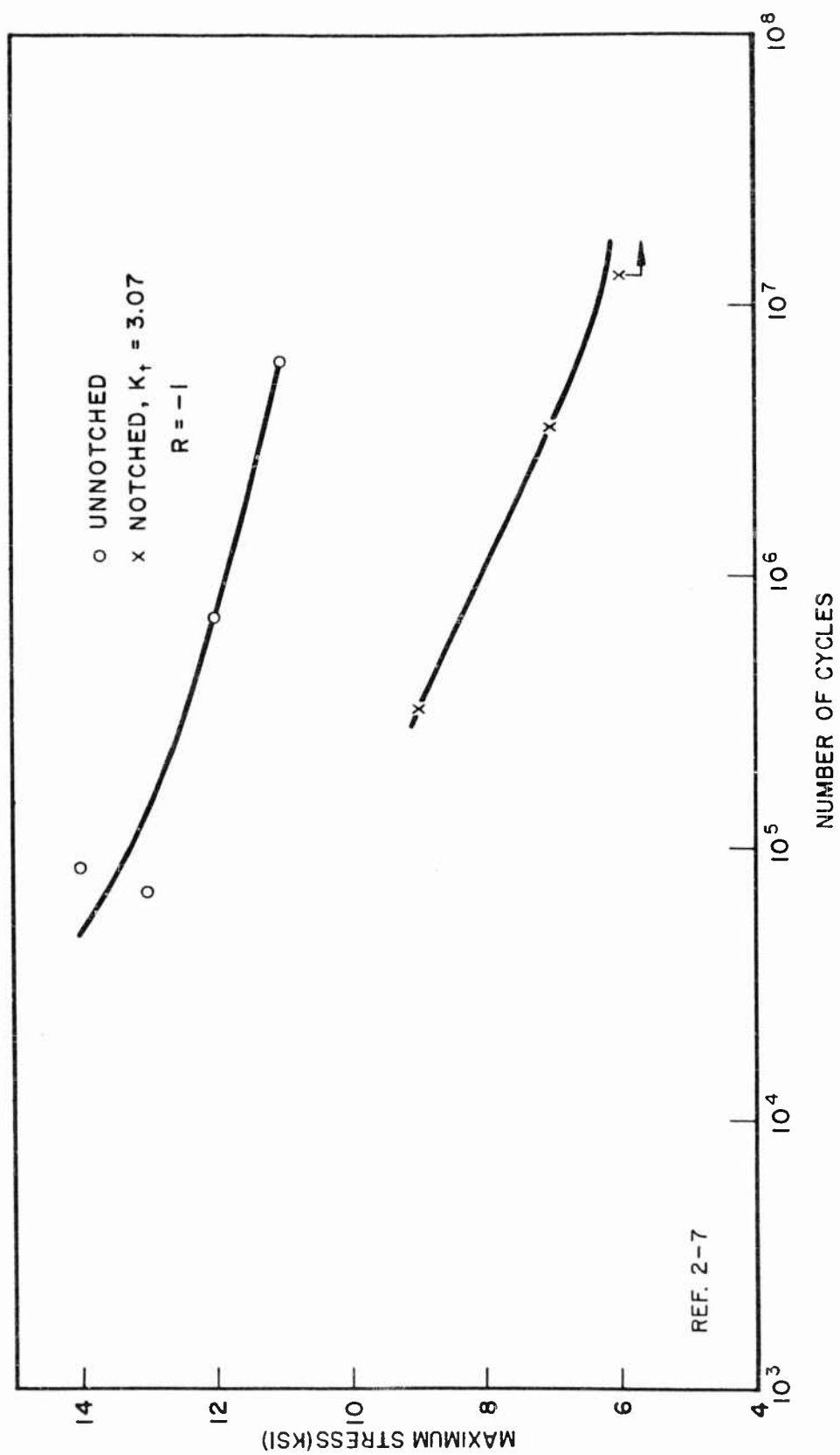


Fig. 2-27 Axial S-N Curves for Hot-Pressed Beryllium Block at 1100°F (2)

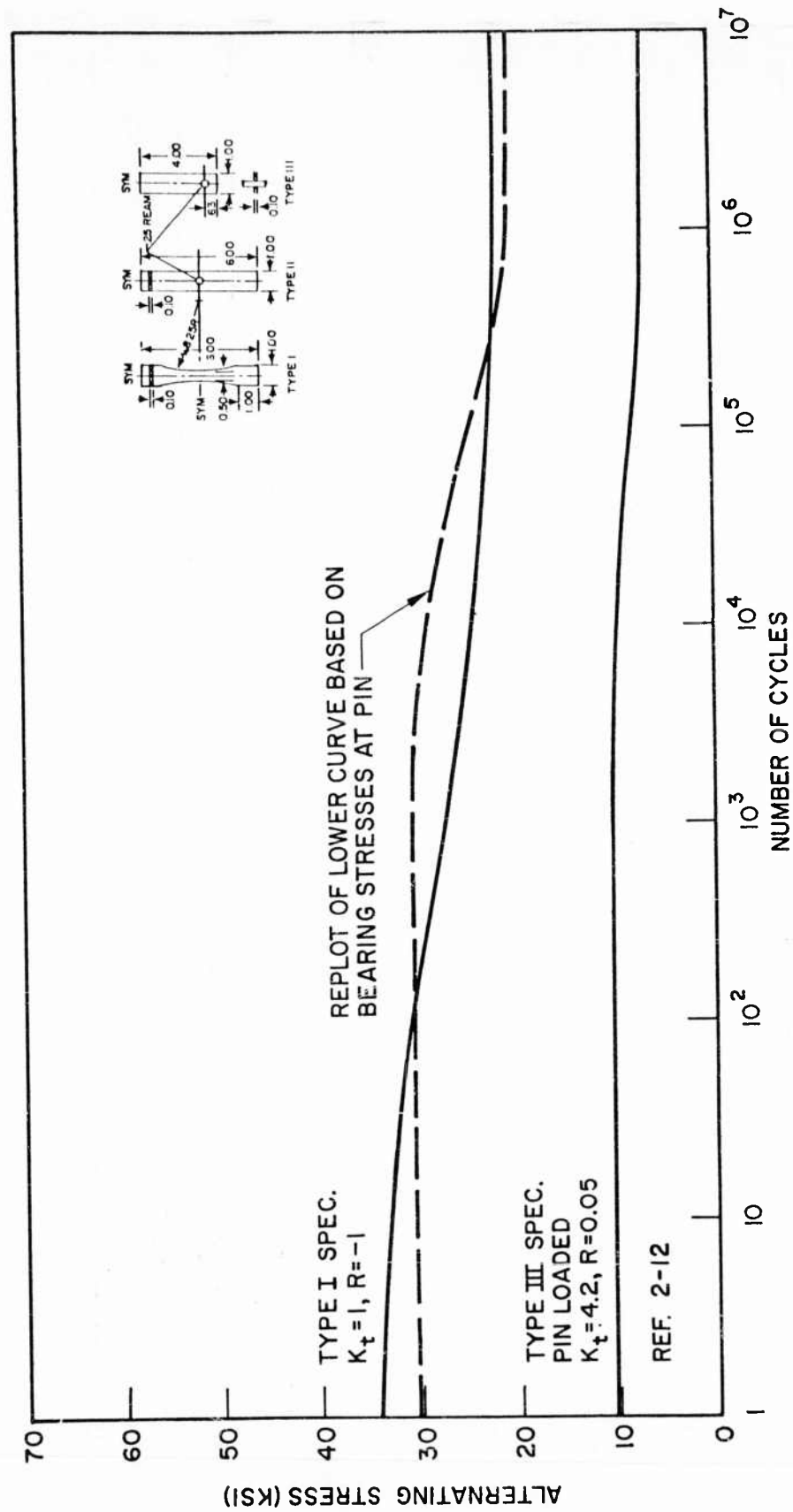


Fig. 2-28 Axial S-N Curves for Hot-Pressed Beryllium Block at Room Temperature (1)

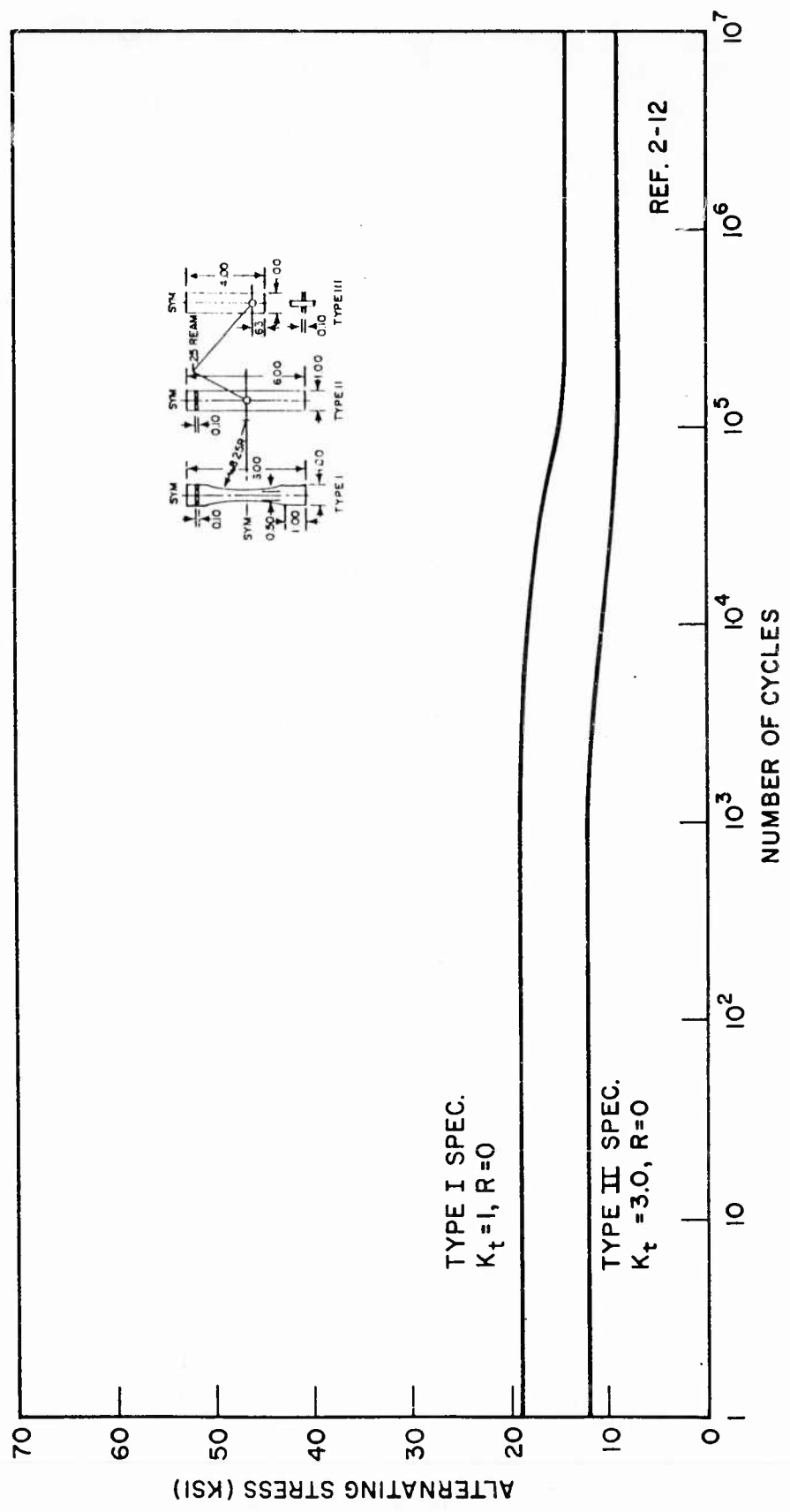


Fig. 2-29 Axial S-N Curves for Hot-Pressed Beryllium Block at Room Temperature (2)

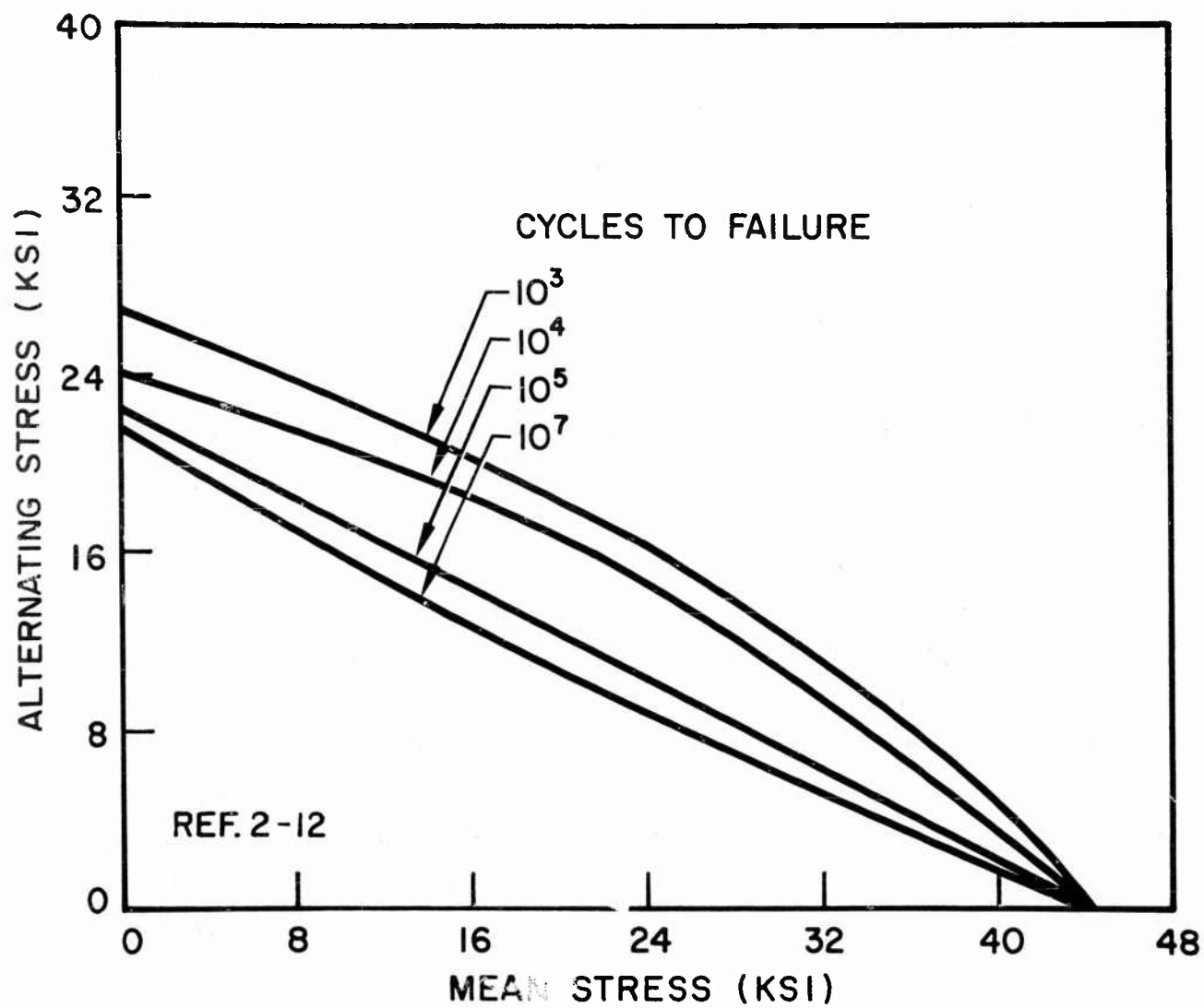


Fig. 2-30 Effect of Mean Stress on the Axial Fatigue Behavior of Unnotched Hot-Pressed Beryllium Block at Room Temperature

Further data at elevated temperatures are given in Fig. 2-31 at 800°F, and Fig. 2-32 at 1200°F. Both of these figures are taken from Ref. 2-13 and cover unnotched specimens having $R = 0$ and -1.0 . They are presented in terms of maximum stress and for a testing frequency of 30 cps. When Fig. 2-32 is compared with Fig. 2-27 for the case $K_t = 1.0$, $R = -1.0$, the approximate effect of testing frequency at elevated temperature may be determined. For a given maximum stress and stress ratio, it is seen that the number of cycles to failure increases with increasing testing frequencies.

Figures 2-33 through 2-37 present information on the fatigue characteristics of joints fabricated from hot-pressed beryllium block. Three types of joints are investigated — those having 2, 4, and 5 fasteners. Sketches showing the arrangement of the fasteners for each type of joint are presented in Fig. 2-33.

All specimens were tested in tension with steel loading and splice plates as shown in Fig. 2-34. Figure 2-35 presents room-temperature data on these types of joints where 3/16-in.-diam. NAS-517 steel screws have been machine countersunk in 1/4-in.-thick beryllium. Likewise, Fig. 2-36 gives data for 1/4-in.-diam. F-260 steel Jo-Bolts machine countersunk in the same thickness of beryllium. Figure 2-37 presents data for the same fastener-thickness combination as in Fig. 2-35 except that the fastener is 1/4 in. in diameter. The stresses shown in these figures are based on net area. The details of the testing are reported in Ref. 2-14. From this reference it can be seen that considerable scatter is present in the curves, and that the curves are drawn along the lower boundary of the scatter. Several types of failure were experienced, including beryllium-sheet failure through the holes, beryllium-sheet failure away from the holes, and beryllium-to-steel bolt shear. The first type of failure was the most common and was of the net tension type rather than the shear tear-out type. In a number of the 4- and 5-fastener specimens, failure occurred through the back row of holes, indicating that the eccentricity of the joint may be an important factor in fatigue strength.

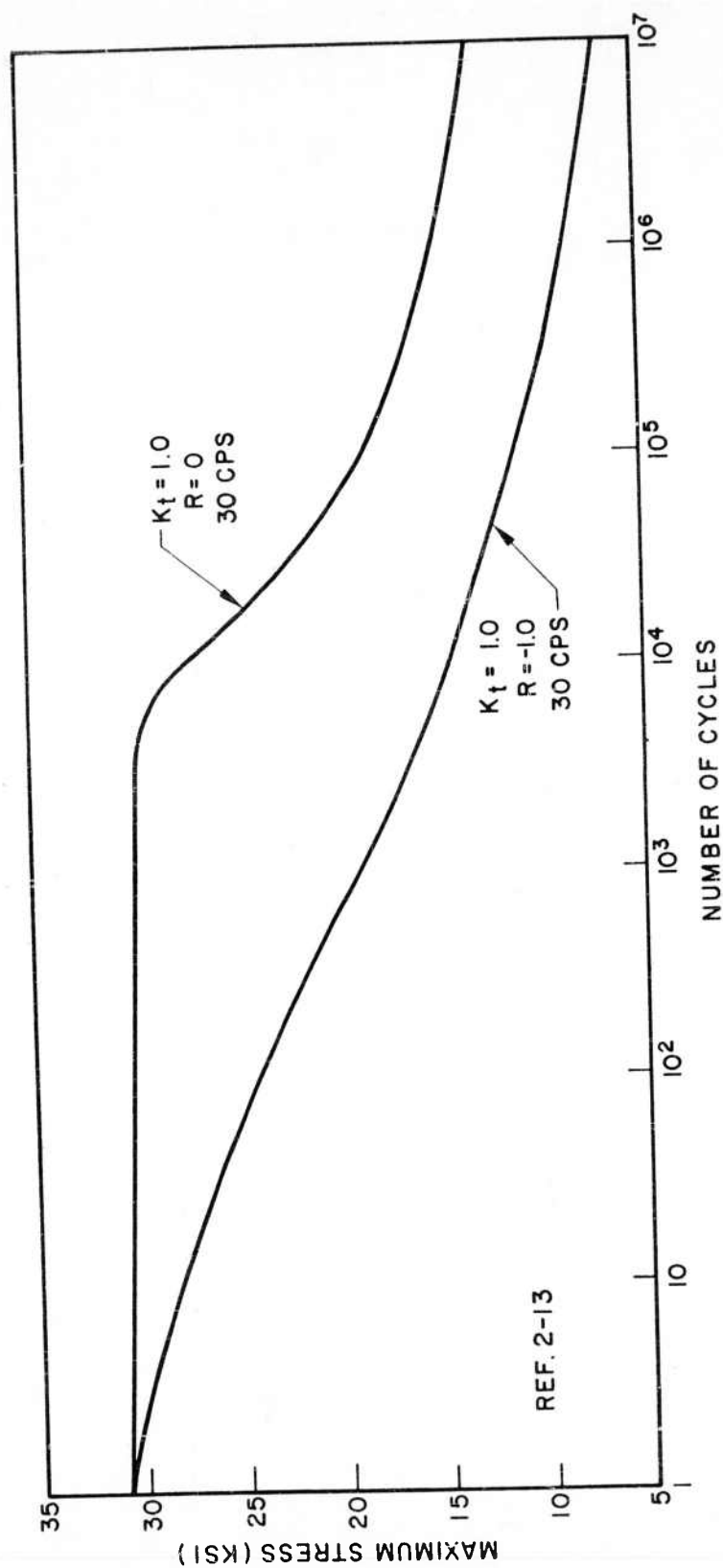


Fig. 2-31 Axial S-N Curves for Hot-Pressed Beryllium Block at 800°F

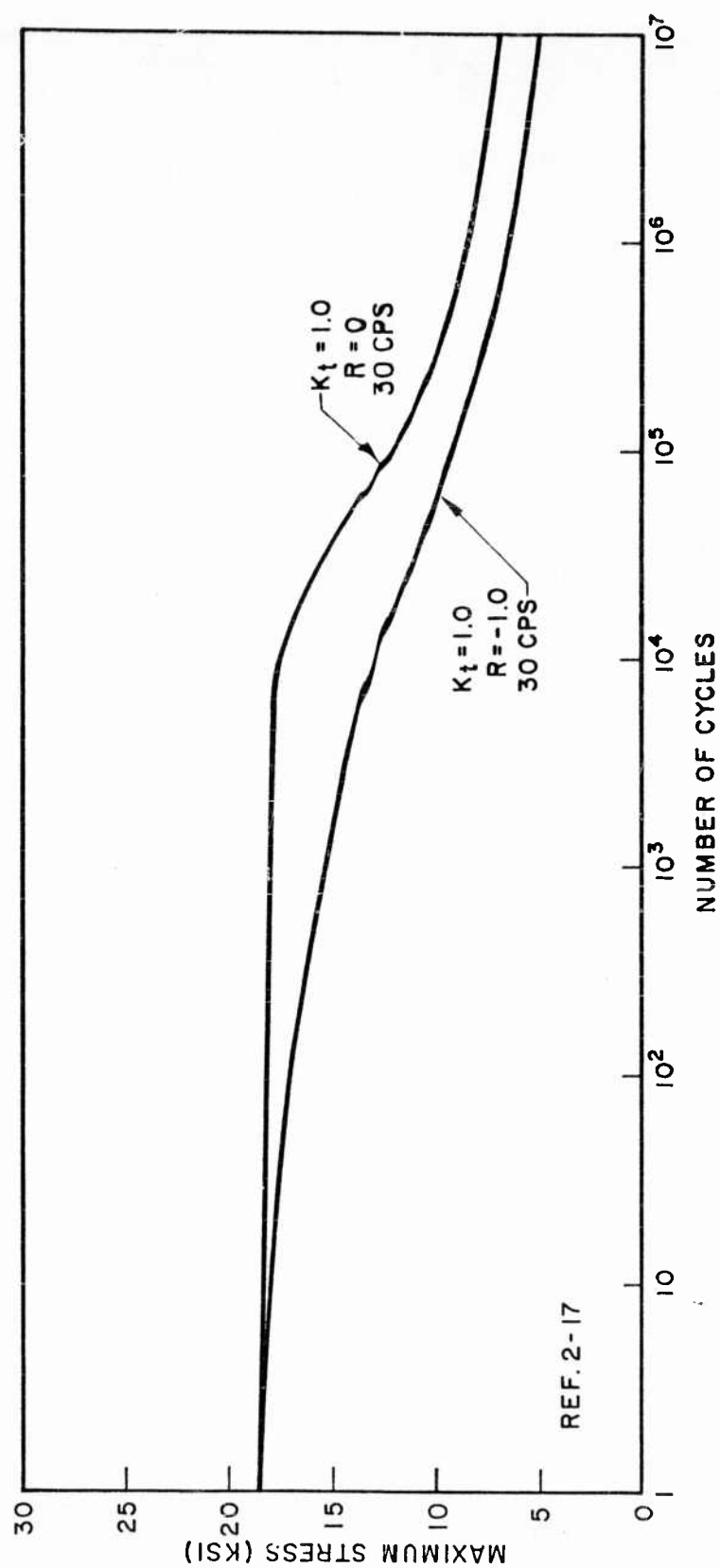


Fig. 2-32 Axial S-N Curves for Hot-Pressed Beryllium Block at 1200°F

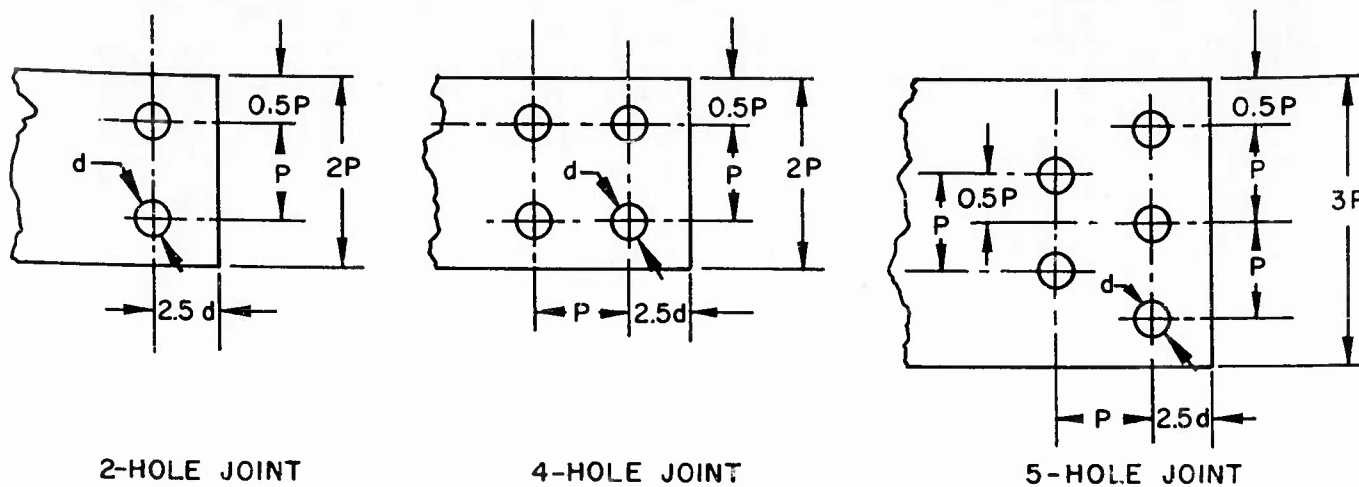


Fig. 2-33. Geometry for 2, 4, and 5 Fastener Joints

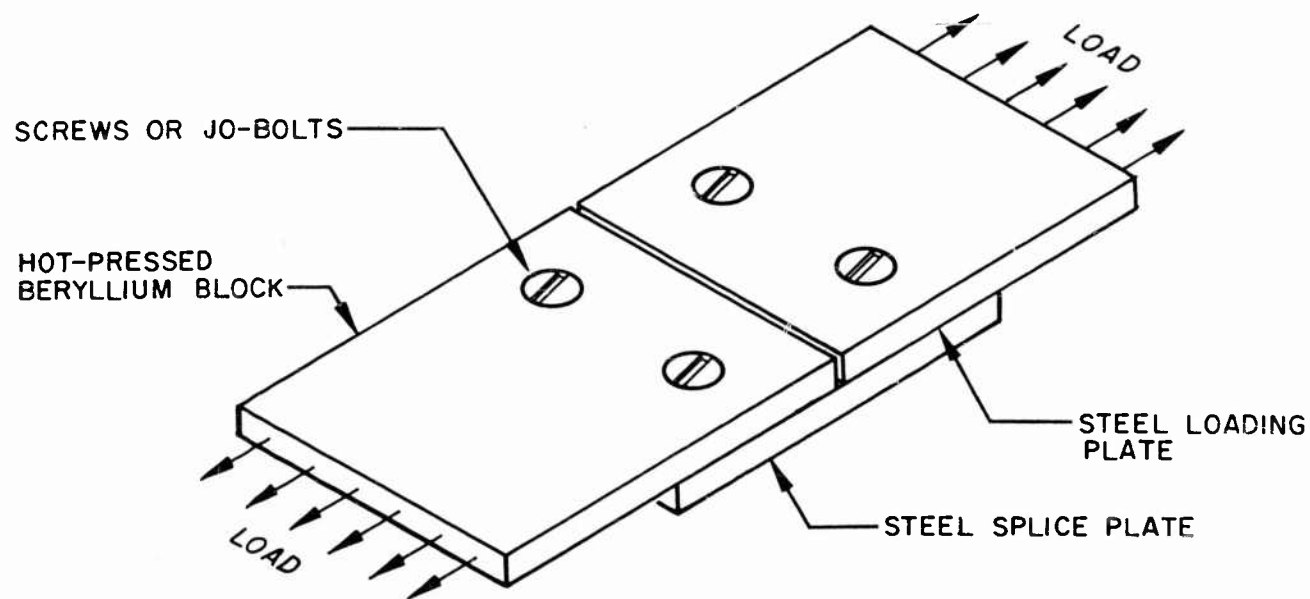


Fig. 2-34 Arrangement for Beryllium Axial Fatigue Joint Tests

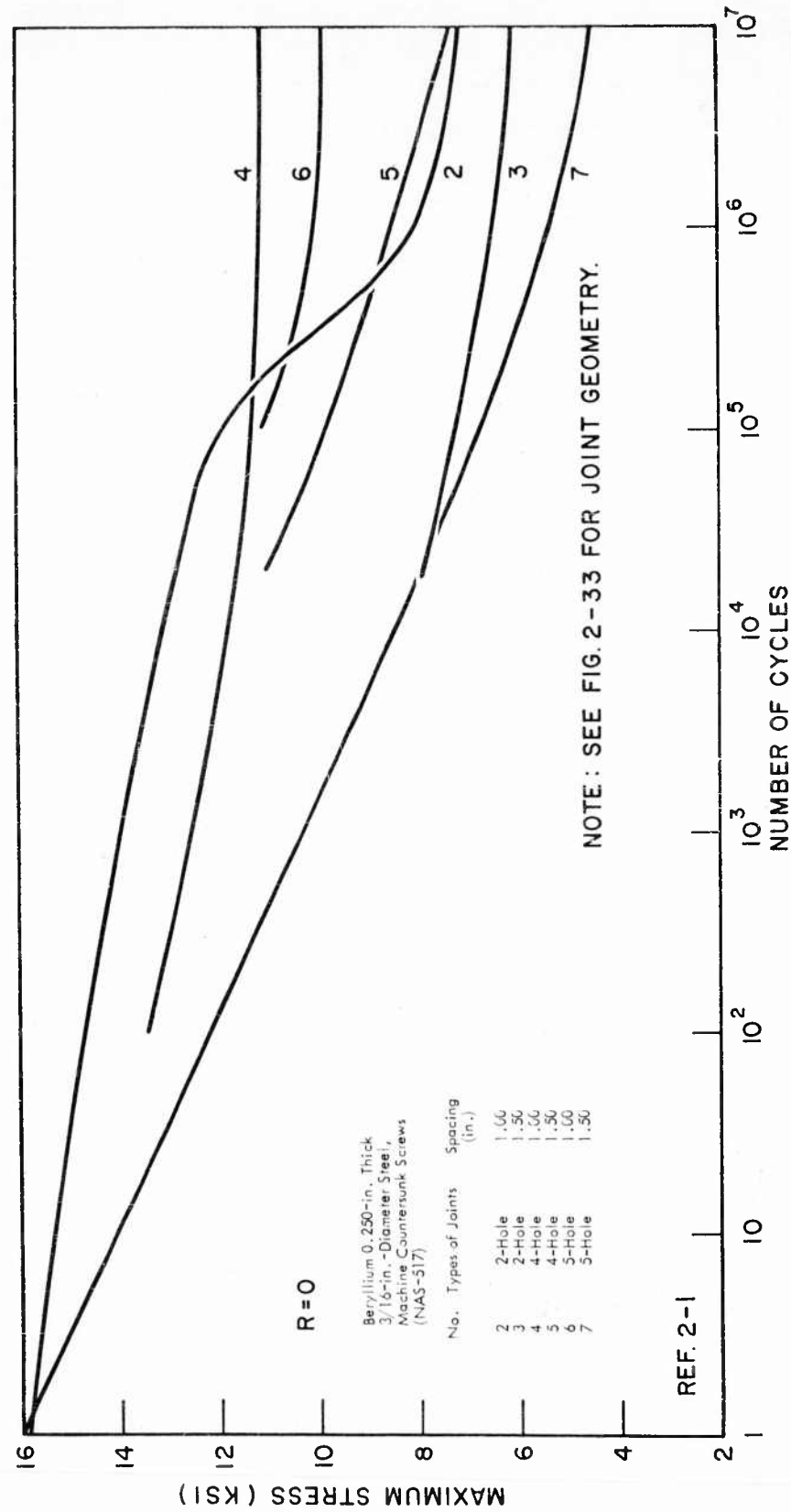


Fig. 2-35 Axial S-N Curves for Hot-Pressed Beryllium Block Joints With 3/16-in. Steel Countersunk Screws at Room Temperature

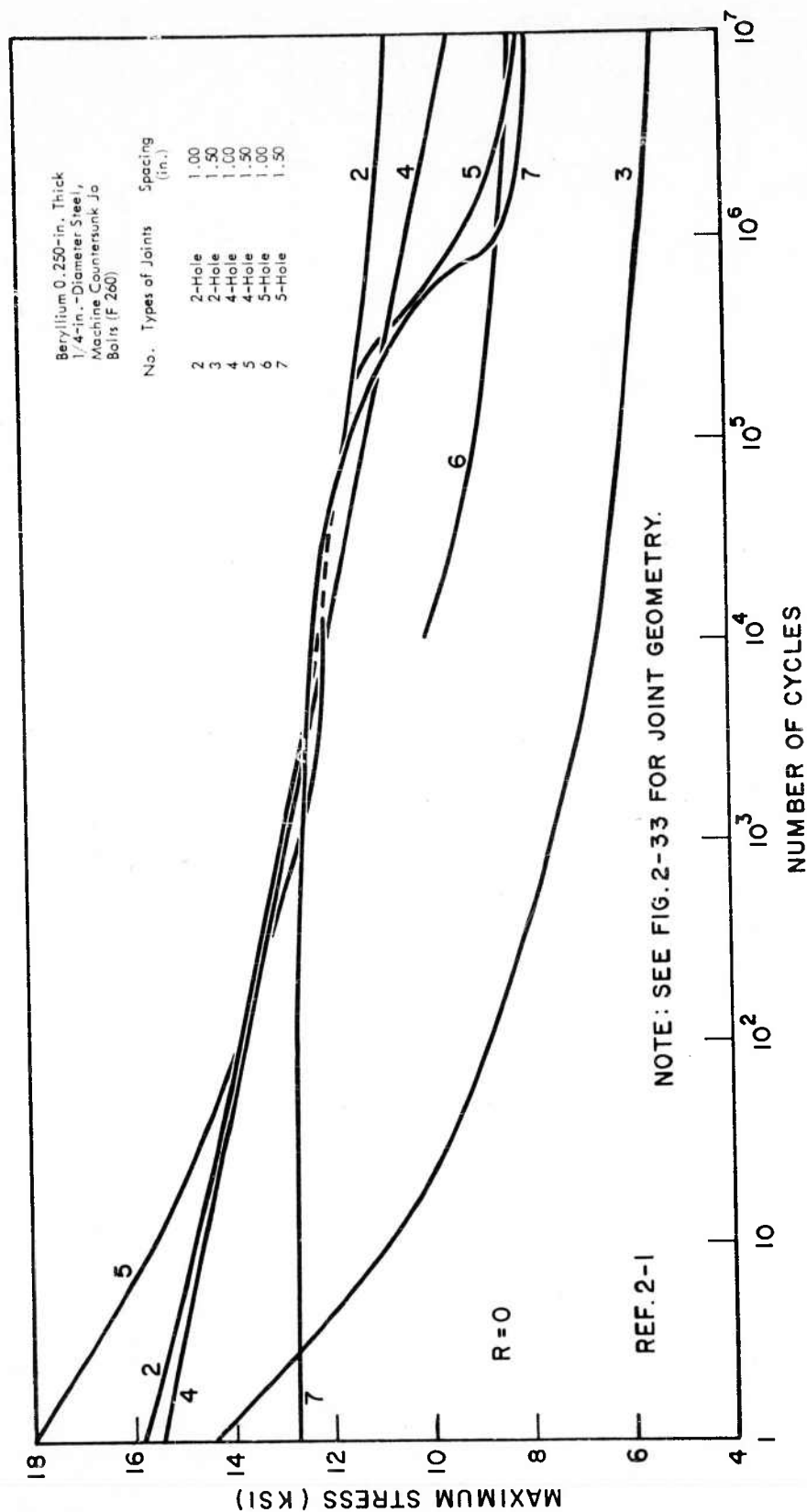


Fig. 2-36 Axial S-N Curves for Hot-Pressed Beryllium Block Joints With 1/4-in. Steel Countersunk Jo-Bolts at Room Temperature

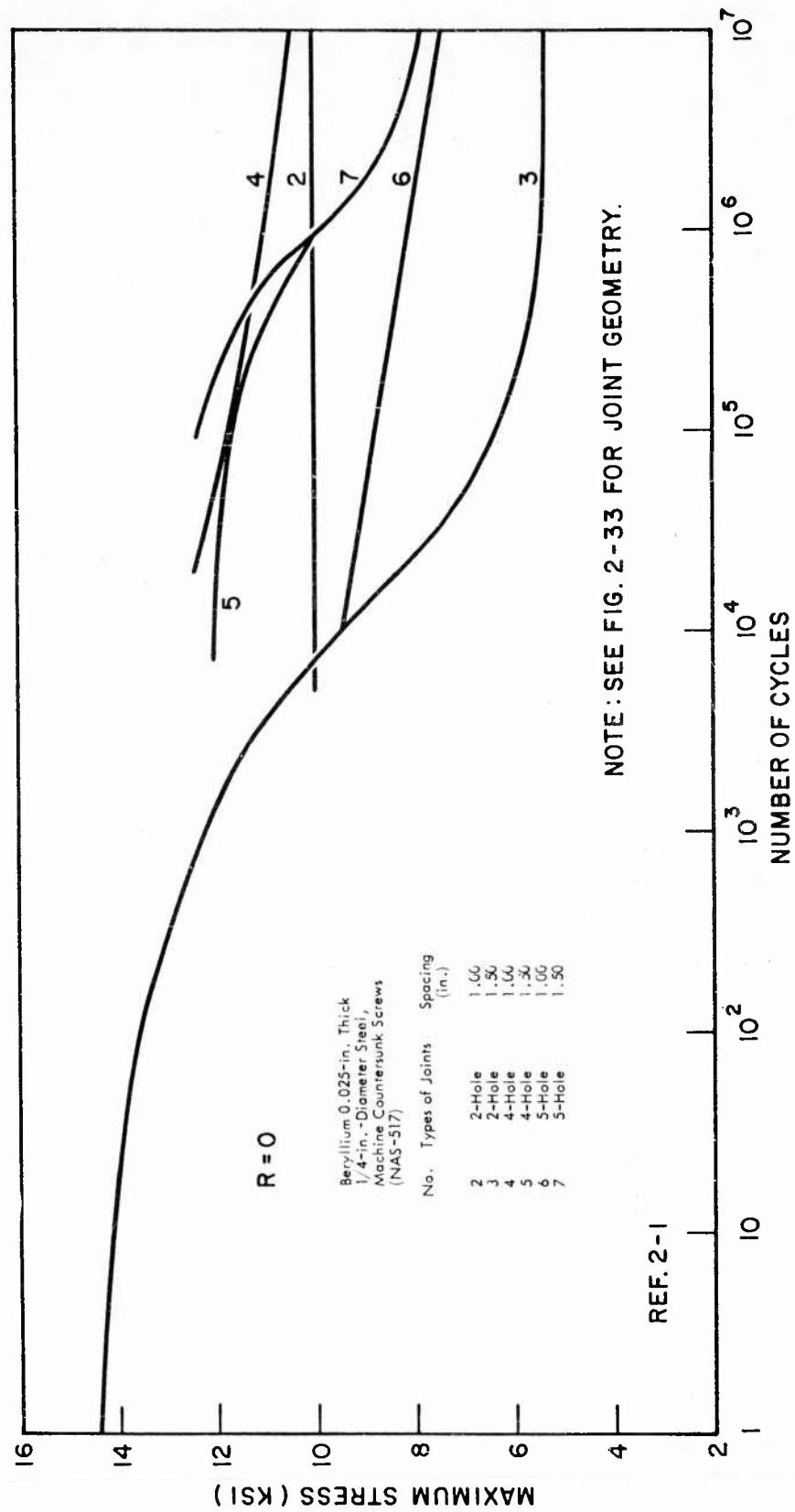


Fig. 2-37 Axial S-N Curves for Hot-Pressed Beryllium Block Joints With 1/4-in. Steel Countersunk Screws at Room Temperature

Figures 2-38 through 2-41 present creep data for hot-pressed beryllium block. Figure 2-38 presents curves for several levels of total deformation at 1000°F. Similarly, Figs. 2-39 and 2-40 present creep data at 1250°F and 1500°F, respectively. These figures are taken from Ref. 2-15. A stress-rupture curve at 1100°F is presented in Fig. 2-41 as taken from Ref. 2-7.

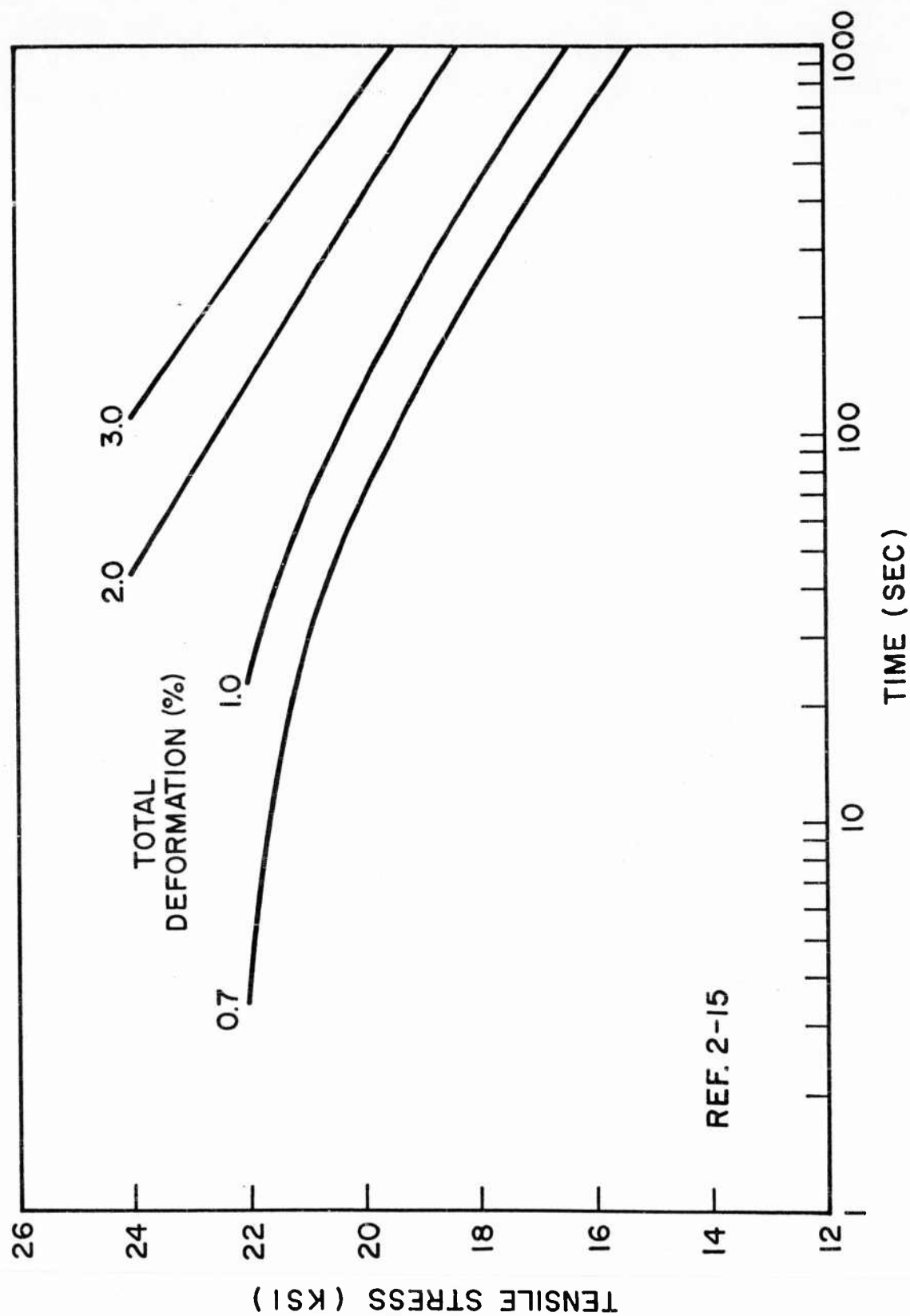


Fig. 2-38 Creep Curves for Hot-Pressed Beryllium Block at 1000°F

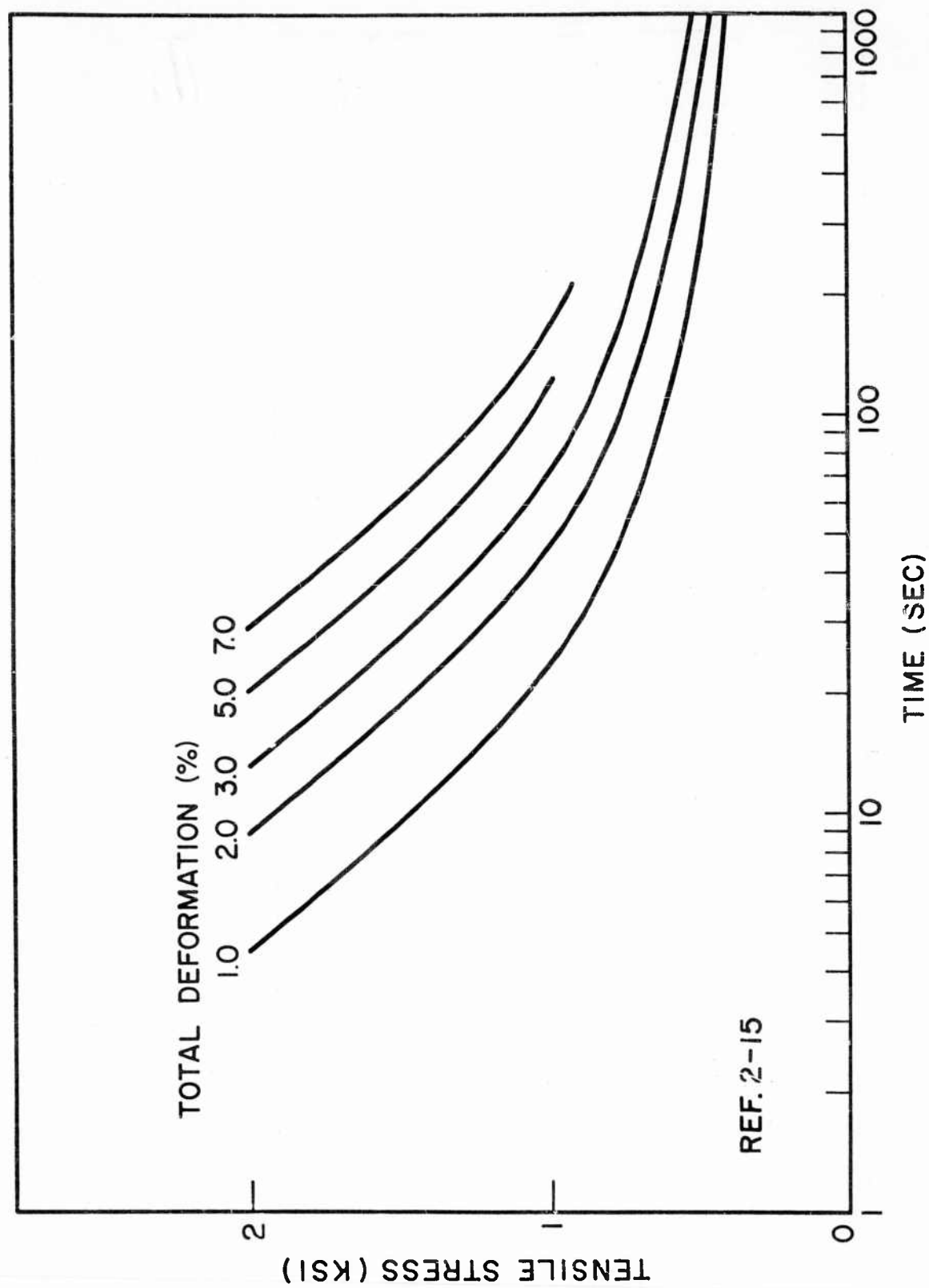


Fig. 2-39 Creep Curves for Hot-Pressed Beryllium Block at 1250°F

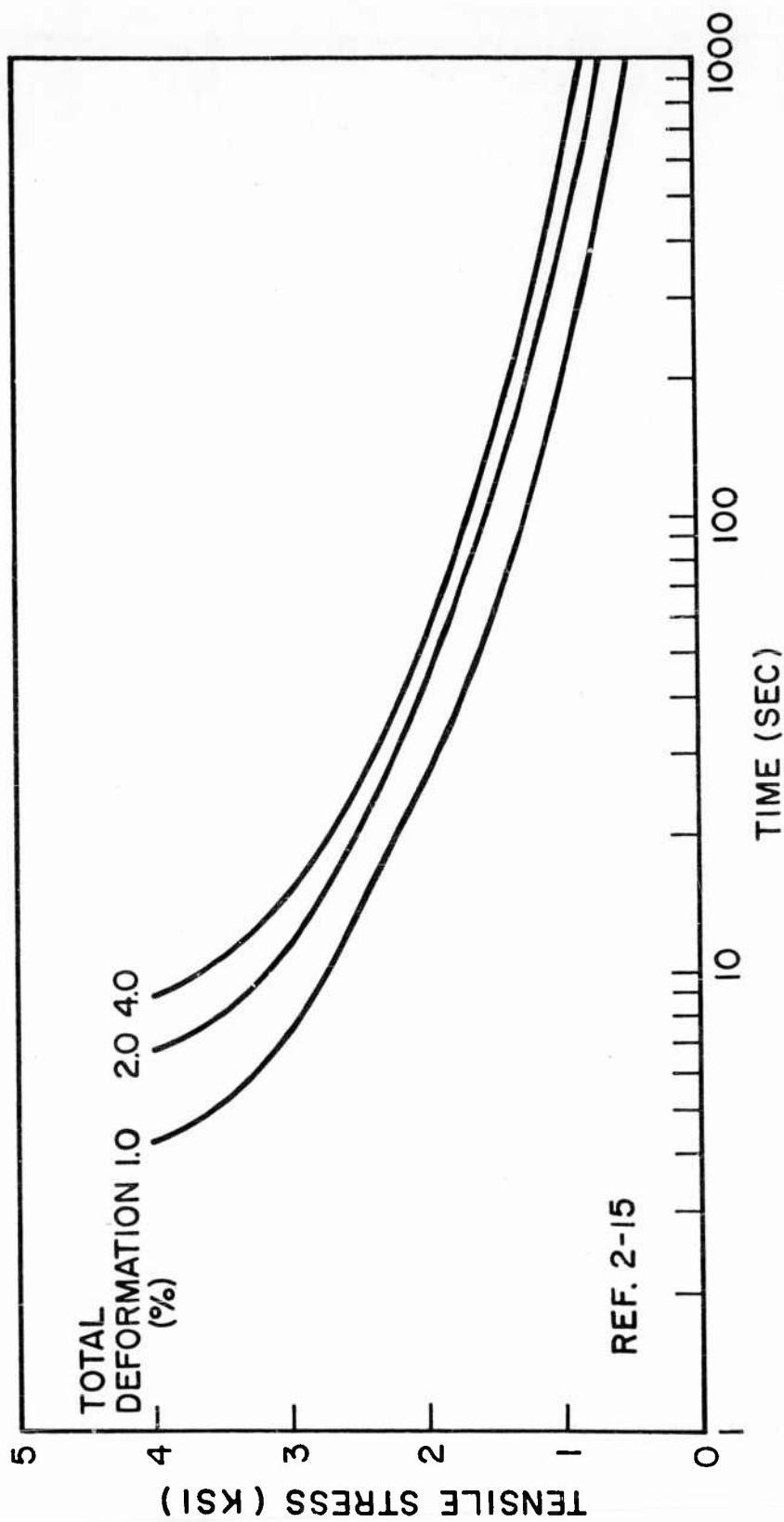


Fig. 2-40 Creep Curves for Hot-Pressed Beryllium Block at 1500°F

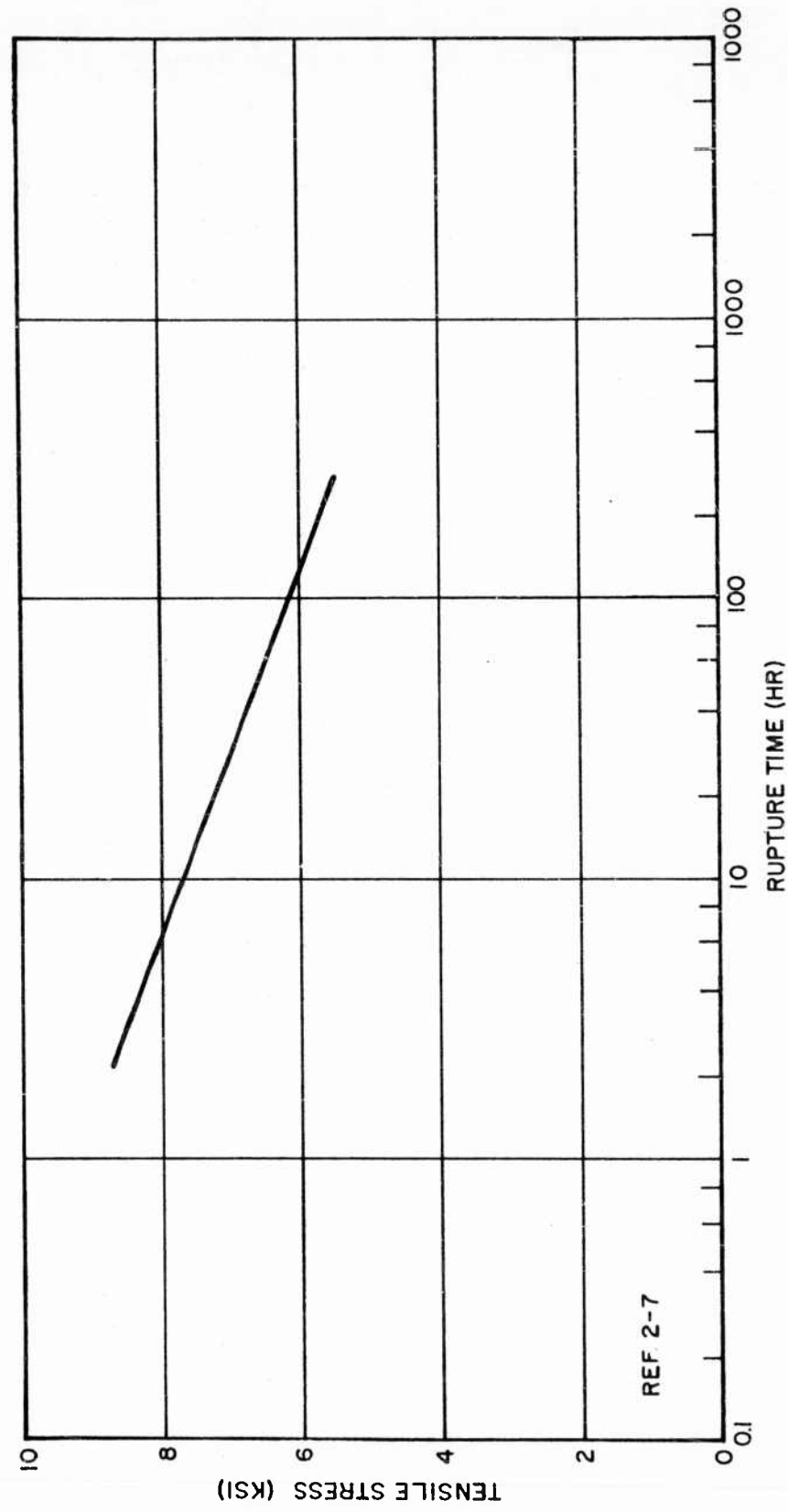


Fig. 2-41 Stress-Rupture Curve for Hot-Pressed Beryllium Block at 1100°F

2.3.2 Cross-Rolled Sheet

Typical design mechanical properties for cross-rolled beryllium sheet are presented in Table 2-2 for room temperature, and in Figs. 2-42 through 2-55 for elevated temperatures. This information is not as complete as that for hot-pressed beryllium block, owing to the shorter period of time that cross-rolled sheet has been commercially available and the commensurate scarcity of published data. All information currently known to exist is included in the table and figures.

The tensile properties of cross-rolled beryllium sheet are the best documented mechanical properties of this material at the present time. Those appearing in Table 2-2 are based on a considerable amount of data and are felt to be quite firm. The tensile properties at elevated temperatures are presented with source references designated on the figures. Considerable variance exists among sources which is probably brought about by the experimental status of the material tested. An average of the extreme maximum and minimum stresses shown for a given temperature is suggested for design purposes. Figure 2-42 presents ultimate tensile stress versus temperature for material tested parallel to the longitudinal grain direction. Figure 2-43 gives ultimate tensile strength in the transverse-grain direction as a function of temperature. The variation of tensile yield-stress with temperature is shown for the longitudinal-grain direction in Fig. 2-44, and for the transverse-grain direction in Fig. 2-45.

The ultimate shear stress of cross-rolled beryllium sheet as a function of temperature is presented in Fig. 2-46, while ultimate- and yield-bearing stresses versus temperature are given in Fig. 2-47. The bearing stresses given in Fig. 2-47 represent the results of an evaluation by LMSC of Ref. 2-5 and associated unpublished data from Thermatest Laboratories. Reference 2-5 reports on bearing tests performed with 3/16-in., 1/4-in., and 5/16-in. -diam. pins and a constant edge distance e equal to 0.5 in. A trend in these data as a function of e/D is not apparent, as was the case in similar tests reported in this same reference for hot-pressed beryllium block

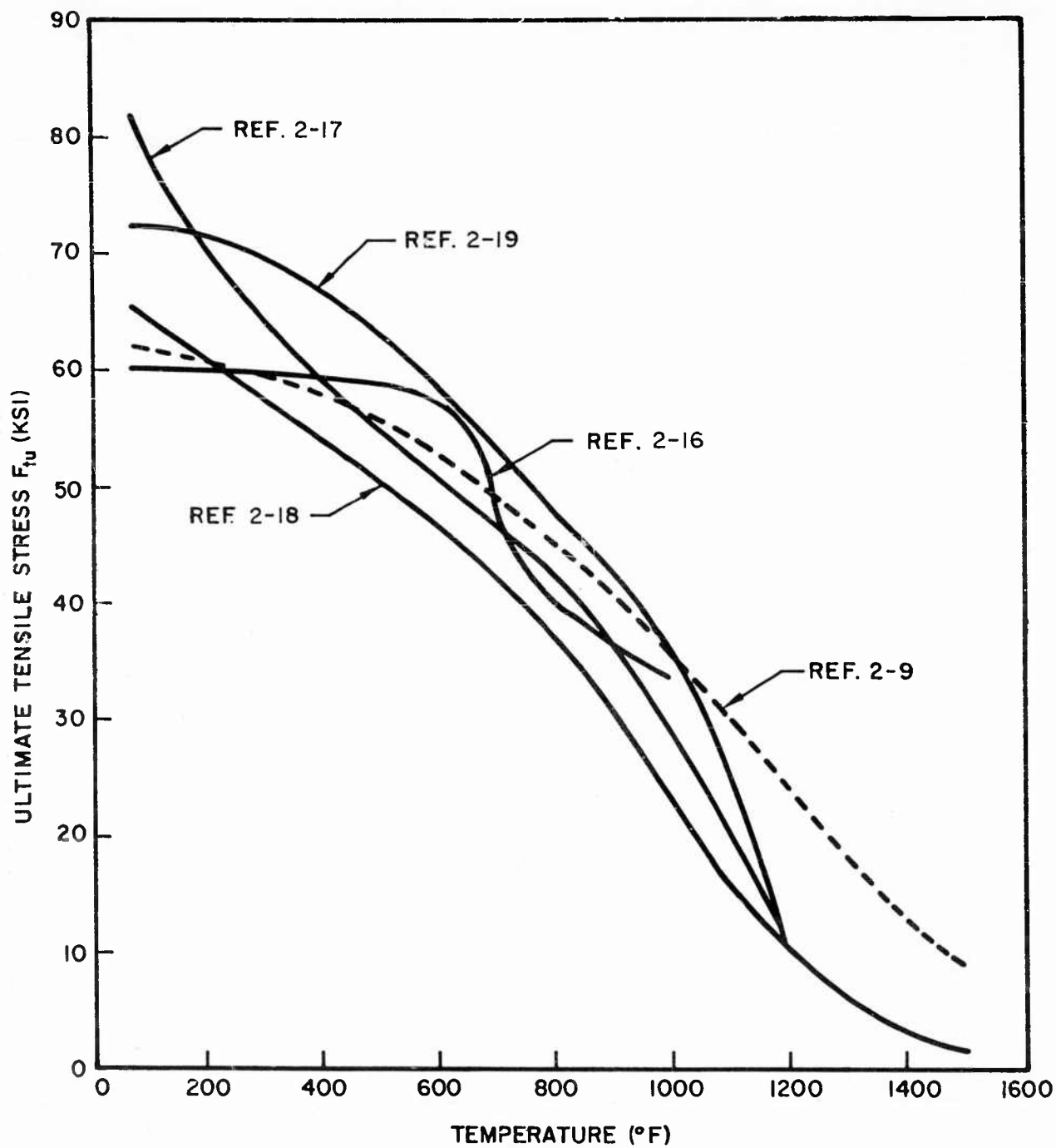


Fig. 2-42 Effect of Temperature on the Typical Longitudinal Ultimate Tensile Stress of Cross-Rolled Beryllium Sheet

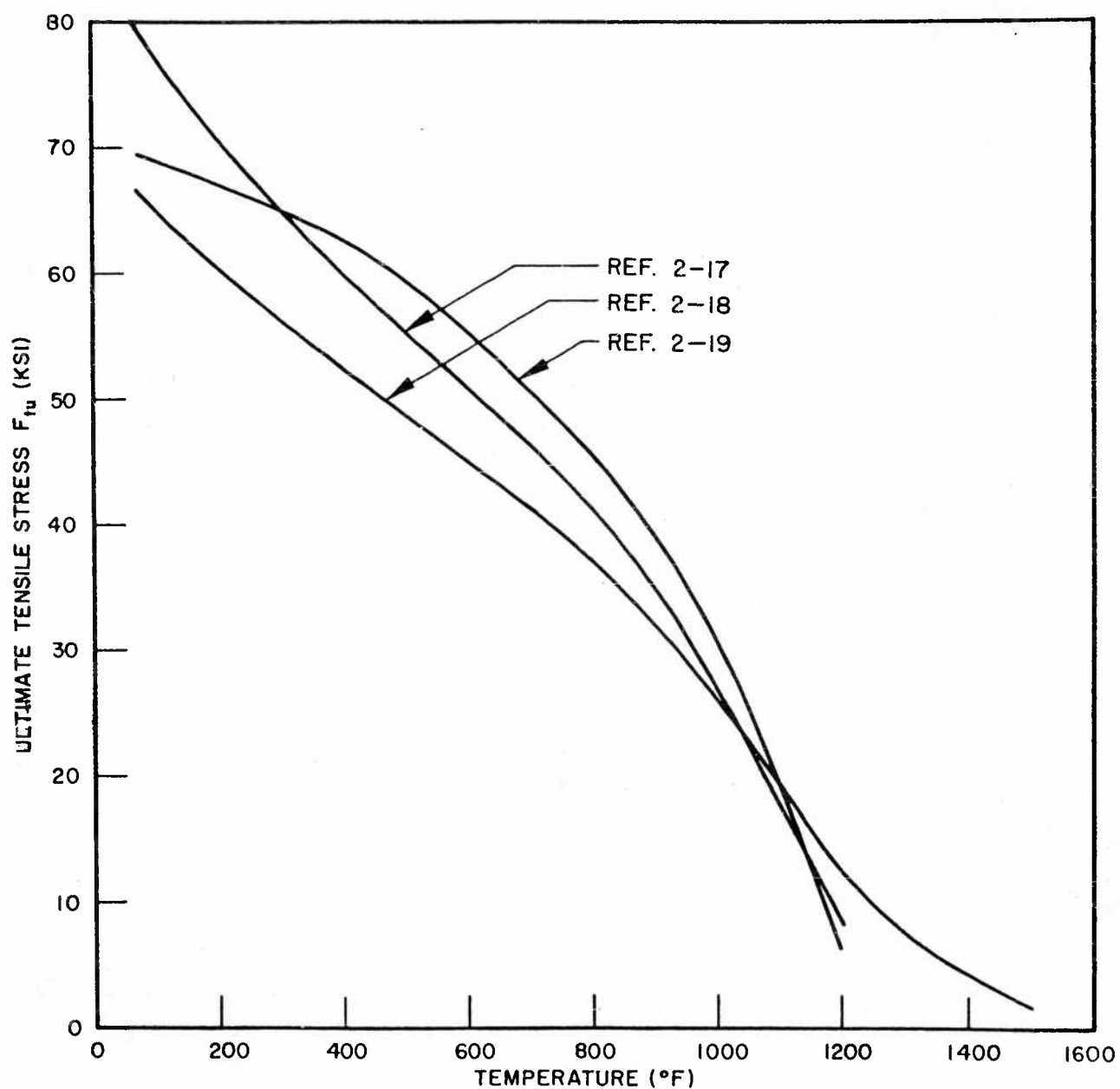


Fig. 2-43 Effect of Temperature on the Typical Transverse Ultimate Tensile Stress of Cross-Rolled Beryllium Sheet

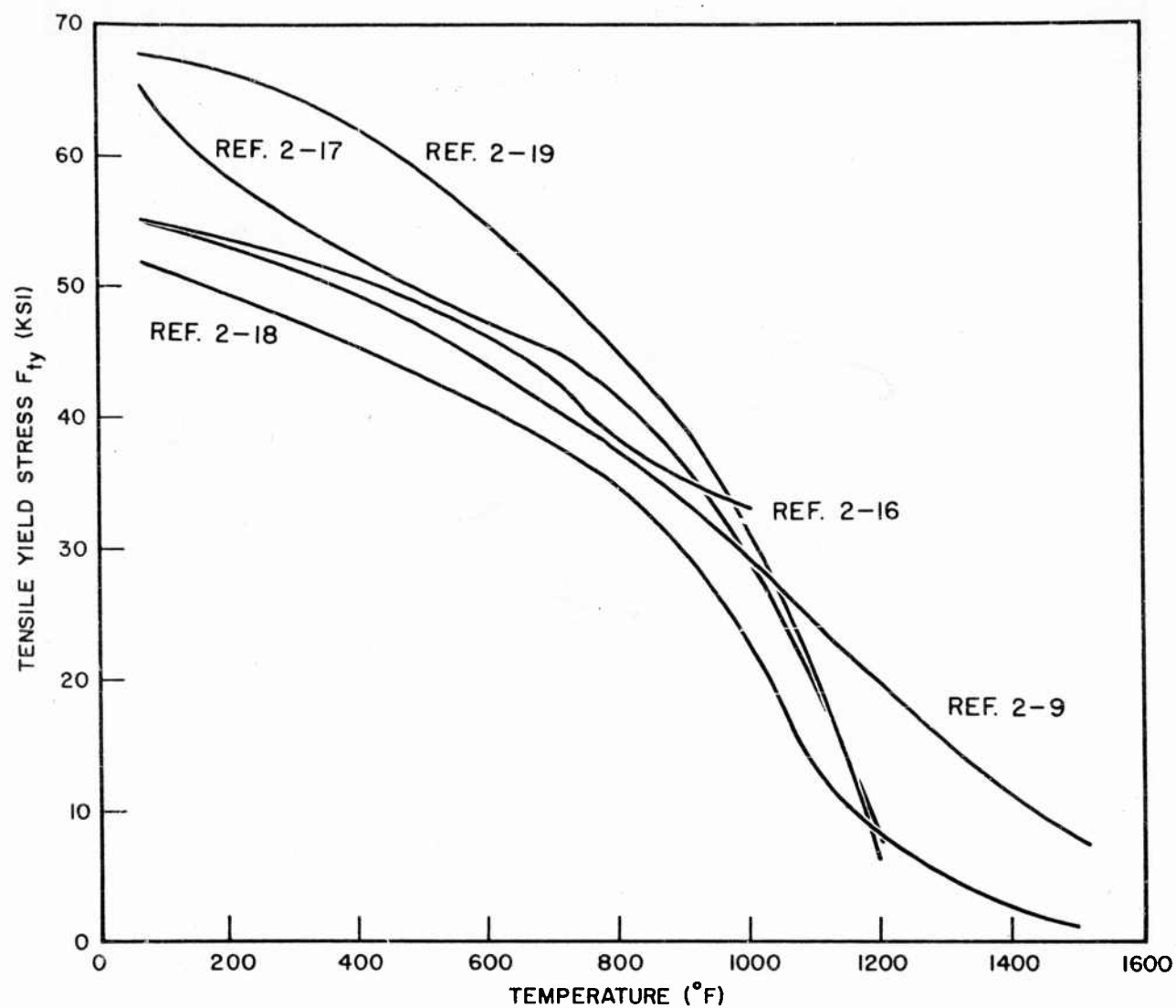


Fig. 2-44 Effect of Temperature on the Typical Longitudinal Tensile Yield-Stress of Cross-Rolled Beryllium Sheet

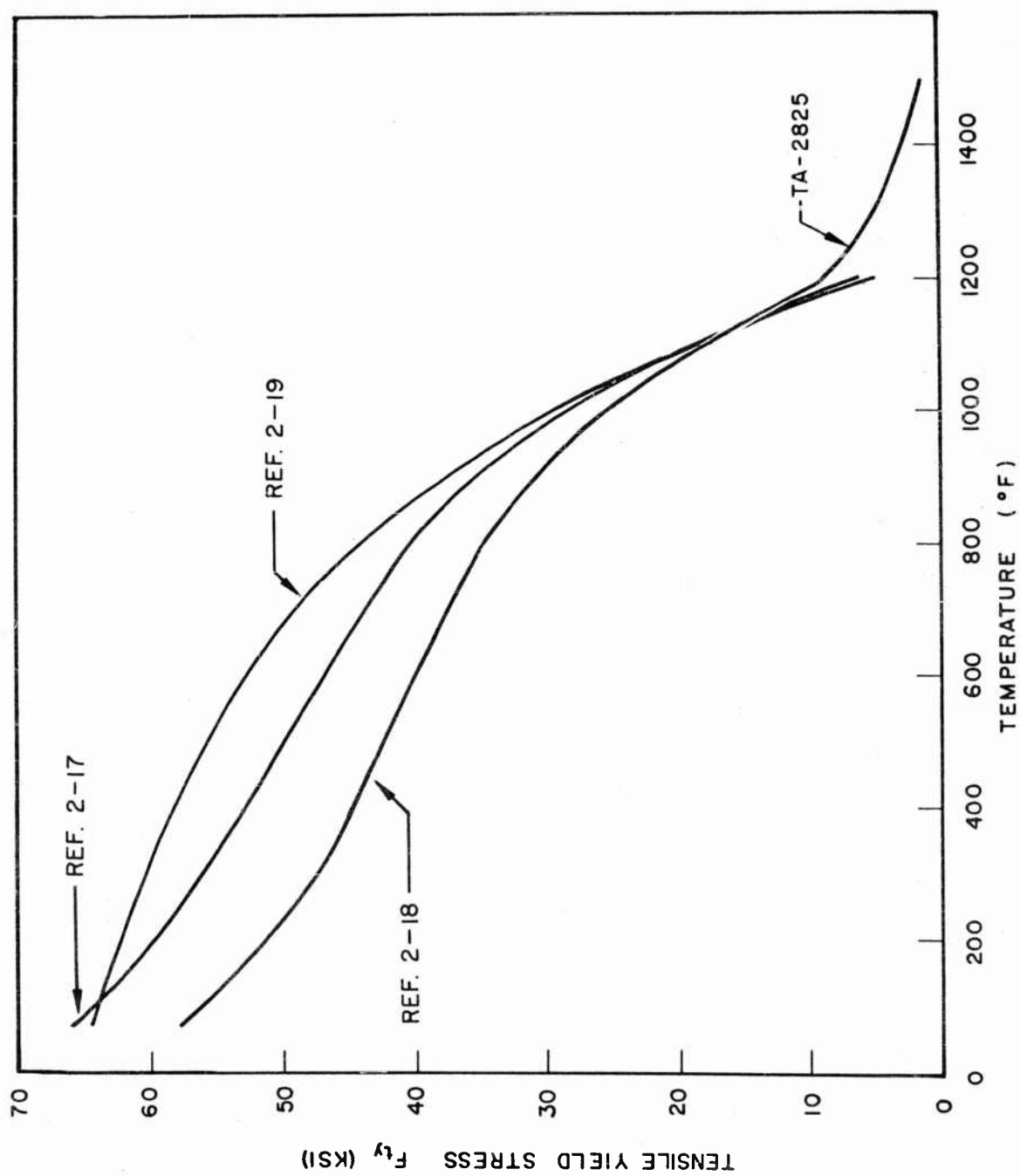


Fig. 2-45 Effect of Temperature on the Typical Transverse Tensile Yield-Stress of Cross-Rolled Beryllium Sheet

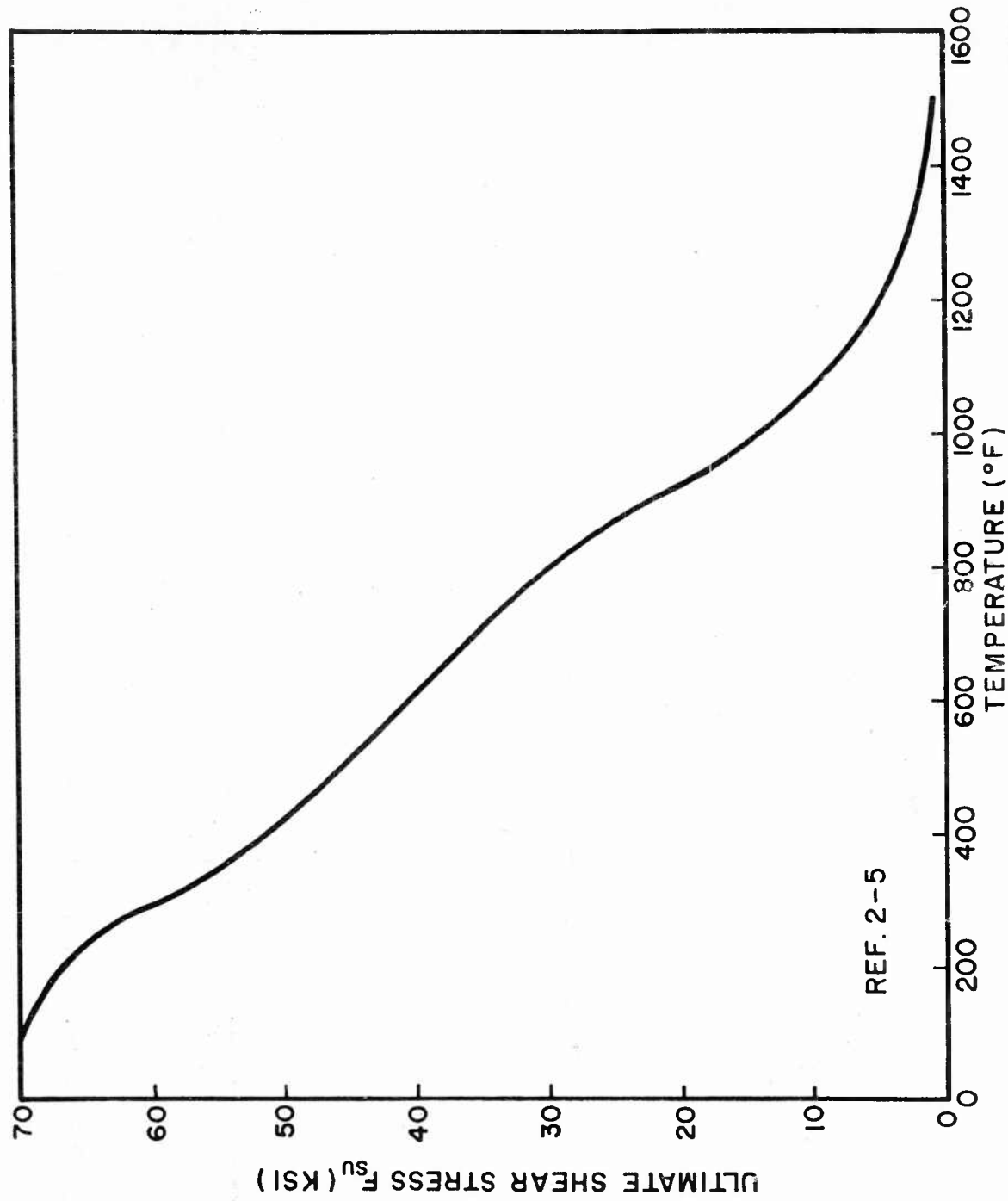


Fig. 2-46 Effect of Temperature on the Typical Ultimate Shear Stress of Cross-Rolled Beryllium Sheet (Shearing Normal to Plane of Sheet)

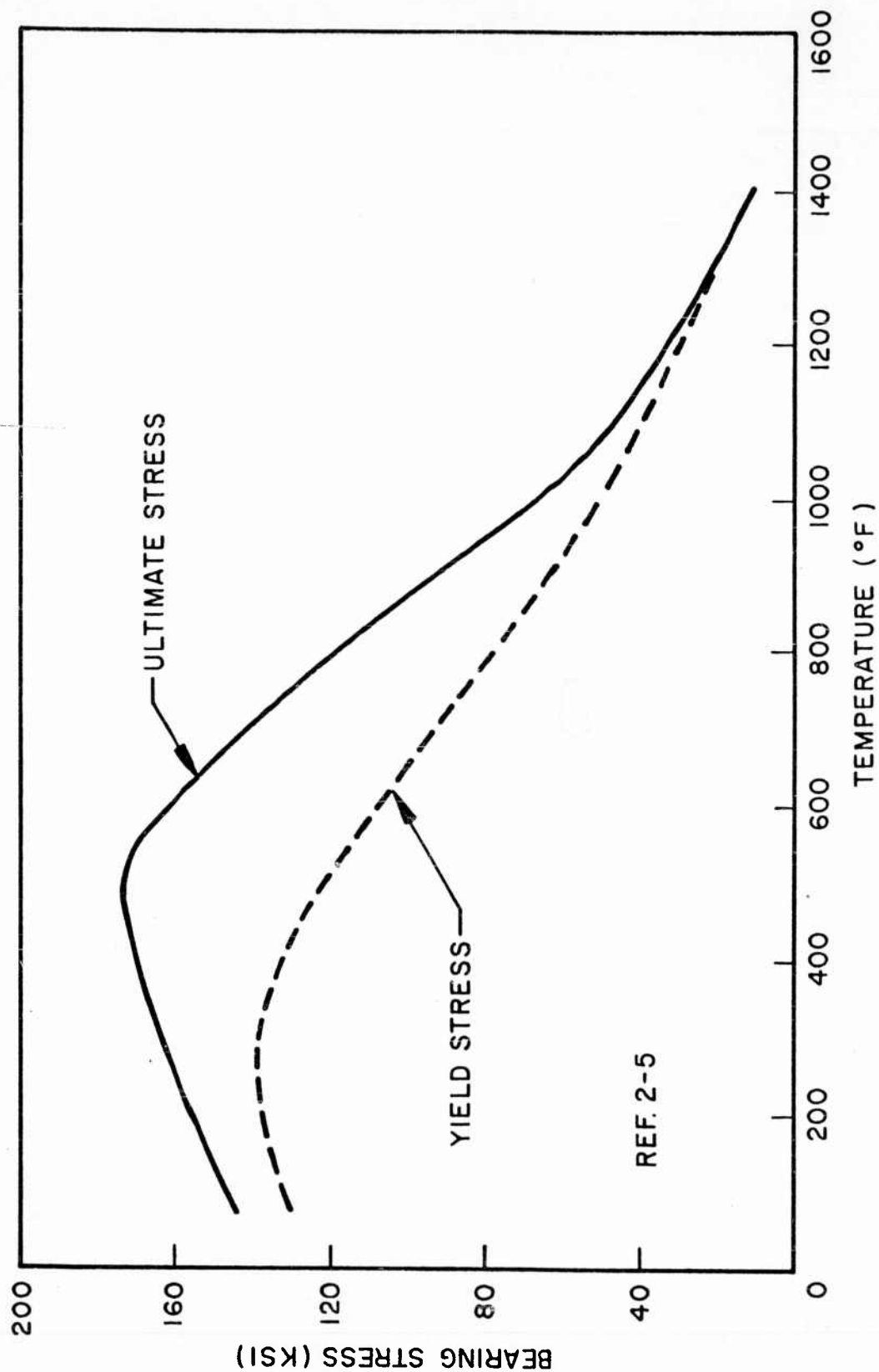


Fig. 2-47 Effect of Temperature on the Typical Bearing Stress of Cross-Rolled Beryllium Sheet

(see Figs. 2-16 through 2-18). Figure 2-47 may therefore be considered typical for the e/D range encompassed by these tests; namely, from 1.6 to 2.67 in.

The variation of the tensile elongation in the longitudinal grain direction of cross-rolled beryllium sheet with temperature is presented in Fig. 2-48. Note that these elongations are substantially greater than those given previously (Fig. 2-19) for hot-pressed beryllium block, and that the characteristic peak in the curve occurs at a slightly lower temperature.

Young's modulus versus temperature is presented in Fig. 2-49 as gathered from several references. The suggested design value is the average of the minimum and maximum values shown for a given temperature. The variation of the compressive modulus of elasticity with temperature is given in Fig. 2-50. Typical tensile stress-strain curves at various temperatures are presented in Fig. 2-51. Figure 2-52 shows some typical compressive stress-strain curves which were obtained from the Boeing Airplane Company (Ref. 2-10) and which are the only curves available. A tensile stress-strain curve obtained from the same lot of material is also shown. It appears, on the basis of this comparison, that the tensile and compressive stress-strain characteristics of the material are similar for a given lot.

Creep information for cross-rolled beryllium sheet is presented in Figs. 2-53 through 2-55. Figure 2-53 gives curves for various levels of total deformation at 1000°F. Figures 2-54 and 2-55 present similar information at 1250°F and 1500°F., respectively.

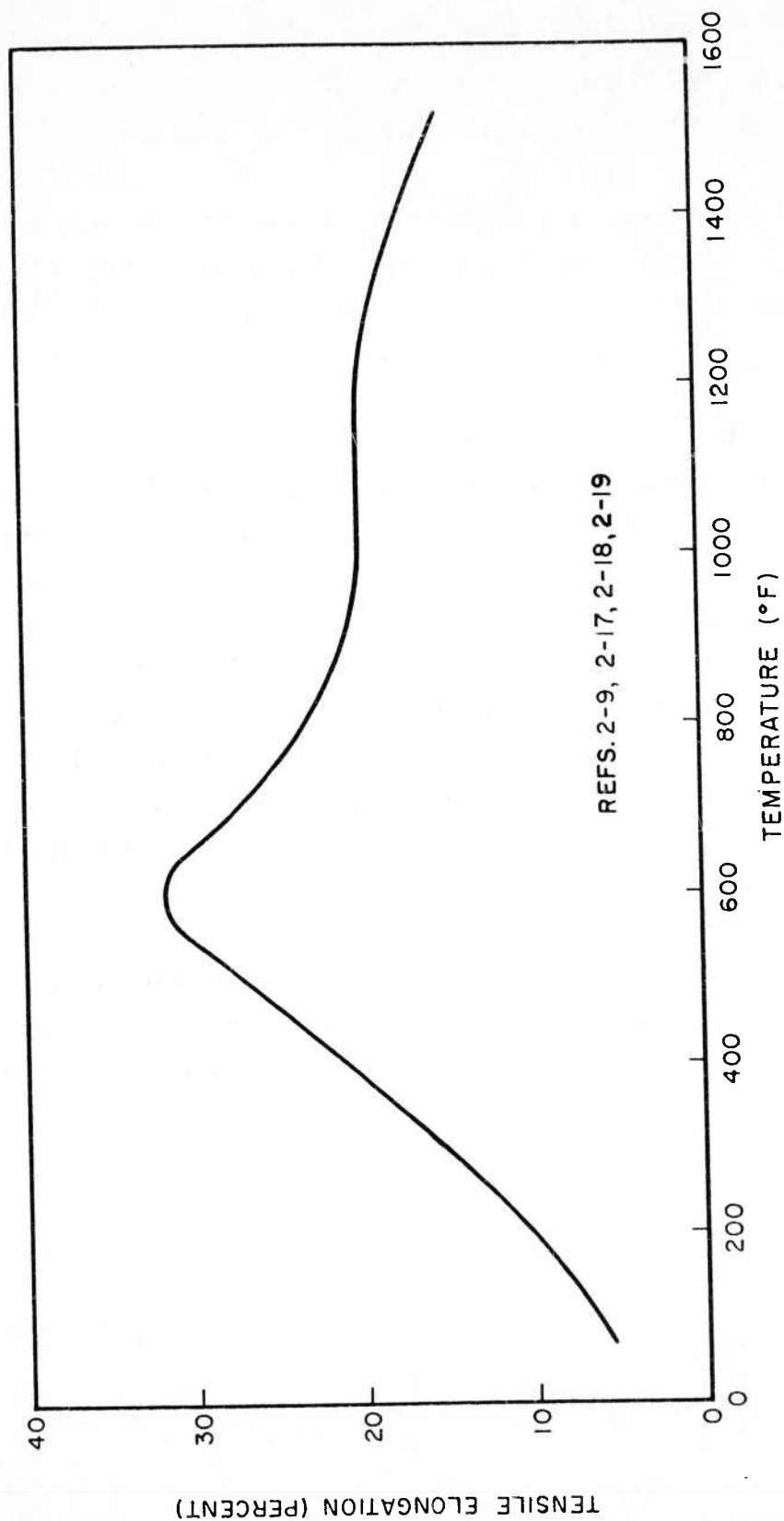


Fig. 2-48 Effect of Temperature on Longitudinal Tensile Elongation of Cross-Rolled Beryllium Sheet

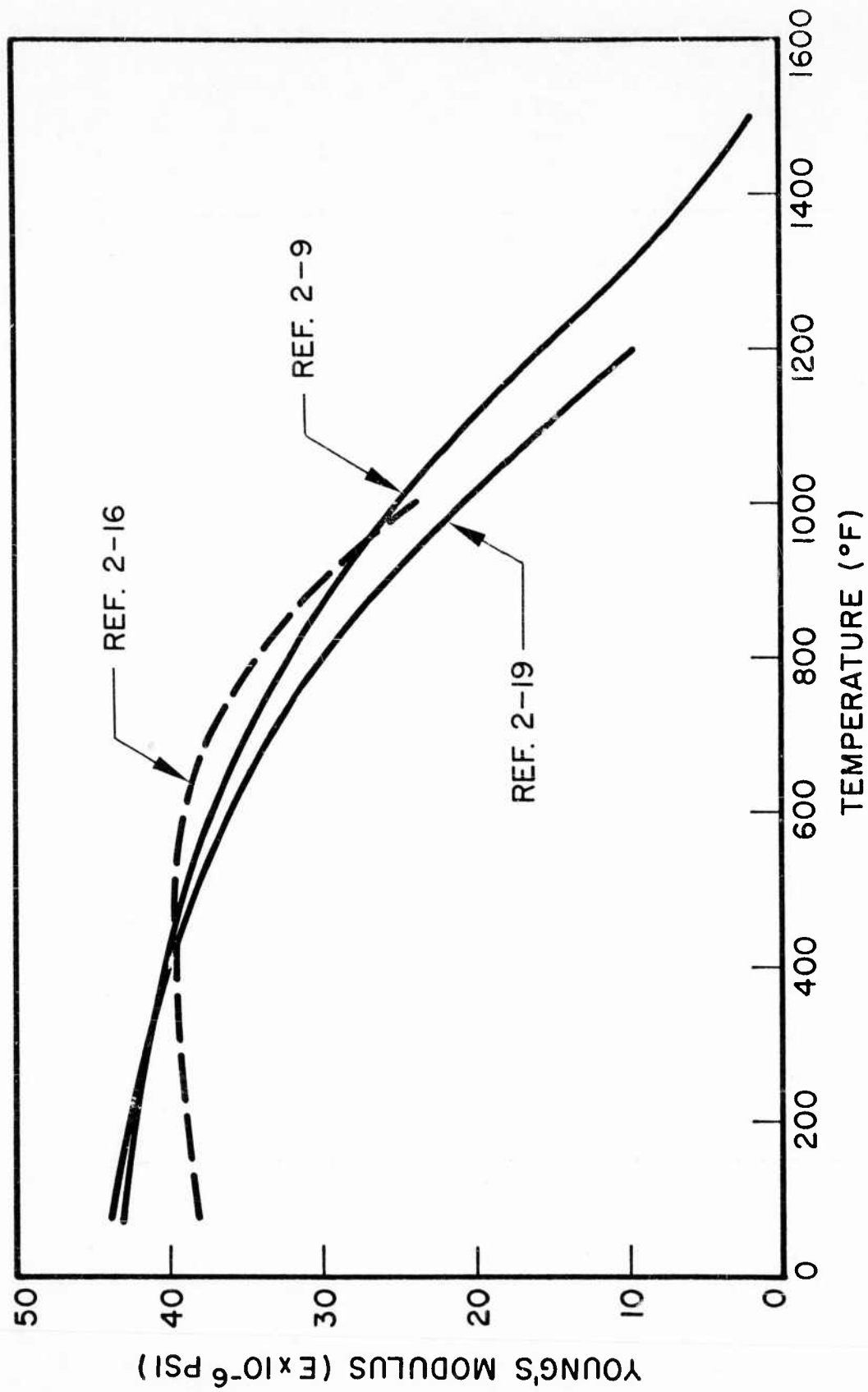


Fig. 2-49 Effect of Temperature on Young's Modulus of Cross-Rolled Beryllium Sheet

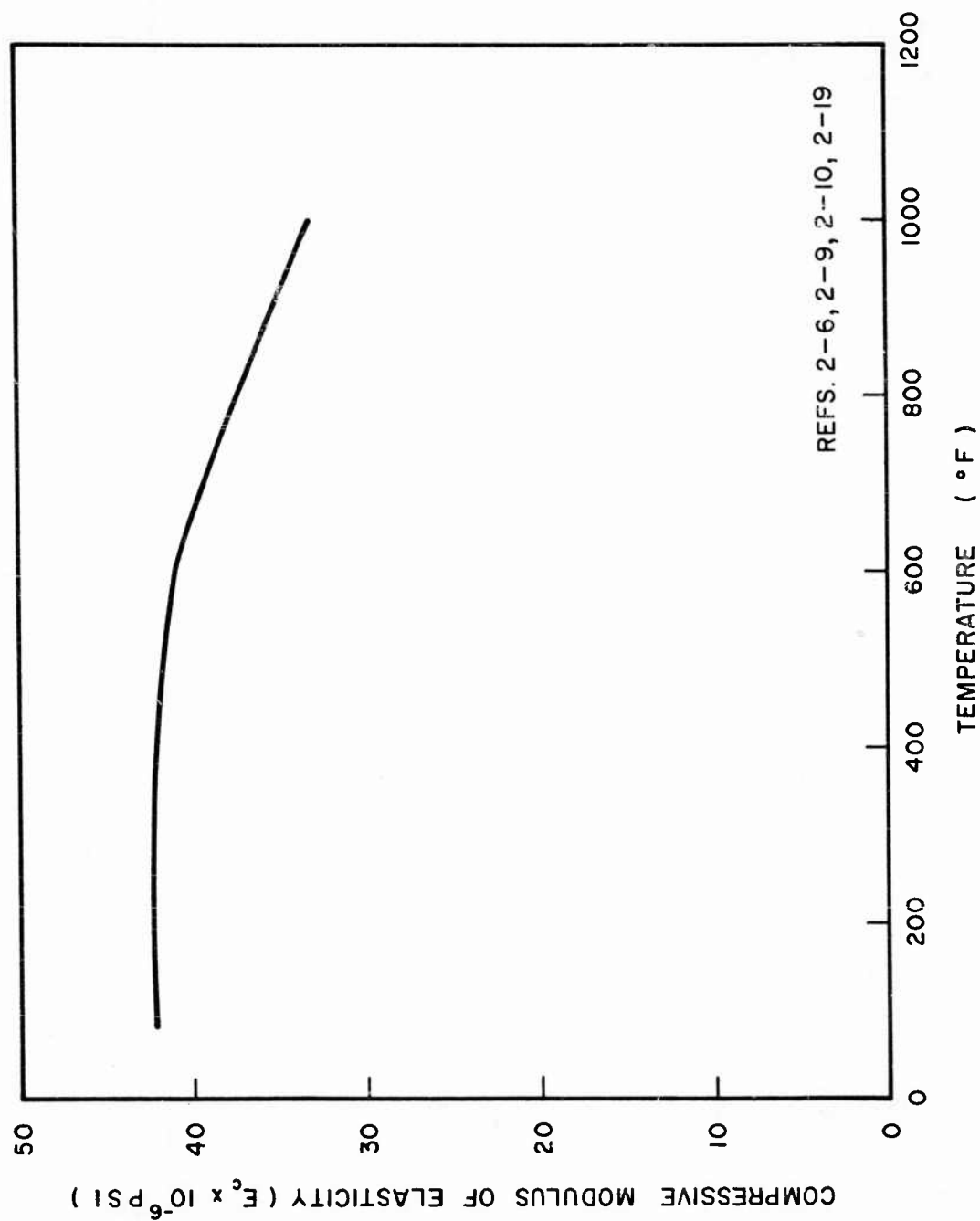


Fig. 2-50 Estimated Effect of Temperature on Compressive Modulus of Elasticity of Cross-Rolled Beryllium Sheet

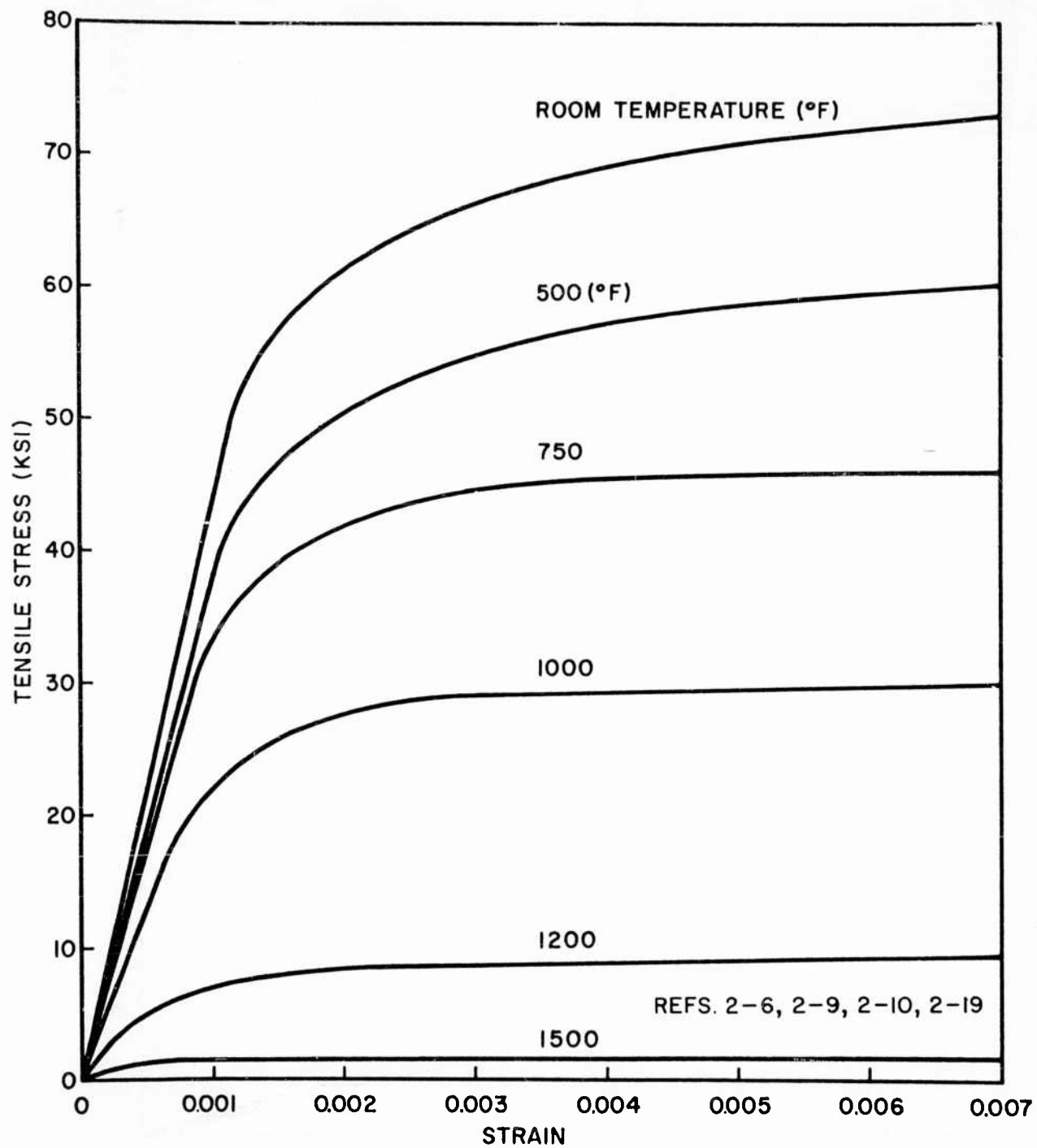


Fig. 2-51 Typical Tensile Stress-Strain Curves at Room and Elevated Temperatures for Cross-Rolled Beryllium Sheet

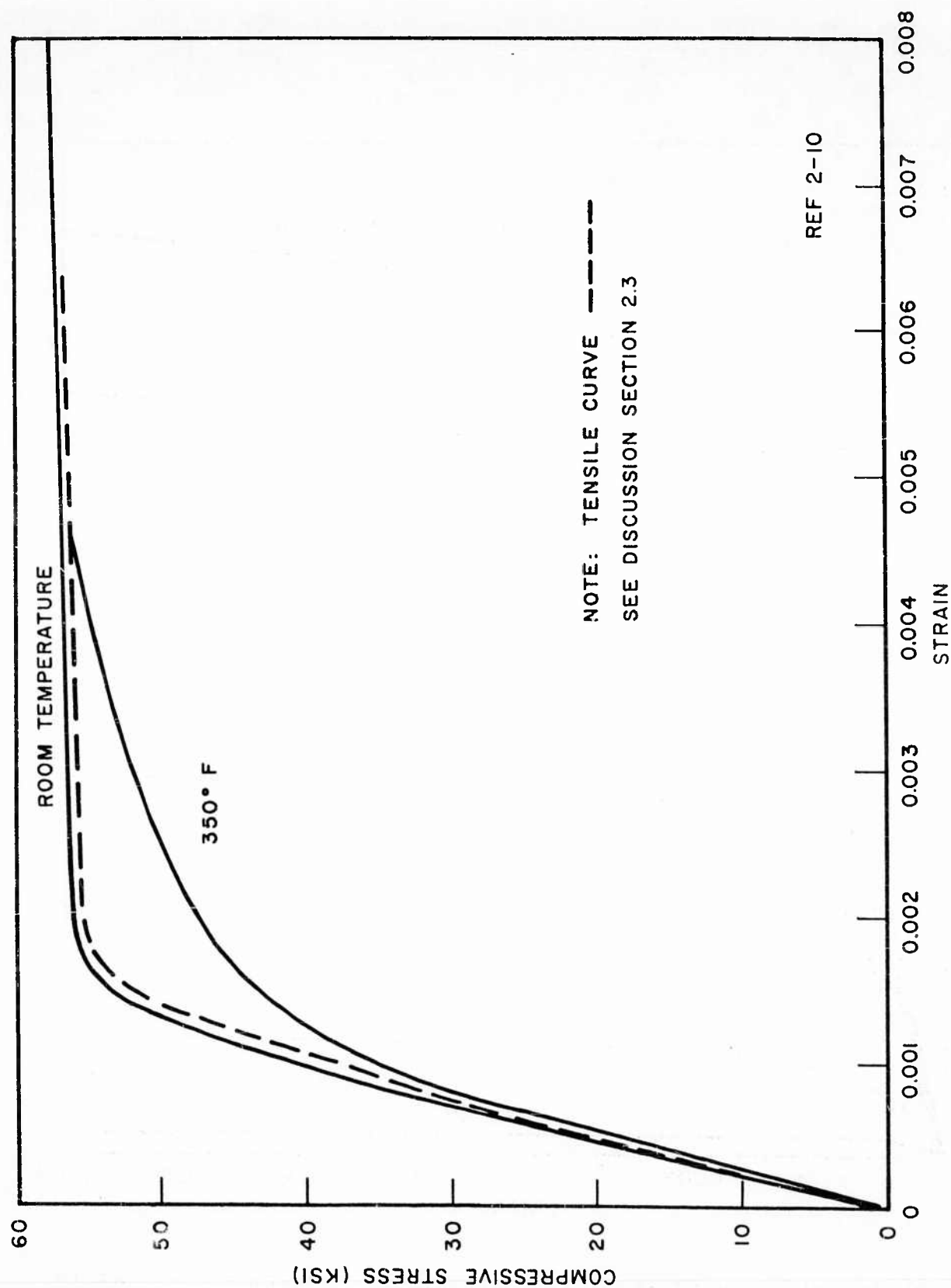


Fig. 2-52 Typical Compressive Stress-Strain Curves at Room and Elevated Temperatures for Cross-Rolled Beryllium Sheet

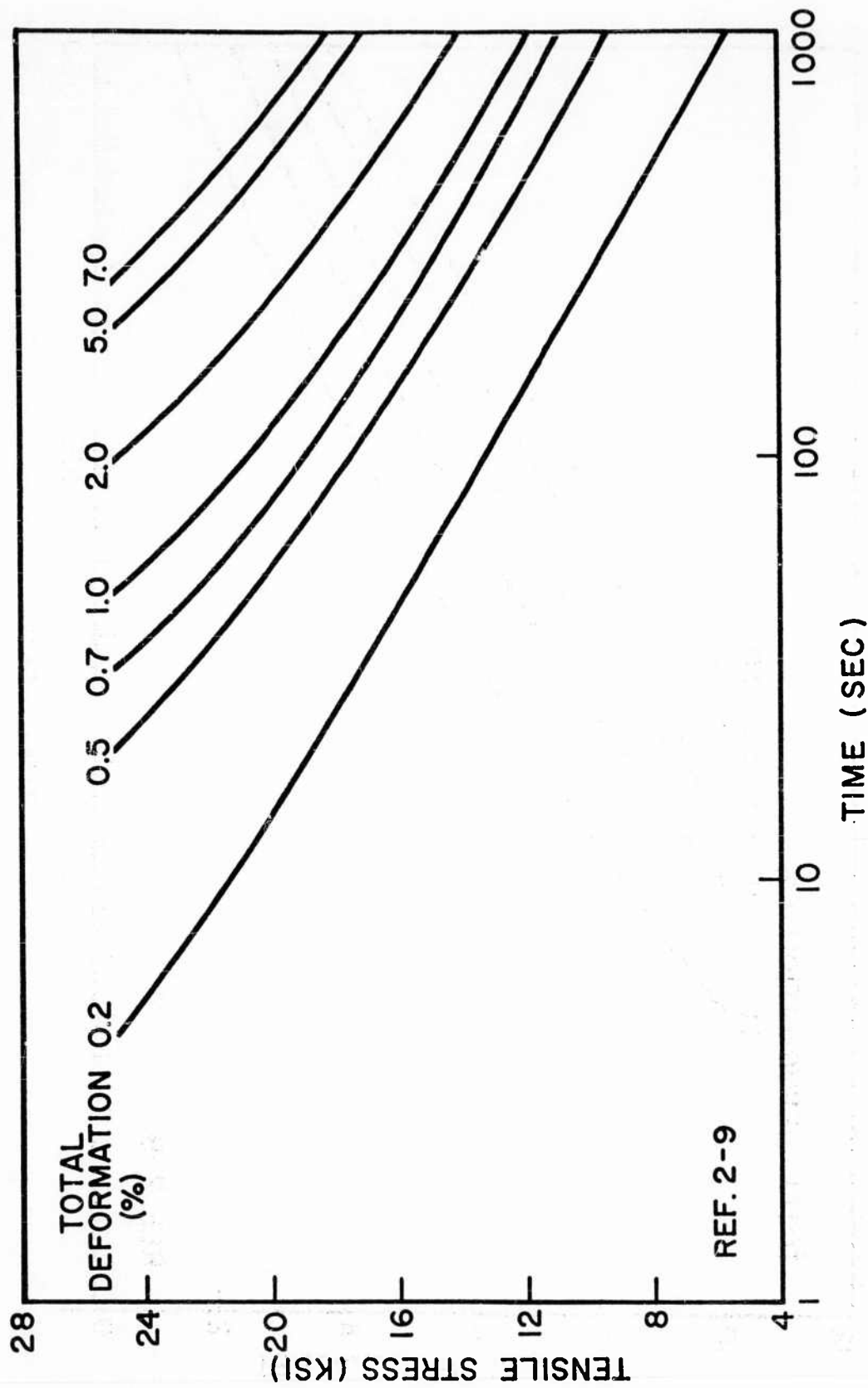


Fig. 2-53 Creep Curves for Cross-Rolled Beryllium Sheet at 1000°F

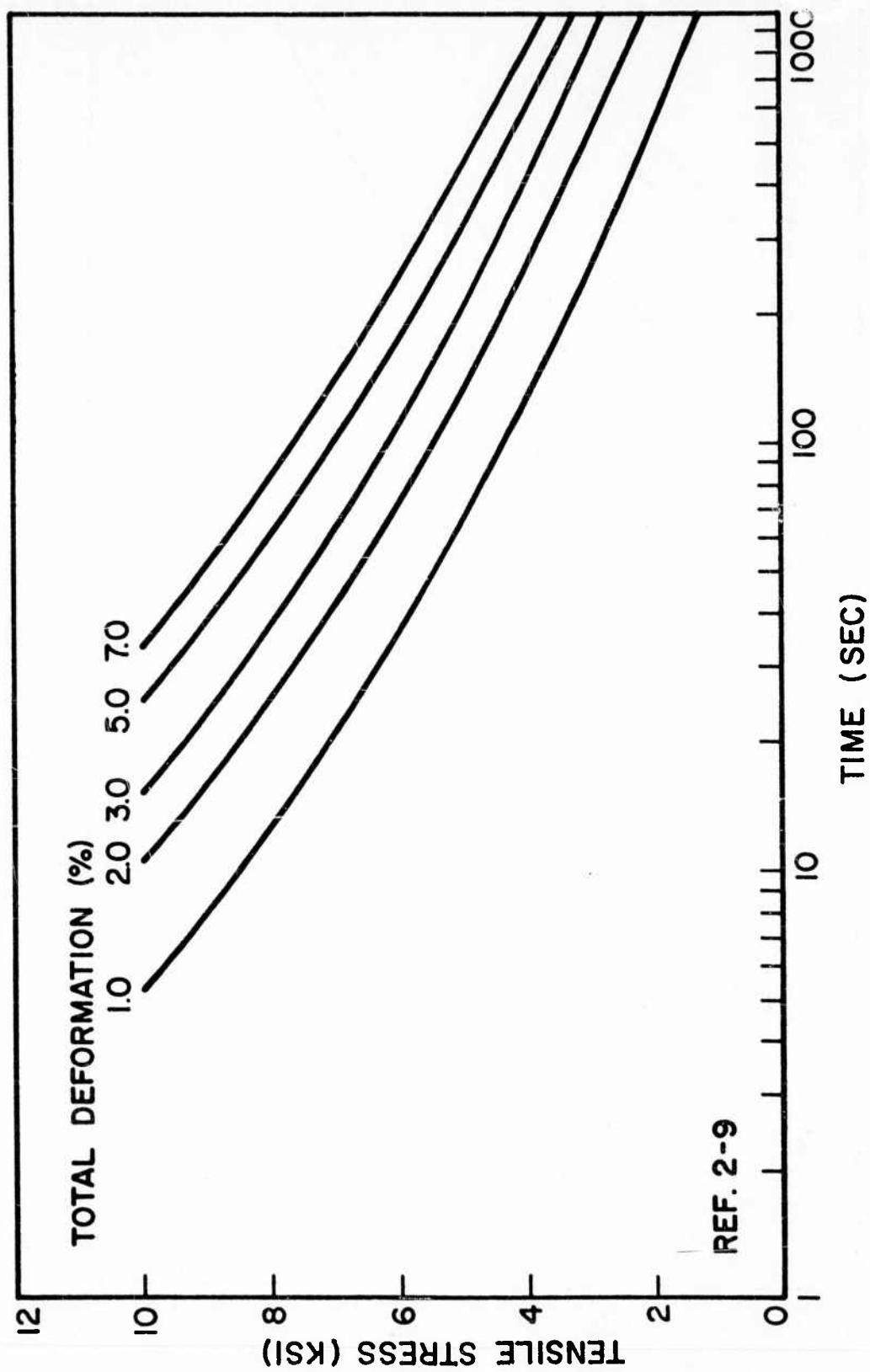


Fig. 2-54 Creep Curves for Cross-Rolled Beryllium Sheet at 1250°F

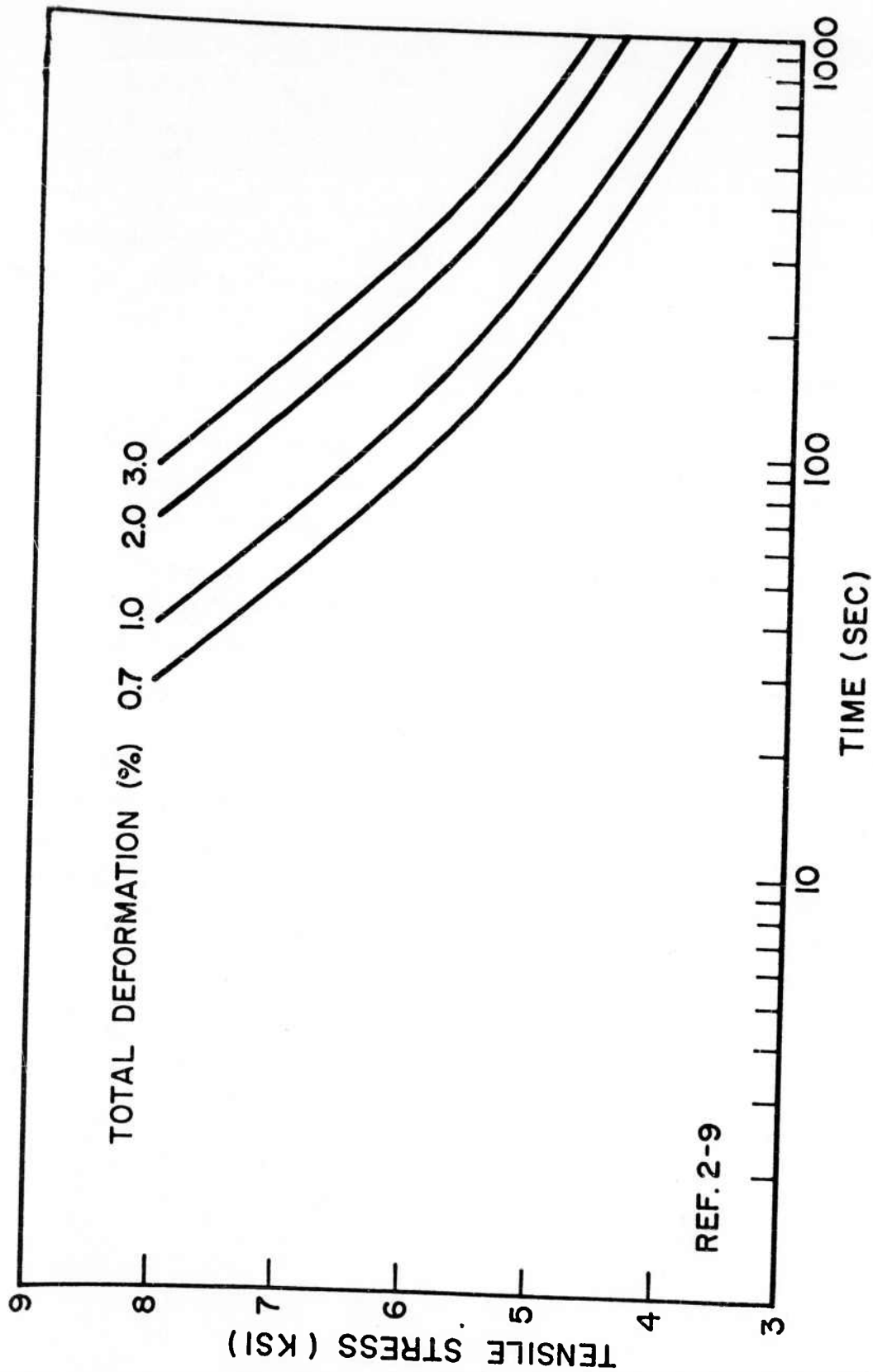


Fig. 2-55 Creep Curves for Cross-Rolled Beryllium Sheet at 1500°F

2.3.3 Hot-Upset Sheet

Typical design mechanical properties for hot-upset sheet are presented in Table 2-2 at room temperature, and Figs. 2-56 through 2-61 at elevated temperatures. The prime source for the data has been the Martin Company which is investigating this material under contract to ASD. Compared to the previous forms of beryllium treated, a very limited number of data are available for hot-upset sheet. The data presented are believed to reflect the current state-of-the-art.

The variation of the compressive yield-stress of hot-upset beryllium sheet with temperature is presented in Fig. 2-56, while tensile elongation versus temperature is given in Fig. 2-57. Note that the elongation curve has the characteristic peak noted in the previously treated forms of beryllium, and that the magnitude and position of the peak is approximately the same as that shown for cross-rolled sheet (Fig. 2-48). Figure 2-58 presents the compressive modulus of elasticity versus temperature. The tensile stress-strain curves for various temperatures shown in Fig. 2-59 are undoubtedly low, but are presented because the general shapes of the curves are believed to be typical. The dotted curve additionally shown on this figure is taken from Ref. 2-6 and represents currently produced material. Figure 2-60 presents compressive stress-strain curves for hot-upset sheet at various temperatures. Some fatigue data, both for bending and axial loadings, are presented in Fig. 2-61 for unnotched specimens tested at room temperature.

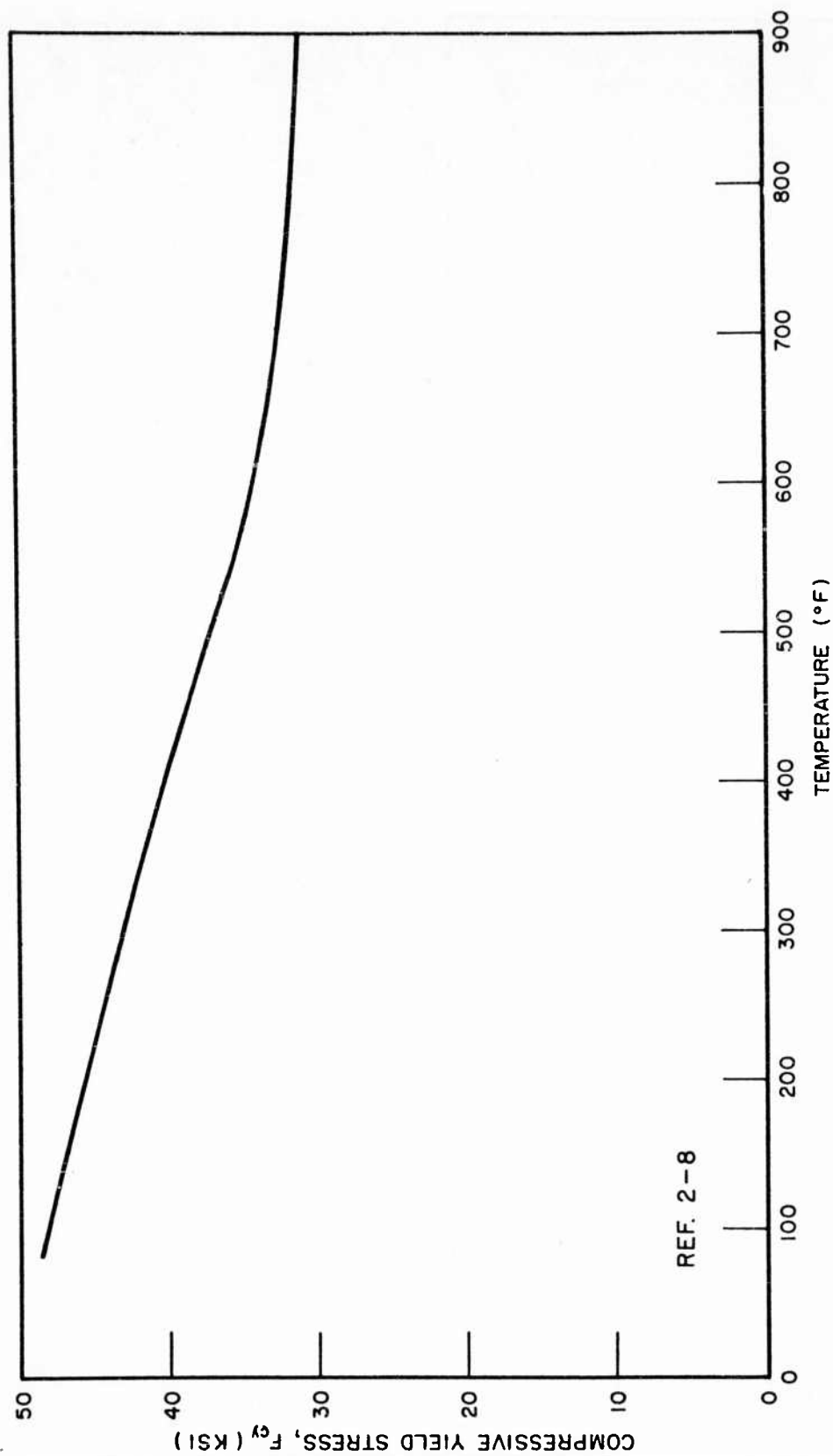


Fig. 2-56 Effect of Temperature on the Typical Compressive Yield Strength of Hot-Upset Beryllium Sheet

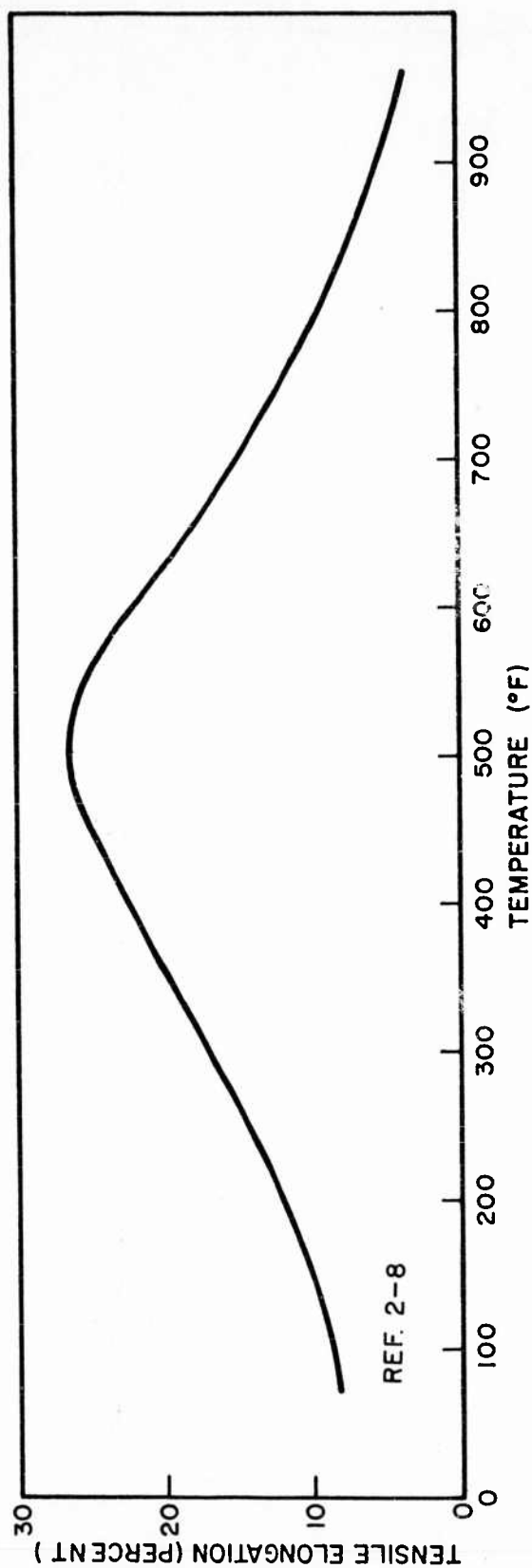


Fig. 2-57 Effect of Temperature on the Tensile Elongation of Hot-Upset Beryllium Sheet

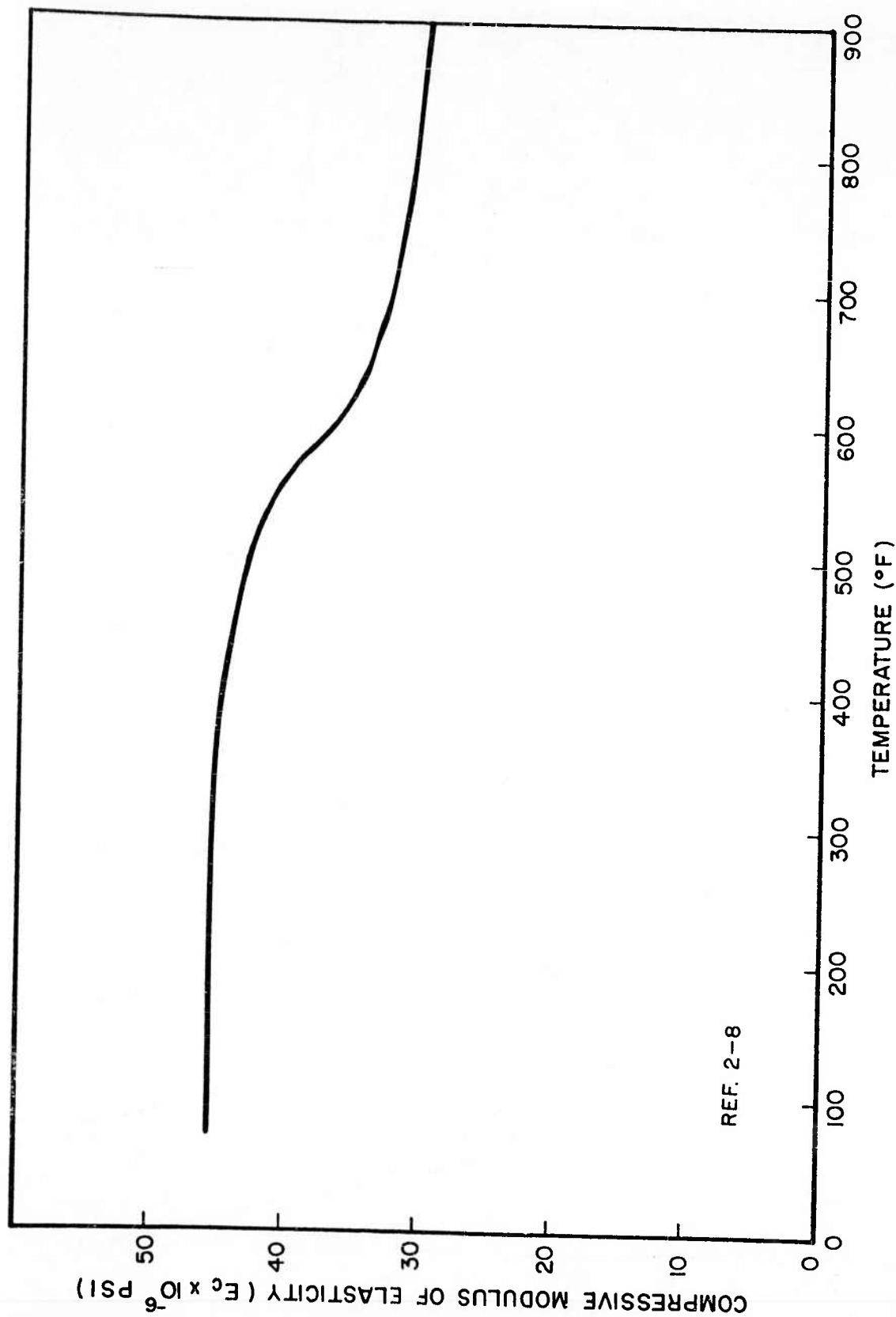


Fig. 2-58 Effect of Temperature on Compressive Modulus of Elasticity of Hot-Upset Beryllium Sheet

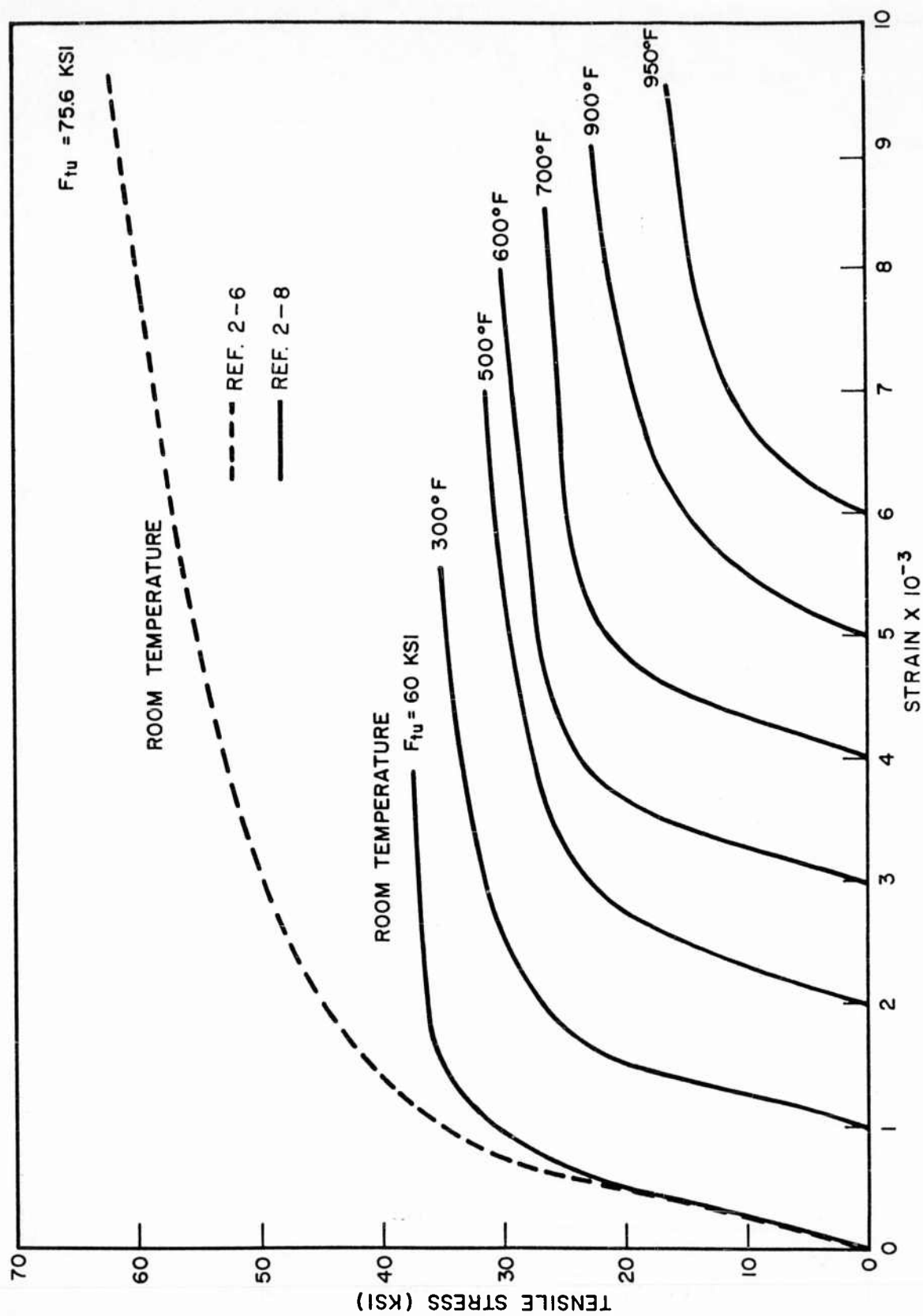


Fig. 2-59 Tensile Stress-Strain Curves for Hot-Upset Beryllium Sheet

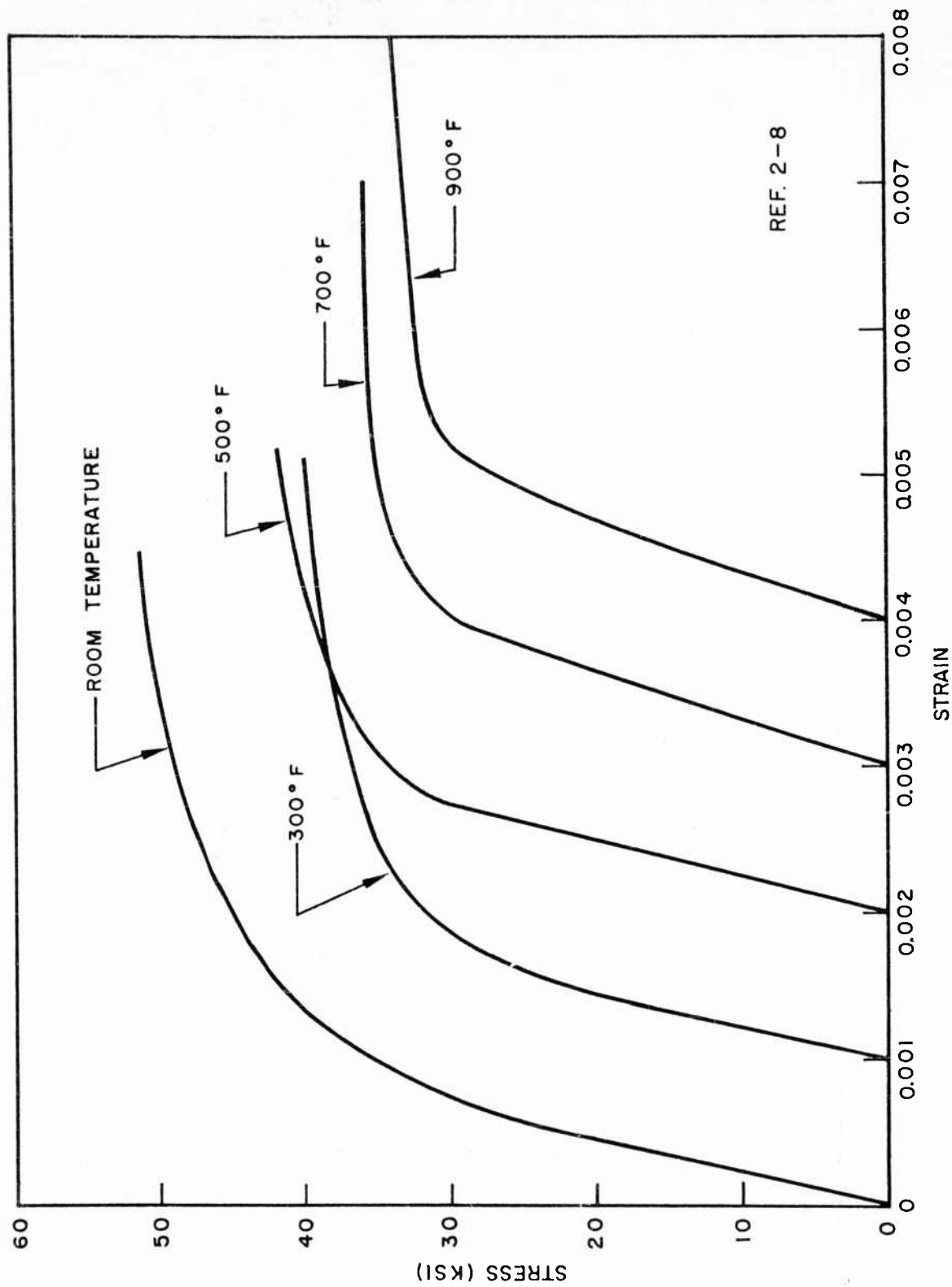


Fig. 2-60 Compressive Stress-Strain Curves for Hot-Upset Beryllium Sheet

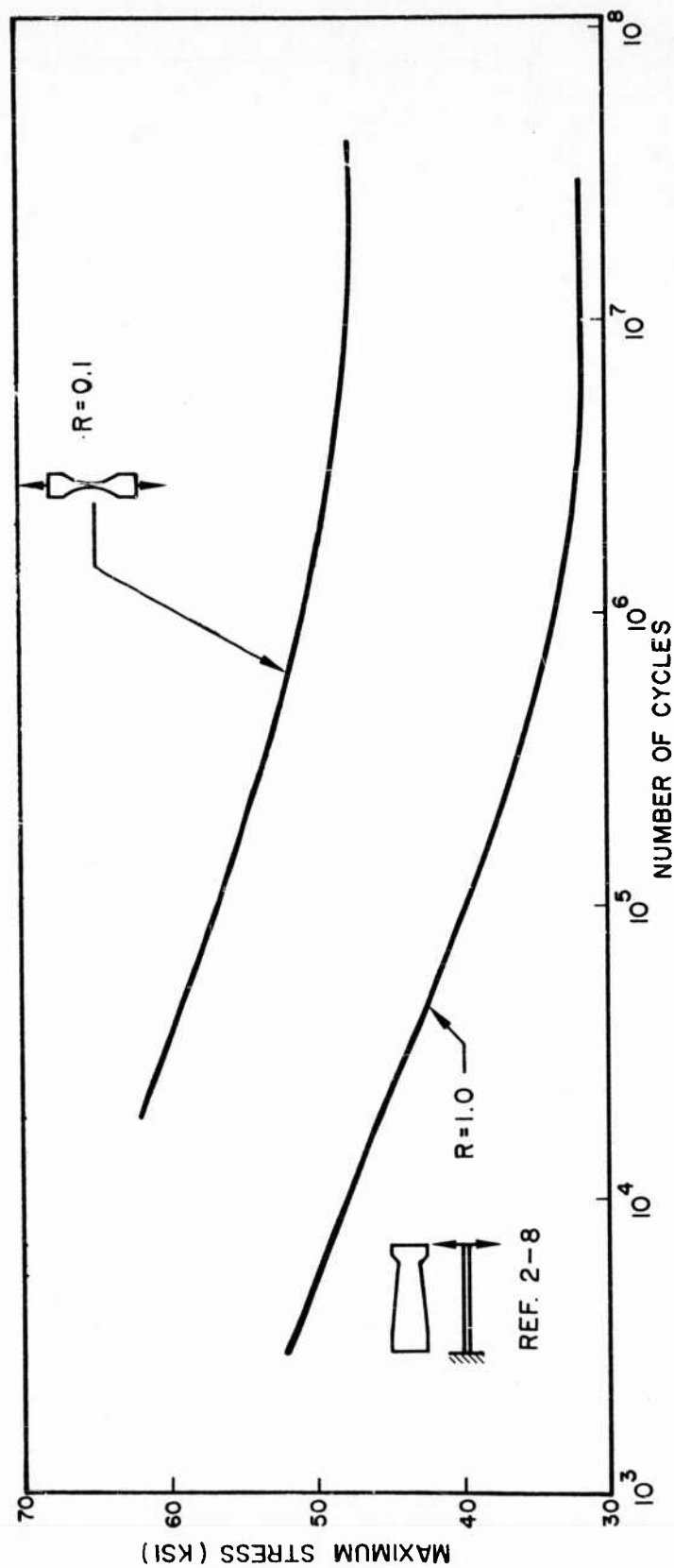


Fig. 2-61 Bending and Axial S-N Curves for Hot-Upset Beryllium Sheet at Room Temperature

2.3.4 Extrusions

Beryllium extrusions at the present time are being produced in small experimental quantities, and mechanical property testing, therefore, has been very limited and highly dependent upon the extruding process. The data presented here, while limited, are intended to provide the reader with some concept of the mechanical properties now being obtained, and are not intended for reference in design. Extruding development programs currently in progress should provide additional data to supplement the present data in the near future.

Table 2-2 presents some room-temperature design mechanical properties for beryllium extrusions. Both higher and lower values have been obtained by varying the extruding process. Figures 2-62 through 2-65 present some elevated-temperature properties. Fatigue data are presented in Figs. 2-62 through 2-64. Figure 2-62 presents axial fatigue data at room temperature for notched and unnotched specimens having a stress ratio of 0.2. Definite differences between the notched and unnotched data can be noted. Figure 2-63 shows similar fatigue data at 1100°F. Here, very little distinction between the notched and unnotched specimens can be observed. When the stress ratio R is decreased to -1, the fatigue characteristics of extruded beryllium at 1100°F are represented by Fig. 2-64. In this case, definite differences between the notched and unnotched data again appear, and scatter about either curve is rather small. The decrease in R from 0.2 to -1.0 at 1100°F is noted to decrease fatigue life considerably.

Figure 2-65 presents stress-rupture data at 1100°F for extruded beryllium.

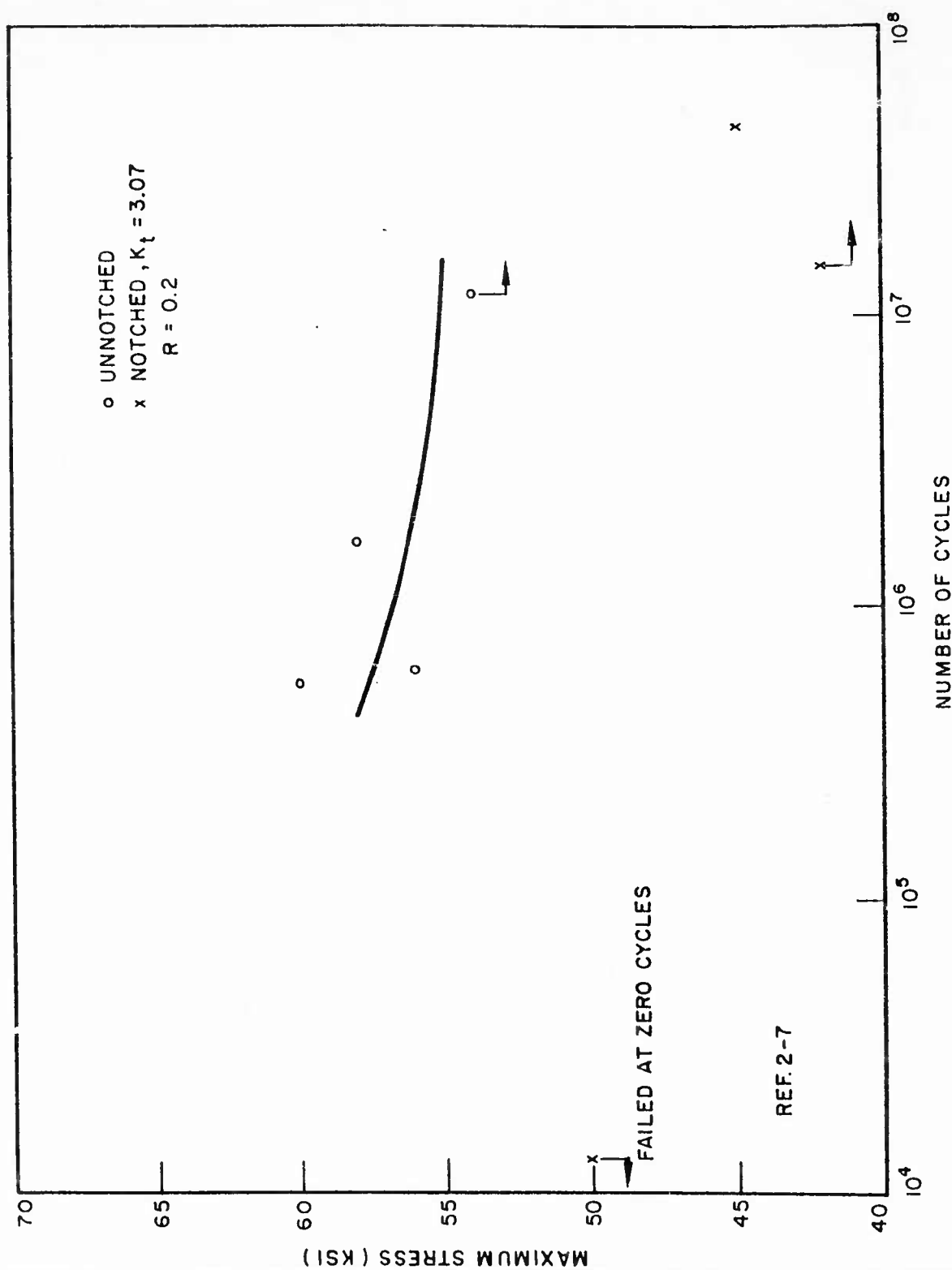


Fig. 2-62 Axial S-N Curves for Extruded Beryllium at Room Temperature

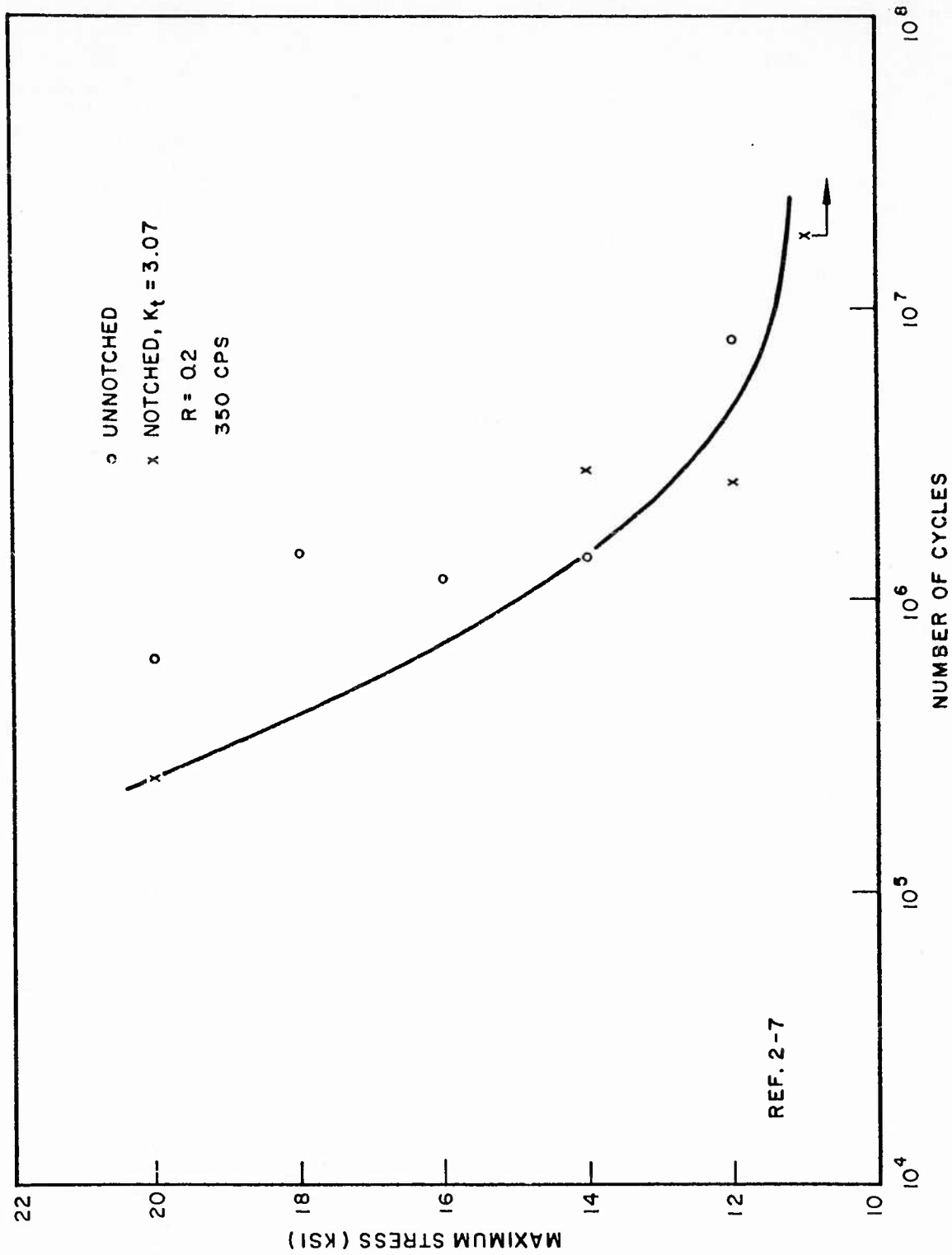


Fig. 2-63 Axial S-N Curves for Extruded Beryllium at 1100°F (1)

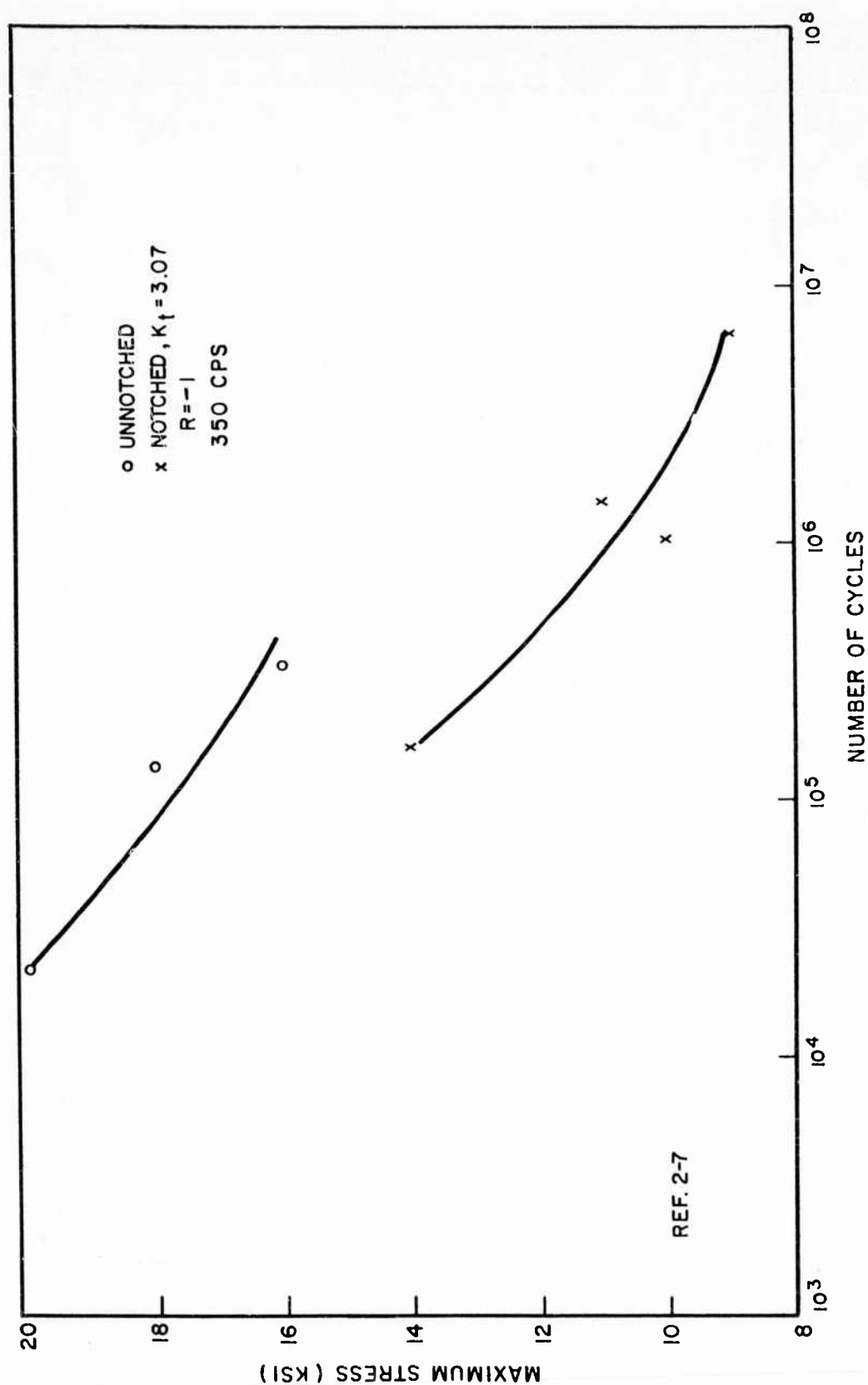


Fig. 2-64 Axial S-N Curves for Extruded Beryllium at 1100°F (2)

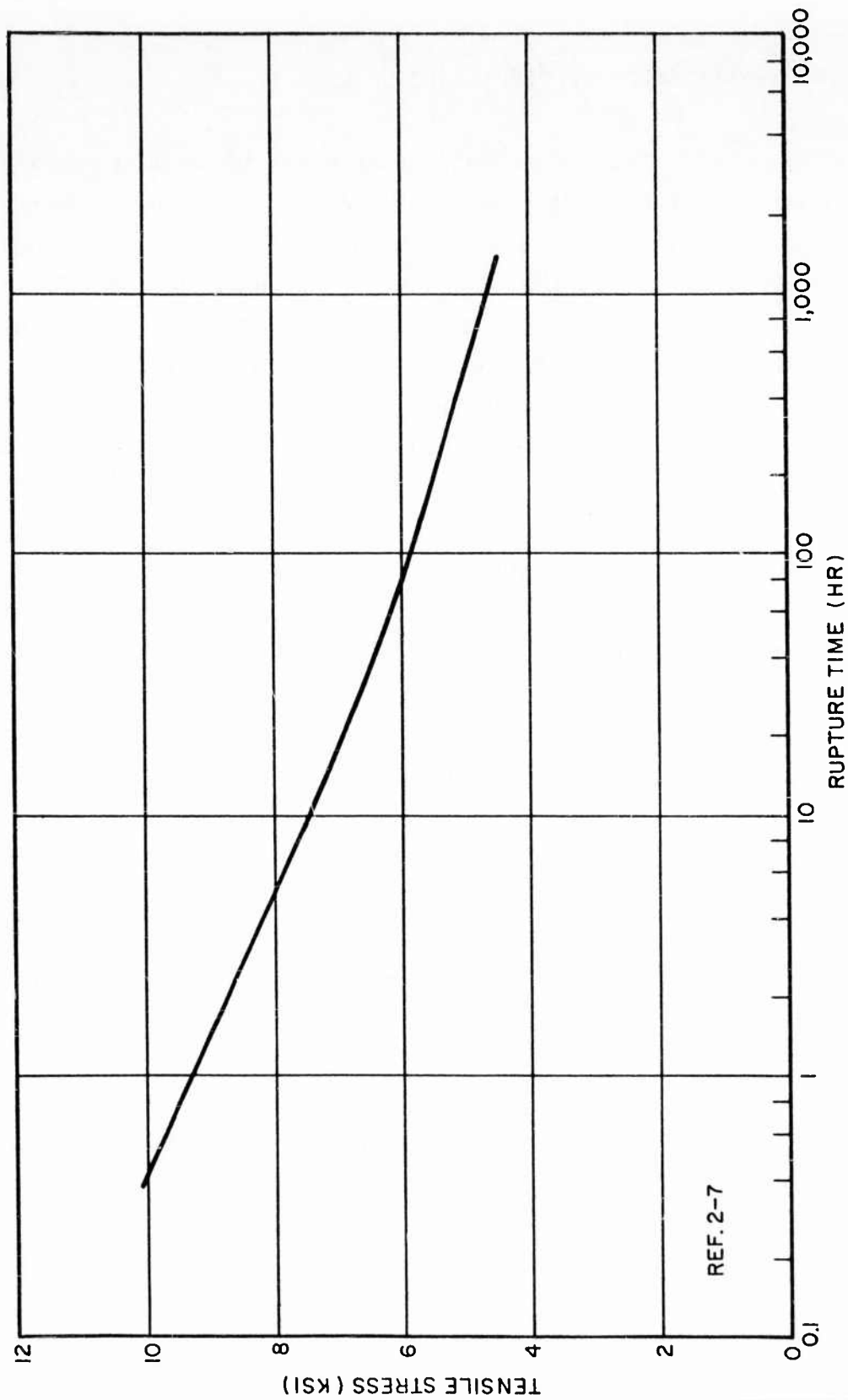


Fig. 2-65 Stress-Rupture Curve for Extruded Beryllium at 1100°F

2.4 NOTCH SENSITIVITY OF BERYLLIUM

The brittleness of beryllium is somewhat demonstrated by the information on its ductility presented previously in this report. However, there appears to be no reliable method by which the structural engineer can convert ductility data into information on the sensitivity of the material to notches or other geometric discontinuities that cause stress concentrations. Since no experimental data on notch sensitivity appear in the literature, a cursory experimental survey of beryllium-block and cross-rolled-sheet notch sensitivity was performed under this contract. A total of 26 notched-block specimens and 16 notched-cross-rolled sheet specimens were tested over the room temperature to 1100°F range.

The notch-sensitivity characteristics of beryllium hot-pressed block and cross-rolled sheet as determined from this survey are shown in Figs. 2-66 and 2-67. The unnotched ultimate strengths used in determining R , the ratio of notched to unnotched ultimate strengths, are given in Fig. 2-68. The block strengths of Fig. 2-68 were obtained from unnotched specimens of the heat from which the notched specimens were cut. The sheet strengths are typical of 1.75-percent BeO sheet. The notch-strength data from which Figs. 2-66 and 2-67 were derived are given in Table 2-3. The notch specimen geometry is shown in Fig. 2-69. Values of the theoretical stress-concentration factors were calculated from charts of Ref. 2-20.

From Figs. 2-66 and 2-67, it is concluded that block and cross-rolled sheet are somewhat notch sensitive at temperatures up to 500°F, although no more sensitive than high-strength steels and titanium alloys. Above 500°F neither form of the material is notch sensitive. The data of Table 2-3 show some inconsistencies and incompleteness. Additional tests should be performed to define more precisely the notch-strength ratios and establish all factors responsible for the trends shown.

Table 2-3
 ULTIMATE STRENGTH OF NOTCHED BERYLLIUM SPECIMENS^(a)

Hot Pressed Block				Cross-Rolled Sheet			
K_T	Notched Strength (ksi)	$R^{(b)}$	Temp. (°F)	K_T	Notched Strength (ksi)	$R^{(b)}$	Temp. (°F)
1.83	53.4	0.99	70	1.55	71.0	0.91	70
2.30	48.0	0.90	↓	2.33	74.8	0.96	↓
2.54	44.3	0.83		5.0	51.6	0.66	
				5.45	49.3	0.63	
4.00	43.0	0.805		11.5	38.5	0.495	
4.40	42.8	0.80					
5.19	49.8	0.93	↓	1.51	74.3	1.22	500
6.00	35.4	0.662		1.90	79.8	1.31	↓
				2.57	71.8	1.18	
1.89	49.4	1.01		5.05	66.7	1.09	
2.48	46.7	0.955		5.50	60.8	0.99	
2.65	48.6	0.99	↓	11.5	68.2	1.12	↓
2.90	57.0	1.16					
4.45	45.6	0.93		2.57	56.0	1.19	
5.48	47.2	0.96		2.65	51.3	1.09	
6.87	46.0	0.94		5.04	51.0	1.085	
			↓				↓
1.94	42.8	1.1		1.52	39.2	1.63	
2.57	46.0	1.18		2.57	48.3	2.01	
2.65	41.2	1.06					
4.45	39.3	1.01					
5.50	43.5	1.11	↓				↓
5.62	44.8	1.15					
6.85	39.0	1.0					
1.94	19.7	0.77	1,100				↓
2.75	34.7	1.35	↓				
4.05	31.8	1.24					
5.42	36.9	1.44					
6.00	18.3	0.71					

(a) Nominal BeO content of all materials is 1.75%.

(b) R = notched ultimate/unnotched ultimate strength. Unnotched strengths taken from Fig. 2-68.

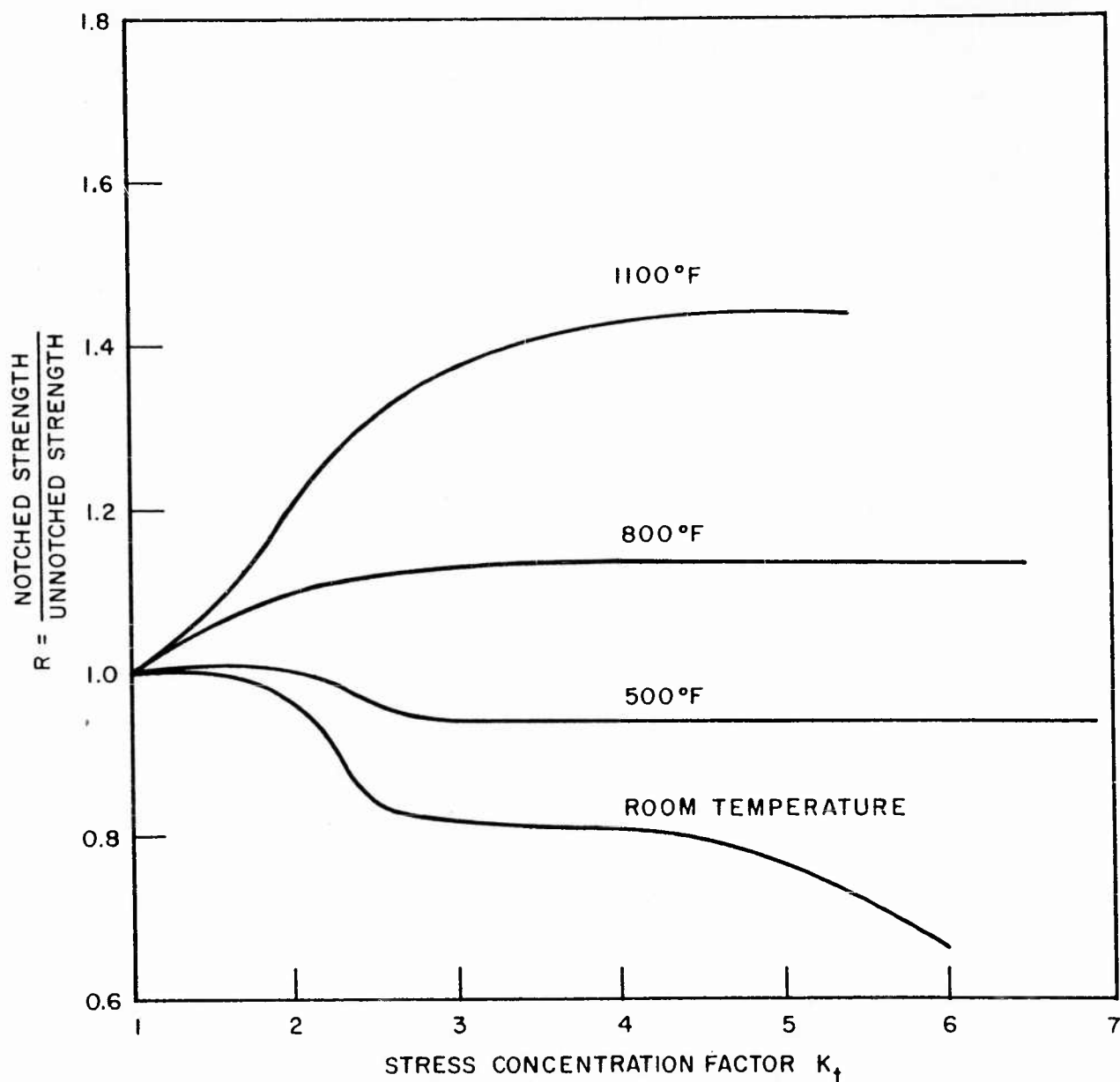


Fig. 2-66 Notch Sensitivity of QMV Hot-Pressed Beryllium Block (1.55% BeO Content)

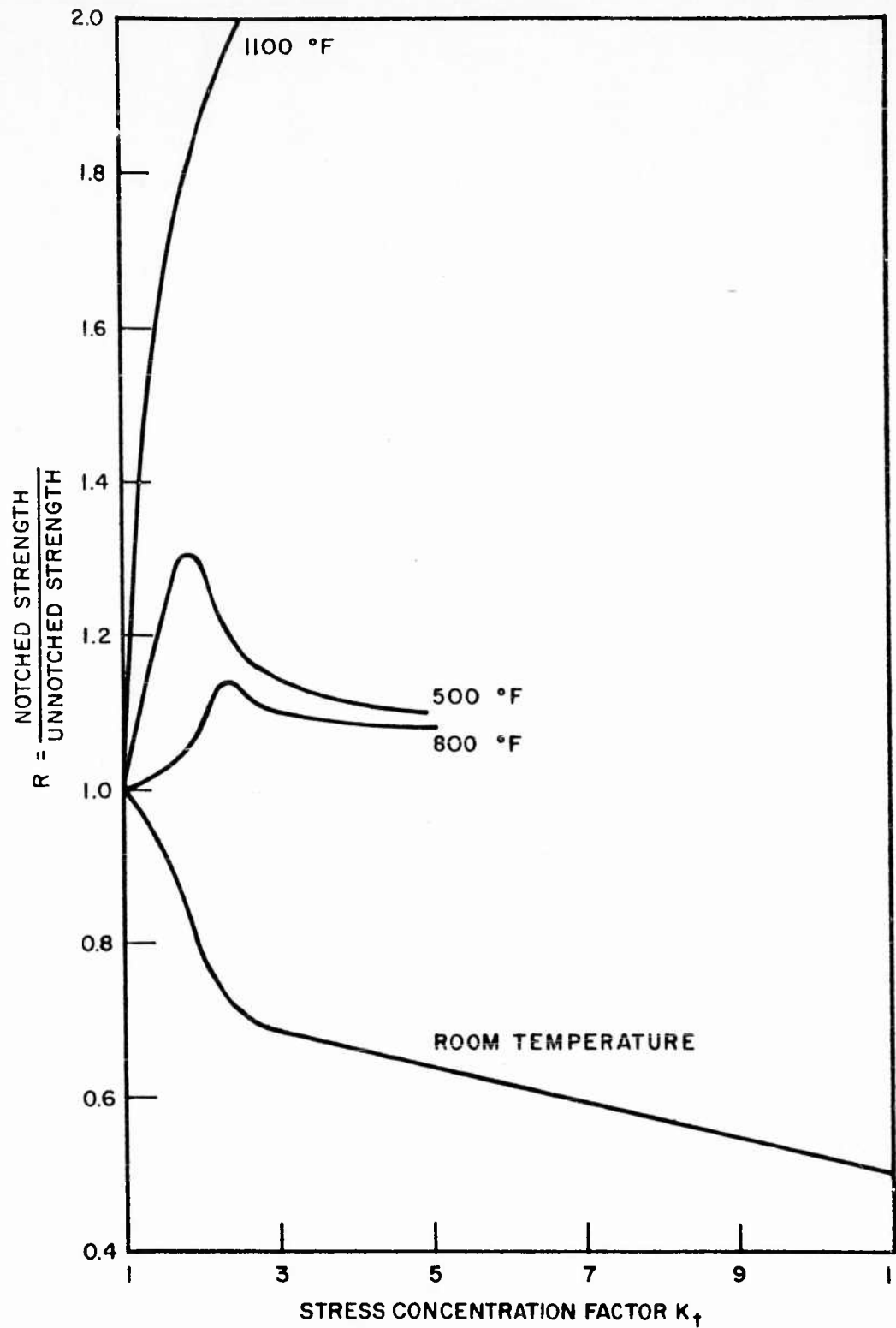


Fig. 2-67 Notch Sensitivity of Cross-Rolled Beryllium Sheet (1.75% BeO Content)

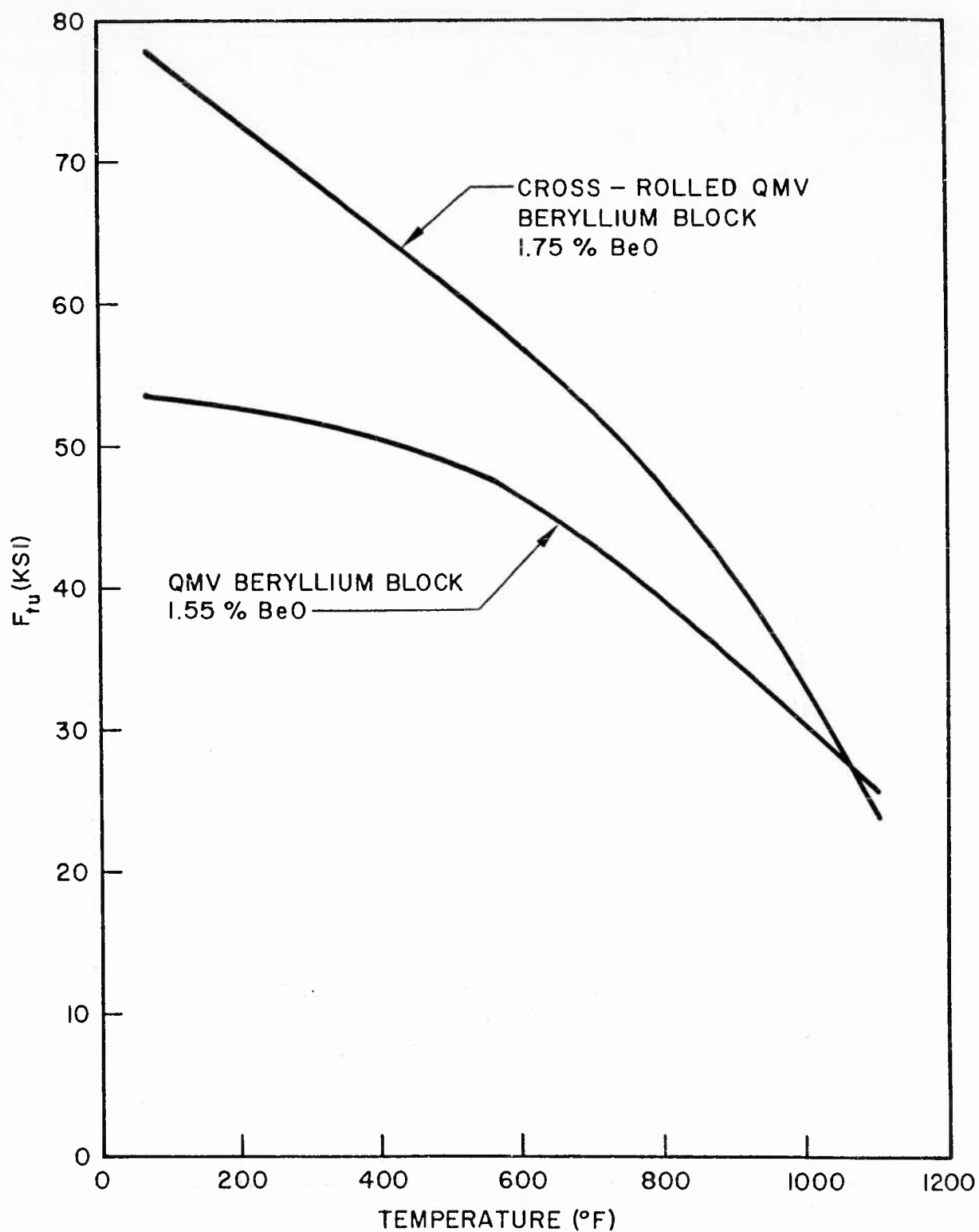


Fig. 2-68 Unnotched Ultimate Tensile Strength of Beryllium

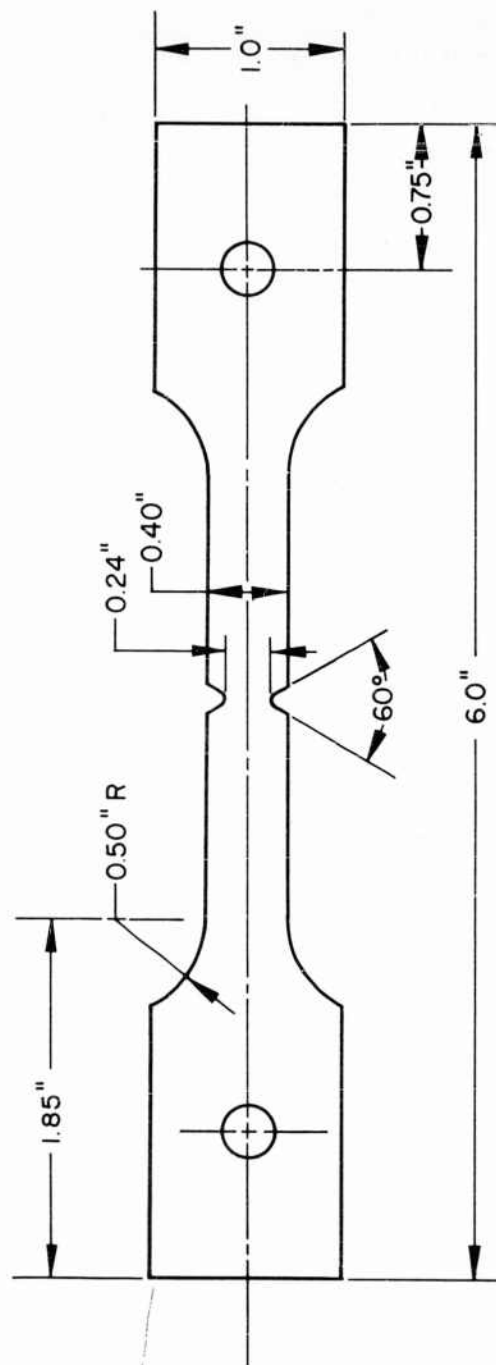


Fig. 2-69 Notch Specimen Geometry

2.4.1 QMV Hot-Pressed Block

The notch-sensitive room-temperature characteristic of block beryllium is chiefly due to the fact that basal plane cleavage is the predominant mode of fracture for the block material at room temperature. Basal plane cleavage is accompanied by little ductility, and Poisson's ratio is quite small (subsection 2.5) which inhibits the development of biaxial stresses at the notch base. However, even if biaxial tension were developed, it is shown in subsection 2.5 that when basal plane cleavage is the predominant mode of fracture, biaxial strengthening does not occur.

Above 800°F, shear of prism planes of the close-packed hexagonal lattice structure of beryllium is the predominant mode of failure. For this mode, biaxial strengthening can and (as shown by the data of Fig. 2-66) does occur. Thus, it is expected that ductile yielding under uniaxial stress occurs at the notch base while biaxial strengthening between the notches accounts for the high strength ratios shown in Fig. 2-66 for 500° and 800°F.

The high notch-strength ratio exhibited at 1100°F may possibly be explained by the fact that the fractures were entirely intergranular, while fracture at the lower temperature was principally transgranular. Perhaps large values of Poisson's ratio under the somewhat viscous action at this temperature led to triaxial tension over much of the area between the notch bases. This could account for the apparent strengthening, but tests in which the ratio of notched area to total cross-sectional area is varied would be necessary to substantiate this conjecture.

2.4.2 Cross-Rolled Sheet

Although the general notch sensitivity characteristics of the block and sheet forms of beryllium shown in Figs. 2-66 and 2-67 are similar, they are probably the results of different phenomena.

The sheet material has a highly oriented grain structure in which the C axes of the lattice structures composing the grains are oriented normal to the plane of the sheet. Accordingly, the basal planes of the lattice structure on which low-temperature fracture occurs in the block material are parallel to the direction of loading in the sheet specimens. Further, Poisson's ratio is virtually zero in the C direction while it is approximately 0.10 in the elastic range in planes normal to the C direction. Thus, the stress at the base of the notch is essentially uniaxial while it is slightly biaxial in the plane of the specimens toward the center from the notches.

In view of these considerations, the high notch sensitivity at low temperatures appears to be the result of brittle fracture in the area somewhat inward from the notch base where the stresses are biaxial but close enough to the notch base to be in the area of high stress concentrations. At the notch base, the stresses are essentially uniaxial and would be relieved by ductility. (Beryllium sheet has been shown to be ductile in uniaxial unnotched tensile tests.) However, inward from the notch base, brittle fracture occurs in the biaxial tension-stress field much in the same manner and for the same reasons that the biaxial tests of subsection 2.5 failed in a brittle manner at room temperature.

At elevated temperatures, a combination of two factors probably explains the strengthening exhibited. First, increased ductility could have relieved the high stress concentration at the notch base. Examination of the specimens shows considerable flow at the notch base was accommodated by contraction in the width direction of the specimens with virtually no contraction in the thickness direction. The flow observed indicates Poisson's ratio was high (approaching unity) and, accordingly, induced tensile stresses in the width direction inward from the notch were high. As explained

in subsection 2.5, this situation can lead to extreme strengthening in beryllium and it appears to have done so in this case.

At 1100°F, the notched-sheet specimens exhibited predominantly transgranular fracture, while at the same temperature the block-specimens fractures were predominantly intergranular. The above explanation of the notch-strengthening effect therefore applies as well to this case. Apparently, rolling causes the grain boundaries to lie chiefly in planes of the sheet. This would reduce stress on the grain boundaries and inhibit that mode of fracture.

In conclusion, two areas of further investigation of notch sensitivity of beryllium are recommended. First, for both sheet and block beryllium, the effect of varying the ratio of notched area to total cross-section area should be determined. In this investigation only one value of that ratio was used, but there is no reason to expect that the results would be the same for other ratios. In fact, the factors responsible for the extreme biaxial strengthening at higher temperatures would probably disappear if the above ratio approached unity (analogous to a scratch) in which case R would also approach unity or less. Secondly, since cross-rolled beryllium sheet is highly anisotropic, it would be valuable to know the effects of notches into the surface of the sheet material. In the present case, the notches were into the edge of the sheet.

2.5 BIAXIAL STRENGTH OF BERYLLIUM BLOCK AND SHEET

Before hot-pressed beryllium powder is extruded, rolled, or otherwise processed in the various ways that can lead to preferred orientation, the grains have a somewhat random orientation with respect to one another, while in themselves they are composed of well-oriented lattice structures. In this condition, the material exhibits brittleness at room temperature with ductilities of less than 2 or 3 percent. When this material is rolled into plate or sheet, the grains assume a preferred orientation. It is clear that yield and fracture criteria for random and preferred orientations will be basically different below their equicohesive temperatures if the grains have directional properties such as those of beryllium. Accordingly, the failure criteria for the two cases are discussed separately. In each case, only biaxial states of stress are discussed.

A summary of some metallurgical and mechanical properties of beryllium is also given. Since much of the information contained in this section is general and available from many sources, only a few specific references are made. Uncited references are listed at the end of the section to aid the reader in finding more general information.

2.5.1 General Metallurgical and Mechanical Properties of Beryllium

The atoms of beryllium crystals are arranged in a "close-packed hexagonal" space lattice. A grain or crystal (these terms are used interchangeably) of beryllium is made up of a large number of connected space lattices. The lattice structure and some of the various planes upon which distortion and fracture occur are sketched in Fig. 2-70.

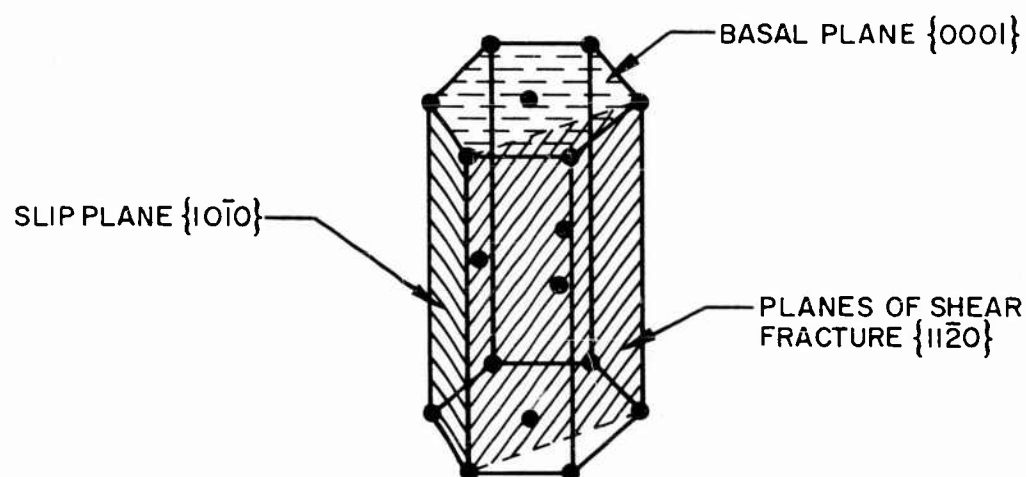


Fig. 2-70 Space Lattice of Beryllium

Single crystals of beryllium have been the subject of intensive investigations. Some of the principal conclusions of those investigations (taken principally from Ref. 2-21) are listed below:

- Cleavage fracture occurs on the basal planes $\{0001\}$, due to tension after only small amounts of slip.

- The $\{10\bar{1}0\}$ planes are the most vulnerable planes for slip or shear distortion between room temperature and 800° to 900° F. Fracture has not been observed on $\{10\bar{1}0\}$ planes. Slip on this family of planes is referred to as "prismatic slip."
- Fracture and discontinuities occur on $\{11\bar{2}0\}$ planes after sufficient amounts of slip on $\{10\bar{1}0\}$ planes.
- At room temperature, the minimum tensile stress required for slip on the $\{10\bar{1}0\}$ planes is 4 to 5 times that required for the small amount of slip on the basal plane that precedes cleavage fracture.
- The tensile strengths mentioned above become equal at approximately 900° F where cleavage strength has increased slightly above room-temperature cleavage strength.
- Very large compressive stresses (250,000 psi) can be sustained by beryllium crystals when stress is applied normal to the basal plane. Fracture then occurs explosively in some unidentified mode.
- Very large ductilities due to prismatic slip are obtained when the lattice is oriented so that basal planes are parallel to the plane of load applications.
- A not fully understood mode of slip becomes operative above 900° F. Some investigators refer to it as a form of "pyramidal slip"; others feel it is slip on twinning planes.
- Twinning is operative at all temperatures and occurs more readily in compression than in tension. Twinning decreases with increased temperature.
- Ductility of single crystals, polycrystalline beryllium, and hot-pressed beryllium is at its maximum at approximately 800° F where $\{10\bar{1}0\}$ slip is least inhibited and thus predominates.

The macroscopic mechanical properties of hot-pressed beryllium block do not readily lead to such precise conclusions as are given above. However, knowledge of these properties of single crystals of beryllium is valuable as an aid to understanding the

macroscopic mechanical properties exhibited by hot-pressed beryllium block, of which the single crystal is the basic constituent. Moreover, where data on the pressed block are nonexistent, knowledge of the properties of the single crystals aids in anticipating the desired information.

Experimental investigations of the physical properties of hot-pressed beryllium block have led to the following conclusions:

- When there is no preferred orientation of grains, fracture occurs principally by propagation of cleavage cracks on $\{0001\}$ planes at room temperature, by $\{11\bar{2}0\}$ fracture following $\{10\bar{1}0\}$ slip at 800° F, and by intercrystalline fracture above 900° F.
- Ductility follows the general pattern shown in Fig. 2-19.
- Compressive yield strength is generally lower than tensile yield strength (Ref. 2-22). This is explained by noting that twinning occurs more readily in compression than in tension, thus providing more favorable slip orientation of crystals. Moreover, ductility can be expected to be larger in compression than in tension because there is no resolved tensile force normal to shear fracture planes to aid in propagating fractures.
- At temperatures above 800° F, the effect of increasing strain rate is to increase yield strength as temperature increases. Some investigators feel that this is proof that intercrystalline deformation is predominant because grain-boundary deformation is viscous in nature and exhibits the same type of response to strain-rate variations. There is some dispute on this conclusion.
- Equicohesive temperature for 3-percent beryllium oxide hot-pressed block appears to be approximately 900° F.

2.5.2 Beryllium Block (Randomly Oriented)

Since cleavage on basal planes is the predominant mode of fracture at room temperature and low temperatures, the maximum normal tension-stress criterion is used to predict fracture in the first quadrant and in parts of the second and fourth quadrants of the biaxial stress plane shown in Fig. 2-71. The maximum normal-stress criterion has been found to be applicable only when cleavage is the predominant mode of fracture; therefore, it is only applied where cleavage fracture is operative or possible. In uniaxial compression, shear is the only mode of deformation that can exist since there can be no resolved tension stress to cause cleavage. Accordingly, the maximum shear-stress criterion, which has been found to satisfactorily predict shear fracture for other metals, should be used in combination with the maximum normal stress criterion to predict fracture, as is shown by the full lines in Fig. 2-71.

Yielding will precede fracture and may be predicted by the inscribed maximum shear-strain energy criterion as shown by the ellipse in Fig. 2-71. This criterion has been found to satisfactorily predict yielding in other metals.

The coordinate axes in Fig. 2-71 are the principal biaxial stresses, σ_1 and σ_2 . The failure criteria of Fig. 2-71 are formulated as follows:

Maximum normal-tension stress:

$$\sigma_1 = F_{tu}$$

and

$$\sigma_2 = F_{tu}$$

Maximum shear-stress criterion:

$$\sigma_1 - \sigma_2 = \pm 2 F_{su} \text{ in quadrants II and IV}$$

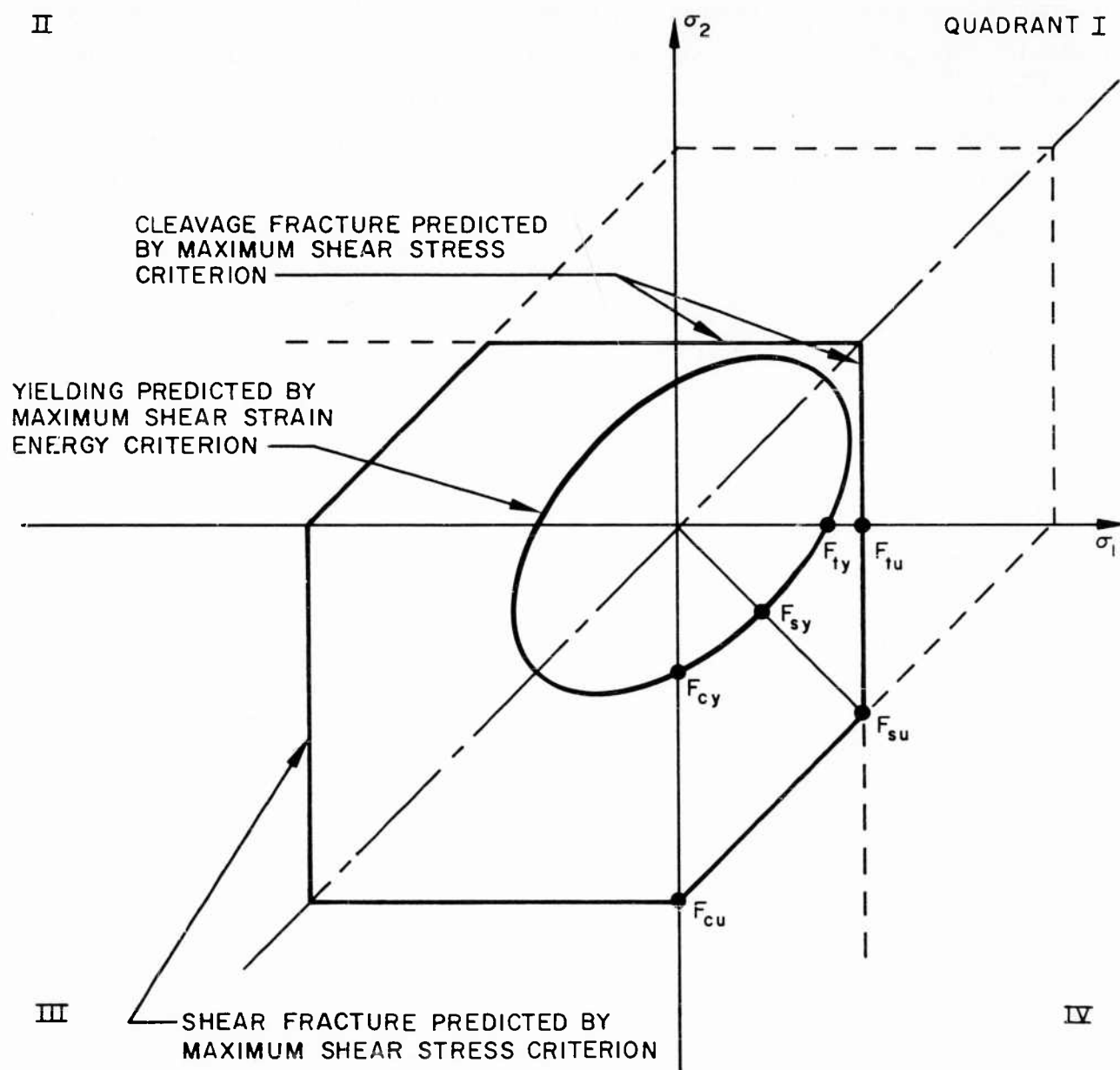


Fig. 2-71 Composite Biaxial Yield and Fracture Criteria for Hot-Pressed Beryllium Block at Low Temperatures

and

$$\sigma_1 = \pm 2 F_{su}$$

$$\sigma_2 = \pm 2 F_{su} \quad \text{in quadrants I and III}$$

Maximum shear-strain energy:

$$\left(\frac{\sigma_1 - \sigma_2}{2}\right)^2 + \left(\frac{\sigma_1}{2}\right)^2 + \left(\frac{\sigma_2}{2}\right)^2 = 2 (F_{sy})^2$$

As temperature increases, the shear-failure criteria given in Fig. 2-71 may be considered to decrease in amplitude while the cleavage-fracture criterion increases (Ref. 2-21). Thus, at some temperature between 400°F and 900°F, the shear-failure criteria would be almost completely operative with the cleavage-fracture criterion outside of the shear criteria. This situation is illustrated in Fig. 2-72.

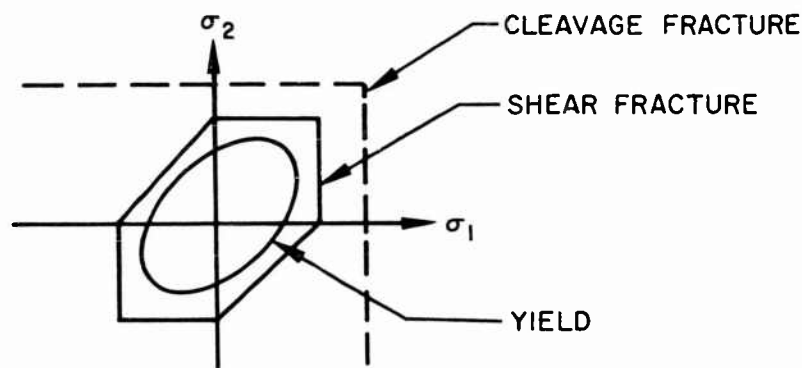


Fig. 2-72 High-Temperature Yield and Fracture Criteria

Above the equicohesive temperature, yield and fracture are expected to obey the maximum shear-stress criterion because of the viscous nature of grain-boundary deformation. Some small amount of strain hardening is to be expected above the equicohesive temperature and is indicated by the difference in amplitude of the two criteria shown in Fig. 2-73.

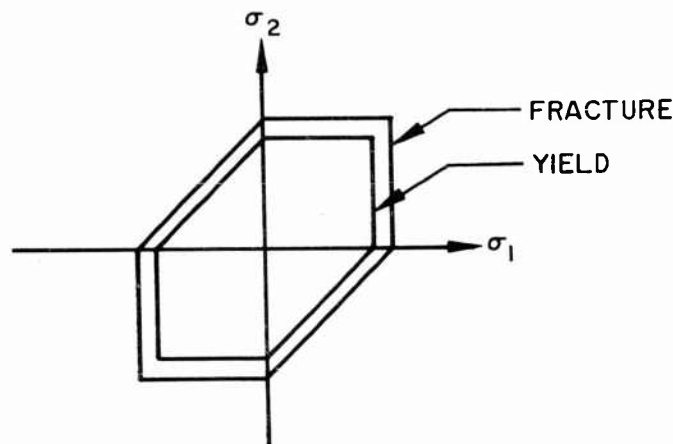


Fig. 2-73 Intercrystalline Yield and Fracture Criteria

It is noted at this point that compressive yield is characteristically lower than tensile yield for hot-pressed beryllium block having random grain orientation as shown in Fig. 2-74. Below the equicohesive temperature (approximately 900°F) the effect may be explained as the result of twinning. Above the equicohesive temperature the cause of the effect is not clear. Whatever may be the cause, in either case the effect is to encumber application of the idealized theories of material failure that have been presented.

Engineering judgment is perhaps the most direct approach to this problem when time, economics, and expediency have limited the investigation to uniaxial testing, only.

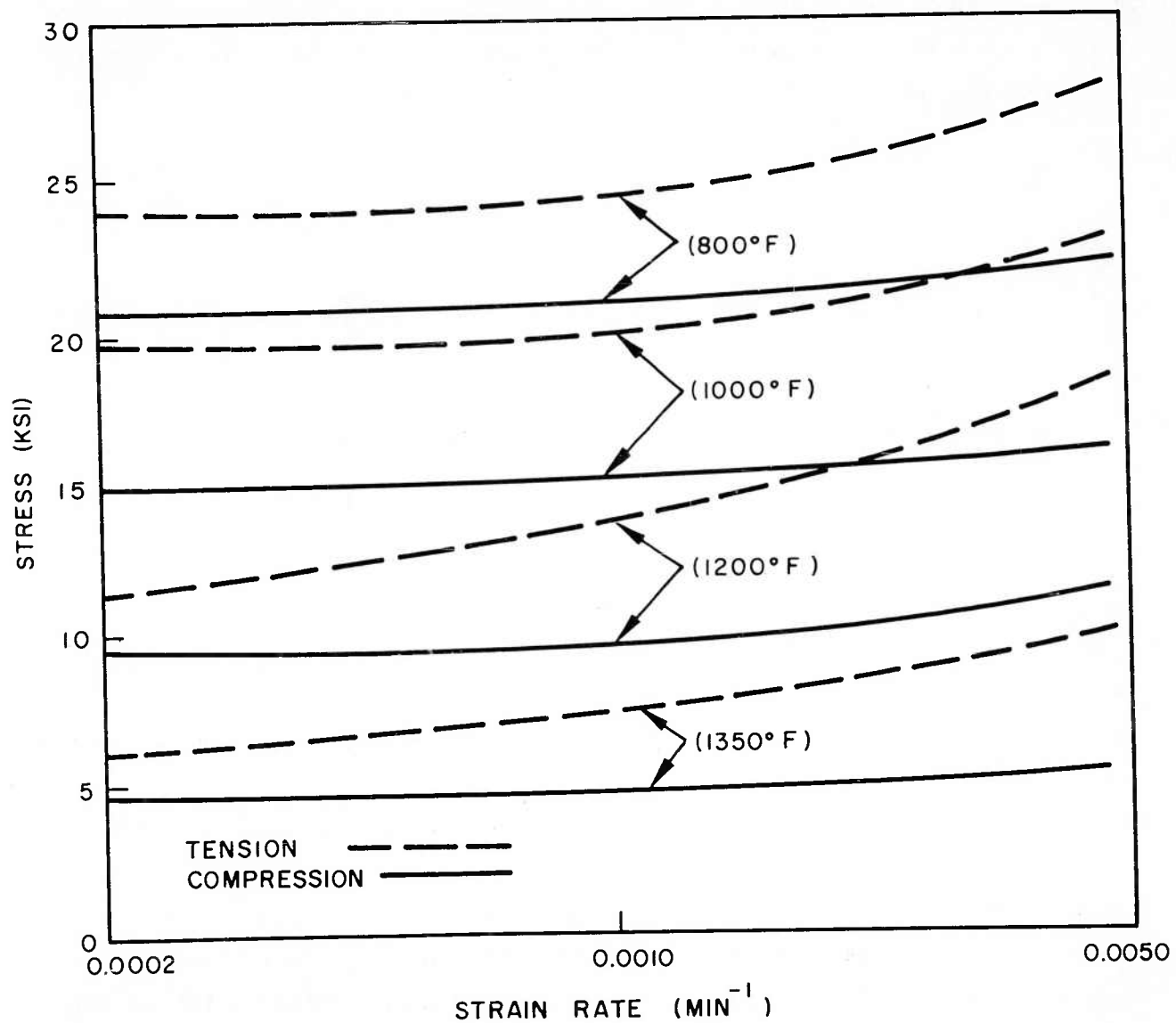
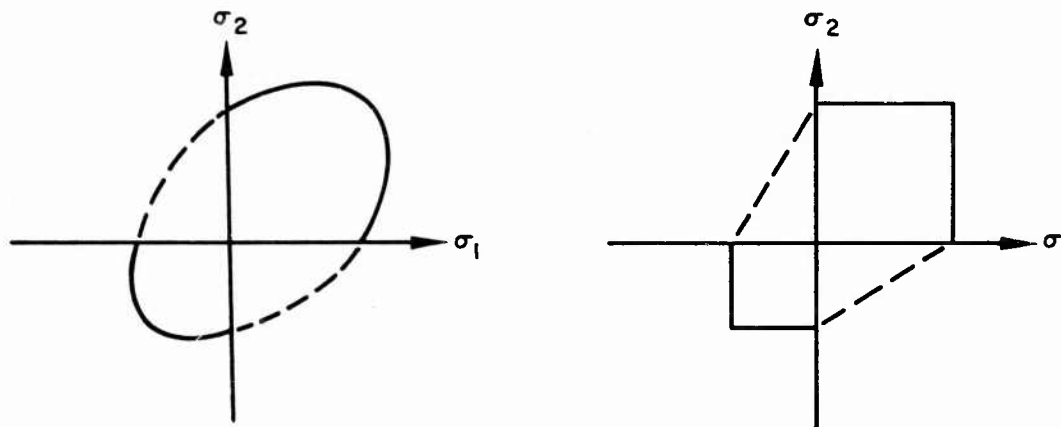


Fig. 2-74 Yield Stress Versus Strain Rate of QMV-S-Y6826 Beryllium (2% BeO) (see Ref. 2-1)

Given experimental values of the intercepts in the $\sigma_1 - \sigma_2$ plane, the maximum shear-strain energy criterion could be constructed through those points as usual to establish the criterion in the first and third quadrants. In the second and fourth quadrants, judgment may exert its influence. The procedure is illustrated in Fig. 2-75a. A similar subterfuge is shown in Fig. 2-75b for the maximum shear-stress criterion for yielding which applies above the equicohesive temperature. It is expected that the shapes of the fracture envelopes, both cleavage and shear, may be unaltered by the effect shown in Fig. 2-74.



(a) Maximum shear-strain energy criterion

(b) Maximum shear-stress criterion

Fig. 2-75 Modified Yield Criteria for Unequal Tensile and Compressive Yield Strengths

It is noted that yielding can occur so that the material continues to yield without increased stress. This phenomenon is commonly known as creep. In such cases, the stresses do not reach the fracture stress envelopes. The problem of fracture is then one of creep rupture in the presence of tensile stresses, and simply continued deformation when tensile stresses are not present. Further treatment of this aspect of the problem is beyond the scope of this report.

Test results from Section 2 and from unpublished results of LMSC investigations are plotted in Figs. 2-76 through 2-78 for beryllium block at room temperature, 800°F, and 1,000°F. In each of these figures, the data have been used to determine the amplitudes of the various criteria discussed. It should be noted that the criteria are not well substantiated by test data over their entire range. Further testing should be performed for this substantiation. However, some confidence in the validity of concepts of composite criteria discussed earlier is to be gained by noting the following in Fig. 2-76:

- The applicability of the maximum normal tension-stress criterion for predicting fracture in both tension and shear
- Yield strengths for both tension and compression are in accordance with the maximum shear-strain energy criterion (experimental values of F_{sy} have not been found)

It should also be noted that Fig. 2-77 implies that at 800°F some cleavage fracture (fracture on basal planes) is still operative since the maximum normal tensile-stress criterion extends somewhat into the fourth quadrant. This is consistent with the single-crystal strength data of Ref. 2-23.

Figures 2-76 and 2-77 show little or no effect of decreased compressive yield strengths at room temperature and 800°F because of twinning or whatever was responsible in data observed by others showing smaller compressive yield strengths than tensile yield strengths at high temperature (see Fig. 2-74).

Finally, it should be noted that no compressive fracture stresses for the third quadrants of Figures 2-76, 2-77, and 2-78 have been found in the literature or elsewhere. It is quite possible, especially at higher temperatures, that fracture in the third quadrant could be produced only by very high rates of straining.

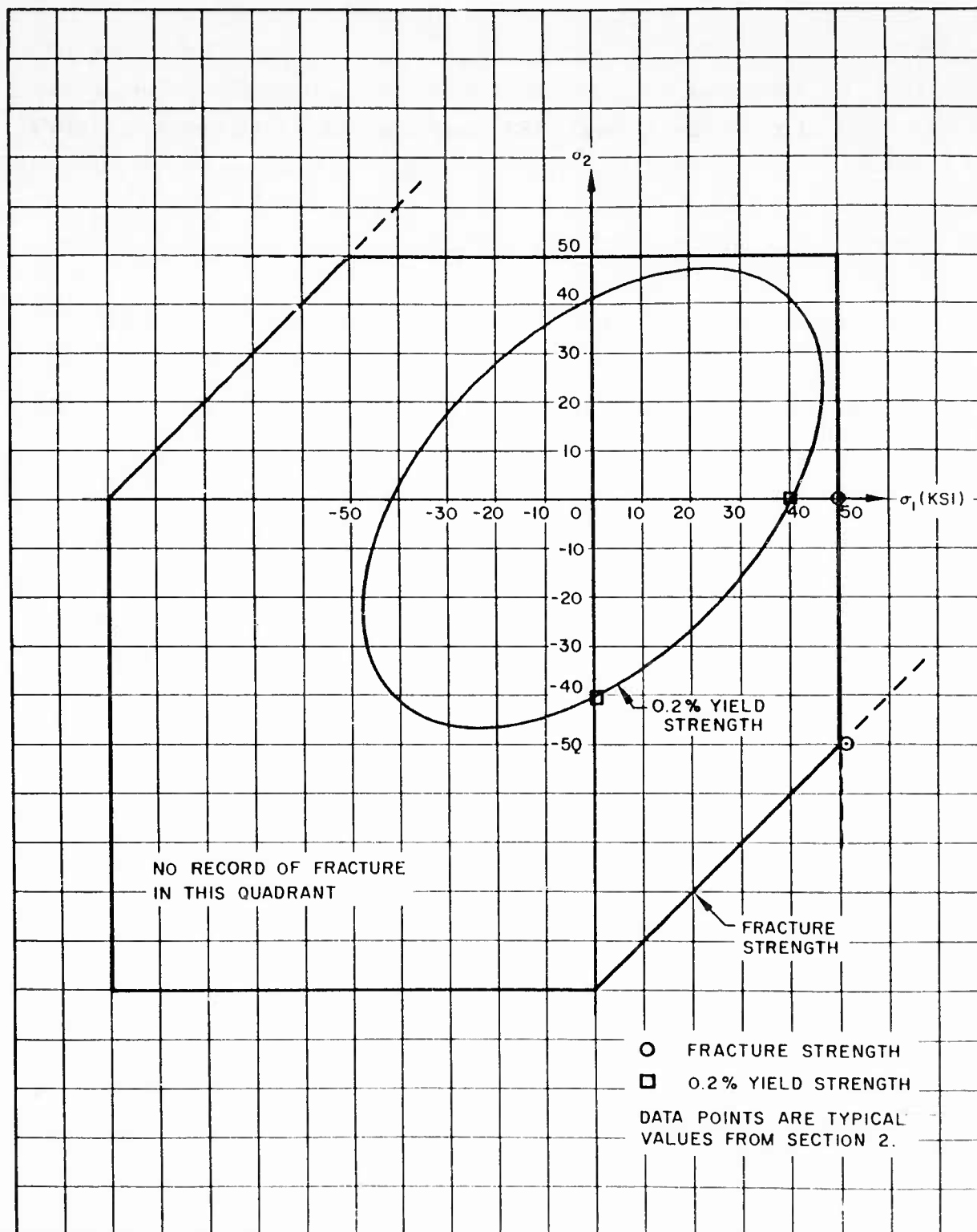


Fig. 2-76 Biaxial Strength Criteria for Beryllium Block at Room Temperature

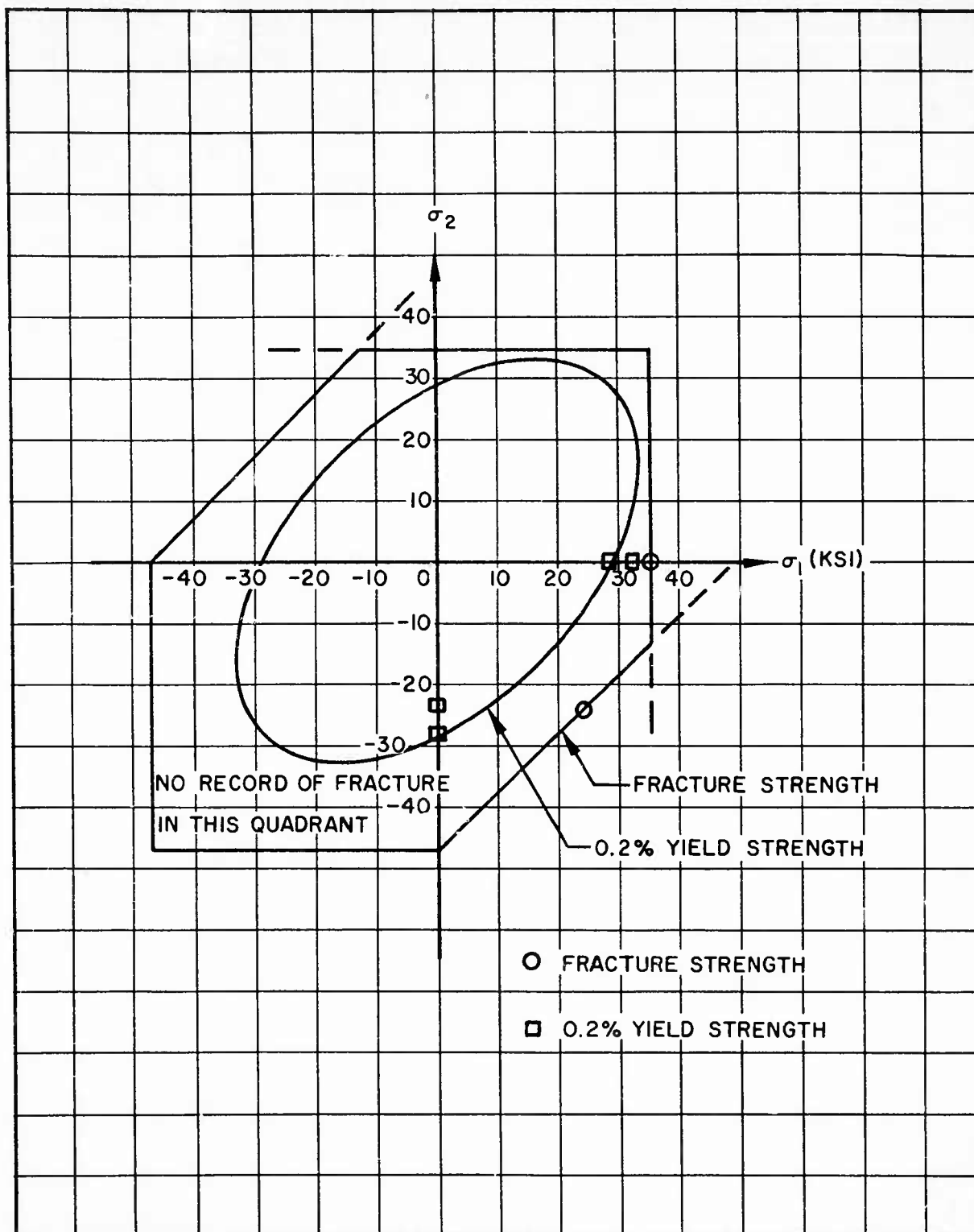


Fig. 2-77 Biaxial Strength Criteria for Beryllium Block at 800°F

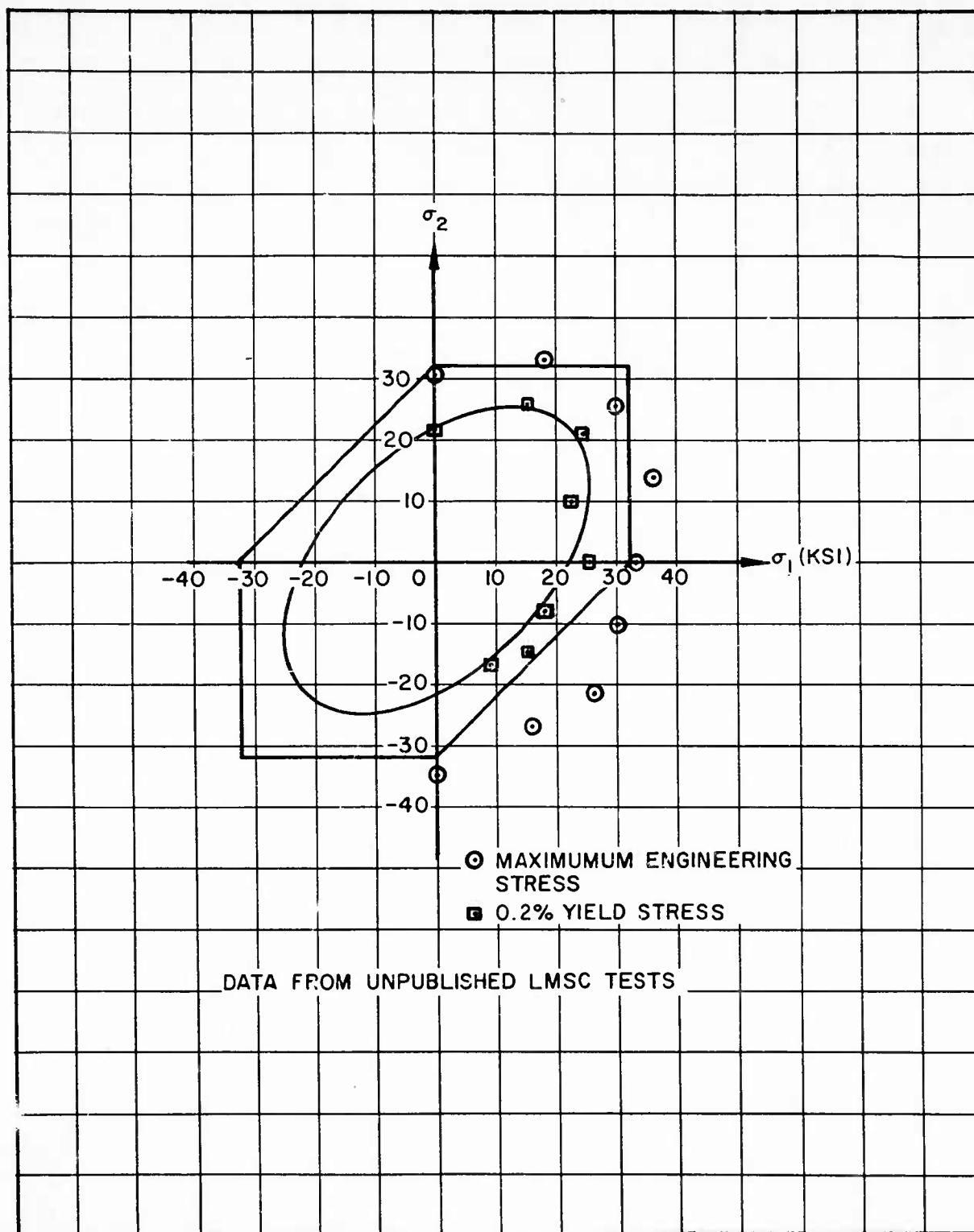


Fig. 2-78 Biaxial Strength Criteria for Beryllium Block at 1000°F

2.5.3 Beryllium Cross-Rolled Sheet

Cross-rolled sheet has a preferred grain orientation in which the basal planes of the lattice structure lie approximately in the plane of the sheet. It is assumed, although it is not precisely correct, that cross rolling produces a random distribution of the lattice orientation about their axes. Thus, macroscopic isotropy is assumed in the plane of the sheet.

One effect of this preferred orientation is that basal-plane cleavage is inhibited for sheet applications where stresses act only in the plane of the sheet and, accordingly, have no components normal to the basal planes. This tends to simplify determination of appropriate failure criteria for in-plane biaxial stresses in the sheet material since basal-plane cleavage is eliminated. However, a complicating factor is also introduced in that critical shearing stress for slip on prism planes is significantly lower than that for the pyramidal planes, at least at lower temperatures (Ref. 2-23). Shearing on the pyramidal planes has not been observed at room temperature, but it has been shown that shearing on those planes is involved in a mode (or modes) of deformation not yet fully defined. At lower temperatures, some investigators state that deformation on those planes is the result of twinning, while others, who have observed slip on pyramidal planes at 950°F in single crystals, contend that it can also occur at lower temperatures (Ref. 2-23).

Nevertheless, there must exist some critical stress value for deformation on pyramidal planes at all temperatures. If the state of stress is such that shear-stress components exist only on pyramidal planes, then deformation on those planes must be admitted for some stress magnitude. Accordingly, the maximum shear-stress criterion and the maximum shear-strain energy criterion are modified here to account for the differences between critical shear stresses for these two types of deformation.

In the following modifications of these two criteria for the anisotropic characteristics of beryllium sheet, it is assumed that each mode of slip can be treated separately,

that no coupling exists between modes, and that the inner envelope of the two treatments will provide the composite failure criterion. It is further assumed, as in the preceding treatment of block beryllium, that the maximum shear-strain energy criterion should be used for predicting yield strength, while fracture strength is predicted by the maximum shear-stress criterion.

For the maximum shear-stress theory, fracture on planes perpendicular to the basal planes will occur when

$$\frac{\sigma_1 - \sigma_2}{2} = F_{su(\text{prismoidal})}$$

Shear fracture will occur in the pyramidal mode when

$$\frac{\sigma_1}{2} = F_{su(\text{pyramidal})}$$

or

$$\frac{\sigma_2}{2} = F_{su(\text{pyramidal})}$$

Thus, the modified maximum shear-stress fracture criterion is represented in σ_1 , σ_2 coordinates as shown in Fig. 2-79 by the solid-line envelope of the two different modes. Similarly, the maximum shear-strain energy theory is modified so that yielding is predicted on planes perpendicular to basal planes by

$$\left(\frac{\sigma_1 - \sigma_2}{2} \right)^2 = F_{sy(\text{prismoidal})}^2$$

and on the pyramidal planes by

$$\left(\frac{\sigma_1}{2}\right)^2 + \left(\frac{\sigma_2}{2}\right)^2 = F_{sy(\text{pyramidal})}^2$$

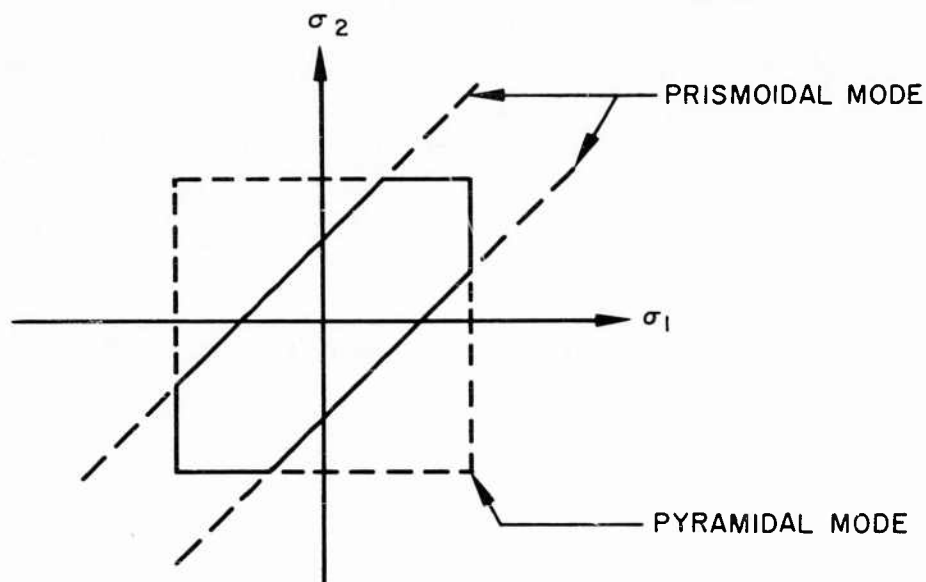


Fig. 2-79 Modified Maximum Shear-Stress Fracture Criterion for Beryllium Sheet

The modified maximum shear-strain energy yield criterion is represented on the $\sigma_1 - \sigma_2$ coordinates shown in Fig. 2-80.

Thus, the modified shear-strain energy yield criterion can be constructed inside the modified maximum shear-stress fracture criterion. These yield and fracture criteria are shown together in Fig. 2-81.

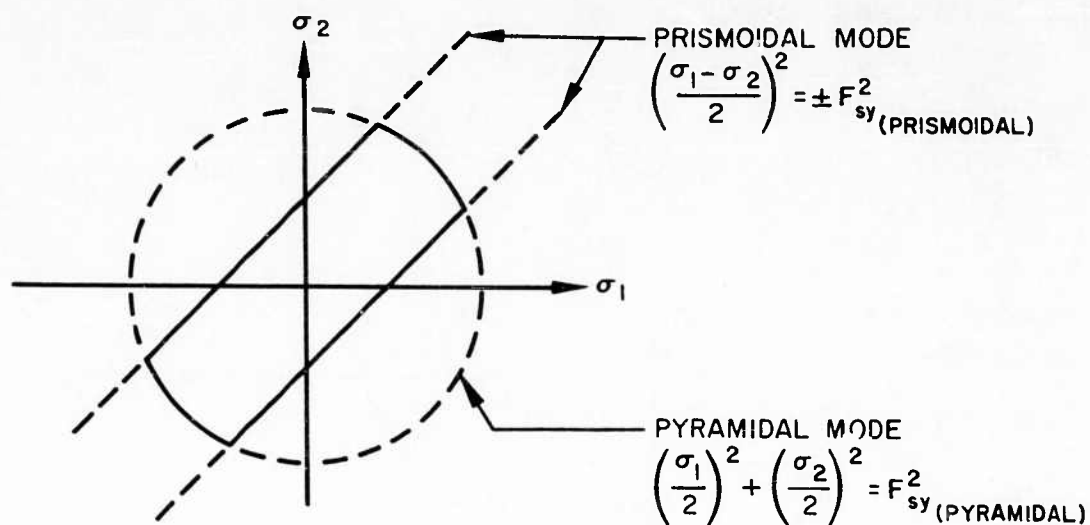


Fig. 2-80 Modified Shear-Strain Energy Yield Criterion for Beryllium Sheet

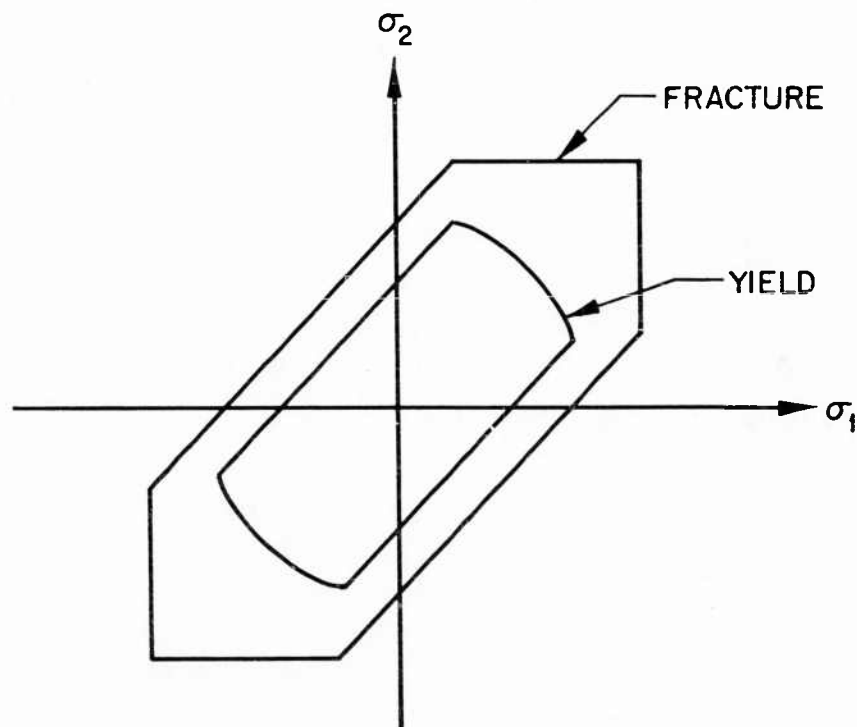


Fig. 2-81 Yield and Fracture Criteria for Beryllium Having Preferred Grain Orientation With Basal Planes Parallel to σ_1 , σ_2 Plane

At temperatures sufficiently above the equicohesive temperature, the grain orientation will have no effect because grain-boundary slip will predominate, in which case the maximum shear-stress criterion of Fig. 2-73 may be expected to apply.

Test results on the fracture strength of beryllium cross-rolled sheet from subsection 2.3.2, from the averaging of all data from the bend tests performed under this program (see Appendix B), and from Ref. 2-24 are plotted in Figs. 2-82 through 2-84. These figures are for room temperature, 400°, and 600°F, respectively. Only fracture strengths are given in these figures because, except for the 600°F test, fracture occurred with only very small amounts of plastic flow. Figures 2-82 through 2-84 are limited to the first quadrant of the biaxial stress plane because test data are available only for that quadrant. The fracture criterion on these graphs is for prismoidal fracture. The fractures were normal to the plane of the sheet and at an angle of approximately 25 deg to the transverse direction. Pyramidal shear would not have had these characteristics.

The uniaxial values of F_{tu} are typical values as determined from the data of subsection 2.3.2. The fracture criteria lines for prismoidal fracture are drawn through the uniaxial values.

The average values of the biaxial strength data are indicated by large four-sided areas representing limits of interpretation of test results. The test results interpreted are the wide-sheet bend tests of this program (see Appendix B) and those of Ref. 2-24.

The wide-sheet bend test, as shown in Ref. 2-25, provides a means by which biaxial stresses may be developed by simply bending a wide sheet. The stresses in the longitudinal direction are those necessary for equilibrating the applied moment. The stresses in the transverse direction are those arising from restraint of anticlastic curvature. The test results in Appendix B prove that anticlastic curvature was indeed completely restrained over most of the loading range. The transverse stress induced by this restraint is equal to Poisson's ratio times the longitudinal stress, since the strains

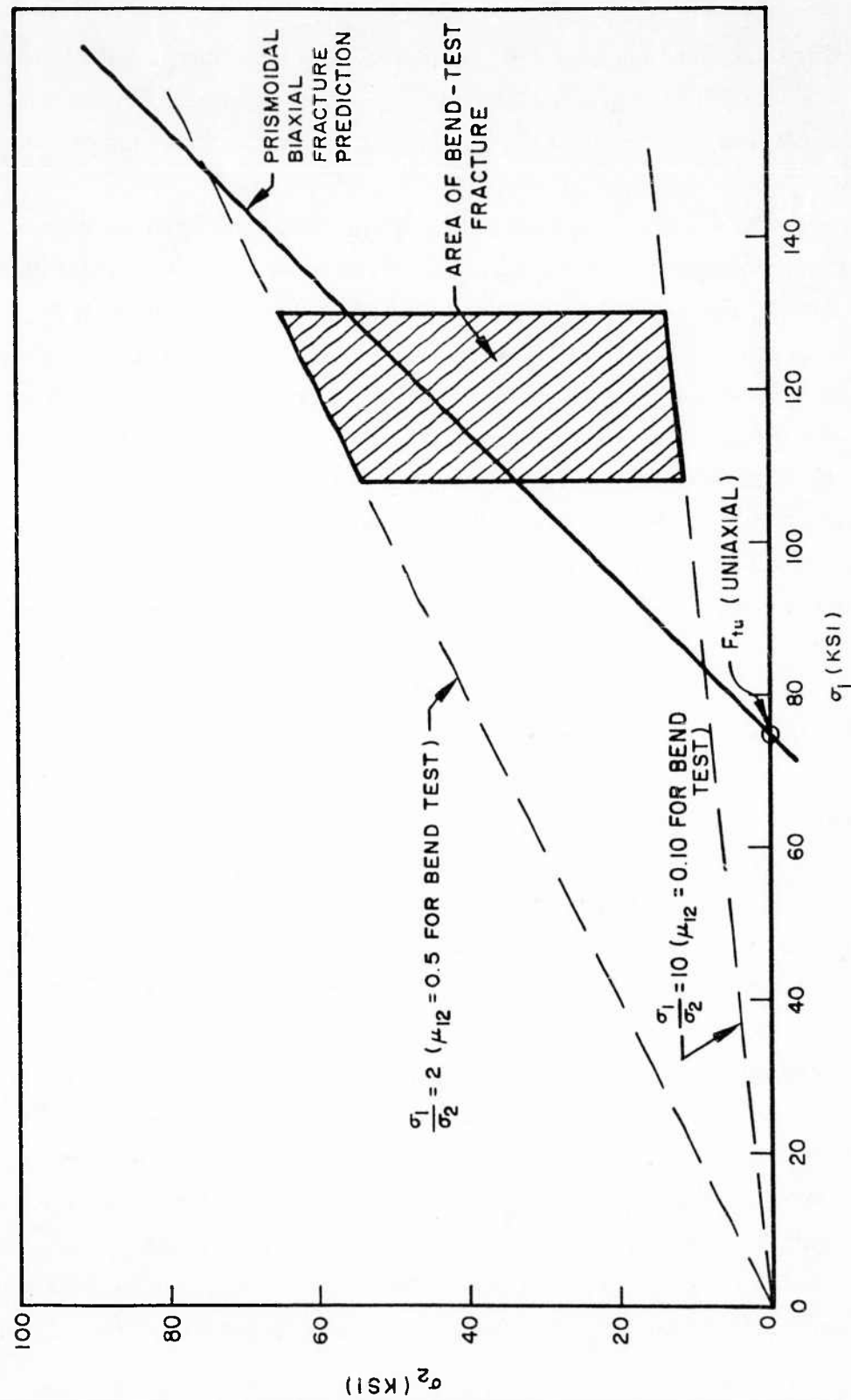


Fig. 2-82 Wide-Sheet Bend Test Results for Cross-Rolled Beryllium Sheet at Room Temperature

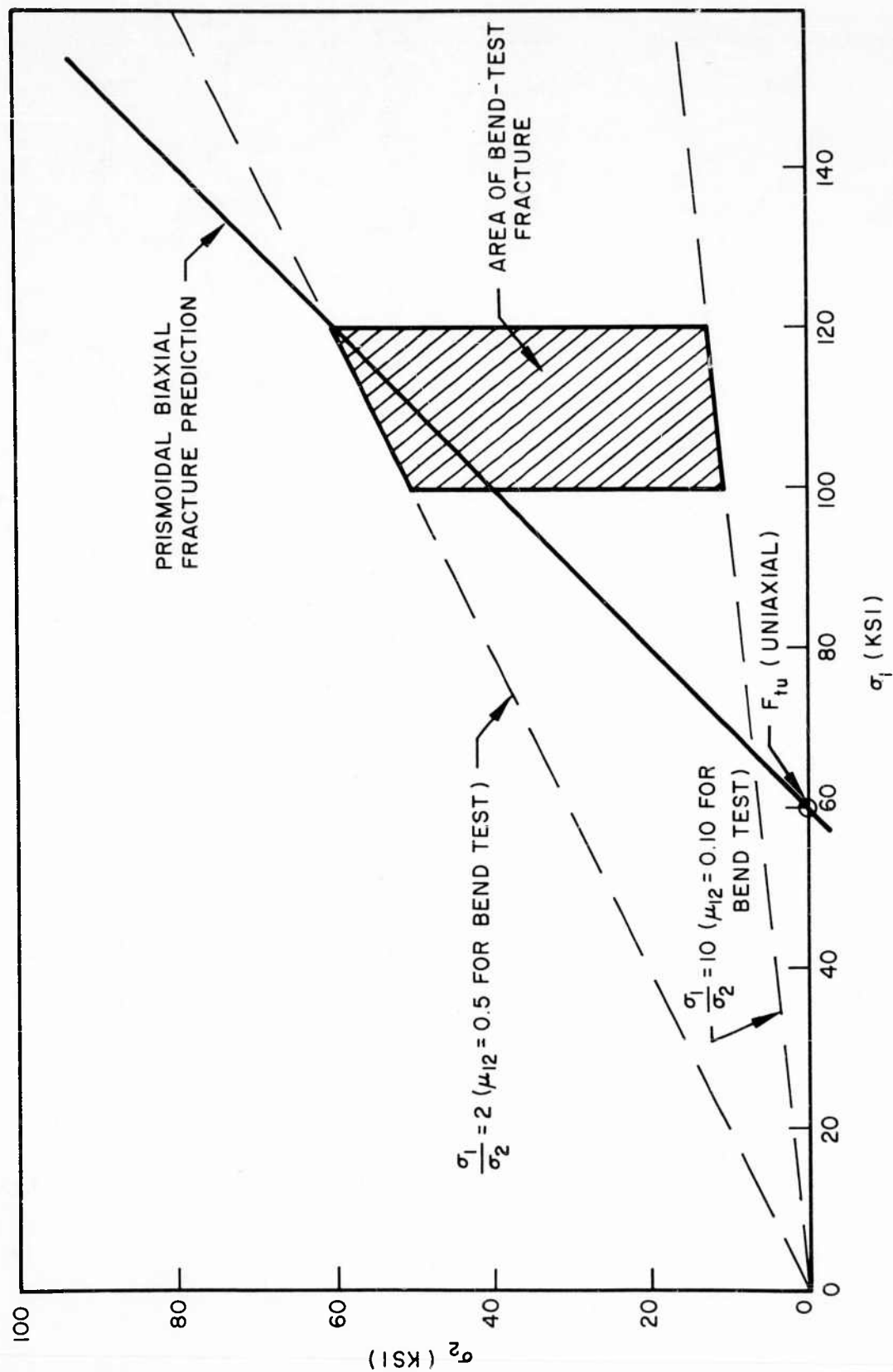


Fig. 2-83 Wide-Sheet Bend Test Results for Cross-Rolled Beryllium Sheet at 400°F

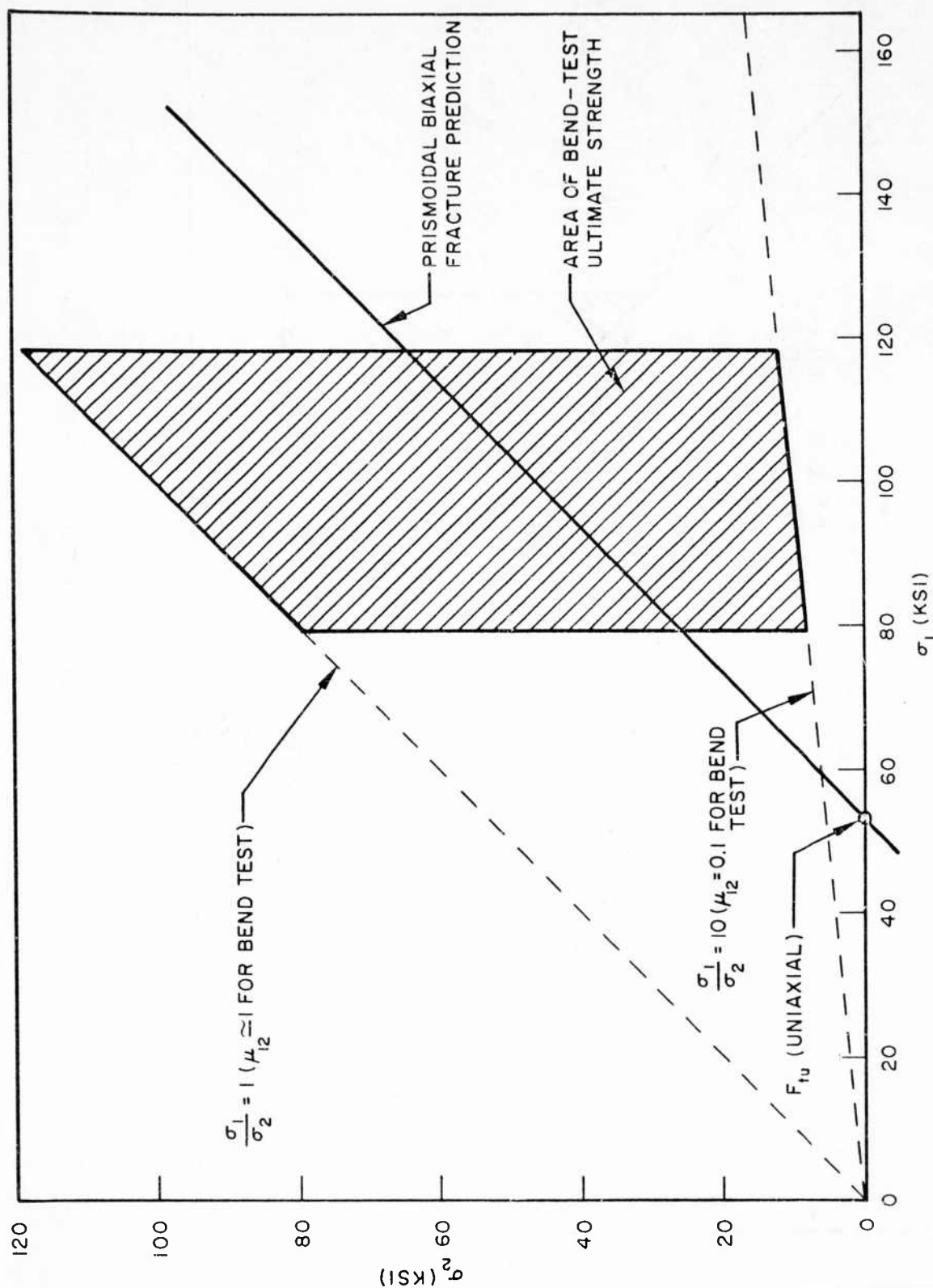


Fig. 2-84 Wide-Sheet Bend Test Results for Cross-Rolled Beryllium Sheet at 600°F

that would occur if the development of anticlastic curvature were not restrained would be Poisson's ratio times the longitudinal strain.

In performing tests of this type, two serious problems arise which make the tests only of qualitative value. First, it is not possible to determine the plastic value of Poisson's ratio to apply when longitudinal stresses become plastic. Therefore, the degree of biaxiality is not known. Second, the extreme fiber longitudinal stress cannot be determined precisely since the distribution of stresses over the cross section of the plate cannot be determined.

In the present case, it was determined experimentally that the value of Poisson's ratio, μ_{12} , in the plane of the sheet is approximately 0.10 in the elastic range. It was also determined that Poisson contraction in the thickness direction resulting from applied tension in the plane of the sheet is much smaller than the above by approximately an order of magnitude. This conclusion applies in both the elastic and plastic regimes. Therefore, induced biaxiality can range between approximately 10:1 and 1:1.

The extreme fiber stress at fracture or ultimate load in these bend tests can range from

$$F_{tu} = \frac{Mc}{I}$$

to

$$F_{tu} = \frac{2}{3} \frac{Mc}{I}$$

depending on whether the stresses are completely elastic or completely plastic, respectively.

In graphically presenting the results of these tests, a four-sided area is given in which the true situation at fracture must lie. The upper and lower boundaries of the areas

are formed by lines for 2:1 and 10:1 biaxility ratios. The lower boundary is for the elastic value of Poisson's ratio while the upper is a very extreme guess as to the plastic value of Poisson's ratio at fracture. It is felt that since the specimens of both this program and Ref. 2-24 failed in a very brittle manner, little plastic flow could have occurred; hence Poisson's ratio could not have been large at failure.

The vertical boundaries for the room temperature and 400°F cases are formed by calculating the extreme fiber longitudinal stresses by the following two formulas:

$$F_{tu} = \frac{Mc}{I}$$

and

$$F_{tu} = \frac{5}{6} \frac{Mc}{I}$$

The absolute minimum value of the stress as computed by

$$F_{tu} \Big|_{\min} = \frac{2}{3} \frac{Mc}{I}$$

was not used in the room-temperature and 400°F cases because, as mentioned above, all of those specimens failed in a very brittle manner and the fully plastic assumption implicit in the above equation is therefore not justifiable. However, that absolute minimum value was used in the 600°F case where fracture did not occur.

It is felt that the results of Figs. 2-82 through 2-84 show quite well that a potentially very large biaxial strength is exhibited by beryllium sheet. In all cases, the minimum value of σ_1 for the biaxial state of stress is at least 50 percent greater than the uni-axial strength.

Ample potentiality is shown by these data to warrant further investigations of this phenomenon by more quantitative means such as long-tube tests in which 2:1 biaxility would be produced, and bulge tests on spherical segments wherein 1:1 biaxility would be produced.

2.6 REFERENCES

2.6.1 Cited References

- 2-1 Lockheed Missiles and Space Division, Beryllium Design Data, LMSD-48472, Sunnyvale, Calif.
- 2-2 Battelle Memorial Institute, Heat Capacity of Beryllium, by J. W. Holladay, DMIC Memo. 36, Columbus, Ohio, 19 Oct 1959
- 2-3 M. Udy, H. Shaw, and F. Boulger, "Properties of Beryllium," Nucleonics, Vol. II, No. 5, May 1953
- 2-4 United States Atomic Energy Commission, Mechanical Properties of Reactor-Grade Beryllium at Elevated Temperatures, by R. G. O'Rourke, J. N. Hurd, K. G. Wickle, and W. W. Beaver, Rpt. No. C00-312, Aug 1956
- 2-5 Thermatest Laboratories, Inc., Room and Elevated Temperatures Bearing and Shear Properties of Beryllium, Rpt. No. 59-1005, Sunnyvale, Calif., 30 Dec 1960 (work performed for Lockheed Missiles and Space Company)
- 2-6 The Martin Company, Relation of Mechanical Behavior of Beryllium Sheet to Fabrication Variables, by C. J. Giemza, Rpt. No. RR-22, Mar 1961
- 2-7 Wright Air Development Division, Mechanical Properties of Beryllium, by A. E. Riesen and R. T. Ault, TR 60-425, Sep 1960
- 2-8 Wright Air Development Center, Development and Evaluation of Structural Beryllium, by C. J. Giemza, TR 59-349, Apr 1959
- 2-9 The Marquardt Corporation, Evaluation of the Short Time Mechanical Properties of Hot Rolled Beryllium Sheet, by E. C. Bennett, Rpt. No. MP63, Van Nuys, Calif., Nov 1959
- 2-10 Boeing Airplane Company, [Letters and Enclosures], from Vincent Dornes, May 1961

- 2-11 G. E. Darwin and J. H. Buddery, Beryllium, Metallurgy of the Rarer Metals-7, New York, Academic Press, 1960
- 2-12 Lockheed Aircraft Corporation, Fatigue Tests of Some Hot-Pressed Beryllium, Rpt. No. 12954, Burbank, Calif., 27 Mar 1958
- 2-13 Lockheed Missiles and Space Division, Fatigue Strength of Beryllium at Elevated Temperature, by R. Lim, LMSD Rpt. No. FL-10, 183A, Sunnyvale, Calif., 15 Apr 1960
- 2-14 Lockheed Missiles and Space Division, Beryllium Butt Joint Fatigue Tests, by R. D. Currier, LMSD-505037, Sunnyvale, Calif., Mar 1959
- 2-15 The Marquardt Corporation, Evaluation of the Short Time Mechanical Properties of Brush QMV Block Beryllium, by E. C. Bennett, Rpt. No. MP65, Van Nuys, Calif., Mar 1960
- 2-16 Convair/Pomona, Tests on Beryllium Sheet, by R. H. Sparling, Rpt. No. ERR-PO-009, 18 Feb 1960
- 2-17 Aircraft Manufacturers Council, Development of Beryllium Sheets Rolled Flat to Gauge, by K. G. Wickle, J. W. Armstrong, and H. N. Perrin, TR 60-7-631, Sep 1960
- 2-18 Lockheed Missiles and Space Division, Tensile Properties of 1/4 Inch Brush Beryllium Sheet, by F. Haskins, Test Rpt. No. FL-2825-A, Sunnyvale, Calif., 27 Jun 1960
- 2-19 Lockheed Missiles and Space Division, Beryllium (Brush QMV Rolled Sheet): Tensile Properties at Room and Elevated Temperatures, by A. Karchem, LMSD-500650, Sunnyvale, Calif., 15 Jan 1959
- 2-20 R. E. Peterson, Stress Concentration Design Factors, 2nd printing, New York, John Wiley & Sons, Sep 1959
- 2-21 D. W. White, Jr., and J. E. Burke, The Metal Beryllium, Cleveland, Ohio, American Society for Metals, 1955

- 2-22 Brush Beryllium Company, Mechanical Properties of Reactor-Grade Beryllium at Elevated Temperatures, by R. G. O'Rourke, J. N. Hurd, K. G. Wickle, and W. W. Beaver, AEC Rpt. No. C00-312, Cleveland, Ohio, Aug 1956
- 2-23 G. E. Darwin and J. H. Buddery, Beryllium, New York, Academic Press, 1960
- 2-24 Lockheed Missiles and Space Division, Beryllium Crack Propagation and Effects of Surface Condition, by C. O. Matthews, M. I. Jacobson, W. E. Jahsman, and W. V. Ward, LMSD-288170, WADD TR 60-116, Sunnyvale, Calif., Jan 1960
- 2-25 E. G. Thomsen and J. E. Dorn, "The Effect of Combined Stresses on the Ductility and Rupture Strength of Magnesium-Alloy Extrusions," J. Aero. Sci., Vol. 11, No. 2, Apr 1944, pp. 125-136

2.6.2 Uncited References

Charles S. Barrett, Structure of Metals, 2nd ed., New York, McGraw-Hill, 1952

Battelle Memorial Institute, Beryllium for Structural Applications—A Review of the Unclassified Literature, Defense Metals Information Center, Rpt. No. 106, Columbus, Ohio, Aug 1958

Alfred M. Freudenthal, The Inelastic Behavior of Engineering Materials and Structures, New York, John Wiley & Sons, 1950

Lockheed Missiles and Space Division, On Determining Biaxial-Stress Yield and Fracture Criteria for Hot-Pressed Beryllium at Room and Elevated Temperatures, by R. F. Crawford, LMSD-49576-1, Sunnyvale, Calif., Jan 1960

Maxwell Gensamer, Strength of Metals Under Combined Stresses, Cleveland, Ohio, American Society for Metals, 1953

A. Nadai, Theory of Flow and Fracture of Solids, Vol. I, 2nd ed., New York, McGraw-Hill, 1950

Earl R. Parker, Brittle Behavior of Engineering Structures, New York, John Wiley & Sons, 1957

Section 3

BERYLLIUM COMPONENT DESIGN DATA

3.1 INTRODUCTION

Data to assist in the structural design of beryllium components are presented in this section. These include buckling and post-buckling design data for flat, unstiffened panels (subsection 3.2); column buckling design data (subsection 3.2.5); design data for the buckling of monocoque cylinders (subsection 3.3); crippling design data (subsection 3.4); plastic bending design data (subsection 3.5); joining data (subsection 3.6); and recommendations for fail-safe design and fittings (subsection 3.7). In addition, it should be noted that applicable design data for stiffened panels and cylinders are presented in Section 4, owing to the presentation of sufficient information in that section to determine the load-carrying ability of nonoptimum geometries, as well as optimum geometries.

Many of the design data presented here have been verified by experimental programs, the details of which are summarized in the appendixes of this report. Test points are shown on the charts and conclusions which may be drawn from the tests are presented appropriately in the text. In general, it may be concluded that the standard methods for deriving such design data as presented in this section may be applied with confidence to beryllium. This conclusion is significant since it dispels the necessity for extensive testing to establish design data for this material. Areas where reasonable doubt regarding this conclusion is apparent are emphasized in the text.

All design charts presented here have been developed for beryllium cross-rolled sheet and beryllium hot-pressed block. Without exception, all design charts show plastic stresses as well as elastic stresses. To be universally acceptable, therefore, the charts must be based on a standardized stress-strain curve, which represents the

typical properties of the material available from the producer. Such stress-strain curves may be found in MIL-HDBK 5 for many materials. In general, this type of presentation is made possible by the existence of military, Federal, or industry material specifications which regulate the material's composition and properties. In the case of beryllium block, it appears that sufficient experience has been gained by both producer and user to establish the composition having 1.75-percent BeO as the standard grade, although as yet no industry-wide material specification has been adopted. Therefore, typical stress-strain curves, such as those shown in Figs. 3-1a and 3-1b, may be obtained which may be approximated by any user ordering this grade of material.

Beryllium cross-rolled sheet, on the other hand, is a relatively new product which is not familiar to many potential users except possibly on a laboratory scale. To date, characteristics of the material have been uncovered which, if improved, would certainly induce more designers to specify this material. Naturally, the producers are currently attempting to improve upon their product and undoubtedly will do so in time. However, at the present time there is no universally acceptable standard grade of cross-rolled beryllium sheet and therefore it is impossible to present design charts for this material which can be thought to apply indiscriminately to millrun, cross-rolled sheet. The data which are presented in this section for cross-rolled sheet are based on "example" stress-strain curves (Fig. 3-2) which represent a compromise between what is currently available from the producer and what the structural designer would settle for on a typical basis. It is emphasized that before using these charts, the designer should be assured that the stress-strain characteristics of the cross-rolled sheet available to him approximate within acceptable limits those shown in Fig. 3-2. If they do not, the appropriate equations presented in the text should be employed and used with the new stress-strain data to derive a new design chart.

Of assistance in comparing other stress-strain data with those shown in Fig. 3-2 are the conclusions which may be drawn from Figs. 3-3 and 3-4. Compressive stress-strain curves are obviously preferred as a basis on which to construct buckling and crippling

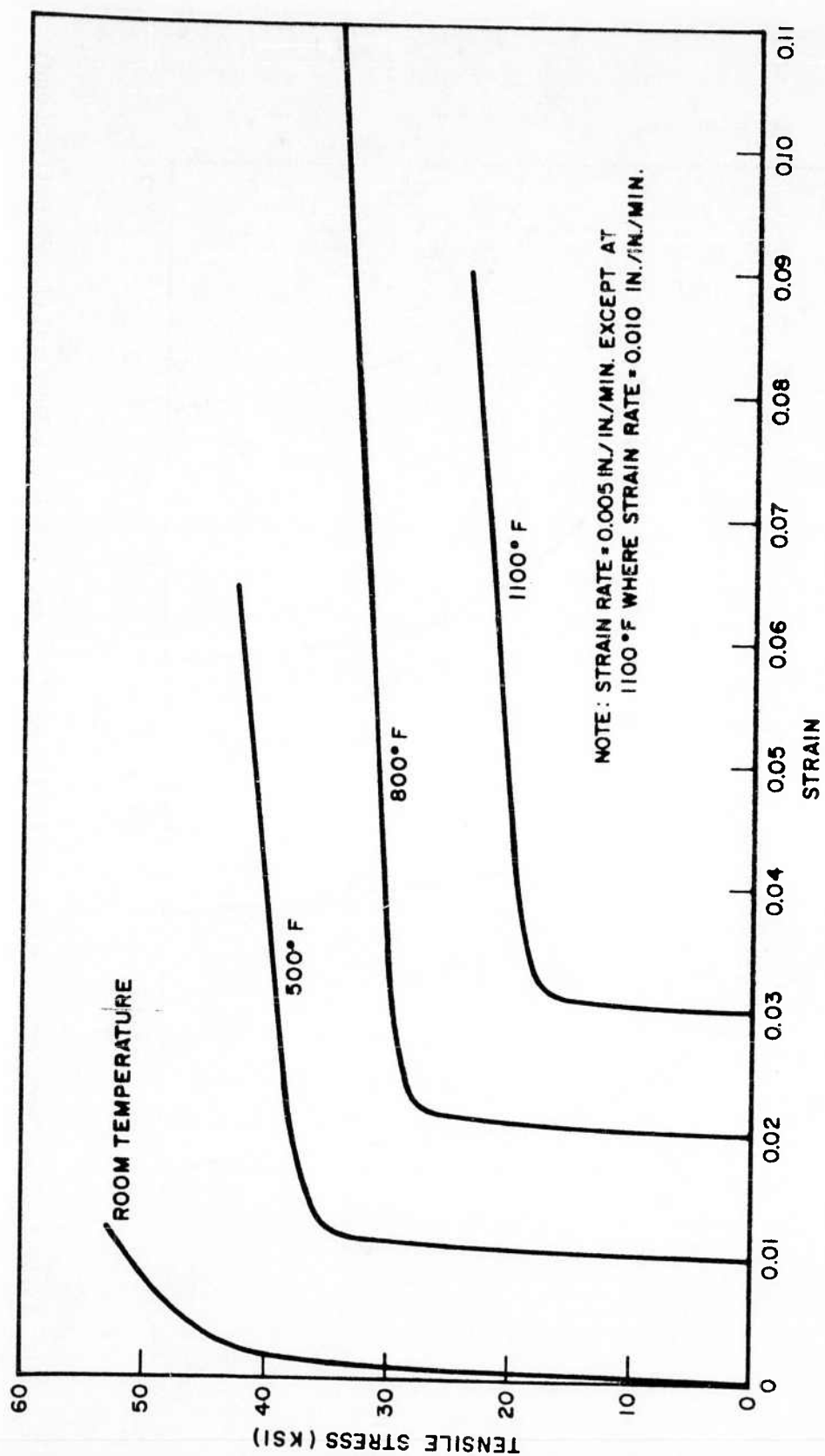


Fig. 3-1a Typical Tensile Stress-Strain Curves for Beryllium Block Material (1.75% BeO Content)

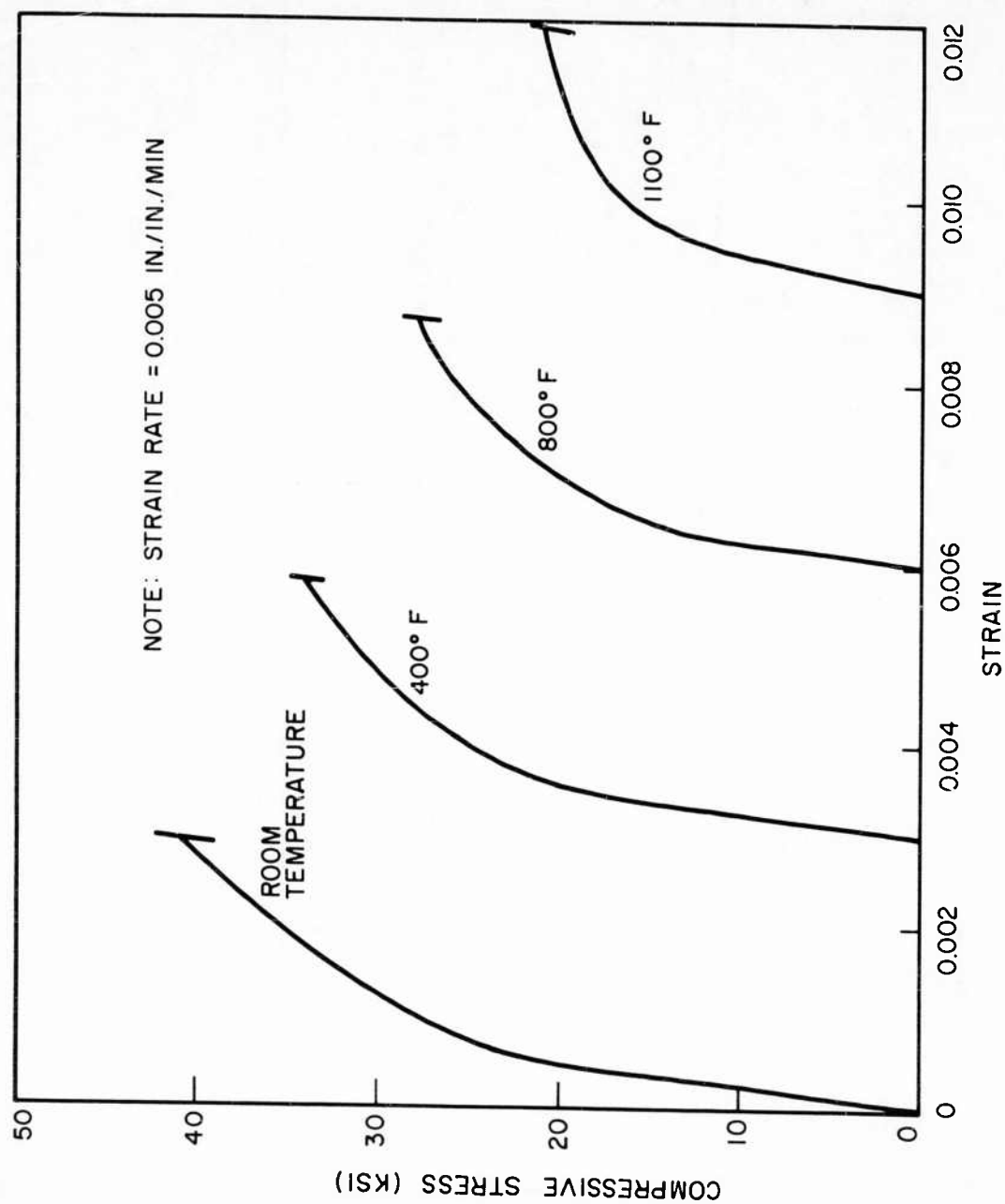


Fig. 3-1b Typical Compressive Stress-Strain Curves for Beryllium Block Material (1.75% BeO Content)

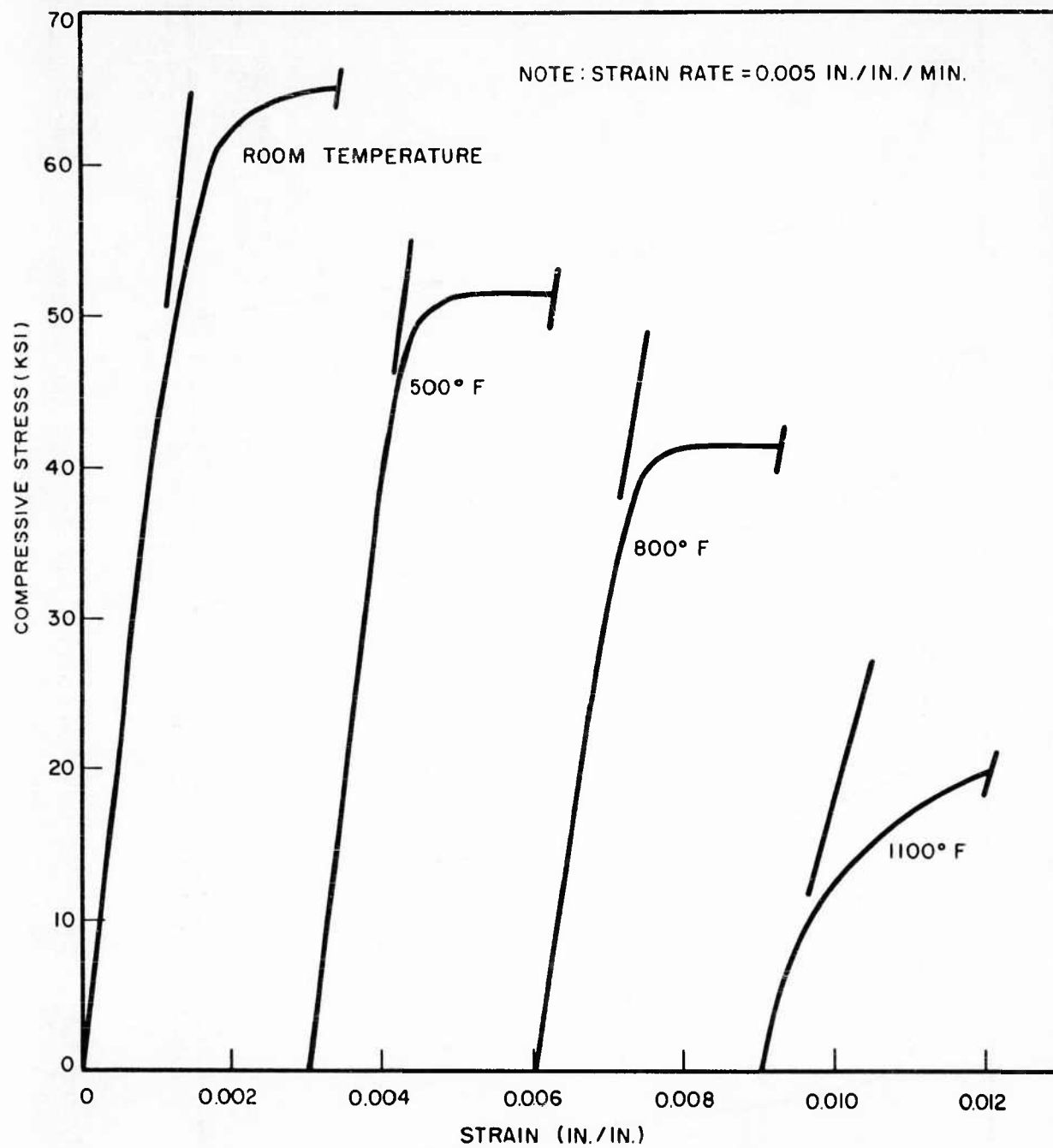


Fig. 3-2 Example Compressive Stress-Strain Curves for As-Received Beryllium Cross-Rolled Sheet (1.75% BeO Content)

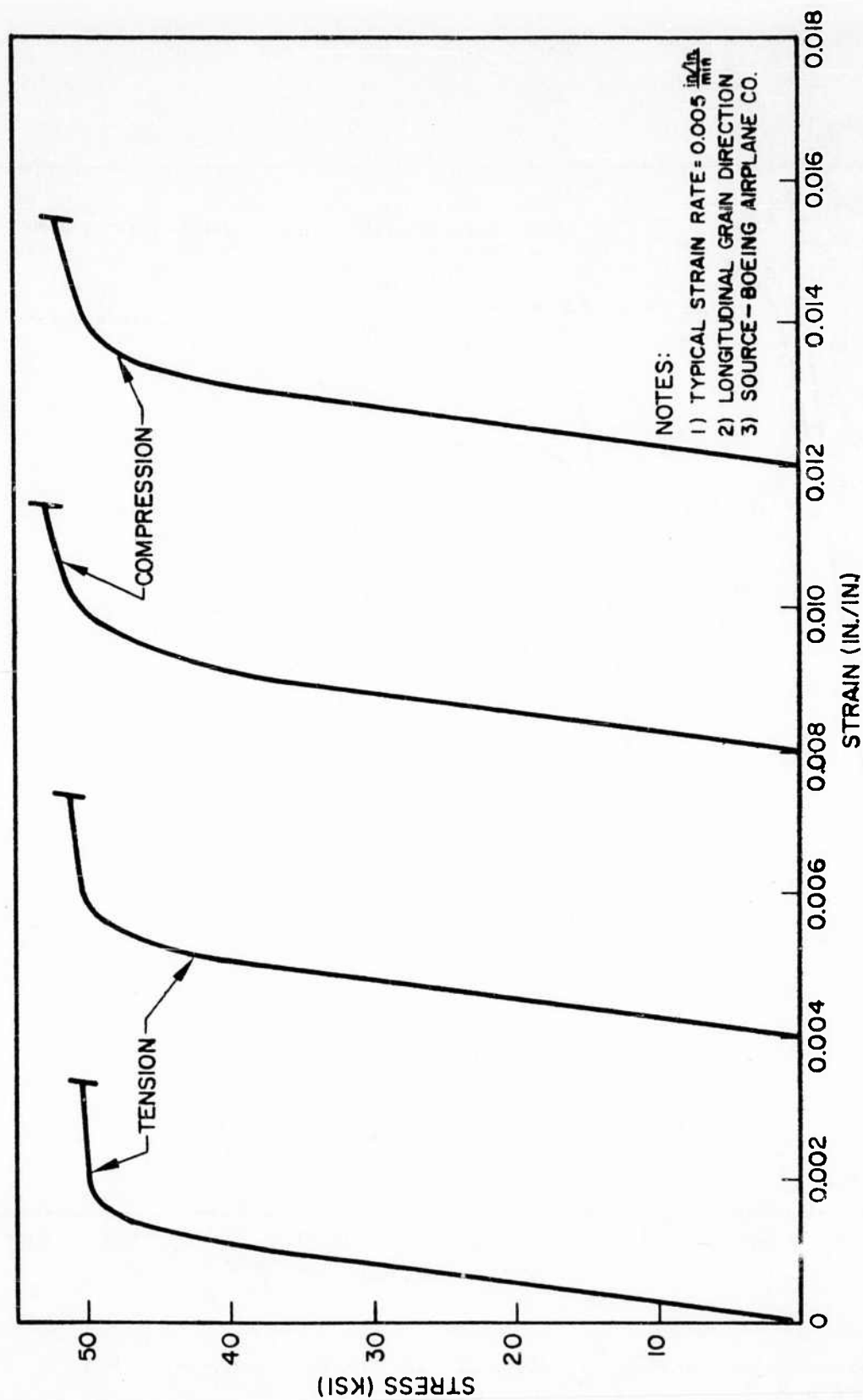


Fig. 3-3 Comparison of Typical Tensile and Compressive Stress-Strain Curves at Room Temperature for Beryllium As-Received Cross-Rolled Sheet

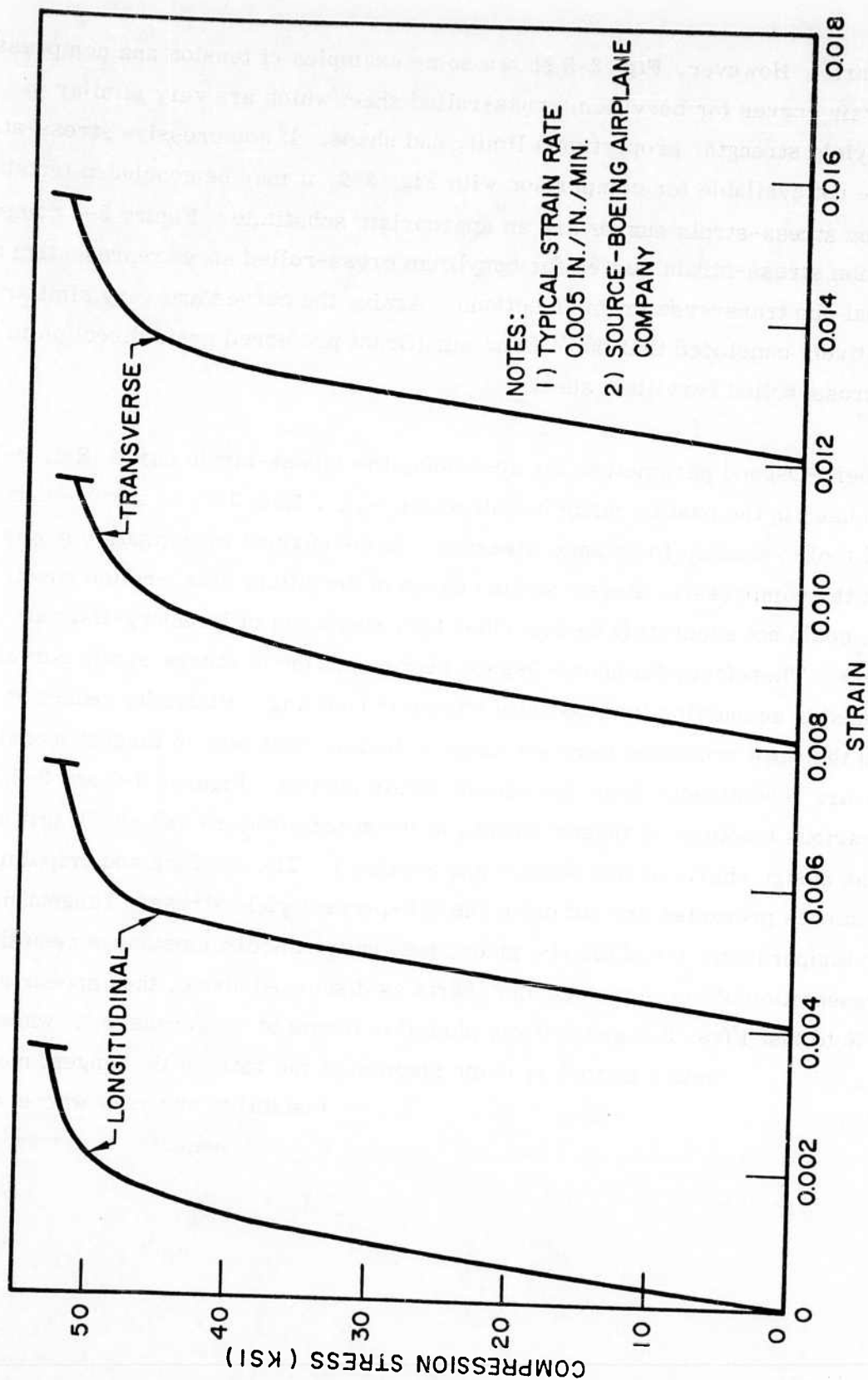


Fig. 3-4 A Comparison of Typical Room-Temperature Compressive Stress-Strain Curves for Beryllium Cross-Rolled Sheet on the Basis of Grain Direction

design charts. However, Fig. 3-3 shows some examples of tension and compression stress-strain curves for beryllium cross-rolled sheet which are very similar in regard to yield strength, proportional limit, and shape. If compressive stress-strain curves are not available for comparison with Fig. 3-2, it may be concluded tentatively that tension stress-strain curves are an appropriate substitute. Figure 3-4 compares compression stress-strain curves for beryllium cross-rolled sheet representing the longitudinal and transverse grain directions. Again, the curves are very similar and it is tentatively concluded that there is no significant preferred grain direction in the plane of cross-rolled beryllium sheet.

The Ramberg-Osgood parameters for describing the stress-strain curve (Ref. 3-1) have been used in the past by many investigators (e. g. , Ref. 3-2) as a convenient analytical tool to account for plastic stresses. In the current investigation it was found that the compressive stress-strain curves of beryllium cross-rolled sheet, Fig. 3-2, could not accurately be described by a single set of Ramberg-Osgood parameters. Therefore, Ramberg-Osgood representation of stress-strain curves was not used in accounting for plasticity effects in buckling. Plasticity reduction factors in the work presented here are taken to be functions only of tangent moduli and these are read directly from the stress-strain curves. Figures 3-5 and 3-6 present various functions of tangent moduli at room temperature and 800°F that are used in the design charts of this section and Section 4. The buckling and crippling strength curves presented are cut off at the 0.2-percent yield stress. Tangent moduli for other temperatures could also be given, but, under the circumstances resulting in the presentation of "example" design charts as discussed above, they appear superfluous. Note that Figs. 3-5 and 3-6 are plotted in terms of σ versus σ/η where η , the plasticity reduction factor, is some function of the ratio of the tangent modulus to the elastic modulus. This format is convenient in instability analyses where σ/η may be found without resorting to iteration procedures, then evaluated in terms of σ by use of charts of the type of Figs. 3-5 and 3-6.

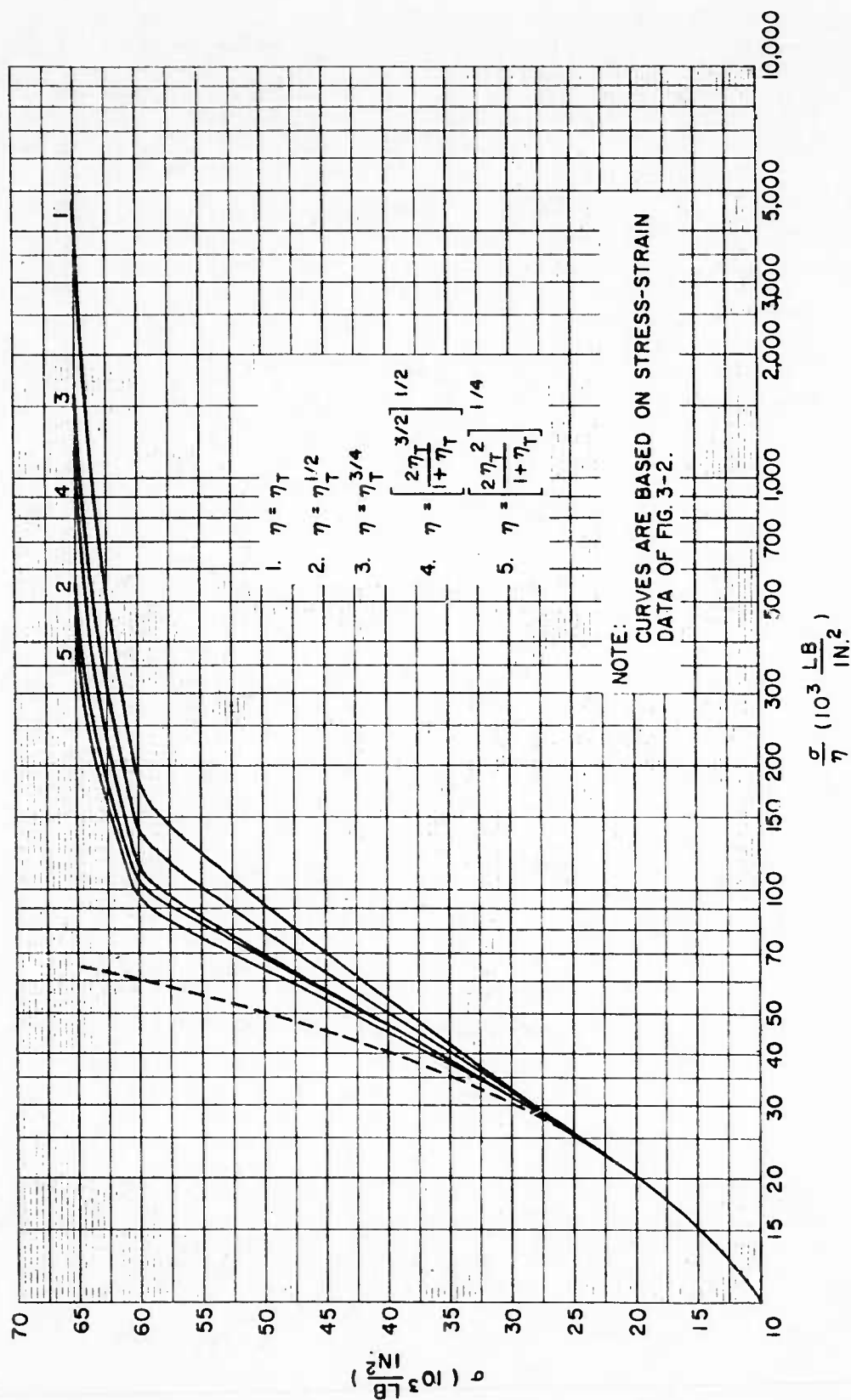


Fig. 3-5 Room-Temperature Plasticity Reduction Factors for As-Received Beryllium Cross-Rolled Sheet (1.75% BeO Content)

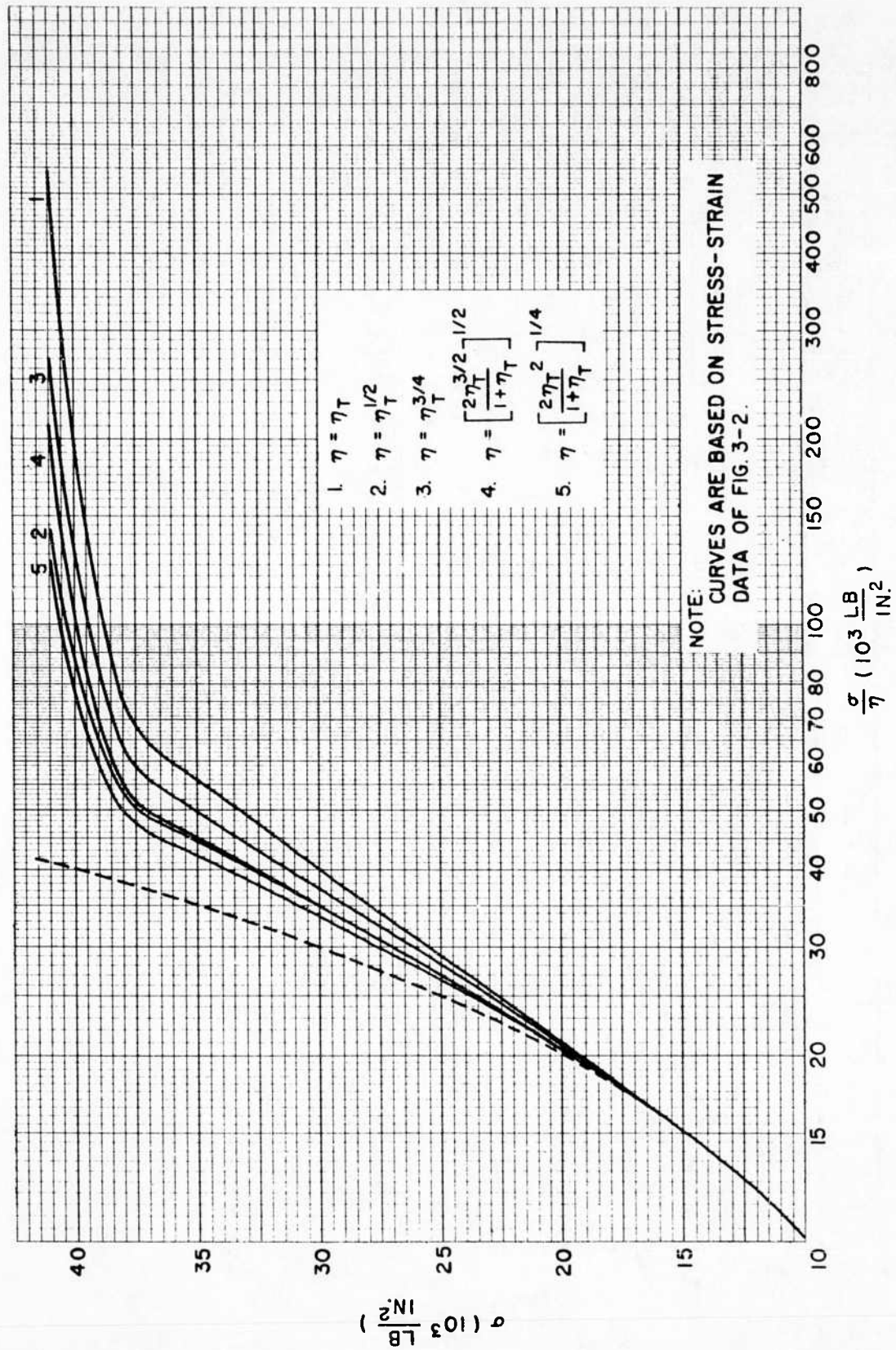


Fig. 3-6 Plasticity Reduction Factors at 800°F for As-Received Beryllium Cross-Rolled Sheet (1.75% BeO Content)

It should be noted that the buckling design charts presented in the following sections are based on a Poisson's ratio of 0.34. This value has subsequently been found to be somewhat high for beryllium cross-rolled sheet as a result of tests conducted late in the period of this contract. Consequently, these charts are unconservative by approximately 5 percent.

3.2 BUCKLING AND POST-BUCKLING DESIGN CHARTS FOR FLAT UNSTIFFENED PANELS

3.2.1 Compression Buckling

Buckling of an unstiffened compression panel may be determined from the classical equation:

$$\frac{F_{c_{cr}}}{\eta} = \frac{\pi^2 E_c}{12(1 - \mu^2)} \left(\frac{t}{b}\right)^2 K_c \quad (3.1)$$

where

- η = plasticity reduction factor
- μ = Poisson's ratio = 0.34
- E_c = modulus of elasticity in compression
- t = thickness of panel
- b = length of loaded edge of panel
- K_c = buckling coefficient

On the basis of tests of materials other than beryllium, a value of the plasticity reduction factor equal to $\sqrt{E_T/E}$ may be specified. Values of the buckling coefficient may be found in Ref. 3-3.

If Figs. 3-5 and 3-6 are used to assess plasticity effects, Eq. (3.1) may be graphically presented as shown in Fig. 3-7. Note that the curves are "example" curves as discussed in subsection 3.1. The maximum buckling stress is assumed to be equal to the compressive yield stress.

The symbols on the chart represent buckling stresses determined experimentally as part of this contract. It can be seen that the curves are generally in close agreement

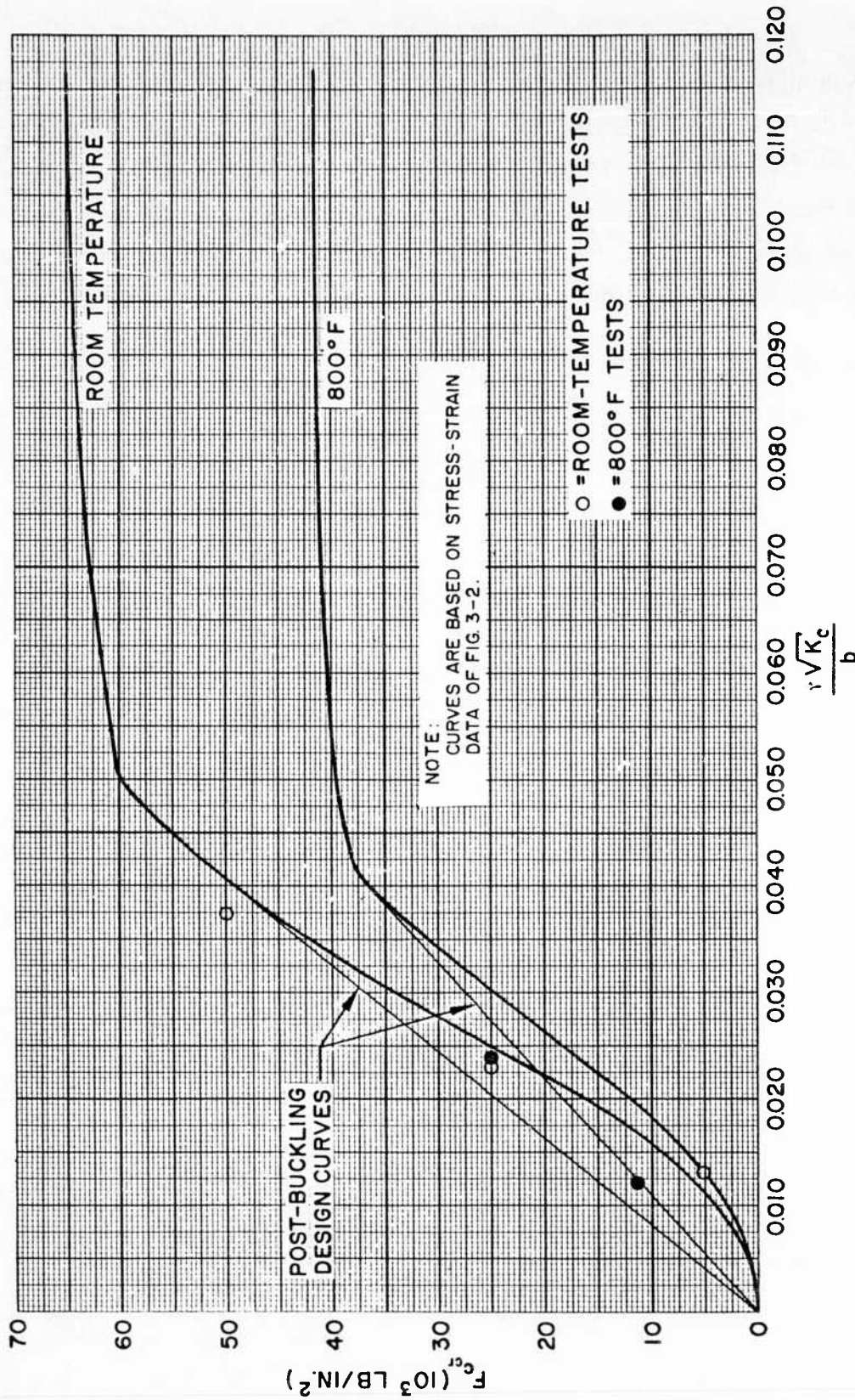


Fig. 3-7 Example Compression Buckling Curves at Room Temperature and 800°F for As-Received Beryllium Cross-Rolled Sheet (1.75% BeO Content)

with the test data over the range of $t \sqrt{K_c}/b$ investigated. It is noted that plastic buckling stresses were obtained in one test. The close correlation between this test and the buckling curve supports the selection of $\eta = \sqrt{E_T/E}$ as noted above. Buckling in all tests was determined from strain-gage data. Visible buckles did not appear until higher stresses were reached. This appears to be a characteristic of the material, perhaps due to its relatively high modulus.

3.2.2 Compression Post-Buckling

The elastic post-buckling behavior of compression panels has been the subject of many investigations, the more widely known of which are listed as references by Mayer and Budiansky (Ref. 3-4). These authors proceed to investigate theoretically the plastic post-buckling behavior of compression panels.

From this information, three post-buckling curves may be obtained: the first based on the theory of Mayer and Budiansky; the second based on square-tube and V-groove tests; and the third based on knife-edge tests of 3-bay plates. These curves have been developed for beryllium cross-rolled sheet and are presented in Fig. 3-8 together with the test points obtained under the present contract. It can be noted that the curves show considerable variance, and that the curve related to Mayer and Budiansky's work is unconservative in relation to the test data. However, the test data correlate very well with the curve based on knife-edge tests of 3-bay plates (extrapolated in Fig. 3-8). It should be noted that the test data were obtained from 3-bay plates having near-knife-edge support, which is the arrangement felt to give the most realistic results.

The buckling curves shown in Fig. 3-8 are taken directly from Fig. 3-7 and carry the same restrictions mentioned in subsection 3.2.1. The curves have been presented in terms of $t \sqrt{K_c}/b$, rather than in terms of $b/t \sqrt{K_c}$, in order to show that a quick, conservative estimate of post-buckling behavior may be obtained by drawing a straight line through the origin tangent to the shoulder of the buckling curve. This curve may be seen in Fig. 3-8 to approximate the curve based on square-tube and V-groove tests.

The test panels represented by the symbols on Fig. 3-8 failed by cracking in the buckle pattern. The cracking was much more severe at room temperature than at 800°F. Buckles were visible in the room-temperature tests of the 0.020- and 0.040-gage specimens prior to failure, although as mentioned in subsection 3.2.1, these buckles appeared at a stress considerably in excess of the experimental buckling

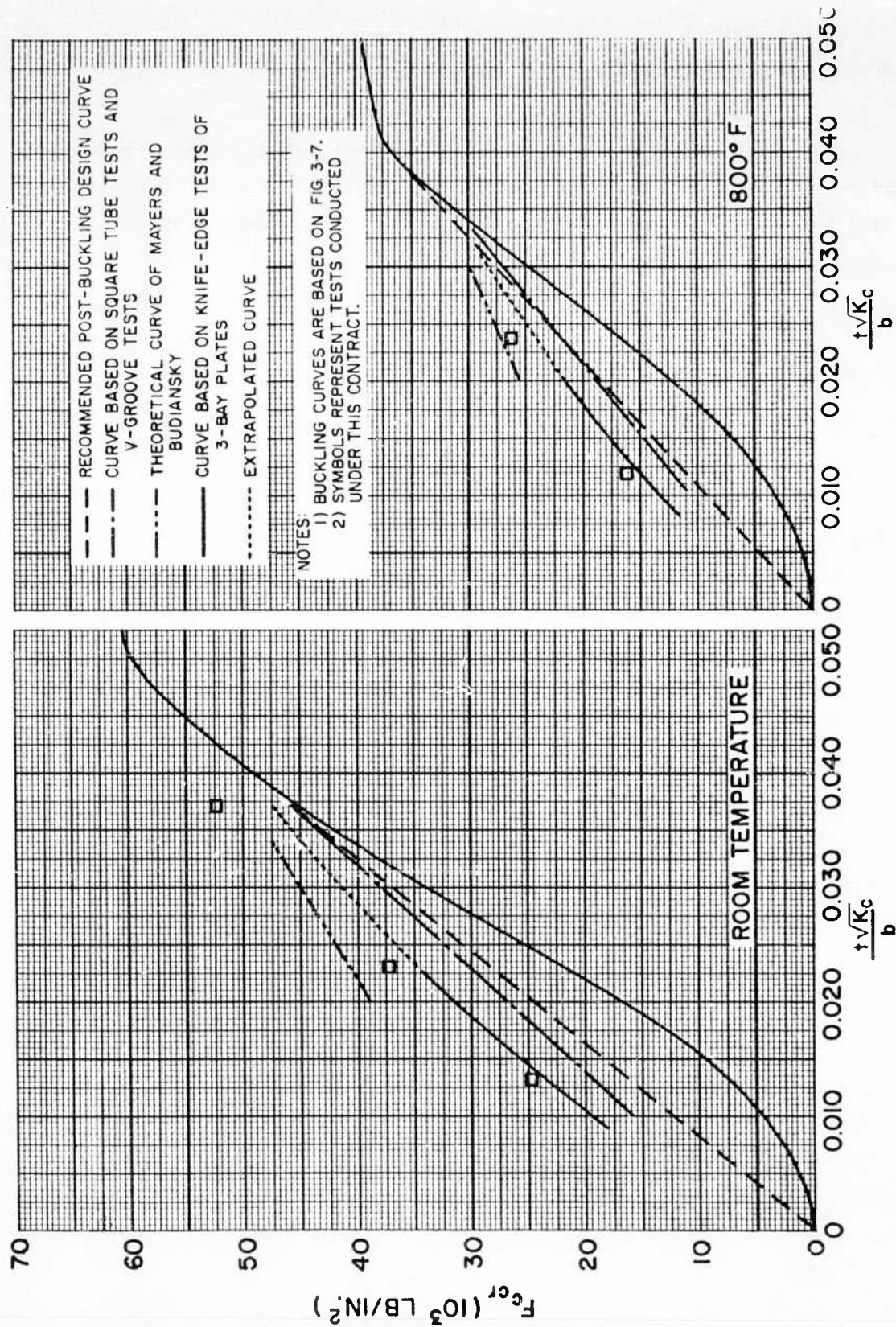


Fig. 3-8 Comparison of Various Post-Buckling Design Curves for Compression Panels With Beryllium Cross-Rolled Sheet Test Data

stress as read from the strain-gage data. Visual observation at 800°F was impossible due to obstruction by the necessary heating apparatus.

In summary, it can be stated that the post-buckling strength of beryllium cross-rolled sheet may be predicted by methods which are based on tests of more common structural materials. However, its post-buckling behavior, namely small buckle amplitude and failure by cracking, is markedly different than that usually observed in these more common materials. The post-buckling curve based on knife-edge tests in 3-bay plates appears satisfactory for beryllium cross-rolled sheet; however, because of limitations of this curve, the straight line drawn through the origin and tangent to the shoulder of the buckling curve is recommended for design purposes at the present time. Additional work appears warranted in this area which, if performed, may lead to more sophisticated design recommendations.

3.2.3 Shear Buckling

The following equation may be used for the determination of shear buckling in a flat, unstiffened panel:

$$\frac{F_{s\text{ cr}}}{\eta} = \frac{\pi^2 E_c}{12(1 - \mu^2)} \left(\frac{t}{b}\right)^2 K_S \quad (3.2)$$

where

- η = plasticity reduction factor
- μ = Poisson's ratio = 0.34
- E_c = modulus of elasticity in compression
- t = thickness of panel
- b = length of short side of panel
- K_S = buckling coefficient

Here η is also specified equal to $\sqrt{E_T/E}$ on the basis of previous experimental data. For values of K_S , see Ref. 3-3.

Using Figs. 3-5 and 3-6 to assess the effects of plasticity, "example" design charts may be derived from Eq. (3.2) as shown in Fig. 3-9. Here the maximum buckling stress is taken equal to $0.61 F_{cy}$ (Ref. 3-2).

The circular symbols on Fig. 3-9 represent experimentally determined buckling stresses. Note that there is little scatter in the test data and that correlation with the theoretical buckling curves is satisfactory. It should be noted here that the buckling stress for each test was determined from a load-deflection chart and represents that point where a definite change in slope occurred. Buckles were not visible in any of the room-temperature tests at the buckling stress. This characteristic is thought to be a result of the exceptional modulus of the material, which resists the formation

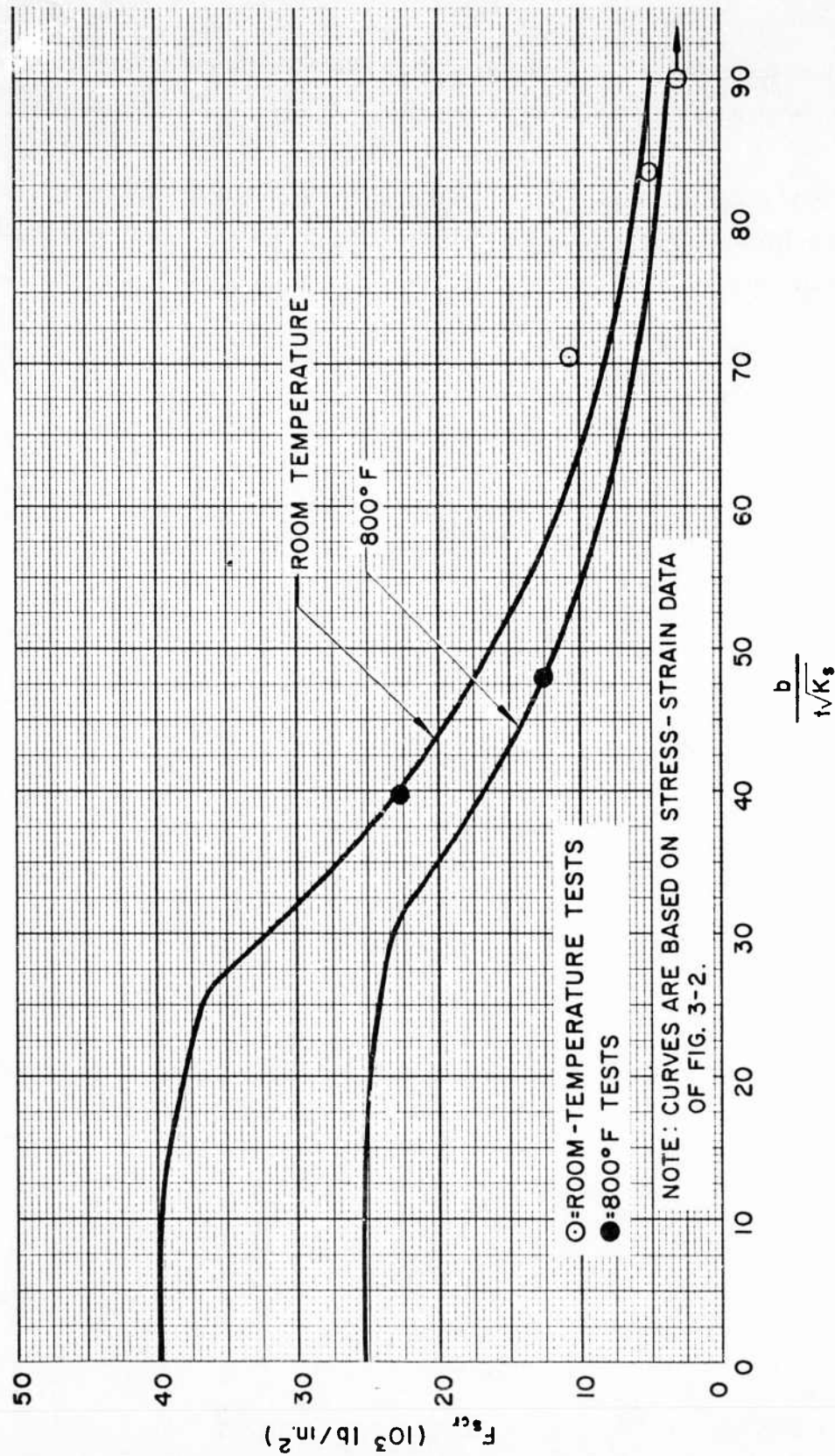


Fig. 3-9 Example Shear Buckling Curves at Room Temperature and 800°F for As-Received Beryllium Cross-Rolled Sheet (1.75% BeO Content)

of buckles in the sheet. The panels tested at 800°F could not be observed owing to the presence of shielding necessary for uniform temperature distribution.

Note that Eq. (3.2) and Fig. 3-9 are also applicable to curved shear panels when buckling coefficients representative of these structures are used. (See Ref. 3-7 for these coefficients.)

3.2.4 Shear Post-Buckling

The post-buckling (or ultimate) strength of flat, unstiffened shear webs fabricated from 2024-T3 and 7075-T6 aluminum alloys may be predicted using the information developed by Kuhn and others (Ref. 3-5). Burns and Terry (Ref. 3-6) have subsequently shown that a good approximation for the shear post-buckling strength of other materials may be obtained by multiplying the 2024-T3 data mentioned above by the ratio of the ultimate tensile stress of the new material to the ultimate tensile stress of 2024-T3 used by Kuhn ($F_{tu} = 62,000$ psi). This procedure has also been found applicable for the determination of elevated-temperature shear-web strengths.

Example post-buckling design curves for beryllium cross-rolled sheet have been determined at room temperature and 800°F according to this procedure and are presented in Fig. 3-10. These curves are based on a room-temperature, ultimate tensile stress of 80,000 psi, and an 800°F ultimate tensile stress of 42,500 psi. Curves for 2024-T3, taken from Ref. 3-5, are also shown. All curves indicate the variation of web-shear strength with the angle of diagonal tension as well as the diagonal tension factor.

The experimental data determined as part of this contract are symbolized on Fig. 3-10. The tests conducted at 800°F (on nominal 0.040-gage sheet) showed the results expected. Buckles formed having an angle of diagonal tension of approximately 45 deg, and the test in both cases was discontinued when excessive elongation for little increase in load was experienced. These test points have the same general relation to the 800°F design curve as Kuhn (Ref. 3-5) shows between 2024-T3 test points and his recommended design curve.

The room-temperature tests, however, show considerable scatter, and are generally low. This is felt to be due in part to the presence of material from more than one heat in the test panels. Coupon tests of material taken from each test panel would probably indicate considerable variance in ultimate tensile stress. If, for example,

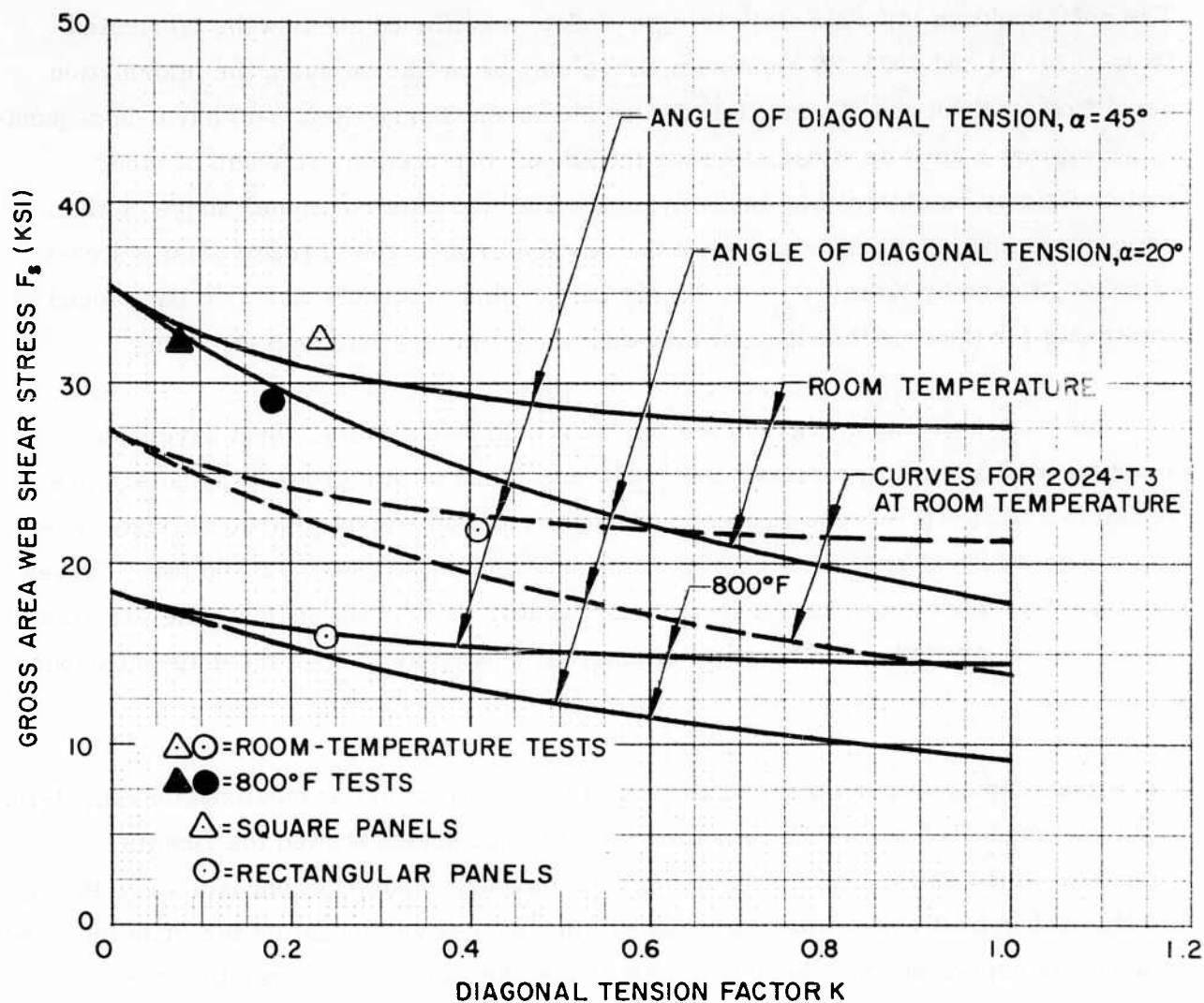


Fig. 3-10 Example Post-Buckling Design Curves at Room Temperature and 800°F for Flat Shear Panels Fabricated From Beryllium Cross-Rolled Sheet

the room-temperature, ultimate tensile stress is better represented by 60,000 psi (which approximates the strength of 2024-T3), it can be seen that all but one of the test points would correlate well with the curves.

All room-temperature test specimens shattered at maximum load. The nominal 0.020-gage panels did not develop visible buckles prior to failure. However, a visible, normal two-buckle pattern did develop in the 0.010-gage panel. Note that a 45-deg angle of diagonal tension was developed by the square 0.02-gage panel and the rectangular 0.01-gage panel. In contrast, a review of the test data for the shattered, rectangular 0.02-gage panel (Fig. A-21) seems to indicate that at failure the panel was attempting to form a buckle across the diagonal, which in terms of angle of diagonal tension is 20 deg. This is not surprising since the picture-frame jig tends to force the buckles across the diagonal of the jig, whether they would normally develop in this manner or not. In actual design practice, an angle of diagonal tension of 20 deg is quite unrealistic for the rectangular panel design. This seems to cast some doubt as to the usefulness of this test. It is surmised that if the test were repeated using a cantilevered jig similar to Kuhn's, an angle of 45 deg would develop and a maximum stress would be obtained which would be more compatible with the other test results.

It is significant to note that the rectangular 0.01-gage panel tested at room temperature attained a diagonal tension factor of 0.41, which represents a post-buckling stress 7.48 times the test buckling stress, and the formation of substantial buckles in the sheet. The remaining room-temperature tests were approximately 3 times over the test buckling stress at failure.

In summary, it may be stated that while beryllium cross-rolled sheet exhibits the unusual characteristics of developing buckles of very small amplitude at the theoretical buckling stress and shattering at failure at room temperature, it appears on the basis of tests performed for this program that conventional methods for determining post-buckling strength are applicable for design purposes. However, the necessity of knowing the mechanical properties of the material at hand is important. Further

tests are required at room temperature to validate the rationalizations presented relating to scatter, which at first glance may appear to the casual observer to be a serious problem.

3.2.5 Column Buckling

Buckling of columns may be determined from the Euler theory:

$$\frac{F_c}{\eta} = \frac{\pi^2 E_c}{(L'/\rho)^2} \quad (3.3)$$

where

η = plasticity reduction factor

E_c = modulus of elasticity in compression

L' = effective column length

ρ = least radius of gyration

The term η is taken equal to E_T/E . Example column buckling curves, based on Eq. (3.3), are presented in Figs. 3-11a and 3-11b for cross-rolled sheet and hot-pressed block, respectively. The plastic stress portions of these curves are based on the stress-strain properties shown in Figs. 3-1b and 3-2. The maximum buckling stress is taken equal to the compressive yield stress.

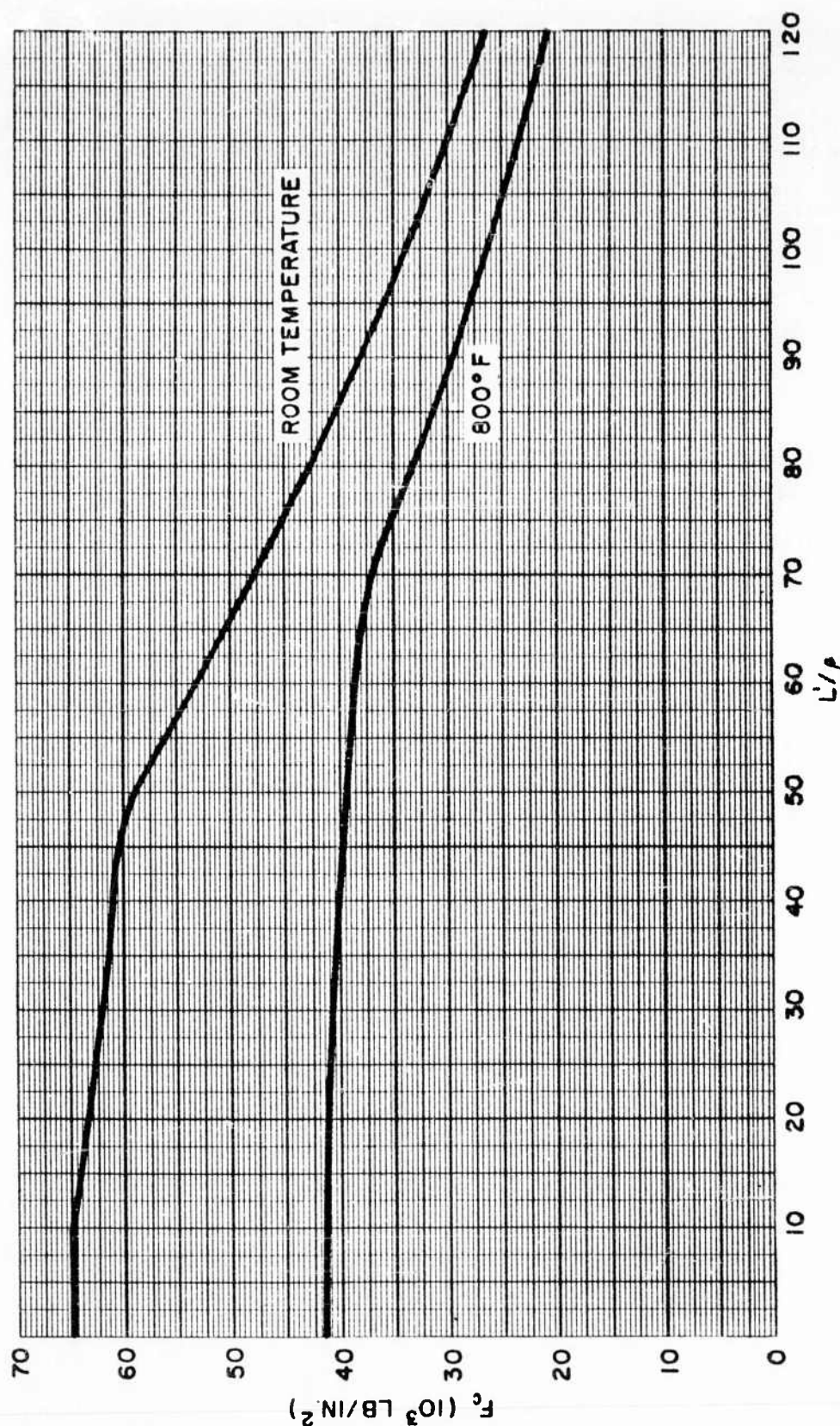


Fig. 3-11a Example Column Buckling Curves at Room Temperature and 800°F for As-Received Beryllium Cross-Rolled Sheet (1.75% BeO Content)

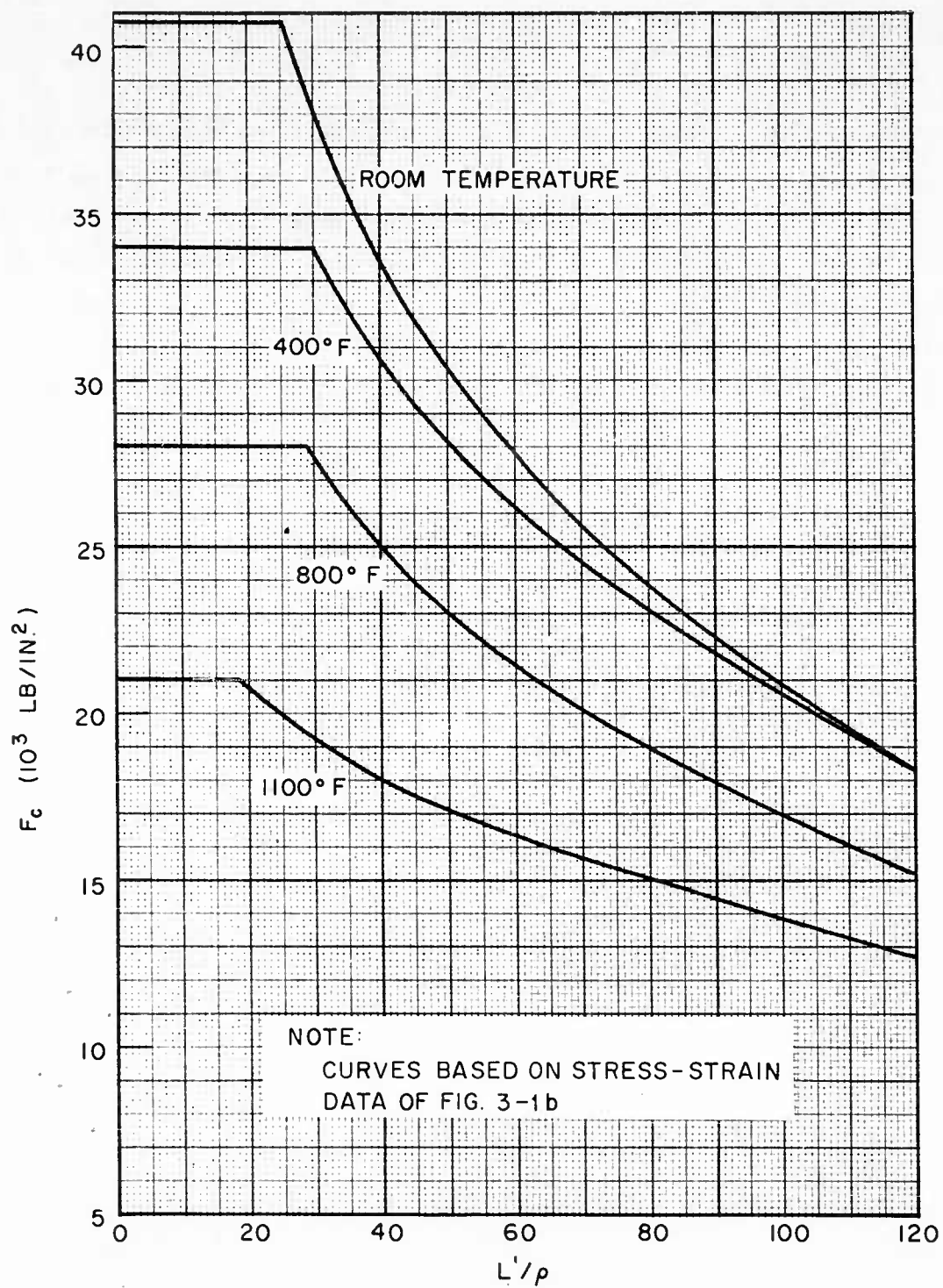


Fig. 3-11b Typical Column Buckling Curves at Various Temperatures for Beryllium Block Material (1.75% BeO Content)

3.2.6 Interaction Formulas

The discussion of the biaxial strength of beryllium presented in subsection 2.5 of this report appears to be the only information currently available relating to the behavior of beryllium under two or more concurrent states of stress. Other interaction combinations are, of course, of interest to the designer, particularly those involving compression, bending, and/or shear as related to shell analysis. In these cases, interaction equations consisting of stress ratios raised to the first power are suggested until such time as tests have been performed to verify more optimistic relationships.

3.3 BUCKLING DESIGN CHARTS FOR MONOCOQUE CYLINDERS

3.3.1 Buckling Due to Axial Compression

The formula for the buckling of a circular monocoque cylinder in axial compression, according to classical small deflection theory, is:

$$\frac{F_{c_{cr}}}{\eta} = C E \left(\frac{t}{R} \right) \quad (3.4)$$

where

- C = buckling coefficient
- η = plasticity reduction factor
- E = Young's modulus
- t = thickness of cylinder wall
- R = radius of cylinder

It is well known that the value of C derived from small deflection theory (0.605) is applicable only over a very small range of R/t values. Consequently, the values of C presented here have been determined in a manner parallel to that suggested by Gerard (Ref. 3-7) but based on more recent data. These are shown in Fig. 3-12. Curves covering three probability levels are given which reflect the scatter in the available test results. Further, Fig. 3-12 is applicable only when $L/R \geq 0.75$ and $t > 0.005$.

Example buckling curves for beryllium cross-rolled sheet are shown in Fig. 3-13 for room temperature and 800°F, based on Eq. (3.4), Fig. 3-12, and taking $\eta = \sqrt{E_T/E}$. The latter quantity has been evaluated using Figs. 3-5 and 3-6. The maximum buckling stress shown on these curves is equal to the compressive yield stress.

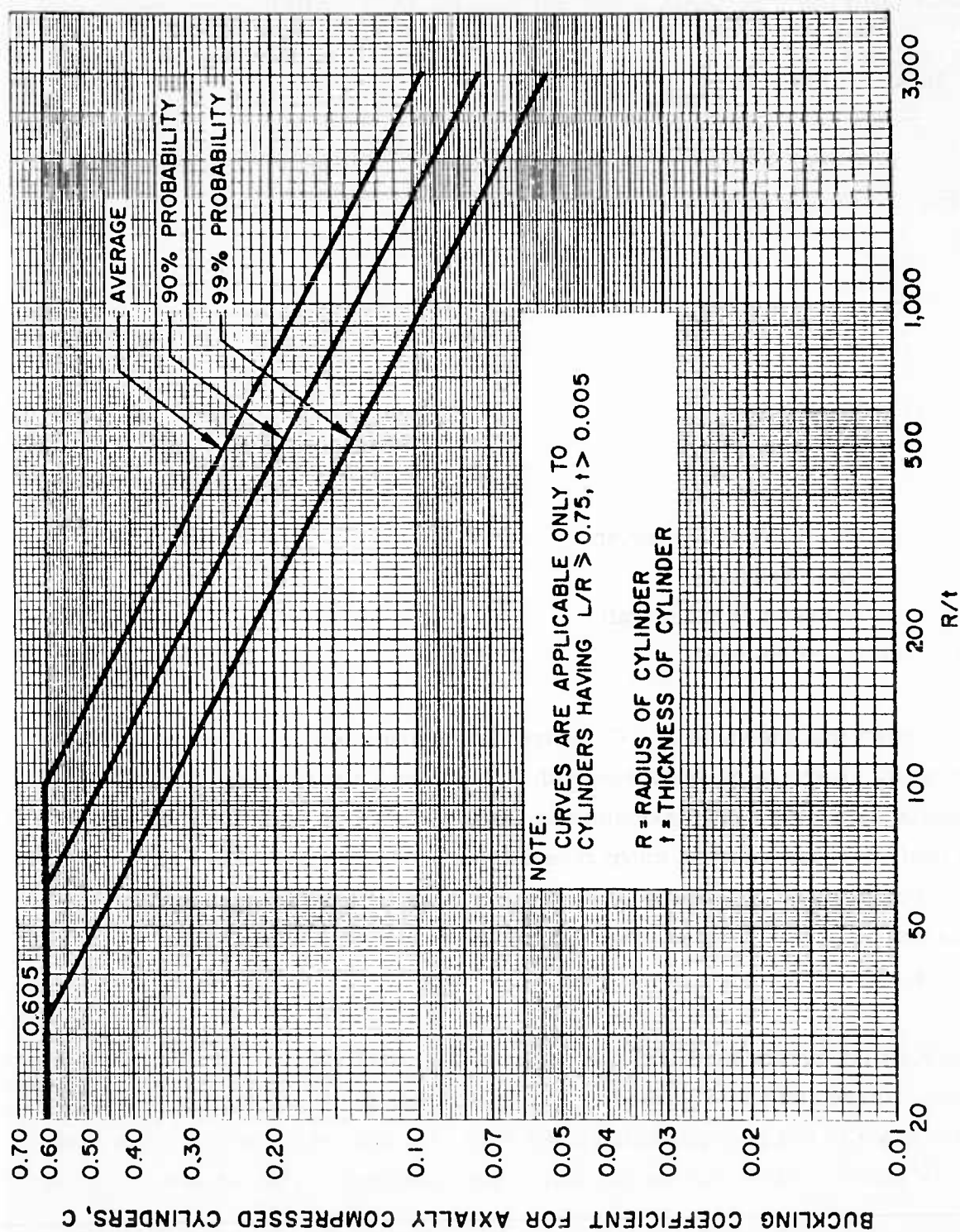


Fig. 3-12 Buckling Coefficients for Long Monocoque Cylinders Subjected to a Uniform Axial Load

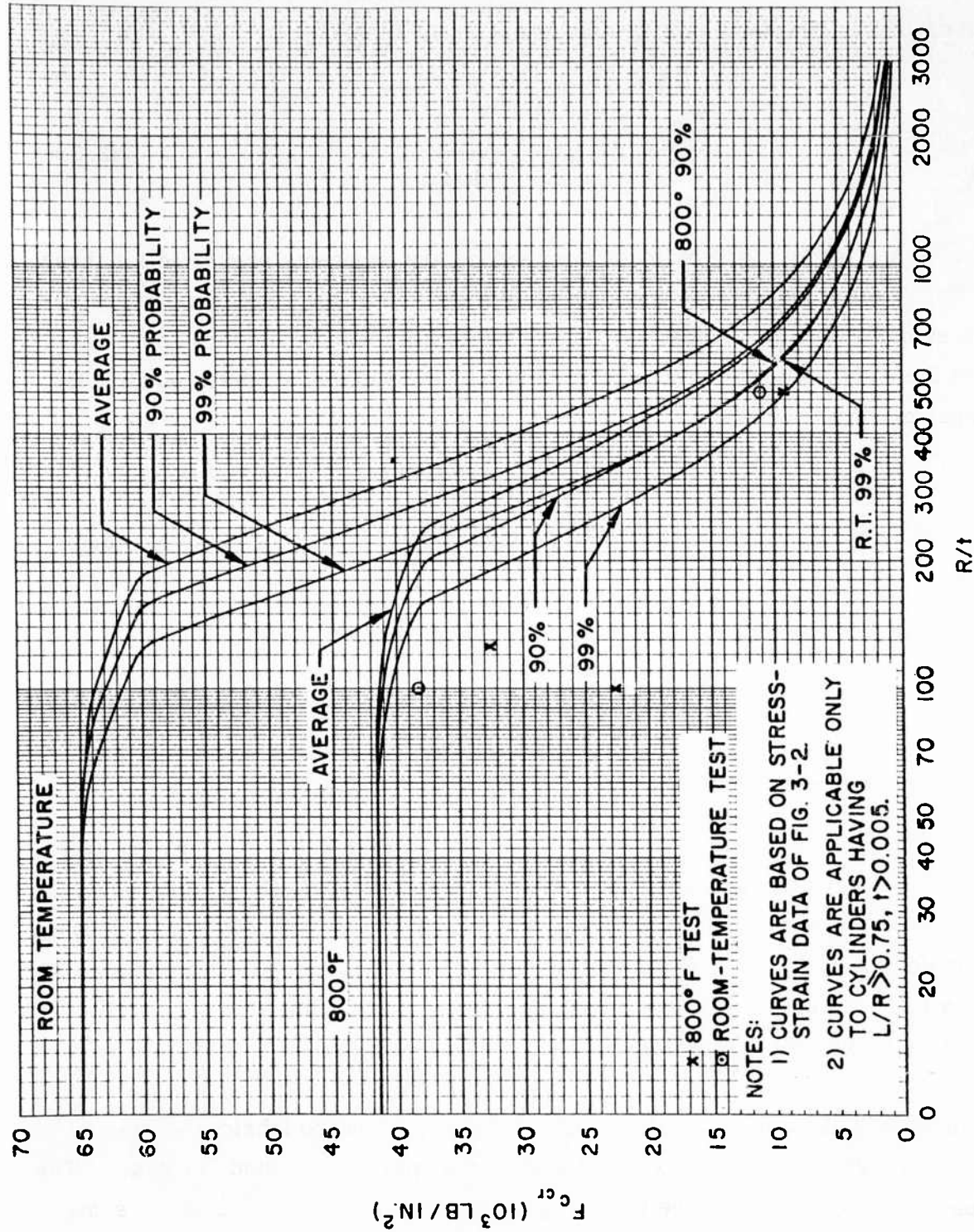


Fig. 3-13 Example Buckling Curves at Room Temperature and 800°F for Long, Axially Loaded Monocoque Cylinders Fabricated From As-Received Beryllium Cross-Rolled Sheet (1.75% BeO Content)

When $L/R < 0.75$ and $t > 0.005$, the recommended empirical formula for buckling of a circular monocoque cylinder under axial load is:

$$\frac{F_{c_{cr}}}{\eta} = \frac{0.871 E}{(R/t)^m (L/R)^n} \quad (3.5)$$

Where L is the length of the cylinder, m and n are exponents presented for three levels of probability as a function of R/t in Fig. 3-14, and the remaining symbols are as previously defined. Because Eq. (3.5) represents short cylinders, edge conditions at the ends of the cylinder govern the minimum buckling stresses obtainable. If the edges are clamped:

$$\frac{F_{\min_{clamped}}}{\eta} = 3.612 E \left(\frac{t}{L}\right)^2 \quad (3.6)$$

If the edges are simply supported:

$$\frac{F_{\min_{S.S.}}}{\eta} = 0.903 E \left(\frac{t}{L}\right)^2 \quad (3.7)$$

Example buckling curves for beryllium cross-rolled sheet at room temperature and 800°F for short cylinders under axial load are presented in Figs. 3-15a and 3-15b. These curves are based on Eq. (3.5), Fig. 3-14, and $\eta = \sqrt{E_T/E}$, where the latter quantity is determined from Figs. 3-5 and 3-6. Again, the compressive yield stress is taken as the maximum buckling stress. Note that the preceding data for axially loaded cylinders may also be applied to axially loaded curved panels (see Ref. 3-7).

A series of five monocoque cylinders having $L/R > 0.75$ were fabricated from cross-rolled sheet and tested in axial compression as part of this study contract. The dimensions of these cylinders, the test temperatures, and the test results are summarized in Table 3-1. These data are also graphically presented in Fig. 3-13.

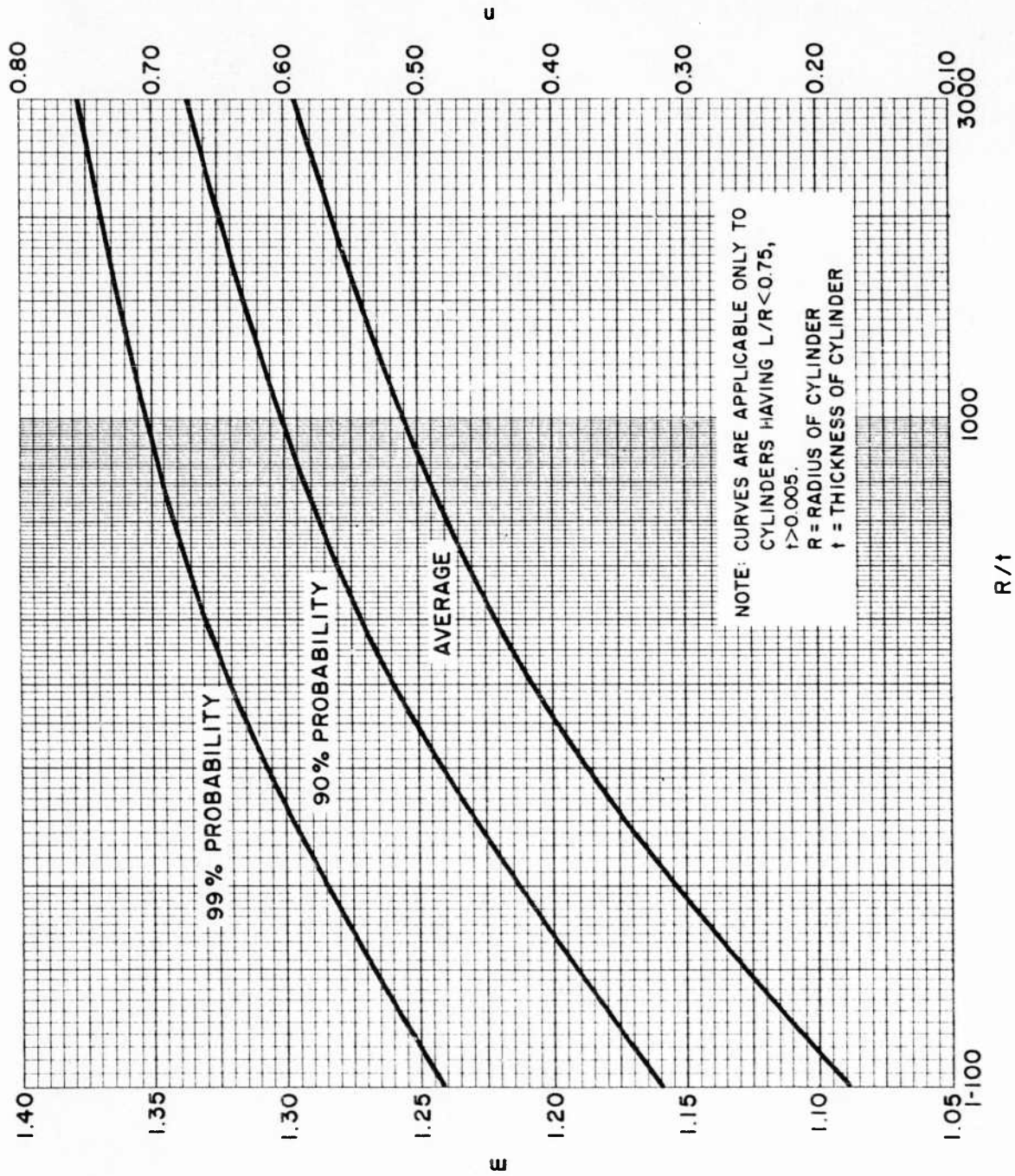


Fig. 3-14 Buckling Exponents for Short Monocoque Cylinders Subjected to a Uniform Axial Load

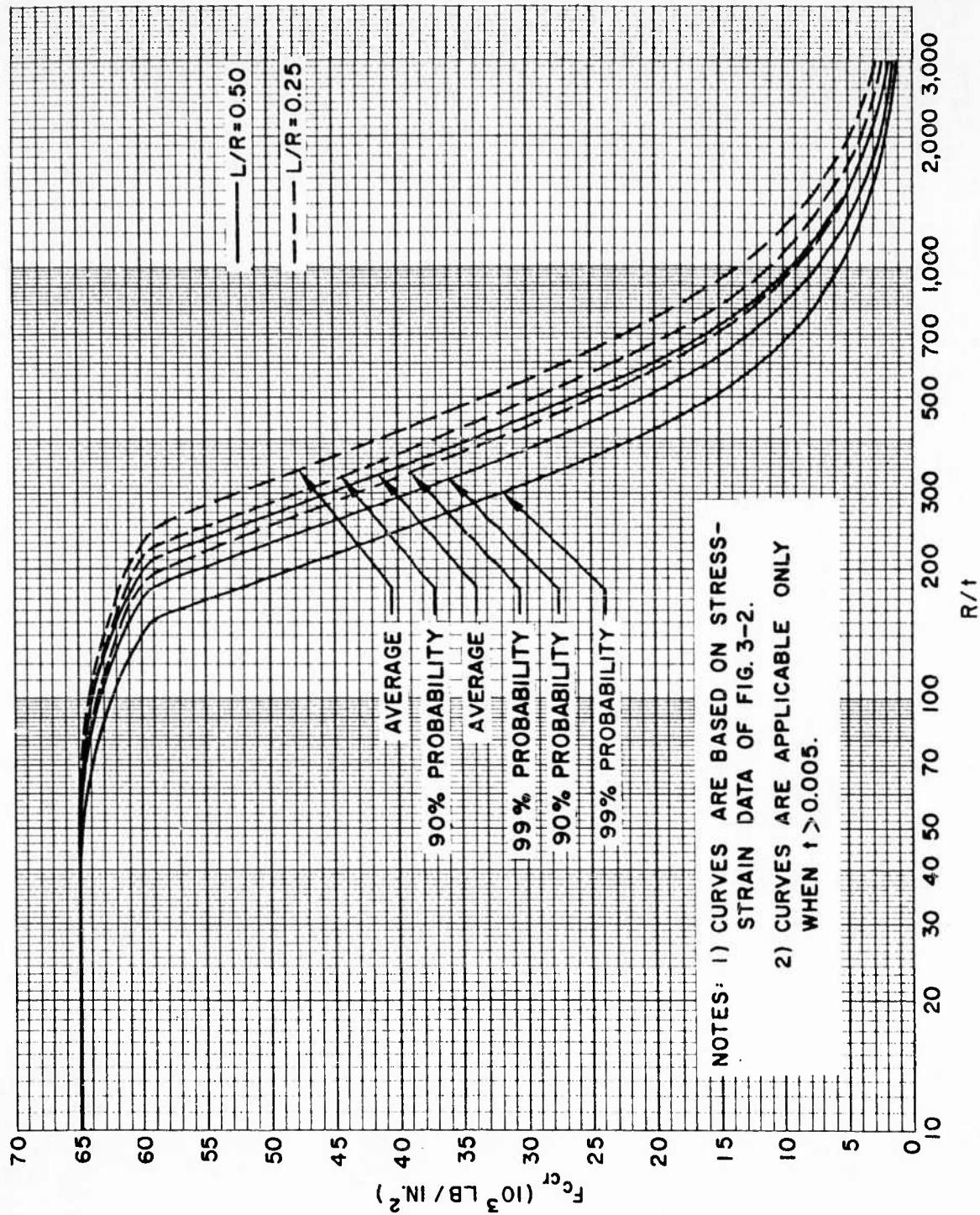


Fig. 3-15a Example Room-Temperature Buckling Curves for Short, Axially Loaded Monocoque Cylinders Fabricated From As-Received Beryllium Cross-Rolled Sheet (1.75% BeO Content)

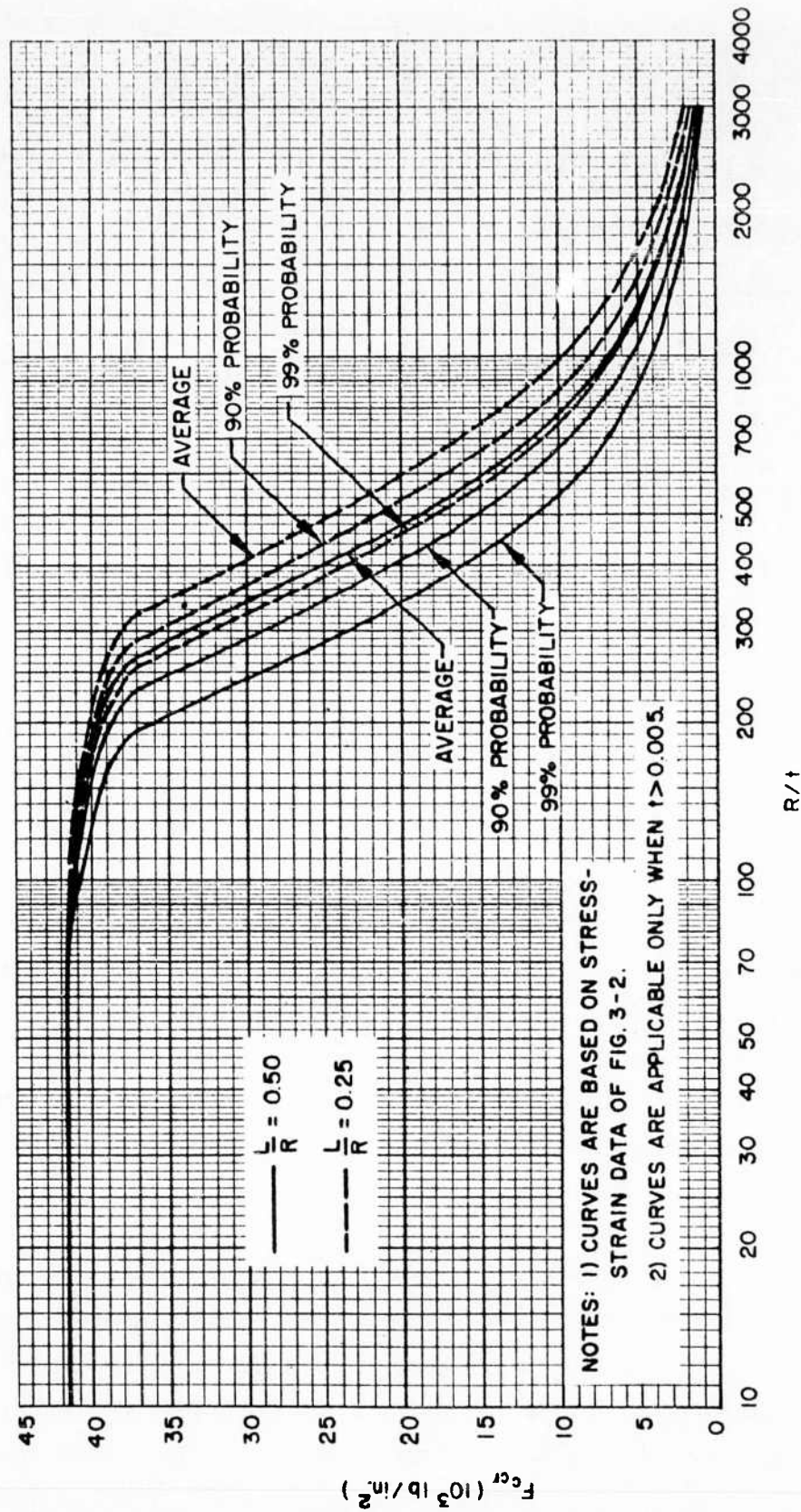


Fig. 3-15b Example Buckling Curves at 800°F for Short, Axially Loaded Monocoque Cylinders Fabricated From As-Received Beryllium Cross-Rolled Sheet (1.75% BeO Content)

Table 3-1

SUMMARY OF PERTINENT DATA AND TEST RESULTS FOR AXIALLY LOADED
MONOCOQUE CYLINDERS FABRICATED FROM
BERYLLIUM CROSS-ROLLED SHEET

Cylinder No.	Radius (in.)	Length (in.)	Nominal Thickness (in.)	Nominal Test Temp. (°F)	Critical Load (lb)	Critical Stress (psi)
1	10	11	0.02	70	13,800	11,000
2	4	10	.04	70	38,400	38,200
3	10	11	.02	800	11,600	9,230
4	5	11	.04	800	41,000	32,600
5	4	10	.04	800	22,600	22,500

Pictures of the failed cylinders and a description of the test procedures are presented in Appendix A.

The correlation between the design curves and the test points in Fig. 3-13 is poor. The elastic test points (cylinders 1 and 3), in fact, generally fall along or below the extreme lower boundary on charts of F_{cr}/E versus R/t which correlate all known elastic test results independent of material. In view of the acceptable correlation between design chart and test for flat compression panels (see subsection 3.2), the low performance of the beryllium in the present tests cannot be rationally attributed to the peculiarities of the beryllium itself. Rather, some deficiency in testing procedure, material properties, or fabrication is suspected.

A common fault of axially loaded cylinder tests in the past has been the uneven application of load, due either to nonparallel and/or uneven cylinder ends, or mismatch between the testing machine loading heads. In the present tests, these factors were found to be within acceptable tolerances, but to provide closer tolerances, bearing plates of a soft material were used between the machine loading heads and the cylinder

ends to ensure even load distribution. Thus, the testing procedure is judged satisfactory.

There is some question of the beryllium mechanical properties represented in the cylinders. It should be emphasized that the tests of cylinders in axial compression under this program are the first such tests using beryllium cross-rolled sheet. Thus, the problems of successfully forming the cylinders and providing an acceptable longitudinal butt joint had to be solved first. The forming was performed by sandwiching the beryllium sheet between mild steel plates and heating this combination in a furnace, followed by removal and slow rolling on standard roll-form equipment. To account for the heat loss due to rolling on unheated equipment, yet be able to roll the material at temperatures above 1000°F, the material was heated to 1400°F in the furnace. What effect, if any, this high-temperature exposure had on the compressive properties of beryllium cross-rolled sheet after cooling is not definitely known, but it is likely that there is some effect. Reference 2-11 reports some tests of beryllium material in which all properties were reduced, and the tensile yield point disappeared after an anneal at 900°C was given the material. Coupons of the cylinder material were not subsequently tested in the present program because of a lack of sheet stock and a lack of funds and time.

A single longitudinal butt joint spliced with stainless-steel foil on both sides and then brazed was found to be a very satisfactory means of finishing the cylinders. The brazing temperature, however, was 1550°F, for up to 30 seconds, and in the range between 1450° and 1550°F for a total time between 2 and 3 minutes. Note that the maximum temperature attained in brazing exceeds the maximum temperature preparatory to rolling the cylinders. Thus the previous comments on the effects of these temperatures on the mechanical properties of the beryllium are even more significant here.

The finished cylinders had a tendency to flare at the ends. This flare probably was increased in the tests as the cylinder ends cut into the soft bearing material. It is well known that unevenness, to which this flare would contribute, is one of the major reasons for scatter in axial compression tests of cylinders.

It should also be recognized that the design curves presented in Fig. 3-13 are based on the stress-strain characteristics of Fig. 3-2, which might not necessarily match the stress-strain characteristics of the test material. This in fact is quite likely in view of the previous comments regarding mechanical properties, and the origin of Fig. 3-2, which was previously stated to take into account improvements in the material which are expected but are not necessarily currently available. This tack is further supported indirectly by the fact that cylinders 2, 4, and 5 failed with the appearance of an axisymmetric buckle, which generally has been observed in tests to occur when the buckling coefficient is near the classical value of 0.605.

None of the cylinders shattered at buckling, although cracks formed at the buckles in the room-temperature tests. The buckles were localized in all tests. Cylinders 1 and 3 failed with the appearance of diamond-shaped buckles. None of the cylinders supported load above the buckling load.

In summary, it may be concluded that while the task of fabricating and testing beryllium cross-rolled sheet cylinders was successfully completed, two factors apparently combined to produce low test results: unexpected reduction of mechanical properties due to fabrication techniques, and a slight flare at the ends of the finished cylinders. It is recommended that studies be undertaken to evaluate the effects of fabrication on the mechanical properties of beryllium cross-rolled sheet.

3.3.2 Buckling Due to Torsion

Buckling of circular monocoque cylinders in torsion may be predicted with small deflection theory which has been modified slightly to show better agreement with test results. The following recommended formulas are taken from Ref. 3-7.

For very short cylinders, the torsional buckling stress may be found from Eq. (3.8):

$$\frac{F_{s_{cr}}}{\eta} = \frac{K_t \pi^2 E}{12(1 - \mu^2)} \left(\frac{t}{L}\right)^2 \quad (3.8)$$

Where K_t is the buckling coefficient for a long flat plate. For clamped edges, $K_t = 8.98$; for simply supported edges, $K_t = 5.35$.

When the cylinder is of intermediate length, that is, when $10\sqrt{t/R} < L/R < 3\sqrt{R/t}$, the following equations apply. For simply supported edges:

$$\frac{F_{s_{cr}}}{\eta} = 0.741 E \left(\frac{t}{R}\right)^{5/4} \left(\frac{R}{L}\right)^{1/2} \quad (3.9)$$

For clamped edges:

$$\frac{F_{s_{cr}}}{\eta} = 0.811 E \left(\frac{t}{R}\right)^{5/4} \left(\frac{R}{L}\right)^{1/2} \quad (3.10)$$

Buckling of long cylinders may be predicted with Eq. (3.11). This equation is applicable when $L/R > 3\sqrt{R/t}$.

$$\frac{F_{s_{cr}}}{\eta} = 0.292 E \left(\frac{t}{R} \right)^{3/2} \quad (3.11)$$

The recommended value of η in each of the above equations is $\sqrt{E_T/E}$. Further, it is recommended that the maximum torsional stress be taken equal to 0.61 times the compressive yield stress. This relationship may also be used to convert compressive stress to torsional stress to obtain η compatible with $F_{s_{cr}}$ from Figs. 3-5 and 3-6. Note that levels of probability are not attached to the equations presented here because of the better agreement between tests and theory as compared to axially loaded cylinders. Probability may be introduced, however, in the mechanical properties of the materials used.

Figure 3-16 presents example buckling curves at room temperature and 800°F for long monocoque circular cylinders in torsion fabricated from beryllium cross-rolled sheet. As in the previous design charts, these curves are based on the example stress-strain data of Fig. 3-2.

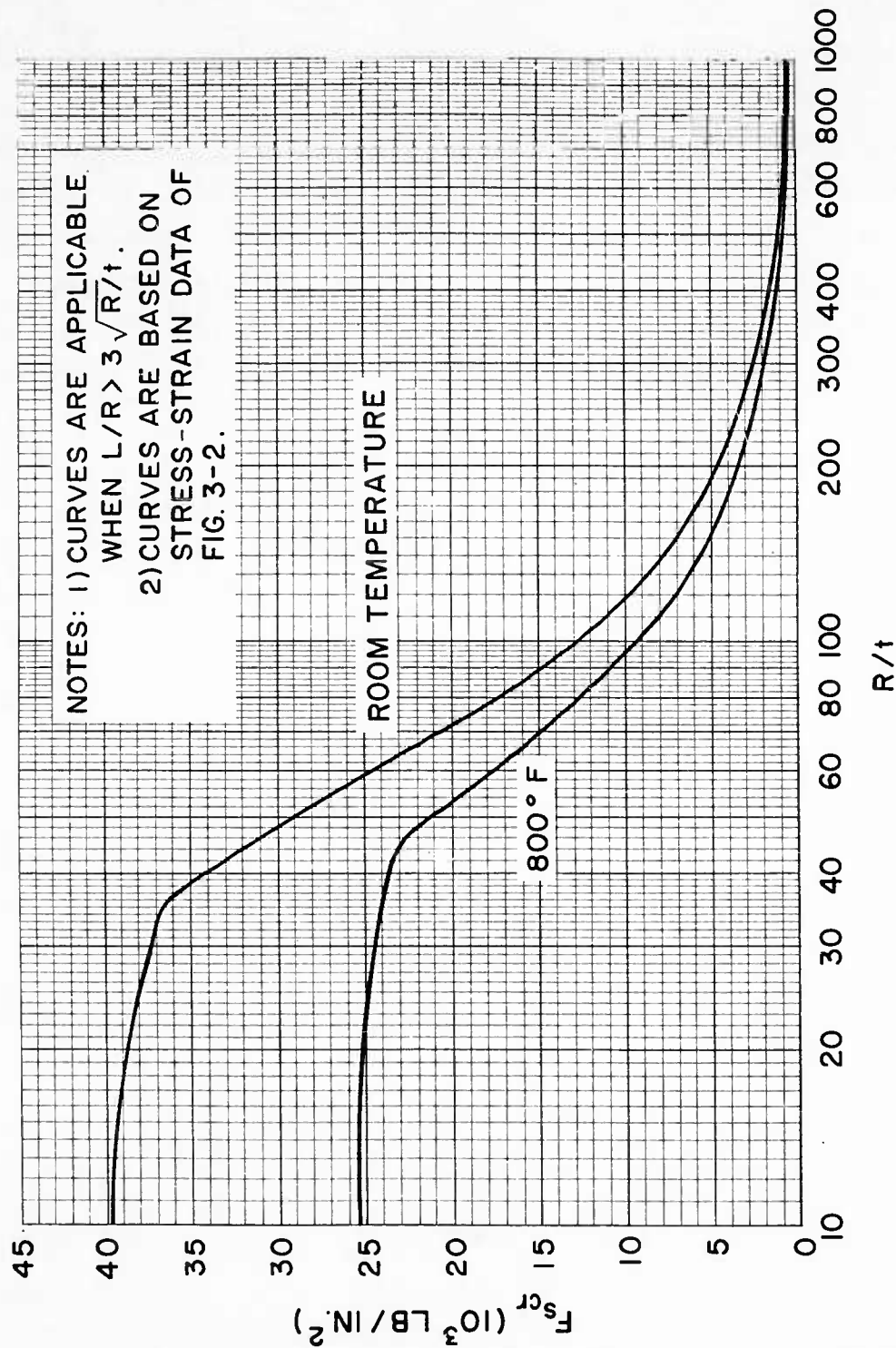


Fig. 3-16 Example Buckling Curves at Room Temperature and 800°F for Long Monocoque Cylinders in Torsion Fabricated From As-Received Beryllium Cross-Rolled Sheet (1.75% BeO Content)

3.3.3 Buckling Due to Hydrostatic or Radial Pressure

A recent comprehensive survey of theoretical and experimental investigations of the buckling of monocoque cylindrical shells subjected to hydrostatic and radial pressure is reported by Pittner in Ref. 3-8. This reference shows that the theoretical difference in the buckling coefficient C_p for hydrostatic and radial pressure at low values of the geometric parameter Z is not substantiated by the test data. Further, edge conditions at the ends of the cylinder apparently had no definite effect on the buckling pressure according to the available test results. Equation (3.12), therefore, may be presented which is applicable for either hydrostatic or radial pressure, without regard to end conditions.

$$p_{cr} = \frac{C_p \pi^2 E}{12 Z \sqrt{1 - \mu^2}} \left(\frac{t}{R}\right)^2 \quad (3.12)$$

where

$$C_p = \frac{0.875 Z + 1.122 \sqrt{Z}}{4.385 + \sqrt{Z}}$$

$$Z = \sqrt{1 - \mu^2} \left(\frac{R}{t}\right) \left(\frac{L}{R}\right)^2$$

$$p_{cr} = \text{buckling pressure} = \frac{\sigma_p}{(R/t)}$$

σ_p = buckling stress due to hydrostatic or radial pressure

R = cylinder radius

L = cylinder length

t = cylinder thickness

E = modulus of elasticity

It should be noted that Eq. (3.12) predicts elastic buckling only, since the effects of plasticity have not, as yet, been satisfactorily treated in the literature. The expression for C_p represents a curve which is very nearly the lower boundary of those tests in which buckling was unquestionably elastic.

A graphical presentation of Eq. (3.12) is shown in Fig. 3-17. This chart may be used to determine the hydrostatic or radial elastic buckling pressure of beryllium cross-rolled sheet, or any other material, at any temperature for which values of the modulus of elasticity are available.

As part of the experimental program performed under this study, a monocoque cylinder fabricated from cross-rolled beryllium sheet was tested under hydrostatic pressure at room temperature. The cylinder had a radius of 10 in., a length of 10.5 in., a nominal thickness of 0.02 in., and failed at 6.55 psi. The predicted collapse pressure according to Fig. 3-17 is 5.40 psi. Thus, for this test, the design curves of Fig. 3-17 are slightly conservative. It is interesting to note that the more optimistic criteria for cylinder wall buckling used in subsection 4.2.7, for the minimum-weight design of ring-stiffened cylinders subjected to hydrostatic pressure, yield a prediction of 7.26 psi which, while slightly unconservative, provides closer correlation than can be shown with Fig. 3-17. Poisson's ratio equal to 0.3 has been used in both predictions. The test failure was catastrophic; without buckles being previously observed, the cylinder shattered into many small pieces. In summary, the design methods presented here for hydrostatically compressed monocoque cylinders have been demonstrated to apply to beryllium cross-rolled sheet. The principal difference between beryllium and other structural materials used in this application appears to be beryllium's mechanism of failure which is catastrophic. The designer should therefore use an appropriate margin of safety. For further testing details, and pictures of the test cylinder after failure, refer to Appendix A.

According to Pittner and Morton (Ref. 3-20), the buckling of a truncated monocoque cone due to hydrostatic pressure may also be predicted using the information in this

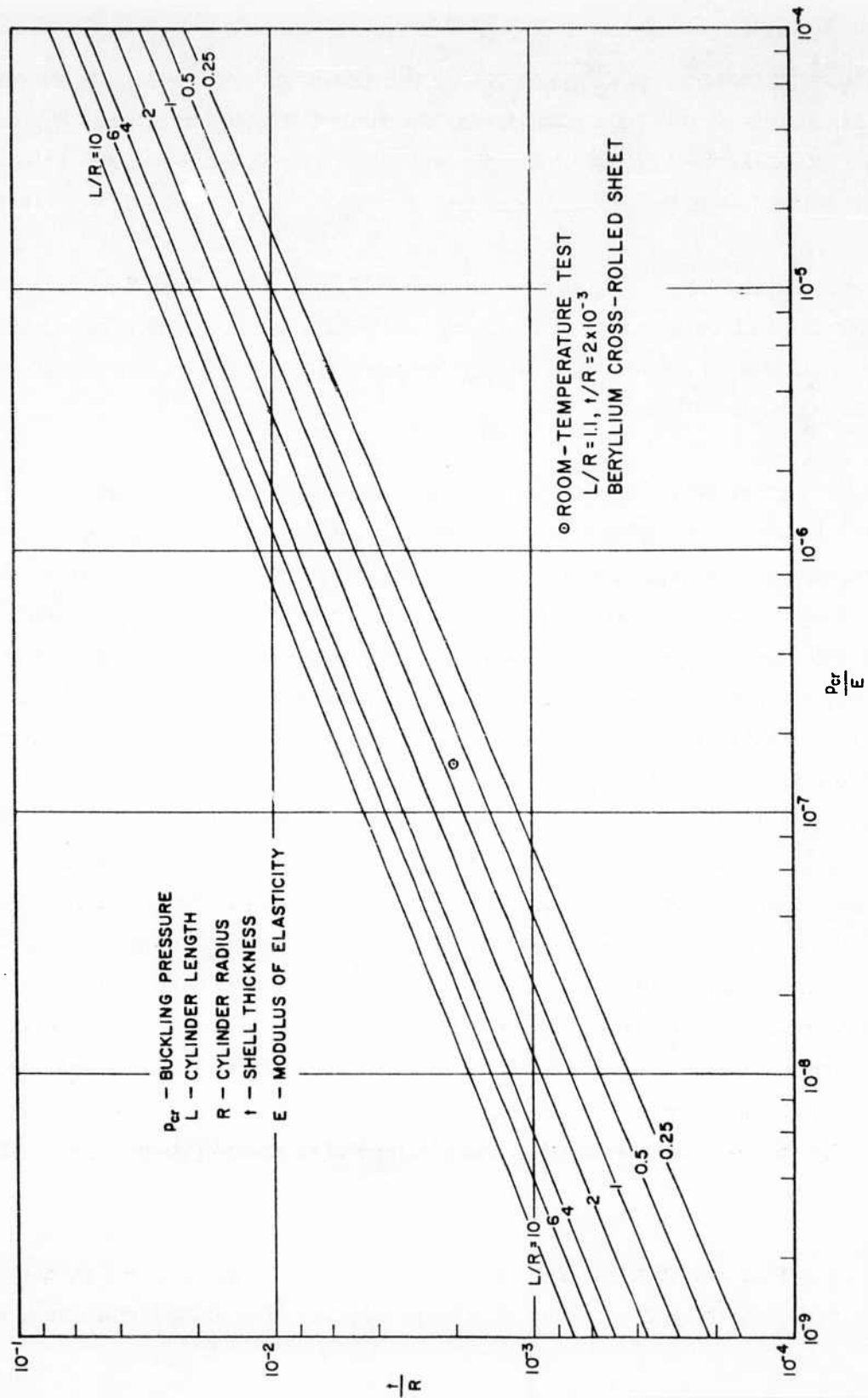


Fig. 3-17 Design Chart for Monocoque Circular Cylinders Subjected to Uniform External Lateral or Hydrostatic Pressure

section by virtue of the "equivalent cylinder" technique. Thus, Eq. (3.12) is also applicable to the design of truncated cones provided the following conditions are met:

$$Z = \frac{\sqrt{1 - \mu^2}}{\eta_r} \left(\frac{L}{R_2} \right)^2 \left(\frac{R_2}{t} \right) \cos \alpha$$

$$\frac{R}{t} = \frac{\eta_r}{\cos \alpha} \left(\frac{R_2}{t} \right)$$

where

$$\eta_r = 0.60 (0.70 + R_1/R_2)$$

L = slant length of the cone

R_1, R_2 = radii of the smaller and the larger ends of the truncated cone, respectively

t = thickness of the shell wall

α = semiapex angle of the cone

Figure 3-17 applies to truncated cones when L/R is replaced by:

$$\left[\frac{L}{R_2} \sqrt{\frac{\eta_r}{\cos \alpha}} \right]$$

and t/R is replaced by t/R_2 , where these terms are as defined above.

3.4 CRIPPLING DESIGN CHARTS

The term crippling as applied here to the strength of beryllium sections is synonymous with post-buckling strength when the latter is limited to in-plane compressive loadings on stiffened plates, or other members composed of several elements, the composites of which can be classed as short columns. The crippling design charts presented in this section are based, with some minor modifications, on the semiempirical method of Cozzone and Melcon (Ref. 3-2). These investigators assume that geometrically identical crippling sections fabricated from different materials will have equal ratios of the average crippling stress to the effective compressive modulus of elasticity, where differences in Poisson's ratio are neglected. Thus, the experimentally determined crippling stresses for 24SRT-10-percent Alclad material presented in Ref. 3-2 may be used to analytically determine crippling curves for other materials. The following equation expresses this basic relationship:

$$\left[\frac{F_{cc}}{\eta E_c} \right]_x = \left[\frac{F_{cc}}{\eta E_c} \right]_{24SRT-10} \quad (3-13)$$

where x represents some candidate material. If η is taken equal to $\sqrt{E_T/E}$ as recommended in Ref. 3-9 and expressed in terms of the Ramberg-Osgood parameters (Ref. 3-1) for 24SRT-10, the following equation results:

$$\left[\frac{F_{cc}}{\eta} \right]_x = (E_c)_x \left\{ \frac{F_{cc}}{9.7 \times 10^6} \left[1 + \frac{30}{7} \left(\frac{F_{cc}}{46000} \right)^9 \right]^{1/2} \right\}_{24SRT-10} \quad (3.14)$$

where values of $F_{cc_{24SRT-10}}$ as a function of section geometry may be found in Ref. 3-2.

Crippling design charts for beryllium cross-rolled sheet and hot-pressed block have been developed and are presented as Figs. 3-18a, 3-18b, and Figs. 3-19a, b, c, d, respectively. These charts have been calculated from Eq. (3.14).

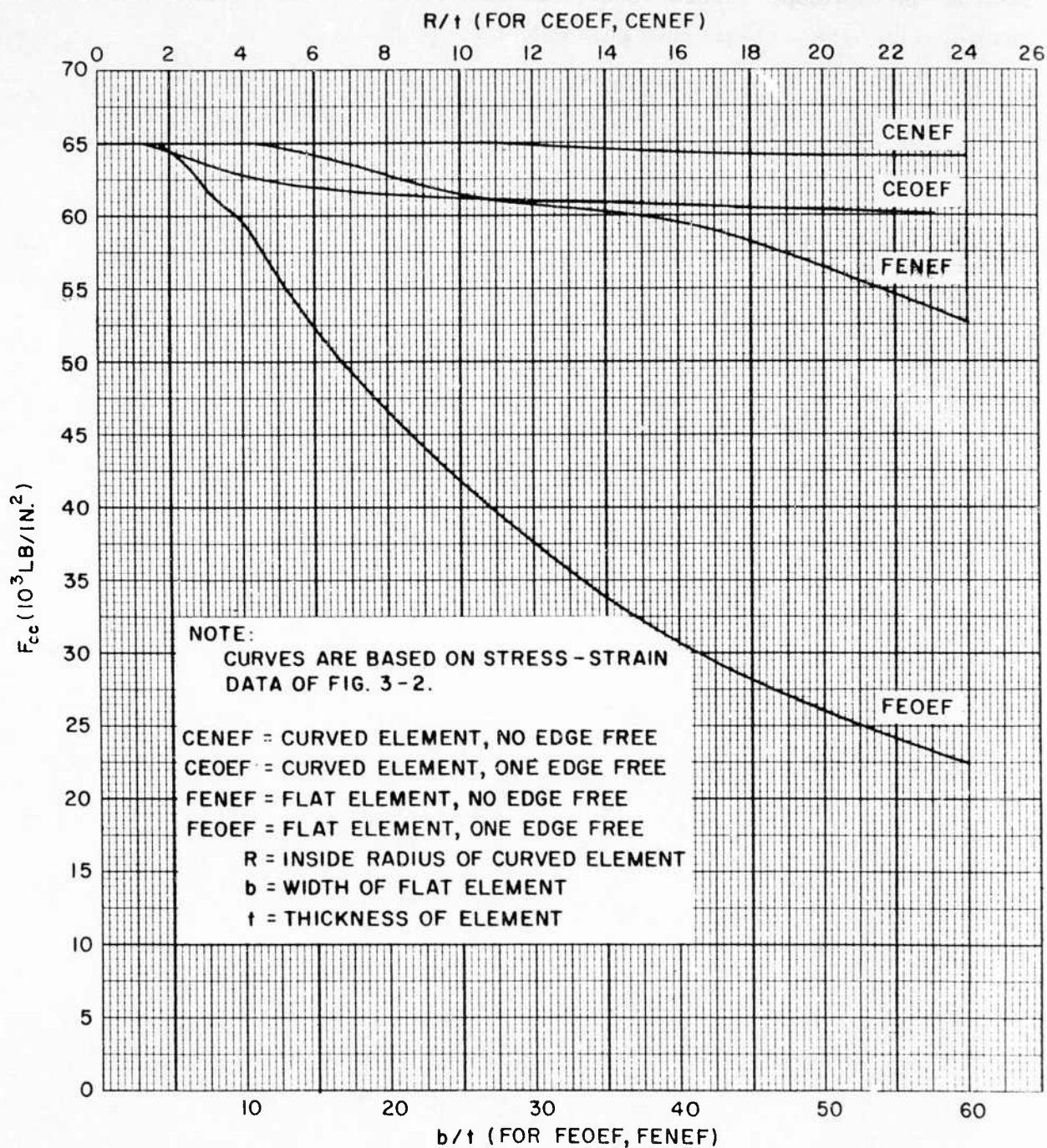


Fig. 3-18a Example Room-Temperature Crippling Curves for Beryllium Cross-Rolled Sheet (1.75% BeO Content)

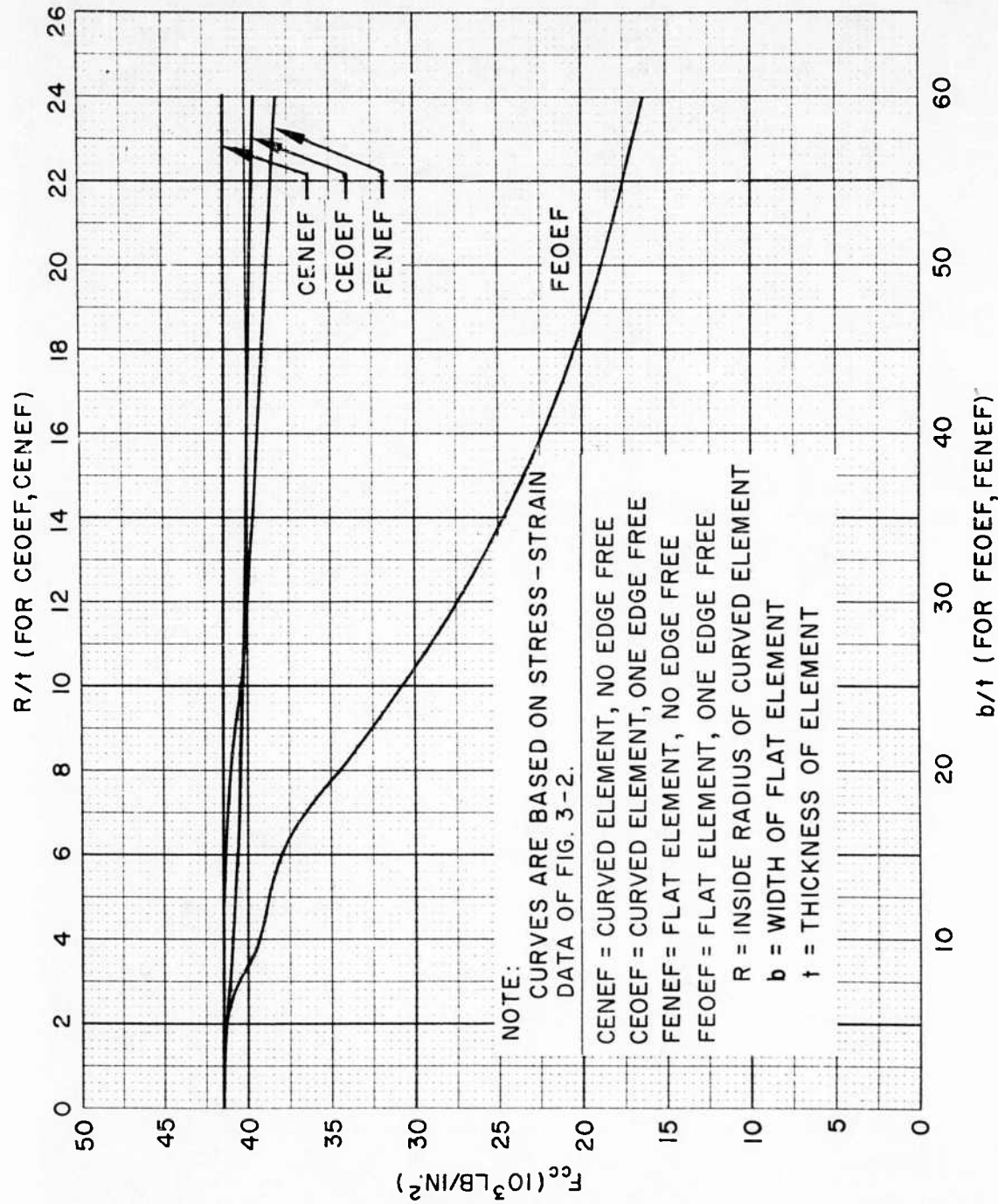


Fig. 3-18b Example Crippling Curves at 800°F for Beryllium Cross-Rolled Sheet (1.75% BeO Content)

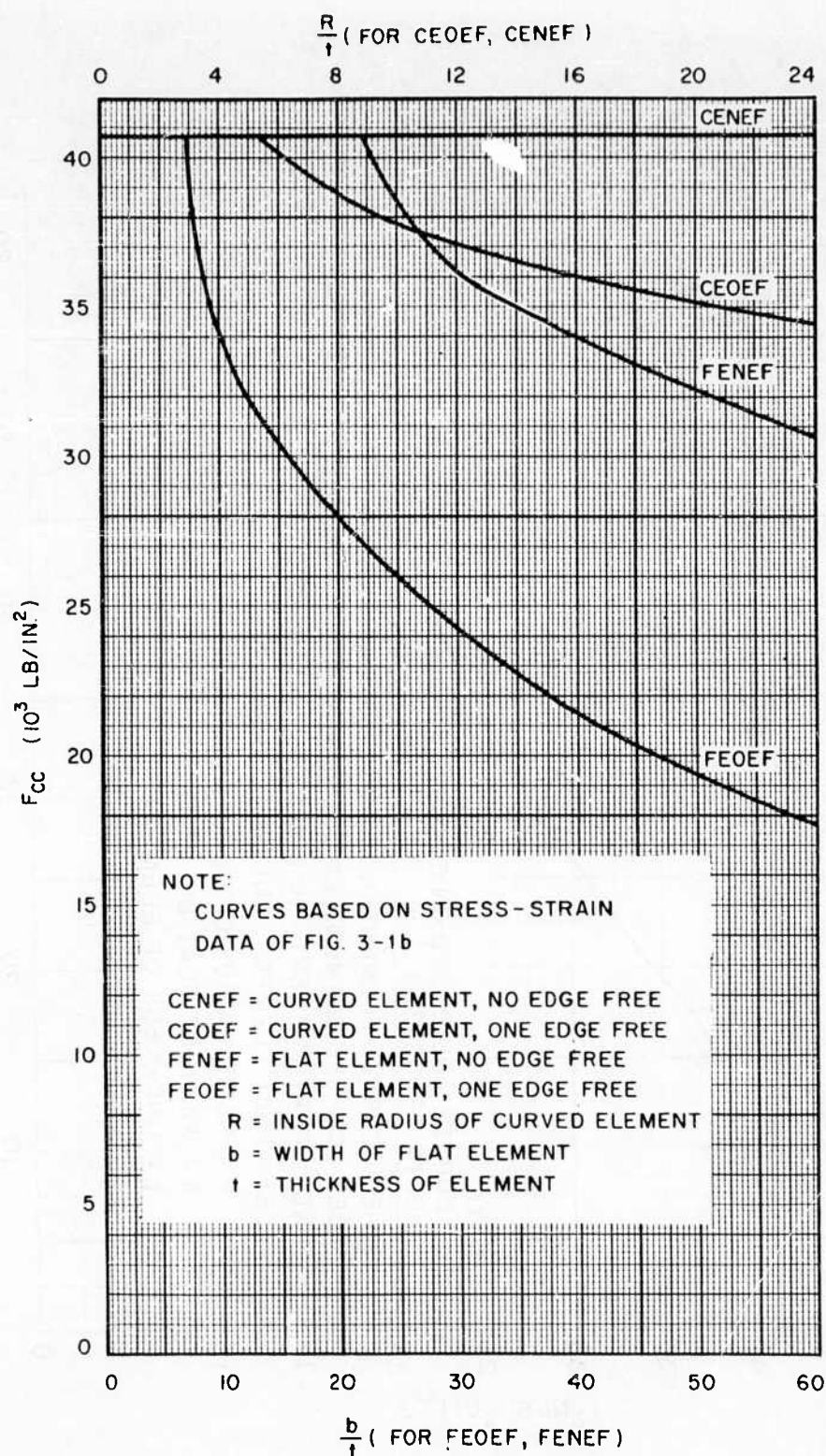


Fig. 3-19a Typical Crippling Curves at Room Temperature for Beryllium Block Material (1.75% BeO Content)

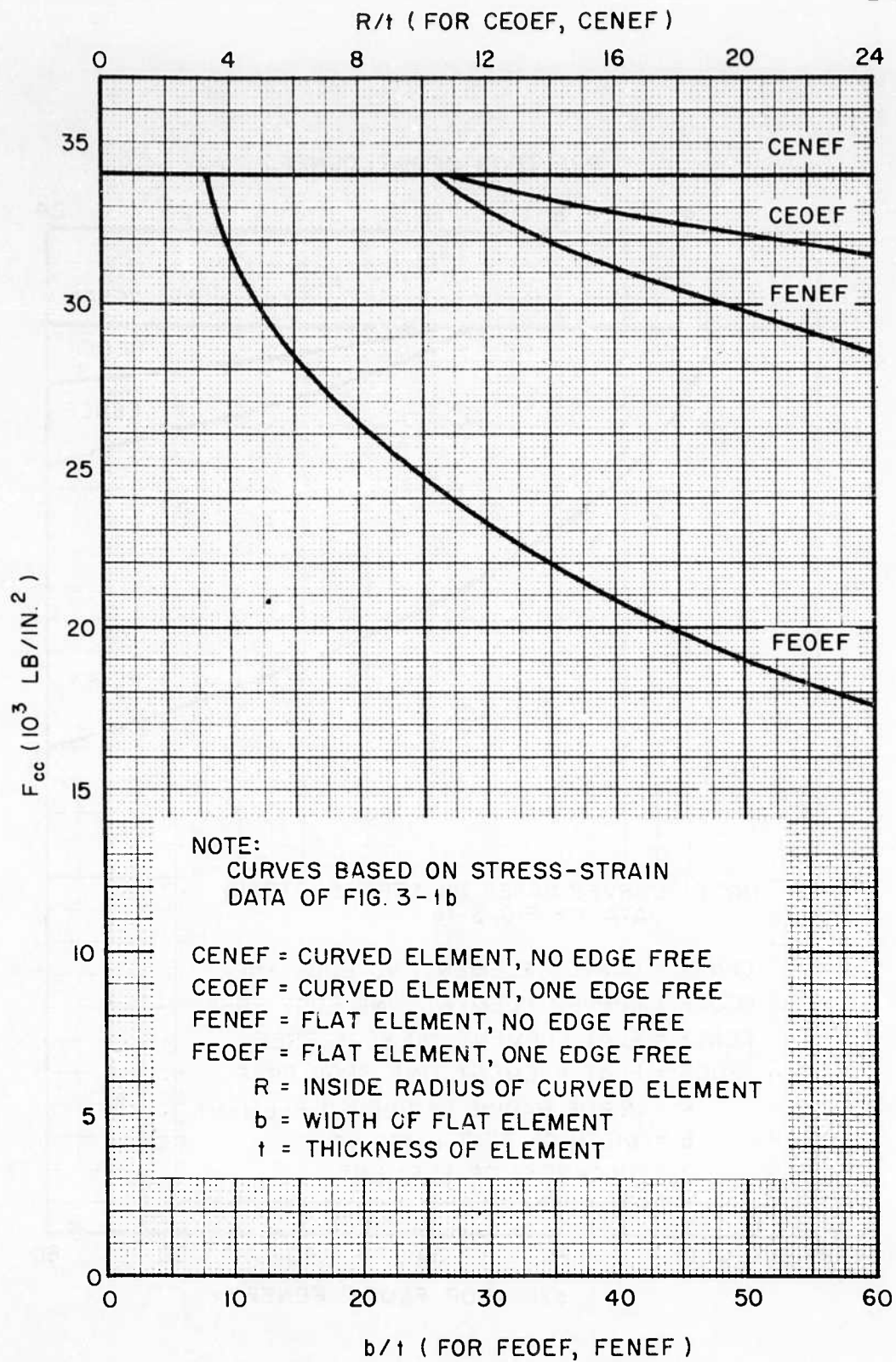


Fig. 3-19b Typical Crippling Curves at 400°F for Beryllium Block Material (1.75% BeO Content)

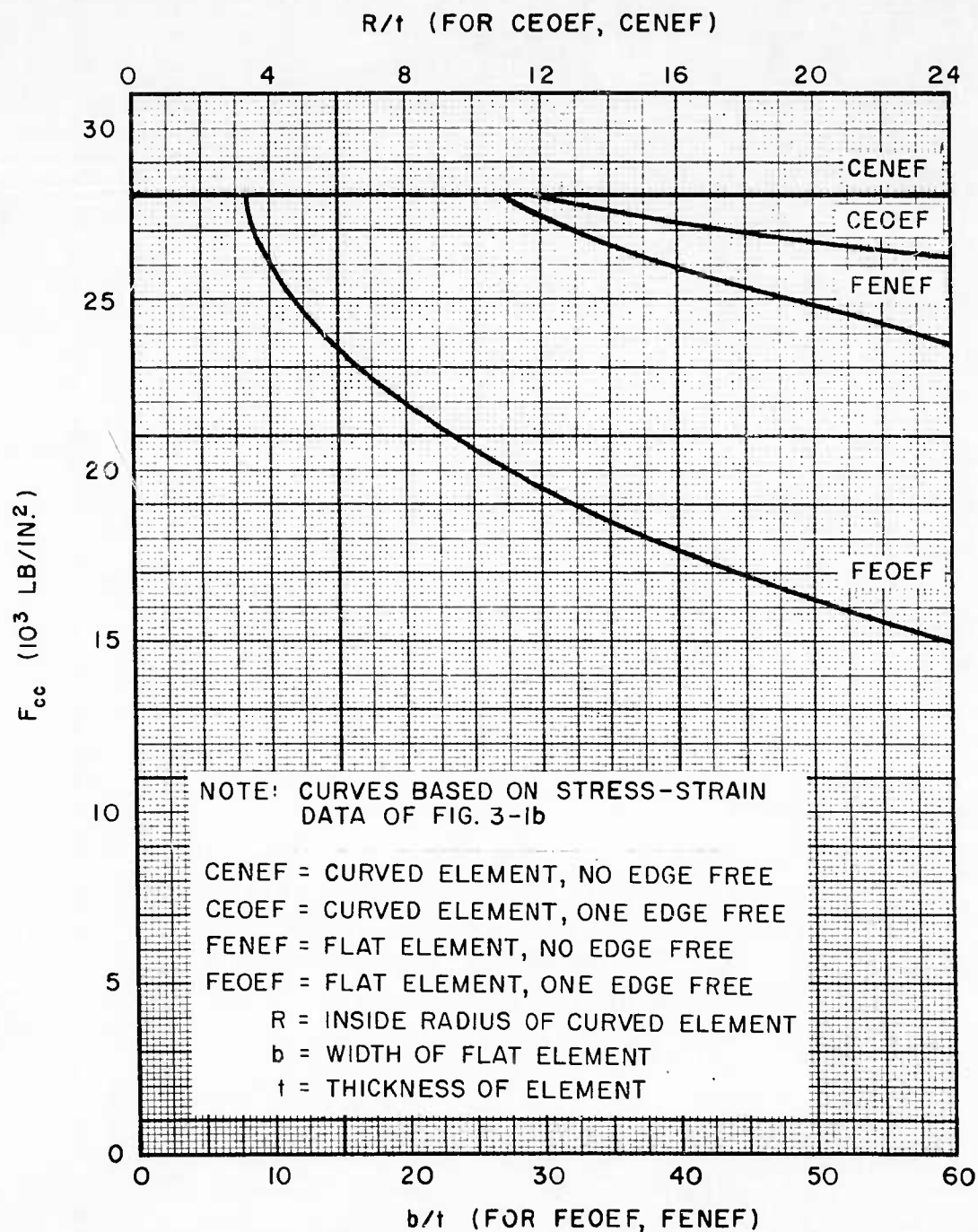


Fig. 3-19c Typical Crippling Curves at 800°F for Beryllium Block Material (1.75% BeO Content)

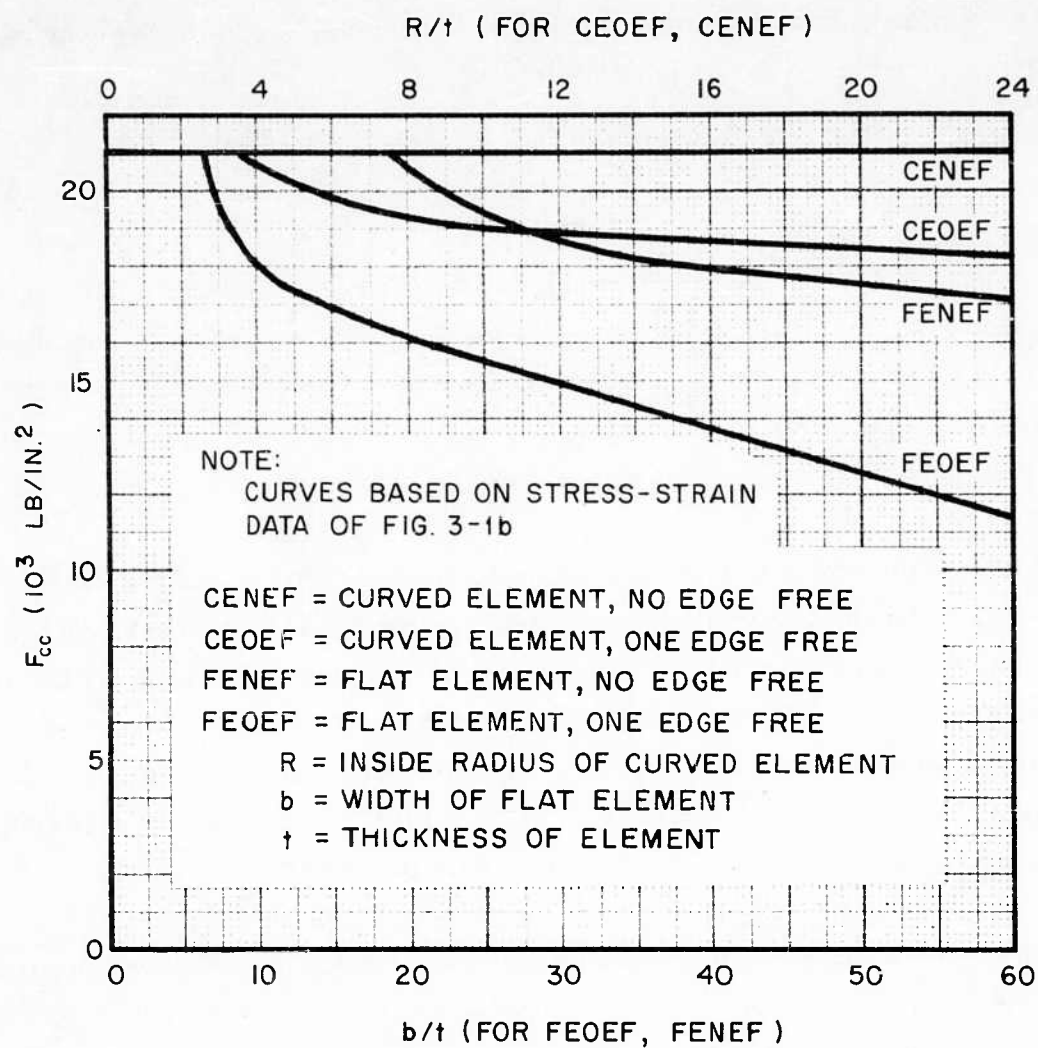


Fig. 3-19d Typical Crippling Curves at 1100°F for Beryllium Block Material (1.75% BeO Content)

3.5 PLASTIC BENDING DESIGN CHARTS

For most compact, stable members subjected to bending, the following conventional beam-stress formula is usually employed:

$$F_b = \frac{Mc}{I} \quad (3.15)$$

The bending modulus F_b is the extreme outer fiber stress which occurs in a beam under a moment M if the action of the beam is completely elastic. The bending modulus corresponding to M_{max} is usually referred to as the modulus of rupture. For beams stressed at the extreme fiber above the proportional limit of the material, the bending modulus is a fictitious stress which is used solely for convenience.

Bending moduli presented in this section are based on the method of Cozzone (Ref. 3-10), and apply to beryllium block material having 1.75-percent BeO content. The typical stress-strain curves for this material are shown in Fig. 3-1a. Curves are presented for several intermediate extreme fiber strains between zero strain and maximum strain so that the designer may determine a bending modulus pertaining to any extreme fiber strain up to maximum strain. These strains may be converted into stress by proper use of the stress-strain data presented in Fig. 3-1a.

Design charts presenting bending moduli versus section factor K as a function of extreme fiber strain are given at room temperature (Fig. 3-20), 500°F (Fig. 3-21), 800°F (Fig. 3-22), and 1100°F (Fig. 3-23). Each of these figures is divided into two charts, a. and b. Chart a. presents bending moduli based on the criteria that extreme fiber strain is measured under load. Chart b. presents bending moduli based on the criteria that extreme fiber strain is measured after load removal. In the latter case, advantage is taken of the elastic recovery of the material after load removal. Obviously, this advantage is most significant at low extreme fiber strains. Note that the manner of converting strain to stress by means of Fig. 3-1a is dependent on the type of strain measurement.

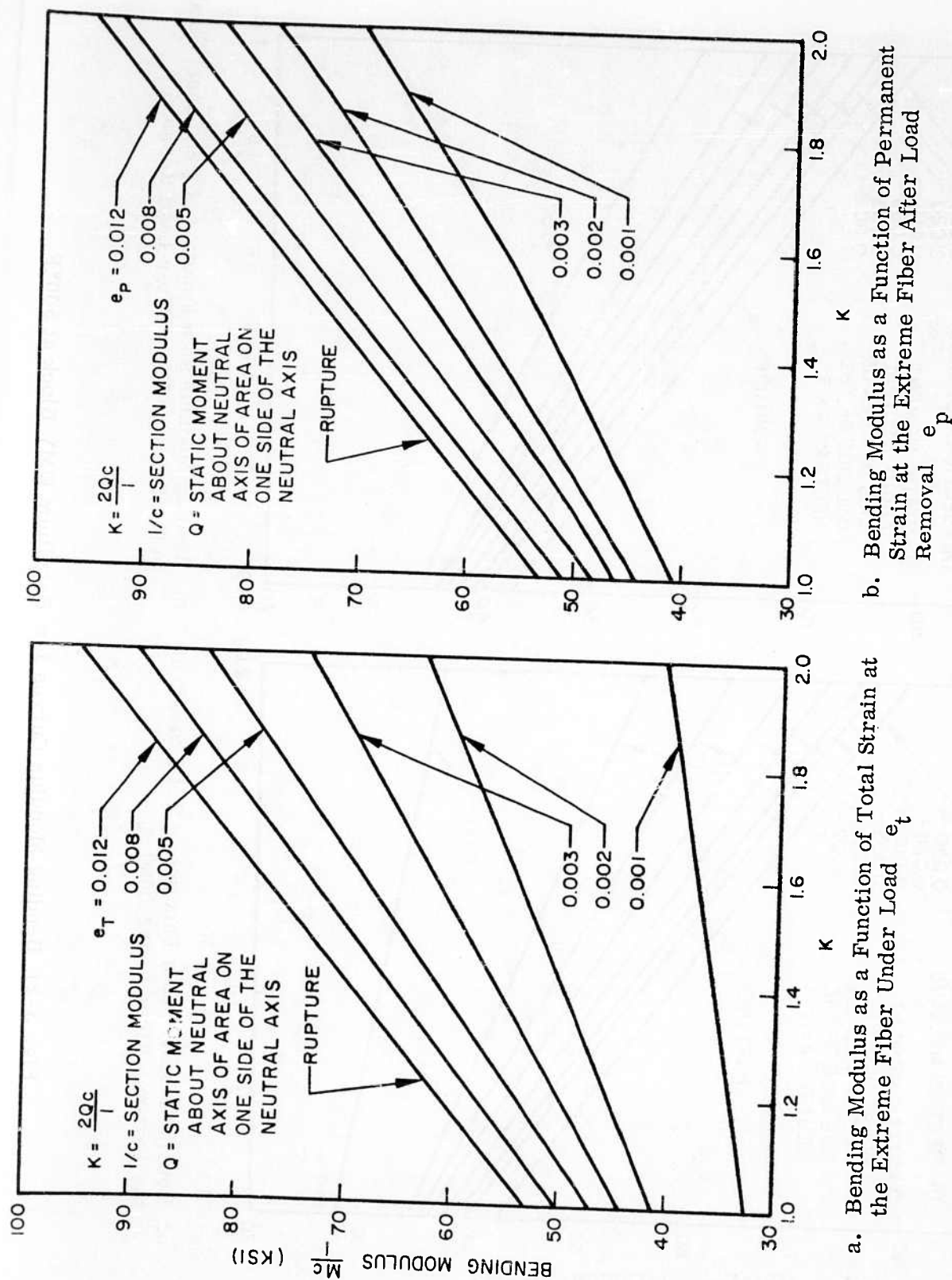
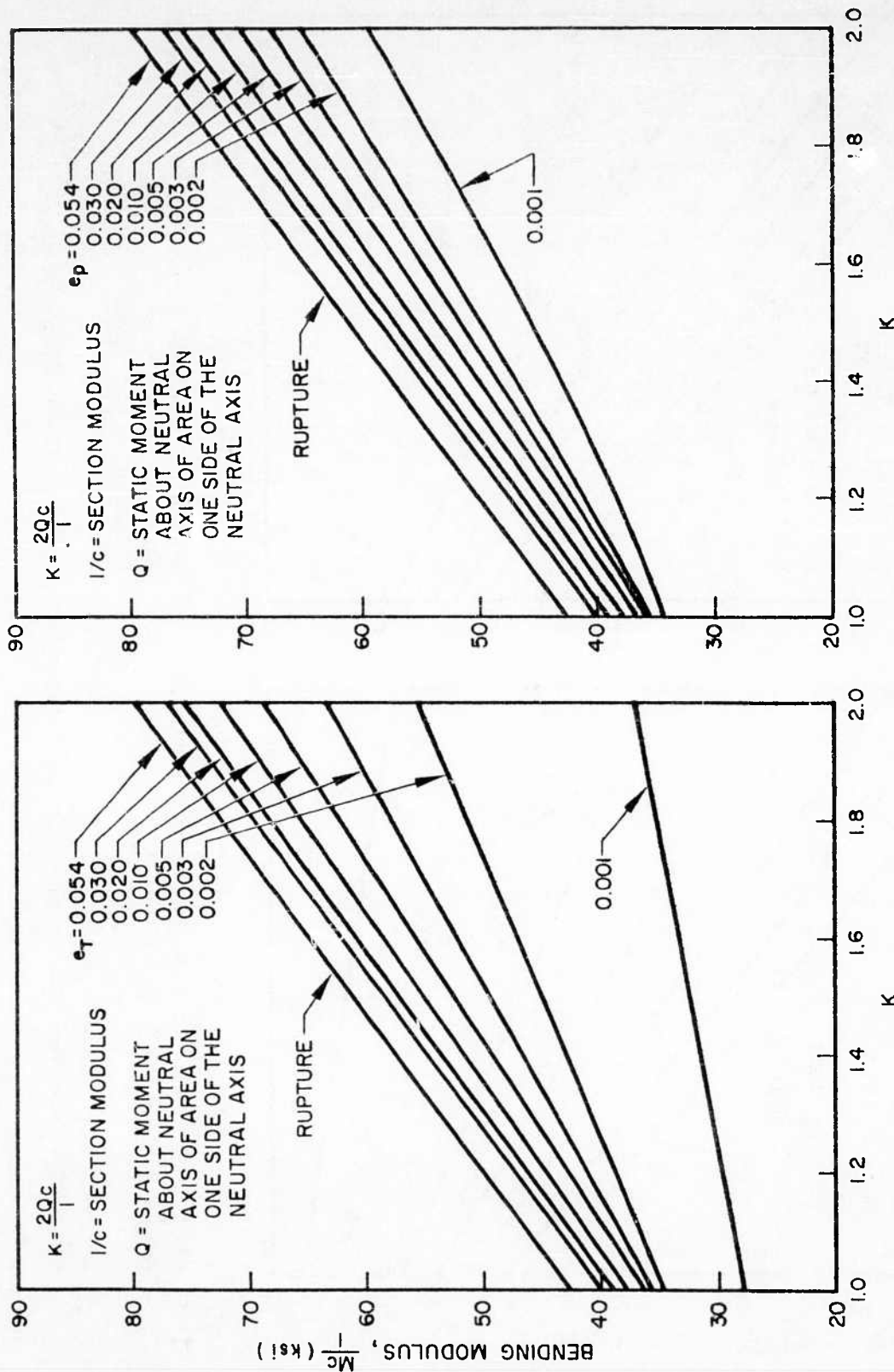
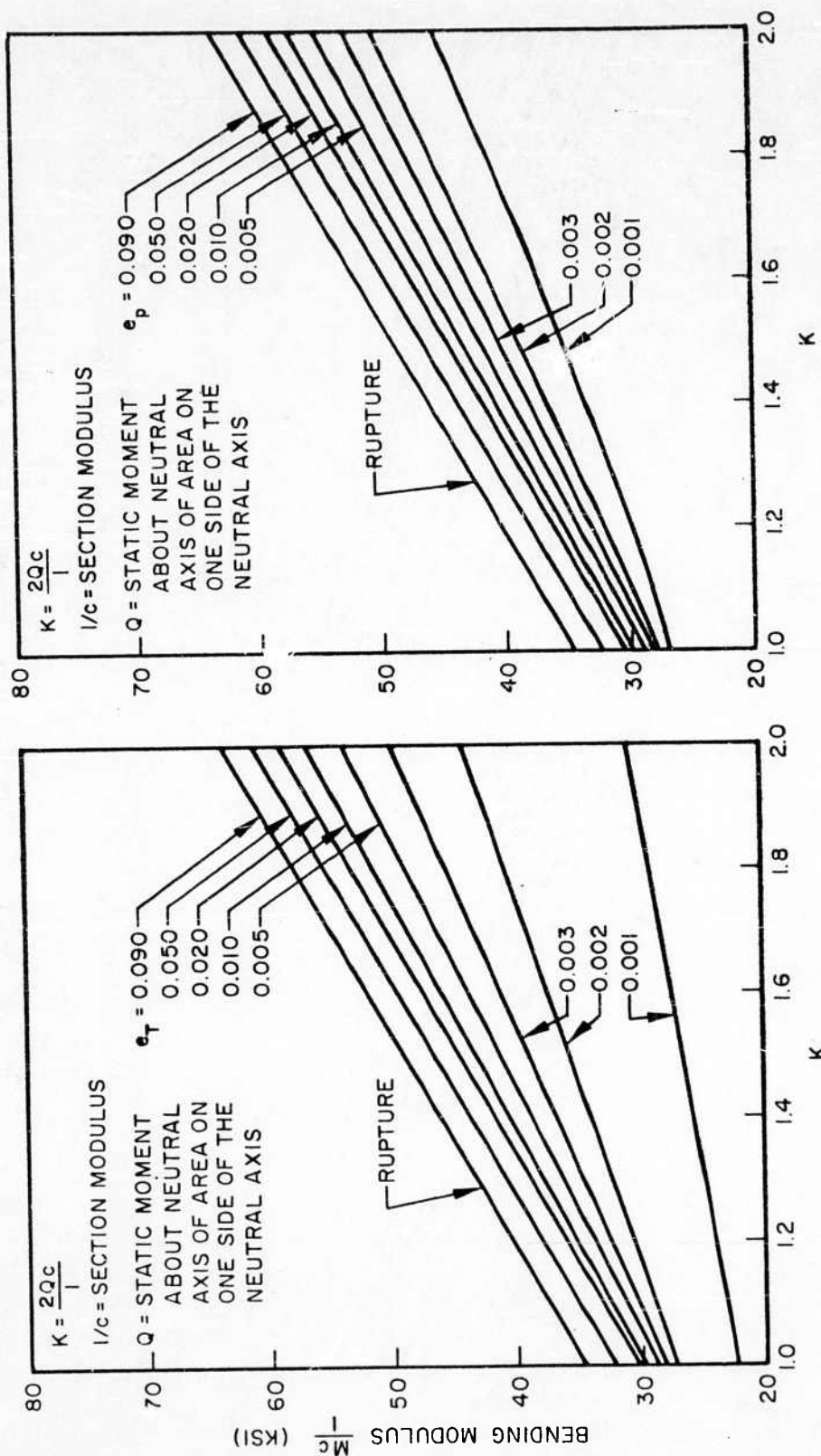


Fig. 3-20 Bending Modulus Curves for Beryllium Block at Room Temperature



a. Bending Modulus as a Function of Total Strain at the Extreme Fiber Under Load e_t
 b. Bending Modulus as a Function of Permanent Strain in the Extreme Fiber After Load Removal e_p

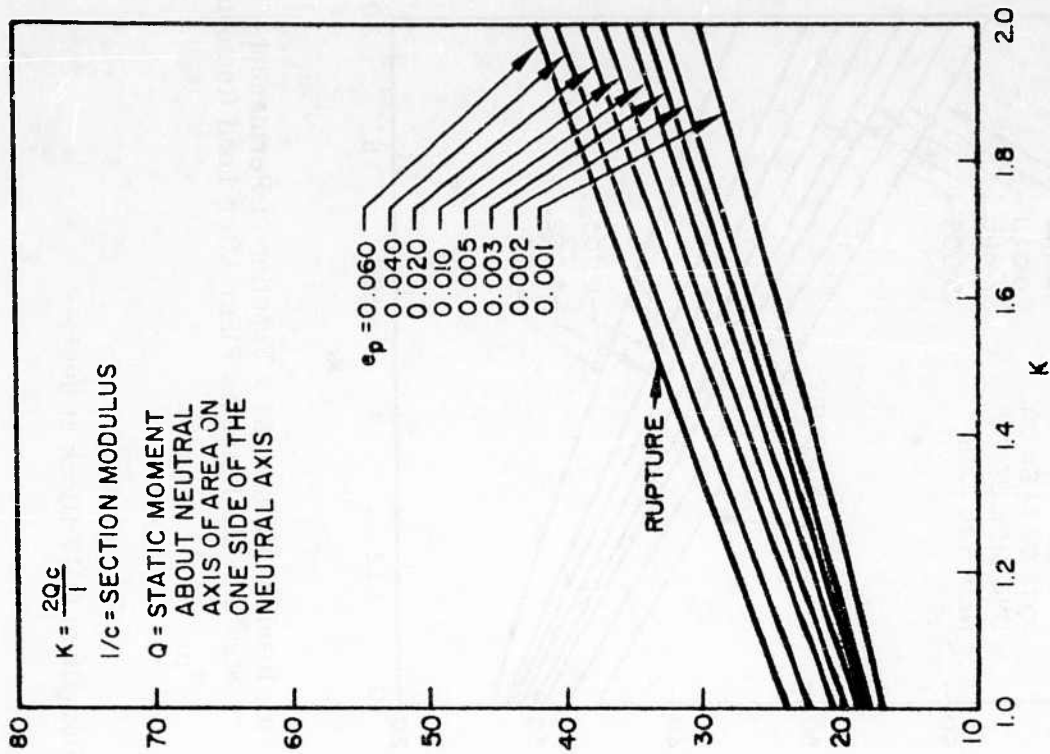
Fig. 3-21 Bending Modulus Curves for Beryllium QMV Block at 500°F



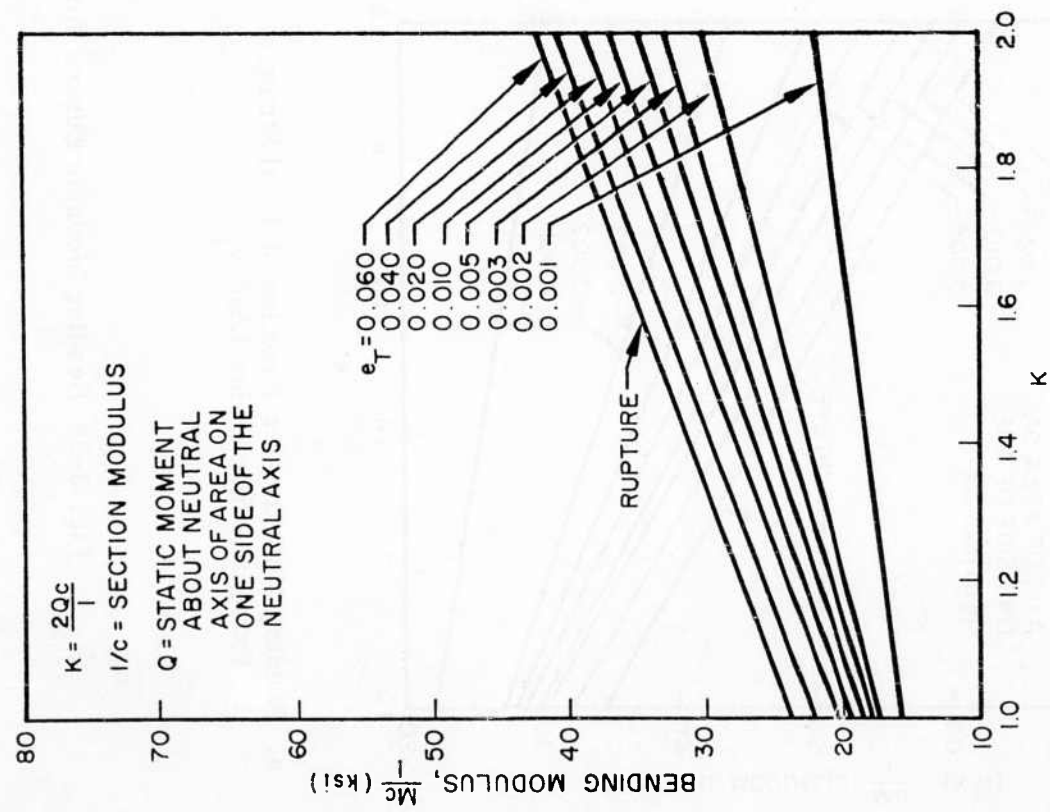
a. Bending Modulus as a Function of Total Strain at the Extreme Fiber Under Load e_t

b. Bending Modulus as a Function of Permanent Strain in the Extreme Fiber After Load Removal e_p

Fig. 3-22 Bending Modulus Curves for Beryllium QMV Block at 800°F



b. Bending Modulus as a Function of Permanent Strain in the Extreme Fiber After Load Removal e_p



a. Bending Modulus as a Function of Total Strain at the Extreme Fiber Under Load e_t

Fig. 3-23 Bending Modulus Curves for Beryllium QMV Block at 1100°F

3.6 BERYLLIUM JOINING

3.6.1 Introduction

A considerable amount of experimental information is available in the literature and from LMSC programs on the subject of beryllium joining. The following discussion and figures summarize this information. Subsection 3.6.1 deals with mechanical joints; subsection 3.6.2 considers metallurgical joints.

3.6.2 Mechanical Joining

The principal sources for the mechanical joining data presented in this section are Refs. 3-11 and 3-12. These reports cover test programs on single splice-plate butt joints using various flush fasteners at room and elevated temperature. Data on the following fasteners are presented, for both the 3/16- and 1/4-in.-diam. sizes: F200 and F260 Jo-Bolts, NAS-560 HK screws, NAS-517 screws, SAL-100 Huckbolts, and a special A-286 hollowend rivet. Joints with single- and double-row fasteners, various spacings, and sheet thicknesses were tested. The single-row specimens consisted of two fasteners; the double-row specimens consisted of two in-line rows of two fasteners each. The geometries of these specimens have been previously presented in Fig. 2-33. All tests in Refs. 3-11 and 3-12 were made in beryllium strip machined from hot-pressed block material, except those of the A-286 hollowend rivet, which were made in beryllium cross-rolled sheet. A constant e/D of 2.5 was maintained in all tests, and the nominal strain rate was 0.01 in./in./min. The following curves, which are presented in terms of maximum load per fastener versus temperature, should be considered typical, since they represent one and two tests per data point. It is recommended that these curves be used in preliminary design and be substantiated with specific tests for the final design configuration.

Figures 3-24 through 3-29 present data on F200 and F260 Jo-Bolts. Figures 3-24 through 3-26 treat the double-row configuration for beryllium block thicknesses of 0.15, 0.25, and 0.375 in., respectively. Likewise, Figs. 3-27 through 3-29 are for the single-row configuration for the same block thicknesses in identical order.

Data on NAS-560 HK screws are presented in Figs. 3-30 through 3-35. The double-row configuration is treated in Figs. 3-30 through 3-32 for 0.15-, 0.25-, and 0.375-in. beryllium block thicknesses, respectively. Figures 3-33 through 3-35 cover the single-row configuration for the same block thicknesses in identical order.

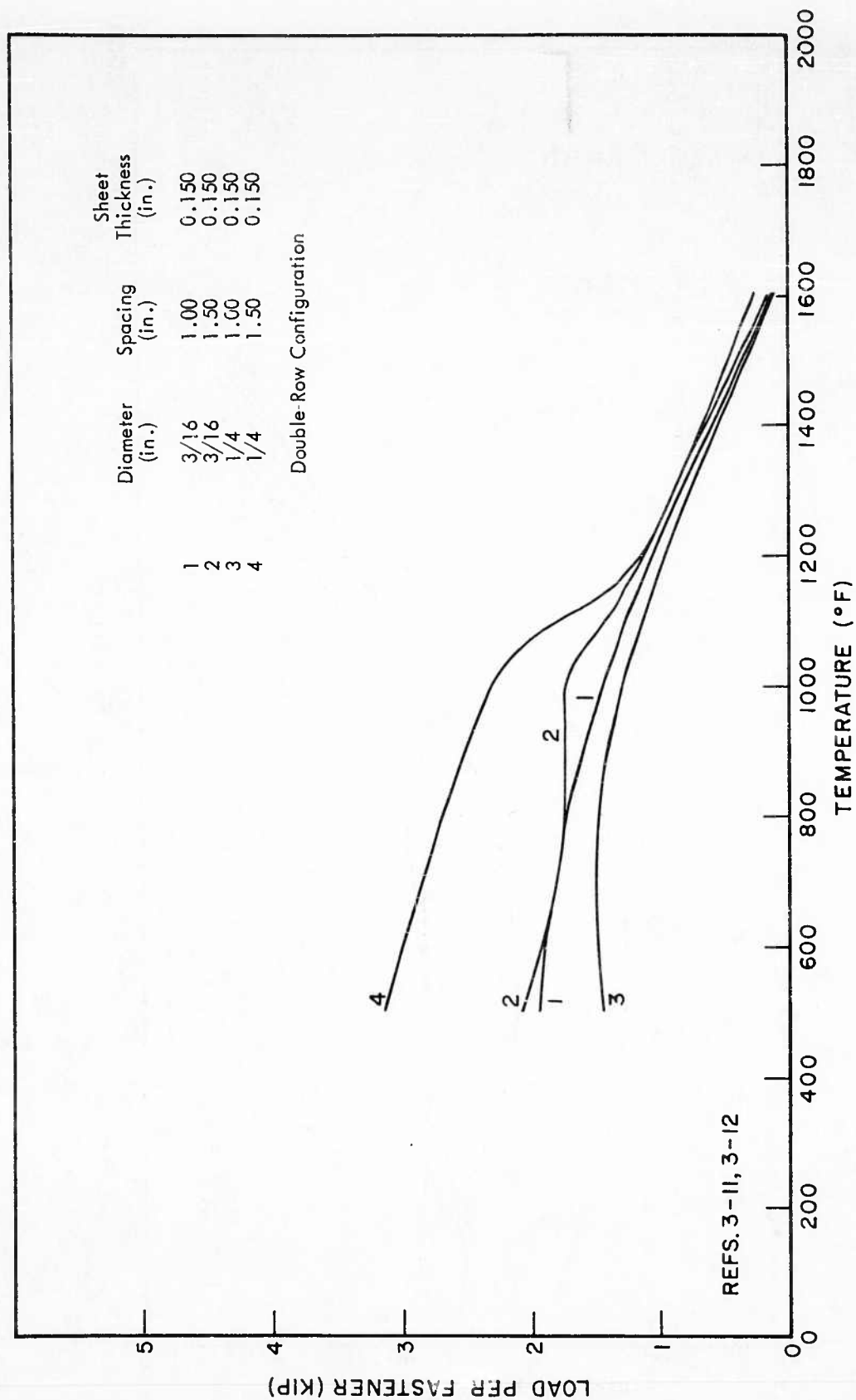


Fig. 3-24 Effect of Temperature on 0.150 Thick Hot-Pressed Beryllium Block Double-Row Butt Joints Fastened With F200 and F260 Jo-Bolts

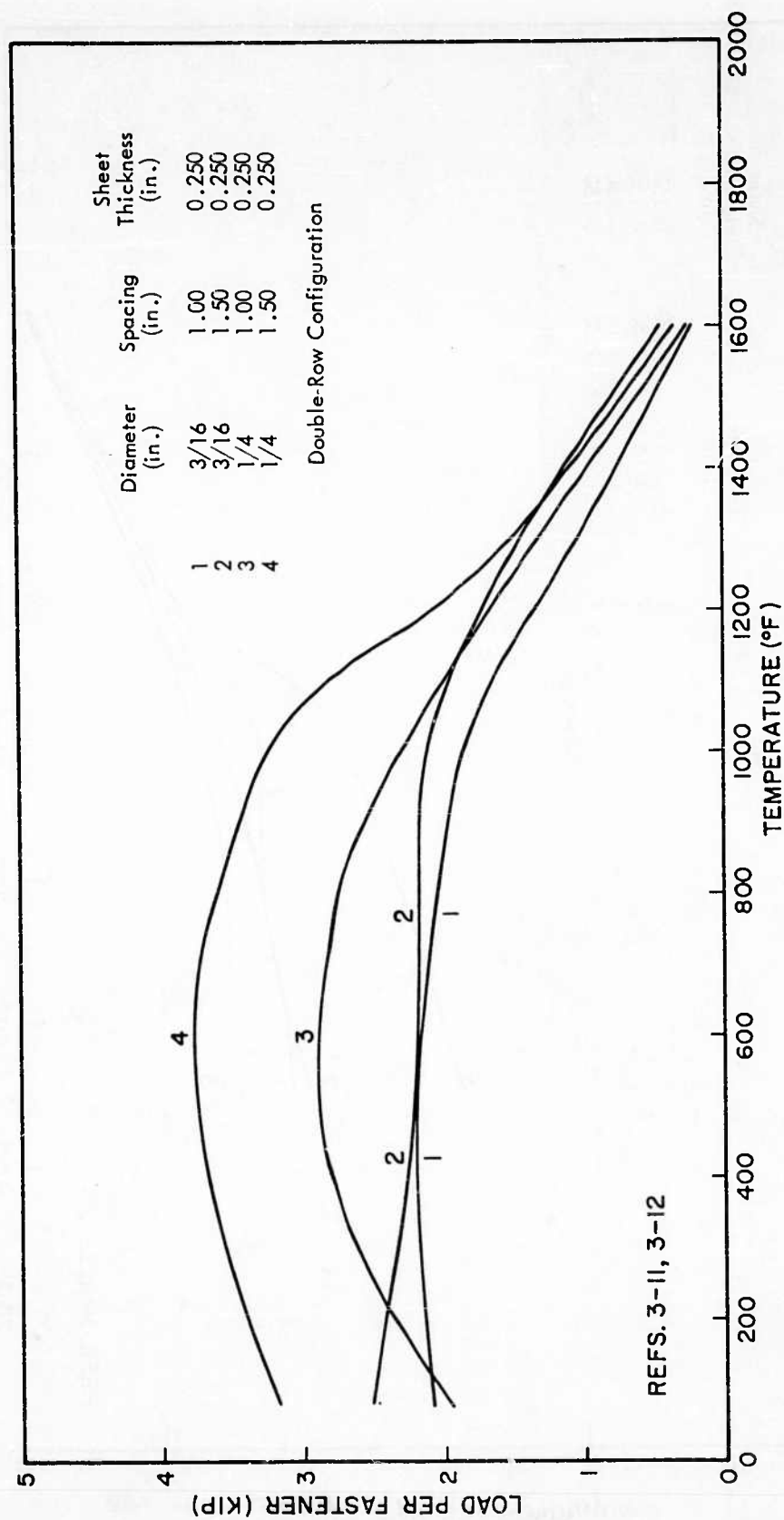


Fig. 3-25 Effect of Temperature on 0.250 Thick Hot-Pressed Beryllium Block Double-Row Butt Joints Fastened With F200 and F260 Jo-Bolts

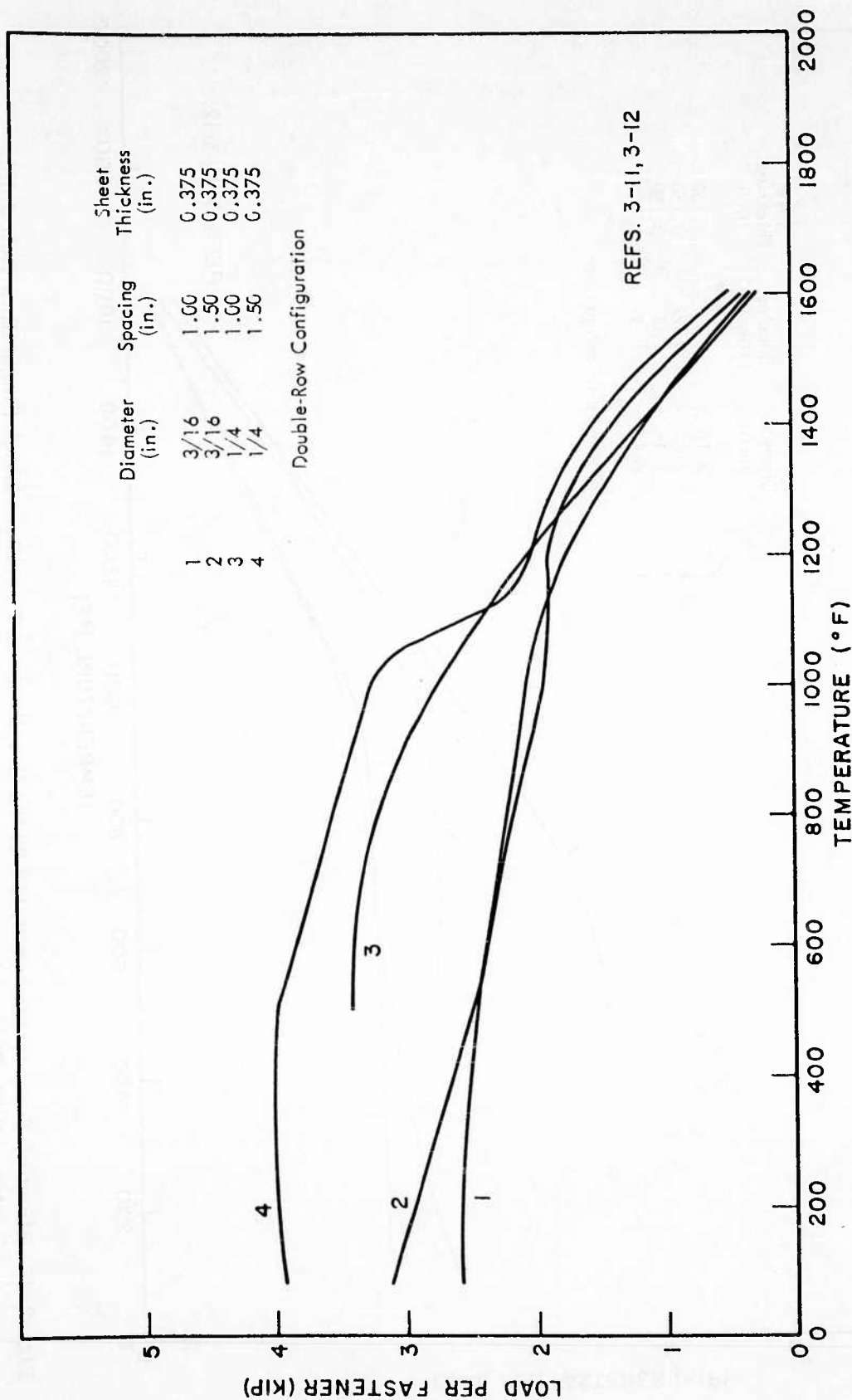


Fig. 3-26 Effect of Temperature on 0.375 Thick Hot-Pressed Beryllium Block Double-Row Butt Joints Fastened With F200 and F260 Jo-Bolts

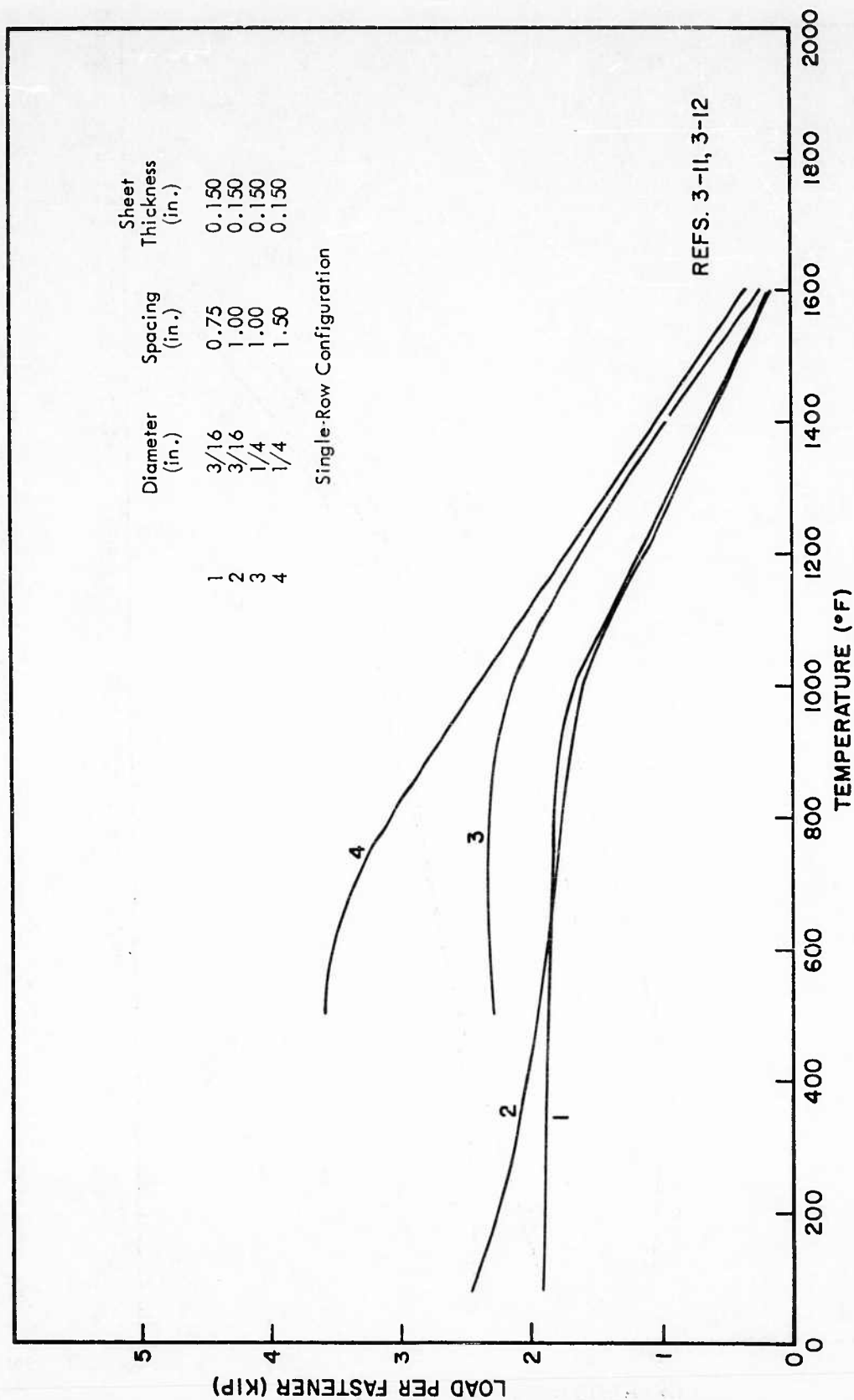


Fig. 3-27 Effect of Temperature on 0.150 Thick Hot-Pressed Beryllium Block Single-Row Butt Joints Fastened With F200 and F260 Jo-Bolts

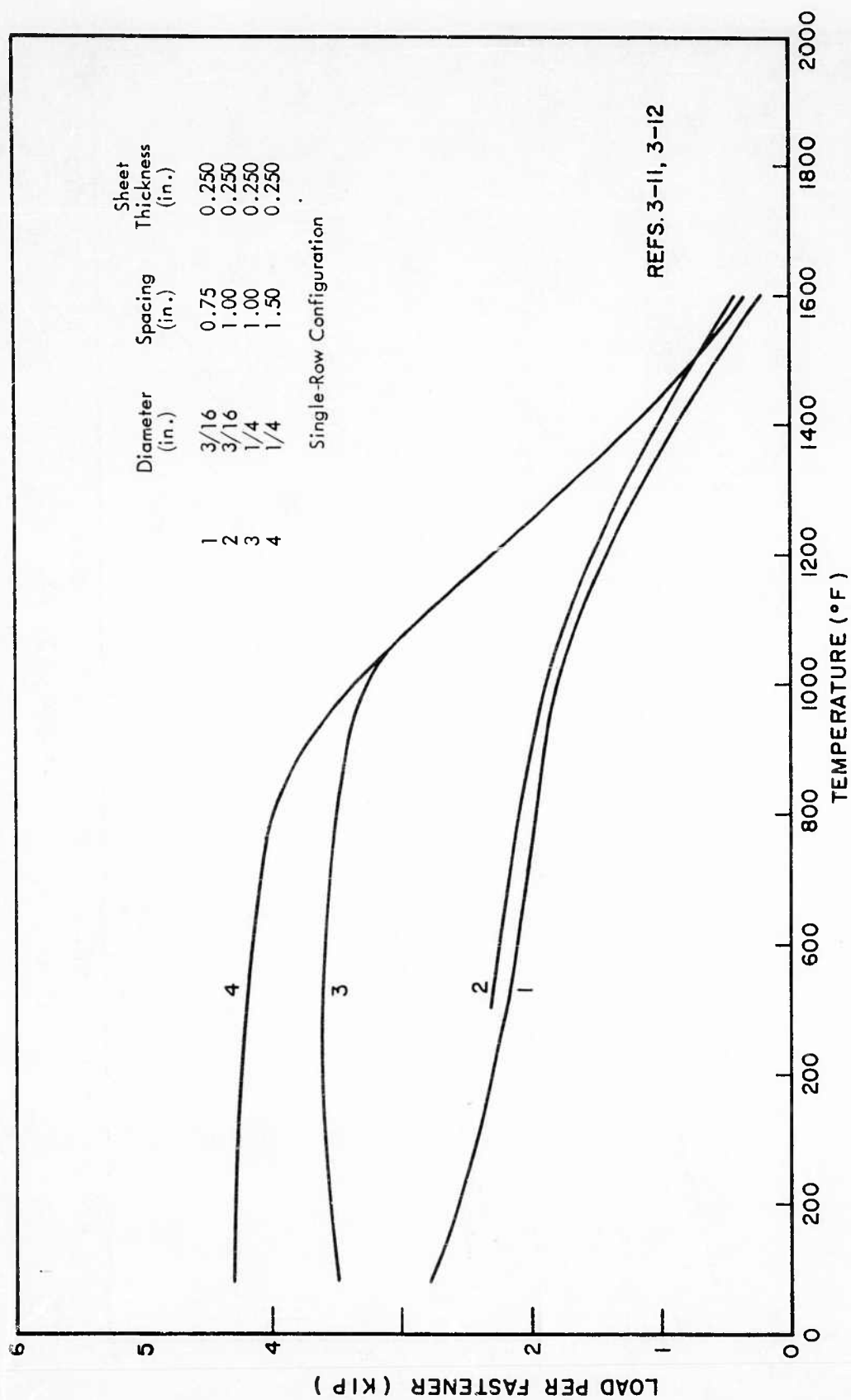


Fig. 3-28 Effect of Temperature on 0.250 Thick Hot-Pressed Beryllium Block Single-Row Butt Joints Fastened With F200 and F260 Jo-Bolts

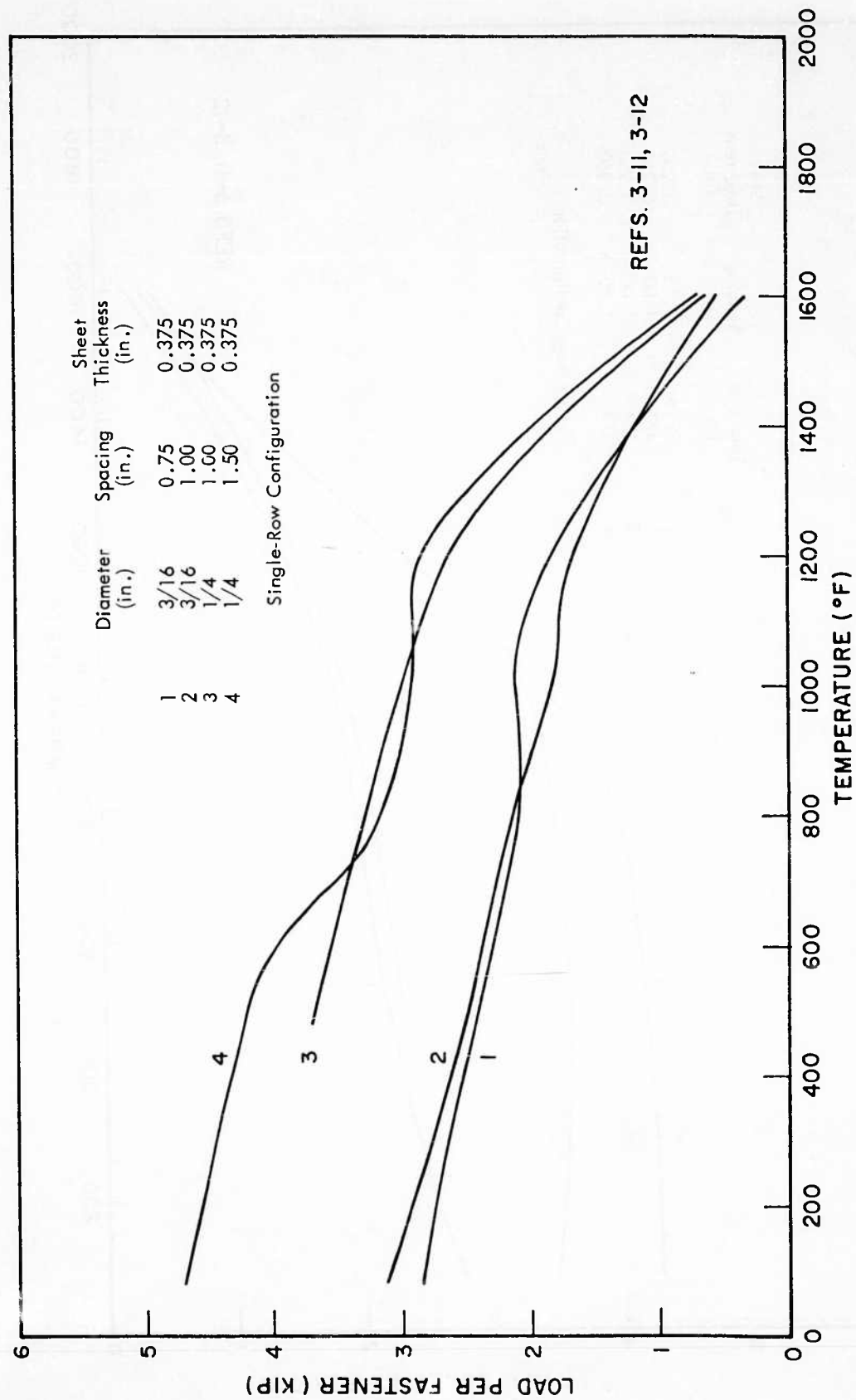


Fig. 3-29 Effect of Temperature on 0.375 Thick Hot-Pressed Beryllium Block Single-Row Butt Joints Fastened With F200 and F260 Jo-Bolts

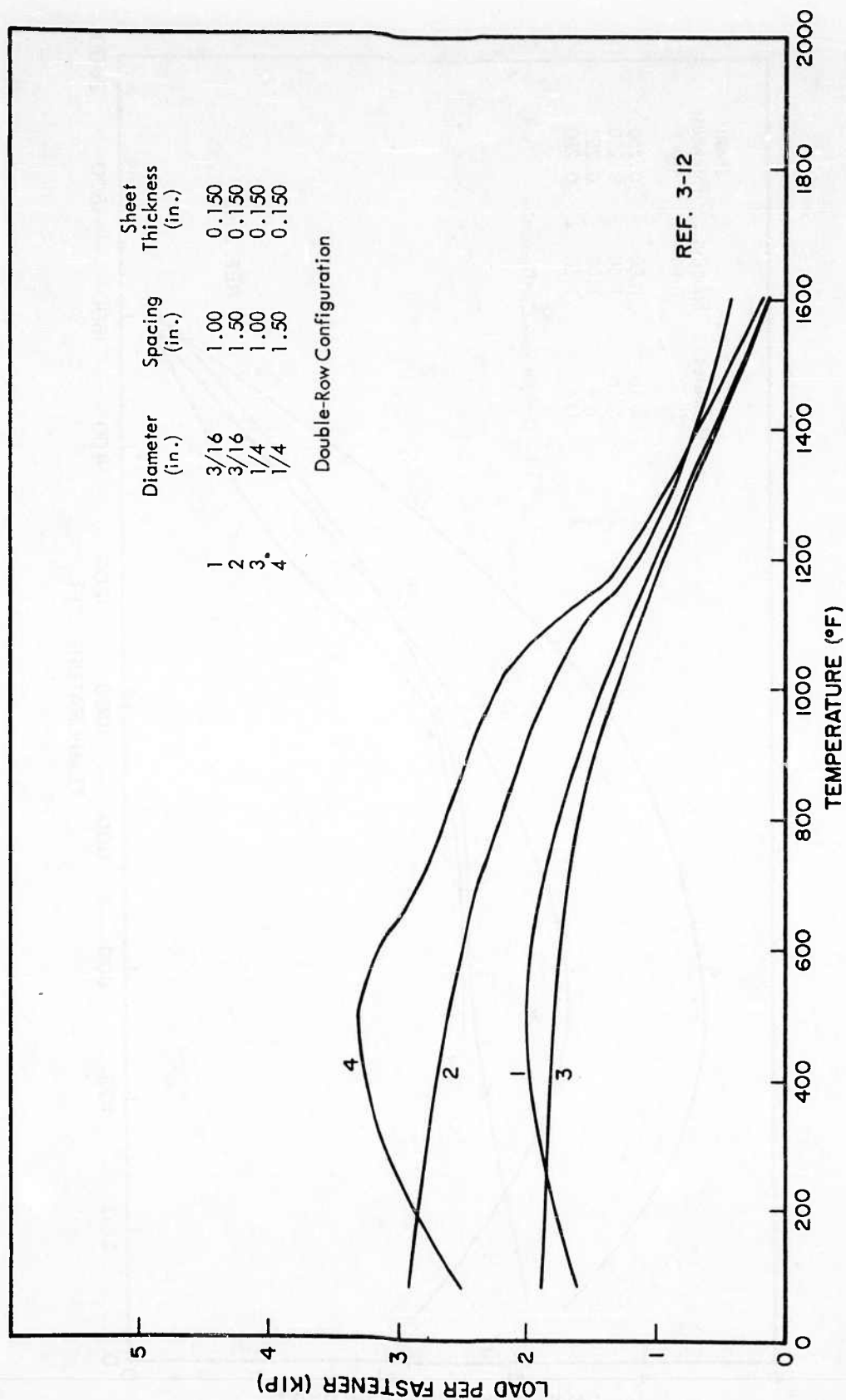


Fig. 3-30 Effect of Temperature on 0.150 Thick Hot-Pressed Beryllium Block Double-Row Butt Joints Fastened With NAS-560 HK Screws

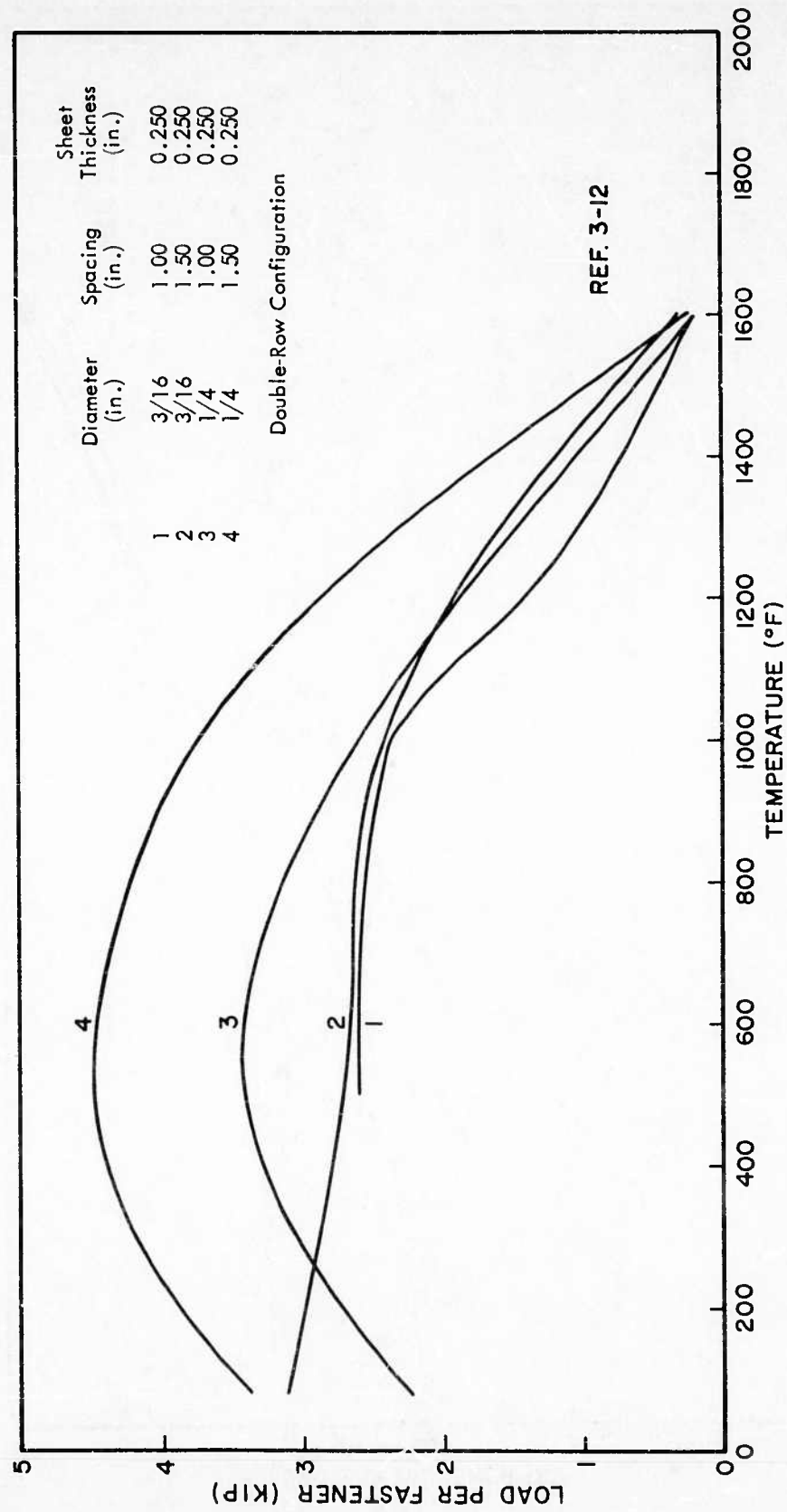


Fig. 3-31 Effect of Temperature on 0.250 Thick Hot-Pressed Beryllium Block Double-Row Butt Joints Fastened With NAS-560 HK Screws

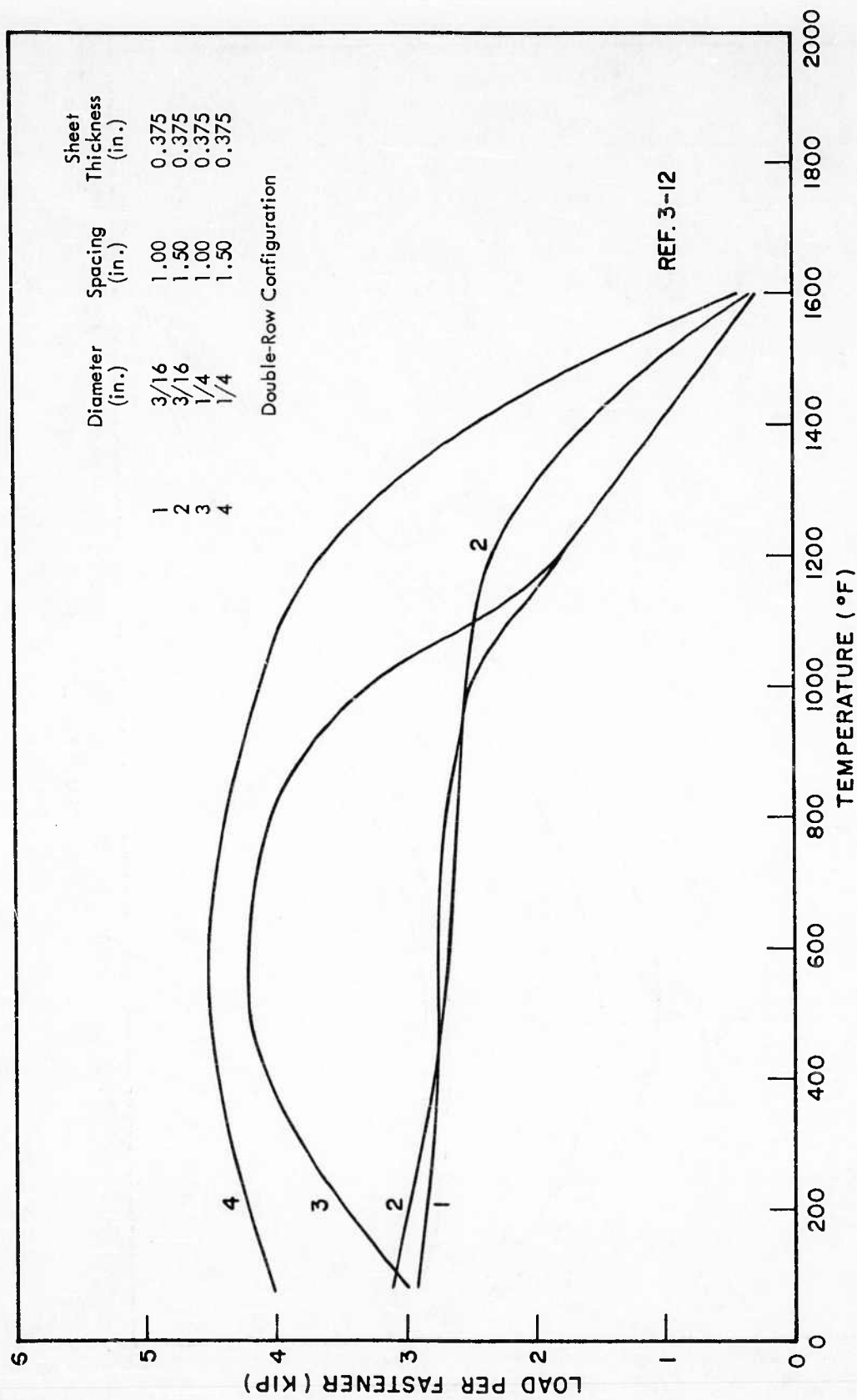


Fig. 3-32 Effect of Temperature on 0.375 Thick Hot-Pressed Beryllium Block Double-Row Butt Joints Fastened With NAS-560 HK Screws

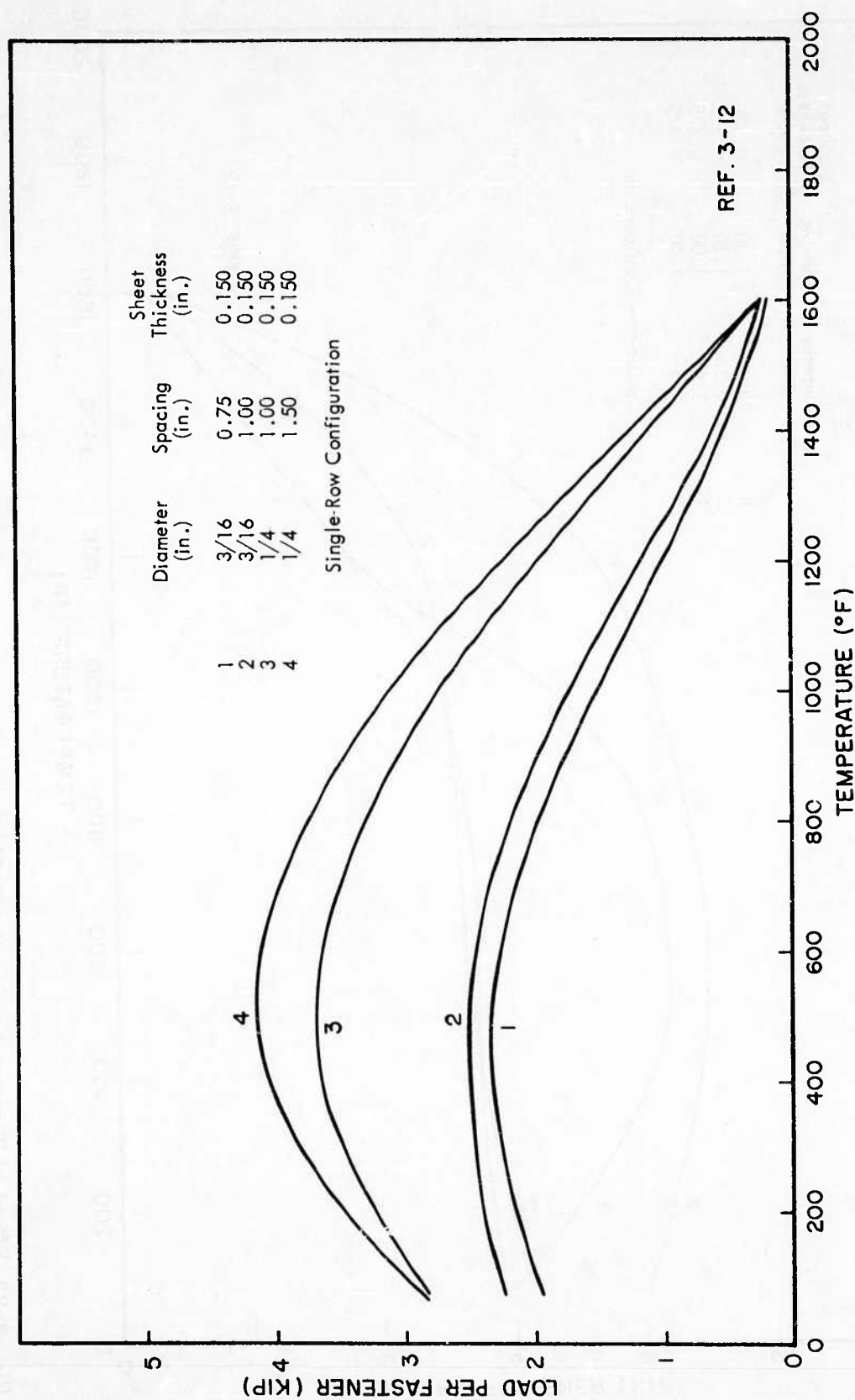


Fig. 3-33 Effect of Temperature on 0.150 Thick Hot-Pressed Beryllium Block Single-Row Butt Joints Fastened With NAS-560 HK Screws

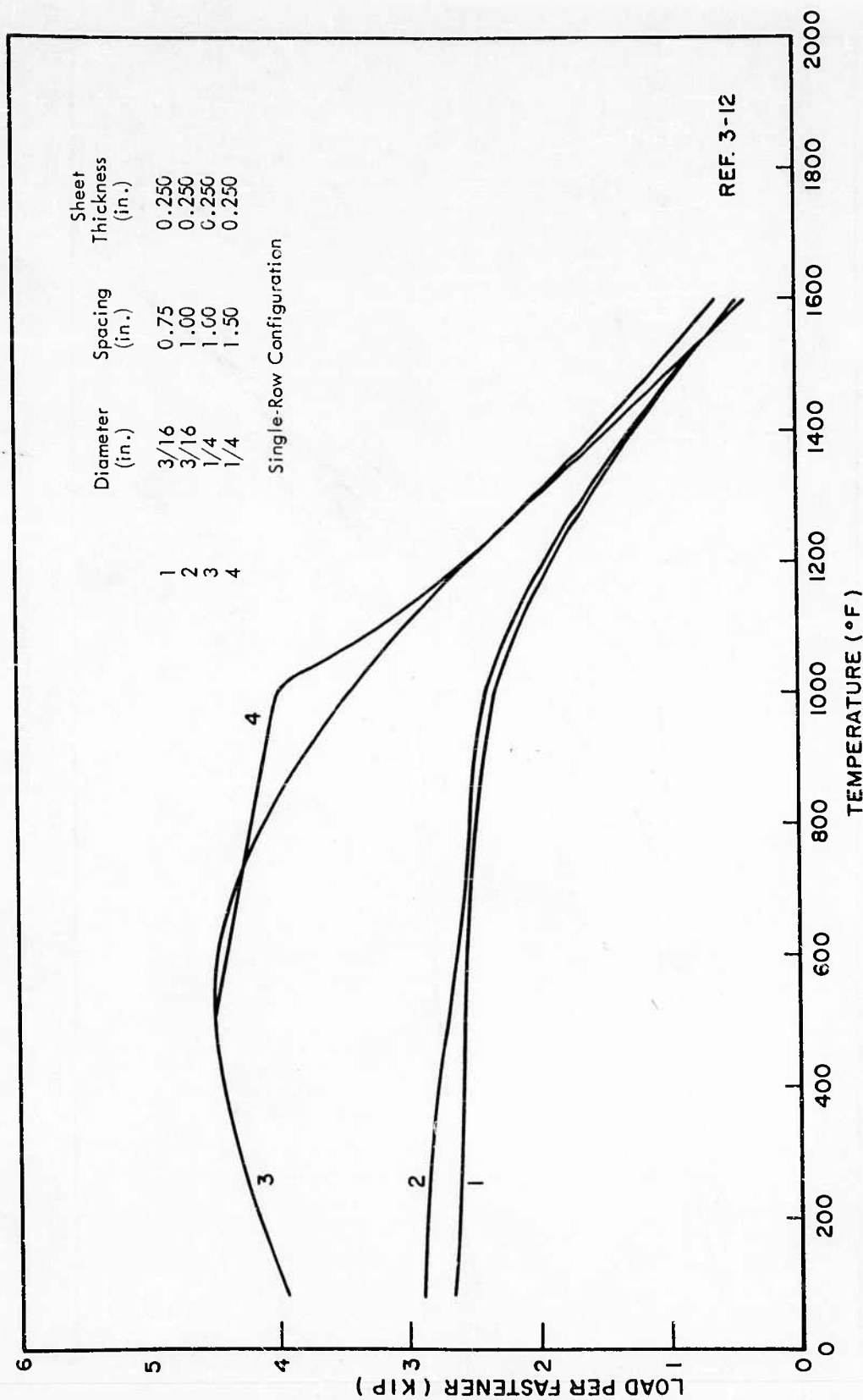


Fig. 3-34 Effect of Temperature on 0.250 Thick Hot-Pressed Beryllium Block Single-Row Butt Joints Fastened With NAS-560 HK Screws

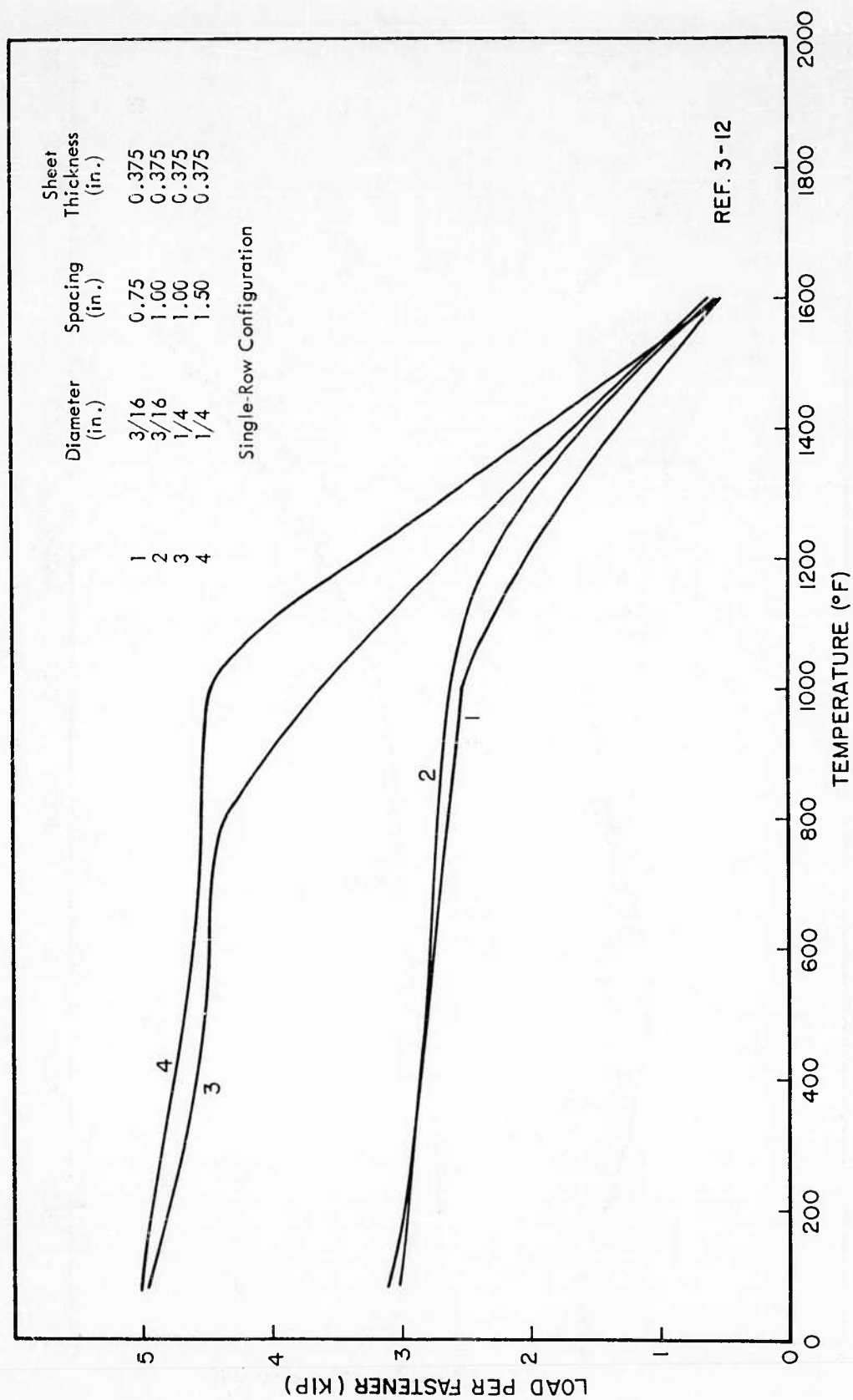


Fig. 3-35 Effect of Temperature on 0.375 Thick Hot-Pressed Beryllium Block Single-Row Butt Joints Fastened With NAS-560 HK Screws

Figures 3-36 through 3-39 are presented for NAS-517 screws. Beryllium block thicknesses of 0.15 and 0.25 in. are treated in Figs. 3-36 and 3-37, respectively, for the double-row configuration. Likewise, the single-row configuration is presented in Figs. 3-38 and 3-39 for these same block thicknesses. Data for NAS-517 screws are limited to the temperature range from 800° to 1400°F.

Figure 3-40 applies to SAL-100 Huckbolts in the double-row configuration, while Fig. 3-41 applies to SAL-100 Huckbolts in the single-row configuration. Both of these figures are based on tests in 0.25-in.-thick beryllium block. These data are limited to the temperature range between 1000° and 1400°F.

As stated previously, the tests of the A-286 hollowend rivet were made in beryllium cross-rolled sheet. Figure 3-42 treats both single- and double-row fastener configurations where the sheet thickness is 0.25 in. Figure 3-43 also treats both fastener configurations, but for a sheet thickness of 0.133 in. Because this fastener is not a standard fastener, a sketch of the rivet geometry is presented for the reader's information as Fig. 3-44.

Reviewing Figs. 3-24 through 3-41 covering Jo-Bolts, screws, and Huckbolts, some trends are noteworthy:

- At room temperature the thinner specimens failed by beryllium sheet tension, while the thickest (0.375 in.) usually failed by fastener shear.
- In the temperature range from 500° to 1000°F, the thin- and intermediate-thickness specimen failed through joint deformation, while the thickest (0.375 in.) failed by fastener shear.
- From room temperature through 1200°F, joint-strength reductions with increasing temperature are mainly due to loss of fastener strength.
- Above 1200°F, the primary source of joint-strength reduction is the loss of strength in the beryllium.
- Beryllium increased in effective strength from room temperature to 500°F because of decreasing notch sensitivity.

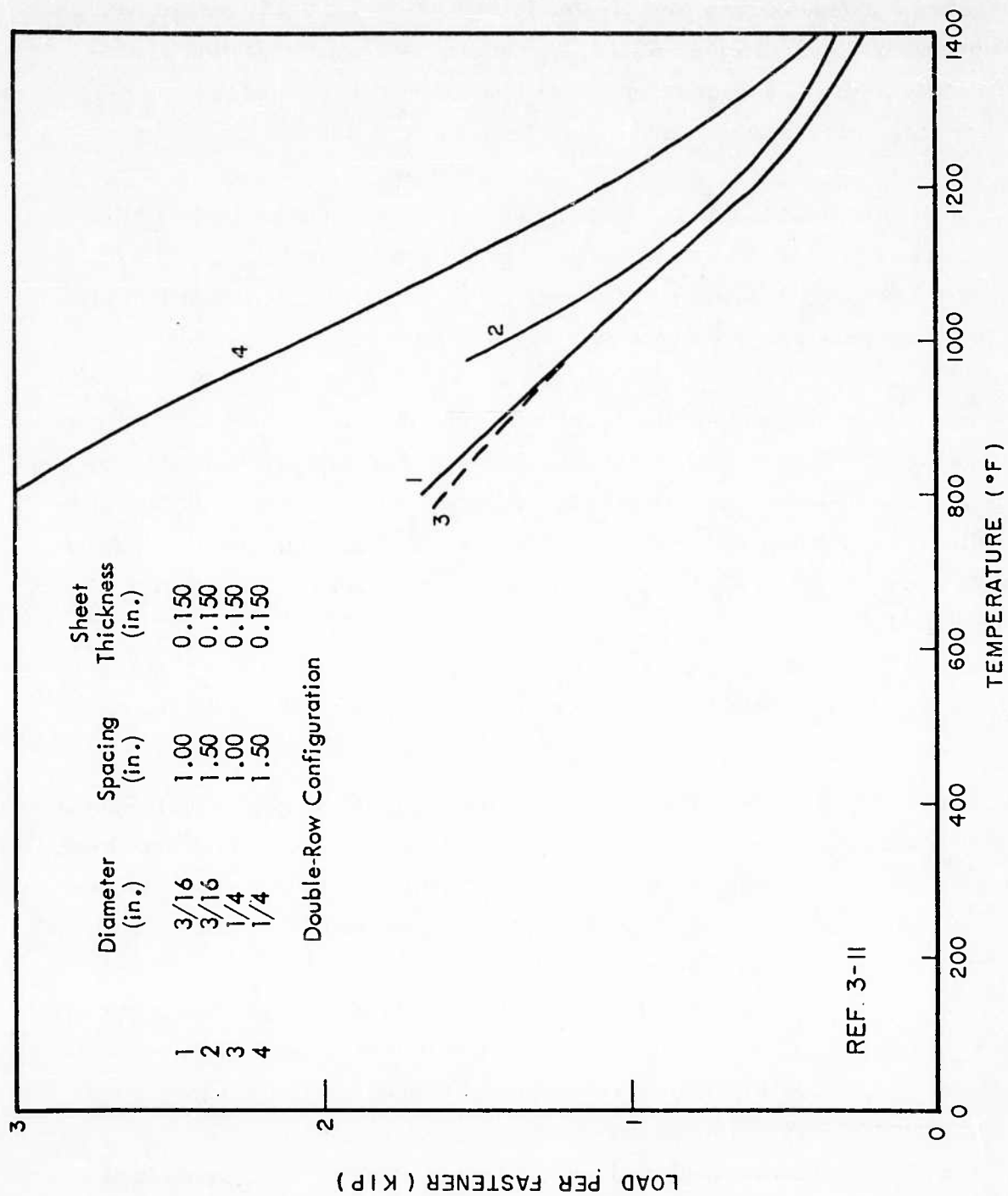


Fig. 3-36 Effect of Temperature on 0.150 Thick Hot-Pressed Beryllium Block Double-Row Butt Joints Fastened With NAS-517 Screws

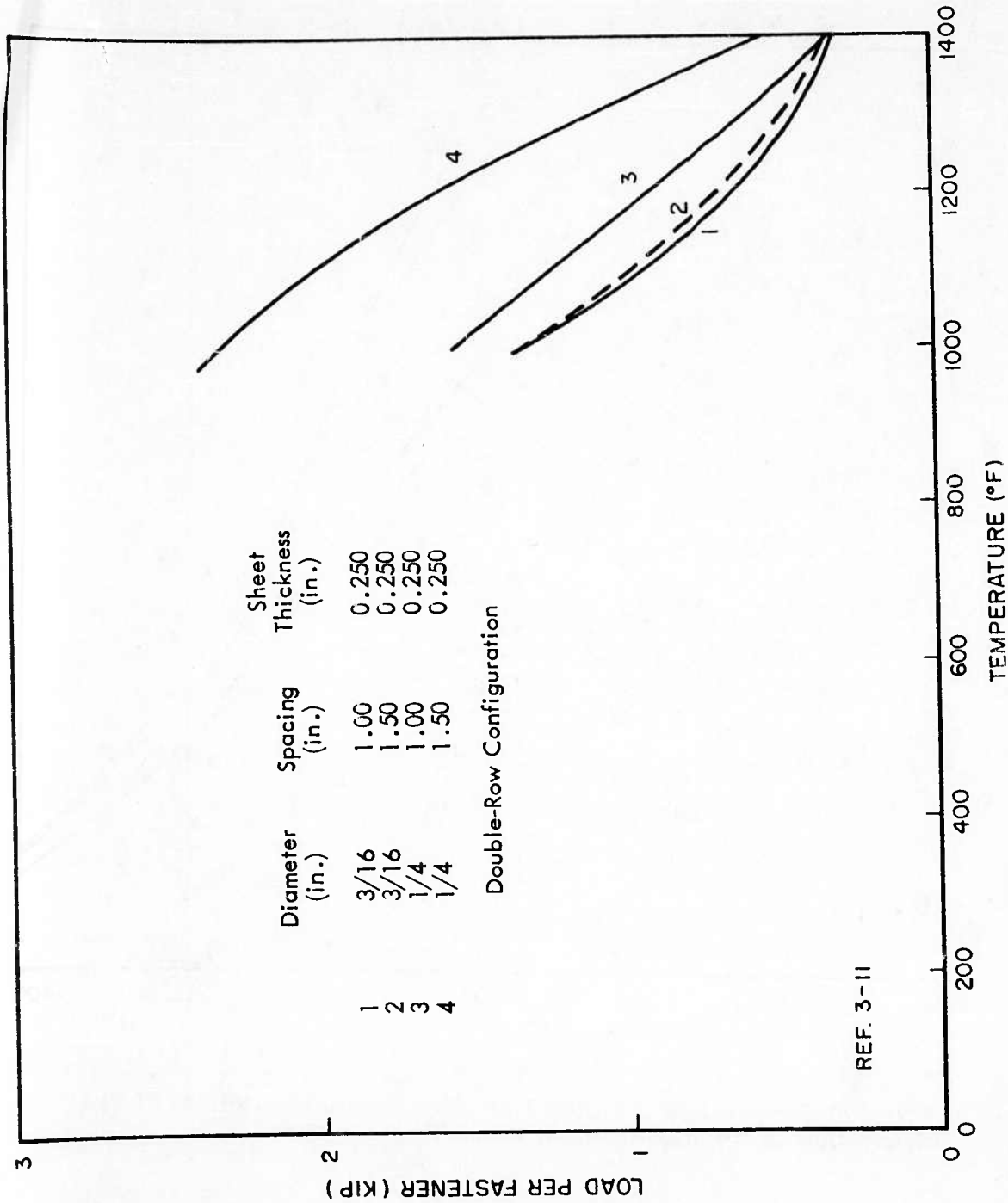


Fig. 3-37 Effect of Temperature on 0.250 Thick Hot-Pressed Beryllium Block Double-Row Butt Joints Fastened With NAS-517 Screws

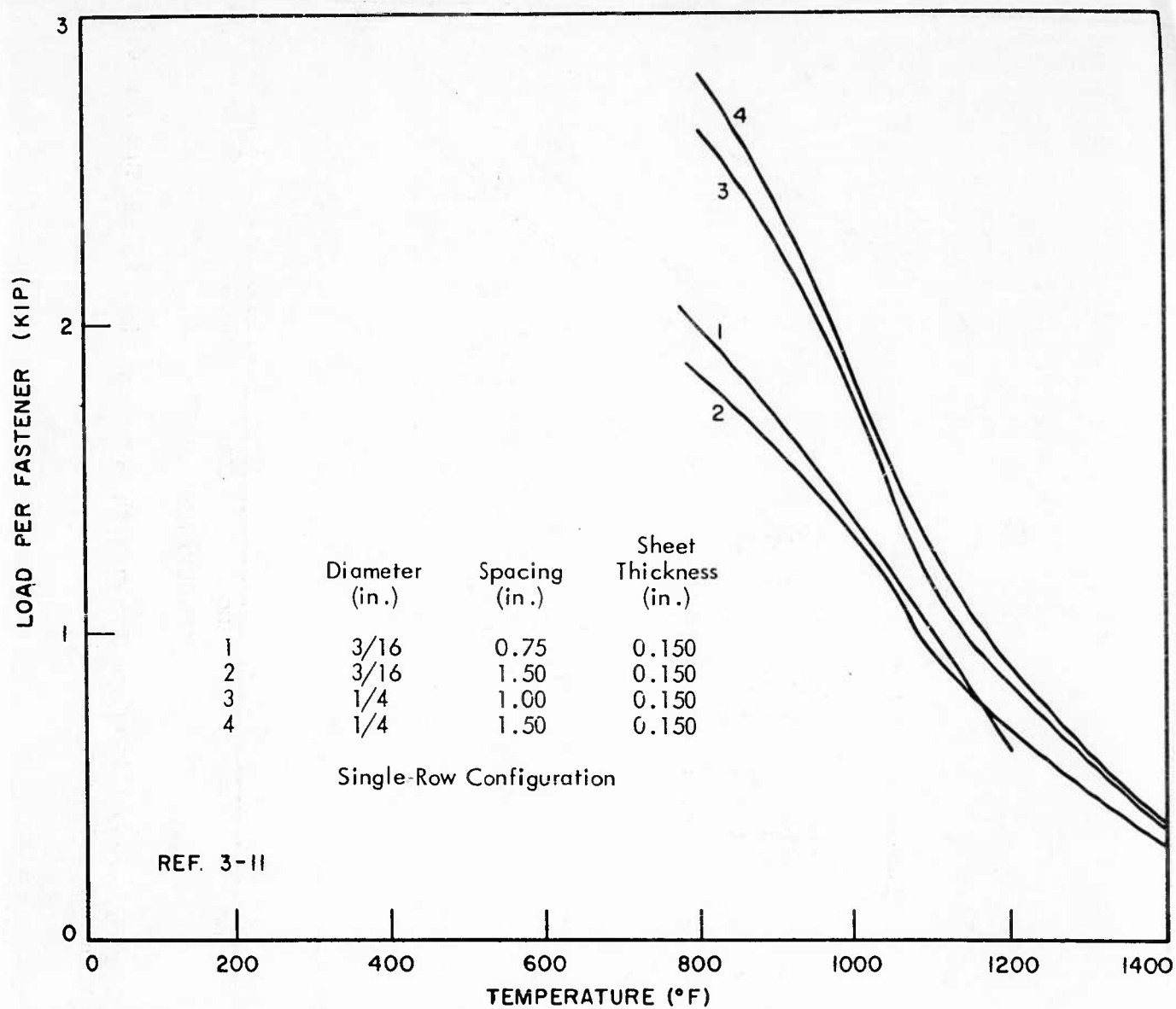


Fig. 3-38 Effect of Temperature on 0.150 Thick Hot-Pressed Beryllium Block Single-Row Butt Joints Fastened with NAS-517 Screws

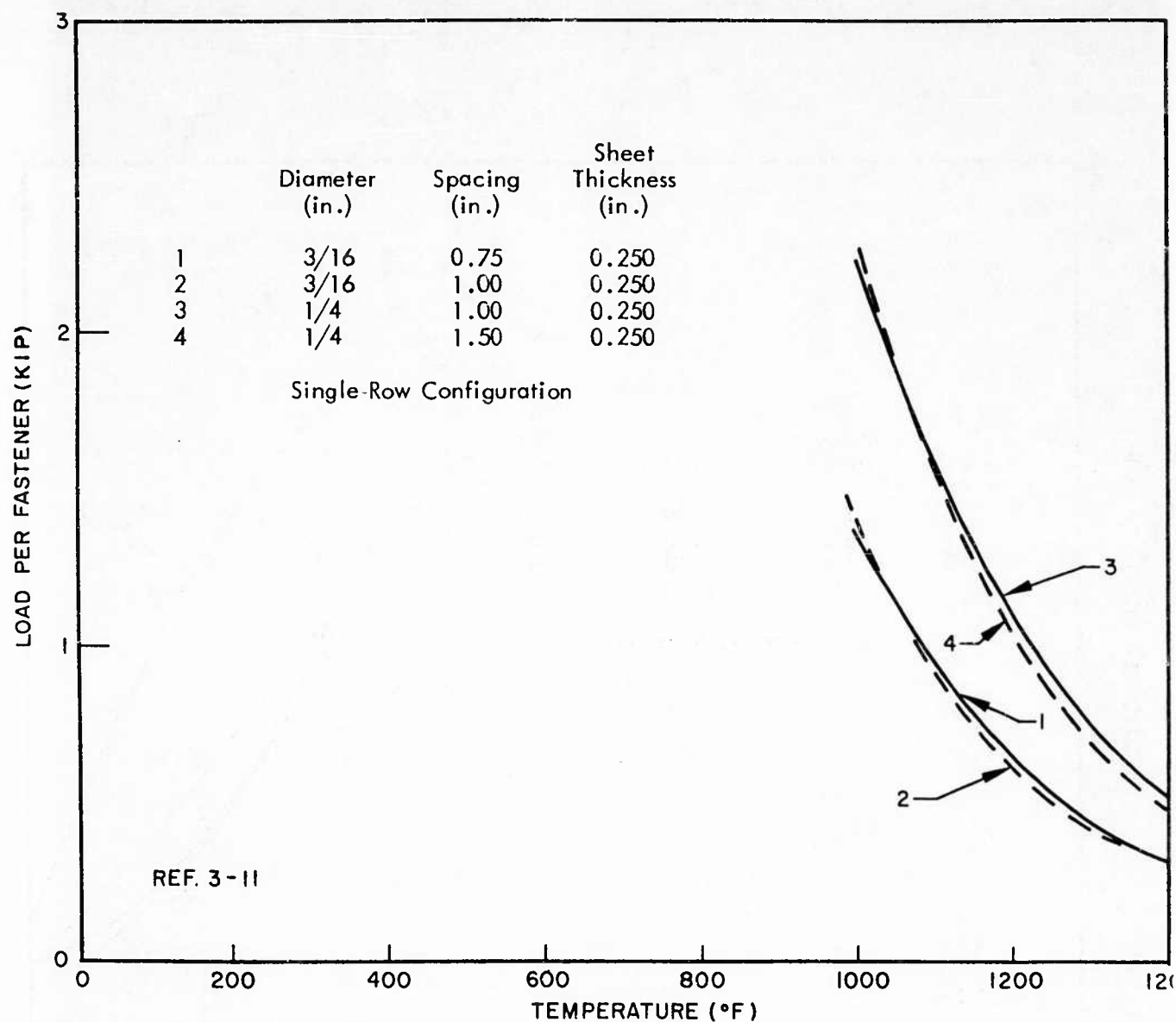


Fig. 3-39 Effect of Temperature on 0.250 Thick Hot-Pressed Beryllium Block Single-Row Butt Joints Fastened With NAS-517 Screws

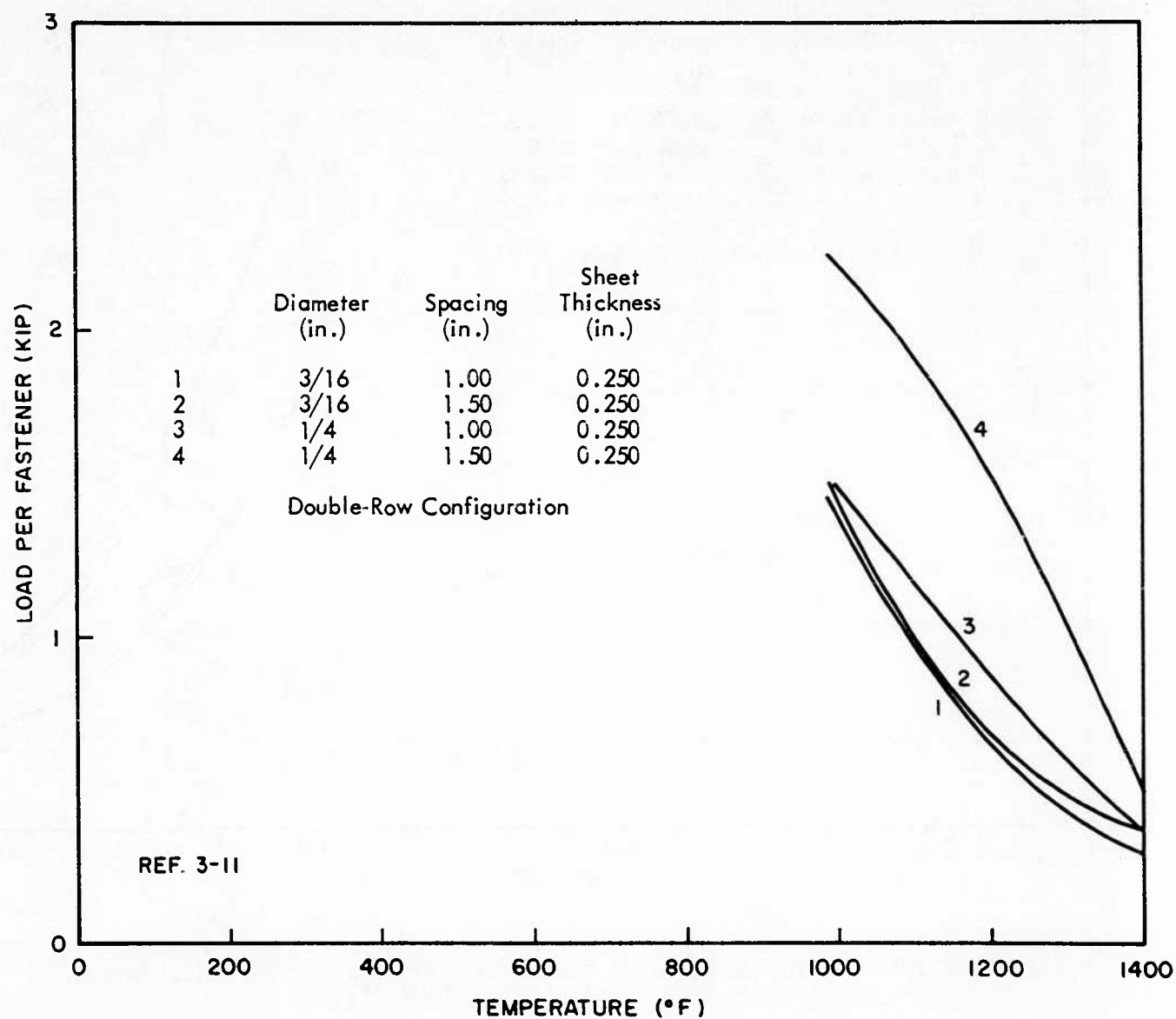


Fig. 3-40 Effect of Temperature on 0.250 Thick Hot-Pressed Beryllium Block Double-Row Butt Joints Fastened with SAL-100 Huckbolts

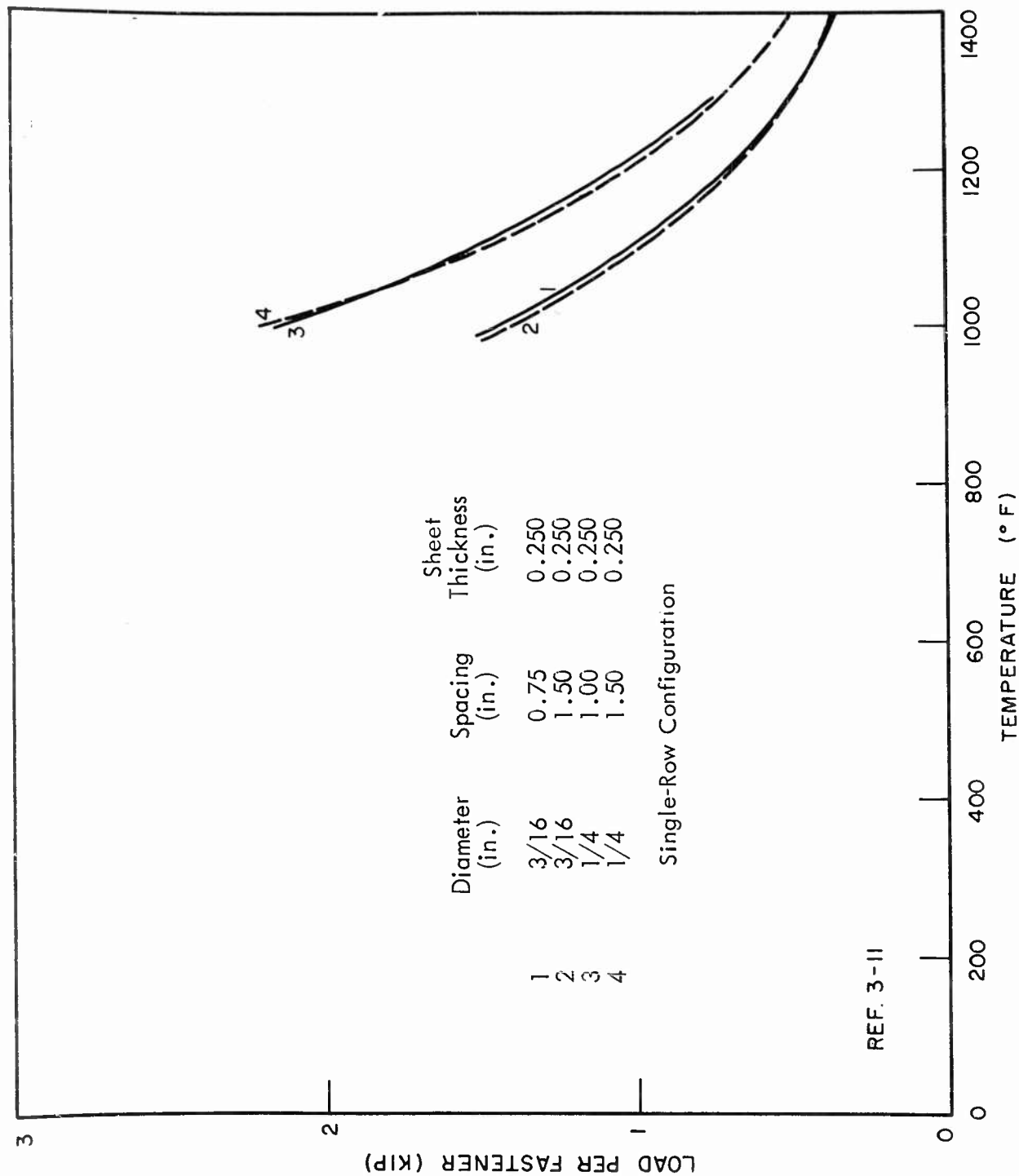


Fig. 3-41 Effect of Temperature on 0.250 Thick Hot-Pressed Beryllium Block Single-Row Butt Joints Fastened With SAL-100 Huckbolts

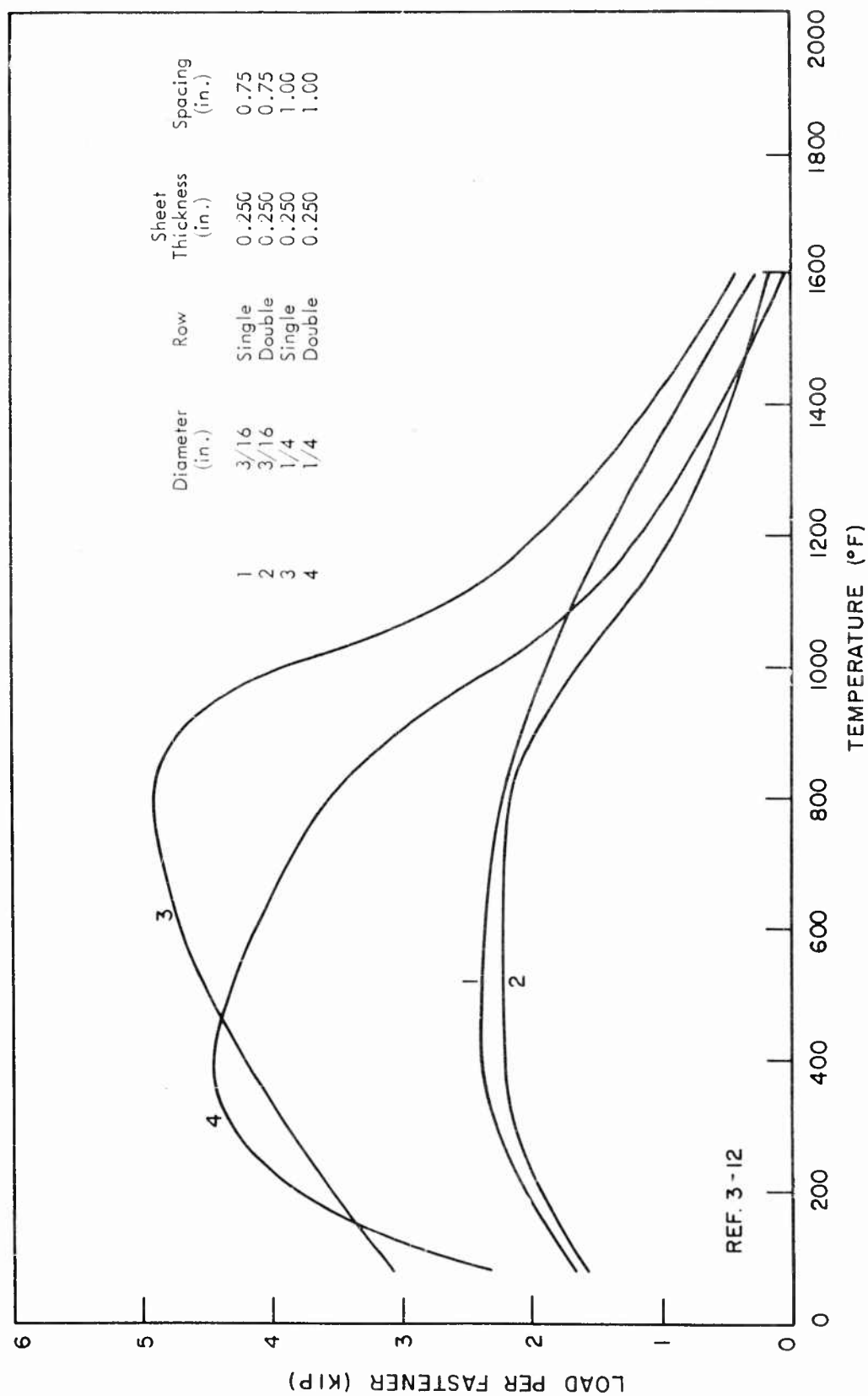


Fig. 3-42 Effect of Temperature on 0.250 Thick Cross-Rolled Beryllium Sheet Butt Joints Fastened With 100-deg Head, Hollowend A-286 Rivets

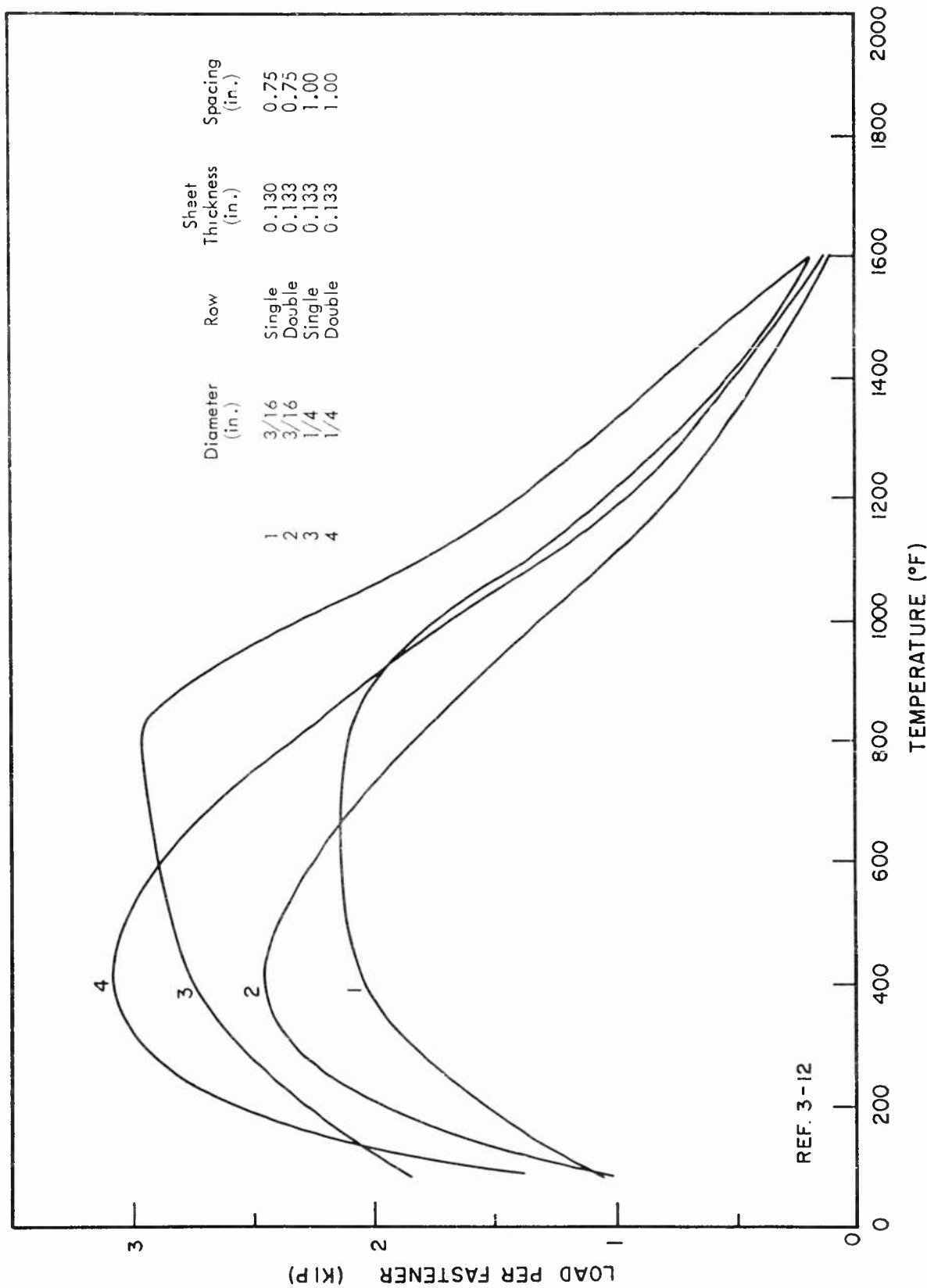
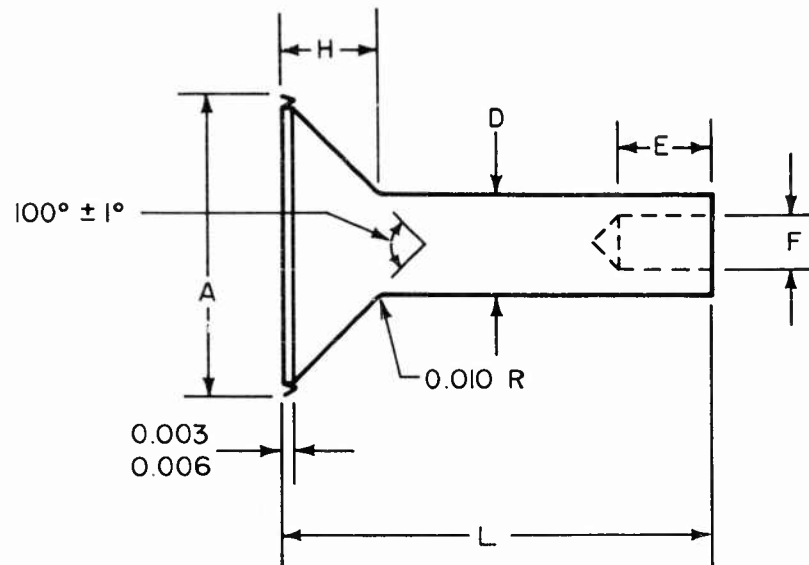


Fig. 3-43 Effect of Temperature on 0.133 Thick Cross-Rolled Beryllium Sheet Butt Joints Fastened With 100-deg Head, Hollowend A-286 Rivets



		D 0.003 .001	E	F	H	L 0.010	A 0.004
3/16-in.-diam. Rivets	for 1/8-in. plate	0.187	0.187	Drill	0.080	0.437	0.353
	for 1/4-in. plate	.187	.187	(3/32-in.)	.080	.687	.353
1/4-in.-diam. Rivets	for 1/8-in. plate	.250	.250	Drill	.106	.500	.476
	for 1/4-in. plate	.250	.250	(1/8-in.)	.106	.250	.476

Material = A-286 Bar Stainless Steel

INSTALLATION OF RIVETS IN JOINTS:

These rivets should be installed with standard-squeeze rivet machines, adjusted so that the upset rivet is as shown below:

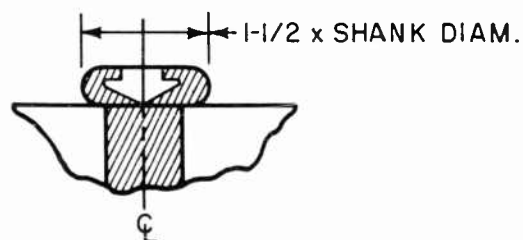


Fig. 3-44 Geometry of Hollowend Rivets

Reference 3-11 also reports on tests of 5-fastener, 2-row joints having three fasteners in the row nearest the specimen edge and two fasteners in a staggered pattern in the second row. These specimens had virtually the same strengths reported herein for the double-row (4-fastener) configuration. This may be explained by noting that the full advantage of both double-row configurations could not be realized because of the high incidence of tensile failures in the beryllium.

Examination of Figs. 3-42 and 3-43 on joints fabricated with A-286 rivets indicates that for these tests, cross-rolled sheet performs in a manner similar to hot-pressed block. The effective strength increases from room temperature to 400°-500° F because of decreasing notch sensitivity. Most specimens failed through tensile failure of the beryllium at room and elevated temperature. The exceptions were the 1/4-in. -diam., single-row rivets at 800° F (beryllium bearing failure), and 3/16-in. -diam., single- and double-row rivets at 400° and 800° F (some fastener shear).

Bolts or blind-type fasteners are preferred to rivets installed by bucking in beryllium because the impact load developed by the gun forces the rivet to fill the hole and the result is an impact tension load around the circumference of the hole. This is very unattractive in view of the low impact resistance of beryllium, and it would aggravate the stress concentration due to service loading. This is why the tests on the special A-286 rivet were performed, and indications are that upsetting of the hollow end is gentle enough to prevent damage to the sheet around the rivet hole.

The effect of a varying e/D ratio, in contrast to the constant e/D ratio of Figs. 3-24 through 3-43, has been investigated and reported on by LMSC for both cross-rolled beryllium sheet and hot-pressed beryllium block. Figure 3-45 presents the effect of varying e/D ratios on butt joints fabricated from 0.082-in. -gage, cross-rolled sheet. As expected, the load per fastener decreases as the edge distance decreases. All specimens, which were in the single-row, 2 fastener configuration, failed in net tension in the beryllium up to 600° F, and in joint deformation at 800° and 1000° F. At 1200° F, the specimens having e/D ratios of 2.0 and 2.5 failed in

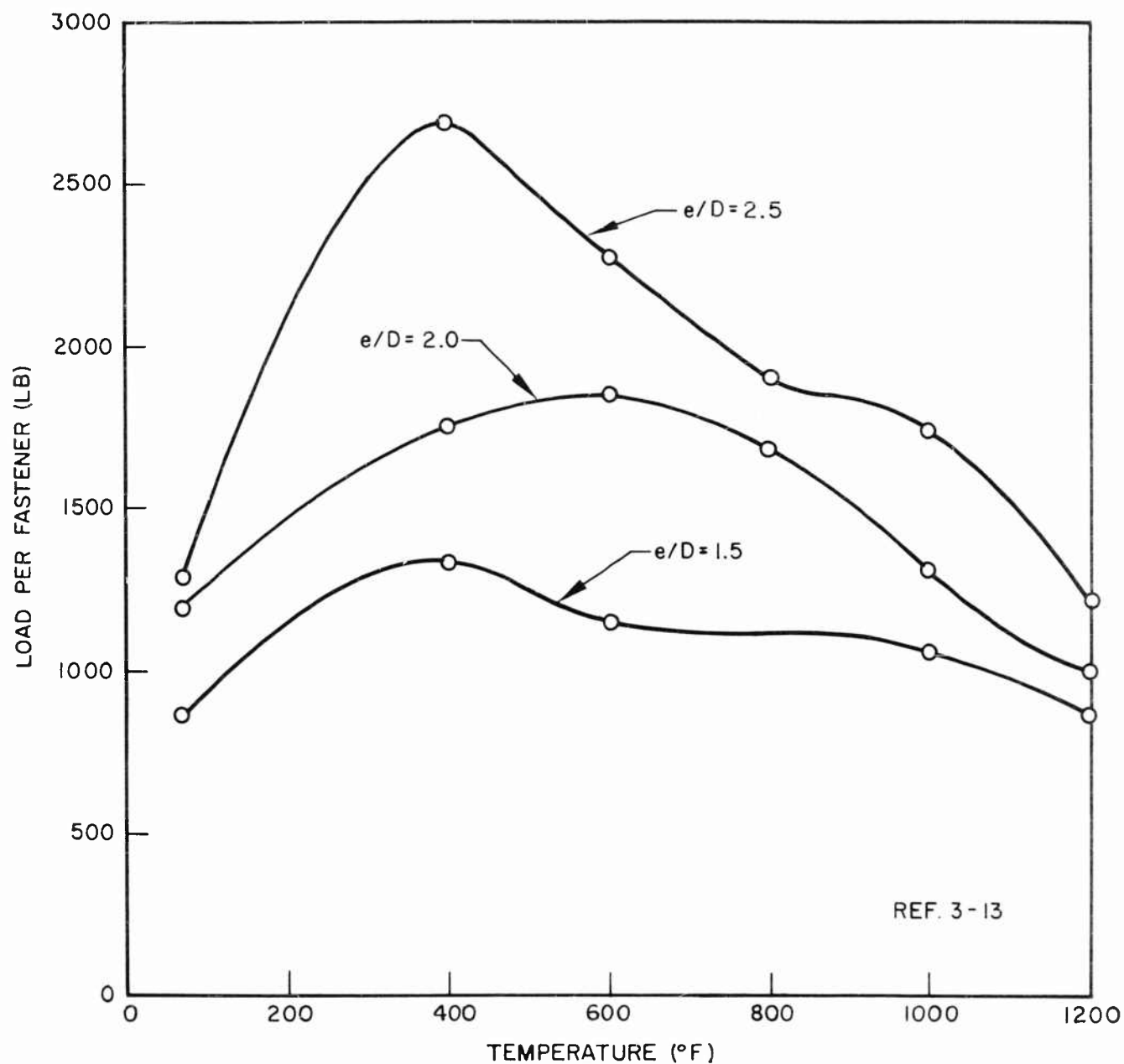


Fig. 3-45 Effect of Temperature and Edge Distance on 0.082-in., Cross-Rolled Beryllium Sheet Butt Joints Using 3/16-in., SAL-100 Huckbolts

fastener shear, while the e/D of 1.5 specimen failed by joint deformation. The fasteners used were 3/16-in.-diam., SAL-100 Huckbolts.

Figure 3-46 shows the effect of varying edge distance on 0.12-in., hot-pressed beryllium block butt joints using SAL-100 Huckbolts (1/4-in.-diam.) and a single-row, 2-fastener configuration. The unexpected favorable comparison for the smaller e/D ratio is believed to be caused by basing the e/D of 2.5 curve on tests conducted in 1957, and the e/D of 1.5 curve on recently conducted tests which take advantage of improvements in material quality over the past four years. All specimens having e/D of 2.5 failed in net tension. The specimens having e/D equal to 1.5 failed in the same modes as described for the e/D of 2.0 cross-rolled sheet specimens of Fig. 3-45.

In conclusion, it is suggested that adhesive bonding might prove to be a useful method of joining. It appears that this method of joining would eliminate the notch-sensitivity problem present when an attachment pattern is drilled in sheet. The lower temperature range where adhesives are most effective is also the area where normal mechanical joining methods are least effective.

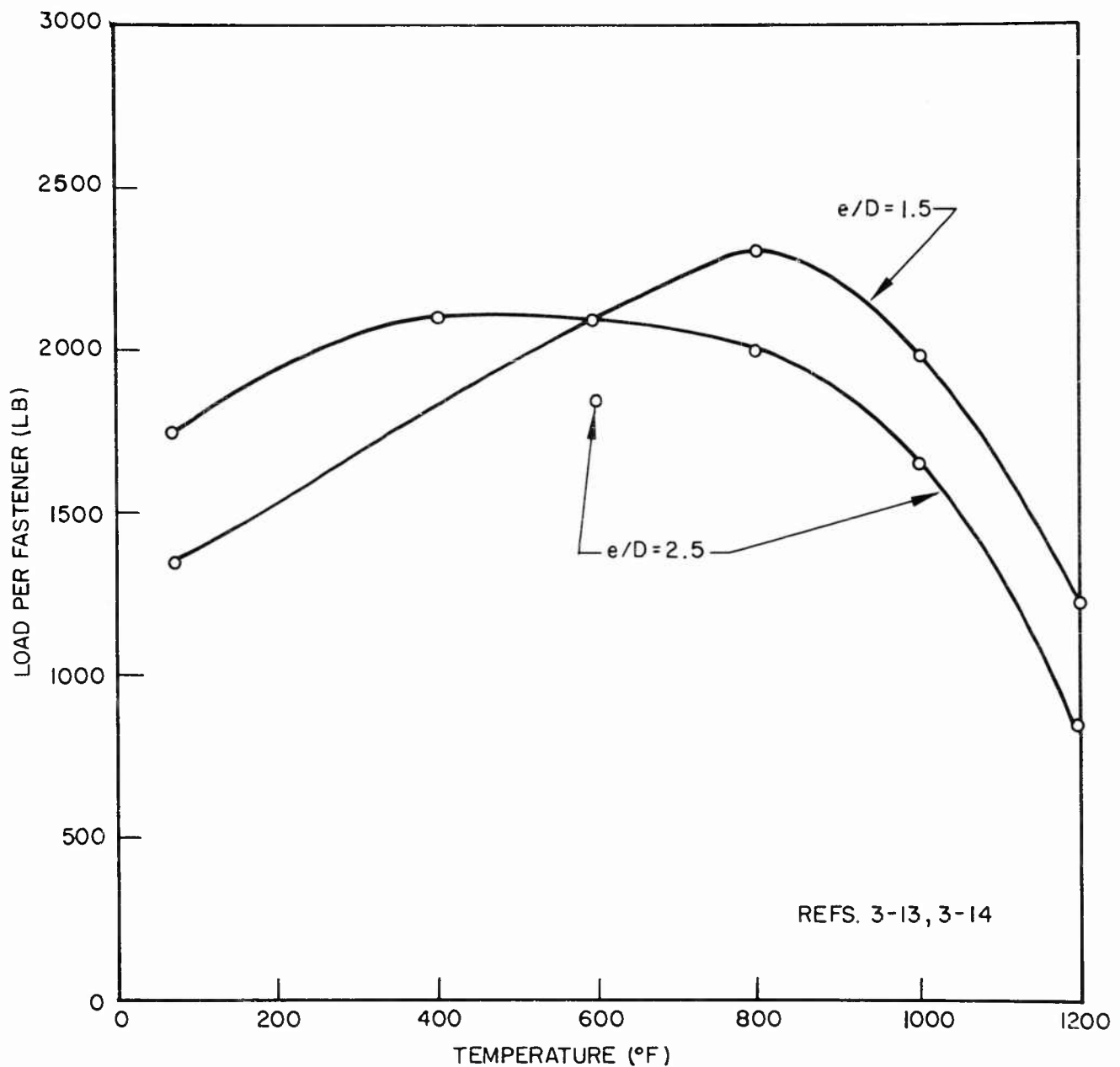


Fig. 3-46 Effect of Temperature and Edge Distance on 0.120-in., Hot-Pressed Beryllium Block Butt Joints Using 1/4-in., SAL-100 Huckbolts

3.6.3 Metallurgical Joining

Reviews of the current literature on the various methods of metallurgical joining of beryllium were made for this study. Some of these methods were found to be well established while others have progressed only to a definition of the problem areas. Fusion, pressure, resistance, and braze welding will be discussed, as well as brazing and soldering.

Fusion welding. Fusion welding of beryllium has not been satisfactory. Hot tearing, grain growth, and porosity have been problem areas for this type of welding. Avco (Ref. 3-15) has conducted a program emphasizing the variables affecting hot tearing as it occurs in hot-pressed block, and their conclusions include the following:

- Fusion welding should be considered for low-stress applications exceeding 1000°F and where pressure welding cannot be used.
- Argon shielding gas and a dry box are recommended to minimize oxidation.
- Susceptibility to hot tearing in beryllium fusion welds is directly proportional to the aluminum content in and above the range found in commercially pure beryllium, up to several-percent aluminum.
- Preheating is necessary, usually in the 800° to 1200°F range, depending upon welding current and arc travel speed. A higher level of preheat is required as current and arc travel are increased.
- High concentrations of impurities were found near the axial tears in the welds decreasing to a minimum 0.060 to 0.070 in. from the tears and increasing to another maximum near the edge of the fusion zone.

The Brush Beryllium Company is investigating fusion welding under ASD sponsorship at the present time.

Pressure welding. Pressure welding in a vacuum is a recommended joining method for all applications where proper jigging can be used. No filler metals are required

in this type of weld. This prevents the forming of brittle intermetallic compounds from the beryllium and the filler metal. The reduced joint efficiencies that normally occur at elevated temperatures when fillers of lower melting temperature are used are avoided. Optimum pressure welding gives 100-percent joint efficiencies with no degradation of the ductility or high-temperature properties of the parent metals.

Avco (Ref. 3-15) has performed an investigation of the effects of surface roughness, welding temperature, aluminum interlayers, and of base material on pressure-welded joints in hot-pressed block material. Some of the important results of this program are:

- Weld strengths increase with higher welding temperature, reach a maximum, and then decline due to grain growth.
- Weld strengths are much better when surfaces are smooth at the lower welding temperatures. Surface roughness does not seem to be significant above a welding temperature of 1920°F.

It should be noted that in the Avco experiments, pressure on the weld increased as the temperature was increased because of the differential thermal expansion of beryllium and the molybdenum jig. The specimens were held at temperature for one hour in a temperature range of 1470° to 2190°F. Pressures were not reported but probably were in the 5000-to 10,000-psi range.

Resistance welding. Some preliminary investigations of resistance welding have been made, but it is believed that this process has little promise because of notch sensitivity of beryllium and cracking of welds.

Braze welding. Braze welding probably is the most widely used method of welding beryllium at the present time. The oxidation problem occurring in the fusion-welding process is reduced because lower temperatures are required to melt the filler metals used in the brazing process. Silver, aluminum silicon, and silver-copper are among the more common braze alloys used. Consumable electrode and inert-gas-shielded

tungsten arc are both used in braze welding. Preplacement of the filler alloy is desirable and minimizes wettability problems.

Avco (Ref. 3-15) has investigated aluminum-12w/o silicon and silver filler metals. The alloys were preplaced between two hot-pressed block plates and butt welded with an inert gas-shielded AC tungsten arc. Some of the conclusions reached include:

- Aluminum -12w/o silicon filler metal is satisfactory for room temperature joints. Transverse joint strengths of 20 to 25 ksi were attained.
- Joint strengths with aluminum-silicon filler were independent of the filler strip thickness used in the range of 1/64 to 3/32 in.
- Purified argon shielding gave cleaner welds than either purified helium or an argon-helium mixture.
- Silver braze welds were not as strong as aluminum-silicon braze welds at room temperature, but are recommended for elevated-temperature applications. Heat treatment below 1400°F is recommended for joints to be used at elevated temperatures to stabilize the silver braze welds.

Brazing and soldering. Brazing is the metallurgical joining method most frequently used at the present time. Other methods previously discussed are being used or investigated, but brazing can give reliable results with a minimum of the porosity, brittleness, and notch buildup that occurs in varying degrees in the various weld processes. Soft solder is effective when a press-fit joint is used.

Keil, Hanks, and Taub of Los Alamos Scientific Laboratory (Ref. 3-16) have made quite an extensive investigation of furnace brazing, induction brazing, and soldering beryllium hot-pressed block to itself. These joints were tested at room temperature. Since beryllium and oxygen have an affinity for each other at elevated temperature, it is necessary to acid-clean or mechanically clean the surfaces prior to brazing, and to perform the brazing operation in an inert atmosphere or a vacuum. A number of furnace brazing materials were tested in flat lap-joints. The most promising were silver; 45 Ag, 15 Cu, 16 Zn, 24 Cd; and 70w/o Ag-30w/o Al. Strong leakproof

joints made by induction brazing with a helium atmosphere and titanium flux are also reported. Promising induction-brazing alloys include: (1) 72 Ag-28 Cu alloy on silver-plated or mechanically cleaned beryllium; (2) 70.1 Ag-27.4 Cu-2.5 Zr alloy on acid-etched or silver-plated beryllium; and (3) pure silver on mechanically cleaned or acid-etched beryllium. In addition, magnesium on a magnesium-coated surface without flux showed good strength. Among the soft solders reported, a Pb-Sn-Zn solder on silver-flame-sprayed beryllium developed the most strength. In the tests reported for the above-mentioned brazed joints, the induction-brazed specimens were the stronger.

The induction-brazing investigation of J. B. Cohen of Avco Corporation is reported in Ref. 3-17. The prime purpose of this work was to develop beryllium-base brazing alloys to produce brazed joints between beryllium pieces with strengths approaching the strength of the base metal above 1300°F. Silver and Be-20 A/O Ag alloy were used as induction-brazing materials for beryllium butt joints. Both brazing materials developed joint strengths of 60 percent of the base metal at room temperature. In the temperature range of 700° to 1450°F, joint strengths were 80 percent of the base metal. A feature of all the specimens was the ductile region around the joint. Silver is one of the few metals having a ductile intergranular relationship with beryllium. Other important points revealed in this investigation are:

- Recrystallization begins after two minutes at 1832°F. This puts a limit on brazing temperatures, because recrystallization has a deleterious effect on the properties of beryllium.
- Silver does not wet beryllium well, as previously reported.
- Silver did not wet beryllium in vacuum (1 to 10 μ).

LMSC has investigated various facets of beryllium furnace brazing and has acquired some interesting data. Reference 3-18 presents a study of the effect of varying temperature and soaking time between 1775° to 1875°F and 0 to 4 min on silver brazing of beryllium to beryllium. While the results are not always consistent, it appeared that

the greater shear strengths occurred with higher temperatures and soak times of 2 to 4 min. Shear strengths were all in excess of 10,000 psi and in many cases reached 20,000 psi. Reference 3-19 discusses a group of beryllium-to-beryllium and beryllium-to-AISI type 430 stainless-steel braze tests. At room temperature, 72 Ag-27.5 Cu-0.5 Li is the superior brazing alloy for the beryllium-to-beryllium brazes. For strength at temperatures of 800°, 1200°, and 1500°F, pure silver or the 99.8Ag-0.2Li alloy is superior. These two alloys have shown shear strengths of 20,000 psi at room temperature and 1,500 psi at 1500°F.

Solar Aircraft Company has fabricated sandwich specimens for the experimental portion of this program (see Appendix C for testing details). The brazing alloy investigated for use on these specimens was 94.8 Ag-5Al-0.2 Mn. The furnace brazing cycle selected was 0.5 min at 1675°F. During the alloy qualification tests, this alloy developed a tensile ultimate stress of 22,730 psi at room temperature. However, braze contamination due to out-gassing of the larger beryllium pieces led to the use of 50 Ag-15.5 Cu-15.5 Zn-16.0 Cd-3.0 Ni for the sandwich fabrication. This alloy has shown somewhat lower strength but is reported by Solar to flow well enough at a peak temperature of 1500°F in an argon atmosphere to permit a very rapid brazing cycle when a proprietary flow promoter is used.

The out-gassing problem was thus overcome by using a brazing alloy and flow promoter which allowed such a short braze cycle time that serious contamination did not have time to occur. The soundness of the joints so produced is demonstrated by the photomicrographs of the joints appearing in Figs. 3-47 and 3-48. Figure 3-47 is a beryllium sheet to beryllium sheet joint in a truss-core sandwich. Figure 3-48 is a beryllium sheet to titanium sheet joint in a beryllium facing sheet - titanium honeycomb core sandwich.

Summarizing, beryllium can be brazed to beryllium or to other metals such as nickel, stainless steel, and copper. The proper choice of the brazing alloy depends upon the application of the component and the metals to be joined. Silver, aluminum,

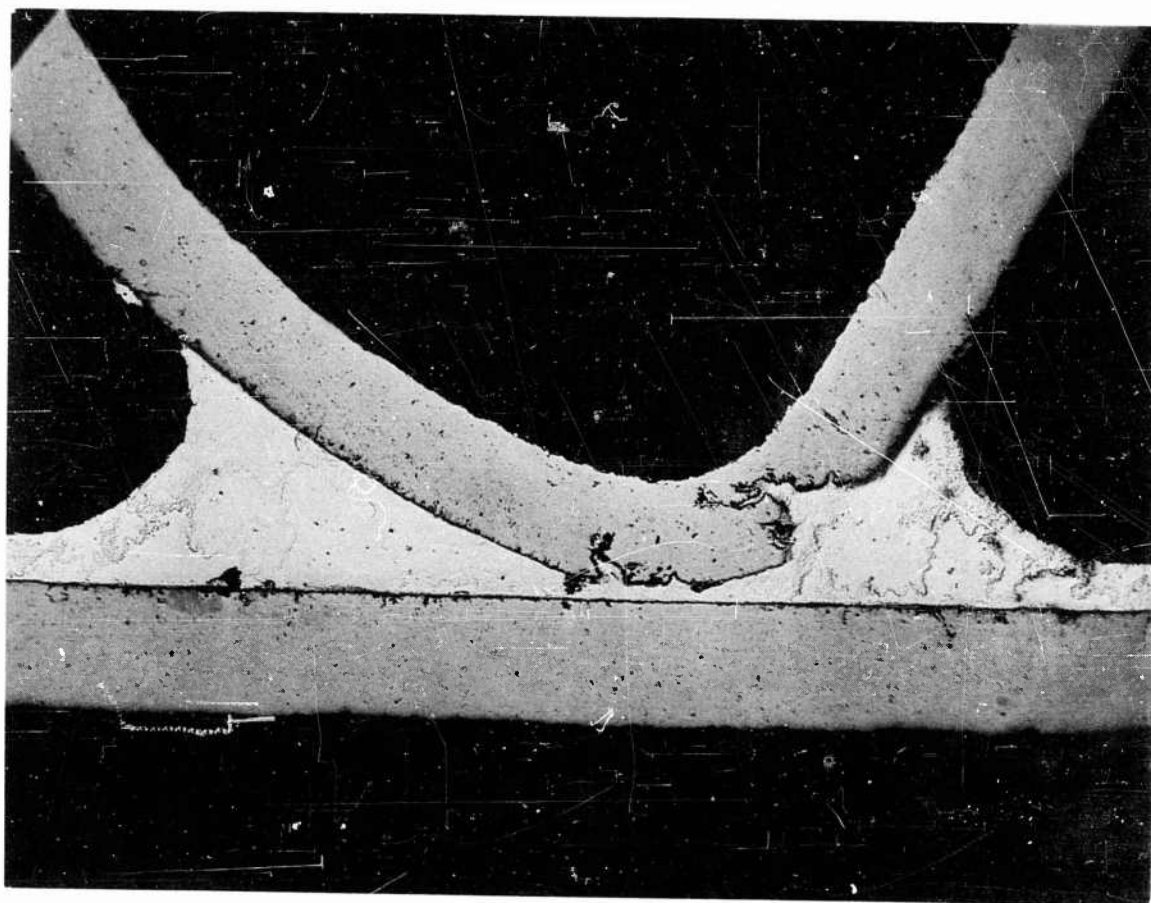


Fig. 3-47a Beryllium Cross-Rolled Sheet to Beryllium Cross-Rolled Sheet Joint in a Truss-Core Sandwich Furnace-Brazed Specimen, Using 50 Ag-15.5 Cu-15.5 Zn-16.0 Cd-3.0 Ni Brazing Alloy. Magnified 60X, Unetched

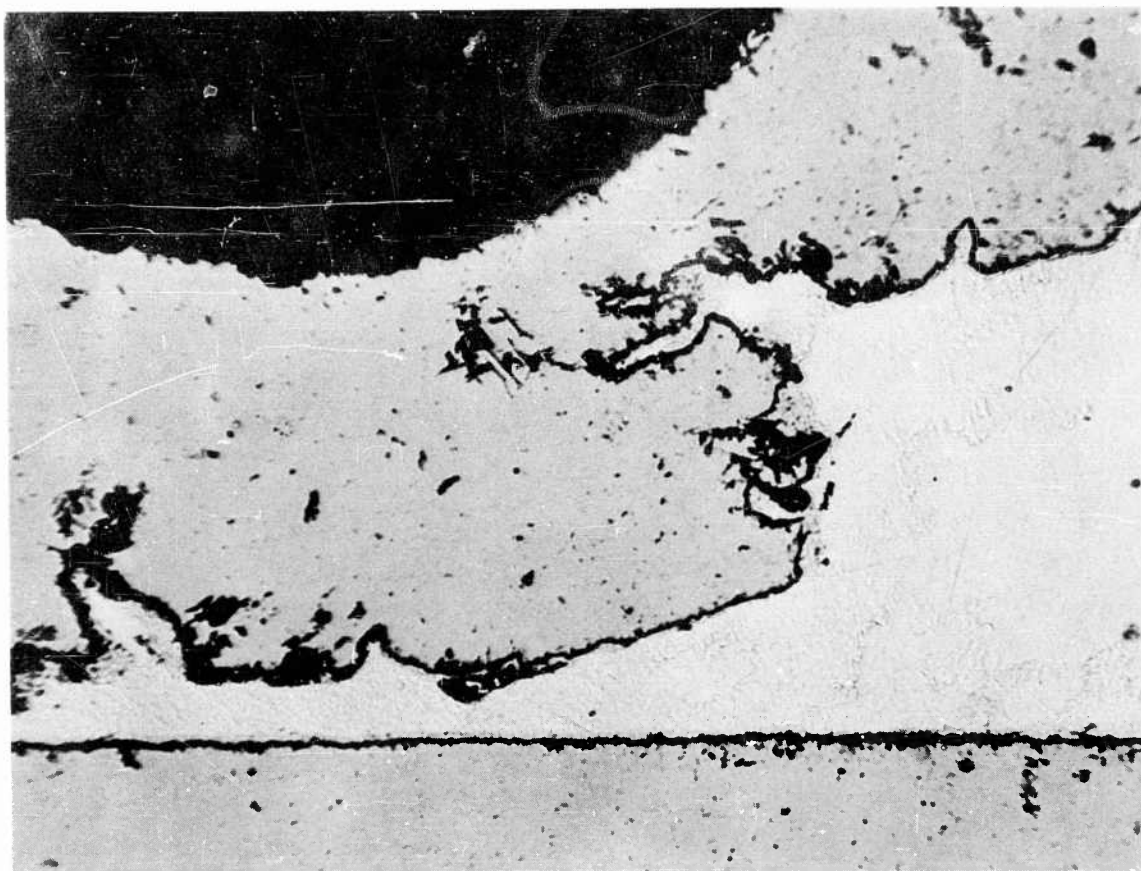


Fig. 3-47b Beryllium Cross-Rolled Sheet to Beryllium Cross-Rolled Sheet Joint in a Truss-Core Sandwich Furnace-Brazed Specimen, Using 50 Ag-15.5 Cu-15.5 Zn-16.0 Cd-3.0 Ni Brazing Alloy. Magnified 240X, Unetched

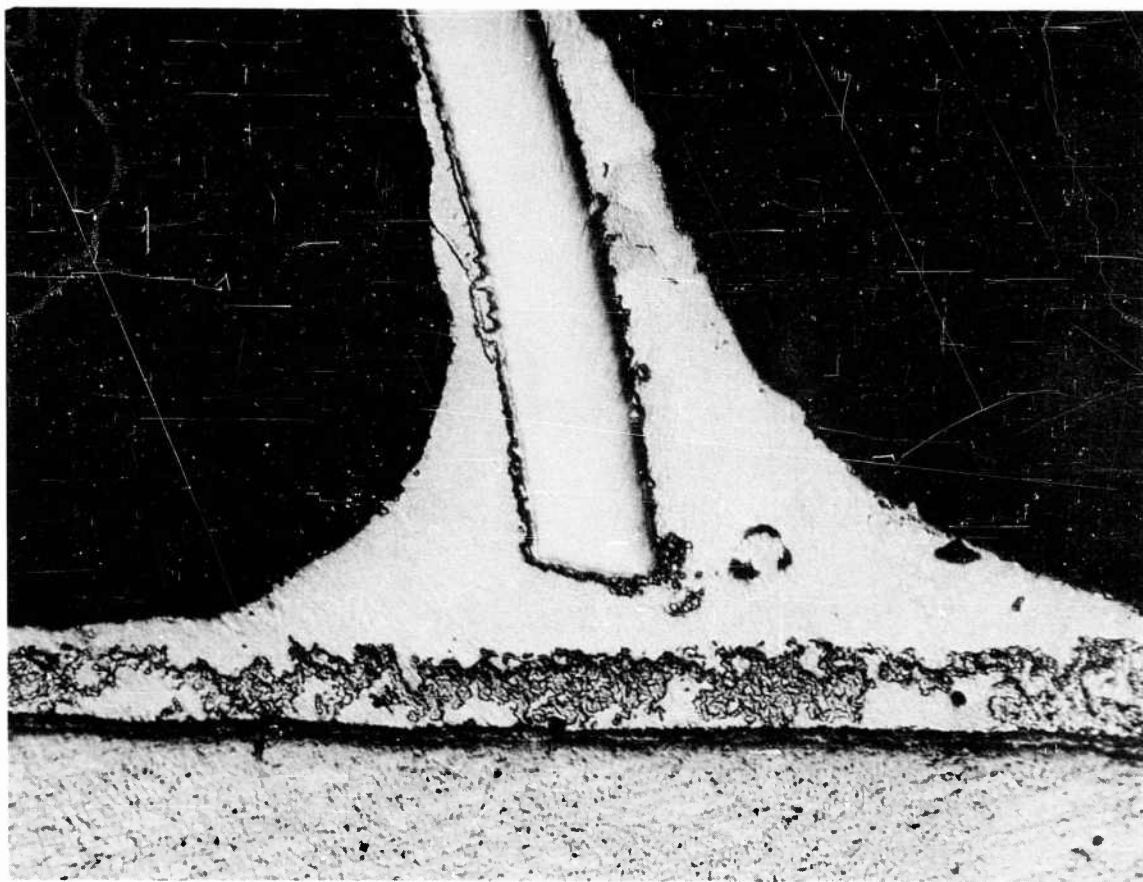


Fig. 3-48a Beryllium Cross-Rolled Sheet to Titanium Core Joint in a Truss-Core Sandwich Furnace-Brazed Specimen, Using 50 Ag-15.5 Cu-15.5 Zn-16.0 Cd-3.0 Ni Brazing Alloy. Magnified 125X, Unetched



Fig. 3-48b Beryllium Cross-Rolled Sheet to Titanium Core Joint in a Truss-Core Sandwich Furnace-Brazed Specimen, Using 50 Ag-15.5 Cu-15.5 Zn-16.0 Cd-3.0 Ni Brazing Alloy. Magnified 500X, Unetched. This joint is adjacent to the joint shown in Fig. 3-48a

silver-copper, and aluminum-silver alloys have been used at room temperature. For elevated-temperature applications, silver seems to be superior. Preplacing the braze material and/or addition of 0.2-percent lithium is preferred practice because of low wettability of beryllium. The oxidation problem is met by brazing in an inert atmosphere or a vacuum. When beryllium is being brazed to another material, it is very important to hold the assembly at the braze temperature for as short a time as possible to avoid the development of intermetallic brittleness that occurs between beryllium and nearly every other metal except silver.

3.7 APPLICATION OF BERYLLIUM IN FAIL-SAFE DESIGN AND IN FITTINGS

3.7.1 Fail-Safe Policy

The concept of fail-safe design in the aircraft industry is an important consideration in civil as well as military aircraft design. Briefly stated, fail-safe design requires that a damaged structure be capable of sustaining a reasonable portion of the design load without complete collapse. This may be accomplished by several methods, usually in combination, as follows:

- Knowledge of crack-propagation properties of the material
- Provision for multiple load-paths for primary loads
- Improved detail design

In general, if a material exhibits a high crack-propagation rate, more attention must be given to multiple load-paths and detail design. High crack-propagation rates are generally found in materials which are notch sensitive.

Beryllium is known to be notch sensitive at room temperature (subsection 2.4), and therefore this material is expected to have a high room-temperature crack-propagation rate although substantiating tests as yet have not been reported in the literature. Until such time as crack-propagation rates for beryllium are experimentally established, it is suggested that the material at room temperature be considered susceptible to high crack-propagation rates and designed accordingly.

3.7.2 Tension-Type Fittings

At present, the use of beryllium in tension-type fittings does not appear economically feasible. Such fittings are generally finish-machined from castings or forgings. In the case of beryllium, these processes as yet have not yielded production quality parts. Therefore, fittings must be machined from hot-pressed block. The expense of parts fabricated in this manner appears to outweigh the advantages of beryllium in most of

these applications. Although tests of tension-type fittings fabricated from hot-pressed block are not reported in the literature, it appears that standard methods of stress analysis are applicable, using the mechanical property data presented in Section 2 of this report.

3.8 REFERENCES

- 3-1 National Advisory Committee for Aeronautics, Description of Stress-Strain Curves by Three Parameters, by Walter Ramberg and William R. Osgood, TN-902, Washington, D. C. , Jul 1943
- 3-2 F. P. Cozzone and M. A. Melcon, "Non-Dimensional Buckling Curves - Their Development and Application," J. Aeronaut. Sci. , Oct 1946, pp. 511-517
- 3-3 National Advisory Committee for Aeronautics, Handbook of Structural Stability, Part I, Buckling of Flat Plates, by George Gerard and Herbert Becker, TN-3781, Washington, D. C. , Jul 1957
- 3-4 National Advisory Committee for Aeronautics, Analysis of Behavior of Simply Supported Flat Plates Compressed Beyond the Buckling Load Into the Plastic Range, by J. Mayers and Bernard Budiansky, TN-3368, Washington, D. C. , Feb 1955
- 3-5 National Advisory Committee for Aeronautics, A Summary of Diagonal Tension, Part I, Methods of Analysis, by Paul Kuhn, James R. Peterson, and L. Ross Levin, TN-2661, Washington, D. C. , May 1952
- 3-6 Chance Vought Corporation, Summary of Shear Panel Design Procedures, by A. Bruce Burns and E. L. Terry, Structures Development Memo 119, Dallas, Tex. , Nov 1959
- 3-7 National Advisory Committee for Aeronautics, Handbook of Structural Stability, Part III, Buckling of Curved Plates and Shells, by George Gerard and Herbert Becker, TN-3783, Washington, D. C. , Aug 1957
- 3-8 Lockheed Missiles and Space Company, Structural Shell Optimization Studies, Vol. I, Survey of Buckling Data for Monocoque Circular Cylindrical Shells Subjected to Uniform External Pressure, by E. V. Pittner, LMSD Tech. Rpt. 3-42-61-2, Sunnyvale, Calif. , 30 Jun 1961

- 3-9 National Advisory Committee for Aeronautics, Correlation of Crippling Strength of Plate Structures With Material Properties, by Roger A. Anderson and Melvin S. Anderson, TN-3600, Washington, D. C., Jan 1956
- 3-10 F. P. Cozzone, "Bending Strength in the Plastic Range," J. Aeronaut. Sci., Vol. 10, No. 5, May 1943, p. 137
- 3-11 Lockheed Missiles and Space Division, Allowable Loads at Temperature for Flush-Type Fasteners in Beryllium Butt Joints, by R. D. Currier, LMSD-502600, Sunnyvale, Calif., 15 Apr 1960
- 3-12 Norair Division of Northrop Corporation, Tensile Tests of Single Splice Plate Butt Joint Beryllium - Stainless Steel Specimens From Room Temperature Through 2000°F, by W. R. Roser, NOR-61-67, Hawthorne, Calif., 28 Mar 1961 (work performed for Lockheed Missiles and Space Company)
- 3-13 Lockheed Missiles and Space Company, Structural Shell Optimization Studies, Vol. II: Optimization of Stiffened Cylindrical Shells Subjected to Uniform External Hydrostatic Pressure, by E. H. Nickell and R. F. Crawford, LMSD Tech. Rpt. 3-42-61-2, Sunnyvale, Calif., 30 Jun 1961
- 3-14 Lockheed Missiles and Space Division, Brush QMV Beryllium/321 Stainless Steel Butt Joints: Strength Characteristics With Double Fasteners at Room and Elevated Temperatures, by Jay F. Burcham, LMSD-2665, Sunnyvale, Calif., 10 Jan 1958
- 3-15 Avco Corporation, Research and Advanced Development Division, Beryllium Joining WADC Sponsored Program, by E. M. Passmore, WADC TR 59-695, Part II, 18 Feb 1960
- 3-16 R. W. Keil, G. S. Hanks, and J. M. Taub, "Brazing and Soldering of Beryllium," Welding J., Welding Res. Suppl., Sep 1960, pp. 406.S-410.S
- 3-17 Avco Corporation, Research and Advanced Development Division, Beryllium Joining RAD Sponsored Program, by J. B. Cohen, WADC TR 59-695, Part I, Apr 1960

- 3-18 Lockheed Missiles and Space Division, Beryllium to Beryllium Brazing, by R. F. Karlak, LMSD Flash Rpt. 1431, Sunnyvale, Calif., 17 Jun 1959 (C)
- 3-19 Lockheed Missiles and Space Division, Pyromet Brazed Beryllium, by R. F. Karlak, LMSD Flash Rpt. 5335-008, Sunnyvale, Calif., 14 Dec 1959
- 3-20 Lockheed Missiles and Space Division, Stress and Stability Analysis of Cylindrical and Conical Shells, Vol. II: A Method of Analysis for Buckling of Monocoque Conical Shells Subjected to Hydrostatic Pressure, by E. V. Pittner and F. G. Morton, Sunnyvale, Calif., 31 May 1961

Section 4

MINIMUM-WEIGHT DESIGN AND COMPARATIVE EFFICIENCY

The current interest in beryllium as a structural material in preference to other more common structural materials, stems mainly from anticipated weight savings in certain military applications. The weight that is saved results in increased performance and, in some instances, in the attainment of technical objectives which otherwise might not be reached as quickly or as easily. In this section, the principles of minimum-weight analysis will be used to determine the most efficient type of construction to carry an applied loading. These principles are discussed in general terms in subsection 4.1. In subsection 4.2, these principles are applied to a number of combinations of structural component, loading, and detailed configuration in order to lay the appropriate groundwork for the minimum-weight design charts for beryllium cross-rolled sheet (subsection 4.3).

Finally, the most efficient constructions determined for particular types of loading are used as a basis for comparing beryllium and other structural materials (subsection 4.4). These comparisons, which are both quantitative and qualitative, show the minimum possible weight to carry the applied load, as well as the optimum material.

4.1 INTRODUCTION TO MINIMUM-WEIGHT ANALYSIS

A minimum-weight analysis indicates:

- The most efficient type of construction
- The detailed geometry within the most efficient type of construction which will carry the applied load
- The material which performs satisfactorily for the lightest possible weight

The method of minimum-weight analysis used to achieve these results is essentially that used by Zahorski (Ref. 4-1), Shanley (Ref. 4-2), Crawford, Burns, and Tilcens (Ref. 4-3), and others, wherein minimum weight results when the structure is so proportioned that the lowest modes of failure have equal critical stresses. To reasonably simplify the analyses, the assumption is made that post-buckling strength cannot be developed in any of the modes of failure considered. Consequently, the modes of failure will be referred to as modes of instability, and those considered are (1) general instability and (2) local instability. General instability is defined as that mode of instability in composite structures (skin plus stiffening elements) wherein instability is characterized by deflection of all elements of the composite structure during buckling. Local instability is defined as that mode of instability in a composite structure which is characterized by the appearance of nodal lines (1) in the skin along (or nearly along) the stiffener-skin juncture when viewed either*parallel or transverse to the load; and/or (2) in the stiffening elements when viewed parallel to the load.

In addition to this assumption, the following restrictions are also imposed:

- A single type of load is applied
- No geometric discontinuities such as holes may be present
- No coupling exists between the general and local instability modes

Applicable equations for general and local instability are presented in each of the parts of subsection 4.2. When these equations are combined according to the methods of minimum-weight analysis, the following general form of an "efficiency" equation may be obtained:

$$\text{Loading - Material Index} = \text{Efficiency Factor} \times [\text{Weight Index}]^n \quad (4.1)$$

The loading-material index usually consists of the loading intensity divided by a specified dimension of the structure and the effective Young's modulus of the structural material, which is the product of the effective plasticity reduction factor and Young's modulus,

denoted $\bar{\eta}E$. The efficiency factor is denoted by the symbol \mathcal{E} . The weight index is always the quotient of a quantity \bar{t} divided by the same dimension of the structure previously specified in the loading-material index, where \bar{t} is the weight-equivalent flat-plate thickness of the stiffened structure. Minimum-weight designs occur when \mathcal{E} , which is a function of the geometric length and/or thickness ratios of the structure, is a maximum. This implies that these ratios are constant for minimum-weight design. It will be seen that this is true; however, the ratios of thickness to length are functions of the loading intensity and vary accordingly. While minimum weight may be expressed mathematically in the form of Eq. (4.1) using the maximum value of \mathcal{E} , a chart showing the relationship between \mathcal{E} and the related length and/or thickness ratios for both minimum and nonminimum weight designs is usually given.

The general form of the efficiency equation [Eq. (4.1)] presented in this section is not always obtained. In some cases, \mathcal{E} is not independent of the loading-material index. The resultant formulation is usually complicated, and is generally presented graphically. The envelope of such a chart, however, forms a line which may be approximated mathematically in the form of the efficiency equation. Auxiliary charts are usually required in this case to show the manner in which all geometric proportions vary with loading intensity. Zee-stiffened compression panels are an example of this type of analysis. Occasionally, solutions to analyses of this type show that the effect of the loading-material index on \mathcal{E} are negligible, and, for practical designs, both the geometric ratios and \mathcal{E} may be considered constant. Examples of such structures are the truss-core sandwich and truss-core semisandwich compression panels.

The local mode of instability may occur in any element in the stiffened structure. An instability equation must be written for each type of element in the structure, and all equations must be considered in the minimum-weight analysis. In this case, the restraint one element exerts on its neighboring elements is neglected, usually by assuming hinge joints between adjacent elements. However, where coupling among the local modes has been considered, a single equation is used for local instability. In this case, the restraint one element exerts on its neighboring element is included. Minimum-weight analyses

based on a consideration of coupling in the local mode of instability are preferred since the assumption of piano-hinge connections is usually conservative, although only to a small degree in some cases (Ref. 4-4). However, it is necessary in some analyses in this chapter to assume piano-hinge connections, because the effect of coupling has not been evaluated for those particular loadings and/or geometries. In other cases, coupling was neglected because its inclusion overcomplicated the analysis.

Some degree of coupling will also exist between local and general instability. Since that type of coupling is very difficult to analyze, has only been analysed for a very few idealized structures, and would grossly complicate this type of analysis, it has been neglected.

It is expected that the minimum-weight design charts presented here will be of greatest value in preliminary design where the basic or predominant type of structure is to be selected. They may be used in stress analysis, too, provided their limitations are recognized. The following design procedures for stiffened structures assume that a single material is used throughout the structure. In addition, Poisson's ratio has been taken equal to 0.30 because this value is typical of many engineering materials.

4.2 NONDIMENSIONAL MINIMUM-WEIGHT DESIGN PROCEDURES

4.2.1 Wide Columns

Introduction. Wide columns are axial-compression members which are free along their unloaded edges; therefore, general instability may be predicted by the Euler column theory. Wide-column analysis is also applicable to compression panels (subsection 4.2.2) if they are sufficiently wide in comparison to their length so that the Euler theory is appropriate.

The minimum-weight analyses presented in the following paragraphs are for wide columns stiffened in the direction of loading and include the effects of coupling between adjacent elements in the local mode of instability. Therefore, local buckling is calculated from a single equation, where the buckling coefficient is dependent upon the relative proportions of the elements of the structure. It is assumed in these wide-column analyses that the structure has a sufficiently large number of stiffeners to permit the column geometric properties \bar{t} and ρ to be based on a unit repetitious width between stiffeners, b_s , even though the end bays may be of width b_s . In addition, simple support along the loaded edges of the column is assumed. For other conditions along the loaded edges, replace the length of the column ℓ in the equations with ℓ/\sqrt{c} , where c is the usual restraint coefficient.

Unstiffened wide column. An unstiffened wide column is of little practical value, but it is included here as a basis on which to compare, at the conclusion of this subsection, the various stiffened wide columns. An unstiffened wide column has a single mode of instability, which is predicted by Euler column theory, Eq. (3.3), where ρ , the radius of gyration, is equal to $t/\sqrt{12}$ and $t = \bar{t}$. Substituting these quantities, and rearranging:

$$\frac{N_x}{\ell \bar{\eta} E} = 0.823 \left(\frac{\bar{t}}{\ell} \right)^3 \quad (4.2)$$

where $\bar{\eta} = \eta_T$, and $N_x/\ell = \sigma_E \cdot \bar{t}/\ell$. Note that Eq. (4.2) is in the general form

of the "efficiency" equation discussed in subsection 4.1. Here $\mathcal{E} = 0.823$. Note that in an unstiffened wide column, \mathcal{E} cannot be maximized. Equation (4.2) is therefore correctly referred to as an efficiency equation, and not a minimum-weight equation. Efficiency equations, and minimum-weight equations incorporating maximized values of \mathcal{E} , will be obtained for stiffened wide columns in succeeding paragraphs.

Unflanged, integrally stiffened wide columns. The following minimum-weight design information for unflanged, integrally stiffened wide columns has been derived from Catchpole (Ref. 4-5), as summarized in Ref. 4-4.

The buckling stress for local instability may be determined from the following equation:

$$\sigma_{cr_L} = \eta_L \frac{E\pi^2}{12(1 - \mu^2)} \left(\frac{t_s}{b_s} \right)^2 K_S \quad (4.3)$$

where values of K_S are given in Ref. 4-6, and $\eta_L = \sqrt{\eta_T}$. The geometric quantities are as defined in Fig. 4-1.

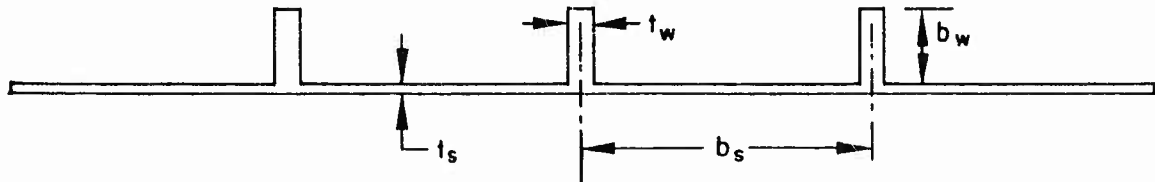


Fig. 4-1 Cross-Sectional Geometry of an Unflanged, Integrally Stiffened Wide Column

The buckling stress for general instability may be determined from the Euler theory as presented in Eq. (3.3). When these equations are combined according to the methods of minimum-weight analysis, the following efficiency equation results:

$$\frac{N_x}{L\bar{\eta}E} = \mathcal{E} \left(\frac{\bar{t}}{L} \right)^2 \quad (4.4)$$

The efficiency factor \mathcal{E} is a function of b_w/b_s and t_w/t_s . Figure 4-2 shows the relationship of these parameters to \mathcal{E} , where it may be seen that

$$\mathcal{E}_{\max} = 0.656$$

$$\left(\frac{t_w}{t_s} \right)_{\text{opt}} = 2.25$$

$$\left(\frac{b_w}{b_s} \right)_{\text{opt}} = 0.65$$

The minimum-weight equation is therefore:

$$\frac{N_x}{L\bar{\eta}E} = 0.656 \left(\frac{\bar{t}}{L} \right)^2 \quad (4.5)$$

It may be noted from Fig. 4-2 that several combinations of t_w/t_s and b_w/b_s may be chosen which are near-optimum, with little sacrifice in efficiency. This characteristic is beneficial for those designs wherein t_w/t_s based on standard gages cannot be made equal to $(t_w/t_s)_{\text{opt}}$.

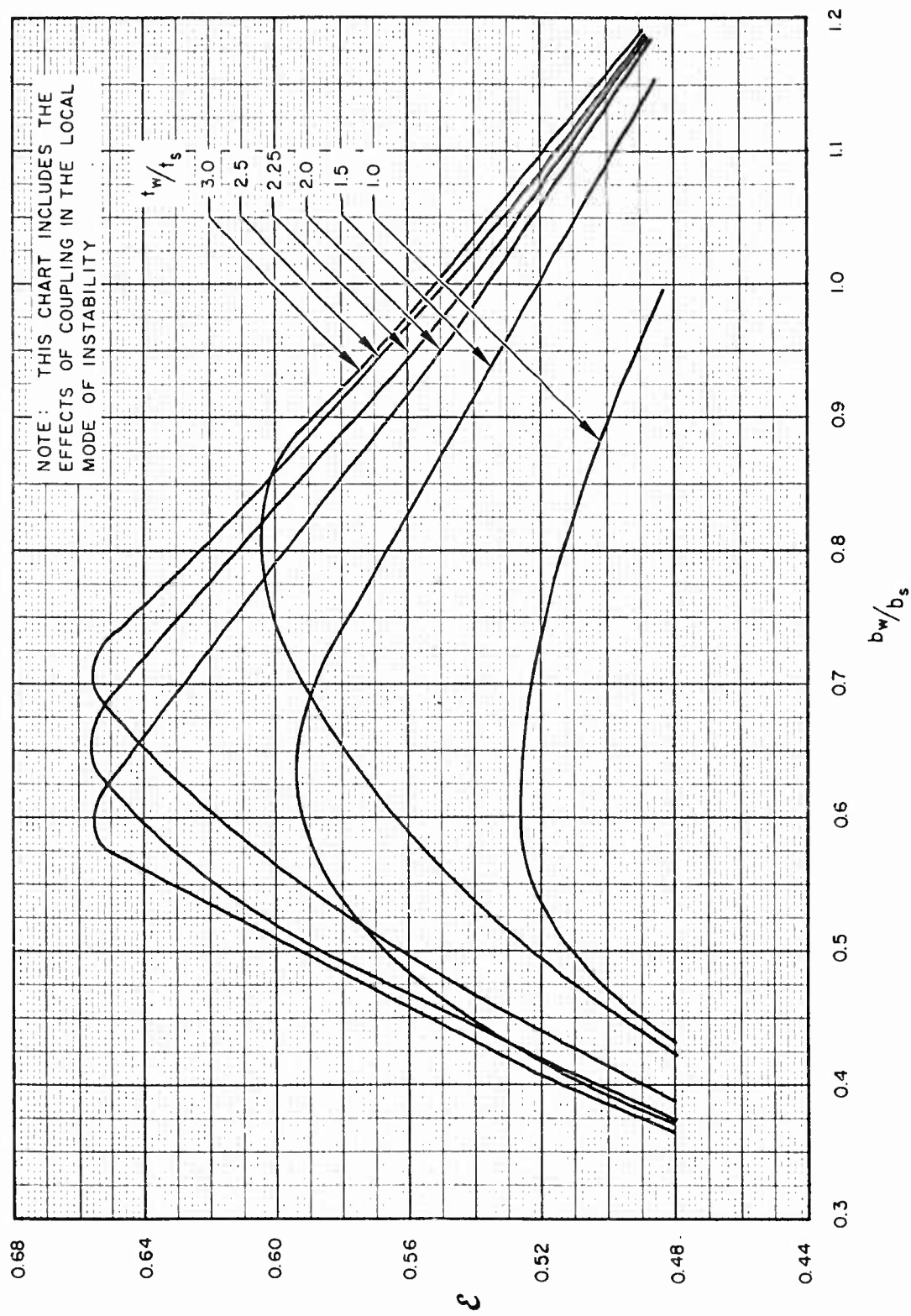


Fig. 4-2 Efficiency Chart for Unflanged, Integrally Stiffened Wide Columns

The following additional equations are necessary to determine the dimensions of the wide-column design:

$$\frac{b_s}{\ell} = 1.1 \left[1 + \frac{t_w}{t_s} \cdot \frac{b_w}{b_s} \right] \sqrt{\frac{\frac{N_x}{\ell \eta_T E}}{\frac{\bar{t}}{\ell} \left[\frac{t_w}{t_s} \left(\frac{b_w}{b_s} \right)^3 \right] \left[4 + \frac{t_w}{t_s} \frac{b_w}{b_s} \right]}}$$

$$t_s = \frac{\bar{t}}{\left[1 + \frac{t_w}{t_s} \cdot \frac{b_w}{b_s} \right]}$$

$$\bar{\eta} = \left[\eta_T \right]^{3/4}$$

Zee-stiffened wide columns. Zee-stiffened wide columns have been treated both theoretically and experimentally, with good agreement between the two approaches. The minimum-weight design information presented here is based on the theoretical work of Farrar (Ref. 4-7) which is also summarized in Ref. 4-4.

Because of the similarity between zee-stiffened and unflanged, integrally stiffened wide columns, Eqs. (3.3), (4.3), and (4.4) apply to both configurations. Values of the buckling coefficient, K_S , may be obtained from Ref. 4-6 for this particular configuration. The following sketch defines the cross-sectional geometry.

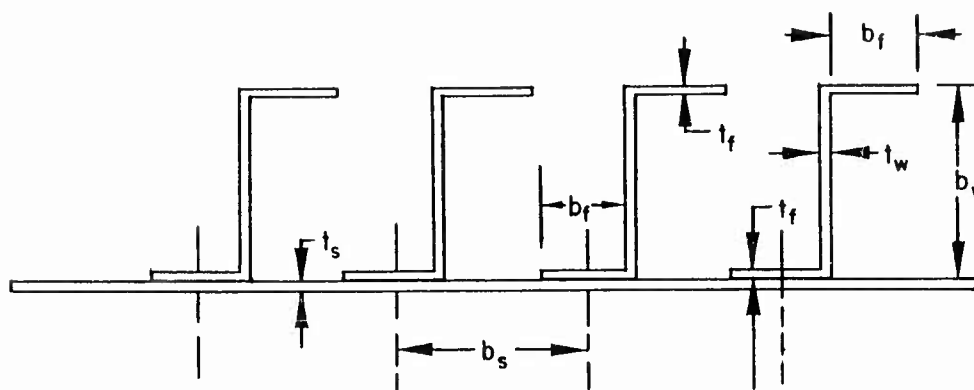


Fig. 4-3 Cross-Sectional Geometry of Zee-Stiffened Wide Column

The efficiency factor \mathcal{E} is again a function of b_w/b_s and t_w/t_s . The relationship of these parameters to \mathcal{E} is given in Fig. 4-4, where it is shown that

$$\mathcal{E}_{\max} = 0.911$$

$$\left(\frac{t_w}{t_s} \right)_{\text{opt}} = 1.06$$

$$\left(\frac{b_w}{b_s} \right)_{\text{opt}} \approx 0.87$$

The minimum-weight equation, therefore, may be written as follows:

$$\frac{N_x}{L\bar{\eta}E} = 0.911 \left(\frac{\bar{t}}{L} \right)^2 \quad (4.6)$$

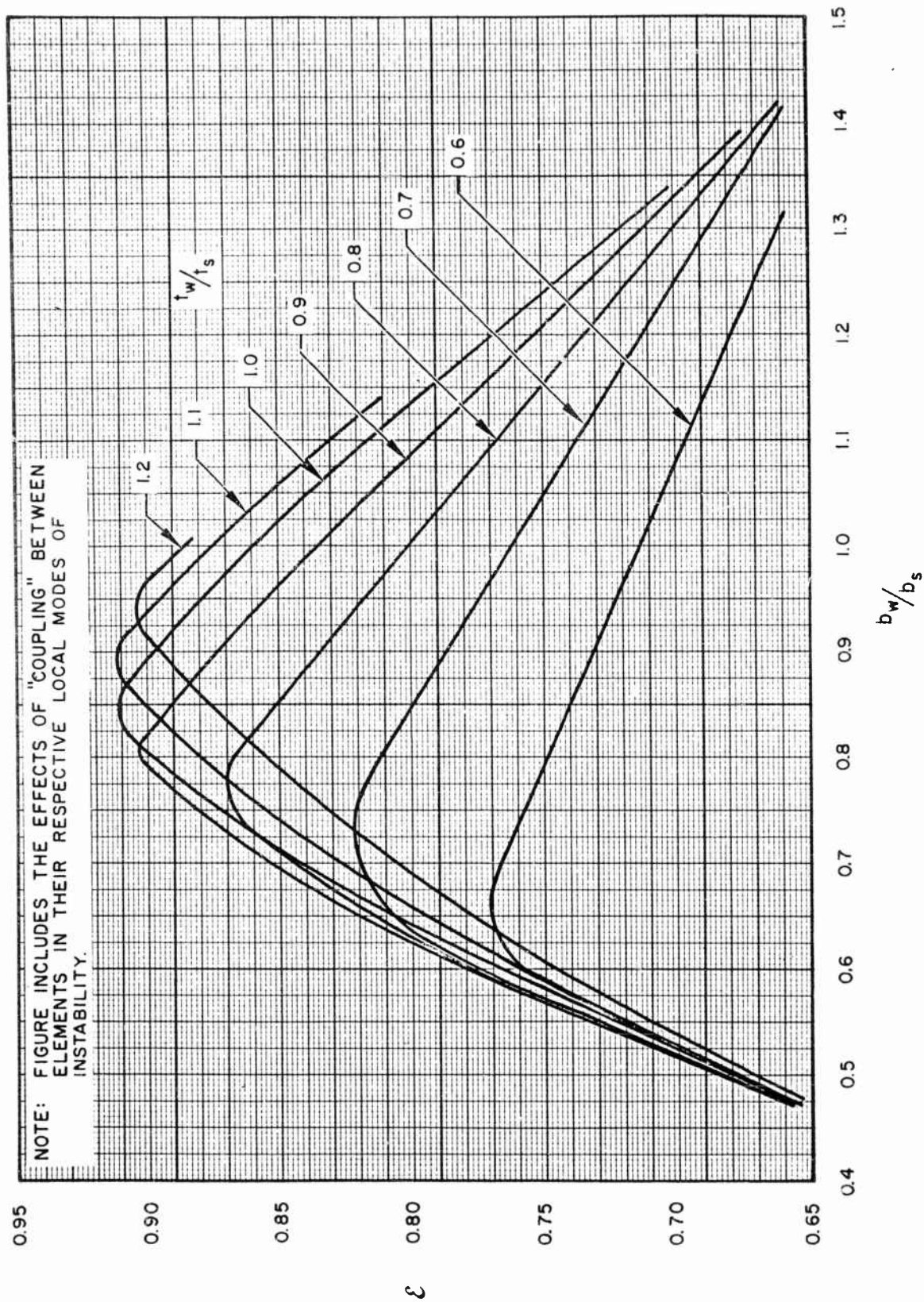


Fig. 4-4 Efficiency Chart for Zee-Stiffened Wide Columns

As indicated by Fig. 4-4, the optimum values of the parameters t_w/t_s and b_w/b_s may vary considerably with little reduction in maximum efficiency. The following equations may be used to complete a zee-stiffened wide-column design:

$$b_f = 0.3 b_w$$

$$t_f = t_w$$

$$t_s = \frac{\bar{t}}{\left[1 + 1.6 \frac{b_w}{b_s} \cdot \frac{t_w}{t_s} \right]}$$

$$\frac{b_w}{l} = \frac{0.4 \left(1 + 1.6 \frac{b_w}{b_s} \cdot \frac{t_w}{t_s} \right)}{\sqrt{\frac{b_w}{b_s} \cdot \frac{t_w}{t_s} \left(1 + 0.59 \frac{b_w}{b_s} \cdot \frac{t_w}{t_s} \right)}} \sqrt{\frac{N_x}{l \eta_T E}} \sqrt{\frac{\bar{t}}{l}}$$

$$\bar{\eta} = [\eta_T]^{3/4}$$

Truss-core sandwich wide columns. The truss-core sandwich wide column is shown in cross section in Fig. 4-5.

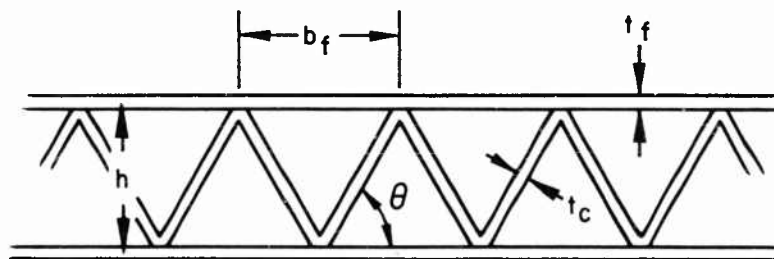


Fig. 4-5 Cross-Sectional Geometry of Truss-Core Sandwich Wide Column

Crawford, Burns, and Tilcens (Ref. 4-3) use the following equations to determine buckling stresses due to local instability and general instability when the facings are of equal thickness:

$$\sigma_{cr_L} = \eta_L \frac{K_x \pi^2 E}{12(1 - \mu^2)} \left(\frac{t_f}{b_f} \right)^2 \quad (4.7)$$

$$\sigma_{cr_G} = \eta_E \frac{\pi^2 D_x}{t \ell^2} \left(\frac{1}{1 + r} \right) \quad (4.8)$$

where

$$\eta_L = \sqrt{\eta_T}$$

K_x is taken from Ref. 4-8 and reproduced as Fig. 4-6

η_E = wide-column plasticity reduction factor based on von Kármán's reduced modulus

D_x = flexural stiffness of sandwich per unit width in x-direction, $D_x = (EI)_x$

$$r = \pi^2 D_x \ell^2 D_{Q_x}$$

ℓ = length of sandwich wide column

D_{Q_x} = transverse shearing stiffness of sandwich on planes perpendicular to x-direction per unit-width

When these equations are suitably combined, and the effects of transverse shearing stiffness are neglected, Eq. (4.4) results. Here, \mathcal{C} is a function of t_c/t_f and θ .

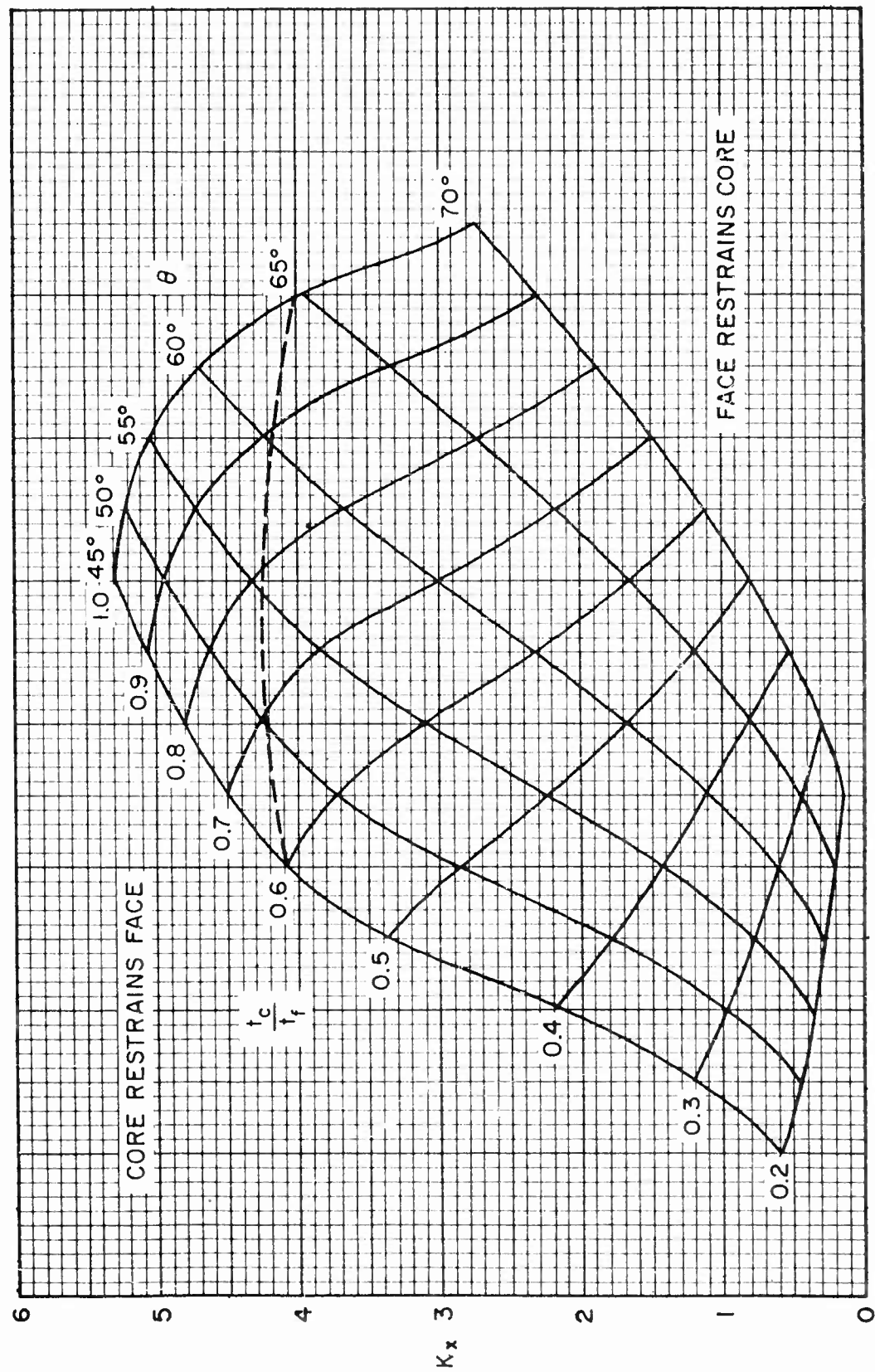


Fig. 4-6 Local Buckling Coefficients for Single-Truss-Core Sandwich and Semisandwich Plates Under Uniaxial Compression in the Direction of the Corrugations

Figure 4-7 shows that:

$$\mathcal{E}_{\max} = 0.605$$

$$\theta_{\text{opt}} = 62^\circ$$

$$\left(\frac{t_c}{t_f} \right)_{\text{opt}} = 0.92$$

The minimum-weight equation is therefore:

$$\frac{N_x}{\ell \eta E} = 0.605 \left(\frac{\bar{t}}{\ell} \right)^2 \quad (4.9)$$

Equation (4.9) is applicable only when $\bar{t}/\ell < 10^{-2}$. Above this value of \bar{t}/ℓ , shear-stiffness effects in the sandwich cannot be neglected, that is, $r \neq 0$, and their inclusion considerably complicates the simple form of Eq. (4.9). Most practical designs have \bar{t}/ℓ values below this cutoff; therefore, procedures for use when $\bar{t}/\ell > 10^{-2}$ are not presented here.

Auxiliary design equations for this configuration are:

$$t_f = \frac{\bar{t}}{2 + \frac{t_c}{t_f} \frac{1}{\cos \theta}}$$

$$b_f = 0.95 t_f \sqrt{\frac{K_X \left(\frac{\bar{t}}{\ell} \right)}{\frac{N_x}{\ell \cdot \eta_L E}}}$$

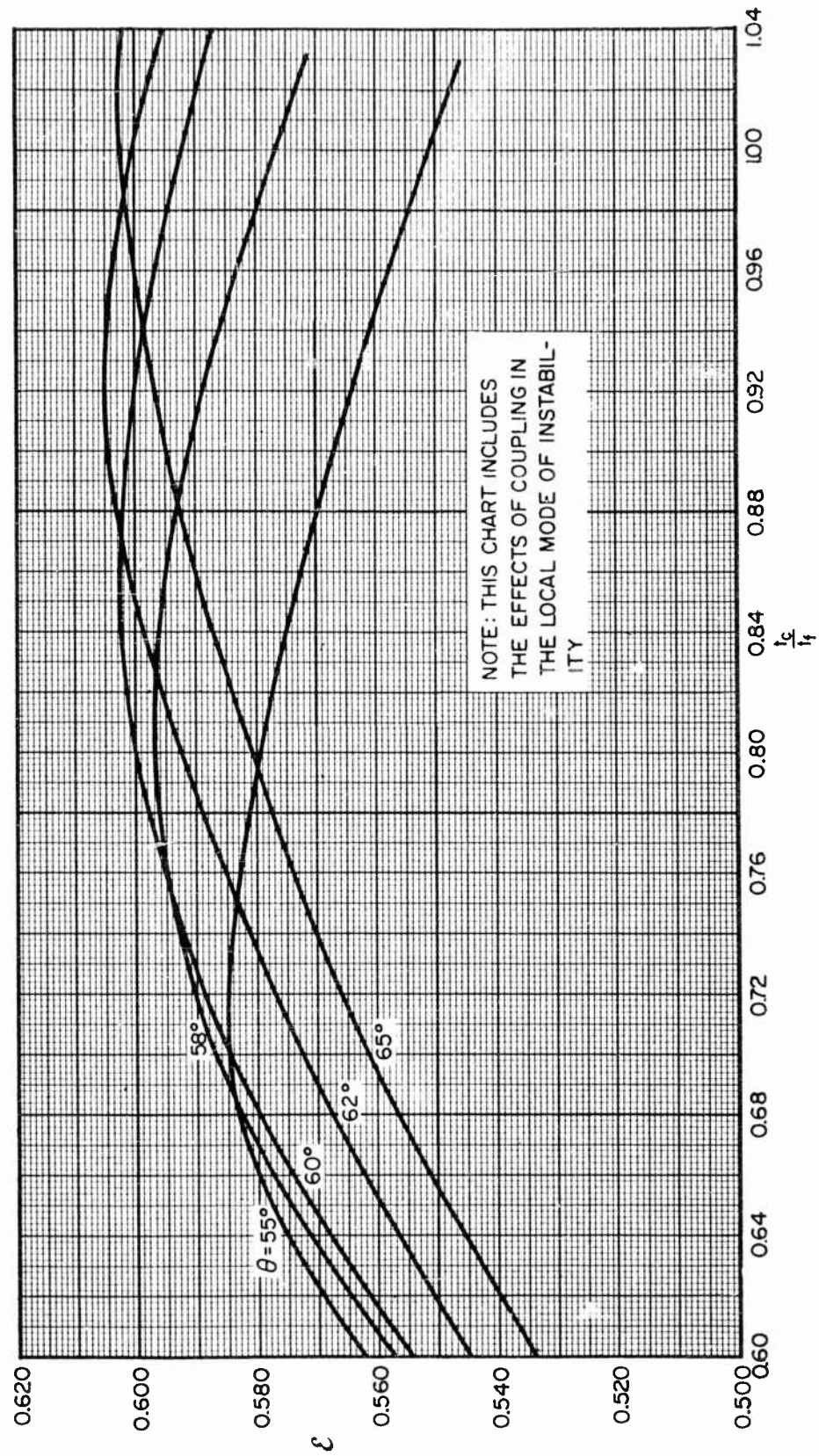


Fig. 4-7 Efficiency Chart for Truss-Core Sandwich Wide Columns

where $\eta_L = \sqrt{\eta_T}$, and K_X is taken from Fig. 4-6.

$$b_c = \frac{b_f}{2 \cos \theta}$$

$$\bar{\eta} = \sqrt{\frac{2\eta_T^{3/2}}{1 + \eta_T}}$$

Note that K_X is equal to 4.13 when the optimum values of θ and t_c/t_f are used.

The relative efficiencies of stiffened wide columns. The minimum-weight equations for wide-column configurations previously presented in this subsection [Eqs. (4.5), (4.6), and (4.9)] are shown in Fig. 4-8 together with Eq. (4.2) for an unstiffened wide column. All stiffened wide-column configurations are far superior to the unstiffened wide column, regardless of the type of stiffening. Further, differences in efficiency between the three stiffened wide-column configurations are rather small. The zee-stiffened wide-column configuration is the most efficient of the stiffened configurations considered. On the basis of the relative positions of the stiffened wide-column configurations shown, it is concluded that the zee-stiffened wide column approaches very closely the maximum efficiency attainable by any wide-column configuration consisting of a flat sheet plus stiffening elements.

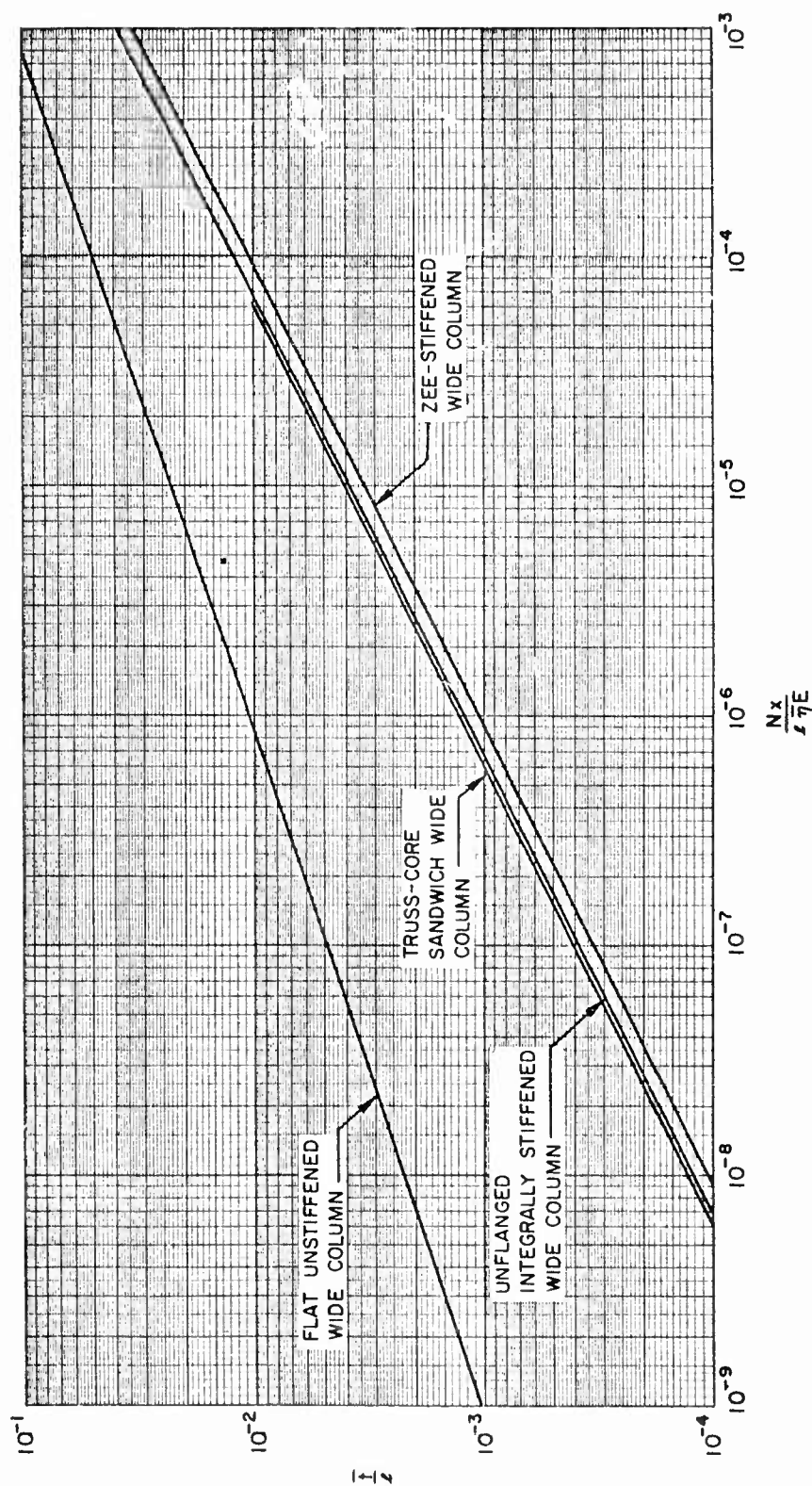


Fig. 4-8 Comparison of the Minimum-Weight Envelopes of Several Types of Stiffened, Wide-Column Construction When Subjected to a Compression Load in the Direction of the Stiffening Elements

4.2.2 Compression Panels

Introduction. Minimum-weight design information is presented in this subsection for long, axially loaded plates that are stiffened in the direction of loading and simply supported along their unloaded edges. These composite structures are referred to as compression panels.

Four types of stiffened compression panels are treated:

- (1) Unflanged, integrally stiffened panels
- (2) Zee-stiffened panels
- (3) Truss-core sandwich panels
- (4) Truss-core semisandwich panels

In addition, the case of an unstiffened compression panel is included for comparative purposes. Types (1) and (2) of the stiffened panels are assumed in their local instability analyses to have piano-hinge connection between adjacent elements, while for types (3) and (4), effects of coupling between adjacent elements are included. The difference in these approaches is discussed in subsection 4.1.

Orthotropic plate theory has been used for the general instability analysis in all cases. This theory is valid when the panel is stiffened with a large number of equally spaced geometrically identical stiffeners. When the optimum number of bays is less than three, as occurs in the case of the highly loaded, unflanged, integrally stiffened panel or the zee-stiffened panel, the modified orthotropic plate theory of Seide and Stein (Ref. 4-9) has been used.

The aspect ratio of the composite stiffened panels, as well as of the individual elemental panels, is assumed sufficiently large to be considered infinite in all cases.

The stiffnesses and weights of the unflanged, integrally stiffened panel and the zee-stiffened panel are calculated assuming the end bay widths are equal to the uniform spacing of the stiffeners.

Unstiffened compression panel. Buckling of an unstiffened compression panel may be determined from Eq. (3.1), where $\eta_L = \sqrt{\eta_T}$, and $K_c = 4.0$ according to the previously defined conditions. If $\mu = 0.30$, $t = \bar{t}$, and $\bar{\eta} = \eta_L$, the following efficiency equation may be obtained:

$$\frac{N_x}{b\bar{\eta}E} = \frac{\sigma}{\bar{\eta}E} \cdot \frac{\bar{t}}{b} = 3.62 \left(\frac{\bar{t}}{b} \right)^3 \quad (4.10)$$

As was noted in a similar manner for the unstiffened wide column, Eq. (4.10) is an efficiency equation, not a minimum-weight equation, because \mathcal{E} is fixed for an unstiffened panel.

Unflanged, integrally stiffened compression panel. A minimum-weight analysis of unflanged, integrally stiffened compression panels has been performed by Burns and Crawford (Ref. 4-4). These investigators found that the usual form of the efficiency equation cannot be obtained since \mathcal{E} is a function of the loading-material index as well as of the geometric proportions of the stiffened panel. The complicated mathematical results of the analysis are most conveniently presented in graphical form, and are shown in Figs. 4-9a and 4-9b. Note that the optimum number of bays steadily decreases as the loading-material index increases. Figures 4-9a and 4-9b alone present insufficient design information. Therefore, Fig. 4-10 is presented as an auxiliary chart to relate \bar{t}/b , N , and b_w/b_s , where N is the number of bays.

These charts are based on the following equation for buckling due to general instability, and Eq. (4.3) for buckling due to local instability, where $K_s = 4.0$.

$$\sigma_{crG} = \eta_G \frac{\pi^2 E}{12(1 - \mu^2)} \left(\frac{t_s}{b_s} \right)^2 K_G \quad (4.11)$$

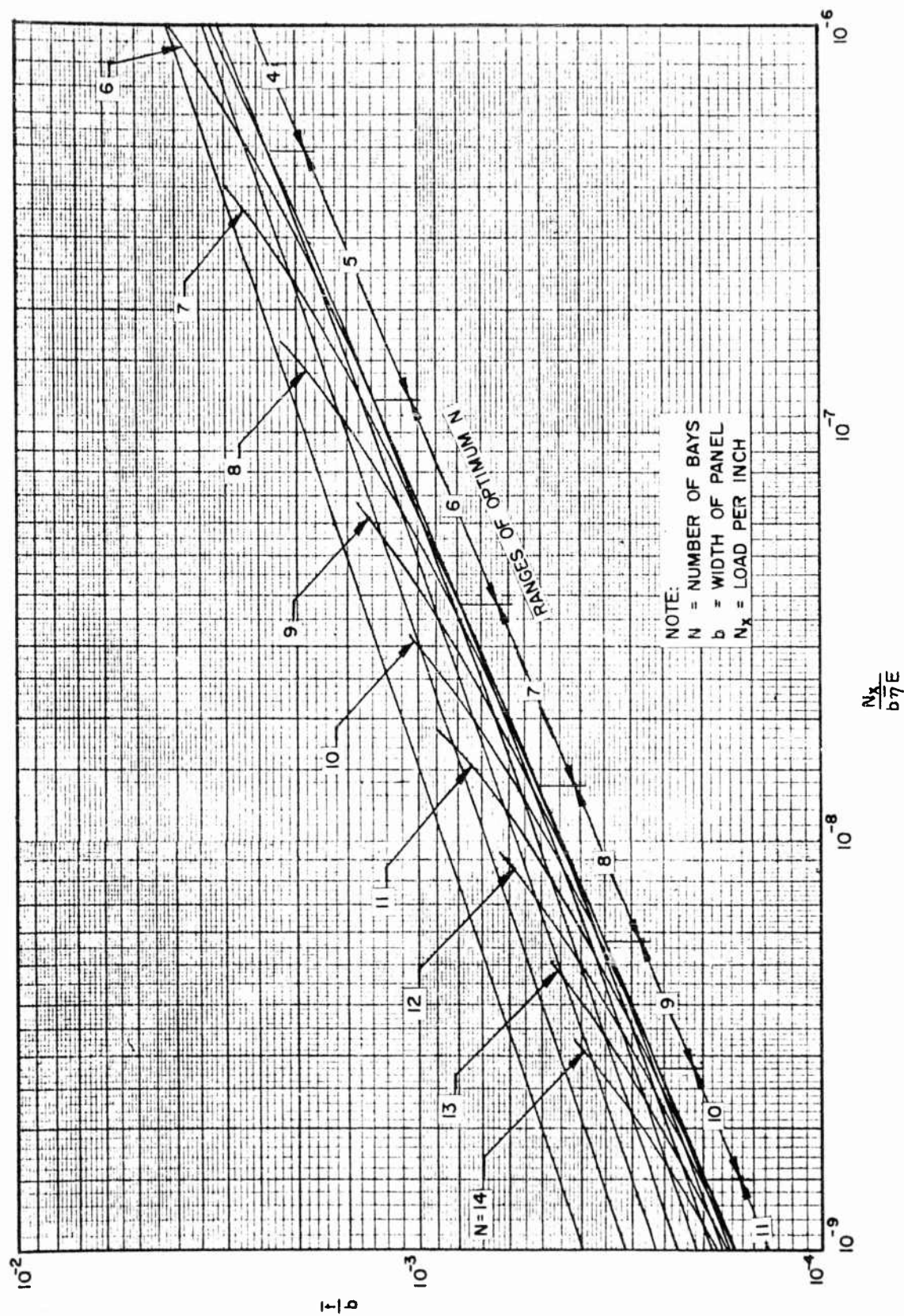


Fig. 4-9a Efficiency Chart for Unflanged, Integrally Stiffened Flat Panels in Compression, Stiffeners Parallel to Load

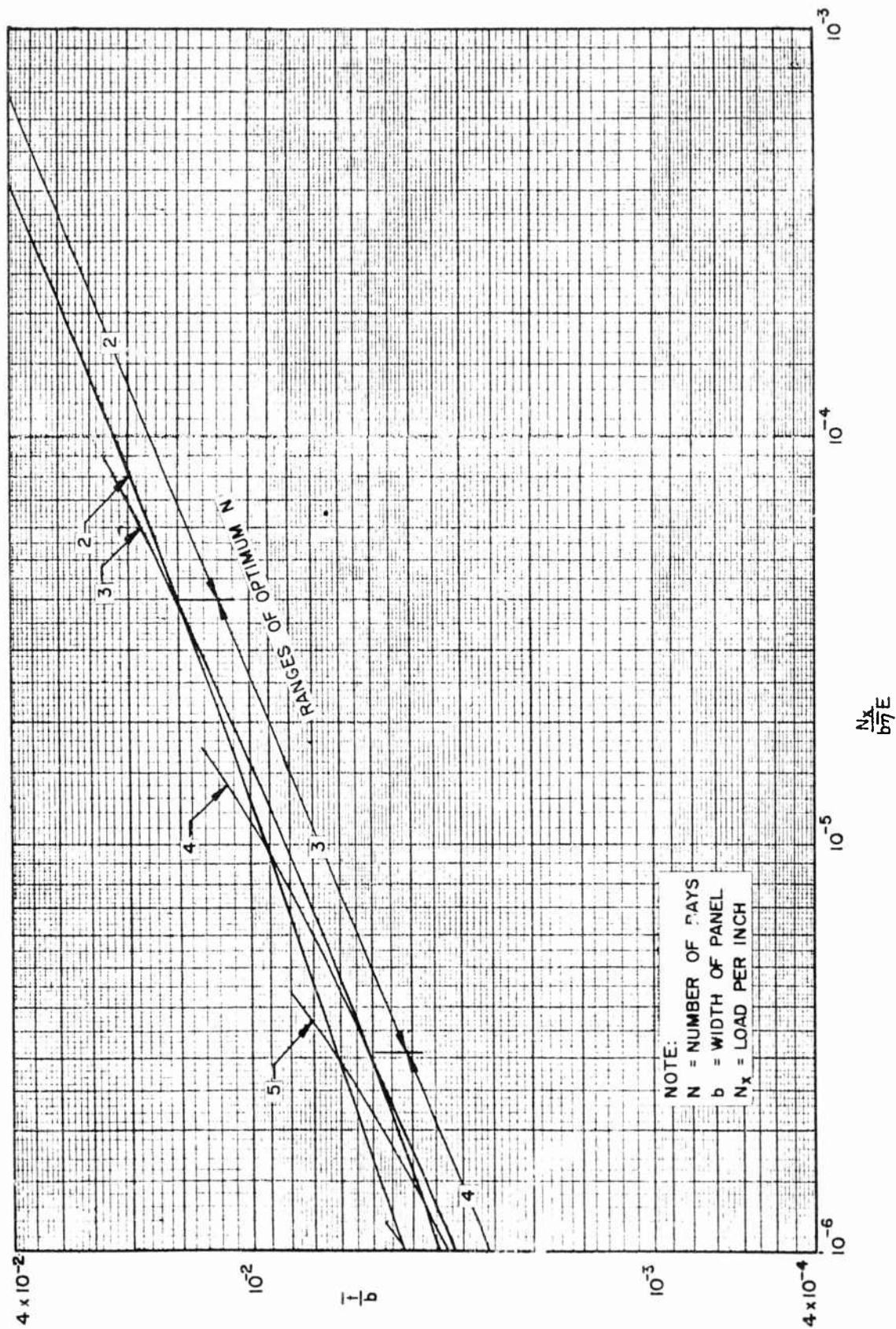


Fig. 4-9b Efficiency Chart for Unflanged, Integrally Stiffened Flat Panels in Compression, Stiffeners Parallel to Load (Continuation of Fig. 4-9a)

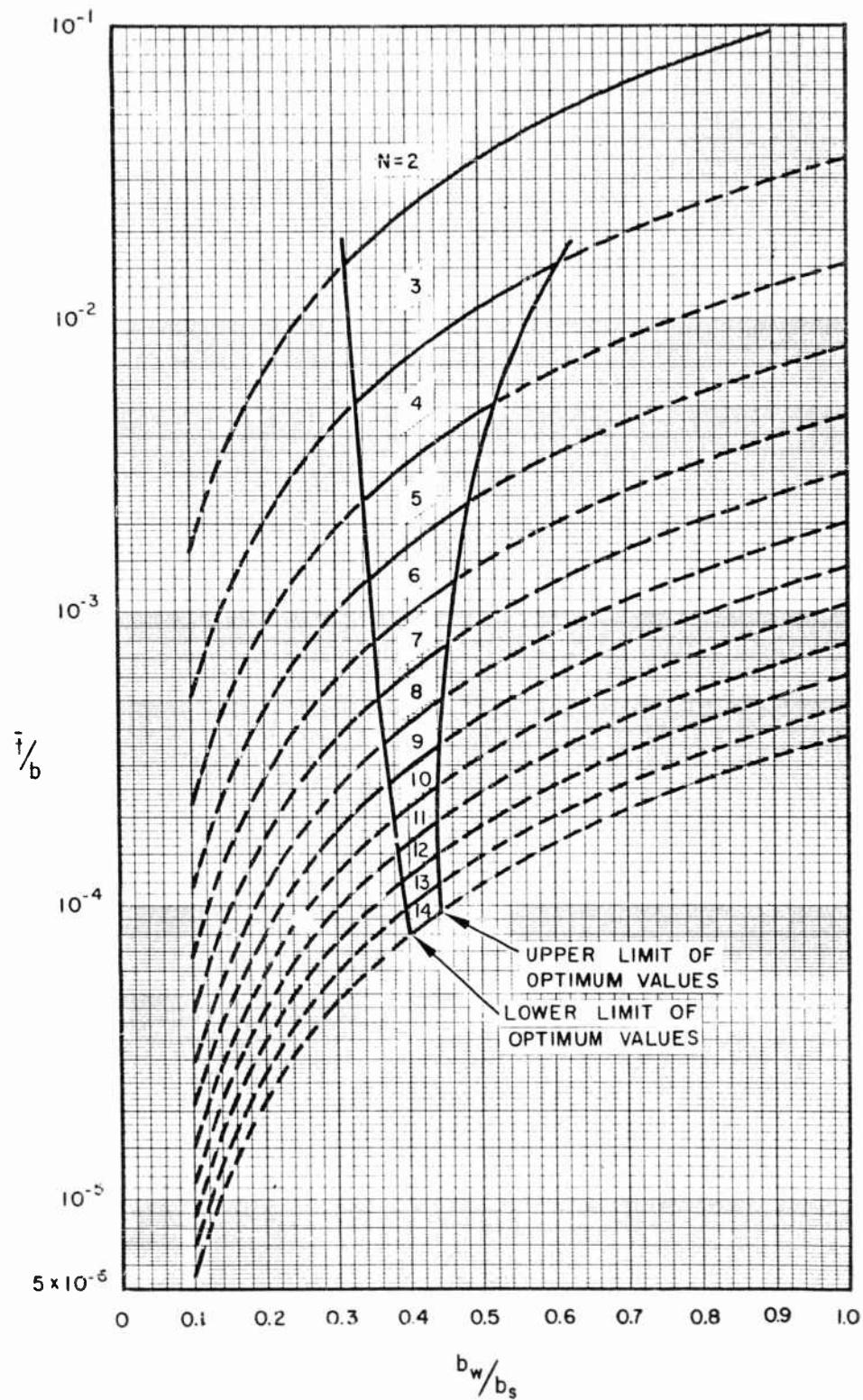


Fig. 4-10 Auxiliary Design Chart for Unflanged, Integrally Stiffened Flat Panels in Compression

where

$$\eta_G = \eta_T$$

$$K_G = \frac{2 \left\{ \left[1 + \frac{N-1}{N} \left(\frac{EI}{b_s D_f} \right) \left(1 + \frac{\frac{A \bar{z}^2}{I}}{\frac{0.88A}{b_s t_s}} \right) \right]^{1/2} + 1 \right\}}{N^2 \left[\frac{N-1}{N} \left(\frac{A}{b_s t_s} + 1 \right) \right]}$$

when $N \geq 3$ (for $N < 3$, see Ref. 4-9)

A = area of stiffener cross section

I = moment of inertia of stiffener cross section about its centroidal axis

$D_f = Et^3/12 (1 - \mu^2)$

E = Young's modulus

\bar{z} = distance from midsurface of skin to stiffener centroidal axis; taken to be approximately $b_w/2$

The cross-sectional geometry for this type of stiffened compression panel is identical to that shown in Fig. 4-1. End bays are also of width b_s . The total width of the loaded edge is denoted as b . The following equations are necessary for design:

$$N_x = \sigma \cdot \bar{t}$$

$$b_s = b/N$$

$$t_s = \frac{b_s \left(\frac{\bar{t}}{b} \right) N}{1 + 2.828 \frac{N-1}{N} \left(\frac{b_w}{b_s} \right)^2}$$

$$t_w = 2.828 t_s \left(\frac{b_w}{b_s} \right)$$

$$\bar{\eta} = [\eta_T]^{3/4}$$

The equation relating t_w/t_s and b_w/b_s results from the assumption of piano-hinge connection between adjacent elements for computing local instability.

For purposes of comparing this type of stiffened compression panel with other types, it may be demonstrated that the envelope of the curves of Figs. 4-9a and 4-9b has approximately the following mathematical equation, which may be regarded as the minimum-weight equation:

$$\frac{N_x}{b\bar{\eta}E} = 0.970 \left(\frac{\bar{t}}{b} \right)^{2.38} \quad (4.12)$$

Zee-stiffened compression panel. Burns and Crawford (Ref. 4-4) have also performed a minimum-weight analysis of zee-stiffened compression panels. As is the case for the unflanged, integrally stiffened compression panel, the usual form of the efficiency equation cannot be obtained for zee-stiffened compression panels since \mathcal{E} is a function of the loading-material index as well as of the geometric proportions of the stiffened panel. A graphical presentation of the results is therefore shown in Figs. 4-11a and 4-11b. An auxiliary chart presenting the relation between \bar{t}/b , N , and b_w/b_s is presented as Fig. 4-12 to provide necessary additional information for design. The number of bays is designated as N ; b is the width of the loaded edge. These charts are based on Eqs. (4.3) and (4.11) for buckling due to local instability and general instability, respectively.

Figure 4-3 shows the cross-sectional geometry which applies to a zee-stiffened compression panel. The end bays are also of width b_s . The following equations are required in addition to Figs. 4-11a, 4-11b, and 4-12 for design purposes.

$$N_x = \sigma \cdot \bar{t}$$

$$b_s = b/N$$

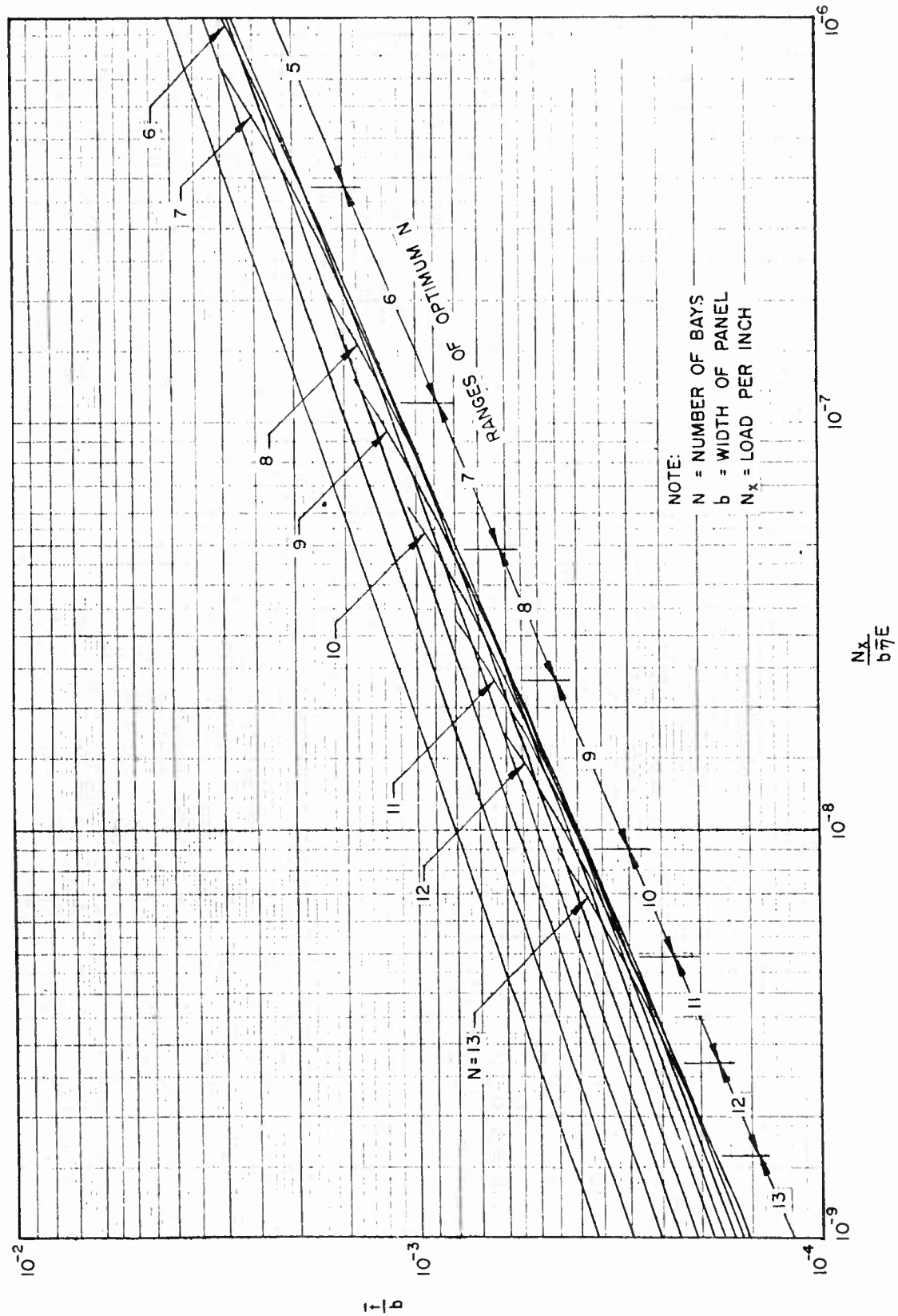


Fig. 4-11a Efficiency Chart for Zee-Stiffened Flat Panels in Compression, Stiffeners Parallel to Load

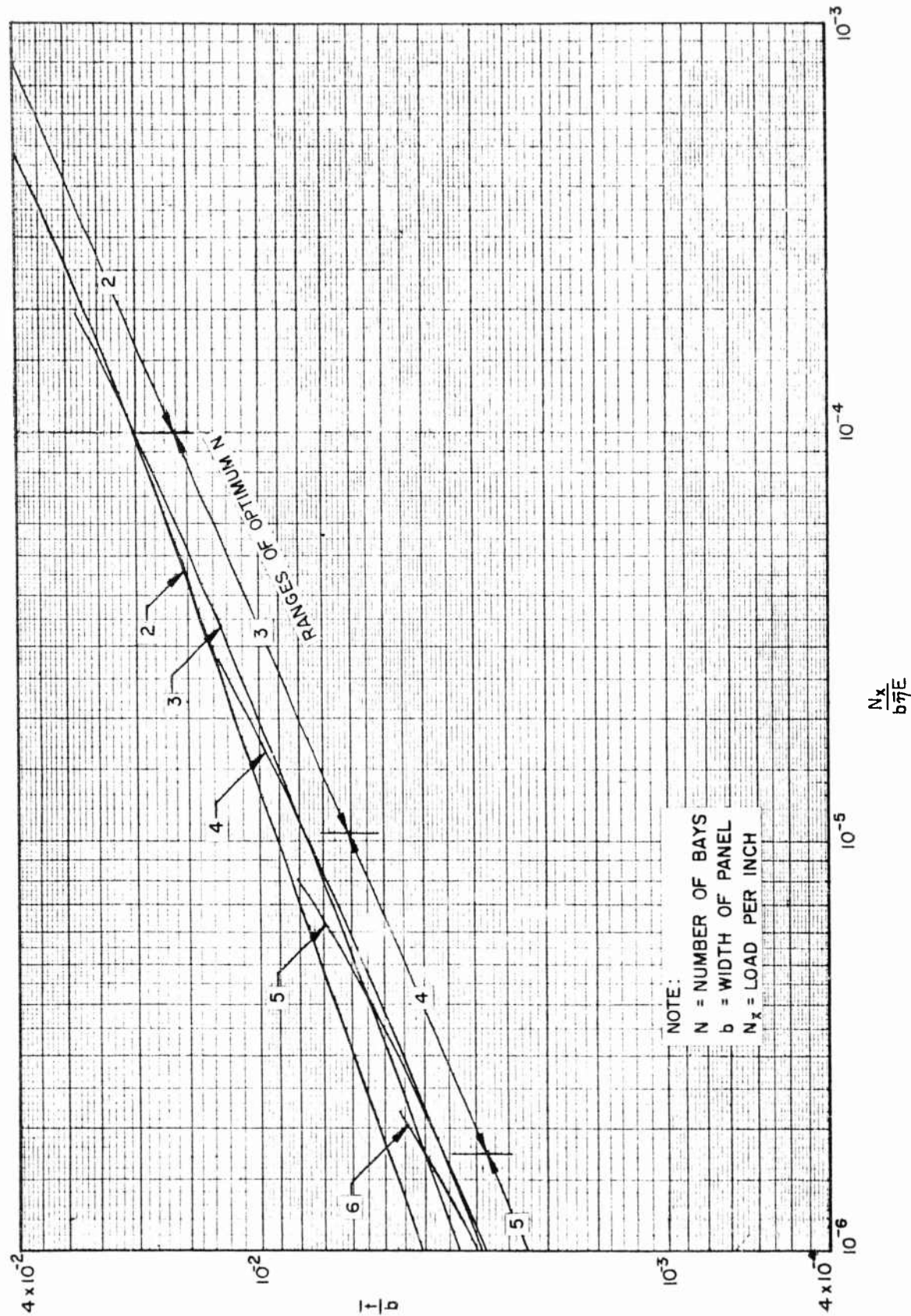


Fig. 4-11b Efficiency Chart for Zee-Stiffened Flat Panels in Compression, Stiffeners Parallel to Load
(Continuation of Fig. 4-11a)

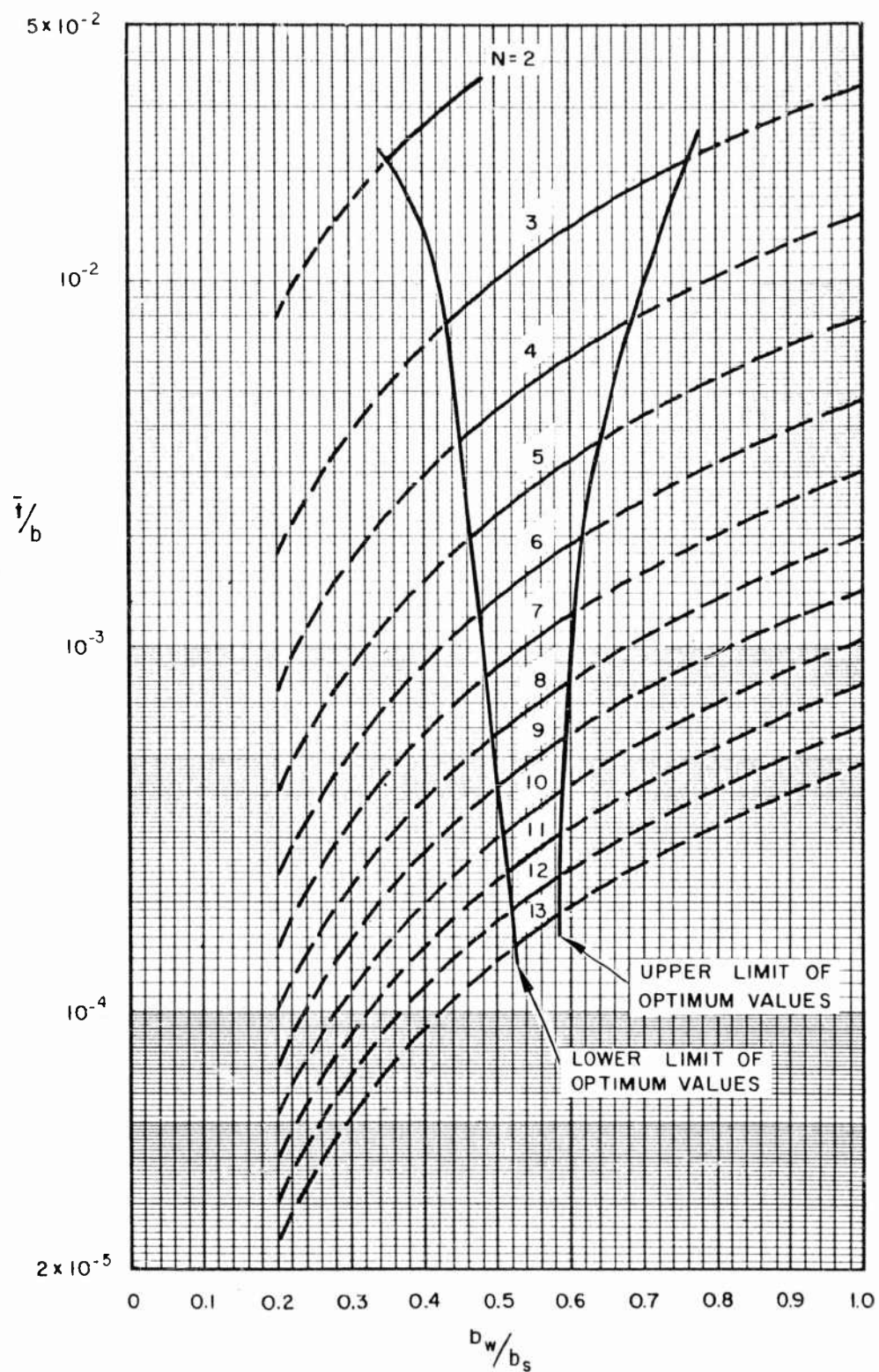


Fig. 4-12 Auxiliary Design Chart for Zee-Stiffened Flat Panels in Compression

$$t_s = \frac{b_s \left(\frac{\bar{t}}{b} \right) N}{1 + 1.707 \frac{N-1}{N} \left(\frac{b_w}{b_s} \right)^2}$$

$$t_w = t_f = t_s \left(\frac{b_w}{b_s} \right)$$

$$b_f = 0.3535 b_w$$

$$\bar{\eta} = [\eta_T]^{3/4}$$

This analysis is based on the simplifying assumption that the thicknesses of the zee flanges and of the zee web are all equal.

The envelope of the curves shown in Figs. 4-11a and 4-11b may be represented approximately by the following mathematical equation:

$$\frac{N_x}{b \bar{\eta} E} = 1.030 (\bar{t}/b)^{2.36} \quad (4.13)$$

This equation is, for comparison purposes, considered the minimum-weight equation for this type of compression panel.

Truss-core sandwich compression panel. The truss-core sandwich cross-sectional geometry is shown in Fig. 4-5. The minimum-weight design information presented here is taken from the analysis of Crawford, Burns, and Tilcens (Ref. 4-3) who use Eq. (4.7) to determine the buckling stress for local instability, and the following equation to determine the buckling stress for general instability:

$$\sigma_{crG} = \frac{2\eta_G \pi^2 D_f s}{\bar{t} b^2} \left(\sqrt{\frac{D_x}{D_f} \frac{D_y}{D_f}} + \frac{D_3}{D_f} \right) \quad (4.14)$$

where

$$\eta_G = \sqrt{\frac{2 \eta_T}{1 + \eta_T}}$$

$$s = \frac{1}{(1 + r)^2}$$

$$r = \frac{\pi^2 D_x}{b^2 D_{Q_x}}$$

D_x = flexural stiffness of sandwich per unit width in x-direction taken equal to

$$D_f \left[\frac{3}{2} \left(\frac{b_f}{t_f} \right)^2 \tan^2 \theta + \frac{1 - \mu^2}{4} \frac{t_c}{t_f} \left(\frac{b_f}{t_f} \right)^2 \frac{\tan^2 \theta}{\cos \theta} \right]$$

D_y = flexural stiffness of sandwich per unit width in y-direction, taken equal to

$$\left[\frac{3}{2} \left(\frac{b_f}{t_f} \right)^2 \tan^2 \theta \right] D_f$$

D_f = flexural stiffness of facing sheet per unit width, taken equal to $E t_f^3 / 12 (1 - \mu^2)$

$D_3 = \mu D_y + D_{xy}$ taken equal to

$$\left[3/2 \left(\frac{b_f}{t_f} \right)^2 \tan^2 \theta \right] D_f$$

D_{xy} = twisting stiffness of sandwich per unit width

D_{Q_x} = transverse shearing stiffness of sandwich on planes perpendicular to x-direction, per unit width

It is assumed that the face sheets are of equal thickness and that the core is made up of straight-line elements.

When Eqs. (4.7) and (4.14) are combined according to the methods of minimum-weight analysis, the efficiency factor \mathcal{E} is found to be a function of the loading-material index as well as of the geometric proportions of the panel. However, Ref. 4-3 shows that this complication may be circumvented if the transverse shear stiffness effects, which were found to be negligible when $\bar{t}/b < 10^{-2}$, are not included in Eq. (4.14), that is, if s in this equation is taken equal to unity. The resulting efficiency equation is

$$\frac{N_x}{b\eta E} = \mathcal{E} \left(\frac{\bar{t}}{b} \right)^2 \quad (4.15)$$

Since sandwich construction is usually reserved for low loading where significant weight savings can be made over flat or other types of stiffened compression panels, the following equations do not include transverse shear effects. The designer, therefore, should limit usage of the following equations to those designs where $\bar{t}/b < 10^{-2}$.

An evaluation of \mathcal{E} is presented in Fig. 4-13. From this chart \mathcal{E}_{\max} is seen to be 1.108 and it occurs when θ is approximately 60 deg and t_c/t_f approximately 0.83. Note

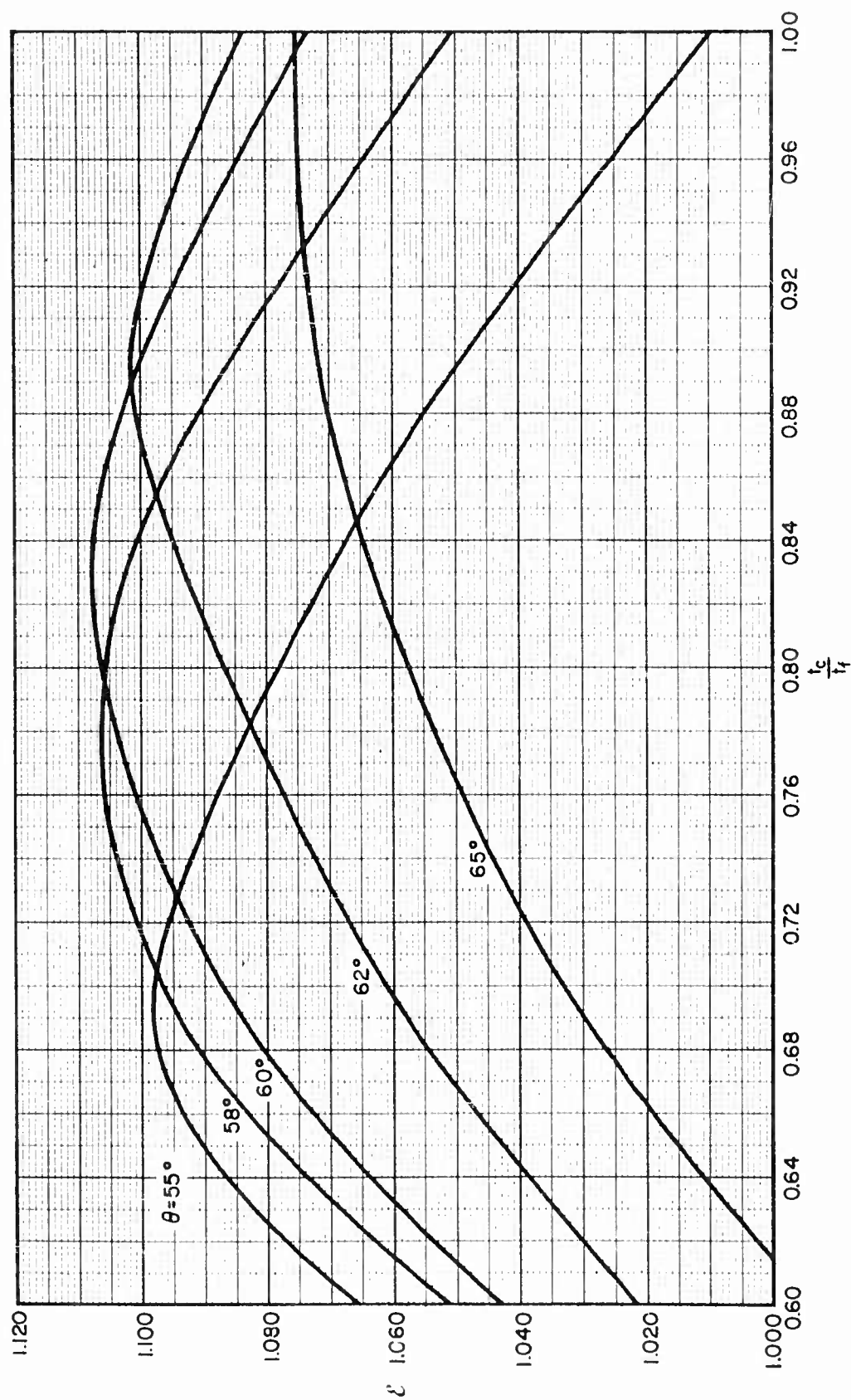


Fig. 4-13 Efficiency Chart for Truss-Core Sandwich Panels in Compression, Corrugations Parallel to Load

that several other combinations of θ and t_c/t_f produce values of \mathcal{E} which are very close to the maximum. The minimum-weight equation for truss-core sandwich compression panels is then

$$\frac{N_X}{b\bar{\eta}E} = 1.108 \left(\frac{\bar{t}}{b} \right)^2 \quad (4.16)$$

For design, Fig. 4-13 and the above equations must be supplemented with the following equations:

$$\bar{\eta} = \left[\frac{2\eta_T^2}{1 + \eta_T} \right]^{1/4} \quad (4.17)$$

$$b_f = 0.95 t_f \sqrt{\frac{K_X (\bar{t}/b)}{(N_X/b\eta_L E)}} \quad (4.18)$$

where $\eta_L = \sqrt{\eta_T}$, and K_X is taken from Fig. 4-6.

$$b_c = b_f / 2 \cos \theta \quad (4.19)$$

$$t_f = \frac{\bar{t}}{2 + \frac{t_c}{t_f} \frac{1}{\cos \theta}}$$

Truss-core semisandwich compression panels. Truss-core semisandwich panels are identical to truss-core sandwich panels, except that one facing sheet has been removed. This configuration is expected to be typical, efficiency-wise, of the large family of corrugation-stiffened panels of various waveforms. Figure 4-5 may be referred to for the definition of cross-sectional geometry, keeping in mind that one of the facing sheets is omitted.

Burns and Crawford have reported the results of a minimum-weight analysis of this type of stiffened compression panel construction in Ref. 4-4. The equations used by these investigators to determine the buckling stress for local instability and general instability are Eqs. (4.7) and (4.14), respectively. Values of the buckling coefficient K_X , appearing in Eq. (4.7), are presented in Fig. 4-6 for the full-sandwich case but are assumed to give a close approximation for the semisandwich case. It is assumed that the core is made up of straight-line elements

The minimum-weight analysis for truss-core semisandwich compression panels is entirely parallel to that for truss-core sandwich compression panels. The resulting efficiency equation is identical to Eq. (4.15).

The efficiency factor \mathcal{E} for truss-core semisandwich panels is presented in Fig. 4-14 as a function of t_c/t_f and θ . The following quantities may be read from this chart:

$$\mathcal{E}_{\max} = 0.59$$

$$\left(\frac{t_c}{t_f}\right)_{\text{opt}} \approx 0.49$$

$$\theta_{\text{opt}} \approx 47\text{-}1/2 \text{ deg}$$

The minimum-weight equation may be written

$$\frac{N_x}{b\eta E} = 0.59 \left(\frac{\bar{t}}{b}\right)^2 \quad (4.20)$$

Owing to the similarity in construction, Eqs. (4.17), (4.18), and (4.19) are applicable here as necessary equations for design purposes. Also necessary is the following equation:

$$t_f = \frac{\bar{t}}{\left(1 + \frac{t_c}{t_f} \frac{1}{\cos \theta}\right)}$$

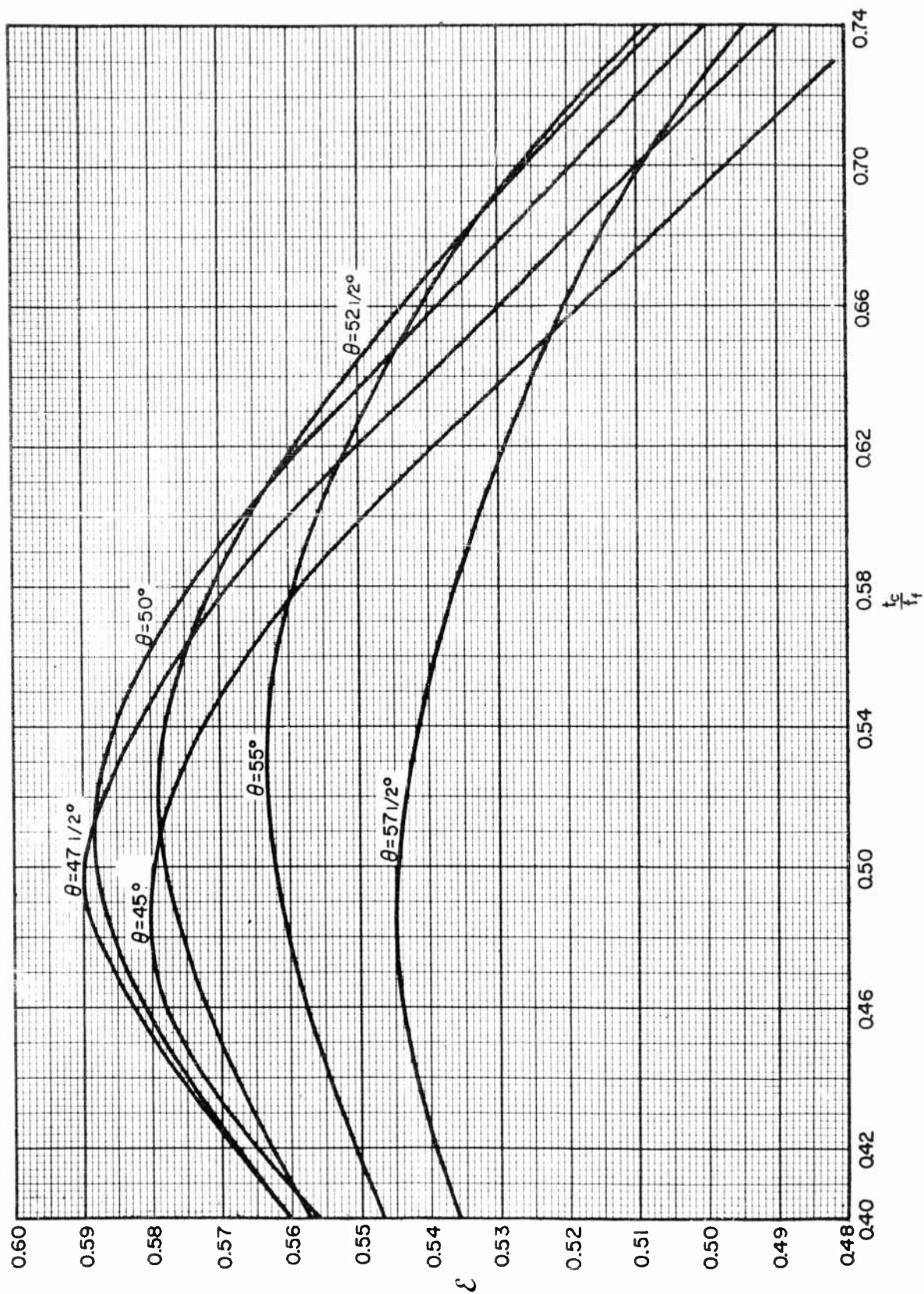


Fig. 4-11: Efficiency Chart for Truss-Core Semisandwich Panels in Compression, Corrugations Parallel to Load

The relative efficiencies of stiffened compression panels. The minimum-weight equations for the several types of flat, stiffened compression panels previously presented in this subsection [Eqs. (4.12), (4.13), (4.16), and (4.20)] are shown in Fig. 4-15 together with Eq. (4.10) for an unstiffened, flat, compression panel. The truss-core sandwich compression panel is the most efficient. The truss-core semisandwich compression panel is almost as efficient as the full sandwich, and may offer economic advantages over the full sandwich which overshadow the weight penalty involved. The more conventional zee and unflanged, integrally stiffened compression panels are considerably more efficient than the flat unstiffened panel, but at the same time are much less efficient than the sandwich compression panels. It is expected that variations on this general approach to stiffening will not improve efficiency significantly over that shown for the zee-stiffened compression panel.

At high values of the loading-material index, the differences between types of compression panels are less pronounced. In fact, it will be demonstrated in subsection 4.3 that when high plastic stresses are developed in each type of construction, no difference in efficiency exists. In this instance, economics rule the choice of type of panel.

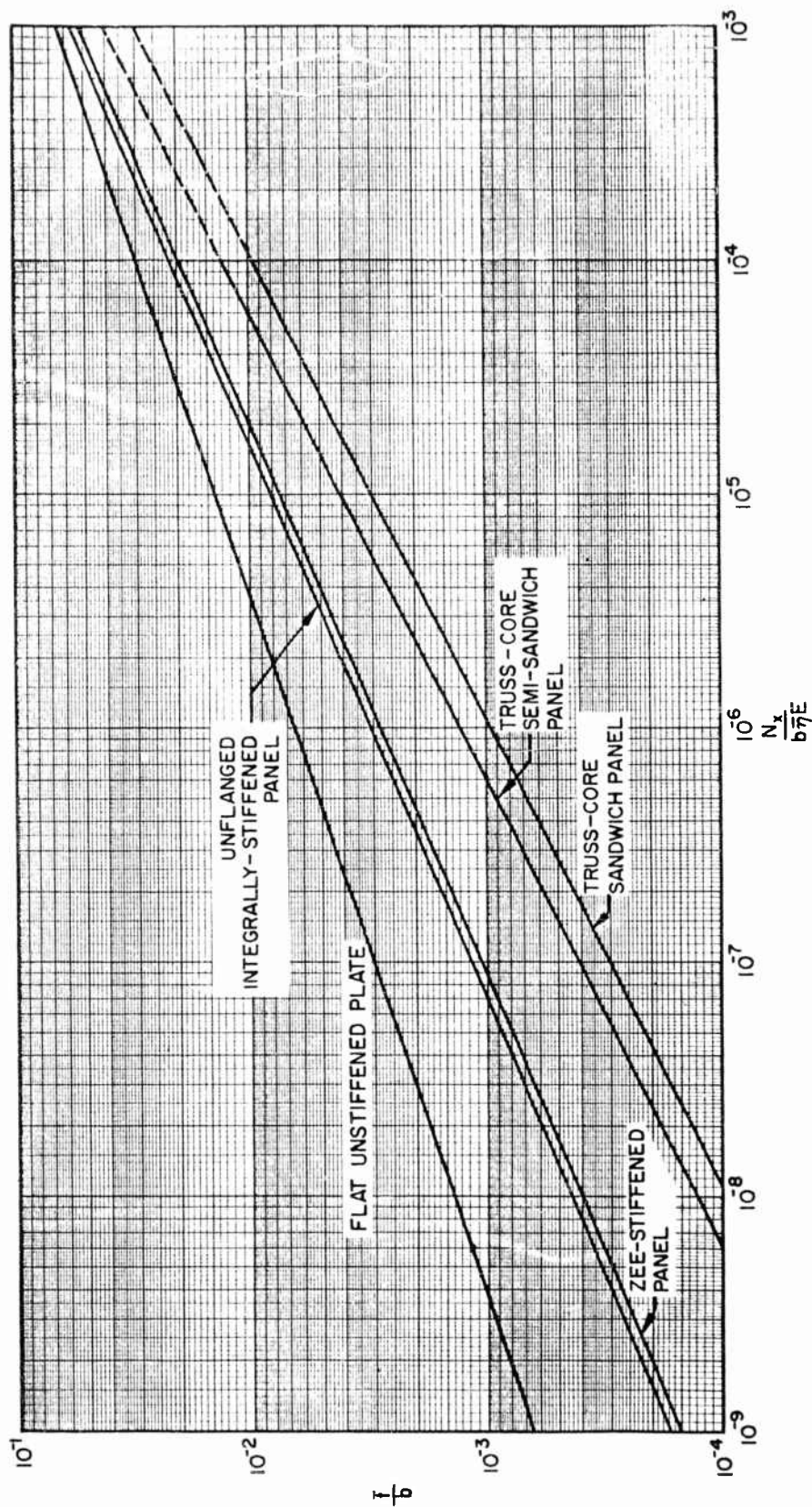


Fig. 4-15 Comparison of the Minimum-Weight Envelopes of the Several Types of Stiffened Panel Construction When Subjected to a Compression Load in the Direction of the Stiffening Elements

4.2.3 Shear Panels

Introduction. Minimum-weight design information is presented in this subsection for truss-core sandwich shear panels. A comparison between this type of shear panel and an unstiffened shear panel is also given.

Unstiffened shear panel. Buckling of an unstiffened shear panel may be predicted with Eq. (3.2). If it is assumed that the aspect ratio of the panel is sufficiently large to be considered infinite, and the edges of the panel are all simply supported, then $K_s = 5.35$. The following elastic efficiency equation may be obtained if, in addition, $\mu = 0.30$, $t = \bar{t}$, and $\eta_L = 1$:

$$\frac{N_{xy}}{bE} = 4.85 (\bar{t}/b)^3 \quad (4.21)$$

N_{xy} is the shear loading per unit length.

Truss-core sandwich shear panel. The following minimum-weight design information is taken from Ref. 4-3, and does not account for effects of either transverse shear stiffness or plasticity. The former effect has been demonstrated to be of negligible importance in lightly loaded truss-core sandwich compression panels (Ref. 4-3), and the same conclusion is assumed to apply for shear loading also. Plasticity correction factors applying to the local and general modes of instability in a truss-core sandwich shear panel are not available as yet. However, since sandwich construction is usually reserved for low loadings where significant weight savings can be made over flat or other types of stiffened shear panels, an elastic analysis appears appropriate and useful here.

The cross-sectional geometry of a truss-core sandwich shear panel is the same as shown in Fig. 4-5. The following equation is used to determine the critical shearing

force for the general mode of instability:

$$N_{xy_G} = \frac{4 \left(16.53 - 3.55 \sqrt{\frac{D_x/D_f}{D_y/D_f}} \right) D_f \sqrt{\frac{D_x}{D_f} \left(\frac{D_y}{D_f} \right)^3}}{b^2} \quad (4.22)$$

Definitions of the various parameters, other than b , are identical to those given in the discussion of truss-core sandwich compression panel in subsection 4.2.2.

The critical shearing force in both the core and the facing elements must be considered for the local mode of instability, since there is no existing analysis that accounts for the interaction between these elements. Therefore:

$$\frac{N_{xy_f}}{E} = \frac{\left(2 + \frac{t_c}{t_f} \cos \theta \right)}{\left(2 + \frac{t_c}{t_f} \frac{1}{\cos \theta} \right)} (\bar{t}) \frac{K_s \pi^2}{12(1 - \mu^2)} \left(\frac{t_f}{b_f} \right)^2 \quad (4.23)$$

$$\frac{N_{xy_c}}{E} = \frac{\left(2 + \frac{t_c}{t_f} \cos \theta \right)}{\left(2 + \frac{t_c}{t_f} \frac{1}{\cos \theta} \right)} (\bar{t}) \frac{K_s \pi^2}{12(1 - \mu^2)} \left(\frac{t_f}{b_f} \right)^2 \left(\frac{t_c}{t_f} \right)^2 4 \cos \theta \quad (4.24)$$

These equations are expansions of the classical buckling equation [Eq. (3.2)] which are in a convenient form for performing a minimum-weight analysis.

Minimum-weight results when the panel is so proportioned that the lowest modes of instability have equal critical stresses. Because the local mode of instability is

represented by two equations, the minimum-weight analysis must deal with the combination of Eqs. (4.22) and (4.23), and also the combination of Eqs. (4.22) and (4.24). The former combination of equations yields the following efficiency equation:

$$\frac{N_{xy}}{b} \frac{1}{E} = \mathcal{E}_f \left(\frac{\bar{t}}{b} \right)^2$$

The latter combination of equations yields this efficiency equation:

$$\frac{N_{xy}}{bE} = \mathcal{E}_c \left(\frac{\bar{t}}{b} \right)^2$$

An evaluation of both \mathcal{E}_f and \mathcal{E}_c is presented in Fig. 4-16, using $K_s = 5.35$ and $\mu = 0.3$. The values of \mathcal{E}_c and \mathcal{E}_f are represented by the positive and negative slopes of the individual θ curves, respectively. Only the critical, or lower, efficiency factor is shown at each value of t_c/t_f and θ . The maximum efficiency factor, \mathcal{E}_{\max} , is 1.725 and it occurs when t_c/t_f is approximately 0.817 and θ is approximately 68 deg. The minimum-weight equation for elastically loaded truss-core sandwich shear panels therefore, is:

$$\frac{N_{xy}}{bE} = 1.725 \left(\frac{\bar{t}}{b} \right)^2 \quad (4.25)$$

The following supplemental equations are necessary for design:

$$t_f = \frac{\bar{t}}{2 + \frac{t_c}{t_f} \cdot \frac{1}{\cos \theta}} \quad (4.26)$$

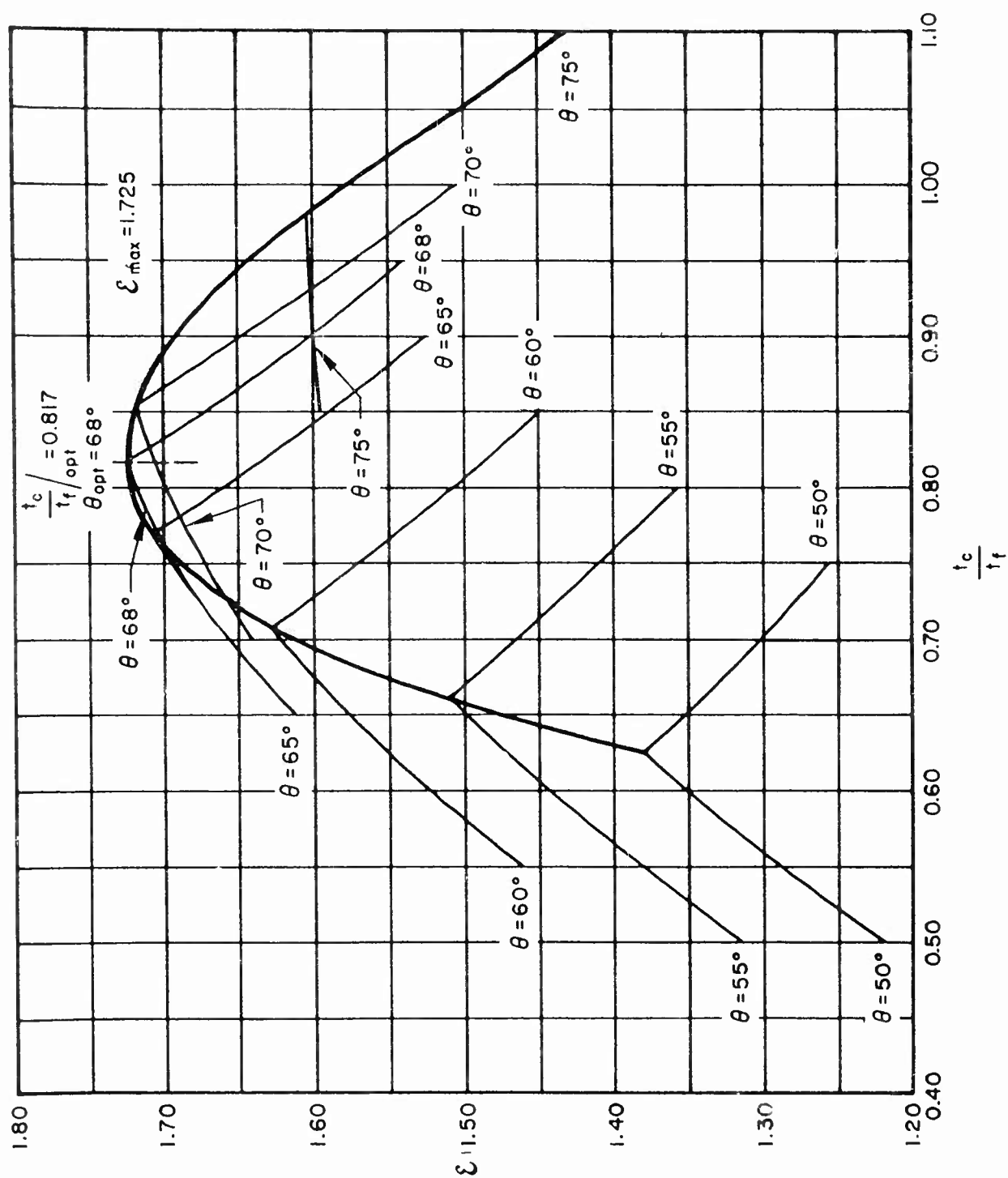


Fig. 4-16 Efficiency Chart for Truss-Core Sandwich Shear Panels

$$b_f = 2.2 t_f \sqrt{\frac{\left(2 + \frac{t_c}{t_f} \cos \theta\right) \bar{t}}{\left(2 + \frac{t_c}{t_f} \frac{1}{\cos \theta}\right) N_{xy}/E}} \quad (4.27)$$

$$b_c = \frac{b_f}{2 \cos \theta} \quad (4.28)$$

The equation for b_f depends upon the highest \mathcal{E} for each θ occurring when both local modes of instability have the same critical stress. When this happens, the efficiency equation may be written in the general form:

$$\frac{N_{xy}}{bE} = \mathcal{E} \left(\frac{\bar{t}}{b} \right)^2$$

Reference to Fig. 4-16 indicates that both local modes of instability do have the same critical stress at the highest value of \mathcal{E} for the θ 's shown. This is represented by the highest \mathcal{E} for each θ occurring at the intersection of \mathcal{E}_c and \mathcal{E}_f . It appears that this will not be the case beginning when θ is something greater than 75 deg; however, since \mathcal{E}_{\max} is considerably greater than any \mathcal{E} obtainable when θ is greater than 75 deg, equations and graphical data covering these latter designs are not presented here.

The minimum-weight truss-core sandwich shear panel, represented by Eq. (4.25), is compared with Eq. (4.21) for a flat, unstiffened shear panel in Fig. 4-17. A truly significant weight advantage is demonstrated by the sandwich shear panel over the unstiffened shear panel, particularly at low values of the loading-material index.

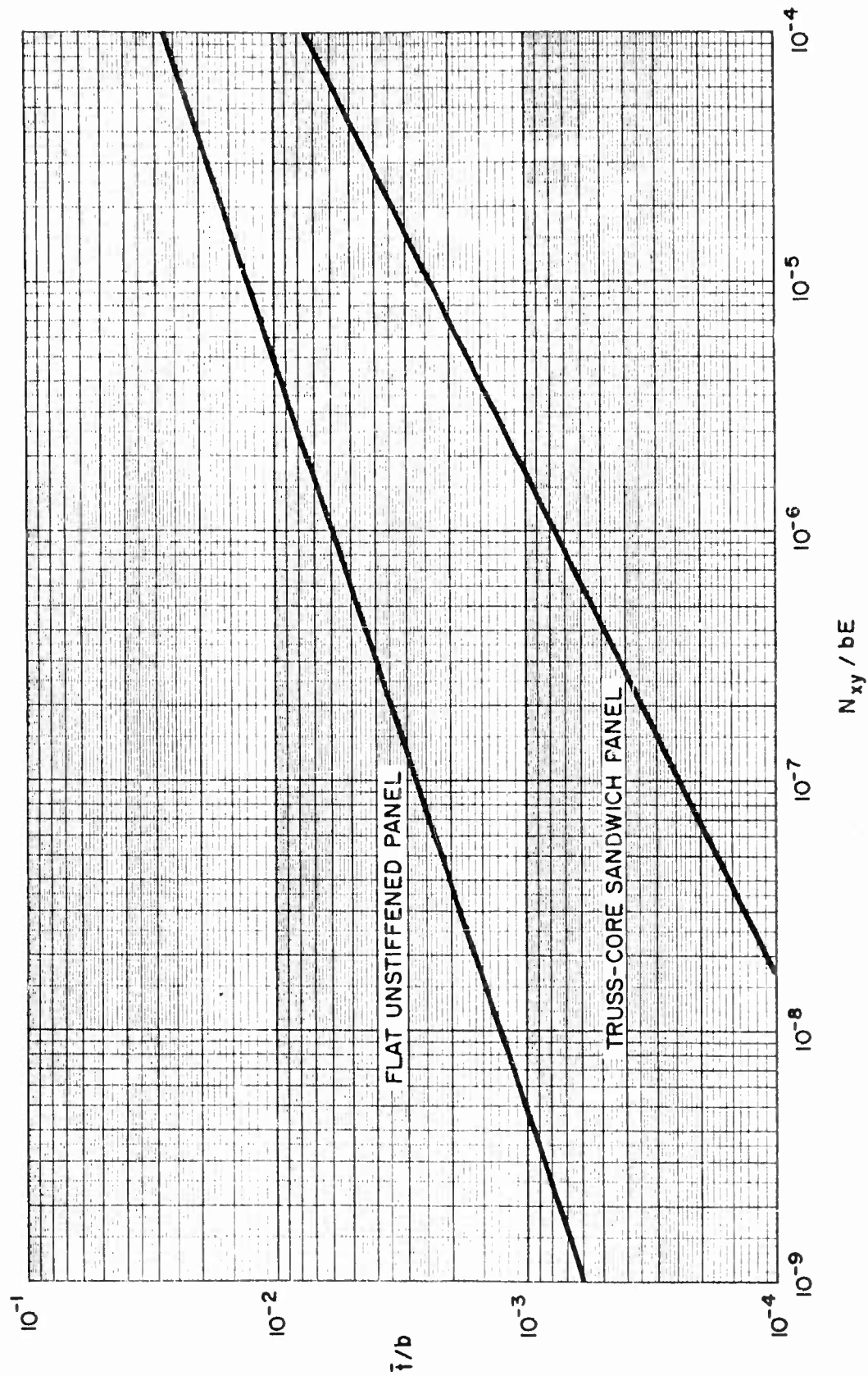


Fig. 4-17 Comparison Between Minimum Weight, Truss-Core Sandwich Shear Panel and a Flat Unstiffened Panel

4.2.4 Multiweb Box Beams

Introduction. Minimum-weight design information for multiweb box beams in pure bending may be developed by determining the most efficient combination of covers and webs, where these elements themselves are optimized according to the minimum-weight design information presented in subsections 4.2.1 and 4.2.2. The information to be presented here applies to rectangular box beams in which the effect of shear buckling in the webs is neglected, and it is assumed that the applied moment is carried only by the covers. It is based on the unpublished analysis of Jacobsen and Crawford (Ref. 4-10), which parallels the work of Crawford and Semonian (Ref. 4-11) and Shanley (Ref. 4-2). Since some new terminology and techniques will be introduced here, a brief resumé of the analysis is presented in the following paragraphs.

Multiweb box beam minimum-weight analysis. The orientation between structure and load to be considered is shown in Fig. 4-18.

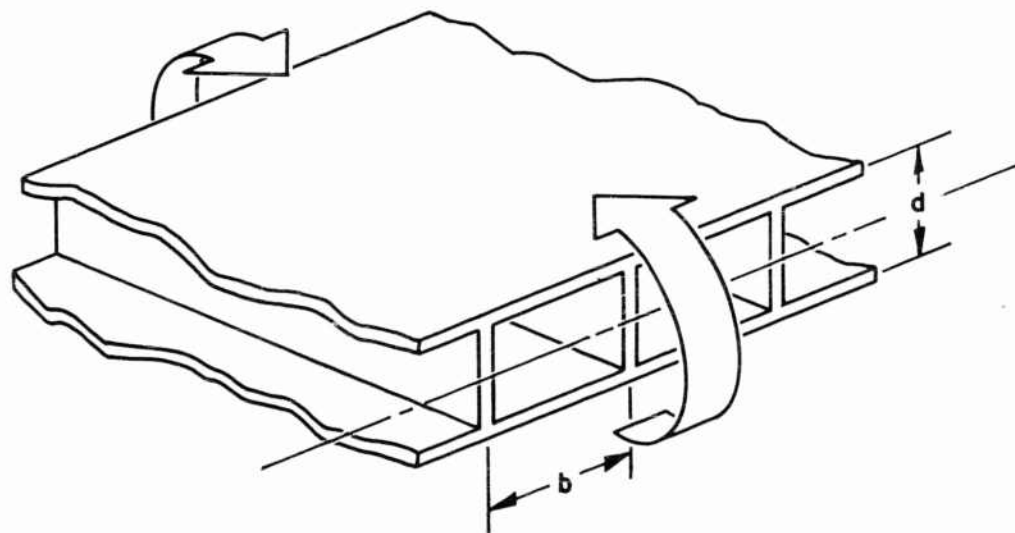


Fig. 4-18 Schematic of Multiweb Box Beam in Bending

Such a structure will be analyzed for the three following modes of instability. As in previous minimum-weight analyses, instability is considered failure; i. e., no post-buckling strength can be developed. Further, it is assumed that there is no interaction between the various modes of instability.

- (1) Local mode of instability in the compression cover
- (2) Wrinkling or general mode of instability in the webs and covers
- (3) Flexure-induced crushing of the webs

The first mode of instability results in lateral deflections of the compression cover while the webs provide straight and rigid lines of simple support. The minimum-weight information of subsection 4.2.2 is applicable here to optimize the cover structure between web supports. The wrinkling or general mode of instability has been analyzed by Semonian (Ref. 4-12), and is characterized by a washboard buckle pattern, principally in the compression cover, brought about by insufficient stiffness in the webs. The third mode of instability can be treated with wide-column analysis if it is assumed that the webs are long in relation to their height, which is usually the case in practice. It is apparent, therefore, that the covers are designed by the first mode of instability, while the webs are designed by the second and third modes of instability, the former specifying stiffness, the latter specifying strength. Crawford and Semonian (Ref. 4-11) have shown that minimum-weight, box-beam proportions do not result when all three modes are critical simultaneously. Therefore, modes (1) and (2) and modes (1) and (3) must be treated separately, with the heavier resulting design governing.

Following are terms which are peculiar to the minimum-weight analysis of box beams in this subsection. Foremost, a weight term similar to \bar{t} in panels and cylinders is required. The term solidity, Σ , will be used, which is defined as the fraction of the total enclosed area of cross section occupied by the compression structure. In addition:

\bar{t}_p = equivalent thickness of the compression cover for weight purposes

\bar{t}_w = equivalent thickness of the webs for weight purposes

M_i = bending moment per unit length of chord

and b and d are as noted in Fig. 4-18. Solidity may therefore be expressed as shown in Eq. (4.29).

$$\Sigma = \frac{\bar{t}_p \cdot b + \bar{t}_w \cdot d}{bd} = \frac{\bar{t}_p}{b} \left(\frac{b}{d} \right) + \frac{\bar{t}_w}{d} \left(\frac{d}{b} \right) \quad (4.29)$$

The loading-material index may be expressed as shown in Eq. (4.30):

$$\frac{M_i}{d^2} \cdot \frac{1}{\bar{\eta}E} = \left(\frac{N_x \cdot d}{d^2} \right) \frac{1}{\bar{\eta}E} = \frac{N_x}{d} \cdot \frac{1}{\bar{\eta}E} = \frac{N_x}{b} \left(\frac{b}{d} \right) \frac{1}{\bar{\eta}E} \quad (4.30)$$

The assumption is made in Eq. (4.30) that all thicknesses and stiffener heights are negligible compared to b and d . The effects of plasticity will not be considered in this analysis. Therefore $\bar{\eta} = 1$ and the loading-material index is simply $\frac{M_i}{d^2 E}$. It will be demonstrated that solidity and the loading-material index can be expressed in an efficiency equation of the form of Eq. (4.31):

$$\Sigma = C \left[\frac{M_i}{d^2 E} \right]^j \quad (4.31)$$

where C and j are quantities which represent a particular combination of structure in the box-beam covers and webs. Note that Eq. (4.31) is in the same form as the efficiency equations developed in subsection 4.2.1 and 4.2.2. These are reproduced in general form as shown below for the elastic case. Note that in these equations the dependent variable is the material-loading index, while in Eq. (4.31) it is the weight index.

$$\frac{N_x}{bE} = \mathcal{E}_p \left(\frac{\bar{t}_p}{b} \right)^m \quad \text{compression panel} \quad (4.32)$$

$$\frac{N_x}{dE} = \mathcal{E}_w \left(\frac{\bar{t}_w}{d} \right)^n \quad \text{wide column} \quad (4.33)$$

Equations for the local and wrinkling modes of instability [modes (1) and (2) previously presented] are combined as follows to yield a solidity equation. The equation for local instability, Eq. (4.32), may be rewritten in the following form after substituting M_i/d for N_x :

$$\frac{\bar{t}_p}{b} = \left(\frac{1}{\mathcal{E}_p} \frac{M_i}{d^2 E} \frac{d}{b} \right)^{1/m} \quad (4.34)$$

Referring to the work of Semonian (Ref. 4-12), it may be shown that when

$$\frac{E \bar{t}_w d^3}{\pi^2 b D_x} > 10 \quad (4.35)$$

the following equation represents the web's equivalent thickness requirements for wrinkling instability:

$$\frac{\bar{t}_w}{d} = \frac{8}{9} b \sqrt{\frac{dE}{D_x}} \left[\frac{M_i}{d^2 E} \right]^{3/2} \quad (4.36)$$

where D_x = flexural stiffness of the composite cover plate. Use of this expression implies that the web-cover joint is monolithic, the web resists cover deflection by only direct stress in the web and the web's stiffness may be spread out over the bay width.

Substituting Eqs. (4.34) and (4.36) into Eq. (4.29), solidity representing the combination of local and wrinkling modes of instability results:

$$\Sigma_{12} = \frac{b}{d} \left(\frac{1}{\mathcal{E}_p} \frac{M_i}{d^2 E} \frac{d}{b} \right)^{1/m} + \frac{d}{b} \left(\frac{8}{9} b \sqrt{\frac{dE}{D_x}} \left[\frac{M_i}{d^2 E} \right]^{3/2} \right) \quad (4.37)$$

It should be pointed out that the criterion of Eq. (4.35) covers most beams of interest.

In a similar manner, equations for the local mode of instability and flexure-induced crushing of the webs may be combined. The latter mode of instability has been treated by Shanley (Ref. 4-2), and by Crawford and Semonian (Ref. 4-11). The following equation, which is a function of both Eqs. (4.32) and (4.33), results:

$$\frac{\bar{t}_w}{d} = \left[\frac{2}{\mathcal{E}_w} \left(\frac{M_i}{d^2 E} \right)^{2 - 1/m} \mathcal{E}_p^{1/m} \left(\frac{b}{d} \right)^{1/m} \right]^{1/n} \quad (4.38)$$

Substituting Eqs. (4.34) and (4.38) into Eq. (4.29), a solidity equation representing the combination of local instability and flexure-induced crushing of the webs can be written:

$$\Sigma_{13} = \frac{b}{d} \left(\frac{1}{\mathcal{E}_p} \frac{M_i}{d^2 E} \frac{d}{b} \right)^{1/m} + \frac{d}{b} \left[\frac{2}{\mathcal{E}_w} \left(\frac{M_i}{d^2 E} \right)^{2 - 1/m} \mathcal{E}_p^{1/m} \left(\frac{b}{d} \right)^{1/m} \right]^{1/n} \quad (4.39)$$

Multiweb box beams of optimum proportions may now be determined by minimizing Σ with respect to $\frac{b}{d}$ in Eqs. (4.37) and (4.39), the larger Σ governing.

It is apparent that the required minimization of Eq. (4.37) cannot be generalized; that is, the factor D_x representing a particular cover geometry must be substituted. Therefore, this minimization will be presented for some specific examples later in this subsection.

However, Eq. (4.39) may be minimized in general terms. The result is shown in Eq. (4.40):

$$\Sigma_{13\min} = A \left[\mathcal{E}_w^{1-m} \mathcal{E}_p^{1-n} \left(\frac{M_i}{d^2 E} \right)^{2m-3+n} \right]^{1/(2mn-n-1)} \quad (4.40)$$

where

$$A = \left(\frac{1-2mn+n}{1-mn} \right) \left[2 \left(\frac{1-mn}{n-mn} \right)^n \right]^{(m-1)/(2mn-n-1)}$$

The optimum value of $\frac{b}{d}$ derived from this minimization is given below:

$$\left(\frac{b}{d} \right)_{\text{opt}} = \left[\left(\frac{1-mn}{n-mn} \right)^{2^{1/n}} \left(\frac{M_i}{d^2 E} \right)^{(2m-1-n)/mn} \mathcal{E}_w^{-1/n} \mathcal{E}_p^{(1+n)/mn} \right]^{(mn)/(2mn-n-1)} \quad (4.41)$$

Values of A in Eq. (4.40) are presented graphically in Fig. 4.19. Note that Eq. (4.40) is an efficiency equation of the form of Eq. (4.31). The foregoing equations will be used to analyze several box-beam configurations in the following paragraphs.

Multiweb box-beam minimum-weight design. Minimum weight for multiweb box-beams simultaneously critical in local instability and flexure induced crushing of the webs may be found for particular types of cover and web construction by substituting \mathcal{E}_w and n for the wide-column (web) designs (subsection 4.2.1), and \mathcal{E}_p and m for the compression panel (cover) designs (subsection 4.2.2) into Eq. (4.40). A series of such substitutions have been made and are shown in Fig. 4-20. The data used in these calculations are shown in Table 4-1.

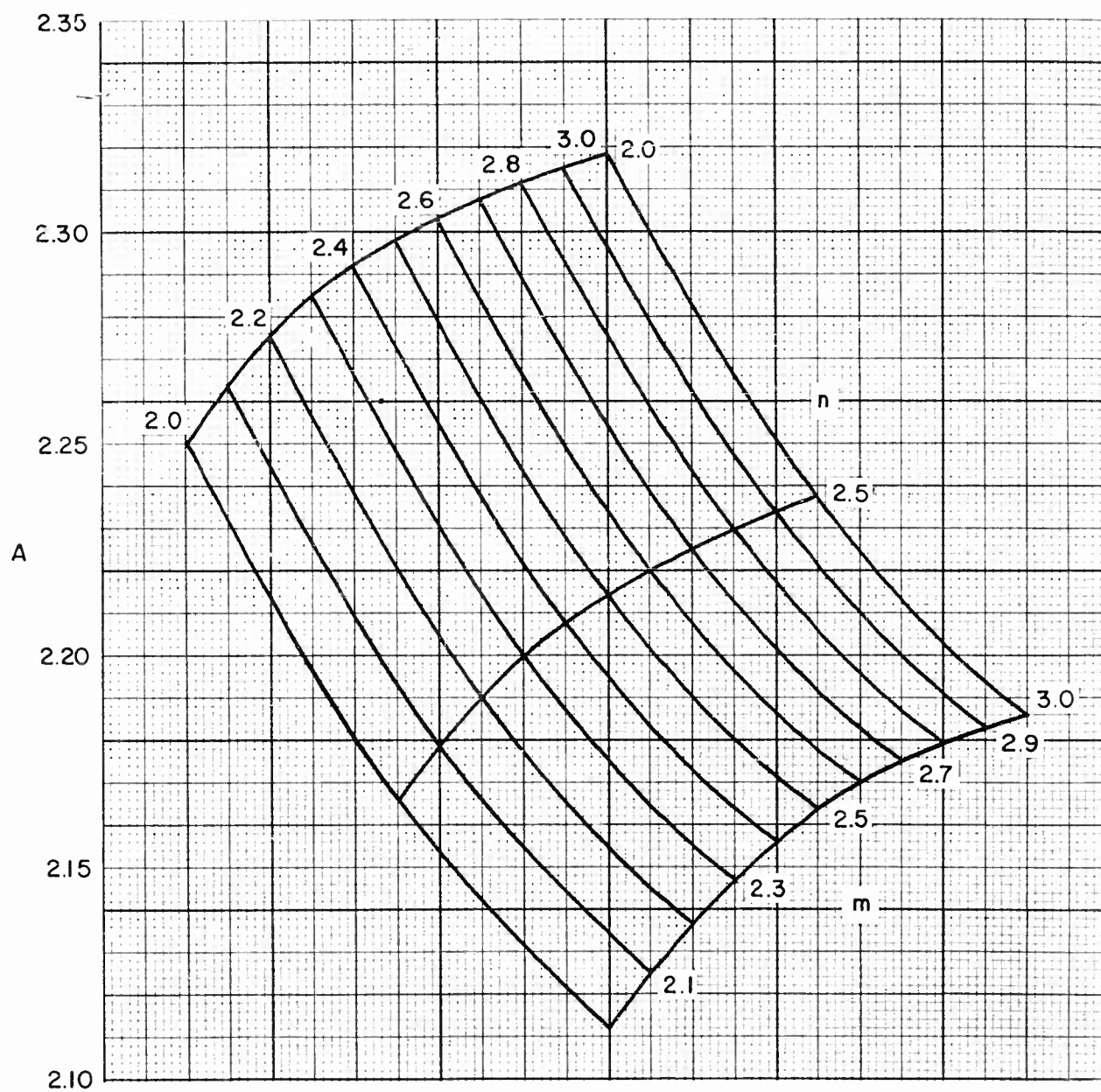


Fig. 4-19 Values of A as a Function of m, n [Ref. Eq. (4.40)]

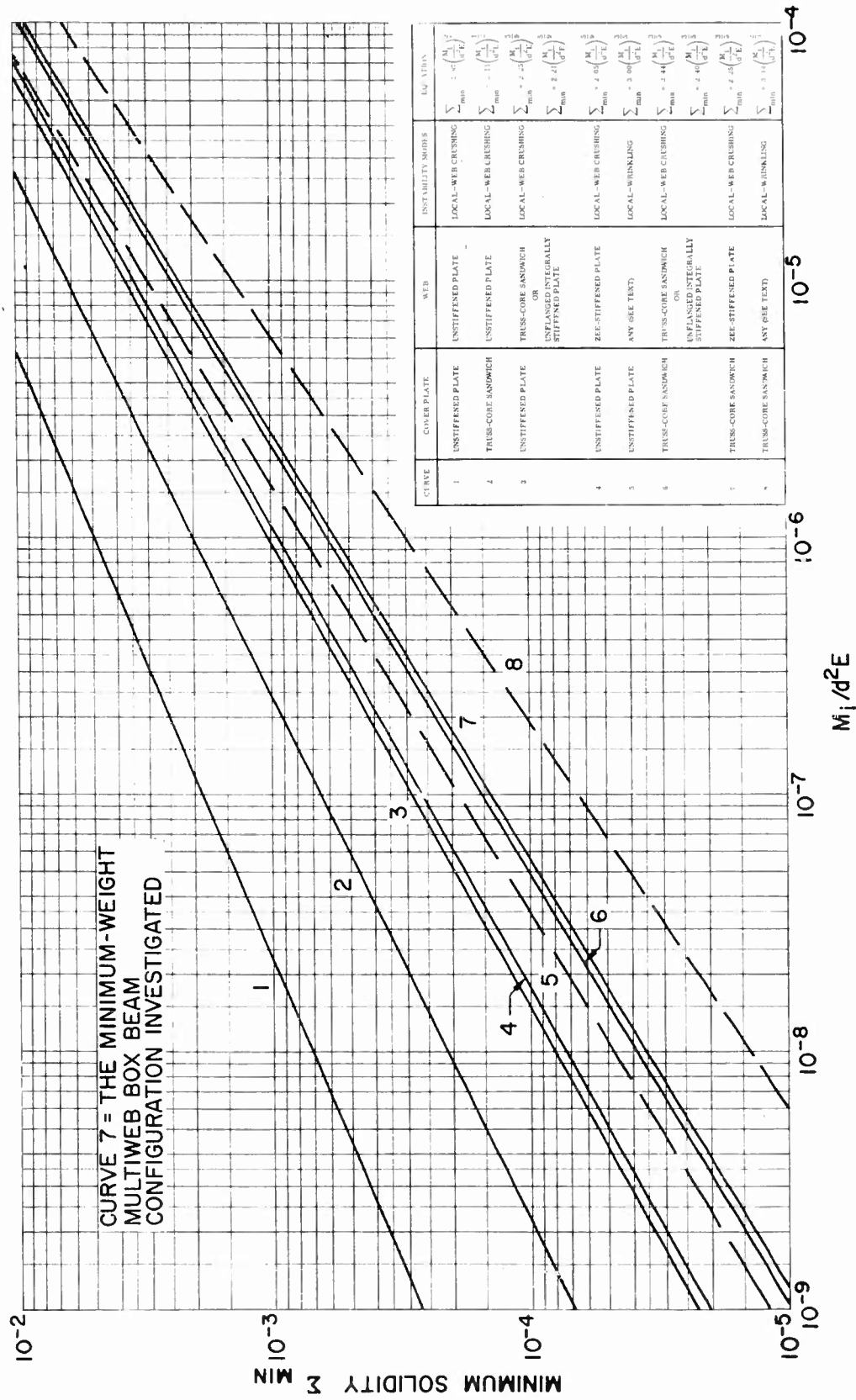


Fig. 4-20 Comparison of the Elastic Minimum-Solidity Equations for Several Multiweb Box Beams Composed of Different Combinations of Cover Plate and Web Construction (Two Combinations of Instability Modes Investigated)

Table 4-1

MINIMUM-WEIGHT EFFICIENCY FACTORS AND EXPONENTS FOR
WIDE COLUMNS AND COMPRESSION PANELS

Construction	\mathcal{E}_p	m	\mathcal{E}_w	n
Unflanged integrally stiffened	0.970	2.38	0.656	2
Zee-stiffened	1.030	2.36	0.911	2
Truss-core sandwich	1.108	2.00	0.605	2
Flat, unstiffened plate	3.62	3.00	0.823	3

Similar calculations follow for particular cover and web geometries when local instability and wrinkling instability are simultaneously critical. The procedure involves substitution of D_x into Eq. (4.37) and minimizing the resulting equation. Note that Eq. (4.37) is a function of cover-plate parameters only. Thus, the choice of web construction is independent of the choice of cover-plate construction. In the following paragraphs, truss-core sandwich cover plates and flat, unstiffened cover plates will be investigated. The resulting equations are applicable for any web construction meeting the requirements set forth in Eq. (4.36).

Truss-Core Sandwich Cover Plates

The expression for D_x may be obtained following Eq. (4.14), rearranged in terms of $\frac{M_1}{d^2 E}$ as shown in Ref. 4-10, and substituted in Eq. (4.37). The equation for $\Sigma_{12_{\min}}$ after substitutions for \mathcal{E}_p and m have been made is shown below:

$$\Sigma_{12_{\min}} = 3.14 \left(\frac{M_1}{d^2 E} \right)^{2/3} \quad (4.42)$$

The corresponding optimum value of $\frac{b}{d}$ is given in Eq. (4.43):

$$\left(\frac{b}{d}\right)_{\text{opt}} = 4.83 \left(\frac{M_i}{d^2 E}\right)^{1/3} \quad (4.43)$$

Equation (4.42) is shown plotted on Fig. 4-20.

Flat Unstiffened Cover Plates

For this construction,

$$D_x = \frac{Et_f^3}{12(1-\mu^2)}$$

where t_f is the thickness of the cover plate. Substituting this equation in Eq. (4.37), minimizing, and substituting for \mathcal{E}_p and m results in Eq. (4.44).

$$\Sigma_{12_{\text{min}}} = 3.00 \left(\frac{M_i}{d^2 E}\right)^{3/5} \quad (4.44)$$

The optimum value of $\frac{b}{d}$ in this case is:

$$\left(\frac{b}{d}\right)_{\text{opt}} = 4.61 \left(\frac{M_i}{d^2 E}\right)^{2/5} \quad (4.45)$$

Equation (4.44) is also shown plotted in Fig. 4-20.

Summary. It can be noted from Fig. 4-20 that the solidity requirements at practical values of the loading-material index for simultaneous buckling due to local instability and wrinkling instability are less than those for simultaneous buckling due to local instability and flexure-induced crushing of the webs for a given cover plate configuration. Thus, the latter combination of instability modes is critical and wrinkling will not occur if proper joint design is provided. Of the box beams investigated for the local-crushing critical combination of instability modes, the one having truss-core sandwich cover plates and zee-stiffened webs is the most efficient.

By referring to Figs. 4-8 and 4-15, it is noted that the zee-stiffened wide-column and the truss-core sandwich compression panel are the most efficient among the wide-column and compression-panel configurations investigated. The obvious may therefore be concluded: The most efficient compression panel (cover) in combination with the most efficient wide column (web) makes the most efficient multiweb box beam.

It may be concluded from Fig. 4-20 that if the designer's choice of an efficient construction is restricted to either cover plates or webs, an efficient web construction should be chosen (compare curves 1, 2, and 3). Further investigation by the designer will show that the web structure has often been overdesigned in the past and that the required web weight for optimum design is a small percentage of the total multiweb box-beam weight. The webs, therefore, are more likely to be critical in shear in an optimum multiweb box-beam design. However, it may be demonstrated that because of the small overall contribution of the minimum-weight webs to total weight of the beam, large percentage increases may be made in the web weight to carry shear without seriously altering the data given in this subsection.

4.2.5 Axially Loaded Cylinders

Introduction. Minimum-weight design information for axially loaded, stiffened cylinders is presently available in the literature only for truss-core sandwich cylinders. This information, together with information for monocoque cylinders, is presented in the following paragraphs. The relative efficiencies of these two types of axially loaded cylinders are discussed briefly.

Monocoque cylinder. Buckling of a long monocoque cylinder may be predicted using Eq. (3.4) presented in subsection 3.3.1. If buckling coefficients based on 50-percent probability are used (Fig. 3-12), and t is taken equal to \bar{t} , η equal to $\bar{\eta}$, the following efficiency equation results:

$$\frac{N_x}{R\bar{\eta}E} = 7.26 \left(\frac{\bar{t}}{R} \right)^{2.54} \quad (4.46)$$

This equation is applicable when $L/R \geq 0.75$, $t > 0.005$, and $R/t > 100$. The quantity $\bar{\eta}$ is taken equal to $\sqrt{E_T/E}$. N_x is the axial load per unit of circumferential length. Equations similar to Eq. (4.46) may be written when $R/t < 100$ and/or $L/R < 0.75$; however, the majority of cylinder designs of interest are represented by Eq. (4.46). Equations for these latter limitations, therefore, are not presented.

Truss-core sandwich cylinder. The minimum-weight analysis for truss-core sandwich cylinders referenced here is that of Crawford and Stuhlman (Ref. 4-13). This analysis pertains to a cylinder geometry wherein the corrugations extend in the axial direction as shown in Fig. 4-21. This analysis is based on existing small-deflection theory. While this theory is known to be inaccurate for monocoque cylinder design, it appears reasonable in this case. Tests of monocoque cylinders generally indicate that the thicker the cylinder wall, the closer the correlation between test and small-deflection theory, even though the size of the average imperfection, to which deviation is generally attributed, remains approximately constant. Thus a sandwich cylinder

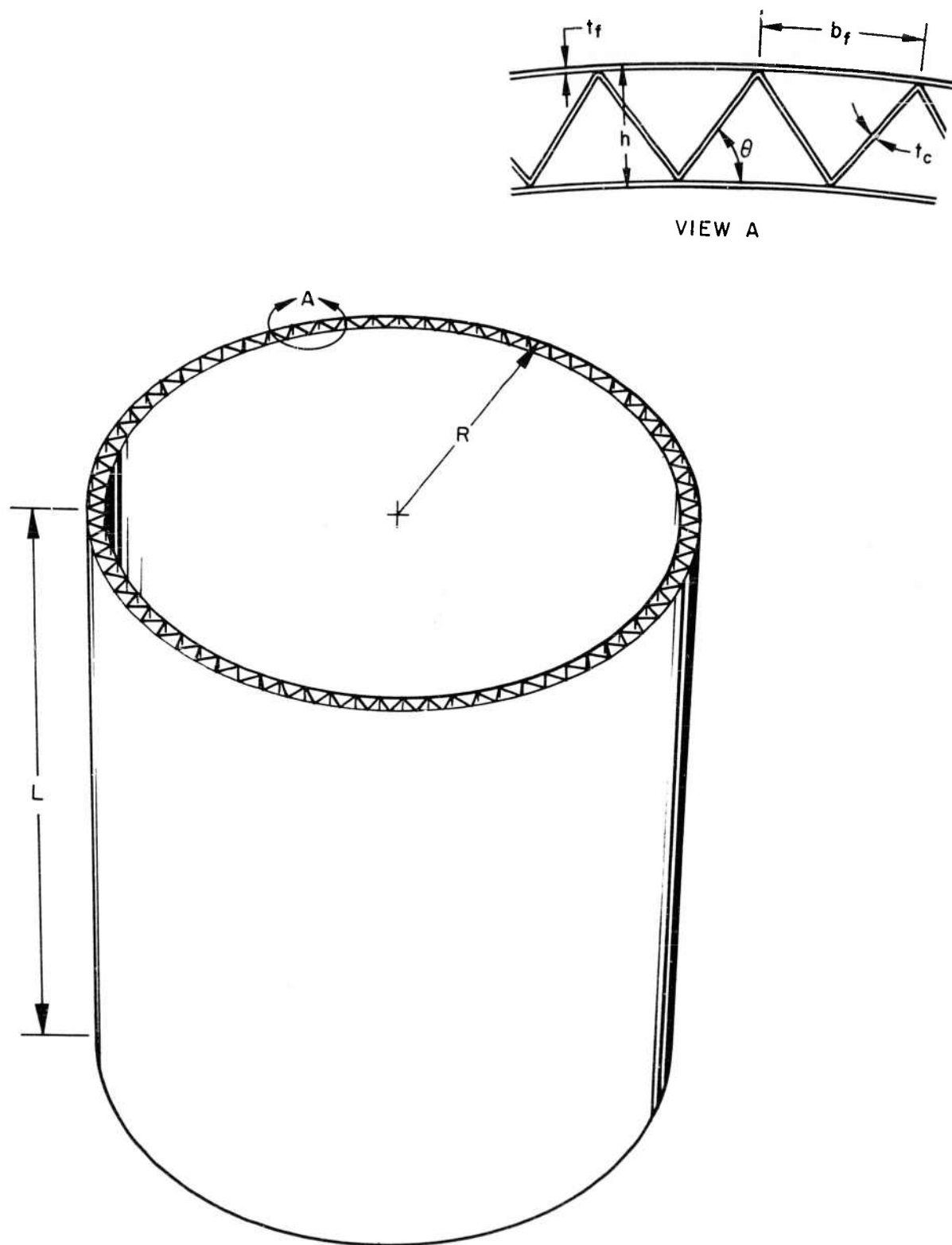


Fig. 4-21 Geometry of Truss-Core Sandwich Cylinder

should be predictable by small-deflection theory in view of its large wall thickness compared to a monocoque cylinder wall thickness of similar load-carrying ability. This reasoning at present has not been validated by test, and should accordingly be viewed with some skepticism. The following data are based on the assumption of sufficient core stiffness and attachment area, which, if available, should prevent premature failure and therefore substantiate the analysis. Thus, details of fabrication are important in obtaining the efficiencies indicated here. It is also assumed that the core and facings are of the same material, and that the facings are of equal thickness. Effects of curvature are included in the general instability analysis but are neglected in the local instability analysis. It is assumed that there is no coupling between these two modes of instability. The effects of transverse shear stiffness have been found to be negligible for the idealized construction as was the case in previous truss-core applications in this report (see subsections 4.2.1 through 4.2.3). The application of the information presented here is limited to cylinders having $R/h (L/R)^2 > 5$.

Buckling due to general instability in a truss-core sandwich cylinder may be determined from the following equation:

$$\sigma_{crG} = \frac{0.50\eta_G E \frac{b_f}{R} \tan \theta}{\left[1 + \frac{1}{2} \frac{t_c}{t_f} \frac{1}{\cos \theta}\right]} \sqrt{\frac{1 + \frac{(1 - \mu^2)}{6} \frac{t_c}{t_f} \frac{1}{\cos \theta}}{(1 - \mu^2)}} \quad (4.47)$$

where

$$\eta_G = \sqrt{\frac{2\eta_T}{1 + \eta_T}}$$

and the geometry is as defined in Fig. 4-21. To determine buckling due to local instability in a truss-core sandwich cylinder, Eq. (4.7) may be used.

The following efficiency equation results when Eqs. (4.7) and (4.47) are combined according to the methods of minimum-weight analysis:

$$\frac{N_x}{R\bar{\eta}E} = \mathcal{E} \left(\frac{\bar{t}}{R} \right)^{5/3}$$

where

$$\bar{\eta} = \left[\frac{2\eta_T^{3/2}}{1 + \eta_T} \right]^{1/3}$$

An evaluation of the efficiency factor \mathcal{E} is presented in Fig. 4-22. From this figure it is noted that \mathcal{E}_{\max} is 0.4423 and that this value of \mathcal{E} occurs when $\theta = 55$ deg and $t_c/t_f = 0.65$. The minimum-weight equation may therefore be expressed as follows:

$$\frac{N_x}{R\bar{\eta}E} = 0.4423 \left(\frac{\bar{t}}{R} \right)^{5/3} \quad (4.48)$$

Additional equations necessary for design purposes are presented below:

$$t_f = \frac{\bar{t}}{2 + \frac{t_c}{t_f} \frac{1}{\cos \theta}}$$

$$b_c = \frac{b_f}{2 \cos \theta}$$

$$b_f = 0.95 t_f \sqrt{\frac{K_x (\bar{t}/R)}{N_x/R\eta_L E}}$$

where $\eta_L = \sqrt{\eta_T}$, and K_x is determined from Fig. 4-6.

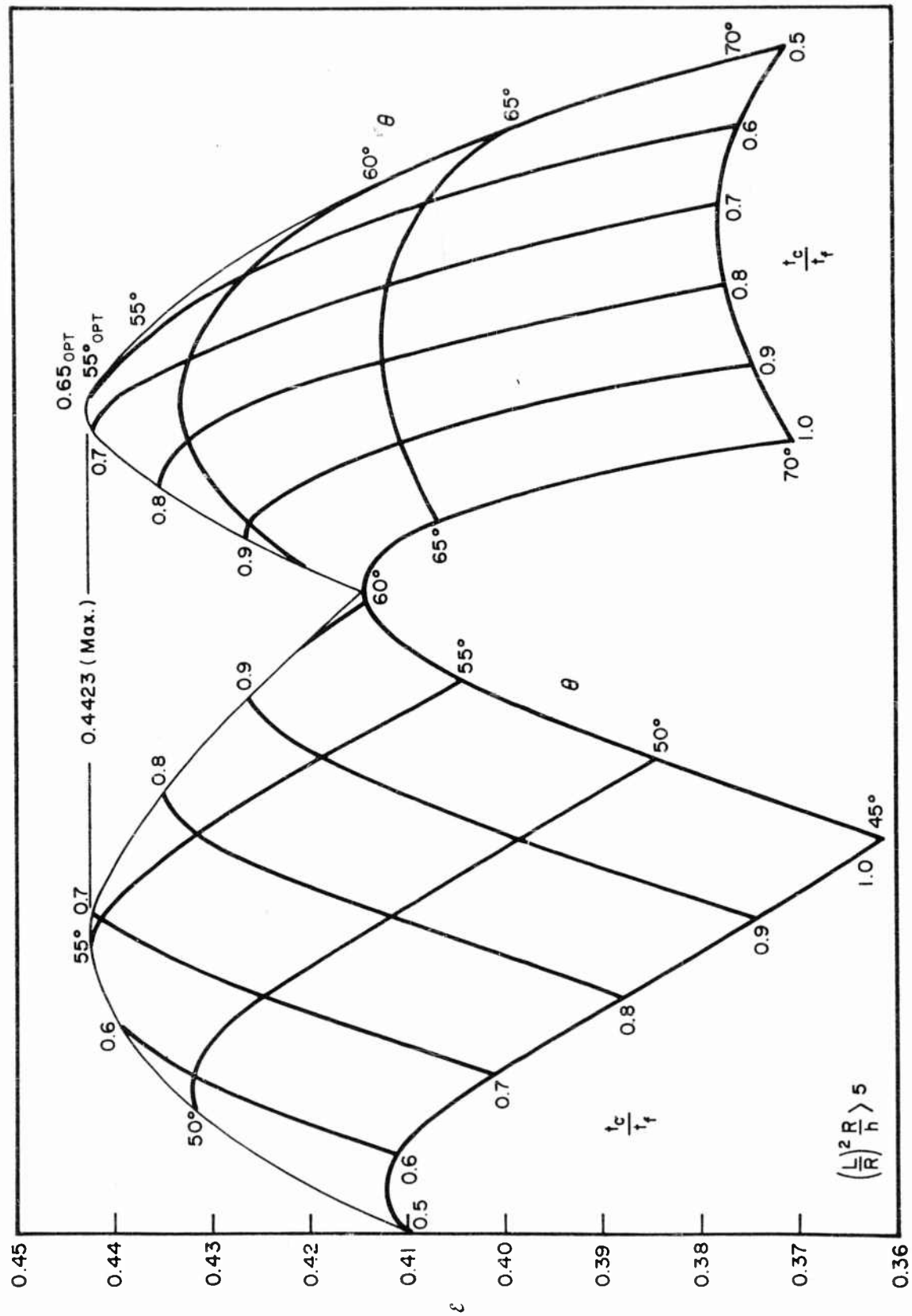


Fig. 4-22 Efficiency Factors for Truss-Core Sandwich Cylinders Under Uniform Axial Compression

The minimum-weight equation for axially loaded truss-core sandwich cylinders [Eq. (4-48)] is nondimensionally compared with the efficiency equation for monocoque axially loaded cylinders [Eq. (4-46)] in Fig. 4-23. The truss-core sandwich construction is seen to be much more efficient than the monocoque construction at low loading-material indexes and to a lesser degree at high loading-material indexes.

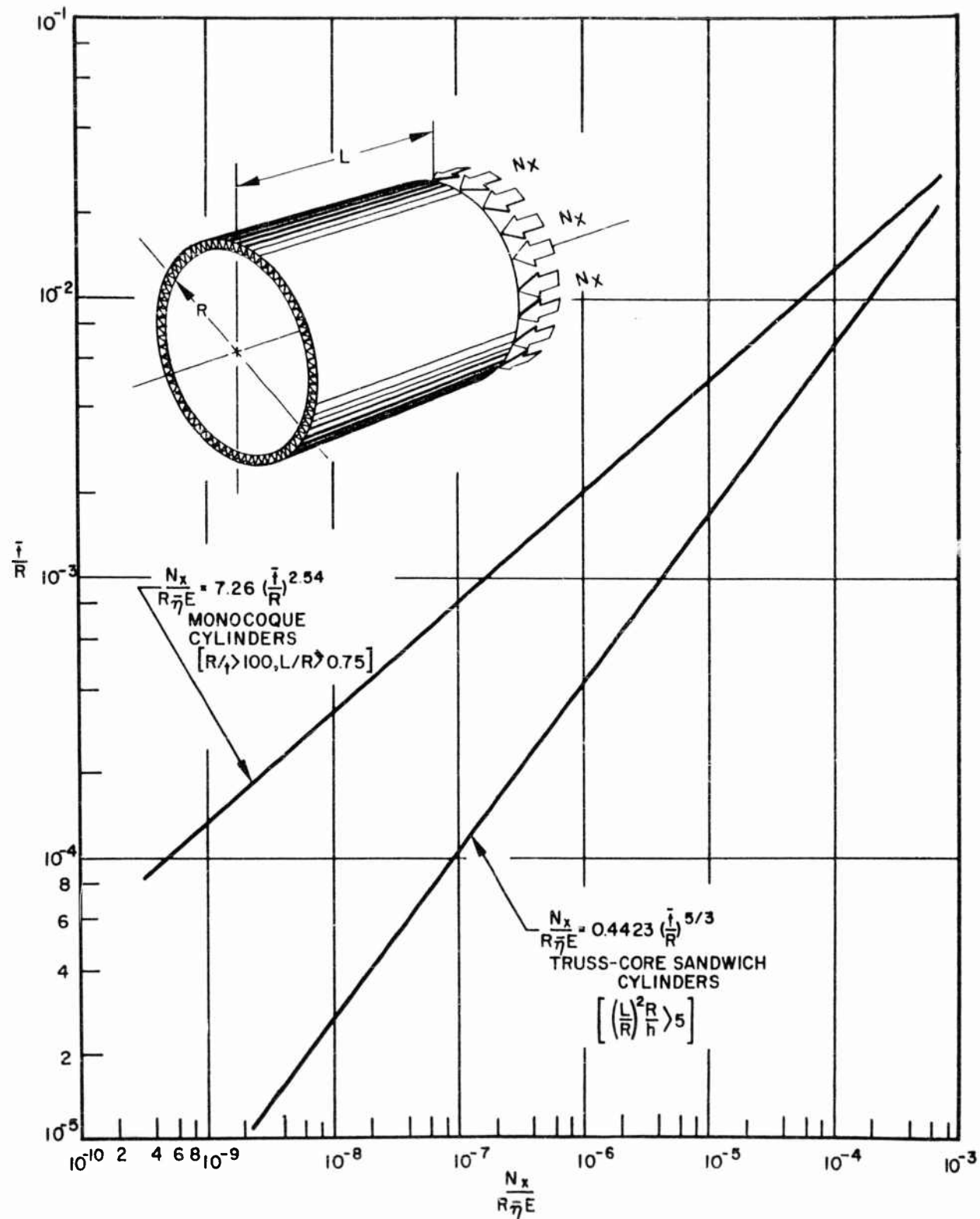


Fig. 4-23 Comparative Efficiencies of Monocoque and Optimum Truss-Core Sandwich, Long Cylinders Subjected to Uniform Axial Compression

4.2.6 Cylinders in Torsion

Introduction. Minimum-weight design information is presented in this section for truss-core sandwich cylinders. An efficiency equation for a monocoque cylinder in torsion is also shown, as are the comparative efficiencies of truss-core sandwich cylinders and monocoque cylinders.

Monocoque cylinder. Equation (3.9), presented in subsection 3.3.2 of this report, may be used to predict buckling of a moderate-length monocoque cylinder in torsion having simply supported edges. For cylinders having $L/R = 1$, the following elastic efficiency equation may be derived:

$$\frac{N_{xy}}{RE} = 0.741 \left(\frac{\bar{t}}{R} \right)^{9/4} \quad (4.49)$$

where $t = \bar{t}$ and N_{xy} is the shear load per unit of circumferential width (commonly referred to as shear flow). Similar equations may be written for moderate-length monocoque cylinders having L/R ratios other than one or clamped-edge conditions, for very short cylinders, and/or for long cylinders in torsion. All may be quickly derived upon referring to the appropriate equations in subsection 3.3.2 and, therefore, will not be presented here.

Truss-core sandwich cylinder. Crawford and Stuhlman (Ref. 4-13) have also performed minimum-weight analyses for both long- and moderate-length truss-core sandwich cylinders. The geometry for this configuration is shown in Fig. 4-21. Neither analysis accounts for the effects of plasticity or transverse shear stiffness. The reasons which justify this approach here are the same as those given in subsection 4.2.3 for truss-core sandwich shear panels.

Moderate-Length Cylinders in Torsion

Equation (4.50) may be used to predict general instability in moderate-length cylinders in torsion:

$$\frac{N_{xy}}{E} = 3.46 \bar{t} \left(\frac{R}{L}\right)^{1/2} \left[\frac{\left(\frac{b_f}{t_f}\right)^2 \left(\frac{t_f}{R}\right)^3 \tan^2 \theta}{8 \frac{\bar{t}}{R} (1 - \mu^2)} \right]^{5/8} \quad (4.50)$$

This equation is applicable between the following limits.

$$\left(\frac{L}{R}\right)^2 \frac{R}{h} > 35 \text{ and } \left(\frac{L}{R}\right)^2 \frac{h}{R} < 30$$

For local instability, equations for the critical shearing force in both the face and the core must be given since there is no existing analysis that accounts for the interaction between these elements. Curvature in the facing elements will be neglected. Therefore, Eqs. (4.23) and (4.24) are applicable.

Upon equating the critical shearing forces N_{xy} for general and local instability according to the principles of minimum-weight analysis, an efficiency equation may be obtained. Two such equations are obtained here: one resulting from equating Eqs. (4.50) and (4.23), and the other resulting from equating Eqs. (4.50) and (4.24). In the former case the resulting efficiency equation is

$$\frac{N_{xy}}{RE} = \mathcal{E}_f \left(\frac{\bar{t}}{R}\right)^{1.77} \left(\frac{R}{L}\right)^{0.3077}$$

In the latter case the efficiency equation is

$$\frac{N_{xy}}{RE} = \mathcal{E}_c \left(\frac{\bar{t}}{R} \right)^{1.77} \left(\frac{R}{L} \right)^{0.3077}$$

The efficiency factors \mathcal{E}_f and \mathcal{E}_c have been evaluated, using $K_S = 5.35$ and $\mu = 0.3$, and are shown in Fig. 4-24. The left-hand portion of the figure presents \mathcal{E}_f while the right-hand portion presents \mathcal{E}_c . Only the critical, or lower, efficiency factor is presented for each combination of θ and t_c/t_f . The maximum efficiency factor \mathcal{E}_{\max} is seen to be 0.5841 and it occurs when t_c/t_f is approximately 0.707 and θ approximately 60 deg. The minimum-weight equation for moderate-length truss-core sandwich cylinders loaded elastically in torsion, therefore, is:

$$\frac{N_{xy}}{RE} = 0.5841 \left(\frac{\bar{t}}{R} \right)^{1.77} \left(\frac{R}{L} \right)^{0.3077} \quad (4.51)$$

Supplemental equations necessary for design are given in Eqs. (4.26) through (4.28). Note that Eq. (4.51) is applicable between the limits $(L/R)^2 R/h > 35$ and $(L/R)^2 h/R < 30$.

It should be pointed out here that for each θ shown on Fig. 4-24, the highest efficiency factor occurs at the intersection of the \mathcal{E}_c and \mathcal{E}_f curves, or, in other words, when both local modes of instability become critical under the applied loading, N_{xy} . Thus, referring to Eqs. (4.23) and (4.24), it is apparent that:

$$2 \frac{t_c}{t_f} \sqrt{\cos \theta} = 1 \quad (4.52)$$

for highest efficiency for any θ .

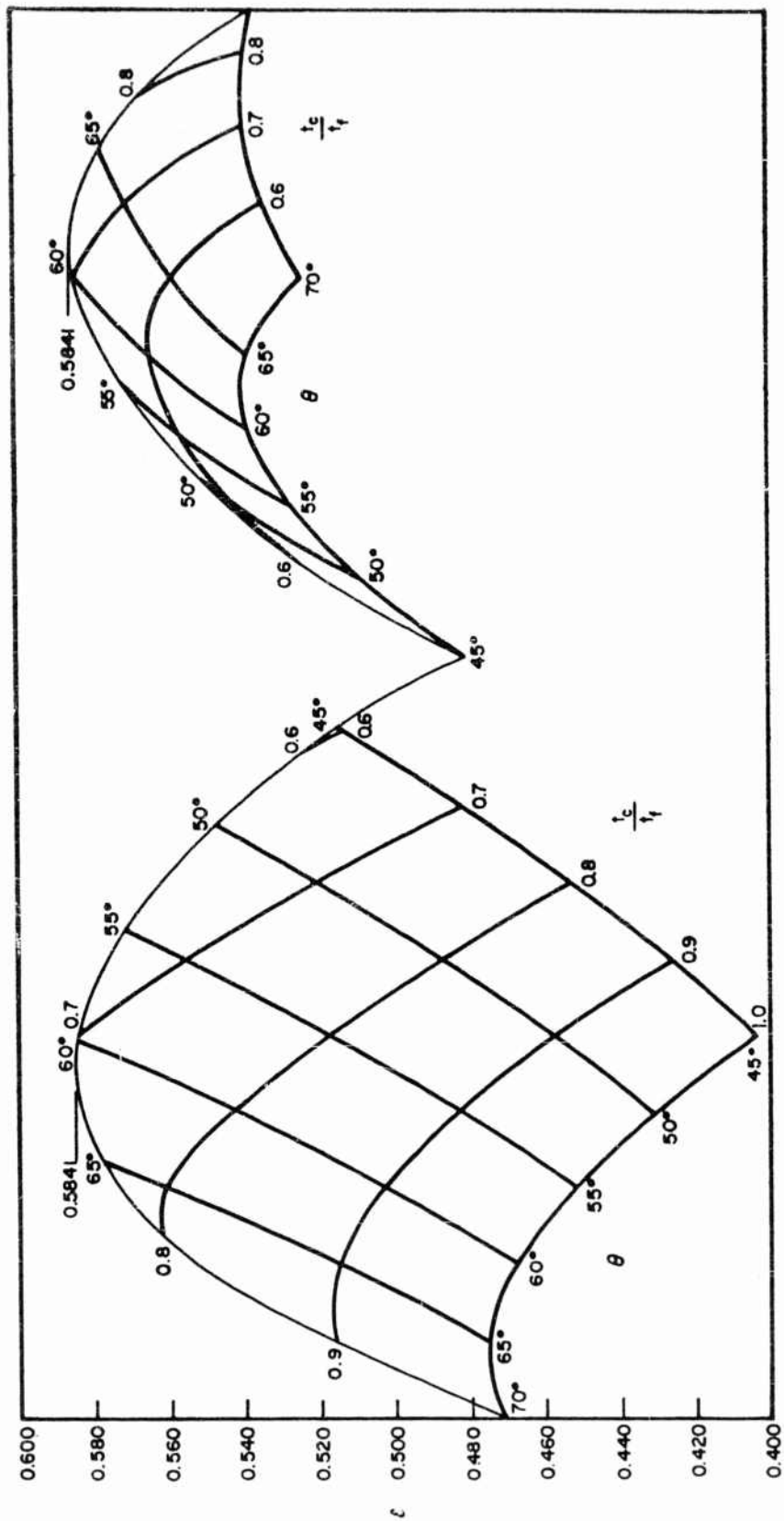


Fig. 4-24 Efficiency Chart for Moderate-Length, Truss-Core Sandwich Cylinders Subjected to Torsion,
 $(L/R)^2 R/h > 35$; $(L/R)^2 h/R < 30$

Long Cylinders in Torsion

General instability in long cylinders in torsion may be predicted with Eq. (4.53):

$$\frac{N_{xy}}{E} = 1.754 \bar{t} \left[\frac{\left(\frac{b_f}{t_f}\right)^2 \left(\frac{t_f}{R}\right)^3 \tan^2 \theta}{8 \left(\frac{\bar{t}}{R}\right) (1 - \mu^2)} \right]^{3/4} \quad (4.53)$$

which is applicable when

$$\left(\frac{L}{R}\right)^2 \frac{h}{R} > 30$$

The same equations for local instability used in the minimum-weight analysis of moderate-length cylinders in torsion [Eqs. (4.23) and (4.24)] are also applicable here. When these equations are combined in a manner entirely parallel to that presented in the previous case, the two following elastic efficiency equations result:

$$\frac{N_{xy}}{RE} = \mathcal{E}_f \left(\frac{\bar{t}}{R}\right)^{1.858}$$

$$\frac{N_{xy}}{RE} = \mathcal{E}_c \left(\frac{\bar{t}}{R}\right)^{1.858}$$

The efficiency factors \mathcal{E}_f and \mathcal{E}_c are presented in Fig. 4-25, where $K_\tau = 5.35$ and $\mu = 0.3$. As was the case in Fig. 4-24, Fig. 4-25 shows \mathcal{E}_c on the right-hand portion of the chart and \mathcal{E}_f on the left-hand portion. Further, only the critical, or lower-efficiency factor, is presented for each combination of θ and t_c/t_f . The maximum-efficiency factor is seen to be 0.3233 and it occurs when t_c/t_f is

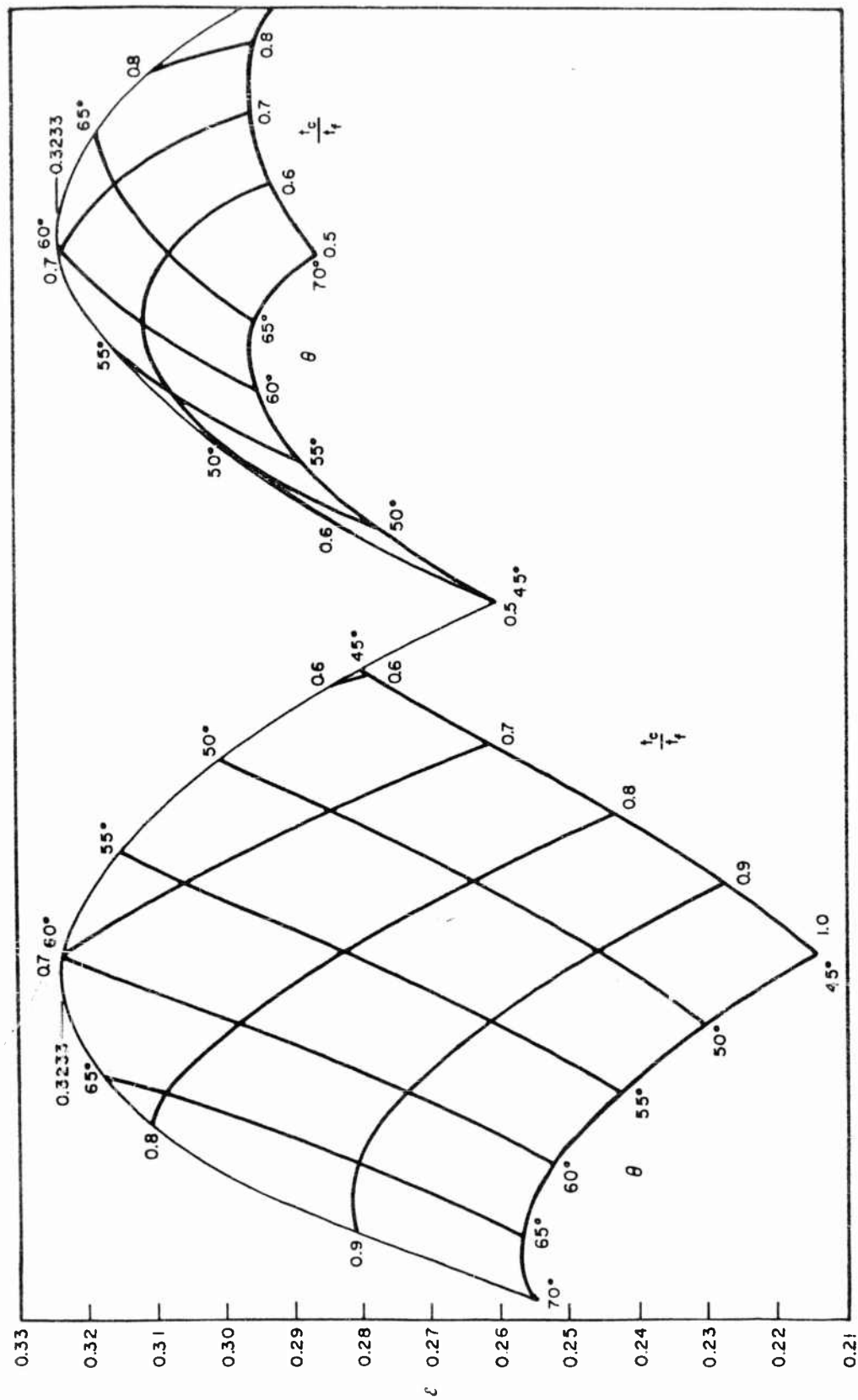


Fig. 4-25 Efficiency Chart for Long Truss-Core Sandwich Cylinders Subjected to Torsion, $(L/R)^2 h/R > 30$

approximately 0.707, θ approximately 60 deg. The minimum-weight equation for long truss-core sandwich cylinders loaded elastically in torsion, therefore, is:

$$\frac{N_{xy}}{RE} = 0.3233 \left(\frac{\bar{t}}{R} \right)^{1.858} \quad (4.54)$$

Equations (4.26) through (4.28) are also applicable in this case as supplemental equations. Note that Eq. (4.54) is applicable when $\left(\frac{L}{R} \right)^2 \frac{h}{R} > 30$.

Reference to Fig. 4-25 indicates that \mathcal{E}_c and \mathcal{E}_f intersect at their maximum values for a given θ . Thus, Eq. (4.52) is applicable to both long- and moderate-length cylinders in torsion of minimum-weight design. Note should also be made that $\theta_{opt} \approx 60$ deg, and $(t_c/t_f)_{opt} \approx 0.707$ in both cases.

A comparison of monocoque and truss-core sandwich cylinders in torsion. Monocoque and truss-core sandwich cylinders of moderate length in torsion are compared in Fig. 4-26 for the case where $L/R = 1$. The curve for monocoque cylinders is a graphical presentation of the efficiency equation given in Eq. (4.49), while the curve for truss-core sandwich cylinders is a graphical presentation of the minimum-weight equation given in Eq. (4.51). It may be concluded from Fig. 4-26 that a substantial weight saving may be effected by specifying truss-core sandwich in moderate-length cylinders loaded elastically in torsion.

Efficiency comparisons may also be drawn for other L/R values or for long cylinders in torsion. In either case, the truss-core sandwich cylinder is superior to the monocoque cylinder to a degree similar to that shown in Fig. 4-26.

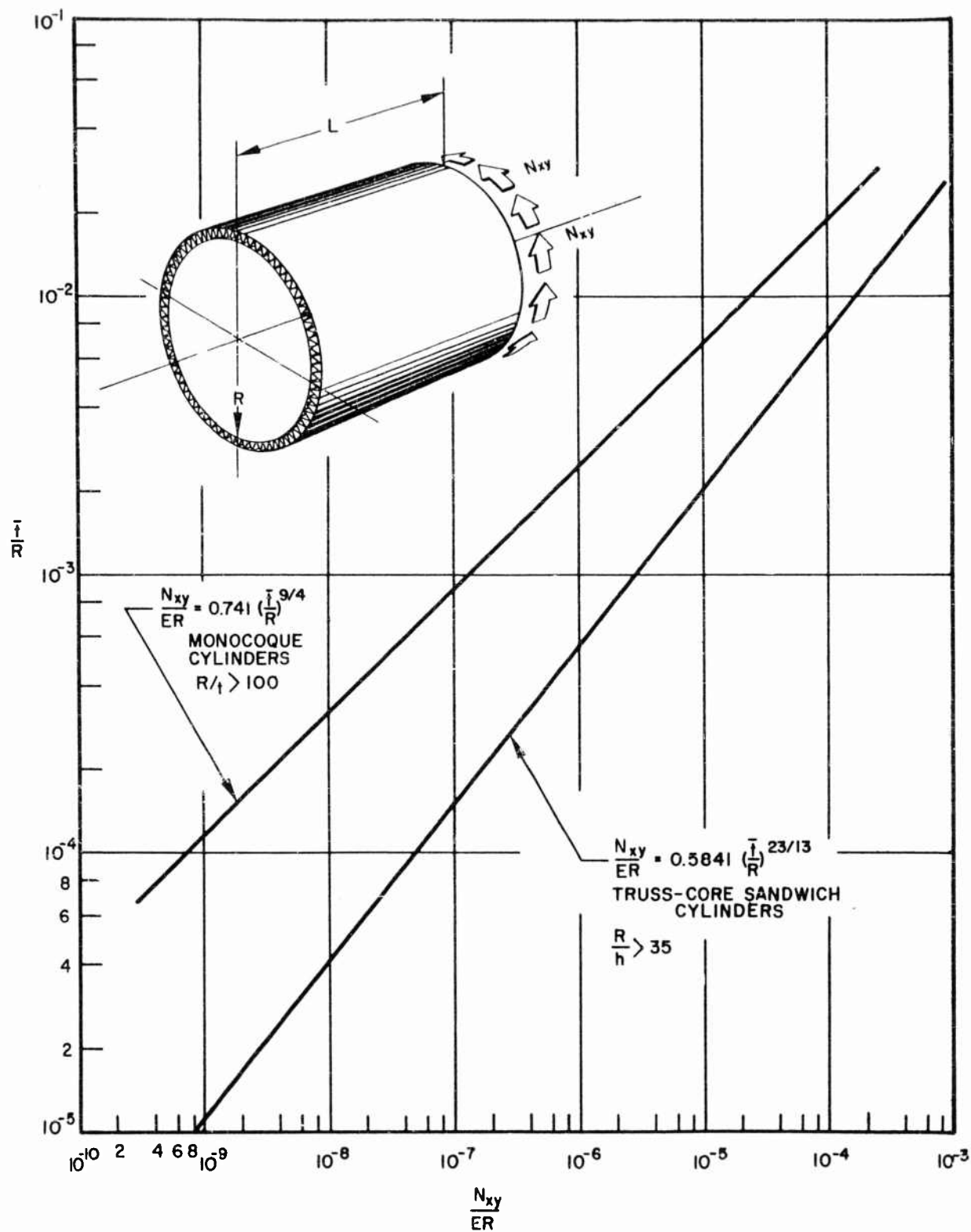


Fig. 4-26 Comparative Efficiencies of Monocoque and Optimum Truss-Core Sandwich Simply Supported Circular Cylinders of Moderate Length in Torsion, $L/R = 1$

4.2.7 Hydrostatically Compressed Cylinders

Introduction. Minimum-weight design information for the following two types of stiffened, hydrostatically compressed cylinders is presented in this subsection:

- (1) Truss-core sandwich cylinders
- (2) Ring-stiffened cylinders

Initially, the efficiency of a monocoque hydrostatically compressed cylinder will be treated, mainly to provide a basis on which to compare the stiffened designs at the conclusion of the subsection.

Monocoque cylinder. The buckling information for hydrostatically compressed monocoque cylinders presented in subsection 2.3.3 may be used here to develop an efficiency equation. However, recent tests by Nickell and Crawford (Ref. 4-14) show that this information is conservative when $Z > 100$, as do the hydrostatic tests of monocoque cylinders conducted under this contract (see subsection 3.3.3). This evidence tends to cast new doubt on tests conducted many years ago about which few details are known other than their low buckling pressures. It is rationalized that the recent tests mentioned above are typical of the specimens available with modern fabrication techniques, and materials having closely controlled mechanical properties. Thus, the expression for C_P suggested by Nickell and Crawford (Ref. 4-14) will be used to derive an efficiency equation for monocoque cylinders, since it is felt to be a more realistic basis on which to compare stiffened cylinders. The buckling pressure for hydrostatically compressed monocoque cylinders, therefore, may be predicted with Eq. (3.12) where:

$$C_P = 1.10 \sqrt{Z} \quad (4.55)$$

and Z is the same as defined in subsection 3.3.3. From these expressions, the following efficiency equation may be derived:

$$\frac{p_{cr}}{E} = \frac{0.971}{(L/R)} \left(\frac{\bar{t}}{R} \right)^{5/2} \quad (4.56)$$

where $\mu = 0.3$, $\bar{t} = t_s$, and p_{cr} is the buckling pressure. This equation applies when $Z > 100$. It is anticipated that most minimum-weight stiffened cylinders under hydrostatic pressure will possess Z 's in this range. Note that Eq. (4.55) closely approximates the buckling coefficients presented by Batdorf (Ref. 4-15) when $Z > 100$.

Truss-core sandwich cylinders. A minimum-weight analysis for truss-core sandwich cylinders subjected to a uniform radial pressure is presented by Crawford and Stuhlman in Ref. 4-13. This analysis is also applicable for uniform hydrostatic pressure when the geometric parameter Z is greater than 100, as can be deduced by reference to Batdorf's paper (Ref. 4-15). The analysis treats both long- and moderate-length cylinders, and does not include the effects of plasticity or transverse shear stiffness, for reasons previously given. The geometry for the truss-core sandwich cylinder is shown in Fig. 4-21.

Moderate-Length Hydrostatically Compressed Cylinders

General instability of a simply supported sandwich cylinder of this category is predicted by the following equation:

$$\sigma_{crG} = \frac{5.51E}{L/R} \left[\frac{\left(\frac{b_f}{R} \right)^2 \tan^2 \theta}{16(1 - \mu^2)} \right]^{3/4} \quad (4.57)$$

when the cylinder geometry is between the following limits:

$$\left(\frac{L}{R}\right)^2 \frac{R}{h} > 100 \quad \text{and} \quad \left(\frac{L}{R}\right)^2 \sqrt{\frac{h}{R}} < 6.75$$

For local instability, the assumption is made that the facing elements are wide, simply supported columns that are uniformly compressed. Therefore, Eq. (3.3) is applicable, which when rewritten in terms of the present parameters becomes:

$$\sigma_{cr_{L_f}} = \frac{\pi^2 E}{12(1 - \mu^2)} \left(\frac{t_f}{b_f}\right)^2 \quad (4.58)$$

It is further assumed that the faces are equally stressed which implies that the core elements are inextensible. The stress in the facing sheet, therefore, to produce instability in the core, assuming the latter also to be wide, simply supported columns is:

$$\sigma_{cr_{L_c}} = \frac{2\pi^2 E}{3(1 - \mu^2)} \left(\frac{t_c}{t_f}\right)^3 \left(\frac{R}{b_f}\right) \left(\frac{t_f}{b_f}\right)^2 \sin \theta \cos^2 \theta \quad (4.59)$$

For minimum weight:

$$\sigma_{cr_G} = \sigma_{cr_{L_f}} = \sigma_{cr_{L_c}} = \sigma = p_{cr} \frac{R}{2t_f} \quad (4.60)$$

Combining Eqs. (4.57) through (4.60) results in the following equation:

$$\frac{\bar{t}}{R} = \frac{0.775}{(\tan \theta)^{6/13}} \left[\frac{p_{cr}}{E} \left(\frac{L}{R}\right)^{4/7} \right]^{7/13} \left\{ 2 + \frac{0.486}{\cos^2 \theta} \left[\frac{p_{cr}}{E} \left(\frac{L}{R}\right)^{3/2} \right]^{4/39} \frac{1}{(\tan \theta)^{11/2}} \right\} \quad (4.61)$$

The parameters of this equation are those that would appear in an efficiency equation; however, it is evident that the relationship between the weight parameter \bar{t}/R and the loading-material index, here p_{cr}/E , cannot be expressed as in the efficiency equations of the previous sections. Therefore, the weight parameter \bar{t}/R is minimized with respect to θ resulting in the following equation:

$$\frac{p_{cr}}{E} \left(\frac{L}{R} \right)^{3/2} = \frac{515.9}{(\tan \theta_{opt})^{14} \left[2 - \frac{40}{39} \csc^2 \theta_{opt} \right]^{39/4}} \quad (4.62)$$

Equation (4.62) is graphically presented in Fig. 4-27 showing values of θ_{opt} for ranges of values of L/R and p_{cr}/E . Associated values of $(\bar{t}/R)_{min}$ may be determined from Eq. (4.61) or Fig. 4-28. It is noted that a minimum-weight equation which is a function of the weight parameter \bar{t}/R and the loading-material index p_{cr}/E cannot be written independent of the geometric ratio L/R . However, when $L/R = 1$, the following minimum-weight equation for moderate-length, hydrostatically compressed, truss-core sandwich cylinders results:

$$\frac{p_{cr}}{E} = 0.2961 \left(\frac{\bar{t}}{R} \right)^{1.74} \quad (4.63)$$

The following three design equations for t_f/b_f , b_f/R , and t_c/t_f are presented graphically for optimum values of these parameters in Figs. 4-29, 4-30, and 4-31, respectively. The equations may be used with either optimum or nonoptimum values of θ .

$$t_f/b_f = 0.845 \left(\frac{R}{L} \right)^{2/13} \left(\frac{p_{cr}}{E} \cdot \tan \theta \right)^{3/13} \quad (4.64)$$

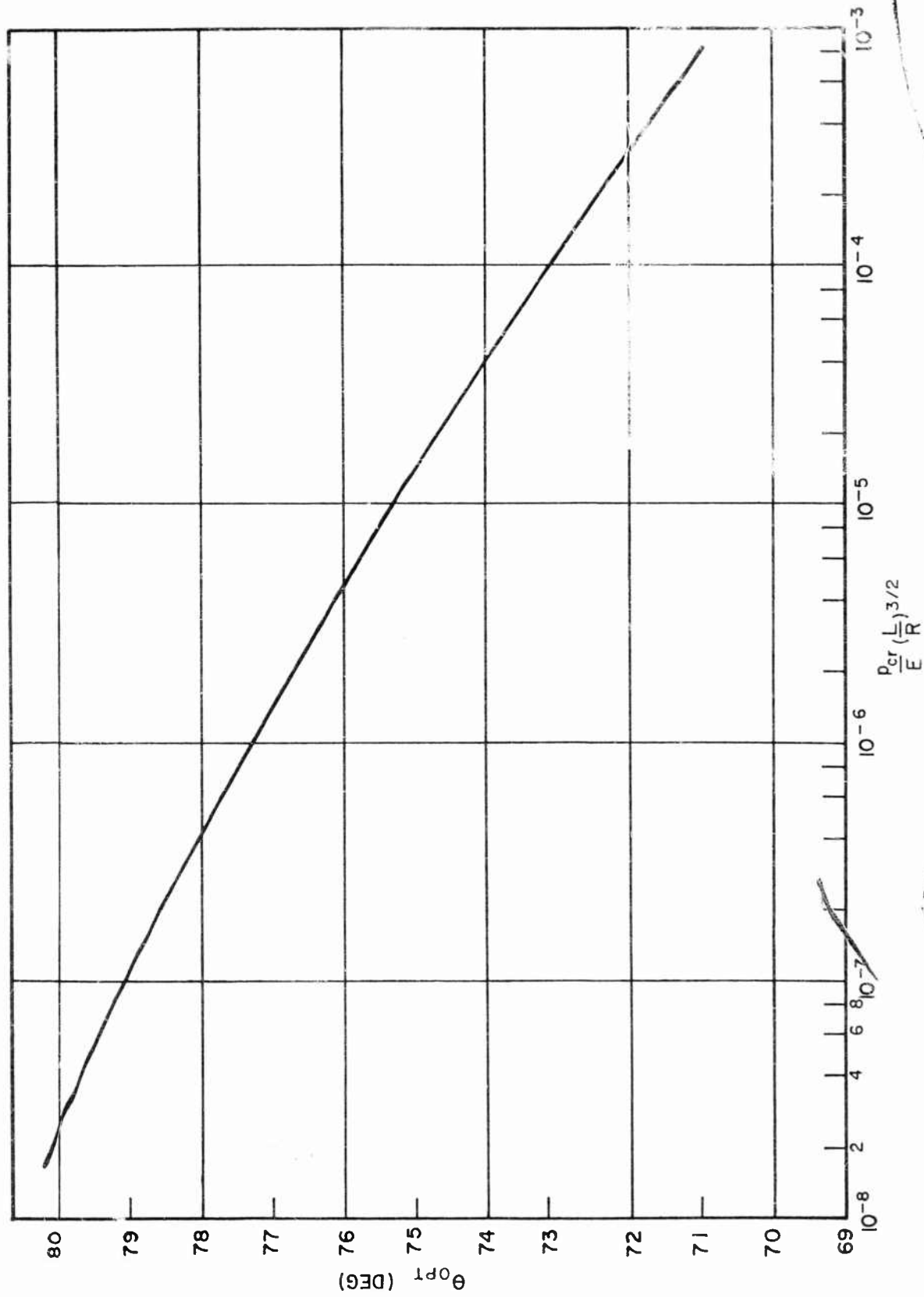


Fig. 4-27 Optimum Values of Truss Angle θ Versus P_{cr}/E and L/R for Moderate Length, Truss-Core Sandwich Cylinders Subjected to a Uniform External Hydrostatic Pressure

2-47-61-2

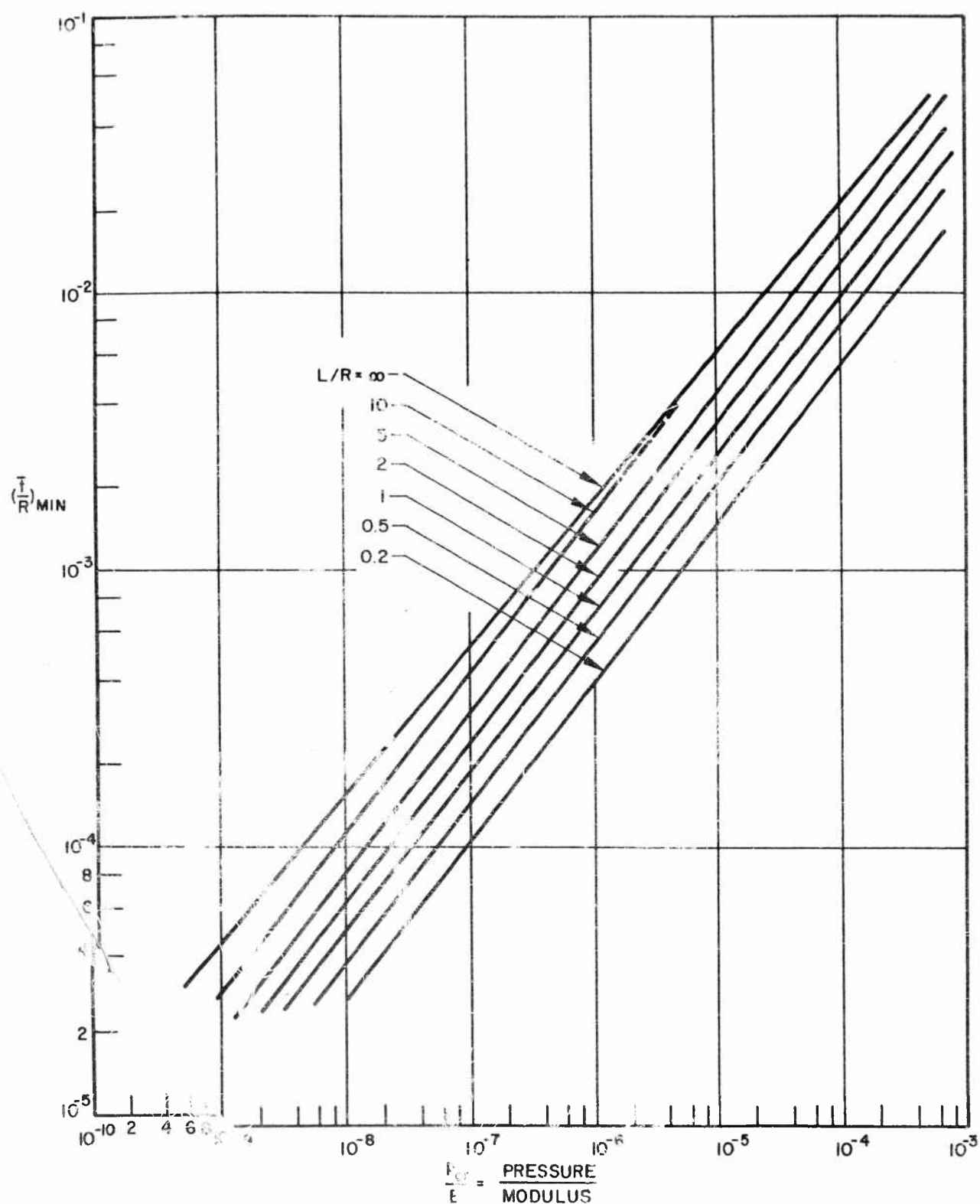


Fig. 4-28 Minimum Values of \bar{t}/R Versus p_{cr}/E and L/R for Truss-Core Sandwich Cylinders Subjected to a Uniform External Hydrostatic Pressure

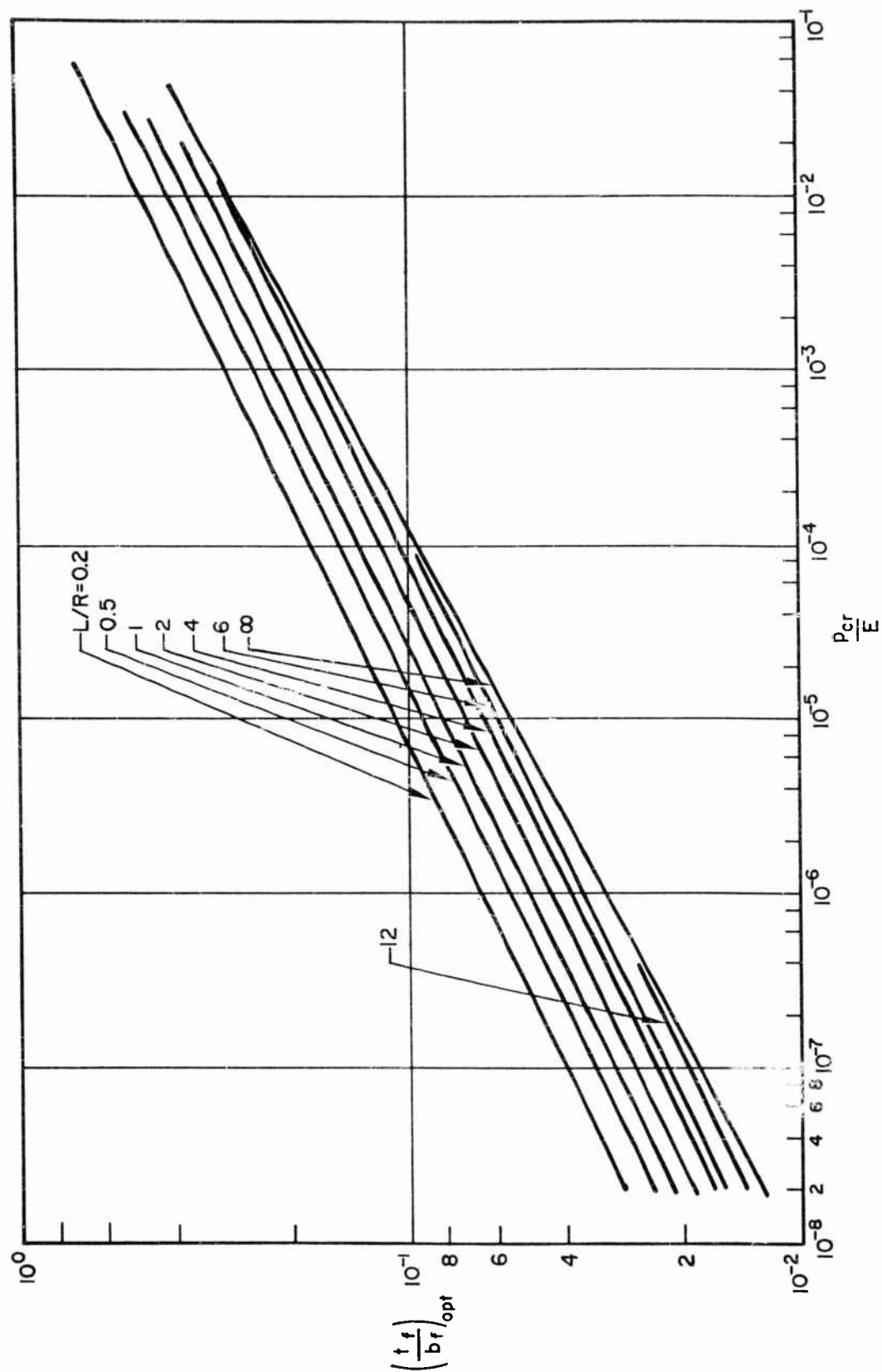


Fig. 4-29 Optimum Values of t_f/b_f for Truss-Core Sandwich Cylinders Subjected to a Uniform External Hydrostatic Pressure

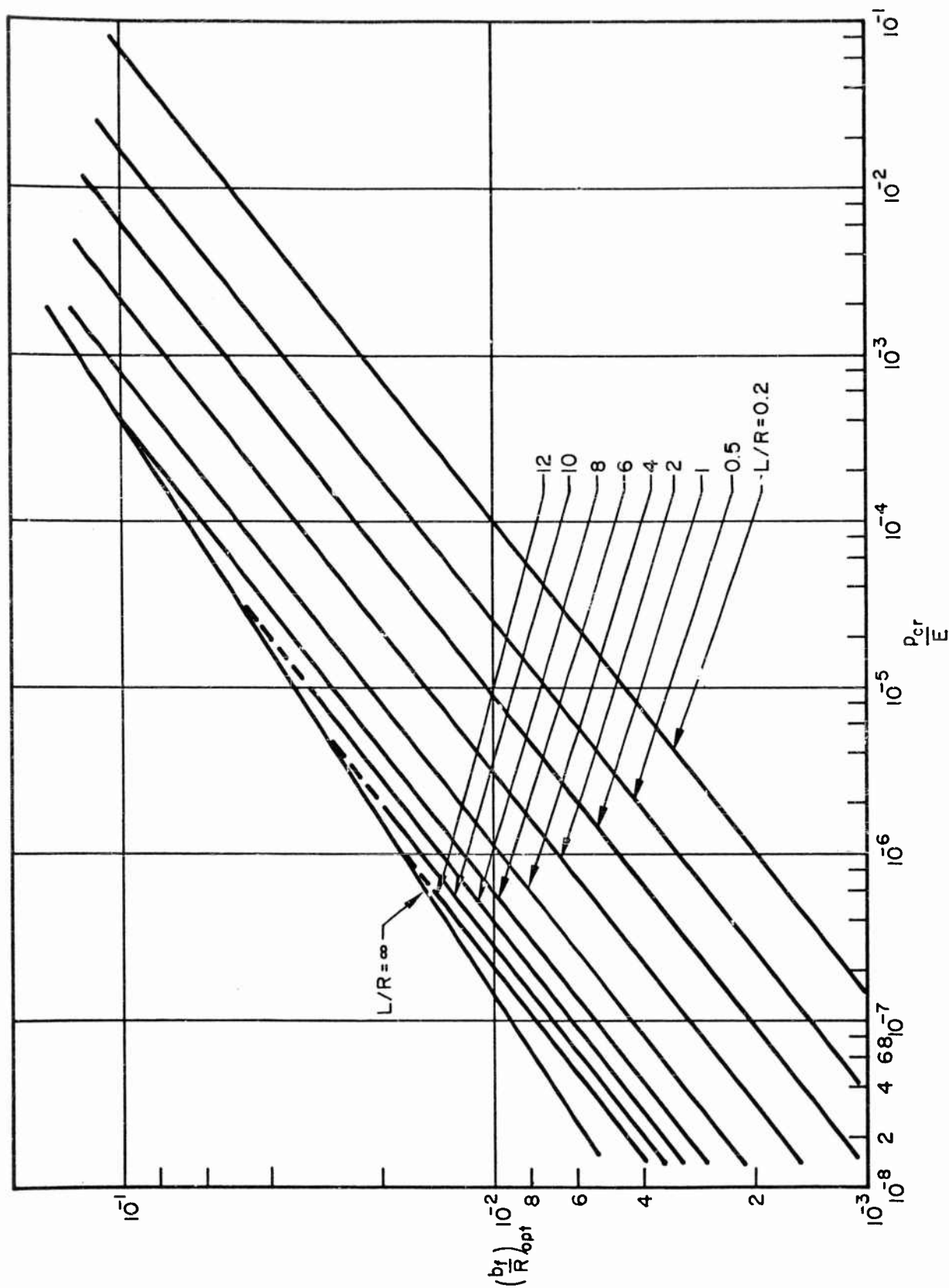


Fig. 4-30 Optimum Values of b_f/R for Truss-Core Sandwich Cylinders Subjected to a Uniform External Hydrostatic Pressure

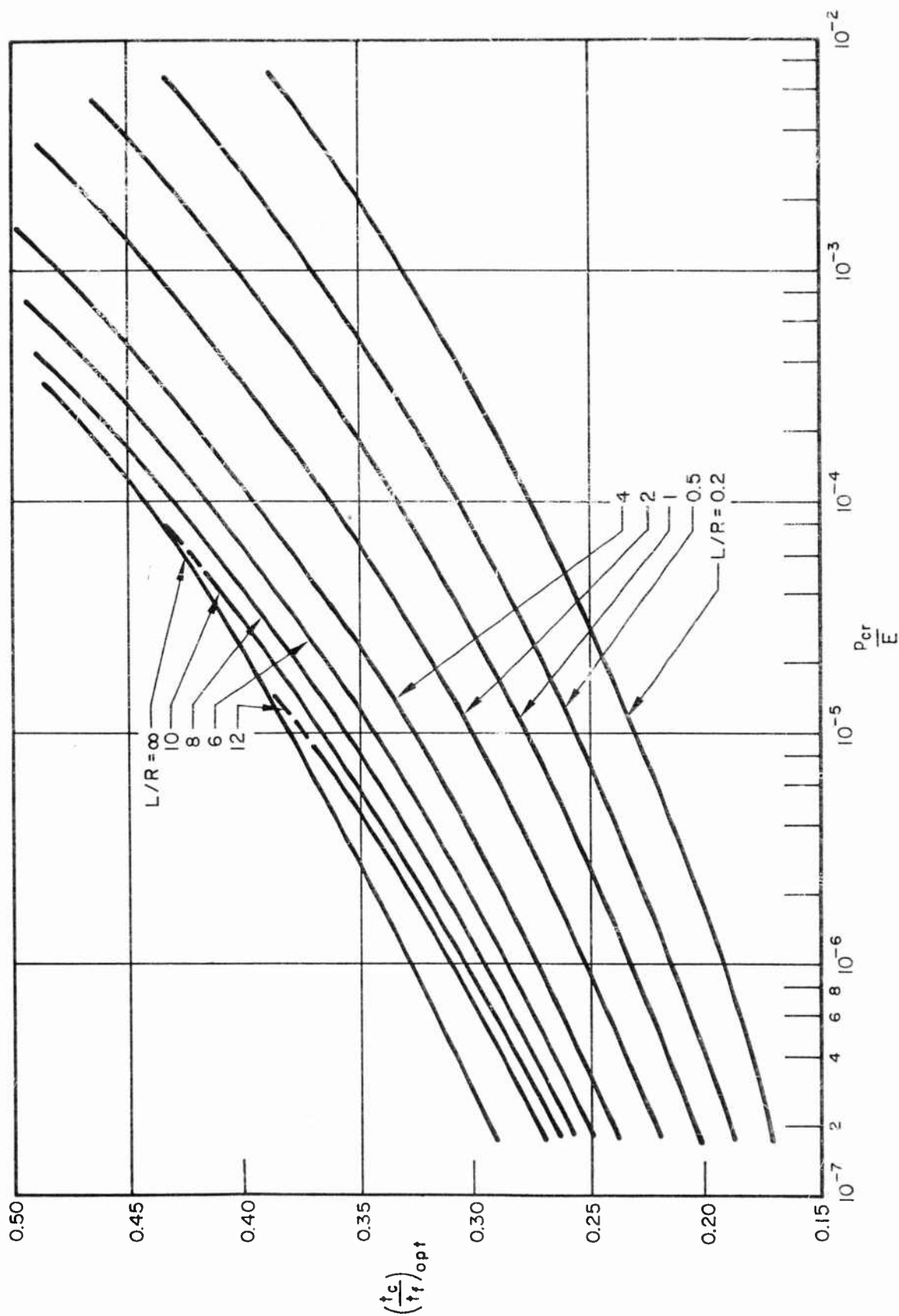


Fig. 4-31 Optimum Values of t_c/t_f for Truss-Core Sandwich Cylinders Subjected to a Uniform External Hydrostatic Pressure

$$b_f/R = \frac{1.145}{\tan \theta} \left(\frac{L}{R} \right)^{2/3} \left(\frac{t_f}{b_f} \right)^{4/3} \quad (4.65)$$

$$t_c/t_f = \left[\frac{b_f}{R} - \frac{1}{\tan \theta} \right]^{1/3} \frac{1}{2 \cos \theta} \quad (4.66)$$

In addition, the relation between b_f and b_c given by Eq. (4.28) is applicable here. Note that Fig. 4-28 is not necessary for design purposes. Note also that the $L/R = \infty$ curve appearing in Figs. 4-28 through 4-31 does not apply to moderate-length cylinders, but only to long cylinders.

Long Hydrostatically Compressed Cylinders

The only difference between this case and the moderate-length case is that a different expression for general instability is used. The long sandwich cylinder may be considered a ring under uniform radial pressure, in which case general instability is predicted by:

$$\sigma_{crG} = \frac{3}{16} \left(\frac{b_f}{R} \right)^2 \frac{E}{(1 - \mu^2)} \tan^2 \theta \quad (4.67)$$

This expression is applicable when:

$$\left(\frac{L}{R} \right)^2 \sqrt{\frac{h}{R}} > 6.75$$

When Eqs. (4.58) through (4.60) are combined with Eq. (4.67), the following equation, similar in form to Eq. (4.61), is obtained:

$$\frac{\bar{t}}{R} = 1.076 \sqrt{\frac{p_{cr}}{E} \cdot \frac{1}{\tan \theta}} \left[2 + \frac{0.572 \left(\frac{p_{cr}}{E} \right)^{1/12}}{(\tan \theta)^{7/12} \cos^2 \theta} \right] \quad (4.68)$$

Minimizing \bar{t}/R with respect to θ leads to the following expression for θ_{opt} :

$$\frac{p_{cr}}{E} = \frac{789.4}{\left[\tan \theta_{opt} \right]^{17} \left[2 - \frac{13}{12} \csc^2 \theta_{opt} \right]^{12}} \quad (4.69)$$

Optimum values of θ for a range of p_{cr}/E values are presented in Fig. 4-32. Corresponding values of $(\bar{t}/R)_{min}$ are shown in Fig. 4-28, where they are represented by the curve for $L/R = \infty$ only. The equation of this curve, which is the minimum-weight equation for long truss-core sandwich cylinders under hydrostatic pressure, is:

$$\frac{p_{cr}}{E} = 0.146 \left(\frac{\bar{t}}{R} \right)^{1.88} \quad (4.70)$$

Optimum values of the geometric parameters t_f/b_f , b_f/R , and t_c/t_f are presented graphically in Figs. 4-29 through 4-31, respectively, where again they are represented by the $L/R = \infty$ curve only. Both optimum and nonoptimum values of these parameters may be calculated from the following equations, by using either optimum or nonoptimum values of θ :

$$\frac{t_f}{b_f} = 0.7165 \left[\frac{p_{cr}}{E} \cdot \tan \theta \right]^{1/4} \quad (4.71)$$

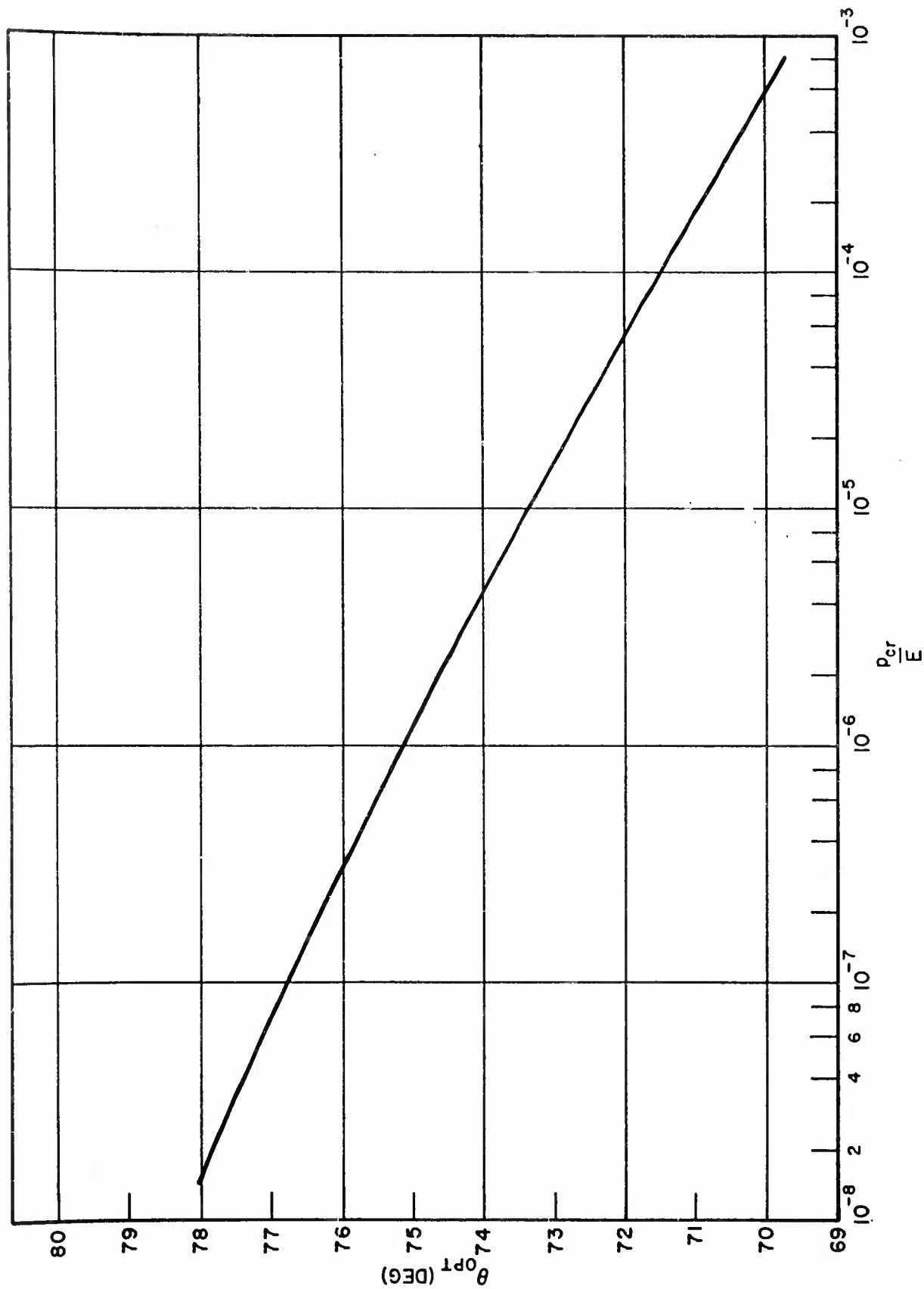


Fig. 4-32 Optimum Values of θ for Long Truss-Core Sandwich Cylinders Subjected to a Uniform External Hydrostatic Pressure

$$\frac{b_f}{R} = \frac{2\pi}{3 \tan \theta} \cdot \frac{t_f}{b_f} \quad (4.72)$$

$$\frac{t_c}{t_f} = \left[\frac{b_f}{R} \cdot \frac{1}{\tan \theta} \right]^{1/3} \frac{1}{2 \cos \theta} \quad (4.73)$$

Equation (4.28) is also applicable here.

Ring-stiffened cylinders. Nickell and Crawford (Ref. 4-14) have analyzed ring-stiffened, hydrostatically compressed cylinders for minimum weight, and the results of their analysis are presented here. The analysis covers only elastic instability, although it may readily be modified for plastic instability. The authors show, however, that most minimum-weight designs are stressed elastically. The rings are of rectangular cross-section.

Three modes of instability are considered. These are:

- (1) Local instability of the rings
- (2) Local instability of the cylinder between rings
- (3) General instability of the composite structure

In previous minimum-weight design procedures involving conventionally stiffened structures (e.g., subsection 4.2.1 or 4.2.2), failure occurred when there were equal stresses in modes (1) and (2). As a consequence, a single equation representing these two modes could be written, as generally discussed in subsection 4.1, which substantially simplified the minimum-weight analysis. However, in the present case, the rings are loaded only by the radial deflections of the cylinder wall at the ring, which are less than those over the major portion of the span between rings. Therefore, modes (1) and (2) here are assumed to occur at equal pressures, but not at equal stresses, for optimum design.

It can be seen that the local instability pressure of the skin is increased as more material is added to the cylinder wall, and that the general instability pressure of the composite structure is increased as more material is added to the rings. General instability may be further increased by shaping the rings to increase the moment of inertia. This can be done for rectangular rings by increasing ring depth in the radial direction and thinning the ring in the longitudinal direction. However, this process is limited by mode (1). Thus, mode (1) becomes important primarily as a check to insure that secondary instability in the ring does not occur prematurely. It will be seen later that the ring depth can be quite short of maximum without significant decrease in efficiency.

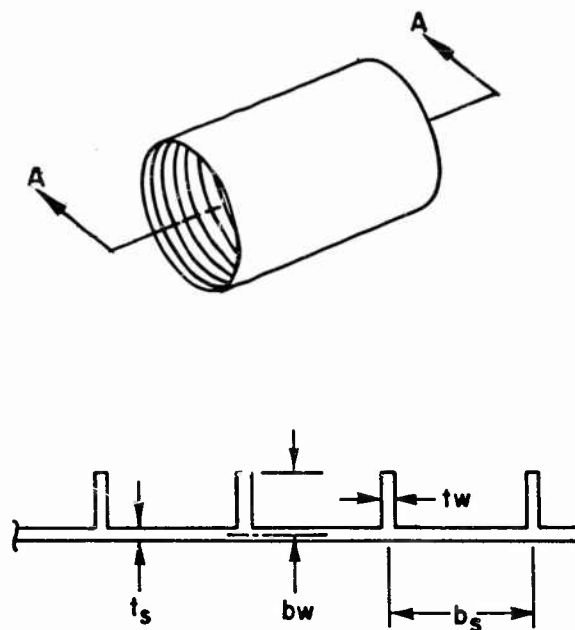
The equation for predicting local instability of the ring, based on a consideration of the radial deflection of the cylinder wall at the ring, is given in Eq. (4.74):

$$\left(\frac{p_{cr}}{E}\right)_{LR} = 0.452 \left(t_s/R\right) \left(\frac{t_w}{b_w}\right)^2 \left[1 + \frac{0.63 A_R}{R^{1/2} t_s^{3/2}} \right] \quad (4.74)$$

where

- t_s = cylinder wall thickness
- R = cylinder mean radius
- t_w = ring thickness
- b_w = ring depth measured to cylinder wall centerline
- A_R = area of ring = $b_w t_w$
- p_{cr} = critical hydrostatic buckling pressure
- E = Young's modulus of elasticity

A cross section taken longitudinally through the cylinder appears in Fig. 4-33 to illustrate some of the above dimensions.



SECTION A-A

Fig. 4-33 Cross Section Taken Longitudinally Through a Ring-Stiffened Cylinder

Local instability of the cylinder wall between rings may be predicted using the information presented previously in this subsection for monocoque cylinders. Taking $L/(n + 1)$ as the ring spacing, where L is the overall length of the cylinder and n is the number of rings, Eq. (4.56) becomes:

$$\left(\frac{p_{cr}}{E}\right)_{LC} = \frac{0.971}{(L/R)} \left(\frac{t_s}{R}\right)^{5/2} (n + 1) \quad (4.75)$$

Note that this equation is applicable when the geometric parameter $Z > 100$.

For general instability of the composite structure, the following expression is applicable:

$$\left(\frac{p_{cr}}{E}\right)_G = \frac{5.84}{(L/R)} \left(\frac{t_s}{R}\right)^{5/2} \left[\frac{(n+1)\bar{I}_R}{t_s^3 L} \right]^{3/4} \quad (4.76)$$

where \bar{I}_R is the effective moment of inertia for the ring, and the remaining symbols are as previously defined. The cylinder wall is assumed to be fully effective in acting with the ring to develop inertia to resist general instability if local instability of the skin has not developed. Nickell and Crawford (Ref. 4-14) present test results substantiating this.

Minimum weight is obtained when general instability of the composite structure and local instability of the cylinder wall have equal critical pressures, with ring geometry limited by local instability of the rings. Therefore, Eqs. (4.75) and (4.76) are equated, and the resulting equation is

$$\frac{\bar{t}}{R} = \frac{L/R}{n(n+1)^{4/3}} \frac{\left(\frac{\bar{t}}{t_s/R} - 1\right)^2 \left(\frac{\bar{t}}{t_s/R} + 3\right)}{t_w/b_w} \quad (4.77)$$

where \bar{t} is the equivalent skin thickness for weight purposes. For minimum-weight design, $(\bar{t}/R)_{\min}$ must be determined. If p_{cr}/E , L/R , and n are assumed, t_s/R may be calculated from Eq. (4.75). Using these values, a range of \bar{t}/R may be calculated from Eq. (4.77) for an assumed range of t_w/b_w . The compatible value of $(\bar{t}/R)_{\min}$ and t_w/b_w may then be selected from this tabulation, after the following condition for ring local instability has been checked:

$$\left.\frac{t_w}{b_w}\right|_{\min} = \left[\frac{2.43 (1 - \mu^2) p_{cr}/E (t_s/R)^{-1}}{1 + \frac{0.63}{n} \cdot \frac{L}{R} \cdot (t_s/R)^{-1/2} \left[\frac{\bar{t}}{t_s/R} - 1 \right]} \right]^{1/2} \quad (4.78)$$

This equation results from rearranging Eq. (4.74) and substituting the geometric formulation for \bar{t}/R :

$$\frac{\bar{t}}{R} = \frac{t_s}{R} \left[1 + \frac{n}{n+1} \frac{A_R}{A_s} \right] \quad (4.79)$$

where

$$A_R = b_w t_w$$

$$A_s = b_s t_s$$

$$b_s = L/(n+1)$$

This procedure has been repeated until all combinations of selected values of the parameters p_{cr}/E , L/R , and n have been investigated. The results of these calculations are presented in Figs. 4-34 through 4-37, which give $(\bar{t}/R)_{min}$ versus p_{cr}/E for various values of n up to 300 when $L/R = 0.5, 1, 2$, and 4 , respectively. These charts indicate that the optimum n is dependent upon p_{cr}/E , and that relatively large values of n are optimum. (Note: the n lines do not form a common curve at their intersections, but cross. The portion of each n line above this intersection has been deleted for clarity.) However, the difference in efficiency between the optimum n and a much smaller n is quite small. The following procedure results in the determination of the design dimensions, assuming p_{cr}/E and L/R are known, and that n and $(\bar{t}/R)_{min}$ have been determined from the previously discussed figures:

- (1) Calculate t_s/R from Eq. (4.75)
- (2) Calculate t_w/b_w from Eq. (4.77)
- (3) Check t_w/b_w calculated in step (2) against $t_w/b_w|_{min}$ calculated from Eq. (4.78)
- (4) Knowing $L, R, t_s, \bar{t}, n, t_w/b_w$, calculate b_w from Eq. (4.79)

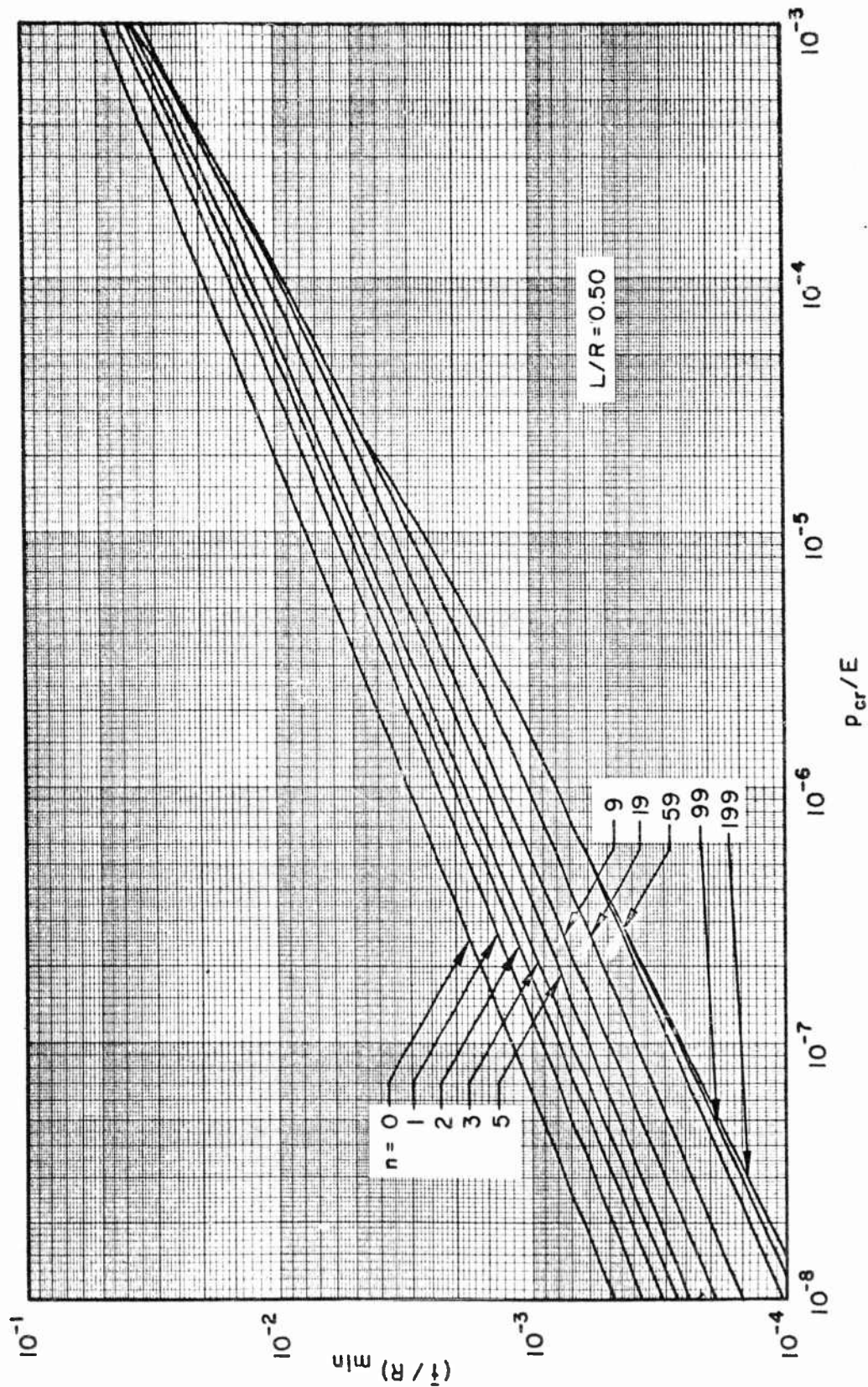


Fig. 4-34 Optimum Design Chart (When n Is Specified) for Ring-Stiffened Cylinders Subjected to a Uniform External Hydrostatic Pressure, $L/R = 0.5$

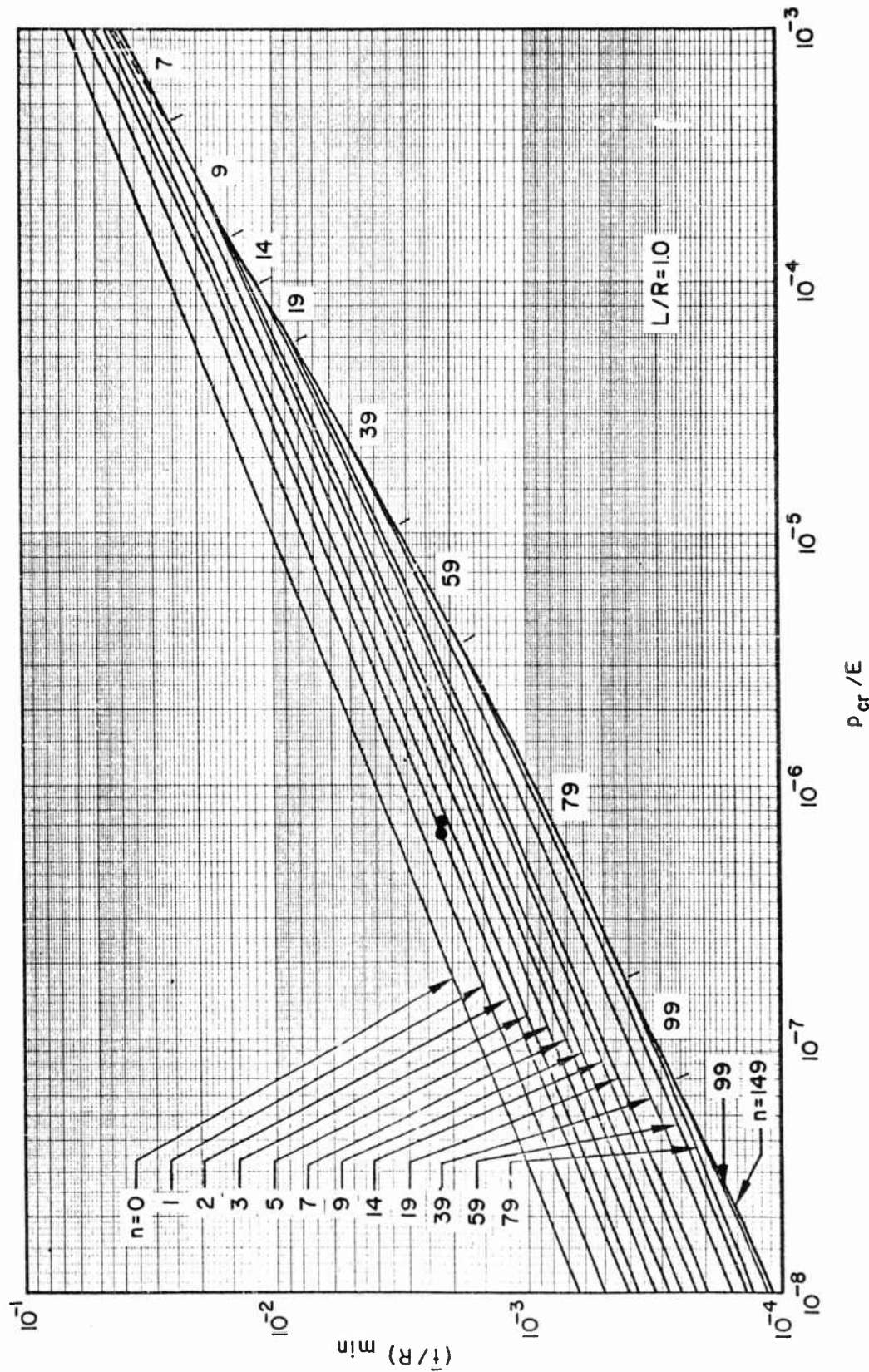


Fig. 4-35 Optimum Design Chart (When n Is Specified) for Ring-Stiffened Cylinders Subjected to a Uniform External Hydrostatic Pressure, $L/R = 1.0$

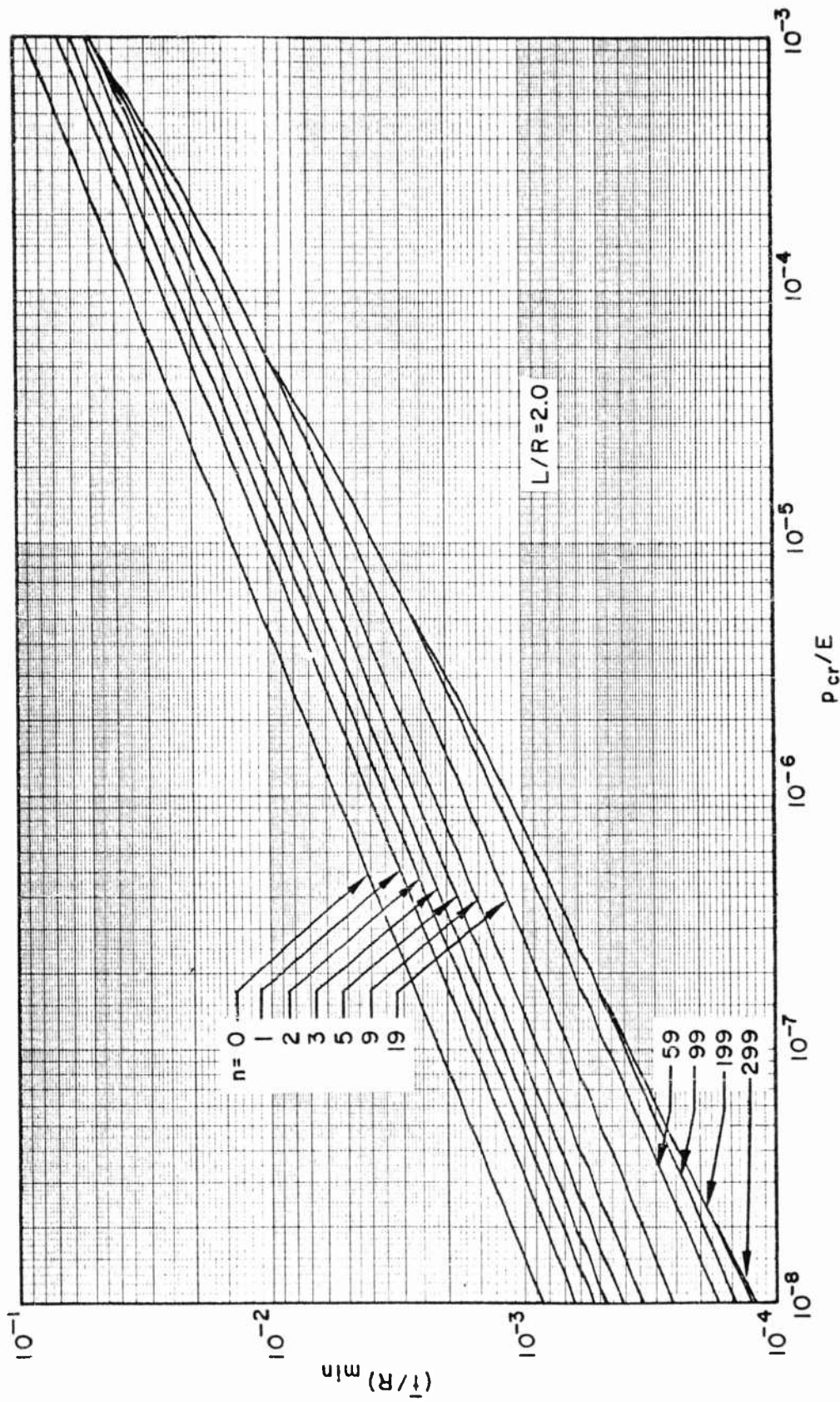


Fig. 4-36 Optimum Design Chart (When n Is Specified) for Ring-Stiffened Cylinders Subjected to a Uniform External Hydrostatic Pressure, $L/R = 2.0$

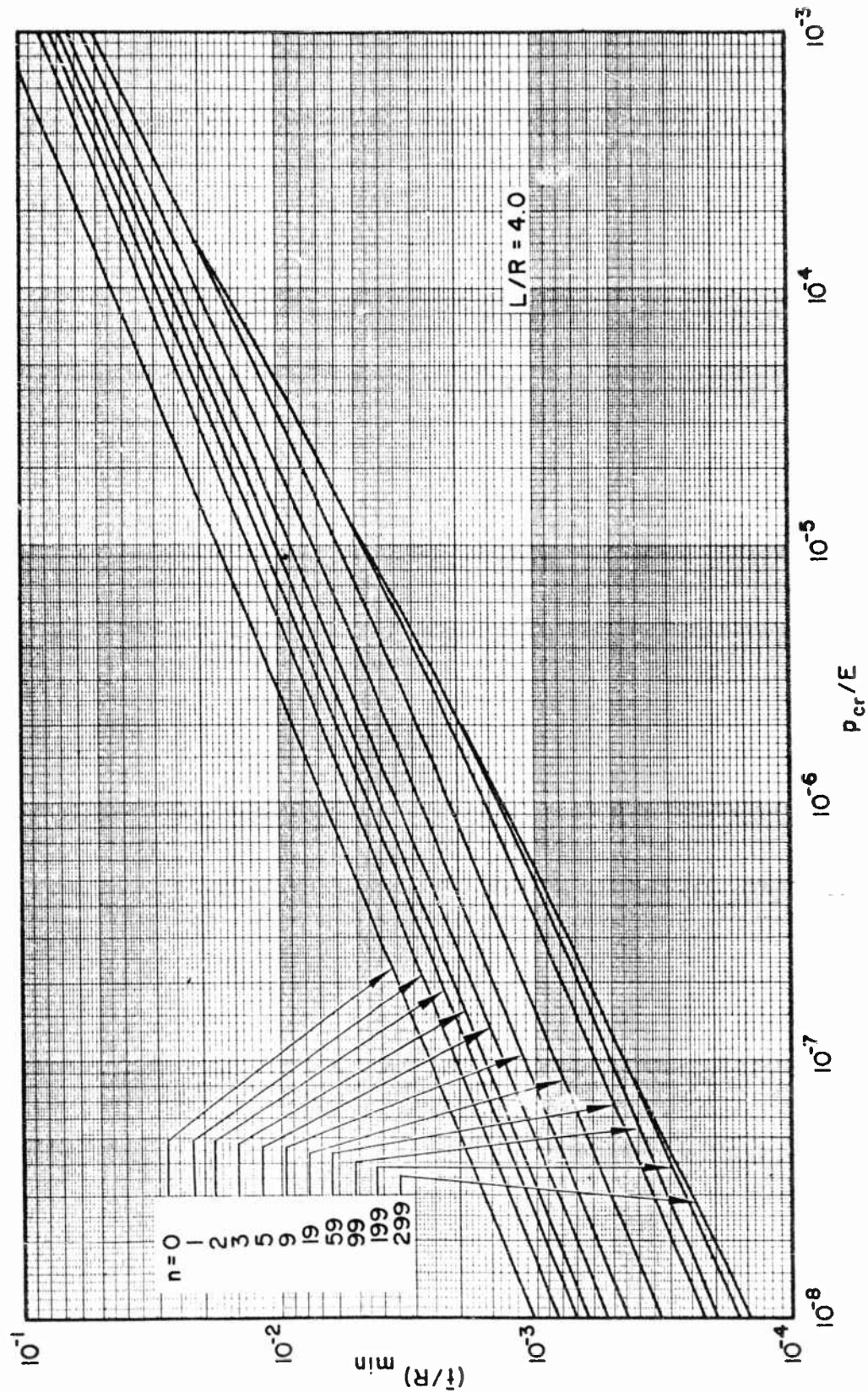


Fig. 4-37 Optimum Design Chart (When n Is Specified) for Ring-Stiffened Cylinders Subjected to a Uniform External Hydrostatic Pressure, $L/R = 4.0$

Forty-two design charts are presented in Ref. 4-14, each graphically showing the variation of $(t_w/b_w)_{opt}$ with \bar{t}/R and p_{cr}/E for a particular combination of L/R and n . While the authors intended that these charts replace steps (2) and (3) in the procedure outlined above, it is beyond the scope of this report to present all of these figures here. Instead, some of the important data contained in these charts will be summarized in tabular form. It is apparent from the design charts that $(t_w/b_w)_{opt}$ is relatively small except for high (p_{cr}/E) 's and that a given optimum value is applicable over a limited p_{cr}/E range. However, considerably larger (t_w/b_w) 's are nearly as efficient as the optimum and are applicable over a much wider range of p_{cr}/E . Table 4-2 presents the maximum t_w/b_w which may be used for a given L/R and n combination to yield approximately a minimum-weight design. Thus, if

Table 4-2

MAXIMUM VALUES OF t_w/b_w FOR NEAR-OPTIMUM DESIGN OF
RING-STIFFENED CYLINDERS UNDER HYDROSTATIC PRESSURE

L/R	n	$(t_w/b_w)_{max}$	p_{cr}/E Limit ^(a)
0.5	1, 2, 3, 5, 9, 19	0.125	2×10^{-4}
	59	0.05	10^{-4}
	99	0.02	10^{-4}
1.0	1, 2, 3, 5, 7, 9, 14, 19	0.125	2×10^{-4}
	39	0.05	2×10^{-5}
	59, 79	0.033	2×10^{-5}
	99, 149, 199	0.02	10^{-5}
2.0	1, 2, 3, 5, 9, 19	0.125	2×10^{-4}
	59	0.05	7×10^{-5}
	99, 199, 299	0.02	2×10^{-6}
4.0	1, 2, 3, 5, 9	0.125	2×10^{-4}
	19, 59	0.05	2×10^{-5}
	99, 199, 299	0.02	10^{-5}

(a) Ring local instability becomes critical above the approximate p_{cr}/E limit shown.

the designer feels that t_w/b_w calculated from steps (2) and (3) above is too small for manufacturing, handling, or other reasons, he may use a larger t_w/b_w , approaching the maximum t_w/b_w specified in Table 4-2, and still maintain a design efficiency very near to that resulting from the use of $(t_w/b_w)_{opt}$. The final t_w/b_w , whether it be calculated or selected, should be used in step (4) of the above procedure.

Test results for two ring-stiffened cylinders fabricated from beryllium cross-rolled sheet are presented in Ref. 4-14, and are summarized in Table 4-3.

Table 4-3

SUMMARY OF BERYLLIUM RING-STIFFENED
CYLINDER TESTS FROM REF. 4-14

Test No.	n	t_w/b_w	\bar{t}/R	p_{cr}/E	L/R
6	4	0.2	2.17×10^{-3}	7.27×10^{-7}	1.0
7	4	0.2	2.17×10^{-3}	6.48×10^{-7}	1.0

These data are also shown on Fig. 4-35. The agreement is shown to be very good, although the curves appear slightly unconservative. This is expected, since the test (t_w/b_w) 's are not optimum (see Table 4-2). [The tests were devised with the belief, later proved to be too conservative, that \bar{I}_R , Eq. (4.76), should consist of ring moment of inertia only.] Therefore, the ring area required for general instability of the composite structure was excessive. This resulted in a larger \bar{t}/R than necessary for minimum-weight design, as well as failure by local instability of the cylinder wall alone (precipitating general instability), rather than in combination with general instability as required by minimum-weight design principles. It should be noted that the criterion used previously in this subsection for buckling of a monocoque cylinder was substantiated by the tests of Ref. 4-14.

The relative efficiencies of stiffened, hydrostatically compressed cylinders. Curves representing minimum-weight, ring-stiffened cylinders and moderate-length truss-core sandwich cylinders are compared in Fig. 4-38 for the case $L/R = 1$. The curve for the former construction is a duplication of the optimum envelope of Fig. 4-35; the curve for the latter construction was calculated from Eq. (4.63). A curve for monocoque cylinders, based on Eq. (4.56), is also shown. It is apparent that truss-core sandwich cylinders are more efficient than ring-stiffened cylinders, although the difference diminishes to a negligible amount with increasing p_{cr}/E . Both stiffened constructions are more efficient than the monocoque construction by a wide margin.

Nickell and Crawford (Ref. 4-14) have also analyzed a waffle cylinder for minimum weight, in addition to the ring-stiffened cylinder. The waffle stiffening is rectangular in cross section and runs parallel and perpendicular to the longitudinal axis of the cylinder. Since the waffle analysis is not as rigorous as the analysis for the ring-stiffened cylinder, it has not been presented here. However, by making allowance for the differences in the two analyses, the authors conclude that the waffle cylinder is slightly less efficient than the ring-stiffened cylinder for any loading. On Fig. 4-38, a curve for waffle cylinders would fall somewhat above the ring-stiffened cylinder curve. It should be noted that the "waffle" is essentially the same as a "ring-stringer" configuration having rectangular cross-section stiffening members. Introductory material by these same authors indicates that a third configuration, stringer-stiffened cylinders, is even less efficient than waffle cylinders, although somewhat more efficient than monocoque cylinders.

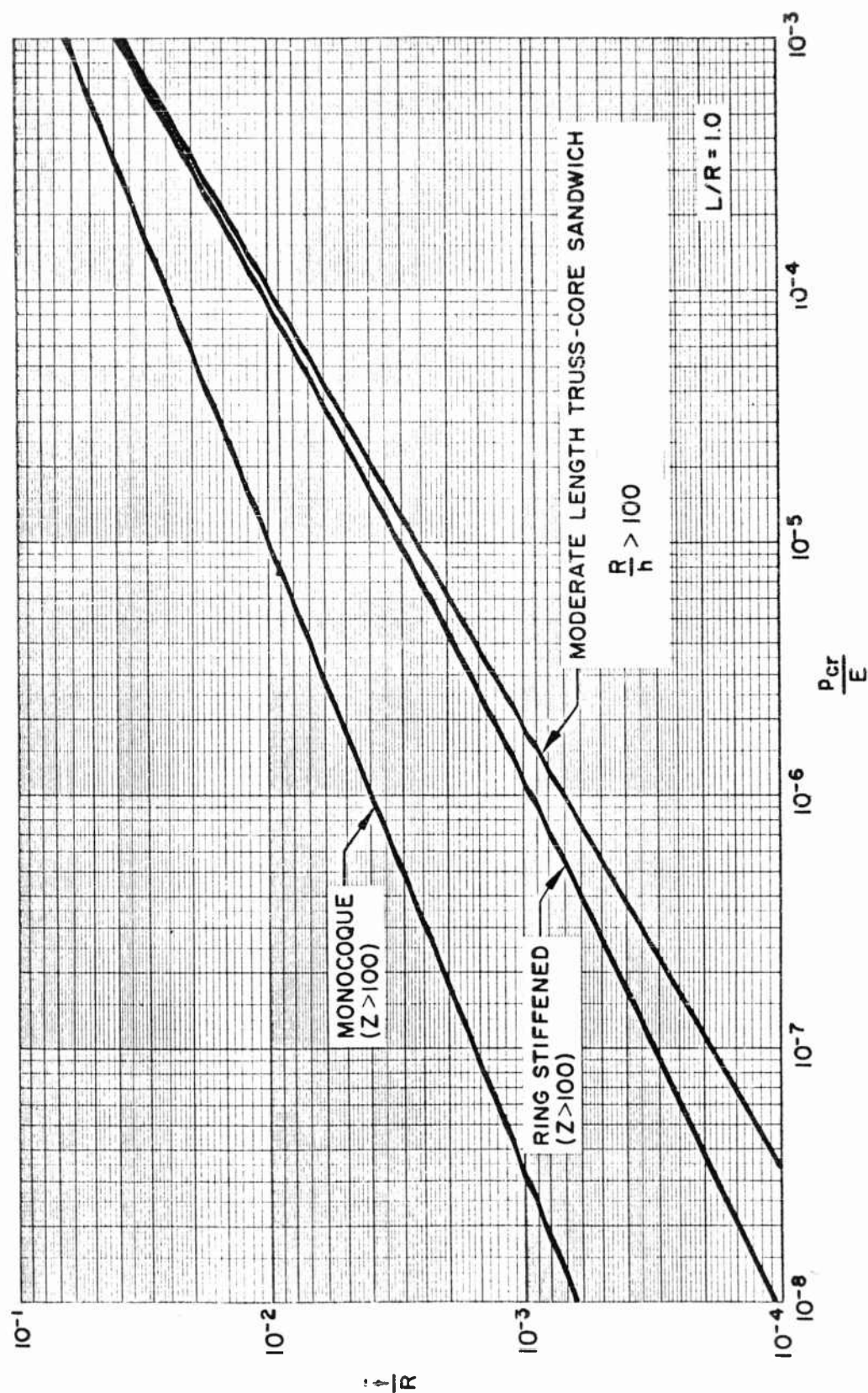


Fig. 4-38 A Comparison Between Minimum-Weight Stiffened Cylinders Loaded Elastically in Hydrostatic Compression

4.3 EXAMPLE MINIMUM-WEIGHT DESIGN CHARTS FOR BERYLLIUM CROSS-ROLLED SHEET

A review of the nondimensionalized minimum-weight design information presented in subsection 4.2 reveals that material properties appear only in the loading-material index of the minimum-weight equations. Thus, minimum-weight design information relating to beryllium cross-rolled sheet consists of the information presented in subsection 4.2 plus a graphical presentation in this section of the minimum-weight equation in terms of weight index versus loading index.

It is convenient to show on a single chart all the types of construction considered for a given combination of loading and structure. Thus, for example, beryllium cross-rolled sheet minimum-weight design information at room temperature for all wide-column constructions is presented in Fig. 4-39. Note that this type of presentation is similar to that used in subsection 4.2 to show relative efficiencies in each subsection. The charts, in fact, are identical except that the quantity $\bar{\eta}E$ (or simply E , in some cases), which represents material properties, has been evaluated and its effect shown in the present charts. To perform this evaluation, charts of σ versus $\sigma/\bar{\eta}$, such as are shown in Fig. 3-5, have been employed, in conjunction with the aforementioned charts from subsection 4.2.

The stress-strain curves of Fig. 3-2 for beryllium cross-rolled sheet have been used in developing the charts in this section. It is emphasized once again that these are "example" curves (see subsection 3.1). On this account, charts are presented only at room temperature and 800°F. The designer should be aware of the stress-strain characteristics on which these charts are based, and be conscientious about deriving similar charts to agree with differing stress-strain characteristics if necessary.

The maximum buckling stress is taken as the compressive yield-stress for those structures carrying axial load. When this condition is translated onto the beryllium design charts, a straight line having a positive 45-deg slope results, to which minimum-weight curves for all constructions eventually become tangent. Thus, at some loading

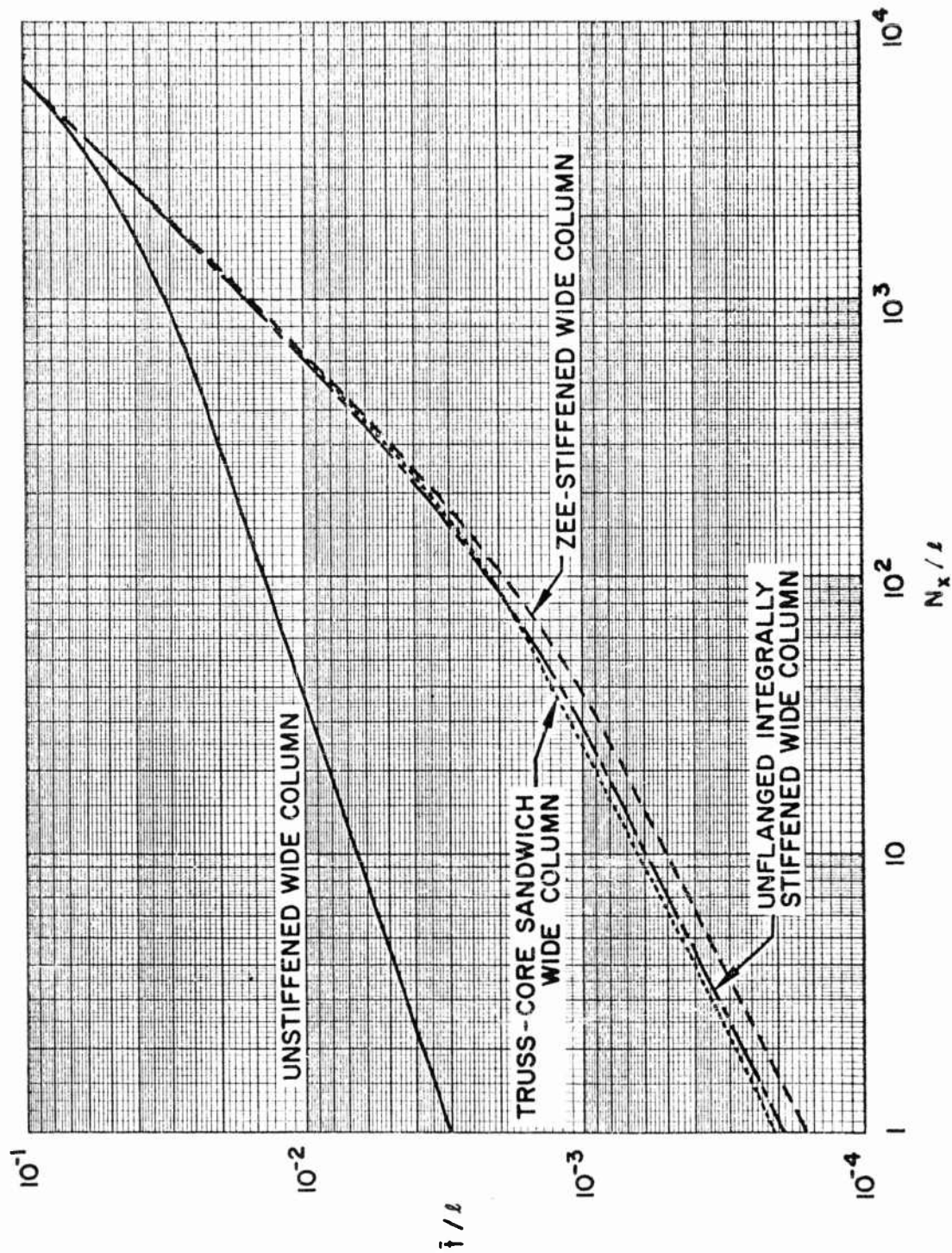


Fig. 4-39 Room-Temperature, Minimum-Weight Design Chart for Cross-Rolled Beryllium Sheet Wide Columns

index, all constructions carry a uniform maximum buckling stress and therefore have equal efficiency. Selection of type of construction under these circumstances should be based primarily on economic considerations. It should be noted, however, that the loading index where all constructions begin to have equal efficiency is usually either above the normal range of the loading index, or can be carried more efficiently by some other material having a higher compressive yield-to-density ratio.

The straight-line portions of the curves to the left of the charts are a function of modulus of elasticity. By noting the point where deviation from the straight line begins, the proportional limit stress for each construction may be determined. It can be seen that the proportional limit occurs at increasingly lower loading indexes as the constructions become more efficient; i. e., as the weight index decreases. This, of course, reflects the basic premise of efficient design: the higher the uniform stress across the cross-section, the higher the efficiency. Minimum-weight design charts derived for a particular material, such as those presented here, are recommended for design applications because of the clear evaluation of the plastic stress-range afforded the designer.

Plastic stress-ranges for structures stressed by other than axial loads are not shown owing to the lack of effective plasticity reduction factors for these cases. Only elastic ranges are shown.

Beryllium minimum-weight design charts for wide columns at room temperature and 800°F are presented in Figs. 4-39 and 4-40, respectively. Similar charts for compression panels are shown in Figs. 4-41 and 4-42. Figure 4-43 gives beryllium minimum-weight design curves for shear panels at both room temperature and 800°F. Beryllium multiweb box beam minimum-weight design curves at room temperature and 800°F are presented in Figs. 4-44 and 4-45, respectively. In a similar manner, Figs. 4-46 and 4-47 show curves for long beryllium axially loaded cylinders. Minimum-weight design curves for beryllium cylinders in torsion at room temperature and 800°F are given in Fig. 4-48. Finally, Fig. 4-49 presents beryllium minimum-weight design charts for hydrostatically loaded cylinders at room temperature and 800°F.

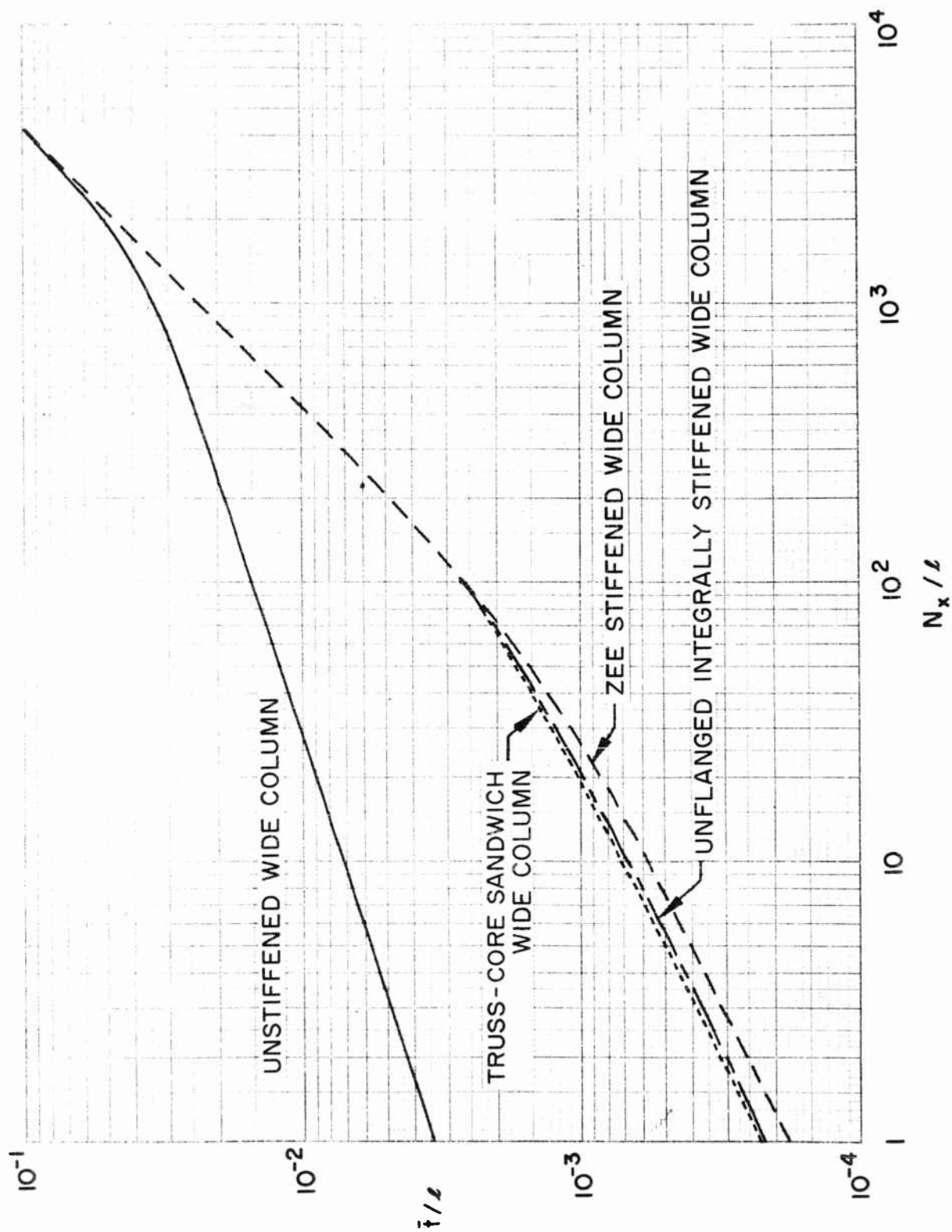


Fig. 4-40 800°F, Minimum-Weight Design Chart for Cross-Rolled Beryllium Sheet Wide Columns

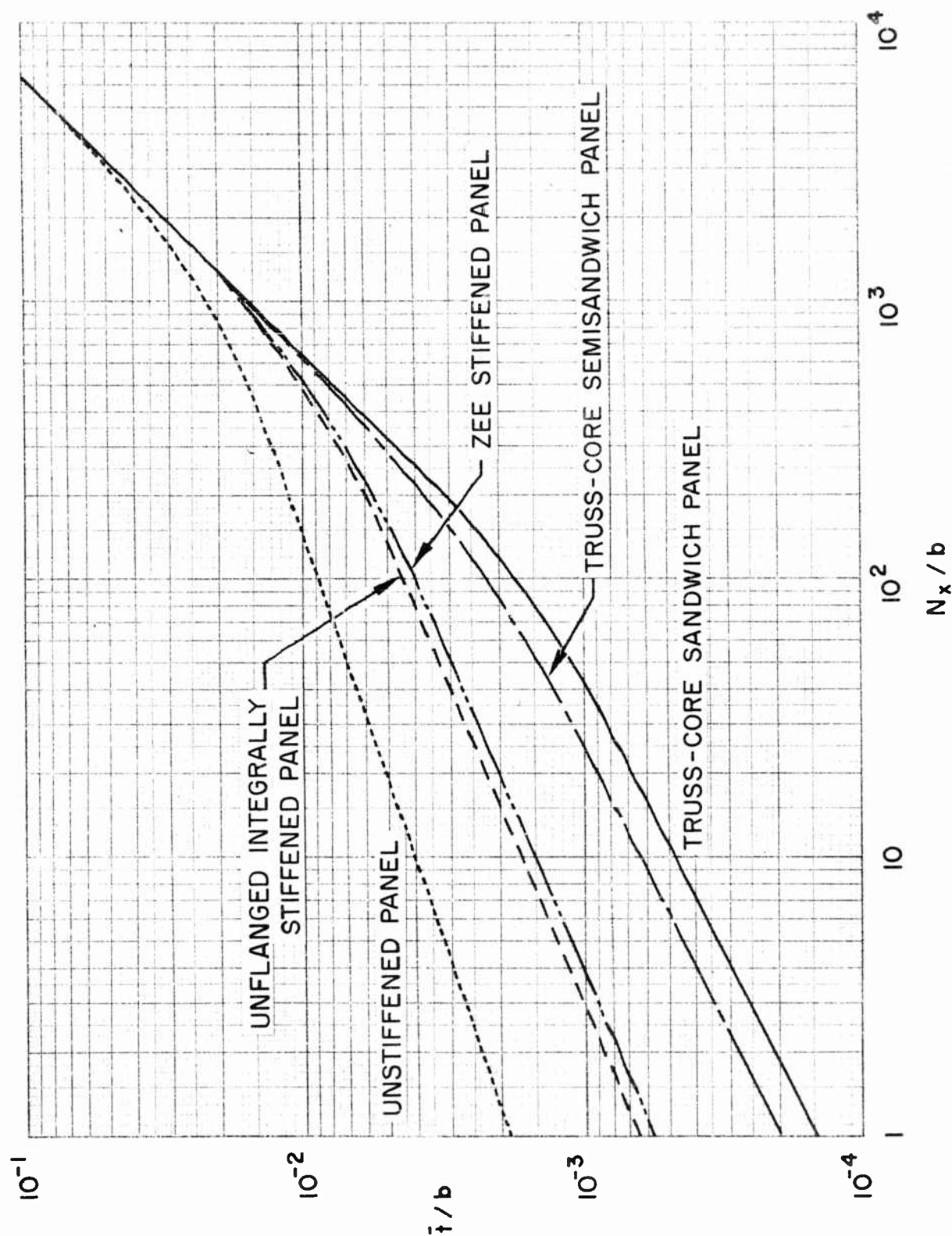


Fig. 4-41 Room-Temperature, Minimum-Weight Design Chart for Cross-Rolled Beryllium Sheet Compression Panels

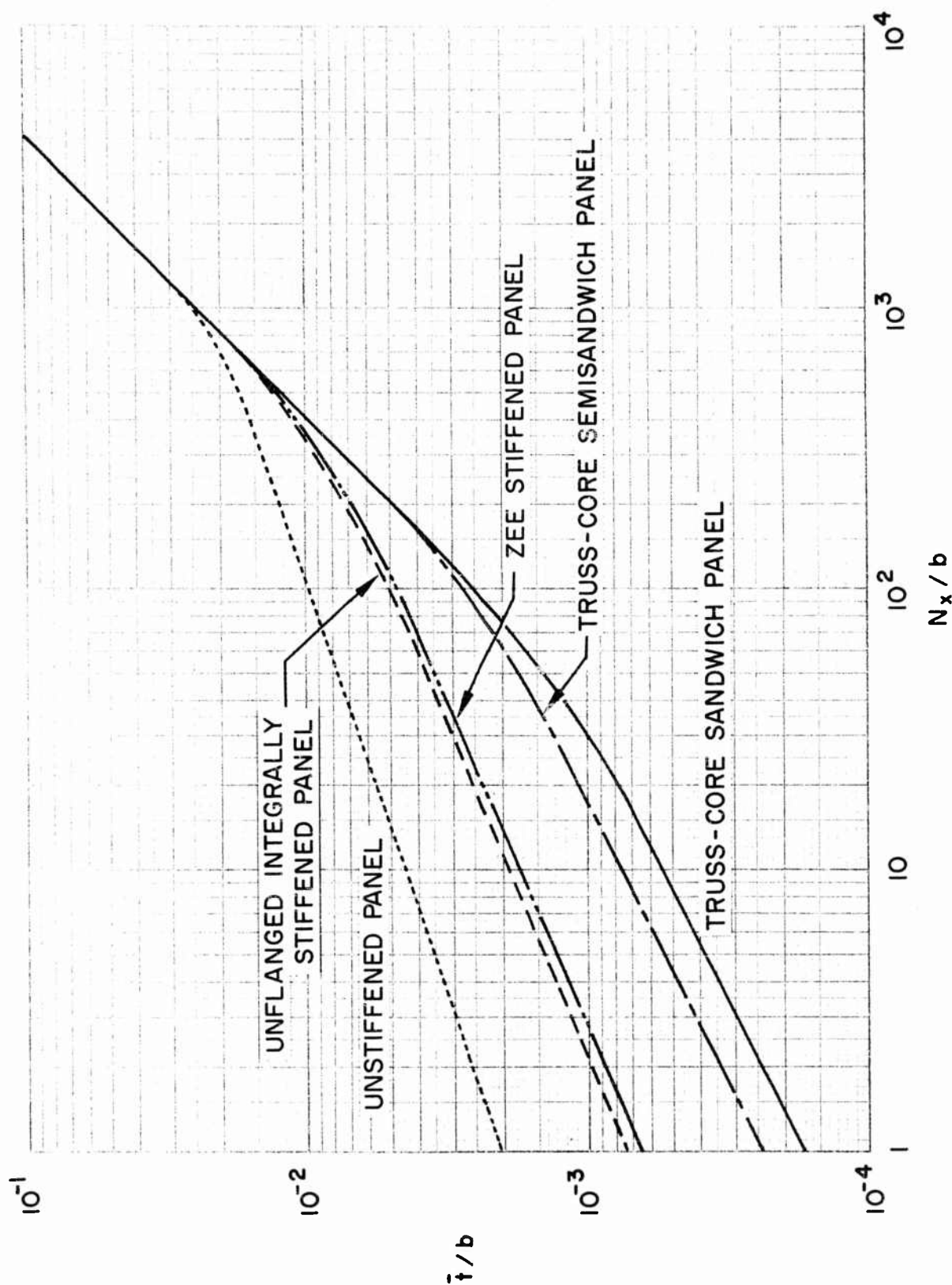


Fig. 4-42 800°F, Minimum-Weight Design Chart for Cross-Rolled Beryllium Sheet Compression Panels

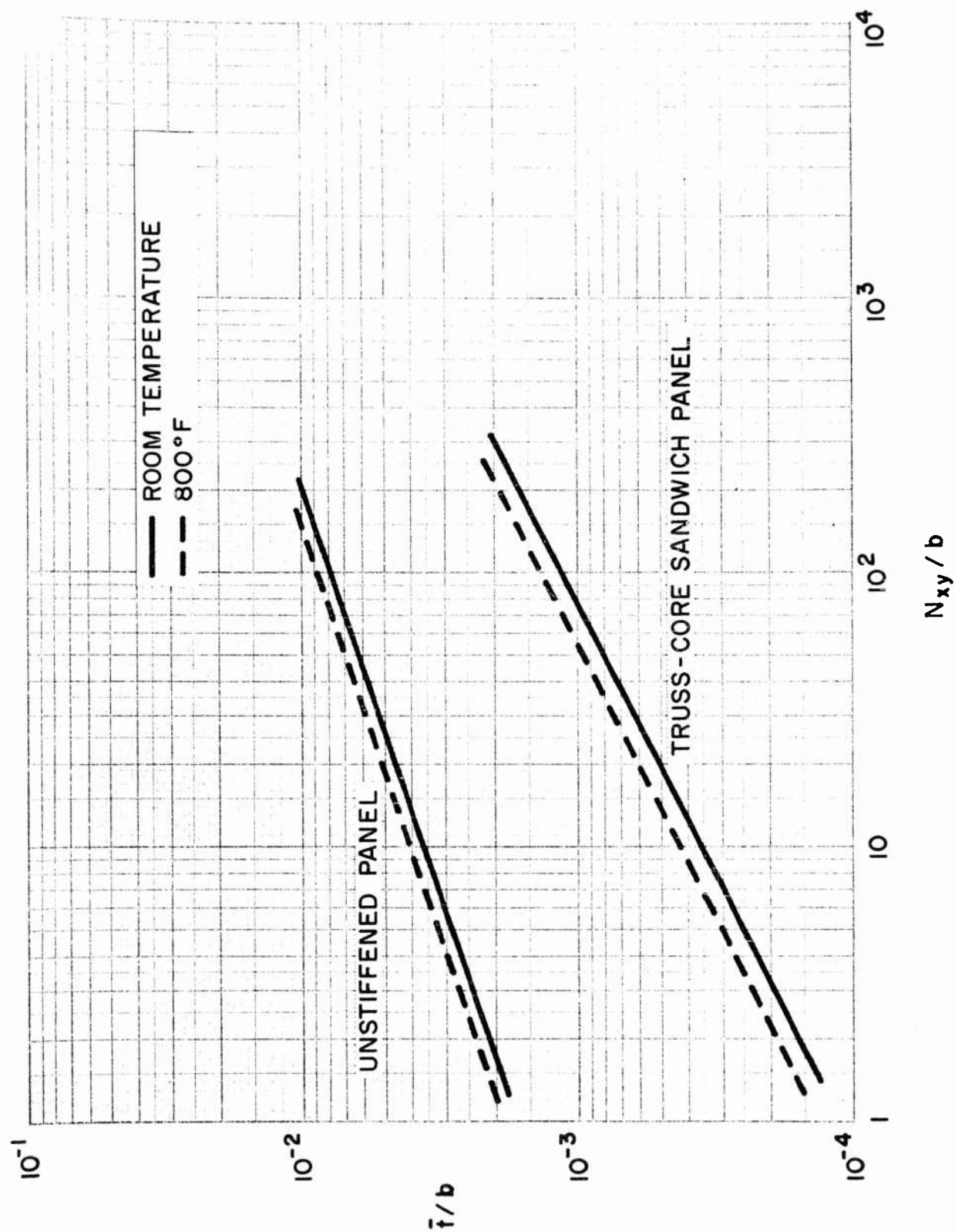


Fig. 4-43 Minimum-Weight Design Chart for Cross-Rolled Beryllium Sheet Shear Panels
At Room Temperature and 800°F

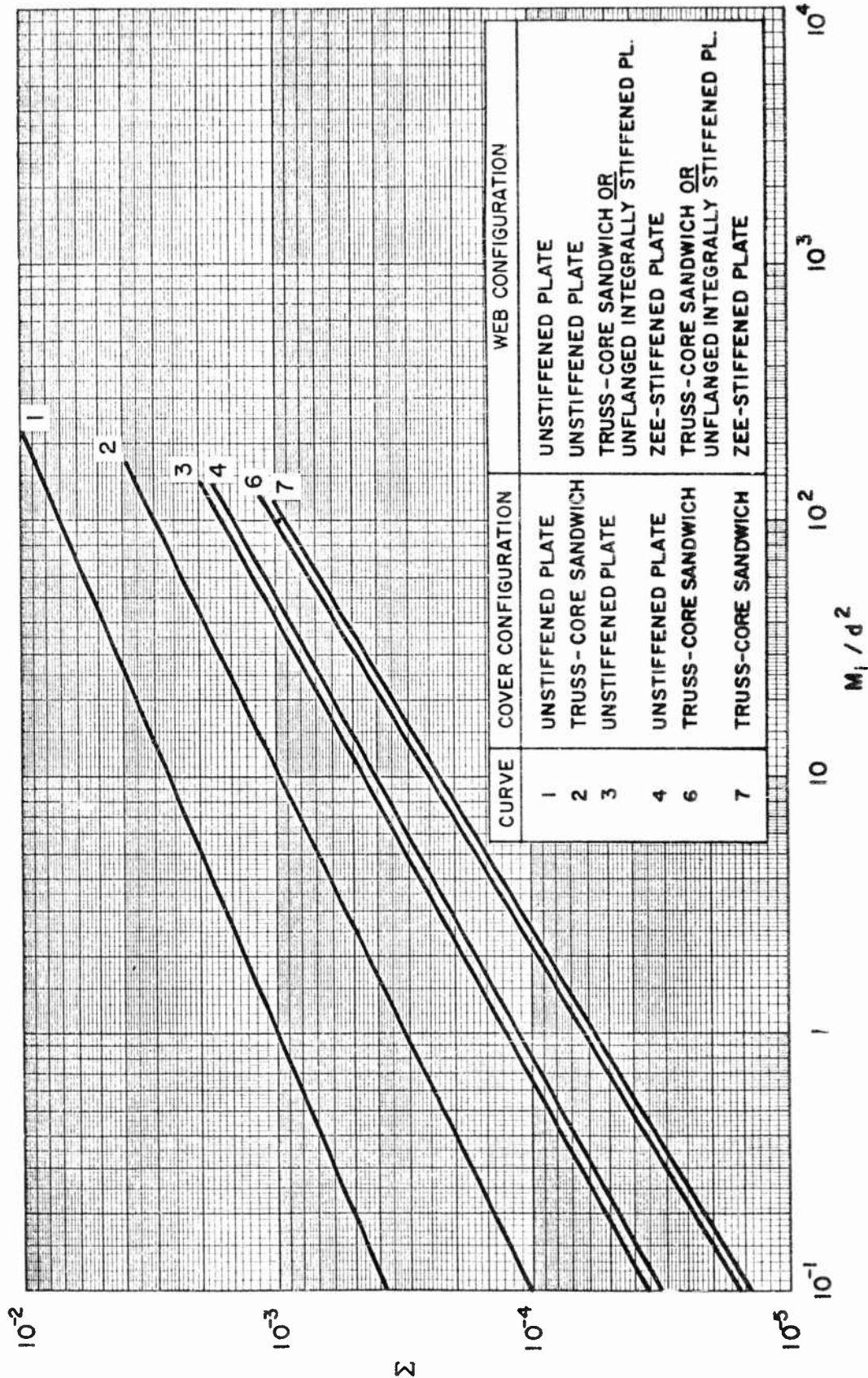


Fig. 4-44 Design Chart for Minimum-Weight Beryllium Cross-Rolled Sheet Multiweb Box Beams Loaded Elastically in Bending at Room Temperature

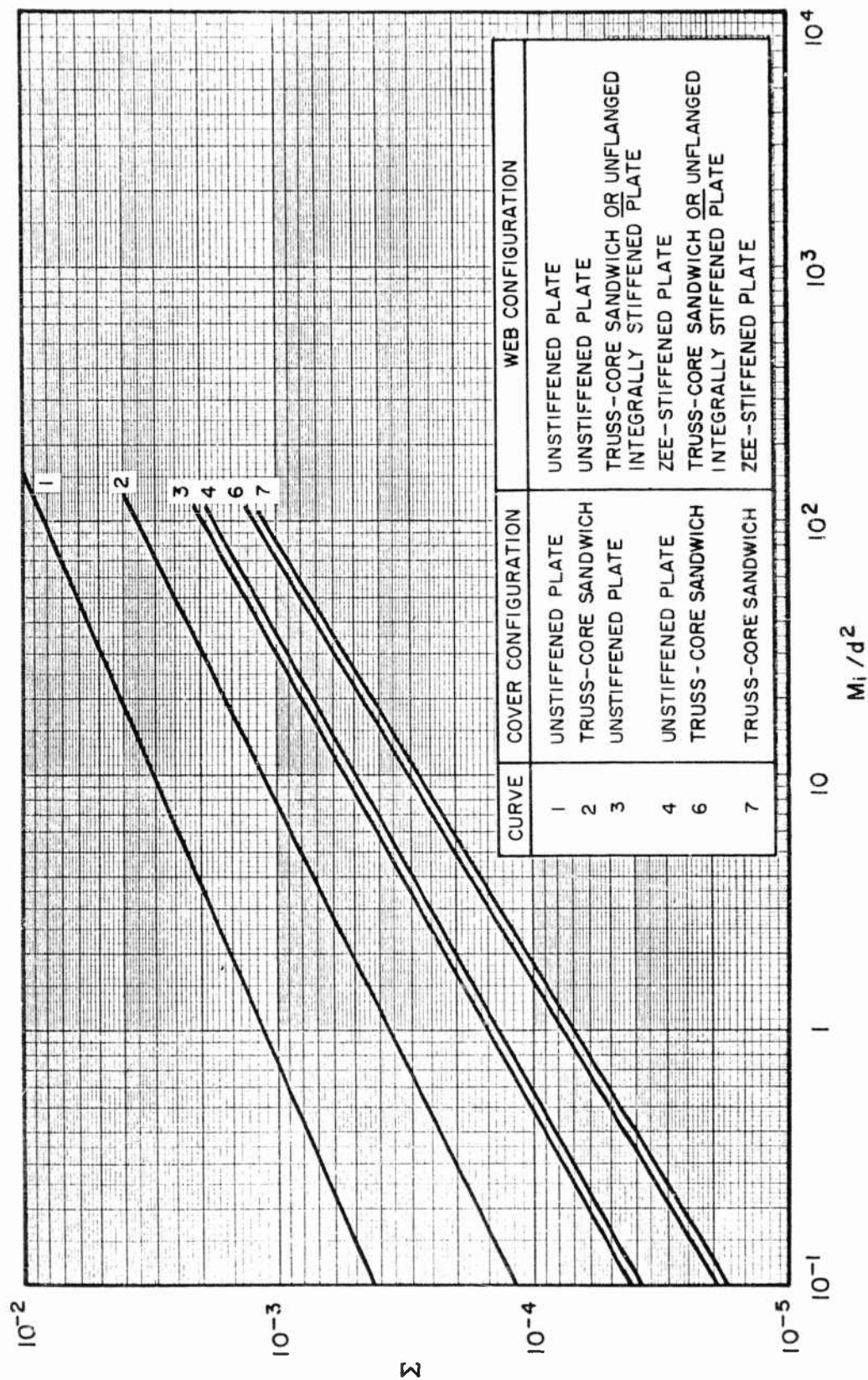


Fig. 4-45 Design Chart for Minimum-Weight Beryllium Cross-Rolled Sheet Multiweb Box Beams Loaded Elastically in Bending at 800°F

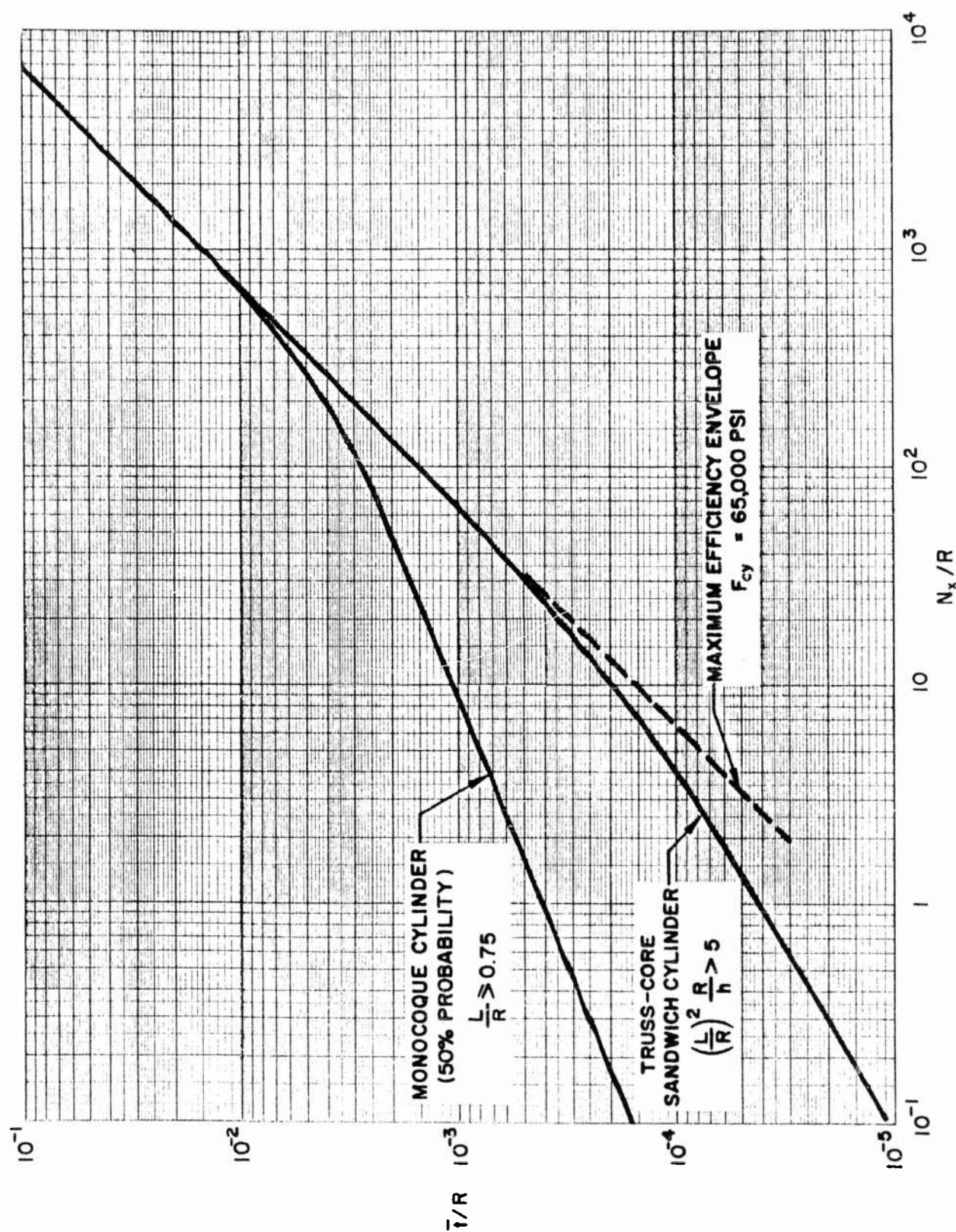


Fig. 4-46 Room Temperature, Minimum-Weight Design Chart for Beryllium Cross-Rolled Sheet Long Cylinders Subjected to a Uniform Axial Load

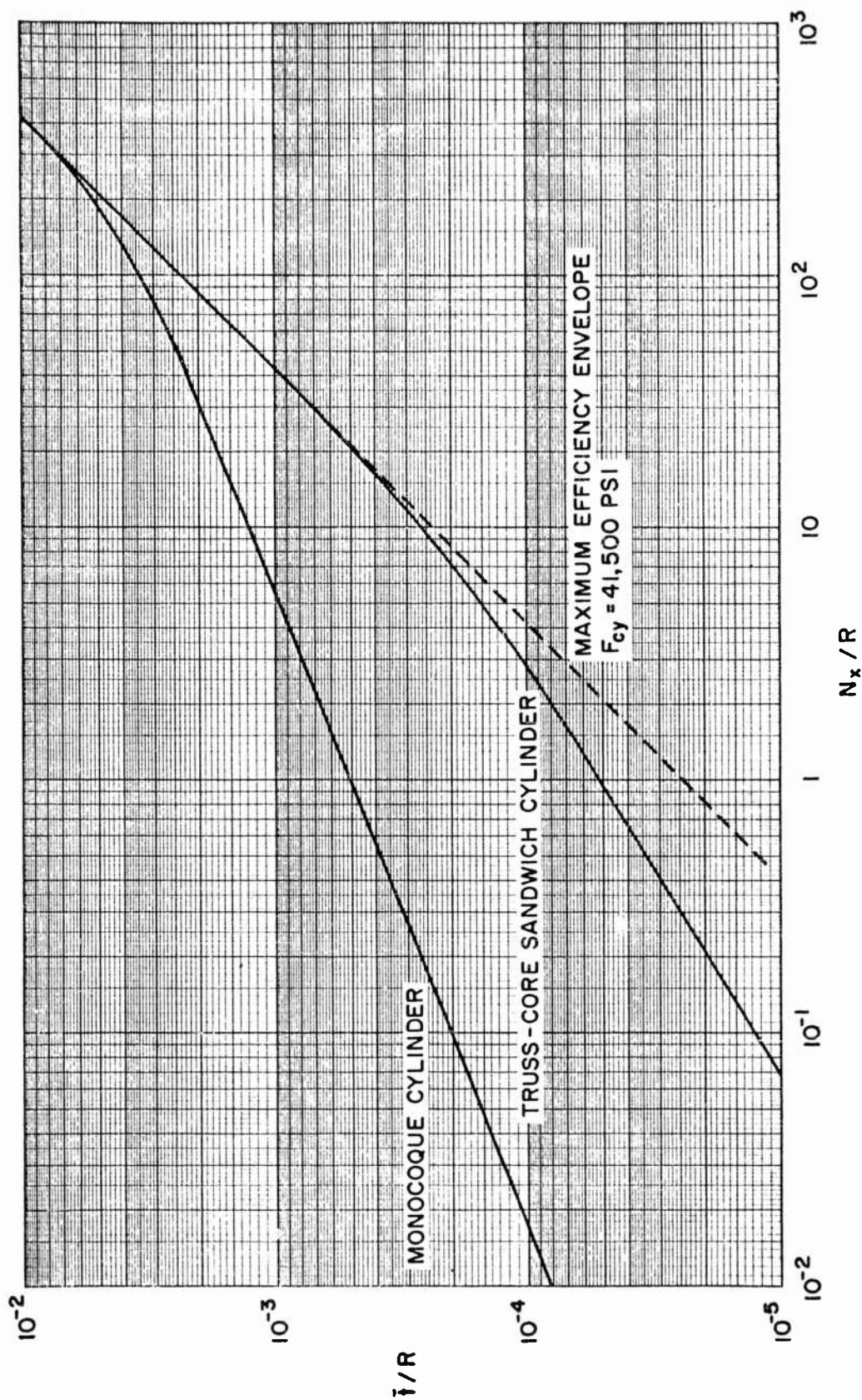


Fig. 4-47 800°F, Minimum-Weight Design Chart for Beryllium Cross-Rolled Sheet Long Cylinders Subjected to a Uniform Axial Load

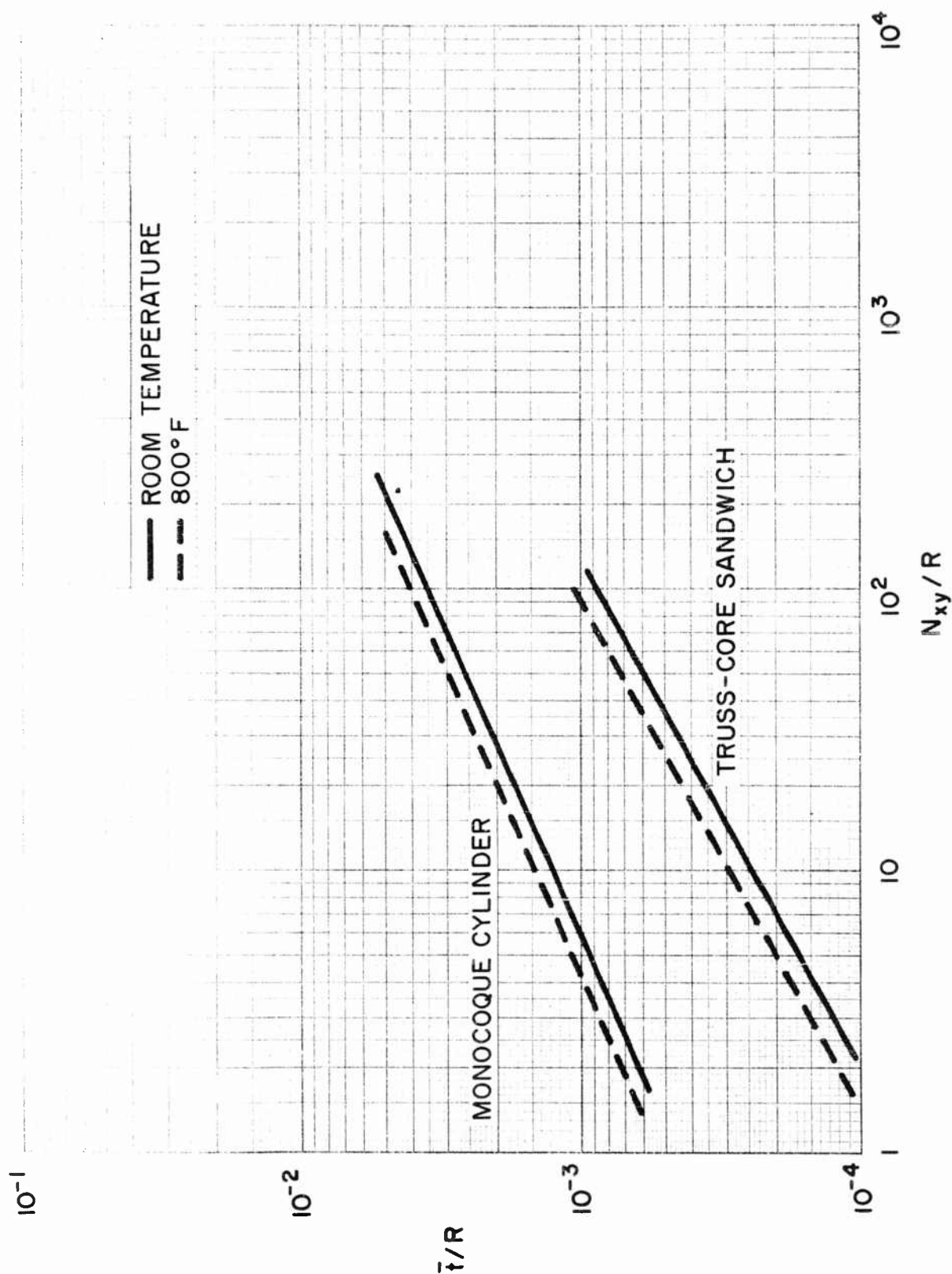


Fig. 4-48 Minimum-Weight Design Chart for Cross-Rolled Beryllium Sheet Moderate-Length Cylinders in Torsion at Room Temperature and 800°F, $L/R = 1$

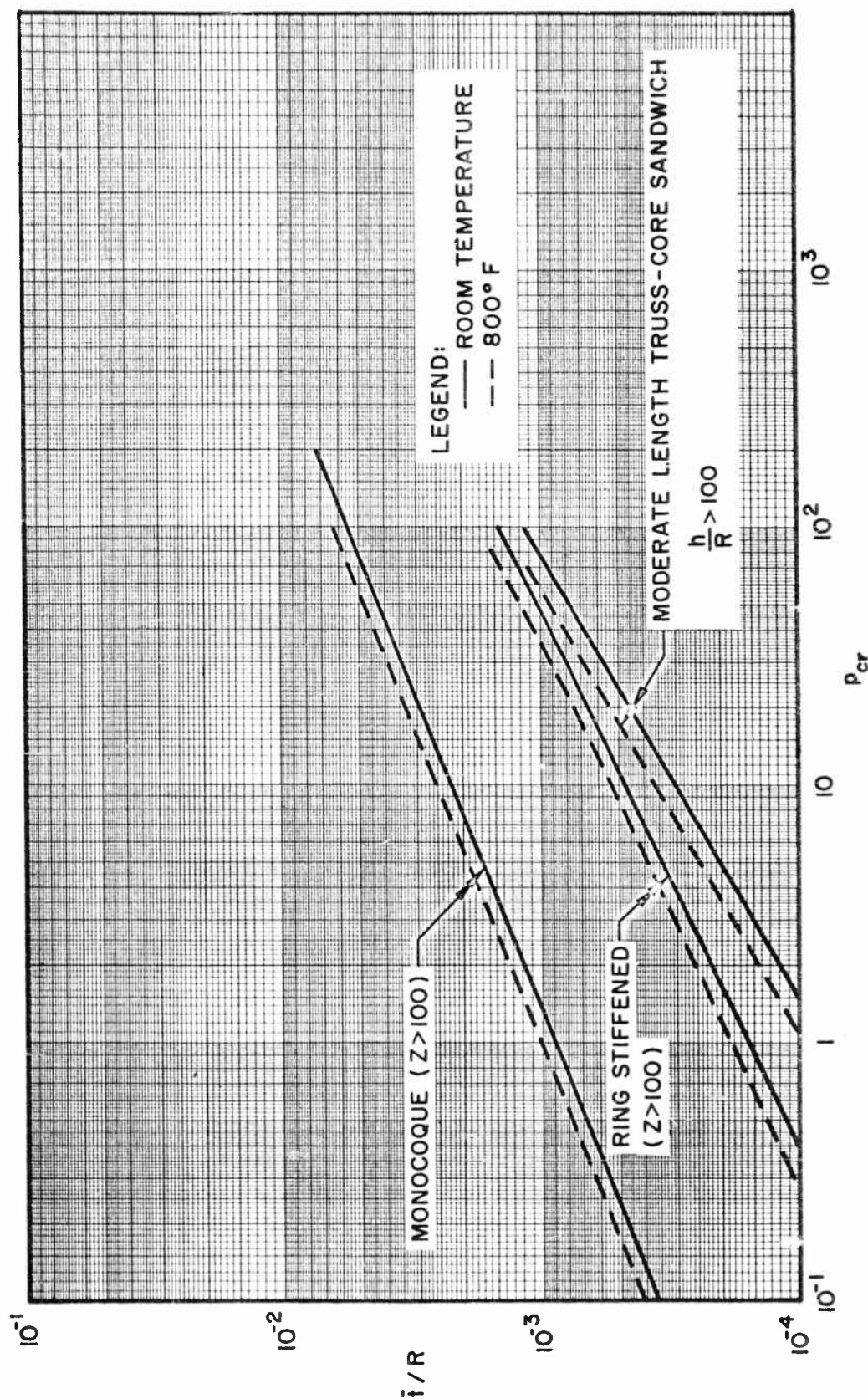


Fig. 4-49 Design Chart for Minimum-Weight Beryllium Cross-Rolled Sheet Cylinders Loaded Elastically in Hydrostatic Compression at Room Temperature and 800° F, $L/R = 1$

It should be noted that the preceding figures are derived from minimum-weight analyses which have assumed a Poisson's ratio of 0.30. This value has been found to be somewhat high for beryllium cross-rolled sheet as a result of tests conducted late in the period of this contract. The consequence of using $\mu = 0.30$ in the following charts may be shown to be slight unconservatism.

4.4 COMPARATIVE EFFICIENCY STUDIES OF BERYLLIUM CROSS-ROLLED SHEET WITH OTHER STRUCTURAL MATERIALS

As discussed in the introduction to this section, a comparison of materials for a given combination of structural component, loading, and detailed configuration should be preceded by minimum-weight analysis. This procedure insures that the weight representing each material for a given load is the minimum weight attainable. As a result, a comparison of materials thus derived has the desirable features of being unbiased toward any material, and showing the true minimum weight associated with each material as well as its standing in relation to other materials. Such comparisons are presented in this subsection, based on the information previously presented in this section.

A comparison of structural materials should be in terms of weight versus load in order to account for differences in densities. Since the minimum-weight equations presented in subsection 4.2 are generally in terms of equivalent thickness per unit width \bar{t} , and load per inch of width, a minimum-weight equation in terms of total weight per unit length W_i and total load P may easily be written. For example, Eq. (4.46), the minimum-weight equation for an axially loaded monocoque cylinder, becomes:

$$\frac{P}{R^2} = 0.428 \bar{\eta} E \left(\frac{W_i}{R^2} \right)^{2.54} \rho^{-2.54} \quad (4.80)$$

where

$$P = 2\pi R N_x$$

$$W_i = 2\pi R \bar{t} \rho$$

Equation (4.80) has been solved for a number of structural materials at room temperature, 250°, 500°, 700°, 1000°, and 1250°F, and these results are presented graphically in Figs. 4-50 through 4-55, respectively. The curves in these figures are drawn up to the proportional limit; that is, $\bar{\eta}$ in Eq. (4.80) has been taken equal to unity and the charts compare elastic stresses only. It can be seen that beryllium

cross-rolled sheet provides the lightest-weight design for this application at all temperatures investigated. Further, the minimum weight required for beryllium (or any of the other structural materials) to carry a given applied load can be found by multiplying W_i/R^2 by the cylinder radius squared and the cylinder length.

It should be noted that the curves presented in Figs. 4-50 through 4-55 are series of parallel lines having a constant relationship. Consequently, it is evident that the information presented in these charts may be summarized on a single chart, such as shown in Fig. 4-56 which presents the ratio of weight of "x" material to the weight of beryllium cross-rolled sheet, denoted W_x/W_{Be} , for the several structural materials as a function of temperature. Here the superiority of beryllium in monocoque cylinders elastically loaded in axial compression is emphasized. Note that the material most competitive with beryllium requires a minimum of twice as much weight to carry the same total load at temperatures up to 1250°F.

The curves of Fig. 4-56 may be mathematically expressed by substituting into Eq. (4.80) for material "x" and for beryllium, then combining the equations for the conditions:

$$\left(\frac{P}{R^2}\right)_x = \left(\frac{P}{R^2}\right)_{Be}$$

$$\bar{\eta} = 1$$

that is, both materials support identical axial loads on cylinders of the same radius, and the stresses are elastic. The resulting equation is:

$$\frac{W_x}{W_{Be}} = \frac{\rho_x}{\rho_{Be}} \left(\frac{E_{Be}}{E_x}\right)^{1/n} \quad (4.81)$$

where n is the exponent found in the minimum-weight equation. It may be shown that Eq. (4.81) is applicable in the elastic stress-range for all combinations of structural components, loadings, and detailed configurations for which minimum-weight

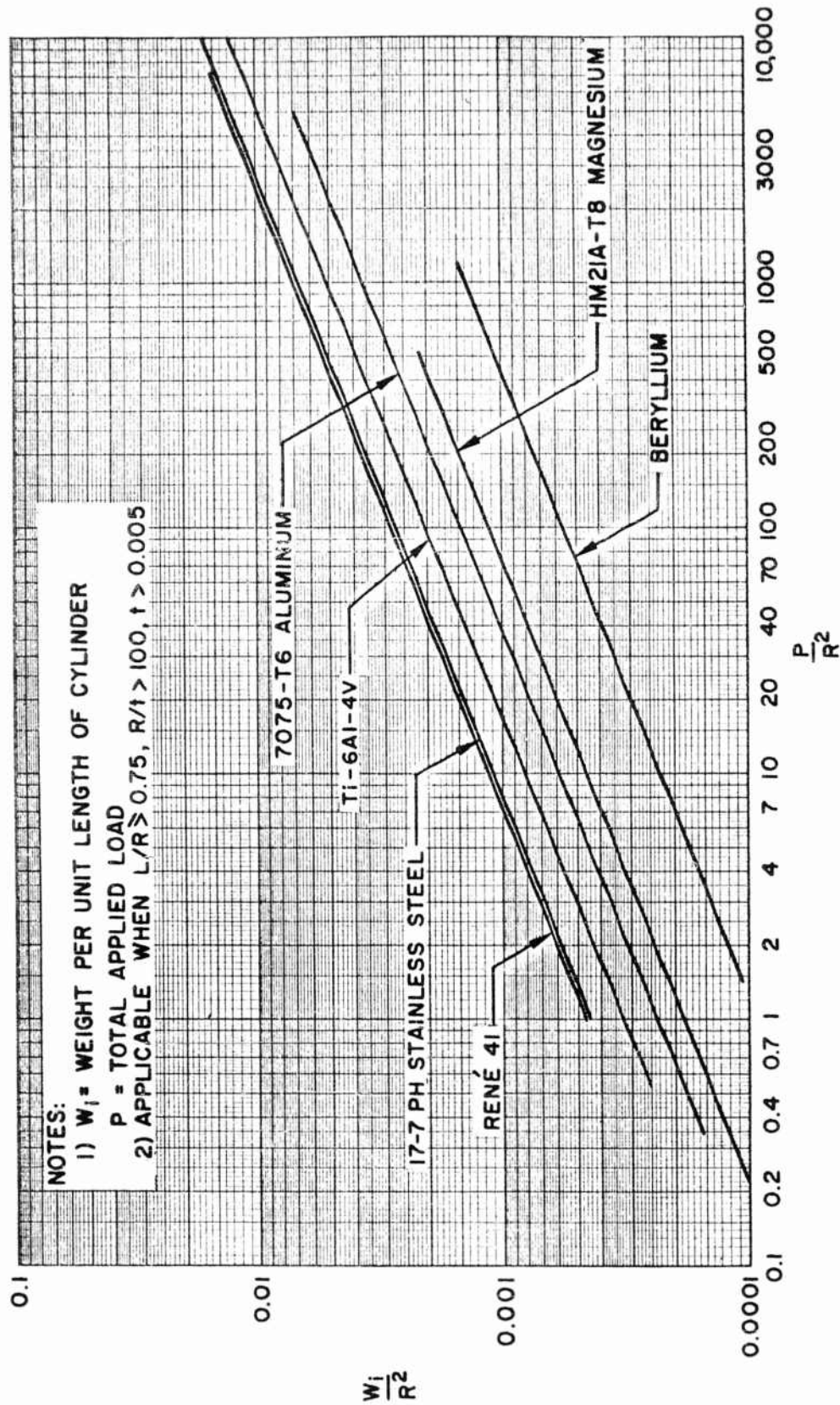


Fig. 4-50 Weight-Load Comparison at Room Temperature of Structural Materials Used in Monocoque Cylinders Elastically Loaded in Axial Compression

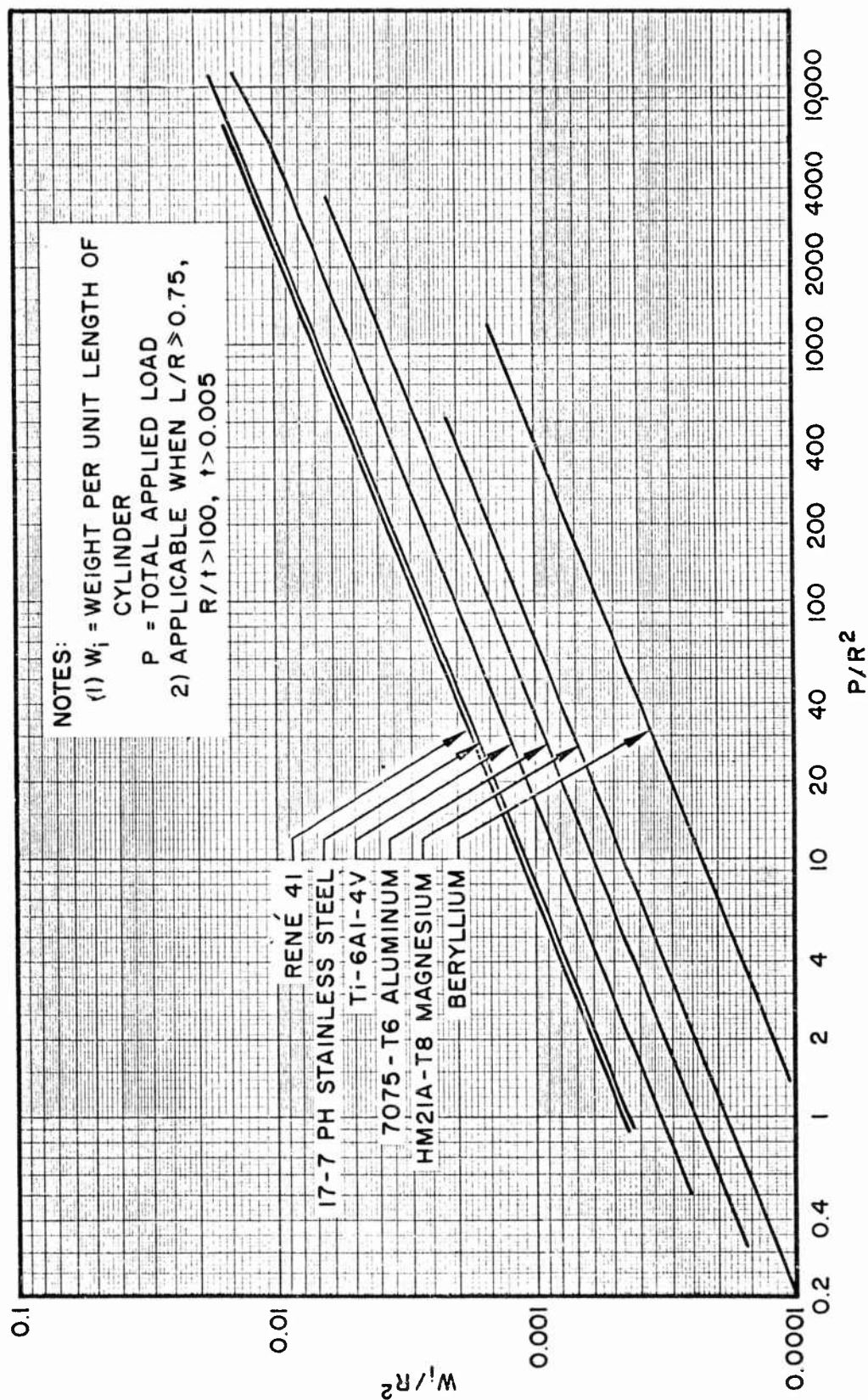


Fig. 4-51 Weight-Load Comparison at 250° F of Structural Materials Used in Monocoque Cylinders Elastically Loaded in Axial Compression

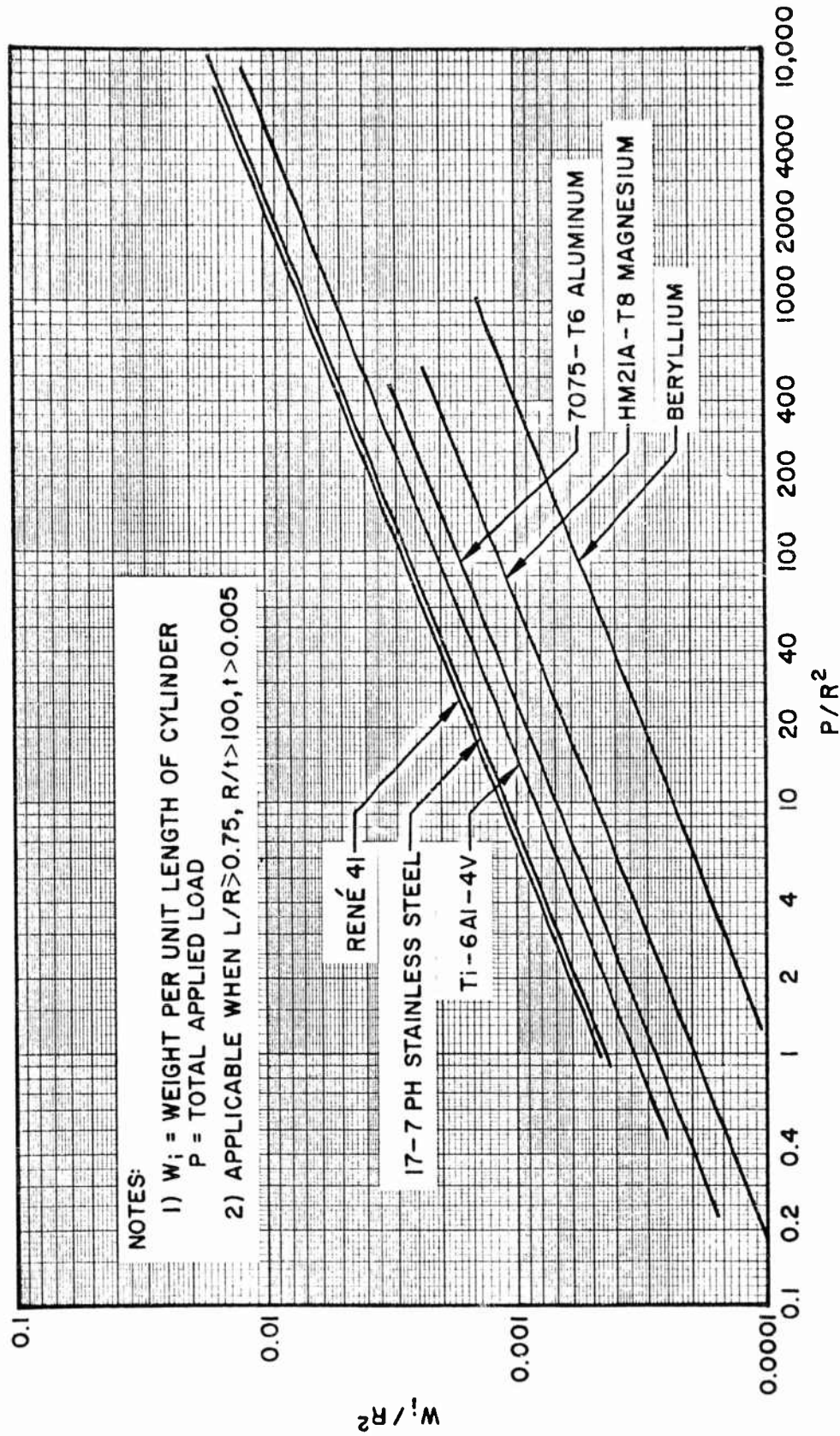


Fig. 4-52 Weight-Load Comparison at 500°F of Structural Materials Used in Monocoque Cylinders Elastically Loaded in Axial Compression

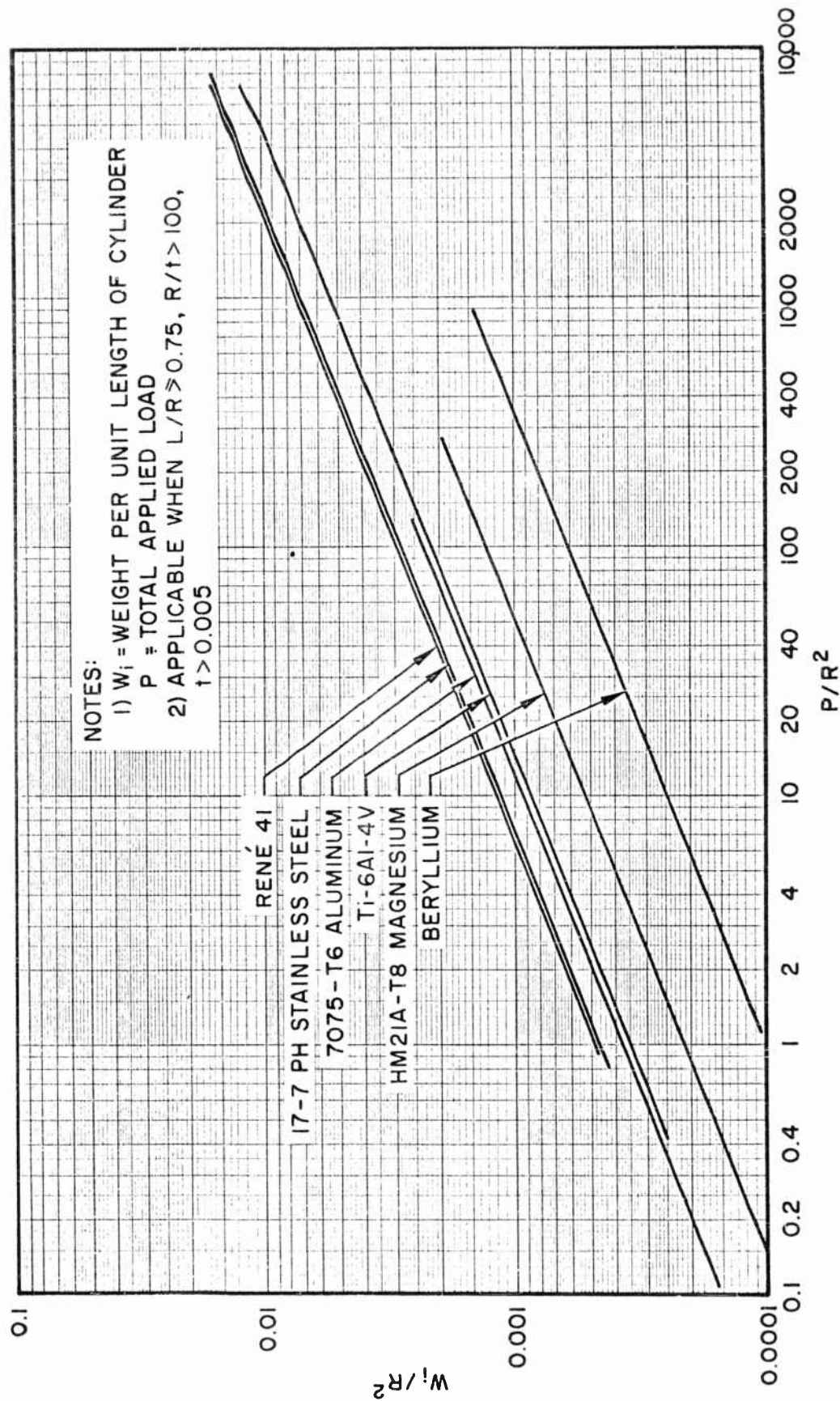


Fig. 4-53 Weight-Load Comparison at 700°F of Structural Materials Used in Monocoque Cylinders Elastically Loaded in Axial Compression

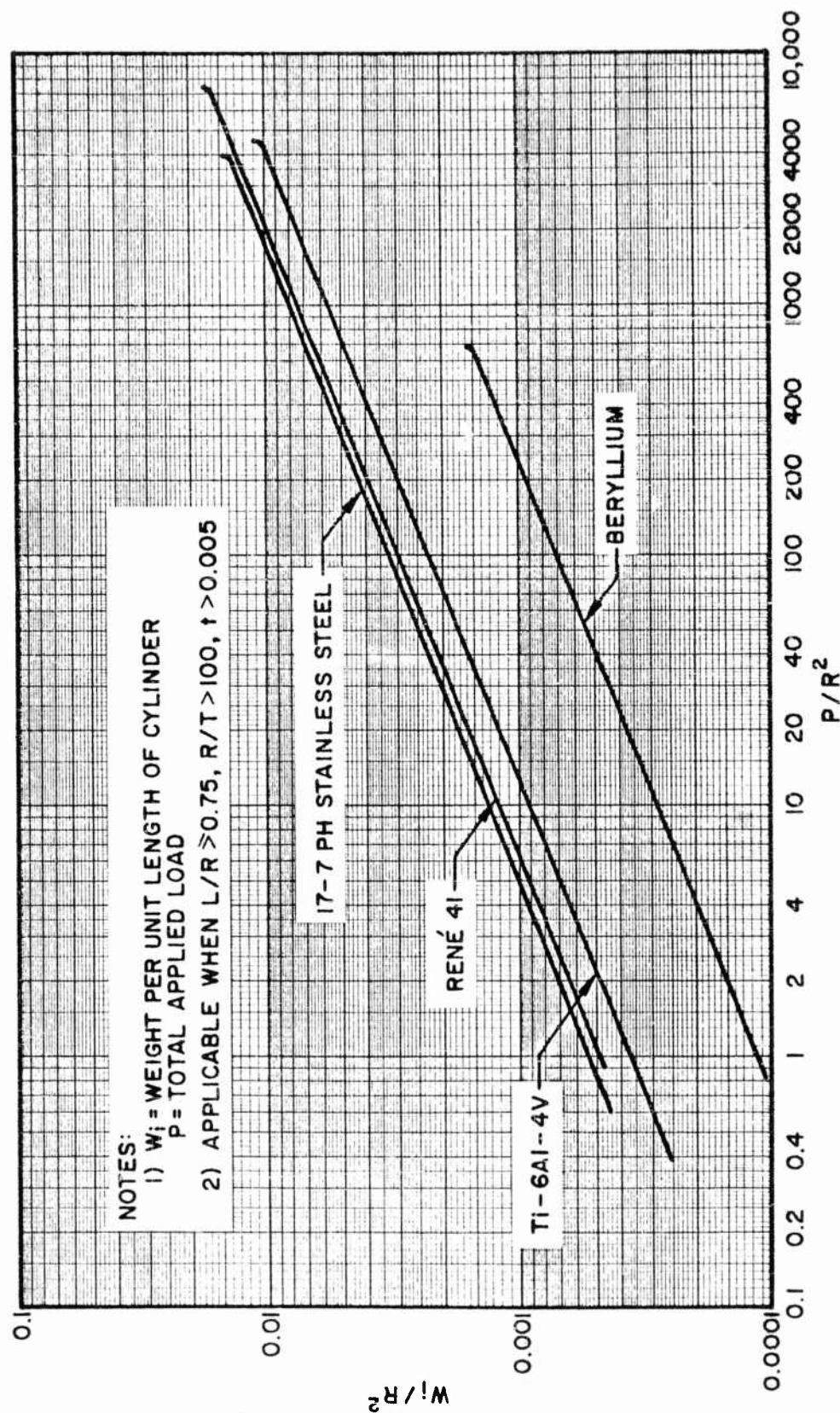


Fig. 4-54 Weight-Load Comparison at 1000°F of Structural Materials Used in Monocoque Cylinders

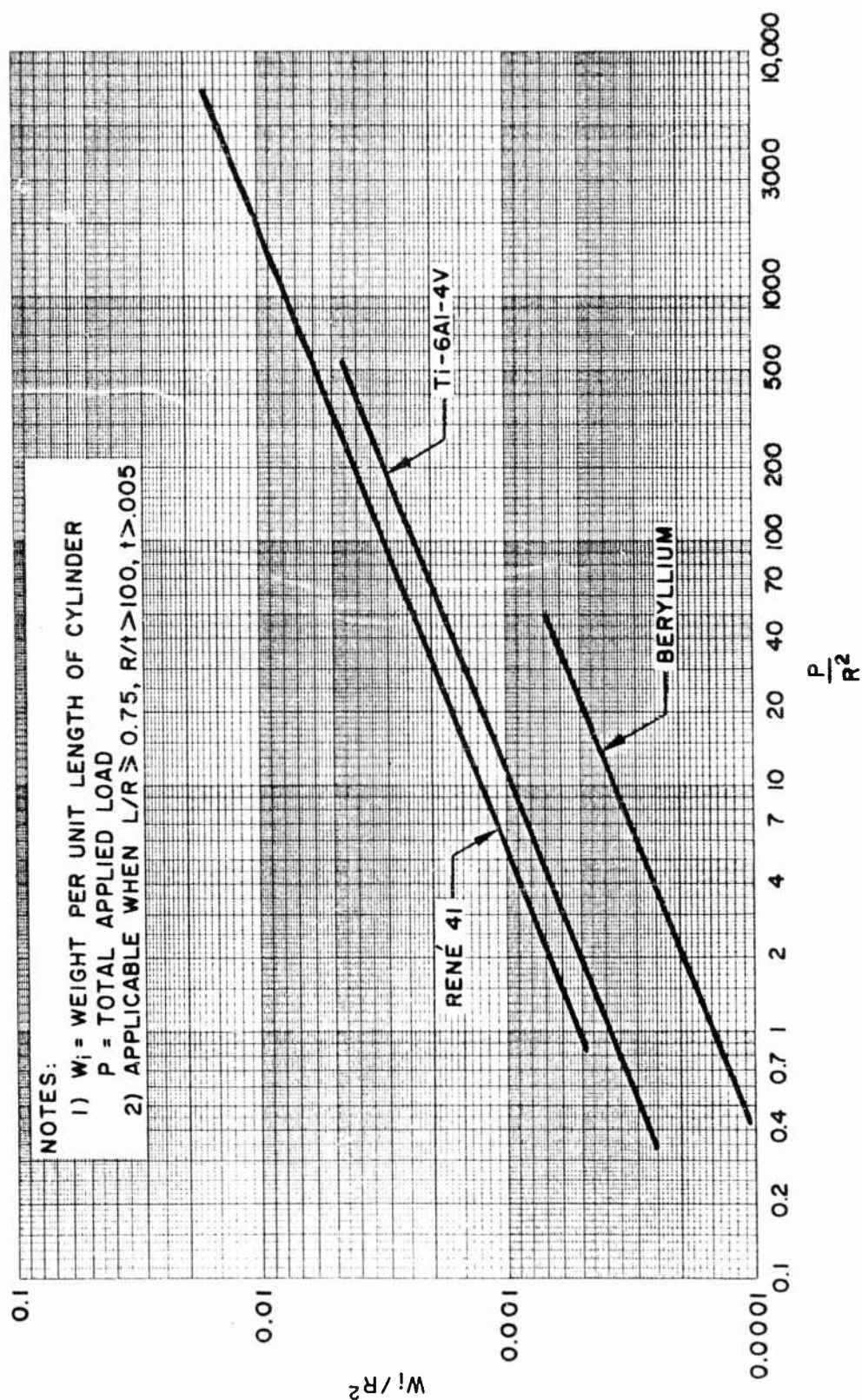


Fig. 4-55 Weight-Load Comparison at 1250° F of Structural Materials Used in Monocoque Cylinders Elastically Loaded in Axial Compression

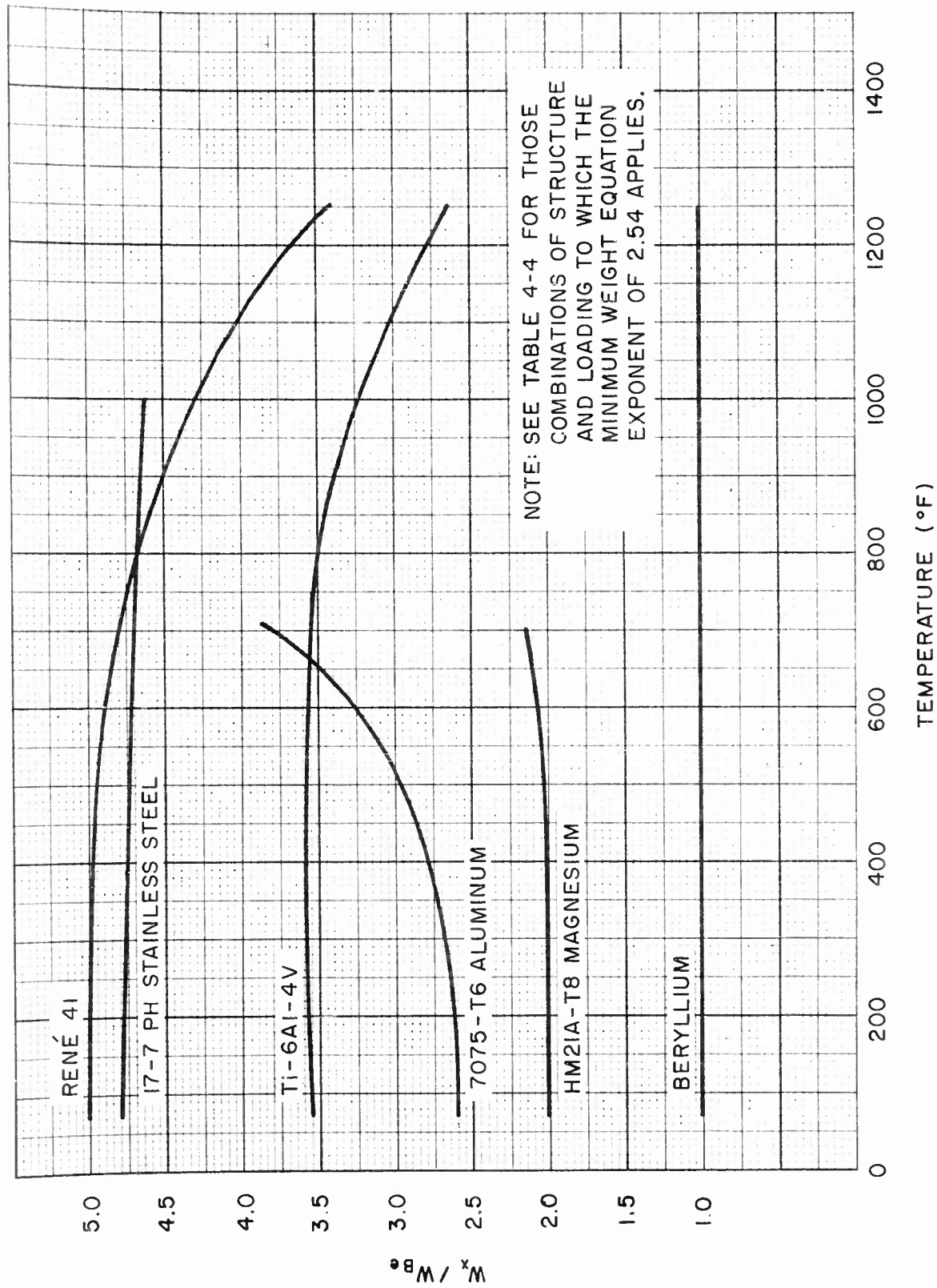


Fig. 4-56 Beryllium-Based Weight Ratios for Elastically Loaded Structures of Optimum Proportions Having a Minimum-Weight Equation Exponent of 2.54

design information is presented in this report. Therefore, material comparisons for each such combination can be made knowing the material densities, elastic moduli, and the minimum-weight equation exponent.

A review of the minimum-weight equation exponents presented in subsection 4.2 shows that several exponents have been duplicated or nearly duplicated in the various minimum-weight equations. Thus, material comparisons based on Eq. (4.81) in many cases apply to more than one combination of structural component, loading, and detailed configuration. Table 4-4 summarizes the combinations considered in this report and their applicable exponent, and indicates which of the succeeding figures (Figs. 4-57 through 4-63) pertains to that exponent. Note that the weight ratios in these figures apply to optimum-proportioned configurations. Note also that the design weight for each of the materials shown may be determined by multiplying the proper W_x/W_{Be} ratio by the weight of the optimum-proportioned beryllium configuration. This latter weight may easily be found at room temperature and at 800°F with the assistance of the beryllium minimum-weight design charts presented in subsection 4.3.

It is apparent from Figs. 4-56 through 4-63 that beryllium cross-rolled sheet provides the lightest-weight design among the structural materials considered for all the combinations of structural component, loading, and detailed configuration considered in this report. As n increases from its minimum value (Fig. 4-63), to its maximum value (Fig. 4-57), the superiority of beryllium decreases. However, even when n is at its maximum value, beryllium's nearest competitor is still a minimum of 1.8 times heavier, except at temperatures exceeding 1400°F. It would appear on the basis of these comparisons that beryllium has high potential as an aerospace structural material for lightly loaded applications in the low-to-medium elevated-temperature range.

The effects of plasticity on minimum-weight design are known for axially loaded components (see subsection 4.2), and these effects have been evaluated for beryllium cross-rolled sheet in subsection 4.3 of this report. Similar evaluations for other structural

Table 4-4

SUMMARY OF MINIMUM-WEIGHT EQUATION EXPONENTS

Figure	n	Applies To Optimum Proportioned
4-56	2.54	(1) Axially loaded monocoque cylinders (2) Hydrostatically compressed monocoque cylinders ($n = 2.5$)
4-57	3.	(1) Flat, unstiffened wide columns (2) Flat, unstiffened compression panels (3) Flat, unstiffened shear panels
4-58	2.36	(1) Zee-stiffened compression panels (2) Unflanged, integrally stiffened compression panels ($n = 2.38$) (3) Multiweb box beams with unstiffened covers and webs ($n = 2.33$)
4-59	2.25	(1) Monocoque cylinders in torsion
4-60	2.	(1) Unflanged, integrally stiffened wide columns (2) Zee-stiffened wide columns (3) Truss-core sandwich wide columns (4) Truss-core sandwich compression panels (5) Truss-core sandwich shear panels (6) Truss-core semisandwich compression panels (7) Multiweb box beams with truss-core sandwich covers and unstiffened webs
4-61	1.858	(1) Long truss-core sandwich cylinders in torsion (2) Long truss-core sandwich cylinders in hydrostatic compression ($n = 1.88$) (3) Ring-stiffened cylinders in hydrostatic compression ($n = 1.826$)
4-62	1.77	(1) Moderate-length truss-core sandwich cylinders in torsion (2) Moderate-length truss-core sandwich cylinders in hydrostatic compression ($n = 1.74$) (3) Multiweb box beams with unstiffened covers and zee-stiffened webs ($n = 1.8$) (4) Multiweb box beams with unstiffened covers and truss-core sandwich webs ($n = 1.8$) (5) Multiweb box beams with unstiffened covers and unflanged integrally stiffened webs ($n = 1.8$)
4-63	1.67	(1) Truss-core sandwich cylinders in axial compression (2) Multiweb box beams with truss-core sandwich covers and truss-core sandwich webs (3) Multiweb box beams with truss-core sandwich covers and unflanged, integrally stiffened webs (4) Multiweb box beams with truss-core sandwich covers and zee-stiffened webs

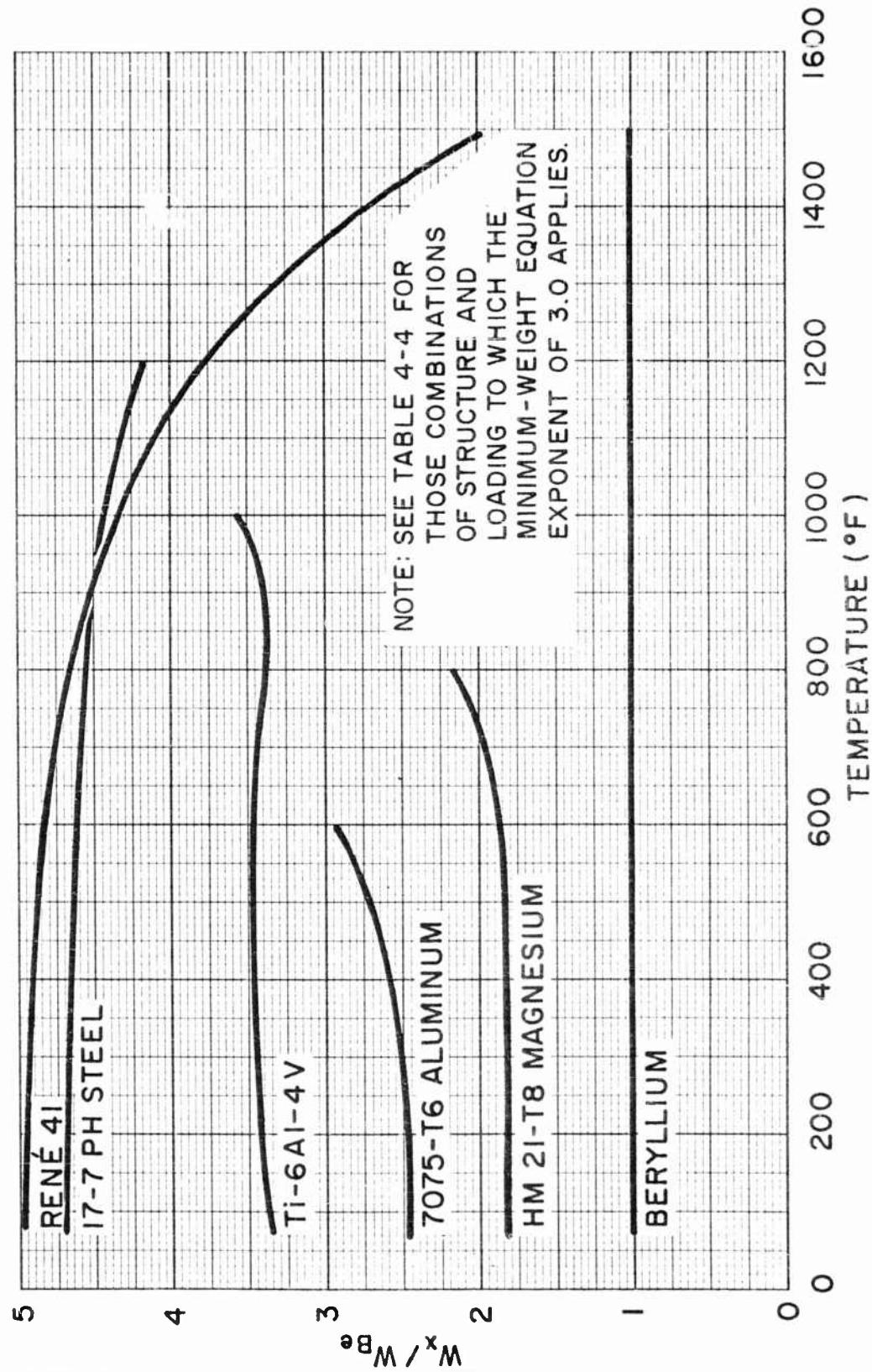


Fig. 4-57 Beryllium-Based Weight Ratios for Elastically Loaded Structures of Optimum Proportions Having a Minimum-Weight Equation Exponent of 3.0

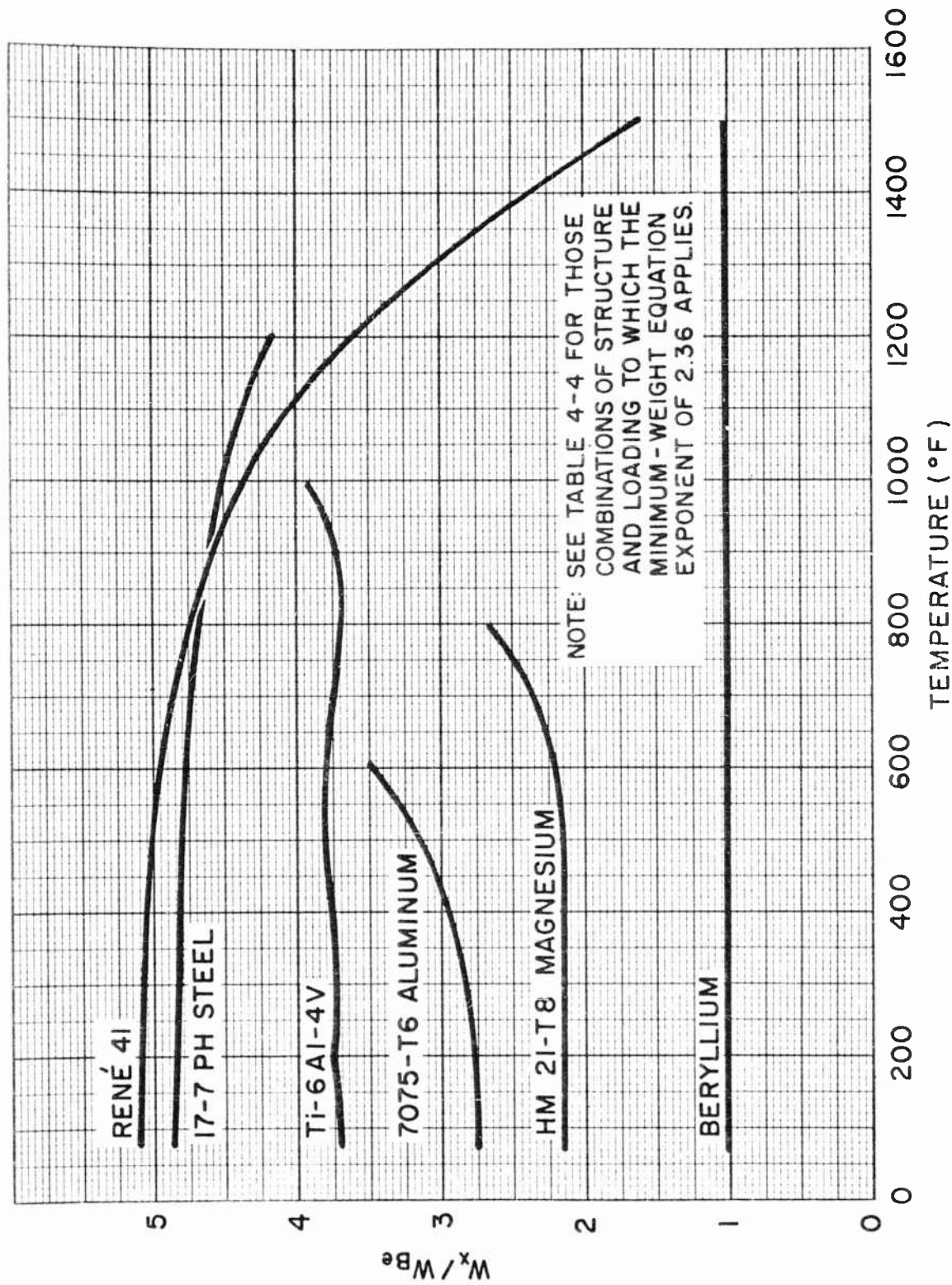


Fig. 4-58 Beryllium-Based Weight Ratios for Elastically Loaded Structures of Optimum Proportions Having a Minimum-Weight Equation Exponent of 2.36

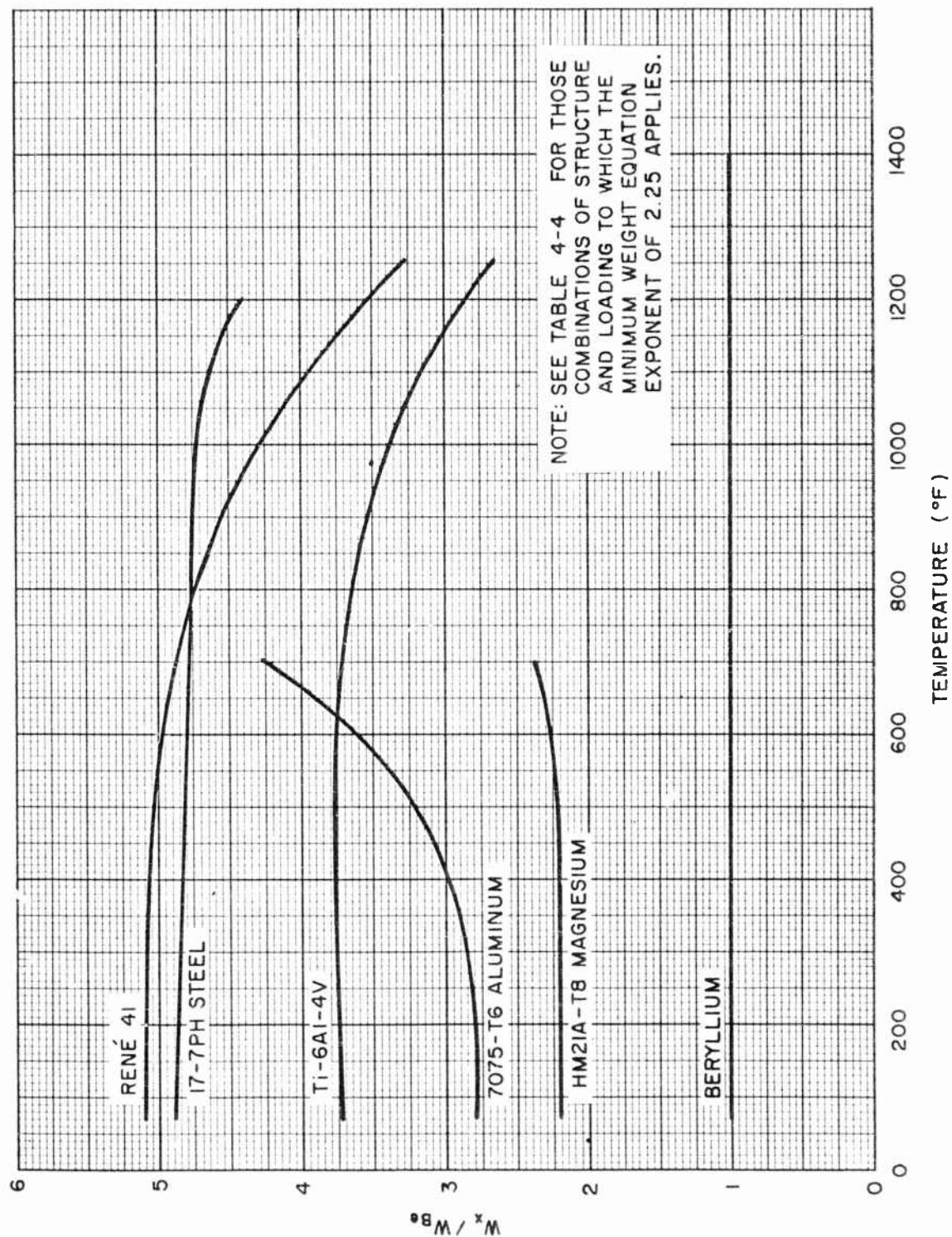


Fig. 4-59 Beryllium-Based Weight Ratios for Elastically Loaded Structures of Optimum Proportions Having a Minimum-Weight Equation Exponent of 2.25

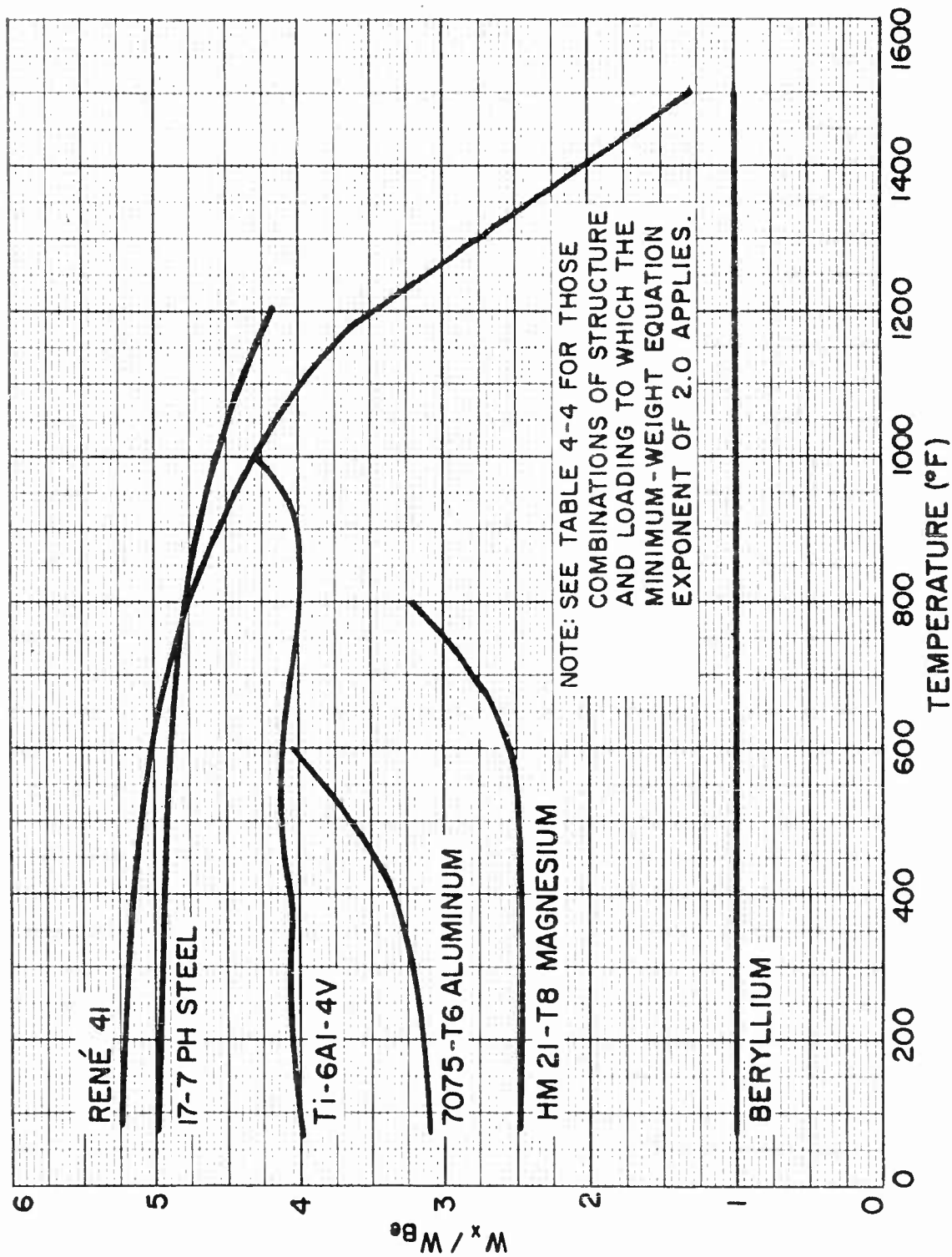


Fig. 4-60 Beryllium-Based Weight Ratios for Elastically Loaded Structures of Optimum Proportions Having a Minimum-Weight Equation Exponent of 2.0

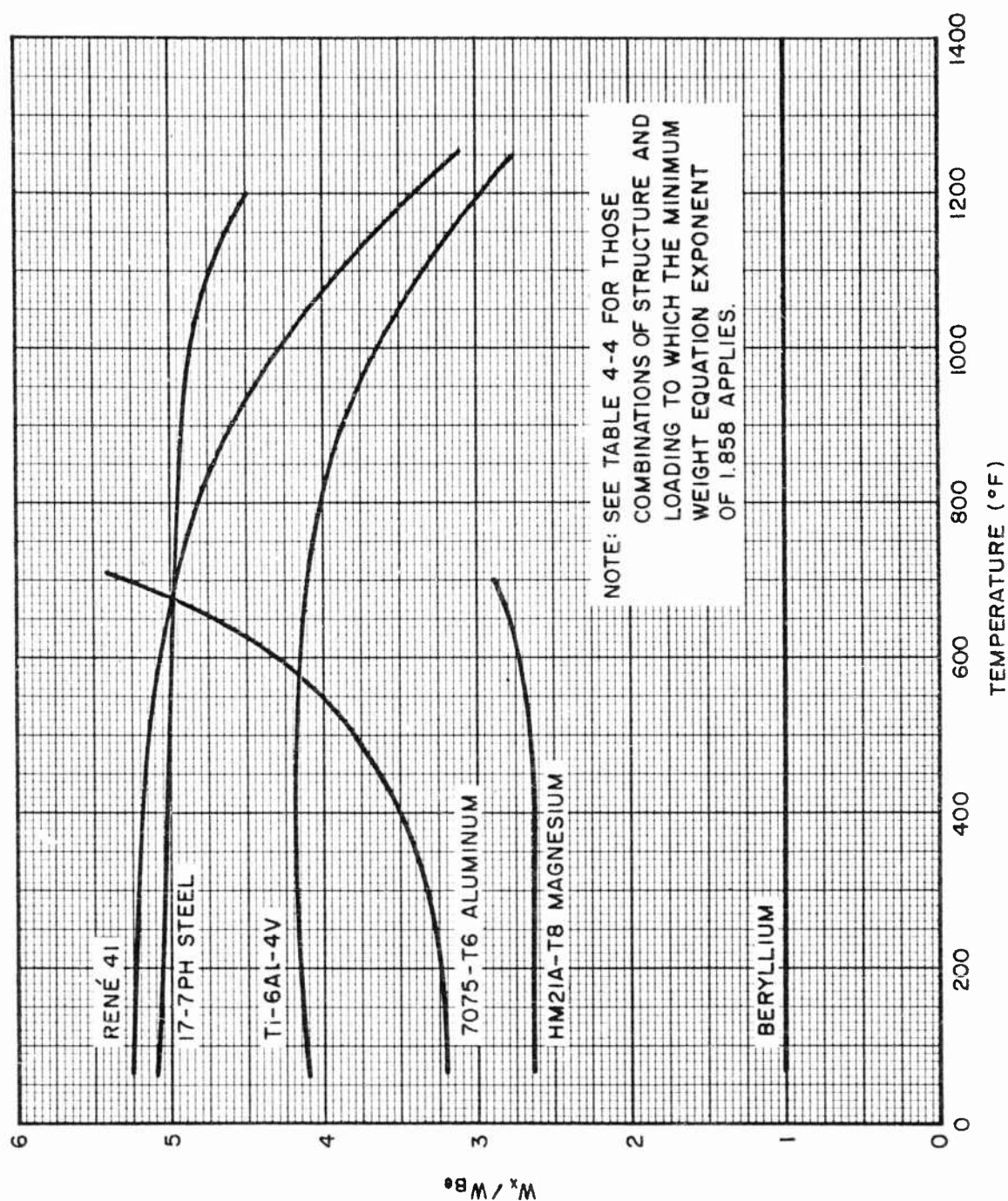


Fig. 4-61 Beryllium-Based Weight Ratios for Elastically Loaded Structures of Optimum Proportions Having a Minimum-Weight Equation Exponent of 1.858

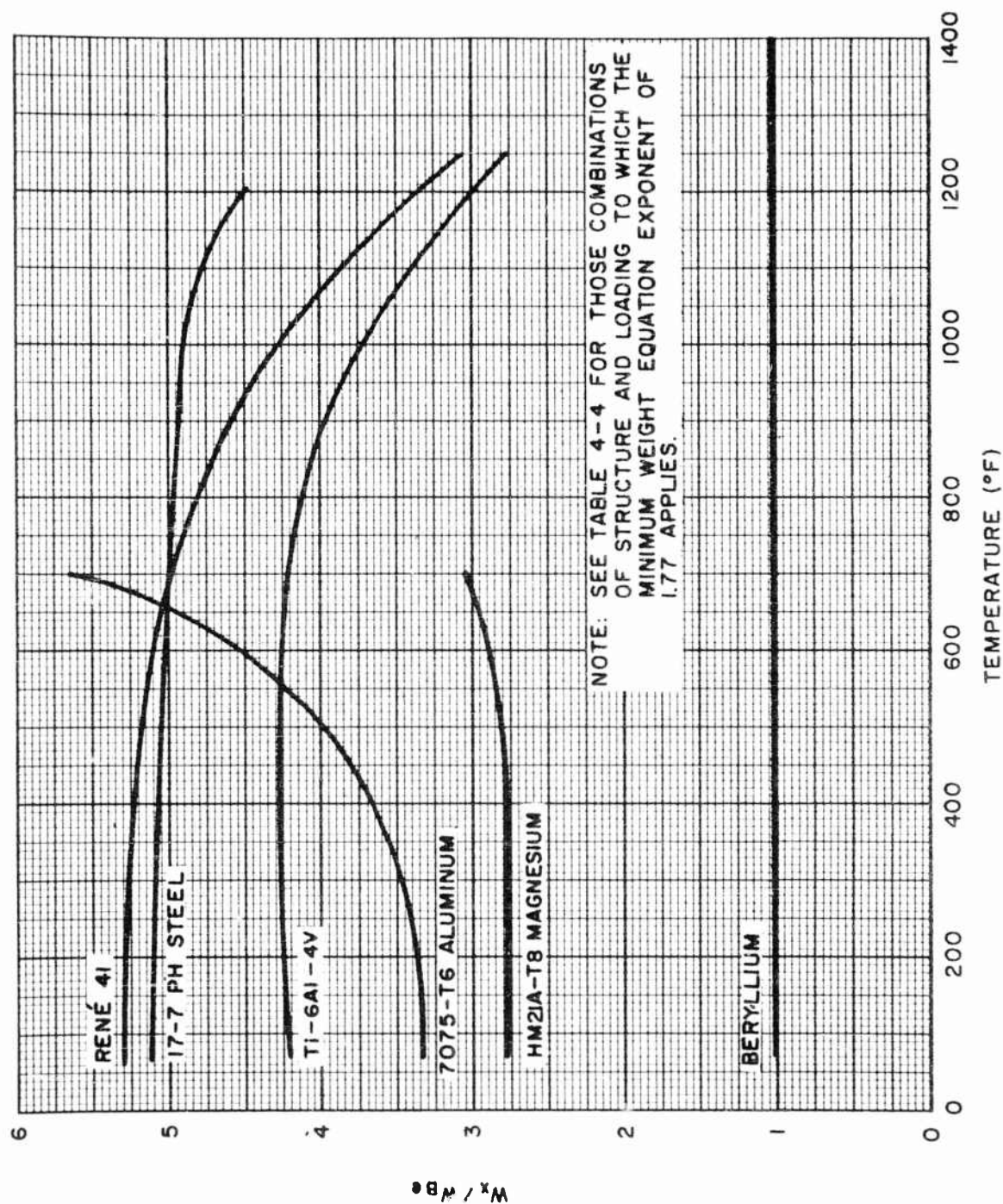


Fig. 4-62 Beryllium-Based Weight Ratios for Elastically Loaded Structures of Optimum Proportions Having a Minimum-Weight Equation Exponent of 1.77

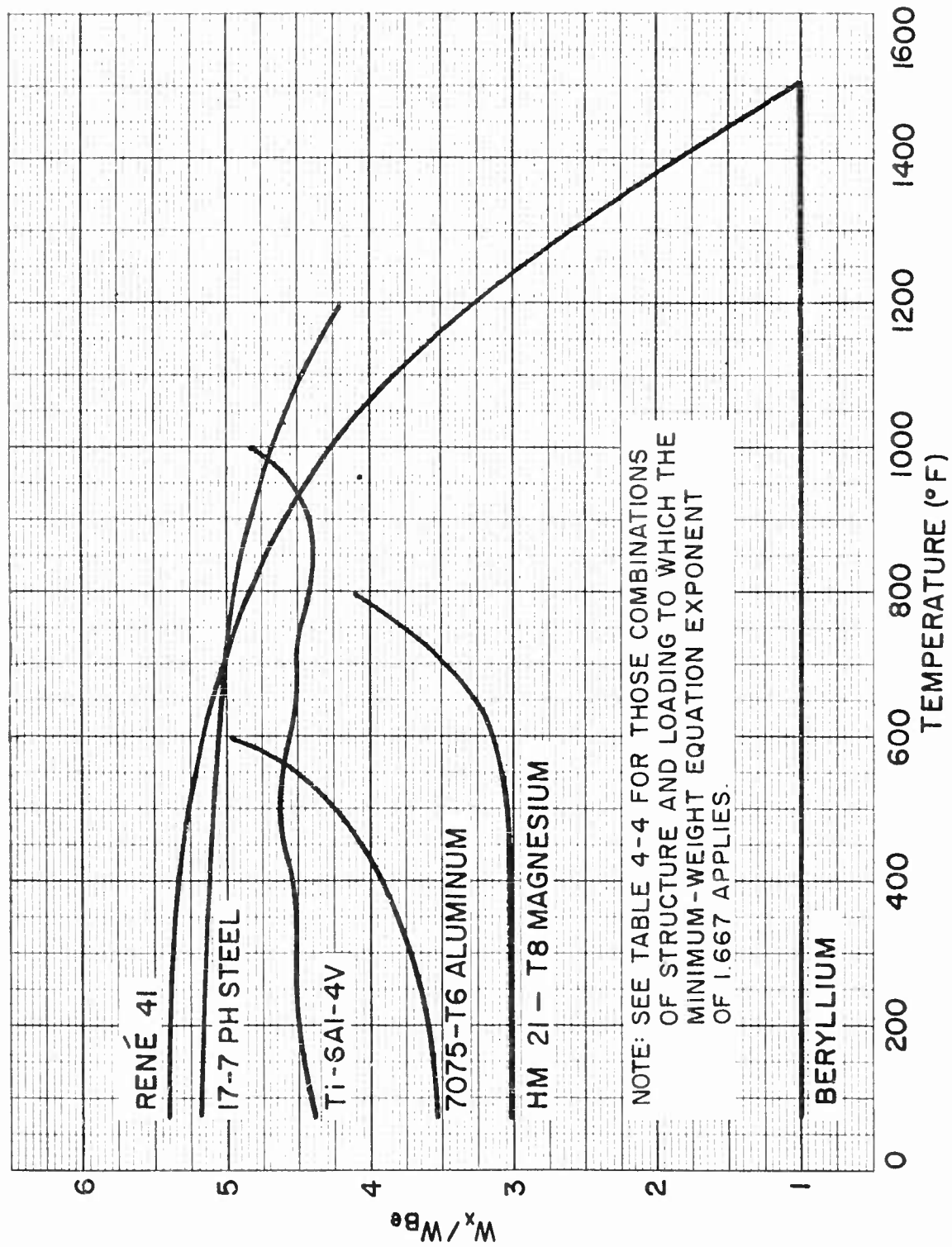


Fig. 4-63 Beryllium-Based Weight Ratios for Elastically Loaded Structures of Optimum Proportions Having a Minimum-Weight Equation Exponent of 1.667

materials have been made for three compression-panel configurations, and, when the parameters W_1 and P are introduced in a manner entirely parallel to that shown in Eq. (4.80), the various materials may be graphically compared. Figures 4-64 and 4-65 present a weight-load comparison at room temperature and 800°F, respectively, of various materials used in flat, unstiffened compression panels. Similarly, Figs. 4-66 and 4-67 show a weight-load comparison at room temperature and 800°F of materials used in truss-core sandwich compression panels of optimum proportions. Finally, Figs. 4-68 and 4-69 give a weight-load comparison at room temperature and 800°F of materials used in zee-stiffened compression panels of optimum proportions. Note that the graphical presentation resulting from Eq. (4.81) is not practical here, since $\bar{\eta}$ is not a constant above the proportional limit. Note further that the temperatures for material comparisons have been limited to room temperature and 800°F owing to the "example" status of the beryllium data as discussed in subsection 4.3. The maximum stress for all materials has been taken equal to the compressive yield stress in all the charts.

As was pointed out in subsection 4.3, the parallel lines to the left on all the charts represent elastic stresses and are a function of modulus of elasticity, while the parallel lines to the right on all the charts represent a plastic stress equal to the compressive yield-stress. The transition range between these extremes represents for each material those stresses between the proportional limit and the compressive yield stress, and is a function of the rate of change of $\bar{\eta}$. On the basis of the information presented in Figs. 4-57, 4-58, and 4-60, the superiority of beryllium cross-rolled sheet under elastic stress conditions is anticipated. However, Figs. 4-64 through 4-69 indicate that at both room temperature and 800°F, beryllium cross-rolled sheet is either equivalent or superior in the plastic stress range to all the structural materials investigated except all-beta titanium (Ti-13V-11Cr-3Al). The superiority of all-beta titanium at room temperature is noted to be rather insignificant. The conclusions reached previously in this discussion in regard to the high potential of beryllium cross-rolled sheet in elastic stress applications may therefore be expanded to include plastic stress applications as well, provided the strengths indicated by the stress-strain data of Fig. 3-2 are obtainable, and operating temperatures do not exceed approximately 800°F.

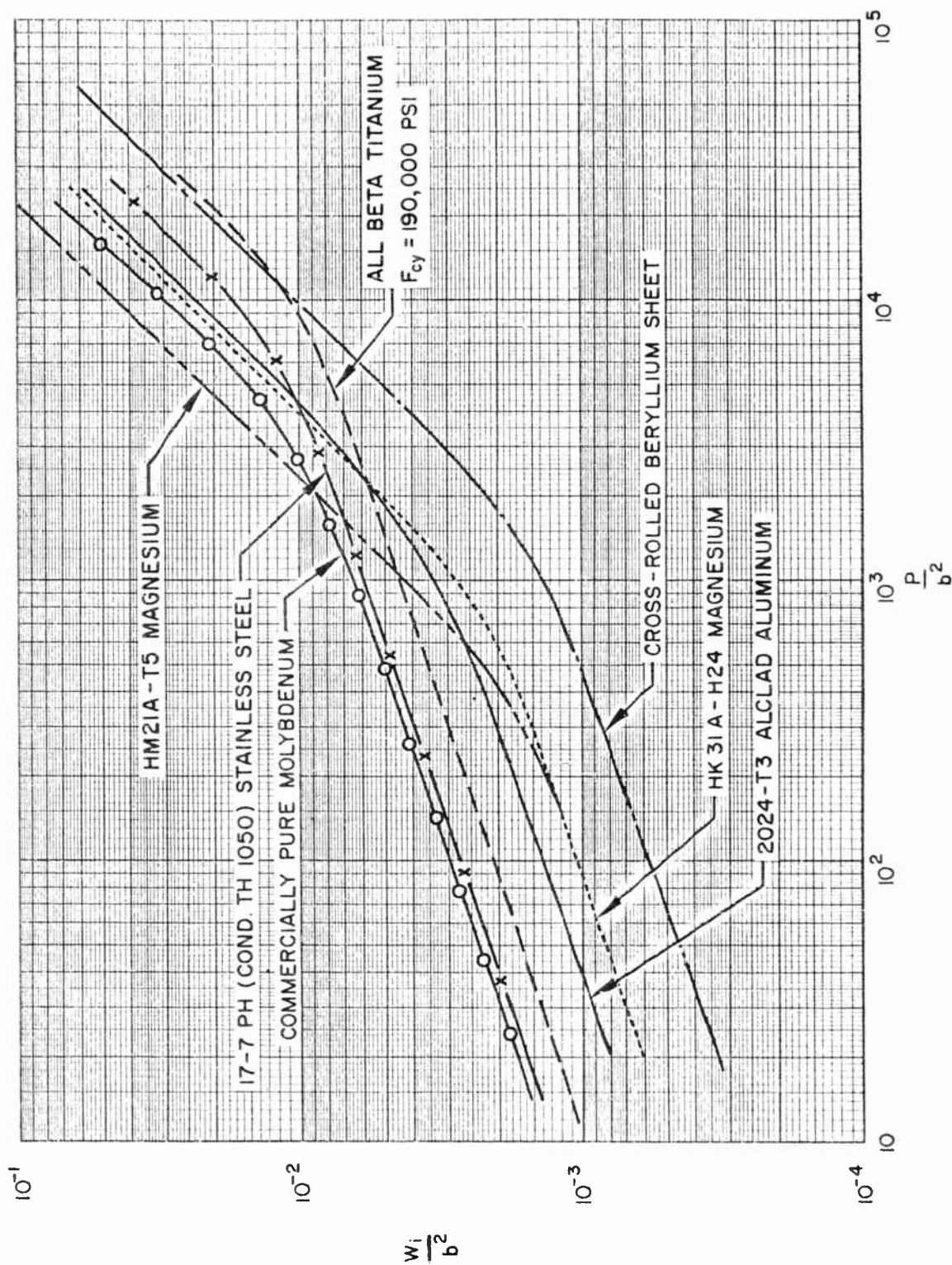


Fig. 4-64 Weight-Load Comparison at Room Temperature of Structural Materials Used in Flat, Unstiffened Compression Panels

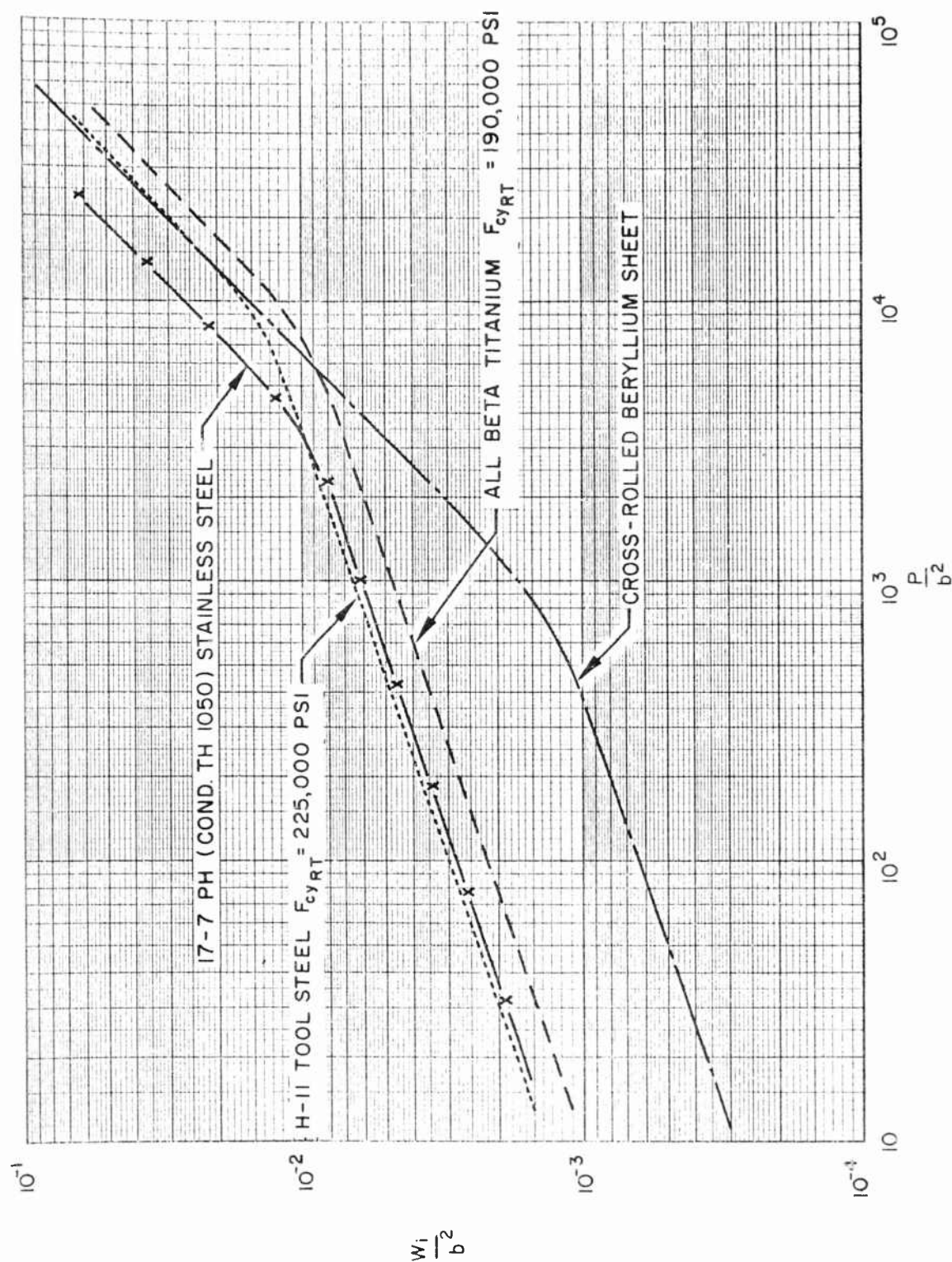


Fig. 4-65 Weight-Load Comparison at 800°F of Structural Materials Used in Flat, Unstiffened Compression Panels

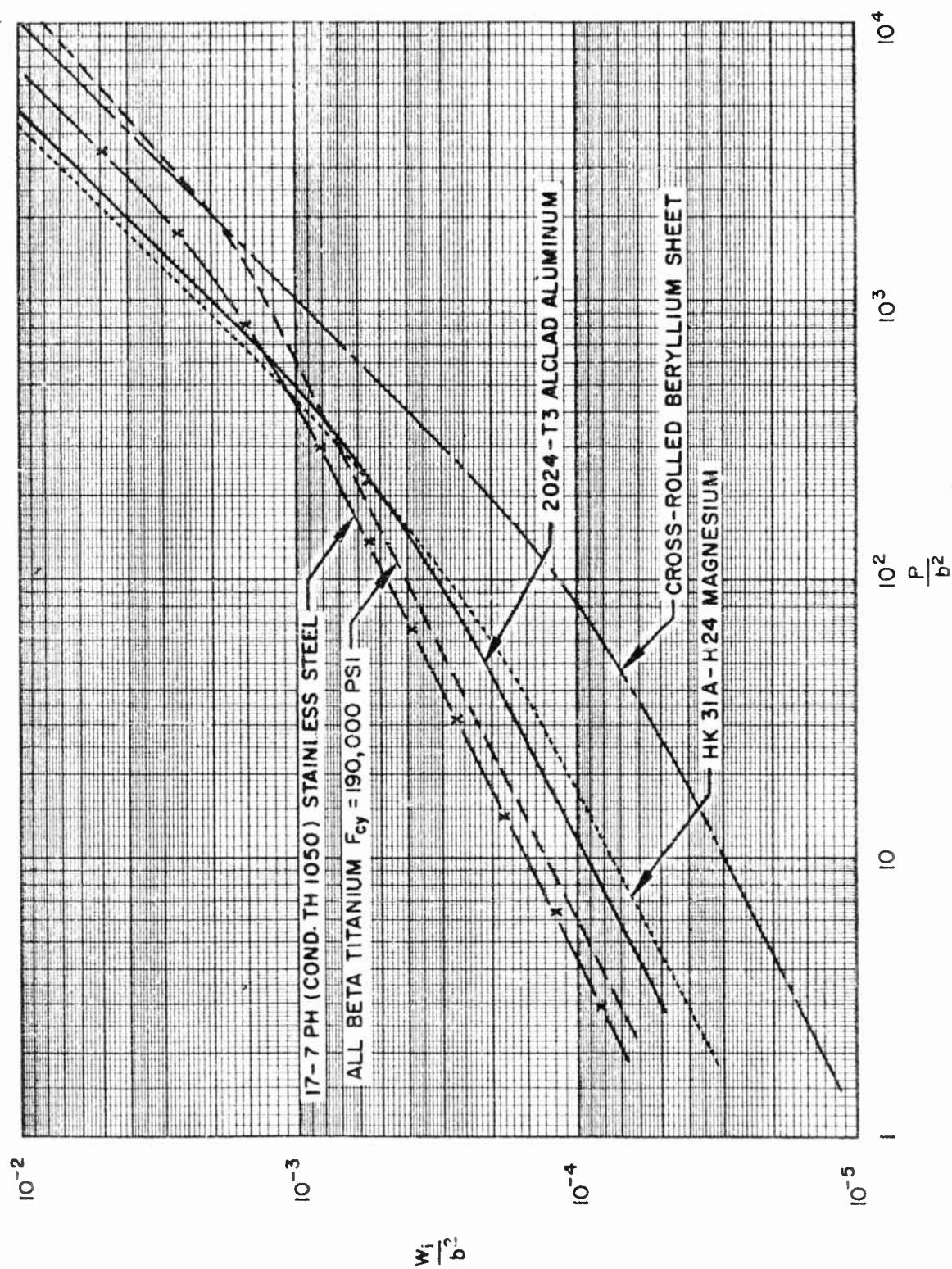


Fig. 4-66 Weight-Load Comparison at Room Temperature of Structural Materials Used in Truss-Core Sandwich Compression Panels of Optimum Proportions

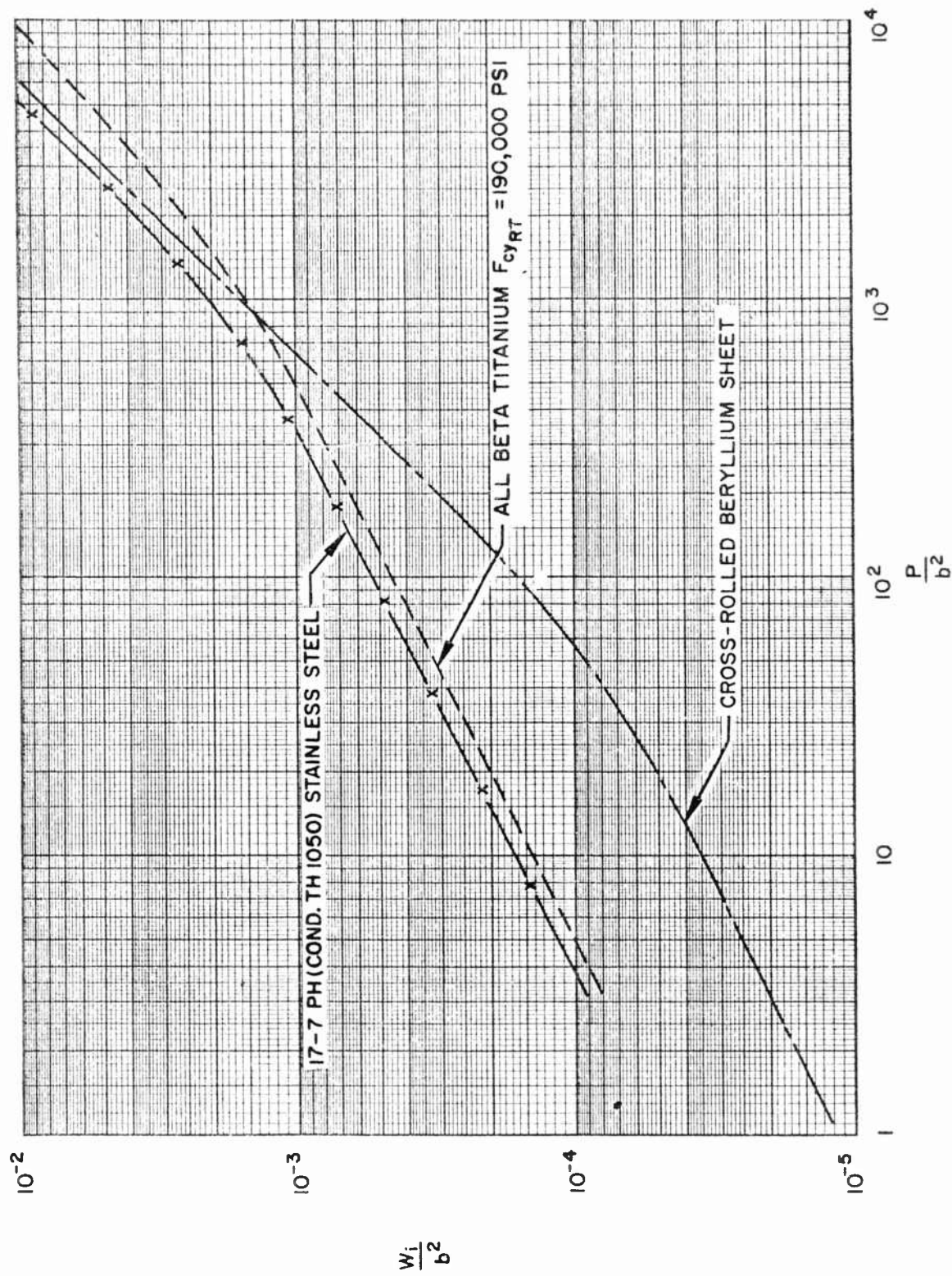


Fig. 4-67 Weight-Load Comparison at 800°F of Structural Materials Used in Truss-Core Sandwich Compression Panels of Optimum Proportions

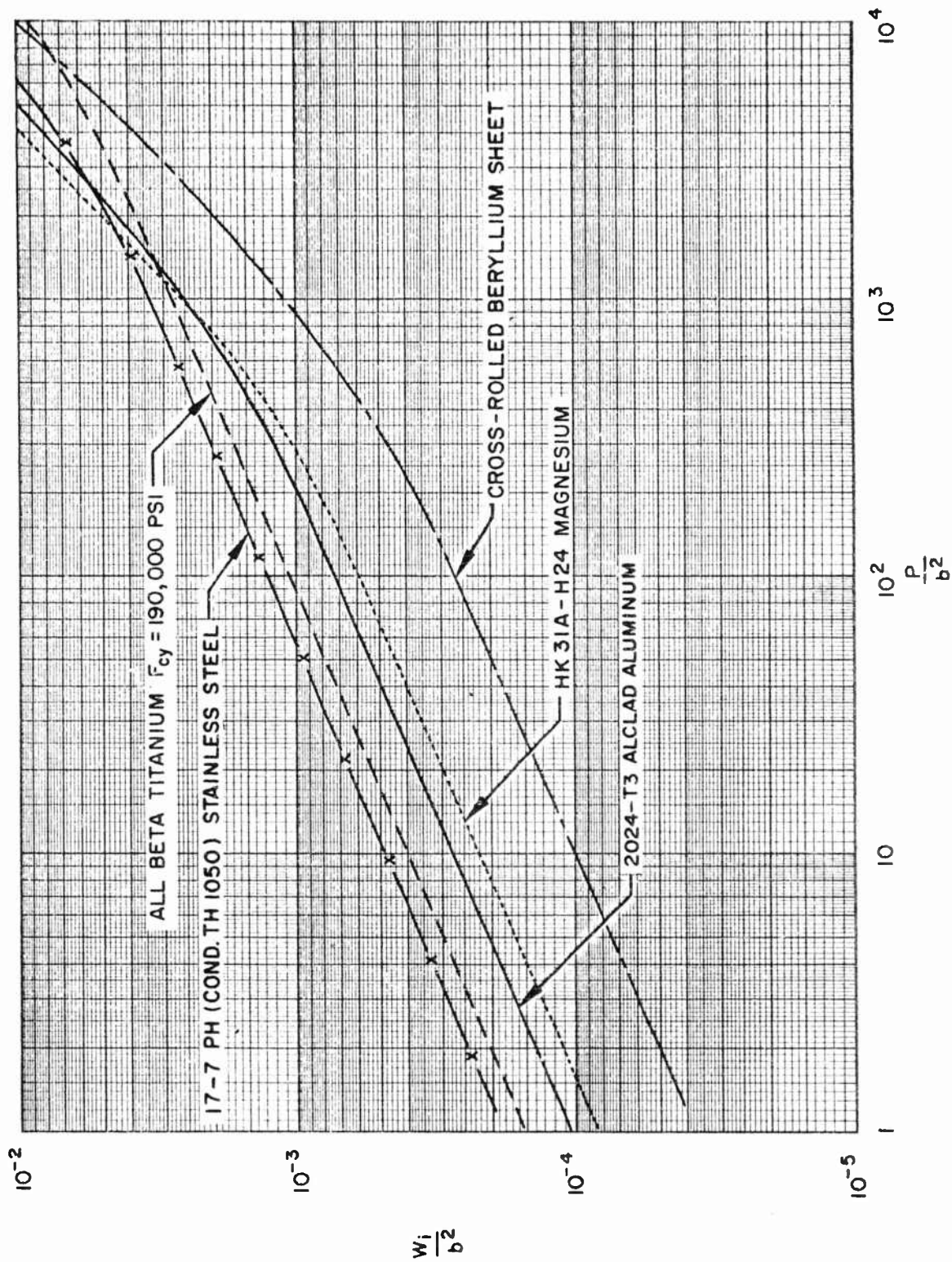


Fig. 4-68 Weight-Load Comparison at Room Temperature of Structural Materials Used in Zee-Stiffened Compression Panels of Optimum Proportions

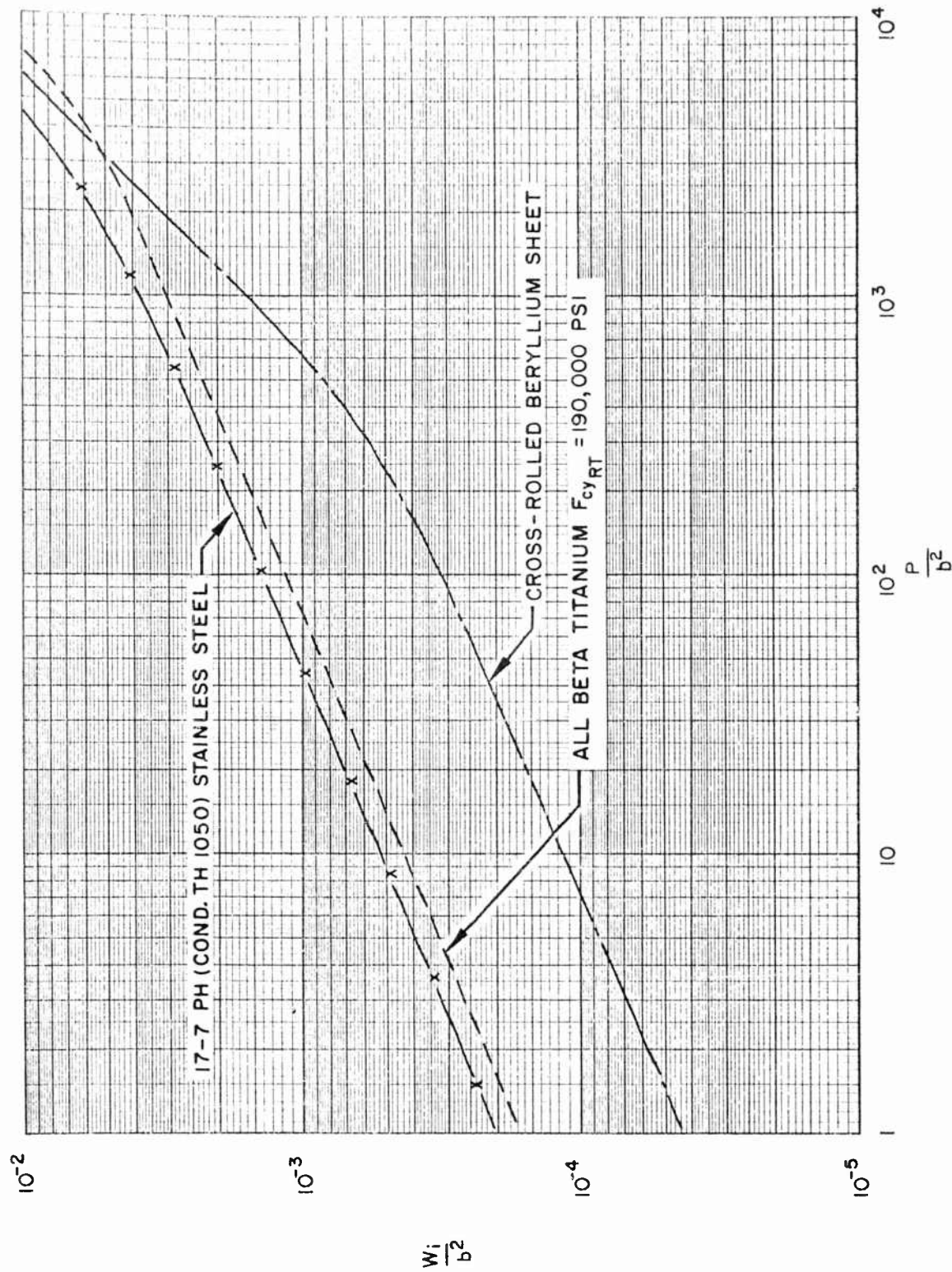


Fig. 4-69 Weight-Load Comparison at 800°F of Structural Materials Used in Zee-Stiffened Compression Panels of Optimum Proportions

4.5 REFERENCES

- 4-1 Adam Zahorski, "Effects of Material Distribution on Strength of Panels," J. Aeronaut. Sci., Vol. 11, No. 3, Jul 1944, pp. 247-253
- 4-2 F. R. Shanley, Weight-Strength Analysis of Aircraft Structures, New York, McGraw-Hill, 1952
- 4-3 Lockheed Missiles and Space Division, Minimum Weight Analyses and Design Procedures for Flat, Truss-Core Sandwich Panels, by R. F. Crawford, A. B. Burns, and L. K. Tilcens, LMSD-704009, Sunnyvale, Calif., Aug 1960
- 4-4 Lockheed Missiles and Space Division, Minimum Weight Analyses for Four Types of Stiffened, Flat, Compression Panels and Their Relative Efficiency, by A. B. Burns and R. F. Crawford, LMSD Tech. Rpt., 2-47-61-1, Sunnyvale, Calif., Jun 1961 (ASTIA AD-267626)
- 4-5 E. J. Catchpole, "The Optimum Design of Compression Surfaces Having Unflanged Integral Stiffeners," J. Roy. Aeronaut. Soc., Vol. 58, No. 527, Nov 1954, pp. 765-768
- 4-6 National Advisory Committee for Aeronautics, Handbook of Structural Stability, Part II, Buckling of Composite Elements, by Herbert Becker, TN-3782, Washington, D. C., Jul 1957
- 4-7 D. J. Farrar, "The Design of Compression Structures for Minimum Weight," J. Roy. Aeronaut. Soc., Vol. 47, 1943, pp. 1041-1052
- 4-8 National Advisory Committee for Aeronautics, Local Instability of the Elements of a Truss-Core Sandwich Plate, by Melvin S. Anderson, TN-4292, Washington, D. C., Jul 1958
- 4-9 National Advisory Committee for Aeronautics, Compressive Buckling of Simply Supported Plates with Longitudinal Stiffeners, by Paul Seide and Manual Stein, TN-1825, Washington, D. C., 1949

- 4-10 Lockheed Missiles and Space Division, "Optimization of Box Beams," by W. E. Jacobsen and R. F. Crawford, (unpublished notes) Sunnyvale, Calif., Aug 1961
- 4-11 Wright Air Development Division, Bending Strength and Efficiency of Multiweb Wings Having Corrugated Webs, by Robert F. Crawford and Joseph W. Semonian, WADC TN-59-399, Wright-Patterson AFB, Ohio, Feb 1960
- 4-12 Wright Air Development Division, The Bending Strength and Structural Efficiency of Full Depth Core Sandwich Wings, by Joseph W. Semonian, WADC TN-59-397, Wright-Patterson AFB, Ohio, Mar 1960
- 4-13 Lockheed Missiles and Space Division, Minimum Weight Analyses for Truss-Core Sandwich Cylindrical Shells Under Axial Compression, Torsion, or Radial Pressure, by R. F. Crawford and C. E. Stuhlman, LMSD Tech. Rpt. 2-47-61-2, Sunnyvale, Calif., Apr 1961 (ASTIA AD-267625)
- 4-14 Lockheed Missiles and Space Division, Structural Shell Optimization Studies, Vol. II, Optimization of Stiffened Cylindrical Shells Subjected to Uniform External Hydrostatic Pressure, by E. H. Nickell and R. F. Crawford, LMSD Tech. Rpt. 3-42-61-2, Sunnyvale, Calif., 30 Jun 1961 (ASTIA AD-267624)
- 4-15 National Advisory Committee for Aeronautics, A Simplified Method of Elastic-Stability Analysis for Thin Cylindrical Shells, by S. B. Batdorf, TR-874, Washington, D. C., 1947

Section 5

BERYLLIUM FABRICATION

5.1 INTRODUCTION

Aside from the advantageous strength-to-weight ratio, modulus-to-weight ratio, and thermal properties of beryllium, its breadth of application will be determined to a large extent by its fabricability. To date, this apparent deficiency has been the principal reason it has not been used more extensively.

Solutions to some of the problems arising in fabricating beryllium have been obtained through developing new processes and methods, as will be discussed in this section. In other instances it will be seen that careful application of existing fabrication methods gives satisfactory results.

In this section, a summary of the methods used for producing the various forms of beryllium stock is given. Following these summaries are several subsections on the various types of machining operations. A list of references follows from which much of the general information of this section was taken.

5.2 HOT-PRESSED BLOCK

Hot pressing is the usual method of making beryllium block material. This is done by placing minus 200 mesh beryllium powder in a mold, then compacting and sintering the powder in a vacuum at 1050°C and a compacting pressure of 100 to 200 psi. This makes a somewhat isotropic material with the strengths and ductilities presented in Section 2. This process is satisfactory when the end products are small or of considerable bulk, but it results in excessive waste when large shell-type units are required. In the future, hot-pressed beryllium will probably be used less as a final form, but more as an intermediate step in making extrusions, forgings, or sheet to be used for structural applications.

5.3 FORGING

In an effort to utilize the material more efficiently and enhance the mechanical properties, hot forging has been adopted. Block material is placed in a mild steel jacket, heated to 1950°F, and hot forged. This process sharply reduces the machining required when using block material, and increases the strength and ductility. Forgings are especially useful for large simple shapes, but are not recommended for complex shapes with sharp corners. The increase in strength depends upon severity of work, but at least 10-percent increase over block properties can be expected.

5.4 SHEET

The two methods for manufacturing sheet material are cross-rolling and the hot-upsetting technique. Cross-rolled sheet is made by cross rolling a billet jacketed in mild steel. In Ref. 5-1, Brush Beryllium Company recommends a 4:1 reduction longitudinally and transversely (16:1 overall) in a rolling temperature range of 1400° to 1500° F. After rolling, an annealing cycle of 10 to 15 min at 1385° to 1400° F promotes better formability, although it does not have a consistent effect on mechanical properties.

Hot-upset sheet is fabricated in the following manner:

- (1) Beryllium powder is placed in a mild steel can and cold compacted to a 50-percent theoretical density.
- (2) A vented cover is placed on the can. The can is then placed in an 1850° to 1900°F argon atmosphere furnace for two hours.
- (3) The can is removed from the furnace, placed in a press, and upset. After furnace cooling, the steel jacket is removed and the sheet is finish-machined. Hot-upset sheet is essentially forged material.

The ultimate tensile strength of sheets made by either of the above processes is in the 70- to 80-ksi range. The tensile yield strength of hot-upset sheet is approximately 50 ksi. Cross-rolled sheet yield strength is between 55 and 70 ksi. Elongation curves for the two types of sheet are similar with the cross-rolled sheet being slightly higher in the longitudinal direction, and hot-upset sheet higher in the short transverse direction.

Techniques for the forming of beryllium sheet are not very highly developed, but various processes have been tried in small components indicating that shearing, spinning, bending, and deep drawing can be applied to beryllium to some degree. A serious problem area in the forming of beryllium has been the presence of inconsistencies in the sheet. Beryllium sheet should be hot formed (800° to 1400° F), preferably in the upper portion of the range. Shearing should be performed above 1000° F. As thickness increases, the temperature should be increased. Satisfactory success in

bending has been consistent, and smaller radii can be used if the material is heated. At room temperature, the minimum bend radius is about $40T$ using $1\frac{1}{2}$ -in.-width strips. At 1300° the bend radii is $3T$. Deep-drawing properties at high temperature are similar to those of carbon steel at room temperature except that total elongation of beryllium is about $\frac{1}{3}$ to $\frac{1}{2}$ that of carbon steel. Appendix B of Ref. 5-1 contains pictures of a $\frac{1}{4}$ -in. wall by 4-in. OD hot-drawn hemisphere and a $\frac{1}{8}$ -in. wall by 8-in. OD hot-spun hemisphere. Hot-spun cones and cups, and double-walled cups are also shown. The Budd Company has made corrugations from 0.012-in.-thick sheet with a height of $\frac{1}{4}$ in. and radius of 0.040 in., though the material had to be reheated for each bend.

5.5 EXTRUSIONS

The conventional method for extruding beryllium has been to extrude a steel-jacketed billet. The purpose of the jacket is to prevent oxidation, minimize toxicity, and protect the tooling. The usual forms of extrusion have been rounds, squares, and rectangles. Under Air Force Contract AF 33(600)-36931, Northrop Corporation and its subcontractors, Nuclear Metals and Wolverine Tube, have been attempting to develop a bare extrusion process to generate complex beryllium shapes to close tolerances. This program is currently in progress. Some of the tentative conclusions from this program as of 1 December 1960 are:

- Higher ram speed gives more consistent results. The current press has speed in excess of 500 in./min.
- Reproducibility has been established.
- A billet temperature of 1750°F seems to yield good extrusions.
- It is believed that there is a narrow lubrication tolerance, but it is not clear whether the composition, quantity, or method of application is critical.

Ultimate strengths of 90 ksi in tension are attained on extrusions. Due to highly preferred orientation, extrusions are brittle in the transverse direction and only axial loadings are recommended. In summary, progress is being made with bare extrusions, but the process still has to be perfected.

The Beryllium Corporation has recently begun a program "Development of Techniques for Producing Beryllium Structural Shapes" under Air Force Contract AF 33(600)-41959. The purpose of this program is to produce angles, channels, zees, tees, squares, and rounds in 60-in. lengths by roll forming and supplemental techniques. These shapes are to have yield and ultimate strengths of 55,000 psi and 75,000 psi, respectively, at room temperature. These shapes will be given a creep-rupture evaluation at elevated temperatures and various loads. This program is in the early stages, but should enhance the use of beryllium.

5.6 MACHINING - GENERAL

With the increased usage of beryllium in recent years in aerospace and atomic energy applications, considerable experience in machining has been accumulated. Beryllium's machinability has been compared with that of cast iron, although beryllium is more brittle and abrasive. Beryllium's rigidity and stability allows minute machining operations and attainment of close tolerances. Inspection of finely machined gyro components is convincing evidence that beryllium machining know-how is available and being successfully applied.

General recommendations for successful machining of beryllium are as follows:

- Since the Atomic Energy Commission has taken the position that "for the present it is safest to regard beryllium metal and all its compounds as potentially toxic," it is recommended that positive action be taken to prevent dispersion of beryllium particles in working areas. This can be accomplished by performing machining operations under high-speed air-exhaust equipment. If this is not possible, a coolant or lubricant of a water-soluble type, inert to beryllium, should be used to suppress dust particles, cool work, and wash away chips. Cutting fluids should not be reused for machining nonberyllium parts. Wet chips and turnings should not be intermixed with clean dry chips and turnings.
- Carbide tools are preferable for turning, milling, and drilling operations. High-speed steel tools can be used, but excessive tool wear is encountered. It is important to keep tool cutting edges in extremely sharp condition. Tools should be promptly replaced at earliest indication of dulling.
- Part sections vulnerable to distortion and vibration during machining should be rigidly supported. Backup fixtures, dampening mandrels, or other tool devices to counteract tool pressure deflection and to assure machining accuracy should be used.

- Machining operations should be performed on heavy-duty equipment with power reserve. Equipment should have a minimum of transmission backlash to permit smooth, no-chatter machining at the desired speed, feed, and cutting depth.

5.7 TURNING

Standard lathe operations such as turning, threading, and boring are performed readily on beryllium. Detailed recommendations for lathe machining of beryllium follow.

- Use single-point cutter tools only. Clamp-in carbide insert tools are preferred because of low cost, availability, and dimensional repeatability. Brazed carbide-tipped cutters may be used.
- Exchange inserts should be the standard triangle or square shape for use with standard-duty tool holders. With carbide inserts, the 5- or 6-deg, positive-side, rake holder units should be used in preference to the 5-deg negative rake units.
- For maximum rigidity, tool overhang should be held to a minimum, and the point of the cutting tool should cut on center.
- Since beryllium is abrasive to all tooling, live centers should be used when beryllium is turned on centers.
- Brazed-carbide cutter tools should be ground as shown in Fig. 5-1 and Table 5-1. Angles may be altered to suit threading and boring requirements. Preferred tip carbides are (1) Grade C-2 (Carboloy 883 or equivalent) for continuous cutting, and (2) Grade C-1 (Carboloy 44A or equivalent) for intermittent cutting.

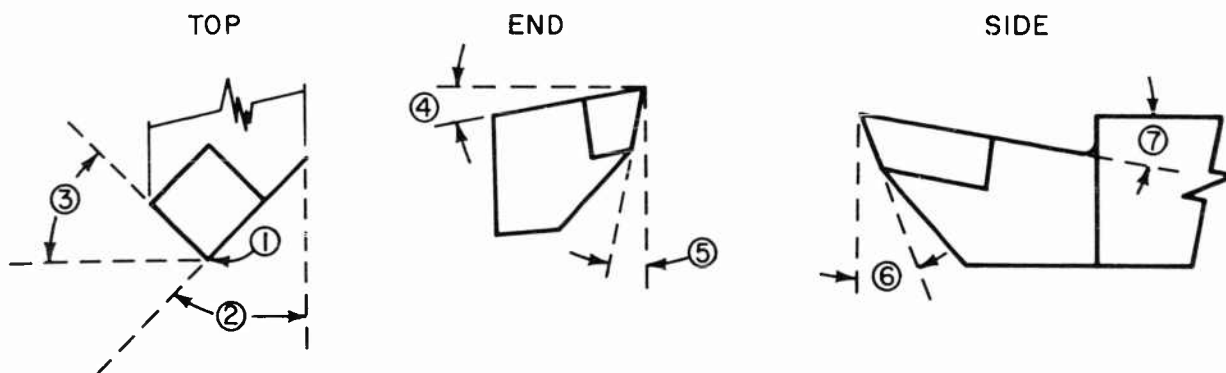


Fig. 5-1 Lathe Tool Geometry, Brazed Carbide (Ref. Table 5-1)

Table 5-1
LATHE TOOL GEOMETRY, BRAZED CARBIDE

No. (a)	Description	Turning	Forming
1	Nose radius (in.) Continuous cutting Interrupted cutting	1/64 to 1/32 1/16	None None
2	Side-cutting-edge angle (deg)	12 to 15	0
3	End-cutting-edge angle (deg)	8 to 15	0
4	Side-rake angle (deg)	7 to 8	0
5	Side-relief angle (deg)	2 to 4	7
6	Front-relief angle (deg)	2 to 4	7
7	Back-rake angle (deg)	0	8

(a) Ref. Fig. 5-1.

- Normal lathe-operating ranges for beryllium are:

Speed (surface ft/min)	150 to 250
Feed (in./rev)	0.01 to 0.015
Depth of Cut (in.)	
Stock cleanup	0.07 to 0.10
Roughing	0.020 to 0.050
Semifinishing	0.005 to 0.010

- Where possible, use a prechamfering operation to prevent spalling as the cutter leaves a lathe pass. Otherwise, passes should start at outer edge and proceed inward, finishing at the part center; or cut inward a short distance, reverse ends, and cut inward from the opposite end to blend with the prior cut.

5.8 MILLING

Milling of beryllium is quite similiar to the turning operations previously discussed. Operational recommendations include the following:

- Carbide cutters are recommended for best tool life, closer tolerances, better finishes, and higher overall operating economics. Preliminary reports of machining studies done at Lockheed show that carbide inserts are very effective.
- Conventional milling rather than climb milling is recommended to obtain the best finish with the most economical use of cutters.
- Backup material should be used to prevent spalling as the cutter leaves the work.
- Suggested design and use of milling cutters:

<u>Tool Geometry</u>	<u>Rough and Finish Milling</u>
Back-rake angle (deg)	0 to 10
Side-cutting-edge angle (deg)	7
Face-cutting-edge angle (deg)	3 to 7
Side-relief angle (deg)	10 to 15
End-relief angle (deg)	10 to 15
Land (in.)	1/32 to 1/16

Speed, feed, and depth of cut:

	<u>Roughing</u>	<u>Finishing</u>
Speed (ft/min)	60 to 100	100 to 150
Table feed (in./min)	3 to 6	3 to 6
Depth of cut (in.)	No data	No data

5.9 DRILLING

Drilling is one of the more difficult machining operations performed on beryllium. However, by exercising care and following proper procedures drilling does not present insurmountable problems. The following methods have proved satisfactory at Lockheed for drilling beryllium:

- (1) Drill the hole full size through the part in one or more operations using a 118-deg included point angle stub drill. A snug-fitting backup block must be used and properly located at the zone of drill exit. This block prevents spalling as the drill emerges through the material. The block should be at least equal to the drill diameter plus $1/4$ in. in all horizontal directions and at least $3/16$ in. thick. A beryllium block is preferred, but a mild steel block may be used where magnetic separation of the resulting steel chips is available.
- (2) Produce the full-sized hole through the part in a series of three operations:
 - (a) Spot drill, using a 60-deg center drill being certain not to pierce the material.
 - (b) Drill an undersize hole through the material using a conventional 118-deg drill. This undersize hole should usually be approximately half the diameter of the final hole. Possible spalling which occurs as the drill emerges should not be a cause for rejection if the fracture is within the full-size hole area.
 - (c) In the final operation, enlarge the undersize hole to full size using a ball-end mill. No backup block is required.
- (3) Drill the full-size hole through the part in a single pass. Use either a rounded corner 118-deg drill or a ball-end mill. No backup is necessary.

Note: Method 1 should be used in preference to methods 2 and 3 when drilling non-perpendicular holes through flat surfaces or when drilling holes through nonflat surfaces. Method 2 is preferred for drilling perpendicular holes through flat surfaces with a machine not equipped with power feed. Method 3 is preferred for drilling perpendicular holes through flat surfaces with a power-feed machine. The 118-deg drills should be used for holes larger than $1/16$ -in. diameter. Drills with a 90-deg, included

point angle, and a web thickness of 0.015 to 0.020 in. must be used for holes 1/16-in. diameter or less. Carbide or carbide-tipped drills, ball-end mills, and countersinks are preferred, though high-speed steel can be used.

The recommended speeds and feeds for drilling and countersinking follow:

Speed (surface ft/min)	
Drilling	70 to 100
Countersinking	60 to 80
Feed (in./rev)	
Under 1/8-in. diam.	0.001 to 0.002
1/8-in. to 1/4-in. diam.	0.002 to 0.004
1/4-in. to 1/2-in. diam.	0.004 to 0.005
Above 1/2-in. diam.	0.005 to 0.007

Reaming is done when a hole with accurate dimensions and fine finish is desired. Reaming is held to a minimum at Lockheed since a ball-end mill gives as good a surface with slightly less accurate dimensions. The following table shows the stock allowances used in machine reaming.

Diameter of Hole (in.)	Stock Allowance (in.)
1/4	0.01
1/2	0.015
1-1/2	0.250

An allowance of 0.001 to 0.003 in. is common practice for hand-reaming operations. The speed is controlled by rigidity of the setup, and by the tolerance and finish required. Excessive speeds can cause chatter, which is harmful to both reamer and finish. The speeds commonly used are about two-thirds of the speeds listed under drilling.

A specialized type of operation is deep-hole drilling. Holes deeper than five times the hole diameter are defined as deep holes. The principal cause of deep-hole drilling

problems is the buildup of heat in the interior of the work piece which can cause seizing. The accumulation of chips in the lower portion of the hole is troublesome, also. Decreasing the diameter of the shank in comparison with the tip and pumping coolant through the drill to the work face are designed to alleviate these problems.

The conventional drill design is a two-flute, oil hole drill with its point ground to a 90-deg included angle. The drill shank should be undercut 0.010 in. on the diameter behind the carbide tip. The carbide tip should back-taper 0.004 in./in. The primary clearance angle should be increased to about 6 deg. Special tool holders are used in conjunction with the above drill. Essentially, they incorporate a spring-loaded clutch which breaks free in case of drill overload.

A second type of drill used for deep holes is the single-flute, carbide-tipped rifle drill. The shank is a seamless steel tube having a diameter slightly smaller than the tip. This tube is brazed to the tip. One side of the tube or shank is depressed to form a "V" groove. This groove extends the entire length of the shank to the point of the drill by removing about one-third of the cross-sectional area of the tip. Two 1/32-in. holes are drilled longitudinally through the tip just below each outer corner of the "V" groove. These holes provide the outlet of coolant from the hollow shank into the cutting site. The "V" groove provides for the outflow of the chip-laden coolant from the cutting site. Longitudinal clearance is present along the tool body to reduce friction and to allow coolant flow around the tip and into the "V" groove. One cutting edge is located on one outside corner of the "V" groove, while the other is formed by the adjacent edge of the "V" groove along the face of the tool extending to the center of the drill. The cylindrical tool body immediately behind the cutting tip rests on the finished surface of the hole to guide the point into the work. On 3/16-in. drills, the guiding elements of the tip consist of a cylindrical land 1/64 in. wide, located below the cutting edge, and a bearing surface 7/32 in. wide, located diametrically opposed to the land. The drill face is ground so the cutting edge in the "V" groove makes a 15-deg angle with the cross section of the drill, and with any line on the face perpendicular to the axis of the drill. Thus, the face recedes from the point and from the

cutting edge of the drill on a compound angle which forms a 15-deg side-cutting angle and a 15-deg end-cutting angle. A clearance is also ground around the coolant hole on the lower side of the drill face. This allows a larger space for flushing chips from the cutting site. This clearance is bounded by a line passing slightly off center between the coolant holes, the lower edge of the "V" groove, and the periphery of the drill.

Speed, feed, and depth of cut for conventional twist drills in drill presses, deep-hole drilling machines, or engine lathes are:

<u>Drilled Hole</u>			
Diameter (in.)	Depth (ft)	Speed (ft/min)	Feed (in./rev)
1/8	2 to 3	70 to 100	0.004

Coolant is kerosene at minimum pressure of 200 psi. Much higher pressures may be used on rifle drills.

5.10 GRINDING

Grinding beryllium is a machining operation used less frequently than others previously discussed. Finishing cuts by other machines usually cannot be improved if the tools are in good condition. Coarse-grained aluminum-oxide wheels with a soft-grade vitrified bond are used for rough grinding. Wheels of medium grain and hardness are recommended for fine-finish grinding. Cut-off wheels range in size from 6 by 0.030 in. to 14 by 0.075 in. using speeds recommended by the manufacturer.

5.11 PARTING

The parting or subdividing of billets is commonly done by the use of a bandsaw. Strain gages are used to measure bowing of the band and the cutting force. Billets are easily sawed using a claw-tooth blade 1 in. wide, 6 to 10 pitch, 0.040 gage, and 0.060 in. set, for work up to 3 in. thick. For work above 3 in. thick, a claw-tooth saw 2 in. wide, 2 pitch, 0.050 gage, and 0.060 in. set is recommended by the Beryllium Corporation.

Saw Speeds Versus Thickness

	Work Height (in.)	Band Speed (surface ft/min)	Feed (in. ² /min)
1-in. saw	1/8	150 to 100	15 to 10
	1 to 3	100 to 85	10 to 5
2-in. saw	3 to 6	150	10 to 7
	6 to 10	150	7 to 4
	10 to 20	145 to 125	2 to 1
	20 to 30	125 to 112	1-1/2 to 1
	30 and over	100 to 95	Less than 1

As mentioned earlier, beryllium sheet should be hot sheared at temperatures in the 1000° to 1400°F range. As thickness increases, the temperature should be increased to the upper part of the range.

LMSC has done a limited amount of sheet cutting at room temperature using an 8-in.-diam. diamond grit wheel with a thickness of 0.024 to 0.032 in. The speed of the wheel is 2300 RPM. A cut of 0.001 in. is taken using a water-soluble cutting fluid.

5.12 REFERENCES

5.12.1 Cited Reference

5-1 Air Materiel Command, Development of Beryllium Sheets Rolled to Flat to Gauge, by K. G. Wikle, J. W. Armstrong, and H. N. Perrin, TR 60-7-631, Sep 1960

5.12.2 Uncited References

Beryllium Corporation, Development of Techniques for Producing Beryllium Structural Shapes, by B. H. Hessler, K. C. Taker, and E. E. Weismantel, AF 33(600)-41959-1 and AF 33(600)-41959-2, Reading, Pa., Aug 1960 - Jan 1961

Defense Metals Information Center, The Machining of Beryllium, by C. T. Olofson, Memo 21, Jun 1959

H. A. Jahnle, "Forming Beryllium Sheet," Product Engr., 20 Jun 1960

Lockheed Missiles and Space Division, Machining Beryllium, by W. Cohenour, MPS 9.12, Sunnyvale, Calif., 14 Mar 1960

Lockheed Missiles and Space Division, Study of Beryllium Machinability, Drilling, by R. A. Kelley, LMSD-480854, Sunnyvale, Calif., 28 Dec 1959

Lockheed Missiles and Space Division, Study of Beryllium Machinability, Lathe Turning, by R. A. Kelley, LMSD-480853, Sunnyvale, Calif., 30 Dec 1959

National Research Council, National Academy of Science, Division of Engineering and Industrial Research, Report of the Panel on Beryllium of the Materials Advisory Board, Rpt. No. MAB-129-M, Washington, D. C., 25 Jun 1958

Northrop Aircraft, Inc., Quality Aircraft Extrusions, Interim Engineering Reports 1 - 10, AF 33(600)-36931

G. A. Toczki and K. Breeze, "Working Beryllium," Amer. Machinist, 17 Oct 1960

Section 6

CONCLUSIONS, RECOMMENDATIONS, AND APPLICATIONS

6.1 CONCLUSIONS

The following conclusions have been reached as a result of the performance of this program:

- Sufficient experience and information have been accumulated for beryllium hot-pressed block and cross-rolled sheet to merit immediate application in design.
- The quality and consistency of beryllium hot-pressed block and cross-rolled sheet are uniform enough for production applications.
- The physical and mechanical properties of beryllium hot-pressed block and cross-rolled sheet are sufficiently documented to permit the design of structural production components.
- Conventional methods of structural analysis are satisfactory to predict the strength of beryllium components, if steps have been taken to ensure proper margins of safety and care in detail design.
- Beryllium can and does develop post-buckling strength in panel applications.
- Beryllium is significantly more efficient through at least 800°F than most materials in structures designed by instability considerations, and beryllium's efficiency advantage is particularly favorable for lightly loaded applications.
- Proper care in the form of appropriate margins of safety should be exercised in beryllium designs to account for the notch sensitivity of the material and the catastrophic post-buckling failure characteristics at room temperature. (Special precautions are not necessary at elevated temperatures greater than 450°F.)
- Buckling at room temperature in both compression panels and shear panels is not visibly noticeable at the theoretical buckling stress because of the low amplitude of the buckles.

- Buckling in axially compressed cylinders occurred at lower stresses than those predicted, apparently because of alterations in the properties of the material brought on by high brazing temperatures.
- The beryllium design charts presented in this report should not be used in design unless the designer is confident that the properties of the beryllium products available to him compare closely with the properties on which the charts are based.

6.2 RECOMMENDATIONS

The following recommendations are made for future investigations:

- Testing of some of the optimum geometric configurations determined theoretically in Section 4 of this report for various stiffened components is recommended where beryllium sheet is the material specified. These tests would be designed to prove out the potentialities indicated by the studies summarized in Section 4, and would provide opportunity to develop the fabrication of more complex structures from beryllium.
- Further notch testing of beryllium sheet is recommended where the notches are cut into the plane of the sheet rather than into the edges of the sheet as in the present program. It has become apparent during the present program that the fracture mechanism varies for these two types of notches. Since notches as represented by scratches, markings, and/or discontinuities usually occur in the surface of the sheet, the investigation of surface notches appears warranted.
- Further experimental investigation of the biaxial strength of beryllium sheet is warranted because of the potentially high biaxial strength shown by theory and test in this work. The test results, although qualitative, indicate biaxial (2:1) strengths at least 50 percent greater than uniaxial strengths. These increased strengths should be substantiated because of possible important design applications.
- The effects of high temperatures and short holding times during brazing on the mechanical properties of beryllium sheet should be determined. This effect

appears to be deleterious. Data regarding exposure-to-temperature effects on the mechanical properties of beryllium sheet should be made available for general engineering use.

- Careful investigation (of the type indicated in this report) is recommended for new, advanced, beryllium sheet products that will become available in the future.

6.3 APPLICATIONS

General applications for beryllium have been analyzed and discussed with the beryllium producers. Information relating to present applications of beryllium, as a general rule, is considered as classified. However, the immediate-future and longer-range potential applications, as outlined by Riedinger (Ref. 6-1), are as follows:

- Immediate-future applications for aircraft
 - (1) Primarily as structure
 - Leading edges
 - Secondary wing skins
 - Some fuselage plating (areas to be determined by acoustic-fatigue limits)
 - Control surfaces
 - (2) Primarily as heat sink
 - Fuselage noses
 - Inlet ducts
 - Brakes
 - Enclosure structure (multiwall) for crew
- Immediate-future applications for missiles and spacecraft
 - (1) Primarily as structure
 - Interconnect structure of upper stages
 - Vehicle nose shell
 - Internal structure in the final stage

(2) Primarily as heat sink

Enclosure structure (multiwall) for various payloads

Heat shields for various parachute-type recoveries, such as that in Project Mercury

(3) Systems or equipment

Gyros

Gears

Linkage and bellcranks

Insulation

Brackets

- Longer-range potential applications

(1) Primarily as structure

Torsional restraint structure for tank clusters

Multiwall structure for space platforms

Reentry structure (except for the extremely high-temperature components)

Wing, empennage, and fuselage structure for aircraft

Internal structure in insulated and cooled structure for various vehicles where temperature control is mandatory (as for manned reentry)

(2) Primarily as heat sink

Internal cabin structure for reentry vehicles

Specific parachute recovery capsules from orbit

6.4 REFERENCE

- 6-1 Lockheed Missiles and Space Division, Beryllium as a Structural Material for Aircraft, Missiles, and Spacecraft, by L. A. Riedinger, LMSD-704028A, Sunnyvale, Calif., Mar 1961 (delivered 1 Mar 1961 before the Metallurgical Section of the AIME, St. Louis, Mo.)

Appendix A
EXPERIMENTAL INVESTIGATION OF BERYLLIUM PANELS AND CYLINDERS

A. 1 INTRODUCTION

Tests simulating four basic structural components were performed on beryllium panels and cylinders at room and elevated temperatures as part of Air Force Contract AF 33(616)-6905.

The four components are:

- (1) Compression panels
- (2) Shear panels
- (3) Axially loaded monocoque cylinders
- (4) Externally pressurized monocoque cylinders

The primary information sought was the buckling characteristics.

In all tests, the material used was cross-rolled QMV beryllium sheet. All future reference to "beryllium" or "sheet" shall mean this material. Interpretations of the test data in this appendix are presented in Section 3 of this report.

Although each structural element required its own special fixtures, instrumentation, and technique, certain basic testing equipment and procedures were used on all or most of the tests. The information common to most of the tests will be discussed in subsection A. 2, while subsection A. 3 will be reserved for details peculiar to each element.

A.2 BASIC TESTING EQUIPMENT AND PROCEDURES

A.2.1 Loading

Loading of all specimens except the pressurized cylinder was by means of the 50,000-lb, screw-driven universal testing machine (Baldwin-Lima-Hamilton Model "FGT"), shown in Fig. A-1. This machine has two load cells incorporated in its cross-head, and the load measured is read on a large, 2-ft.-diam. dial. Four load ranges are available - 50,000, 10,000, 2,500, and 1,000 lb. The most sensitive dial that would cover the anticipated load was always used. The finest subdivision of the dial is 0.2 percent of full scale, and the manufacturer's guaranteed accuracy is ± 0.5 percent of load or 0.1 percent of dial, whichever is greater. Maximum loads given in this report were read on this dial. A precision potentiometer was connected to the load-indicator shaft. By this means, a voltage output proportional to load was used to record the load on an oscillograph on which strains (from strain gages) were simultaneously recorded. The accuracy of this device, which recorded the load values given in the succeeding tables, is 1 percent.

On all tests, the loading rate used was at, or very near, the minimum possible. In all tests, the flexibilities of the loaded systems differed, and on most tests they even varied during the test. For this reason, the loading rate differed with each test even though the cross-head motion was very nearly the same in all tests. In some tests, where considerable deformation of the specimen occurred after buckling or yielding, the cross-head motion was increased somewhat so as not to prolong the test excessively. Where average loading rates are given, they do not include this accelerated portion of the test. In no cases were the load rates such that they could not classify as essentially "static load tests."

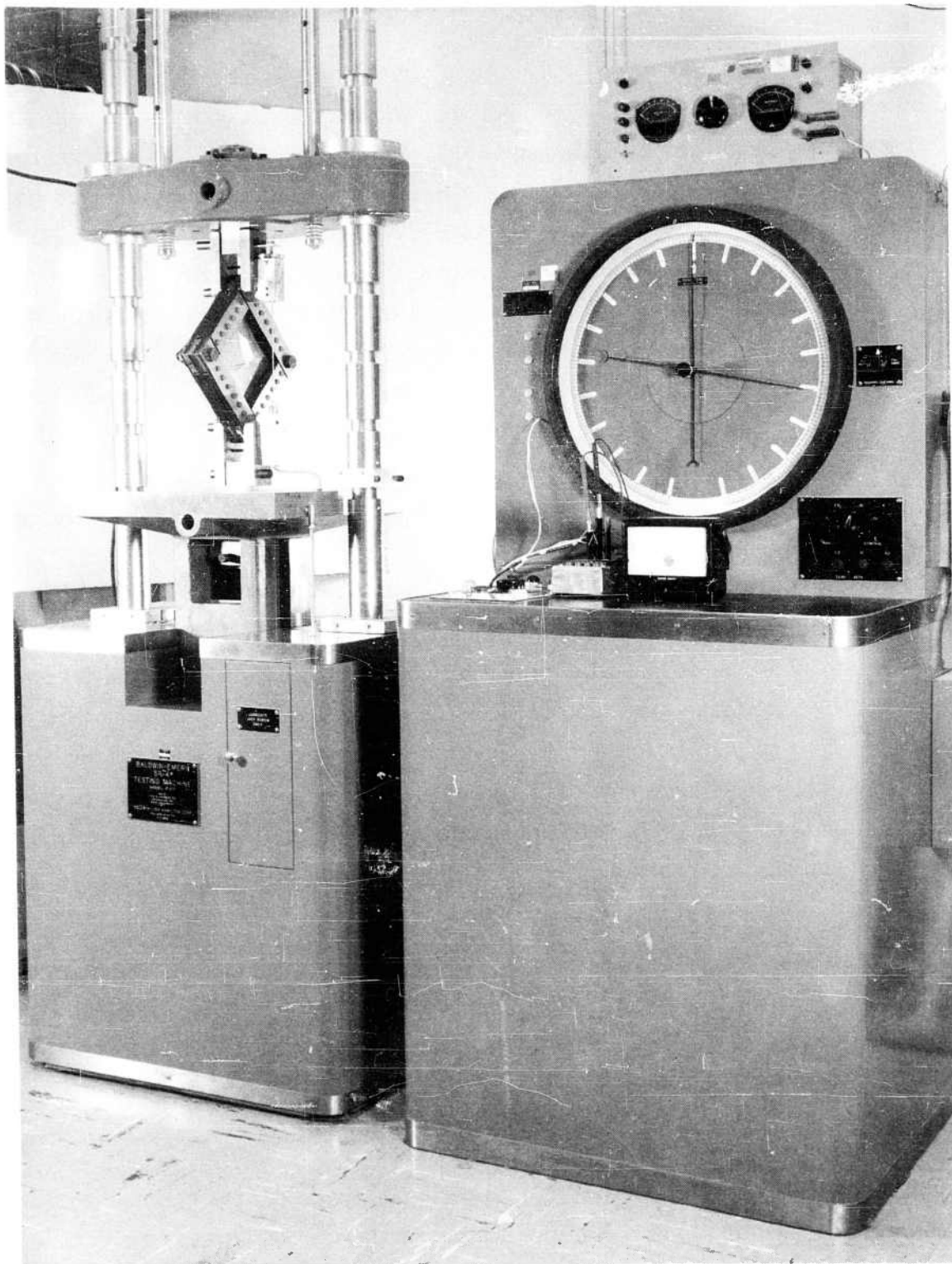


Fig. A-1 Universal Testing Machine, 50,000 lb

A.2.2 Strain and Elongation Recording

Strain or elongation of some part of the specimen was measured on all tests with strain gages or extensometers, using strain gages to measure the motion. All strain gages were incorporated into DC-powered bridges with excitation voltages between 4.5 and 9.0 volts. The power supply for these was an Era Pacific Inc., transistorized, DC power supply, Model TR 32-8, connected in parallel to several batteries of the desired voltage. With the bridges connected, the output of the DC power supply was adjusted so that voltage across the batteries was the same as the open circuit voltage of the batteries. Thus there was little or no current drain on the batteries during the test, and the batteries "regulated" the bridge voltages which were found free of variations greater than ± 0.25 percent. This voltage was monitored on a Kintel DC voltage standard, Model 301 R. Special boxes provided a means of balancing, voltage trimming, and calibrating (by shunting) the strain-gage bridges.

The output signals were connected directly to highly sensitive pencil galvanometers (Midwestern Model 102 A-40) installed in a multichannel optical oscillograph (Midwestern Model 607 F). Where large strains would have produced nonlinear recordings, the galvanometer was "stepped" back into its linear range by shunting the leg of the bridge which caused an output voltage opposite to the signal voltage. The magnitude of the steps was determined after the test by actual measurement on the chart. Since the strains were changing very slowly, the strain "lost" or obscured during the 30-millisecond duration of the step did not cause a perceptible loss of accuracy.

Without amplification and with galvanometers of low natural frequency (40 cps), this DC system was found to be free of drift and noise. Shielded cables were used wherever feasible. Sensitivity on the chart was as high as 150 microstrain/in. on some of the tests, so that using care, the chart resolution could be as high as ± 5 microstrain.

Resistance measurements pertinent to the reduction of strain data were made with a Wheatstone bridge reading to five significant figures, four of which were retained in calculations.

In room-temperature tests, strain measurements are subject to ± 3.5 percent. This is based on a total of the following possible sources of error:

Excitation voltage fluctuation	$\pm 0.25 \%$
Strain-gage resistance	± 0.10
Calibration shunt resistance	± 0.10
Manufacturer's gage factor	± 1.00
Resolution at calibration	± 1.00
Resolution at any load	<u>± 1.00</u>
Total	$\pm 3.5 \%$

In tests where the maximum strains were less than 500 microstrain, the accuracy should be stated thus: ± 3.5 percent or ± 5 microstrain, whichever is greater. For tests where maximum strains exceeded 500 microstrain (i.e., where less sensitivity was used), the accuracy was ± 3.5 percent or ± 10 microstrain, whichever was greater. Sensitivity was controlled by changing the bridge voltage.

In tests where shattering of the specimen could have "opened" one of the bridge legs, the galvanometer was protected by putting a Zener diode across the "openable" leg and powering the bridge at a voltage slightly below twice the Zener voltage of the diode. In these cases, sensitivity was controlled by a variable resistor in series with the galvanometer.

Test procedure with all strain gages was to set the bridge voltage at approximately the desired (precalculated) voltage. Just prior to the test, with the recorder running, a shunt (calibration) resistor was momentarily applied to the appropriate leg of the bridge, at each bridge successively. With gage resistance, shunt resistance, and gage factor known, a known calibration strain was represented on the chart by a "step" of a measurable number of inches (usually 1.5 to 2 in.). From this, a microstrain/inch value was established for each strain gage. These differed somewhat. For instance, in one test with eight strain gages, they ranged from 290 to 357 microstrain/in. At various load values, the deviations of the strain-gage traces (from a zero strain datum)

were measured in inches. Then all the values of one column representing deviations of any one gage versus load were multiplied by the microstrain/inch values to give a column of strain versus load for that gage, and so on.

At elevated temperatures, the only difference in the accuracy is the gage-factor item. The manufacturer (Baldwin-Lima-Hamilton) supplies a rough curve of gage factor versus temperature, but implies by its representation that this is subject to about ± 5 -percent accuracy. The curves show a gage factor in the neighborhood of 2.0 for the range from 600° to 1000°F. This value was used throughout the data reduction. The final accuracy of strain-gage readings at elevated temperature is probably ± 7.5 percent. Since these gages were used primarily to indicate the onset of buckling (the specimen being completely enclosed by the heating system), the fact that the absolute value of strain measured is off by 7.5 percent is not a drawback. It is probable that in these nearly steady temperature tests, the relative accuracy of any two strain readings on one strain gage is better than ± 1 percent. (All items except the item called "resolution at any load" are constant throughout the test.)

An additional procedure at elevated temperature is the measuring of the resistance of the strain gages at test temperature. This is accomplished by careful selection of resistors completing the bridge. Two of these resistors must be exactly equal (to within 0.1 percent), the third, used adjacent to the gage and in the opposite half of the bridge to the two equal ones, must be of known value and somewhat greater value than the gage. If, at test temperature and just prior to load application, the bridge is brought to balance by shunting the third (and known) resistor with a precision potentiometer, the value of the gage resistance is established by the fact that it must be equal to the combined value of the third resistor and its known shunt. Leads to the gages were as short as possible and of the maximum feasible size so that lead resistance was not a significant source of error. During temperature rise, comparatively little apparent strain was observed. Gages used will be discussed in subsection A-3 for each specific test.

Oscillograph chart speed on all tests was 0.05 in./sec, and time lines were applied to the chart at 10-sec intervals. Since the tests all lasted several minutes and the measured functions varied slowly (except at the instant of buckling), traces were never steep. During the test, the slope of the traces usually changed gradually if at all. Just prior to buckling, slope changes were no longer gradual but still smooth. At buckling, some of the gages usually "stepped" abruptly to a new strain level. Where this occurred, the strain value just prior to and just after the step is given (with no change in load). If no value is given beyond a certain load, the gage went off-scale completely when buckling occurred. In all tables where strain-gage readings are given, values are stated in microstrain – and are compression unless followed by (T), in which case they are tension.

A.2.3 Heating of Specimens

In all elevated-temperature tests, heating of specimens was by radiant heat lamps. These were General Electric quartz envelope lamps of 1,000- or 2,000-watt nominal rating (see specific tests for applicable wattages). These were powered by a Research Incorporated ignition-controlled power supply with 130-kva maximum output. Temperatures were controlled manually. In the large shear-panel tests, as many as 60 lamps were wired in parallel. It was found that to maintain a test temperature of approximately 800°F, 180 amps were required with a voltage drop of 30 volts across the 60 lamps. In the compression-panel and shear-panel tests, gold-plated, air-cooled reflectors containing 5 lamps each were used. In these reflectors (made by Research Incorporated), compressed air is fed into a plenum chamber behind the reflector and bleeds out into the reflector space through numerous small holes in the reflector face. These reflectors are 2 in. wide and, like the lamps, 12 in. long.

A.2.4 Strain Gages

All strain gages used were manufactured by Baldwin-Lima-Hamilton. All room-temperature gages had a 0.25-in. gage length and a resistance of 120 ohms. Paperback gages were bonded with Duco cement and foil gages (room temperature) were bonded with Eastman 910. Gage factors were around 2.0; exact values (given to ± 1 -percent accuracy) were used in data reduction.

All elevated-temperature gages were of the HT series, free-filament gages of 0.25- or 0.31 (5/16)-in. gage length and with nominal resistances of 350 ohms. Gages were bonded to the specimen with PBX Dry-Mix Cement. This ceramic cement requires two 2-hr curing cycles, one at 200°F and one at 600°F for each of the three coats applied. The first coat acts as an insulator, the second coat bonds the gage to the first coat, and the third coat seals the gage. Curing was done in a thermostatically controlled furnace.

These free-filament gages are supplied with Nichrome leads about 1 in. long. These were connected to Fiberglas-insulated Niclad wire by pinching a small copper collar around the wire and lead laid side by side. The Niclad wire was connected to a shielded (room-temperature) cable as soon as it left the elevated-temperature zone.

A.2.5 Temperature Measurement and Recording

All temperature measurements were made with Chromel-Alumel thermocouples. With the exception of a few thermocouples incorporated into the strain gage by the manufacturer, all thermocouples were type K, 28-gage, Fiberglas-insulated solid wire welded to the specimen. In the compression-panel and shear-panel tests, resistance welding was used and the two wires of the thermocouple were spaced 0.06 in. apart on the specimen. It was noticed that quite often this produced a small crack in the beryllium sheet. After the elevated-temperature tests, these cracks had sometimes opened to the point where light shone through, but apparently no propagation of the crack had occurred. Figure A-2 shows such a crack on the square shear-panel test. The white part is light shining through from behind the specimen.

On the cylinders, capacitance or "compression" welding was used. In this method, the two wires of the thermocouple are fused together in a ball of about 0.02-in. diameter. This ball-ended junction is brought into contact with the specimen using some force. At the moment of contact, a capacitive discharge fuses the ball into the surface of the specimen. No cracks were visible in the beryllium in the vicinity of these thermocouple junctions.

In the thermocouples incorporated into strain gages, a similar but smaller junction of the thermocouple wires is held near the surface of the specimen by the cement of the strain gage.

To determine the general temperature distribution over the specimen, 15 to 20 thermocouples were used. Continuous recording for three of these was available on Bristol strip chart recorders (1200° F full scale). The other thermocouples were connected to a switching box so that any one selected at the switching box could be read on a Bristol recorder. Just before and just after each test, a survey was made of all thermocouples. Temperatures given in this report are the averages of the temperatures just prior to and just after the test. Although the accuracy of the Bristol recorders is $\pm 5^\circ\text{F}$, some

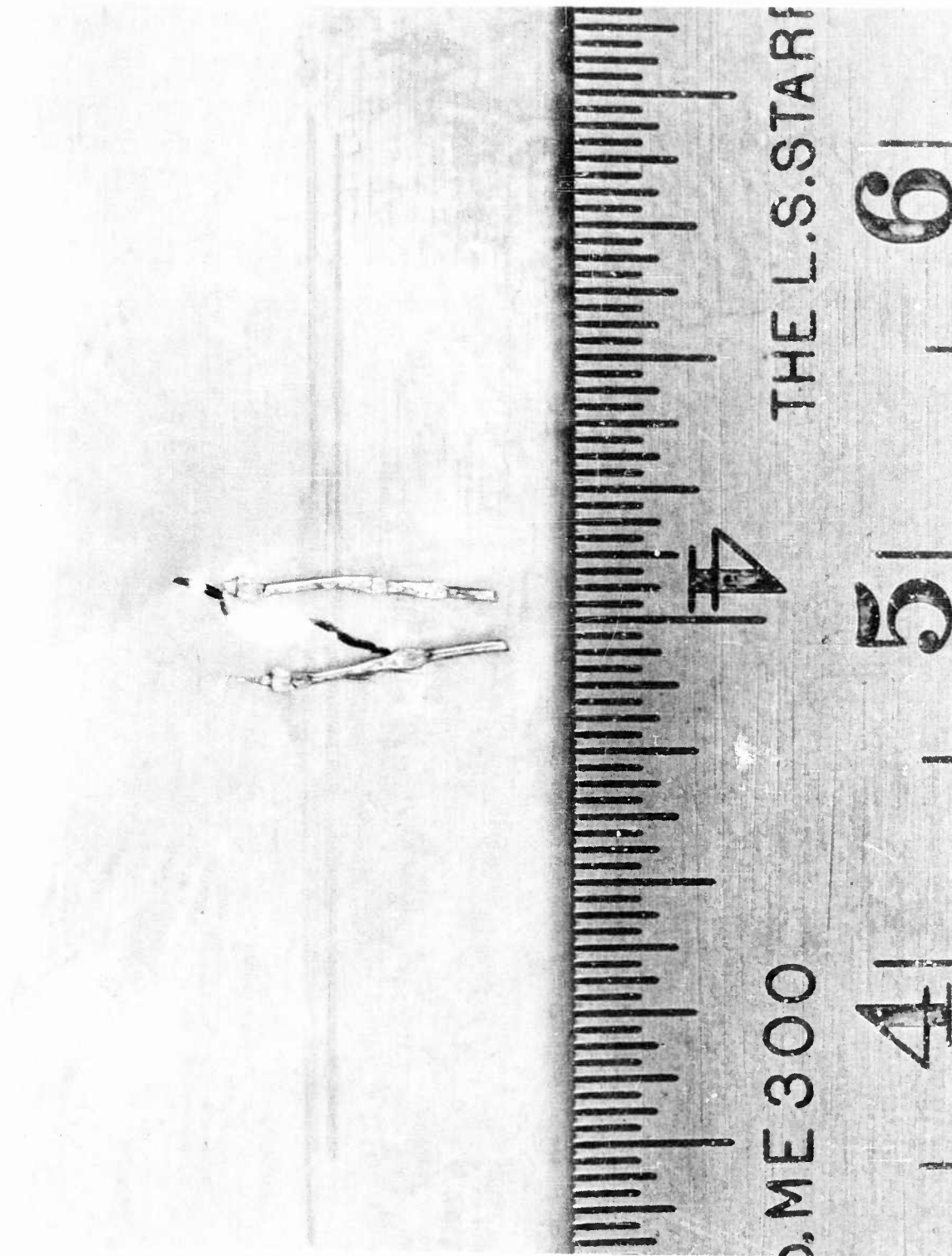


Fig. A-2 Cracking at a Resistance-Welded Thermocouple After Test

accuracy is lost in the switching operation and in the averaging process. Stated temperatures are subject to $\pm 10^\circ \text{F}$ accuracy. These statements apply to the compression-panel and cylinder tests. For the shear-panel tests, the Bristol recorders were not available and the thermocouple millivolt outputs (after the switching box) were measured with a 102 A-40 galvanometer in the oscillograph already described. Accuracy of this system is $\pm 15^\circ \text{F}$.

Where a "test temperature" is given in a table, it is an estimate of the most representative temperature based on averages and/or interpolations.

A.2.6 Measurement and Geometry of Specimens

Overall dimensions of the specimens are given and are accurate to ± 0.03 in. Thicknesses given are the average of 16 or more measurements taken around the edges of the plate or cylinder with a micrometer. A blade micrometer was used on the cylinders. The diameters of the 20-in. cylinders are only accurate to ± 0.10 in. because the cylinders were too flexible to permit very accurate measurement.

Where specimens appear shiny in the photographs, it is because varnish was applied to emphasize buckling undulations.

A.3 DETAILS OF SPECIFIC TESTS

A.3.1 Compression Panels

Five rectangular sheets, 11 by 12 in., were loaded axially so that a uniform compressive load was applied along each of the 11-in. edges.

For the test, a sheet was set in a vertical plane (with the 12-in. dimension vertical) and was divided into three equal longitudinal panels 3.5 in. wide horizontally. At the four vertical panel divisions, eight rigid plates, lying in a vertical plane at right angles on either side of the test sheet, acted as restraint against lateral buckling. These restraining plates, with their edges ground to a truncated point, were butted together in four pairs with the test sheet between them (Figs. A-3, A-4, and A-5). Figure A-5 is a photograph showing the test-fixture frame with three of the restraining plates removed from one side to show the interior construction of the fixture. The restraining plates could be moved laterally in their slots to adjust for the different thicknesses of sheet tested, and could be tightened at their proper location so that no further horizontal movement occurred.

A summary of basic information for each of the five sheets tested is given in Table A-1.

Special precautions were taken to insure a uniform distribution of load across the full width of the plate. Bars of annealed copper were placed between the edge of the beryllium sheet and the loading surfaces. The loading surfaces were of small radius (0.50 in.) to insure that indenting of the soft copper would occur on both faces of the bar (Fig. A-5). For specimen 1, where stresses were considerably lower, lead bars were used instead of annealed copper.

The bearing surfaces of the test sheets were flat and parallel to ± 0.002 in. over their length, and the loading surfaces of the universal testing machine and fixture were flat and parallel to ± 0.001 in. over their loaded width.

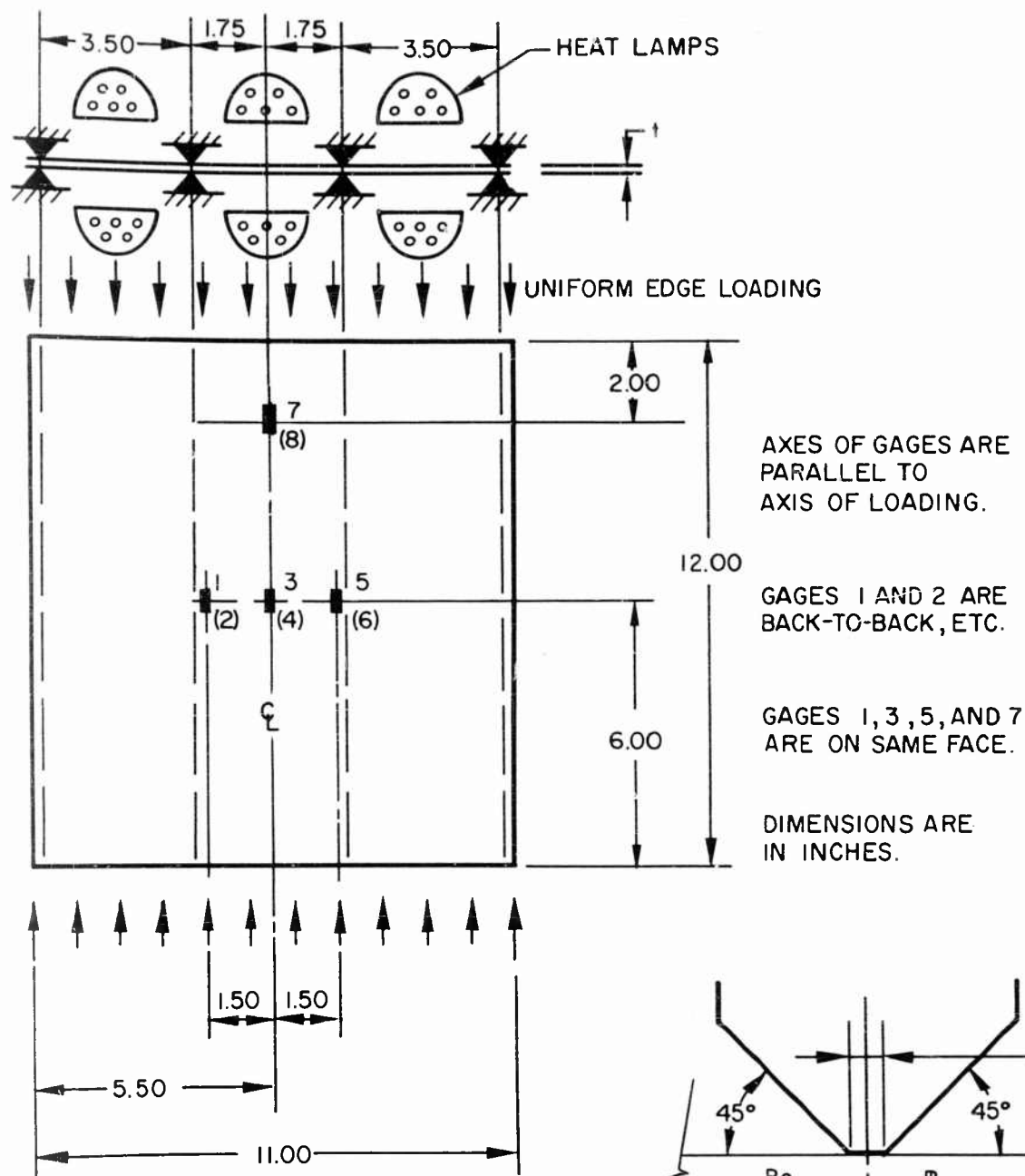


Fig. A-3 Geometry of Compression-Panel Tests

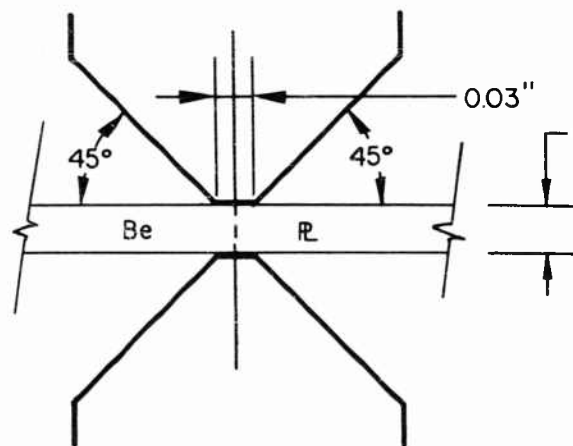


Fig. A-4 Detail of Knife-Edge Restraints

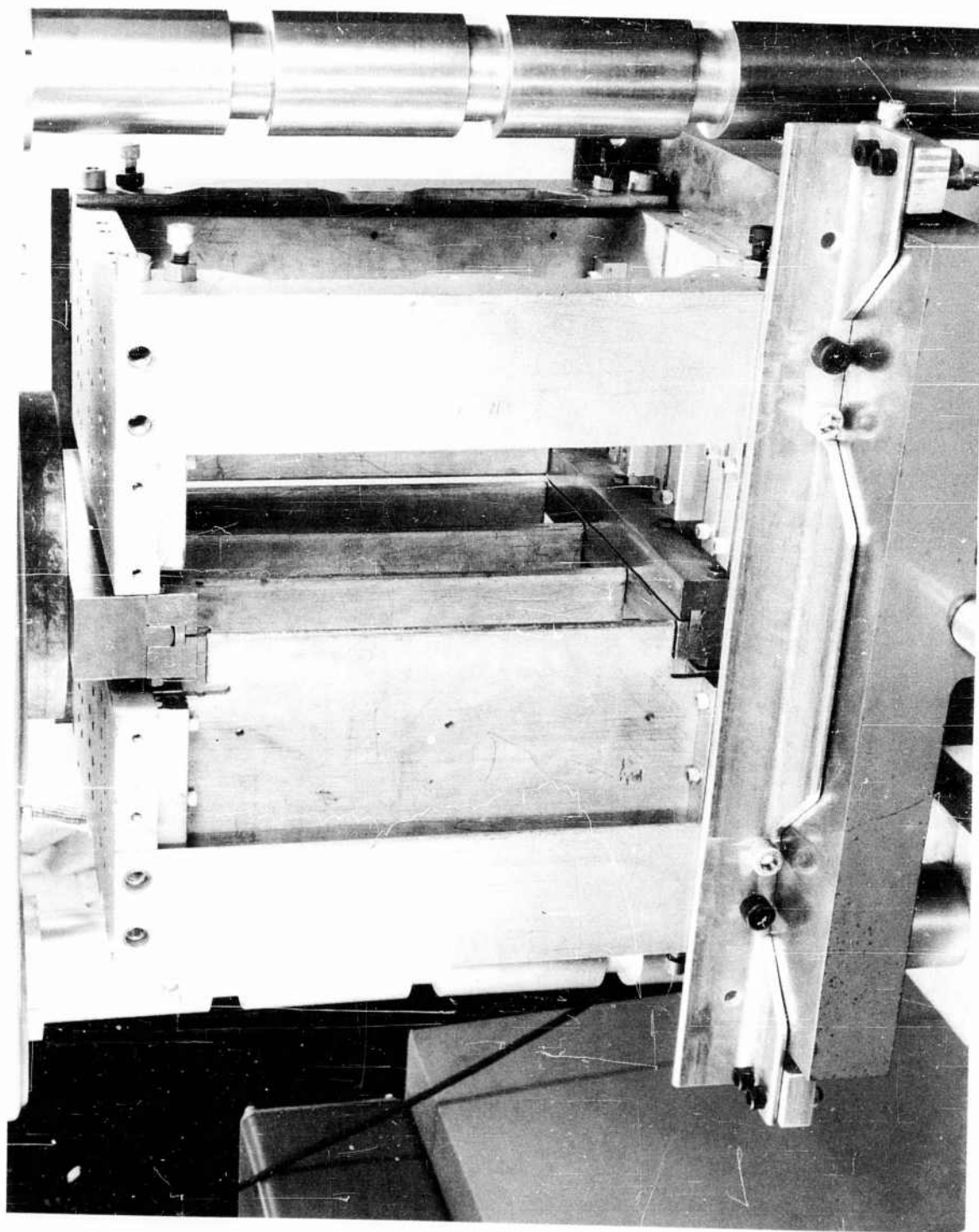


Fig. A-5 Compression-Panel Test Fixture

Table A-1

SUMMARY OF COMPRESSION-PANEL TESTS

Test Data	Specimen Number				
	1	2	3	4	5
Actual Thickness (in.)	0.022	0.039	0.063	0.022	0.038
Test Temperature (° F)	R. T.	R. T.	R. T.	680	680
Buckling Load (lb)	1,210	10,700	34,600	2,500	11,400
Buckling Stress (psi)	5,000	25,000	50,000	10,330	24,800
Maximum Load (lb)	6,000	16,000	36,500	3,580	11,500
Maximum Stress (psi)	24,790	37,500	52,240	14,800	27,500
Average Loading Rate (lb/min approx.)	150	1,500	700	1,700	6,000
Number of Gages Used	6	6	6	2	2

The "knife edges" of the restraining plates were straight and parallel to each other (within opposed pairs) to ± 0.001 in.

At room temperature, six strain gages were used. They are shown numbered 1 through 6 in Fig. A-3. At elevated temperature, two gages were used and these are numbered 7 and 8 in Fig. A-3. Tables A-2 through A-6 give strain-gage readings at various loads for the five specimens. Figures A-6 through A-13 show plots of load versus strain. All values are given in microstrain and are compression unless followed by (T) for tension.

Figure A-14 shows the location of 22 thermocouples mounted on both specimens 4 and 5. Tables A-7 and A-8 give temperatures at these locations before and after test. Thermocouple F on side 1 did not function on specimen 5.

For the elevated-temperature tests, six 5-lamp reflectors were installed in the spaces between the stiffening plates. Figure A-15 shows the fixture with the two end-stiffening plates removed to show the reflector and the lamps. Visible in the photograph is the Fiberglass packing used around the reflectors to seal off the heated area and form a furnace. The only openings left were below the reflectors. Since compressed air was leaving the reflectors, its only exit was at this base opening. This downward-moving air counteracted the "chimney" tendency and helped to reduce the vertical nonuniformity of temperature distribution. The photo also shows the thermocouple wires installed on the buckled specimen 4.

Elevated-temperature specimens were brought to test temperature by slowly heating for one hour. During this time, the loading head was raised so that the specimen could expand freely, and the stiffening plates were loosened on one side of the specimen but locked tight on the other to retain alignment. After reaching temperature, the specimens were allowed to soak for one hour before the stiffening plates were tightened and the load applied. Loading rates are given in Table A-1.

Table A-2

SPECIMEN NO. 1 STRAIN-GAGE READINGS AT VARIOUS LOADS^(a)

Time (min)	Load (lb)	Strain Gage Number					
		1	2	3	4	5	6
0	0	5(T)	0	10(T)	0	10(T)	0
6.85	500	25	35	15(T)	10	30(T)	10
8.93	750	60	55	5	26	25(T)	10
10.65	1,000	120	80	30	43	15(T)	25
12.17	1,250	165	110	82	46	10	35
13.58	1,500	210	130	140	31	40	40
15.33	1,750	265	160	225	10(T)	75	80
16.33	2,000	295	160	265	44(T)	90	95
17.83	2,250	370	200	340	84(T)	125	170
18.58	2,500	420	230	375	120(T)	165	200
19.75	2,750	460	260	420	150(T)	205	250
20.75	2,950	480	350	430	197(T)	235	280
20.83	3,000	480	350	370	166(T)	245	285
23.17	3,250	570	395	375	194(T)	345	365
25.33	3,500	630	430	380	218(T)	420	435
27.17	3,750	690	460	390	256(T)	495	490
29.25	4,000	750	480	410	285(T)	560	510
32.25	4,250	830	500	440	335(T)	665	570
38.17	4,500	990	530	470	391(T)	755	620
44.25	4,750	970	560	525	446(T)	840	640
52.00	5,000	1,000	565	580	590(T)	885	660
52.42	5,500	1,180	650	780	850(T)	985	720
53.33	6,000	1,500	930	1,060	1,260(T)	1,190	960

(a) All values in microstrain compression unless followed by (T).

Table A-3

SPECIMEN NO. 2 STRAIN-GAGE READINGS AT VARIOUS LOADS^(a)

Time (min)	Load (lb)	Strain Gage Number					
		1	2	3	4	5	6
0	0	0	0	0	0	10	0
0.25	500	10	10	10	28	0	30
0.50	1,000	30	20	30	68	45	75
0.58	1,500	60	45	60	87	70	100
0.75	2,500	110	100	105	150	120	150
1.42	5,000	240	230	225	285	235	290
1.62	6,000	270	260	255	345	250	310
2.00	6,500	295	275	280	370	285	325
2.75	7,000	310	300	280	403	315	350
3.33	7,500	335	315	305	428	340	365
3.92	8,000	355	340	330	450	370	385
5.08	9,000	415	380	425	432	460	410
5.33	9,100	445	385	465	432	490	420
5.34	9,200	460	375	480	413	500	420
5.71	9,500	475	380	495	420	520	480
6.37	10,000	495	415	480	440	550	580
7.08	10,500	520	455	440	475	590	540
7.83	11,000	560	495	400	475	650	590
8.58	11,500	615	530	400	435	700	630
9.42	12,000	680	560	430	368	780	700
10.25	12,500	720	615	465	310	860	740
11.08	13,000	780	665	500	254	940	780
12.00	13,500	835	715	525	190	1,030	825
13.00	14,000	890	785	560	140	1,135	880
14.00	14,500	960	840	590	100	1,250	935
15.08	15,000	1,055	920	640	250	1,380	990
16.33	15,500	1,170	985	720	85(T)	1,560	1,040
18.33	16,000	1,475	1,000	1,260	400(T)	1,950	810
19.37	16,000	1,600	800	1,900	800(T)	2,200	600
19.40	Failure						

(a) All values in microstrain compression unless followed by (T).

Table A-4

SPECIMEN NO. 3 STRAIN-GAGE READINGS AT VARIOUS LOADS^(a)

Load (lb)	Strain-Gage Number					
	1	2	3	4	5	6
0	0	0	0	0	0	0
1,000	20	20	20	15	0	20
2,000	60	70	60	60	40	40
3,000	120	110	100	94	70	80
4,000	140	140	120	130	100	100
5,000	180	160	160	160	130	140
6,000	220	200	180	190	160	180
7,000	260	230	220	220	220	210
8,000	290	260	240	250	220	240
9,000	320	290	270	290	250	260
10,000	360	320	300	320	280	290
11,000	380	350	340	350	300	330
12,000	440	380	370	390	340	350
13,000	460	410	400	410	380	390
14,000	490	440	420	450	400	420
15,000	520	470	440	475	430	460
16,000	560	500	480	510	460	490
17,000	590	520	500	540	500	510
18,000	620	550	530	570	520	540
19,000	660	580	560	600	560	580
20,000	680	640	580	640	580	640
21,000	720	660	660	675	660	640
22,000	760	700	680	710	670	680
23,000	780	730	700	735	740	740
24,000	810	760	730	765	760	760
25,000	850	790	760	800	790	800
26,000	880	820	780	835	820	820
27,000	920	840	820	870	840	860
27,900	950	880	840	900	880	880
28,100	900	940	810	940	880	880
29,000	930	970	840	980	910	920
30,000	980	990	860	1,010	940	940
30,200	1,000	1,000	870	1,010	940	960
30,300	1,080	940	920	970	940	960
31,000	1,120	950	940	980	980	980
32,000	1,170	970	1,000	1,000	1,020	1,010
33,000	1,220	990	1,010	990	1,060	1,050
34,000	1,240	1,040	1,080	1,020	1,110	1,090
35,000	1,320	1,100	1,080	1,100	1,180	1,180
36,000	1,420	1,240	940	1,280	1,280	1,280
36,500	1,440	1,400	790	1,420	1,340	1,460
36,200	1,480	1,680	700	1,450	1,400	1,540
36,000	1,500	1,800	720	1,340	1,500	1,540
35,000	1,760	2,120	800	1,150	1,540	1,500
Failure						

(a) All strain-gage values in microstrain compression.

Table A-5

SPECIMEN NO. 4 STRAIN-GAGE READINGS AT VARIOUS LOADS^(a)

Load (lb)	Strain Gage 7	Strain Gage 8	Average of Strain Gages 7 and 8
0	0	0	0
600	15(T)	65	25
800	20(T)	110	45
1,000	30(T)	165	68
1,200	50(T)	205	78
1,400	65(T)	265	100
1,600	95(T)	320	112
1,800	125(T)	360	118
2,000	155(T)	410	128
2,200	175(T)	460	142
2,400	205(T)	480	138
2,600	185(T)	510	162
2,800	140(T)	480	170
3,000	80(T)	440	180
3,200	5(T)	360	178
3,250	5	350	178
2,950	335(T)	670	168
3,200	220(T)	700	240
3,400	160(T)	585	212
3,580	90(T)	170	40

(a) All values in microstrain compression unless followed by (T).

Table A-6

SPECIMEN NO. 5 STRAIN-GAGE READINGS AT VARIOUS LOADS^(a)

Load (lb)	Strain Gage 7	Strain Gage 8	Average of Strain Gages 7 and 8
0	0	0	0
1,000	0	60	30
2,000	20(T)	220	100
3,000	20(T)	340	160
4,000	20(T)	420	200
5,000	20(T)	520	250
6,000	40(T)	600	280
7,000	60(T)	660	300
8,000	80(T)	760	340
9,000	95(T)	820	362
10,000	135(T)	940	402
10,500	305(T)	1,020	358
11,000	340(T)	1,140	400
11,500	325(T)	1,240	453

(a) All values in microstrain compression unless followed by (T).

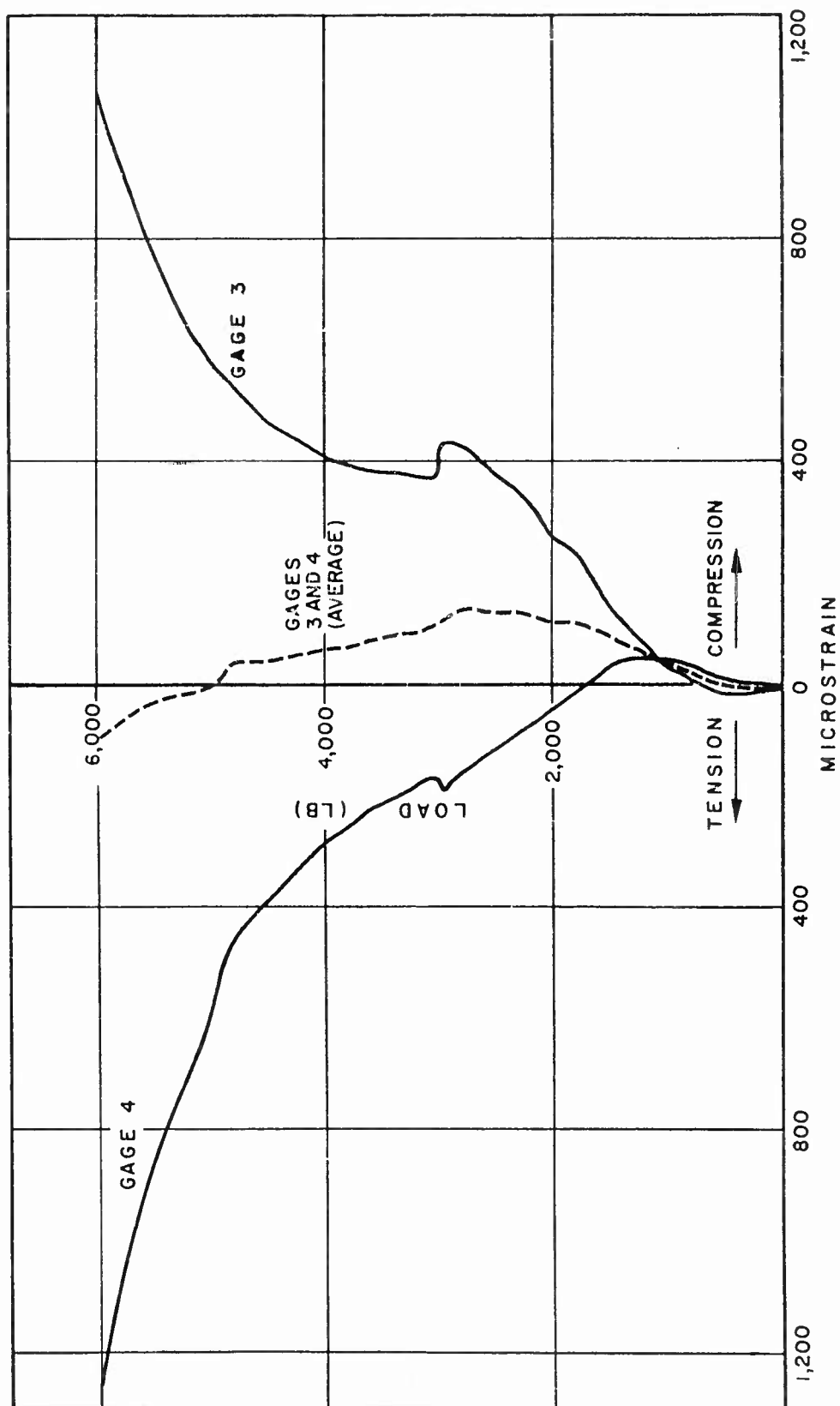


Fig. A-6 Specimen 1 Load Versus Strain Gages 3 and 4

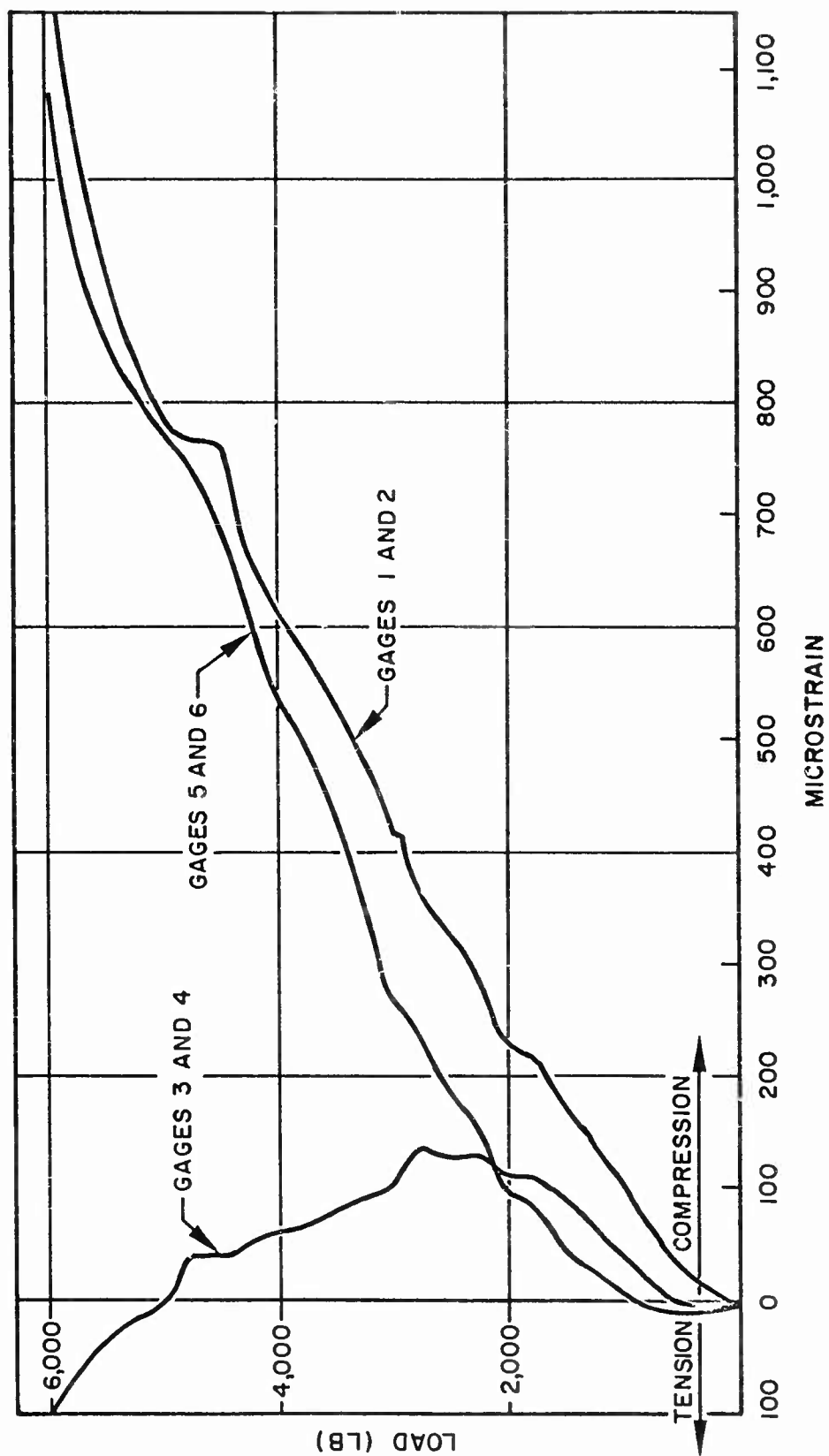


Fig. A-7 Specimen 1 Load Versus Strain Averages of Gages 1 and 2, 3 and 4, and 5 and 6

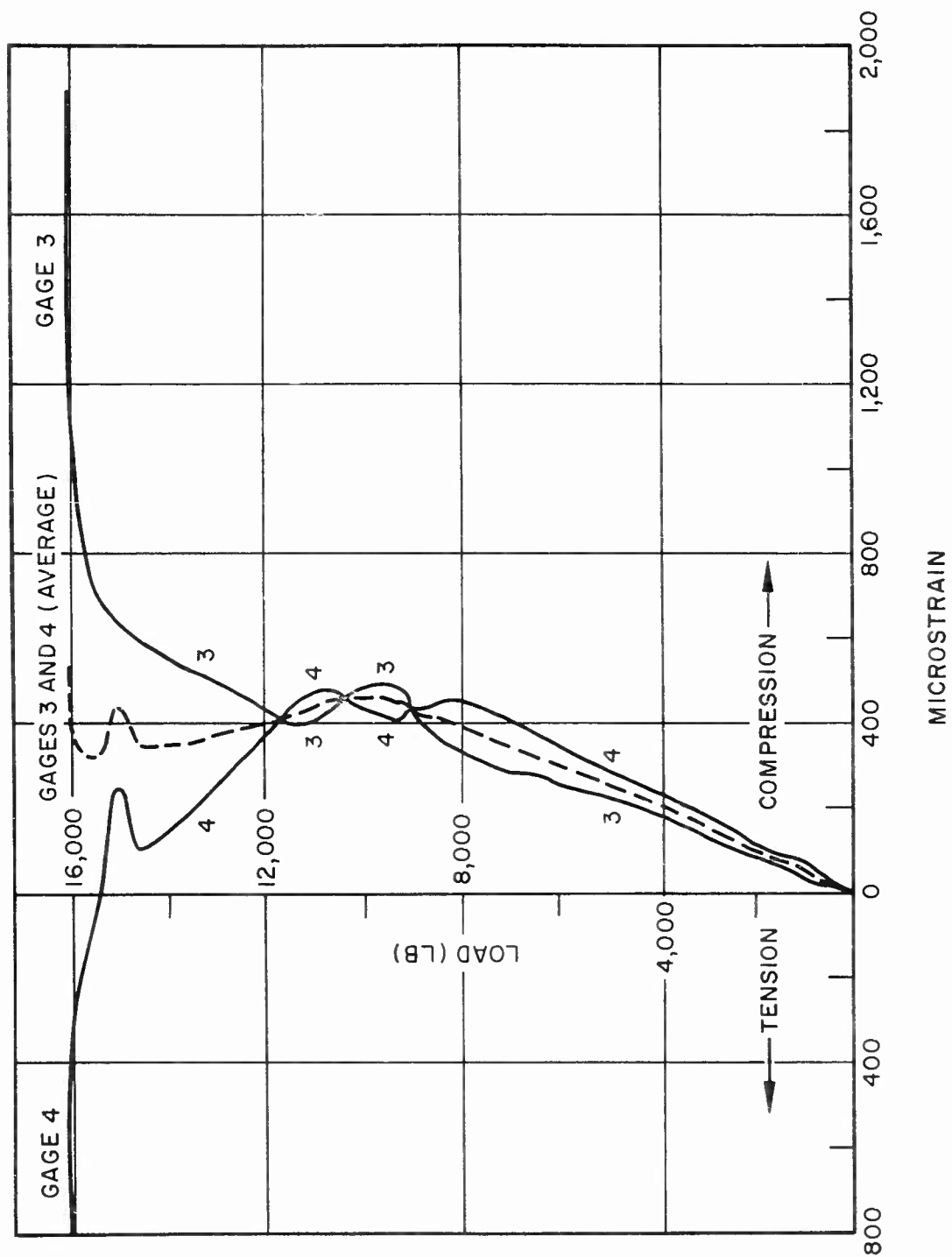


Fig. A-8 Specimen 2 Load Versus Strain for Gages 3 and 4

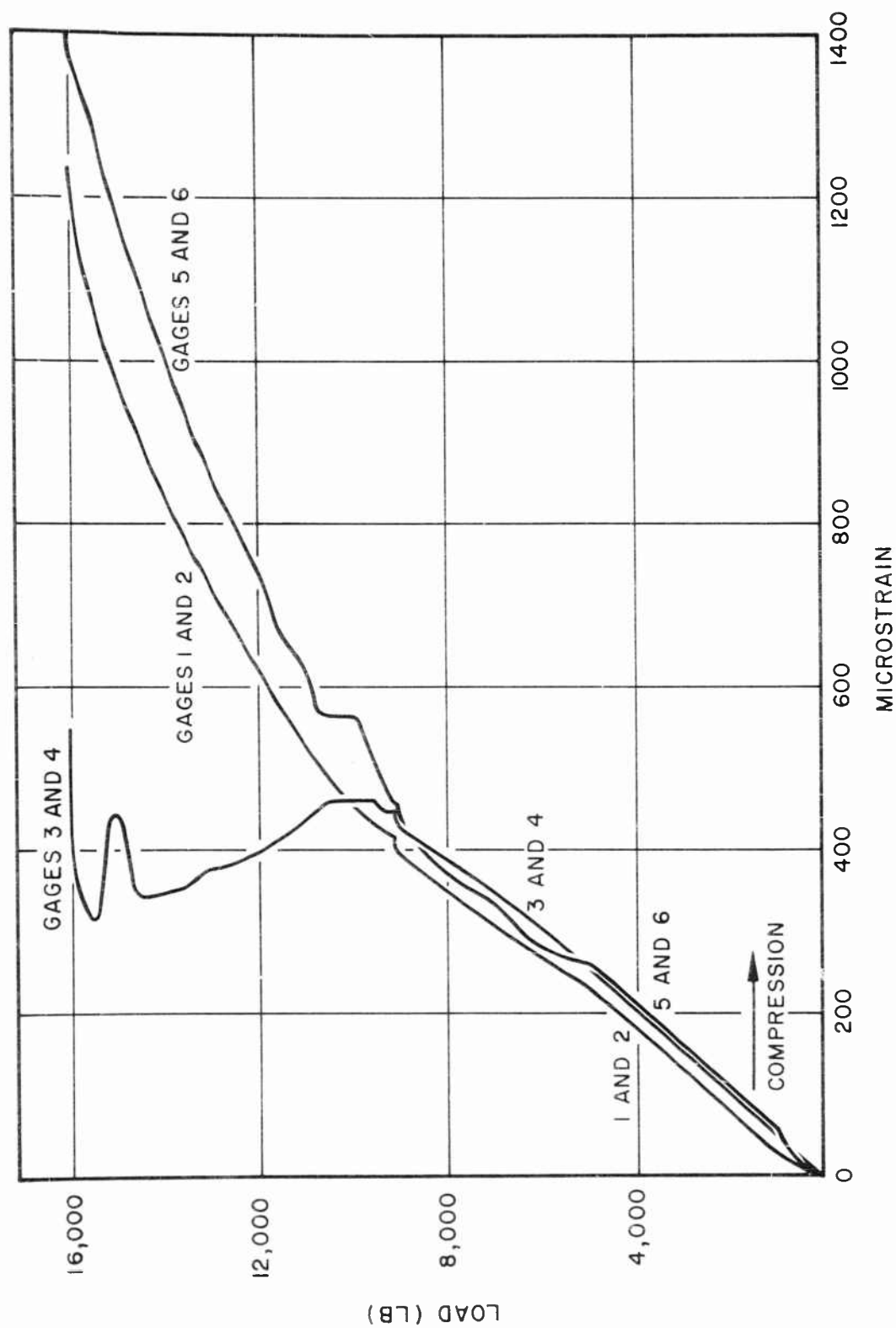


Fig. A-9 Specimen 2 Load Versus Strain Averages of Gages 1 and 2, 3 and 4, and 5 and 6

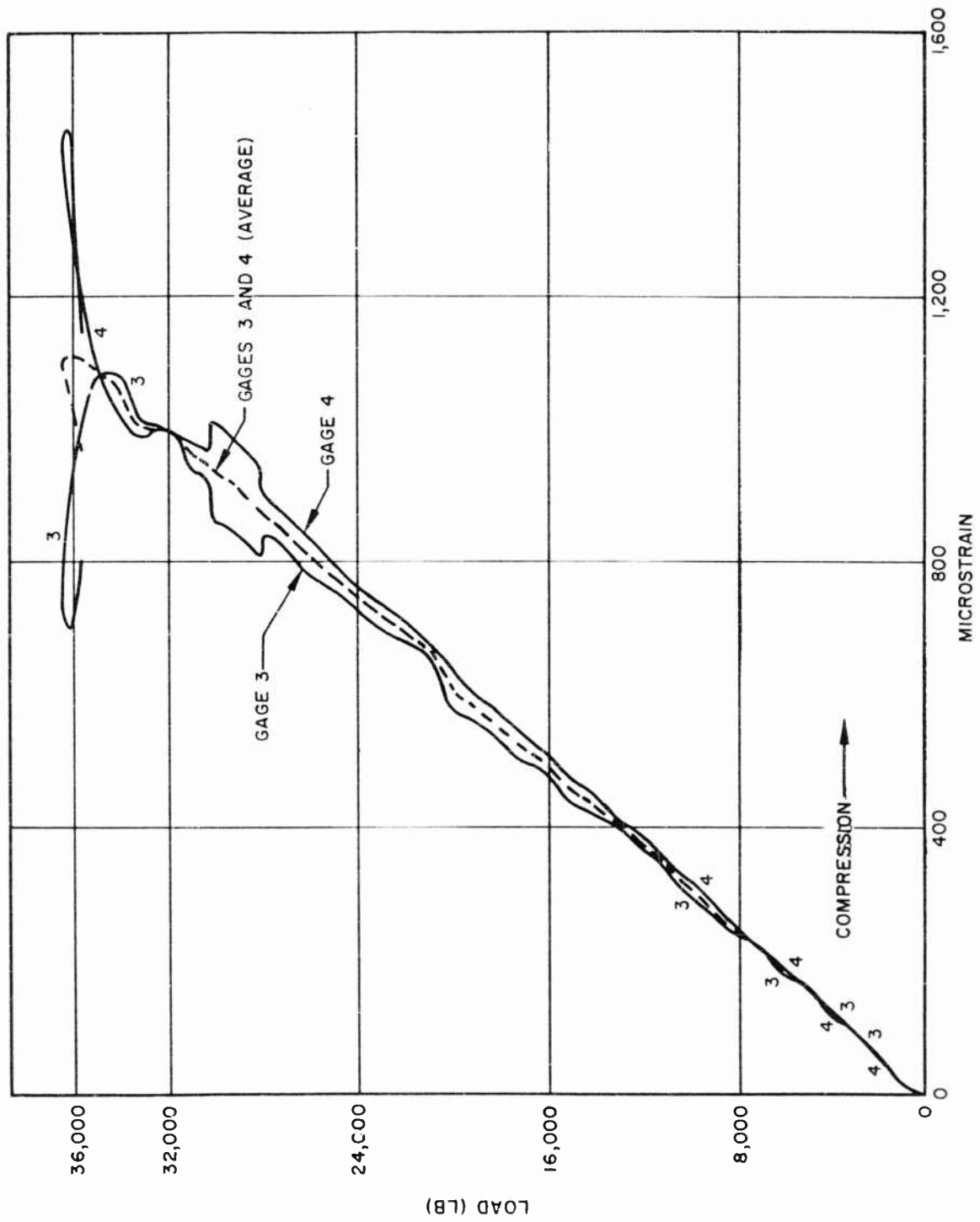


Fig. A-10 Specimen 3 Load Versus Strain Gages 3 and 4

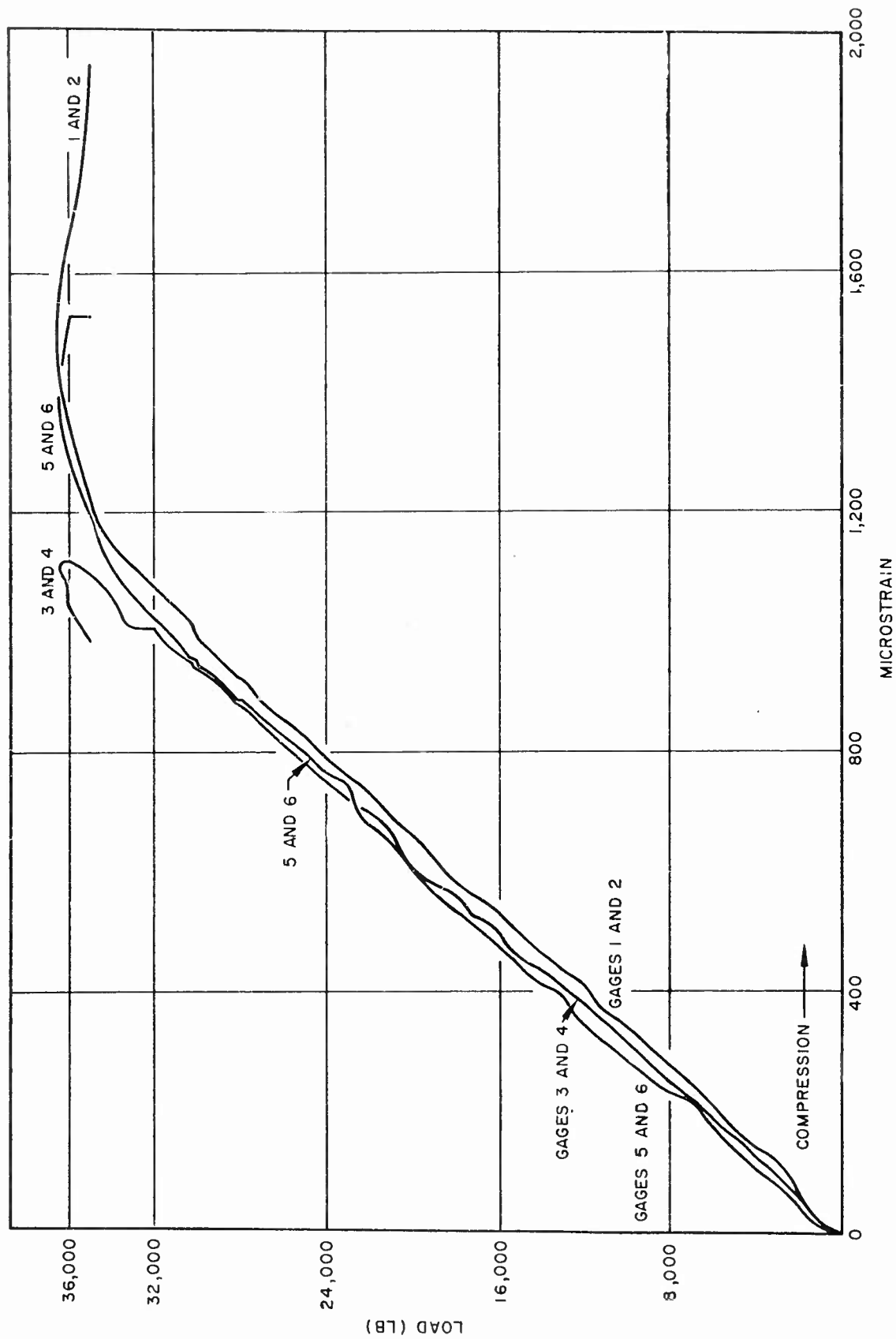


Fig. A-11 Specimen 3 Load Versus Strain Averages of Gages 1 and 2, 3 and 4, and 5 and 6

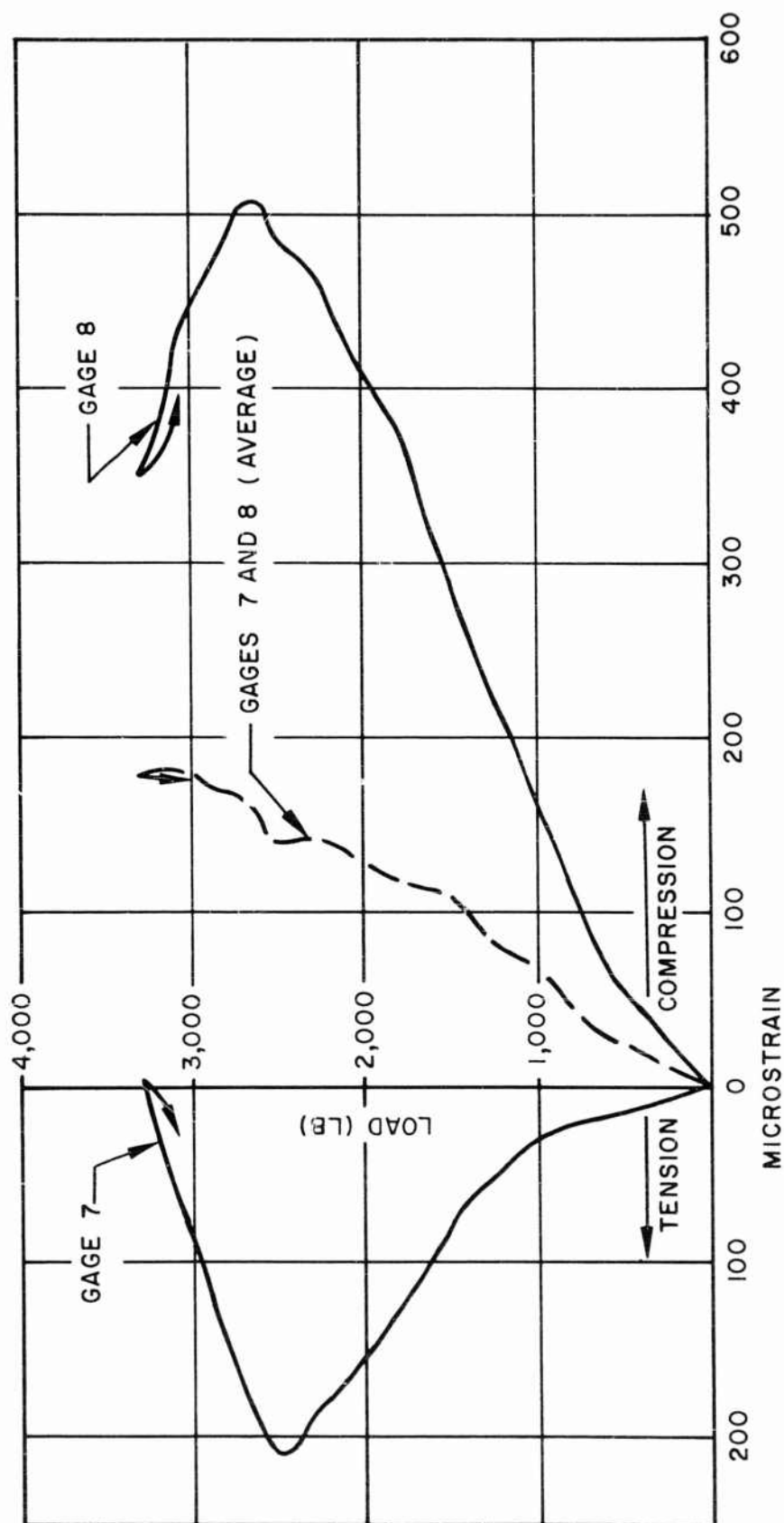


Fig. A-12 Specimen 4 Load Versus Strain Gages 7 and 8

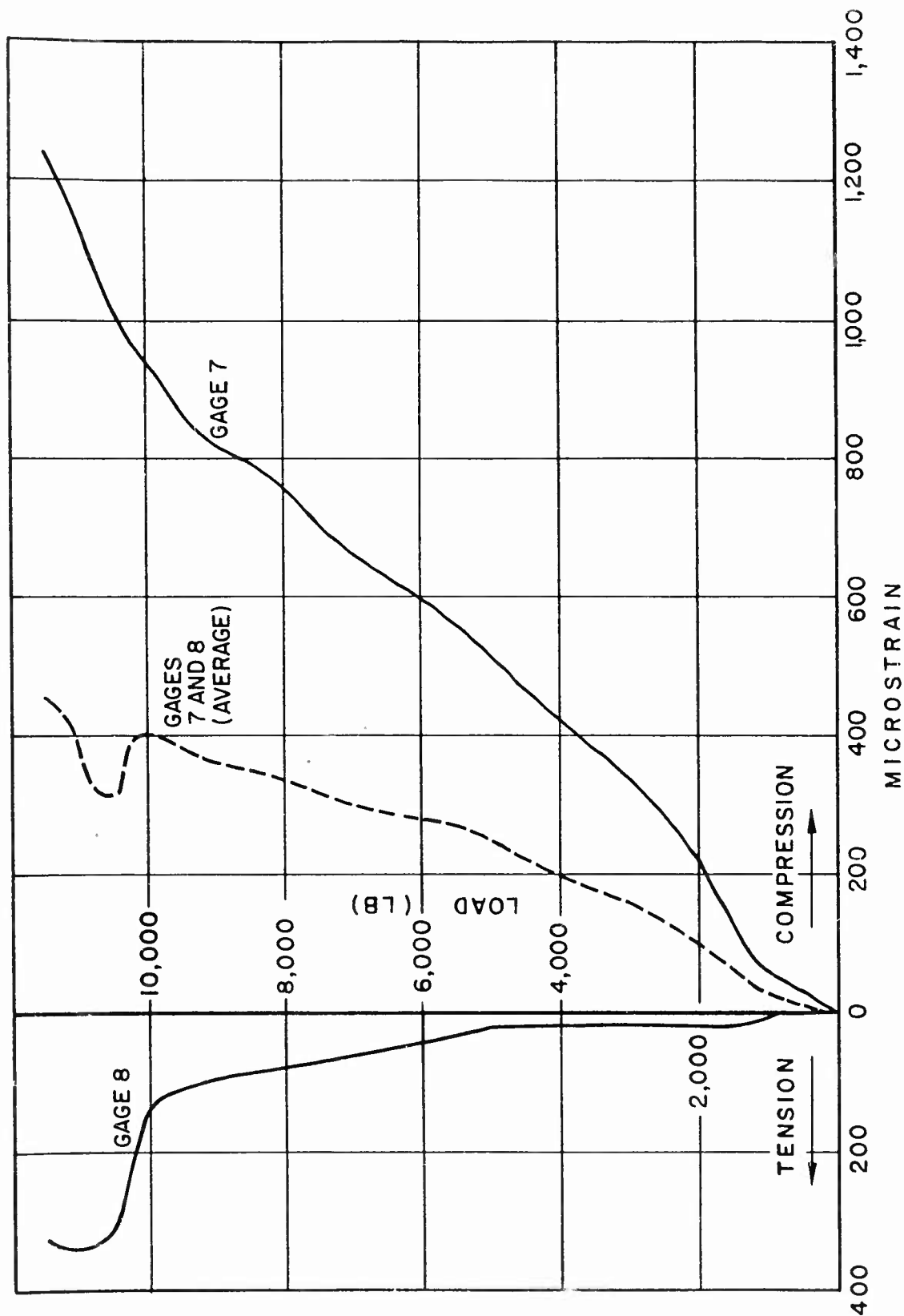


Fig. A-13 Specimen 5 Load Versus Strain Gages 7 and 8

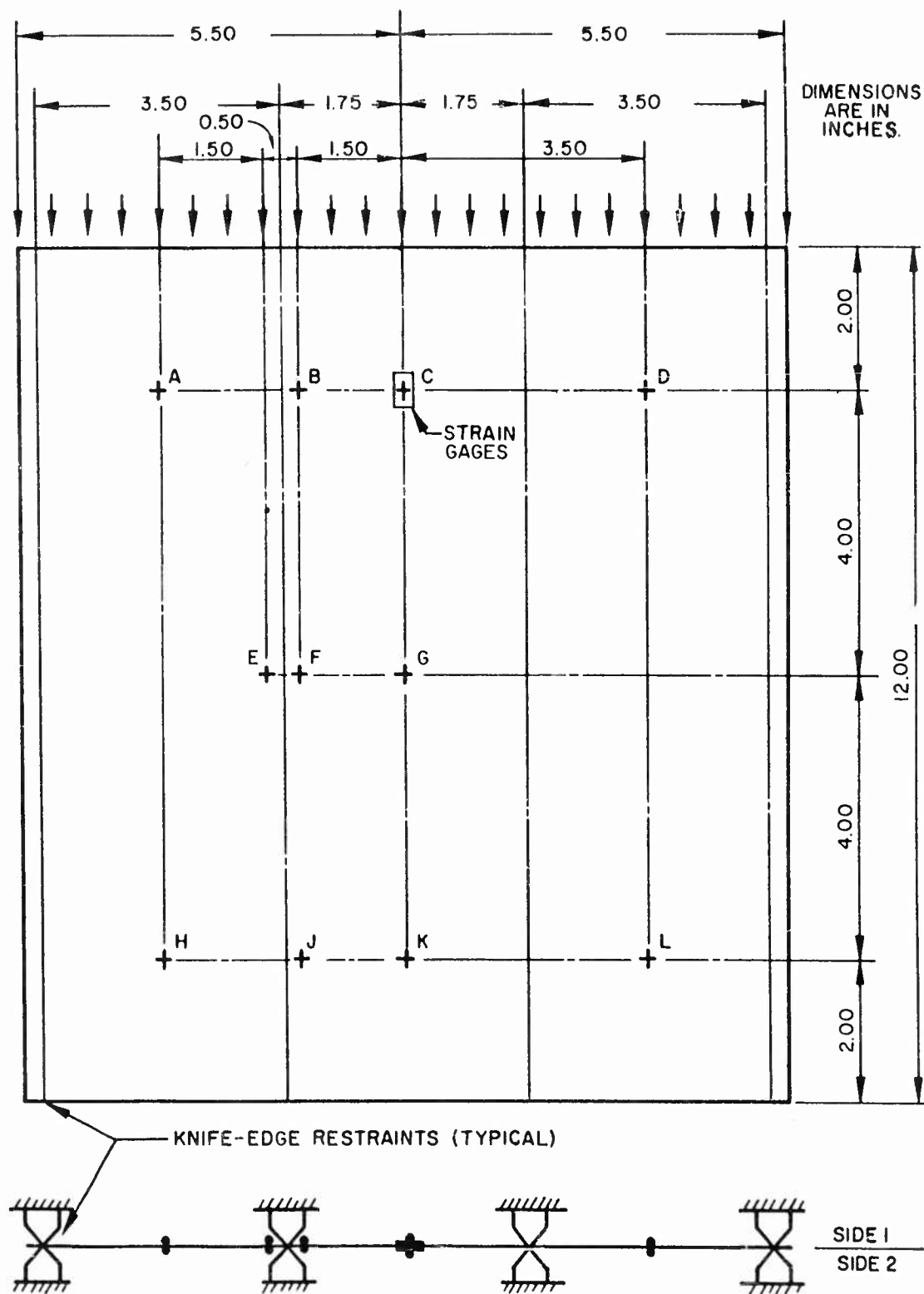


Fig. A-14 Thermocouple Locations on Compression-Panel Tests

Table A-7

SPECIMEN NO. 4 TEST TEMPERATURES

Location	Just Prior To Test (° F)		Just After Test (° F)	
	Side 1	Side 2	Side 1	Side 2
A	660	660	666	666
B	638	670	662	648
C	826	804	876	826
D	657	653	625	621
E	750	750	748	750
F	762	760	758	758
G	775	775	775	775
H	642	640	646	646
J	652	652	666	670
K	679	681	690	692
L	643	643	652	652
Average	703.0	698.9	705.8	700.3

Table A-8

SPECIMEN NO. 5 TEST TEMPERATURES

Location	Just Prior To Test (° F)		Just After Test (° F)	
	Side 1	Side 2	Side 1	Side 2
A	592	590	600	595
B	600	597	634	632
C	827	703	781	686
D	629	629	617	617
E	757	755	756	756
F	—	768	—	768
G	794	724	804	768
H	655	648	650	646
J	672	668	662	662
K	684	679	676	672
L	643	648	670	648
Average	685.3	673.5	685.0	676.9

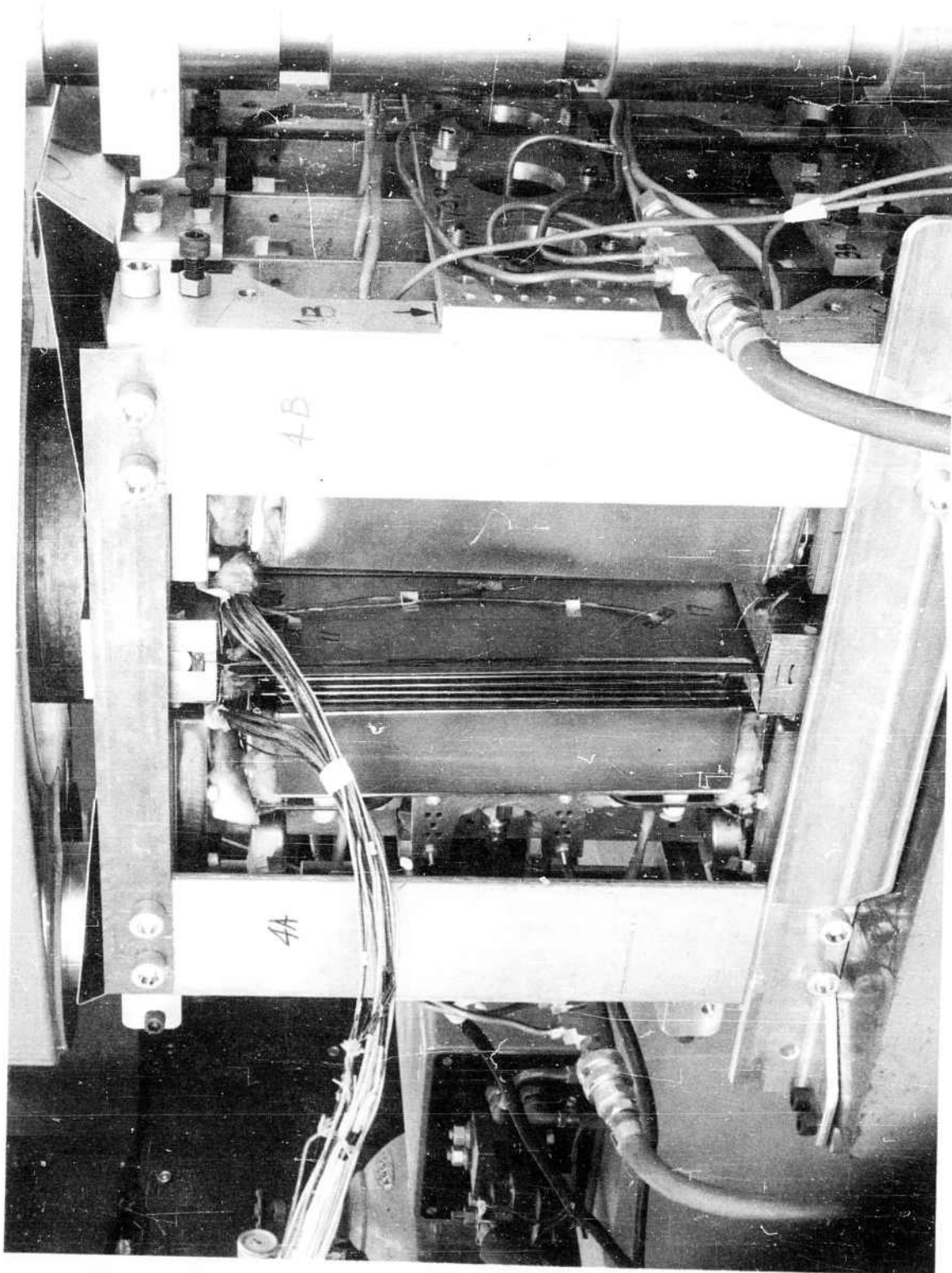


Fig. A-15 Compression-Panel Test Fixture With Heat Lamps Installed

Figure A-16 shows specimens 1, 2, and 3. The lower one is specimen 1. Failure occurred in the thinnest region (0.002 in. less than the average, 0.022 in.). Specimen 2 is the upper left one. Failure of this specimen occurred by the shattering of all three panels without indication of which shattered first. Detached pieces (almost rectangular) are lying on the lower half of the plate. Specimen 3 (upper right hand) shattered like specimen 2 but the pieces were not separated from the sheet. The black streaks on specimens 2 and 3 are molybdenum disulphide, a lubricant-like graphite that was used to reduce friction between the sheet and stiffening plates. Some of the load was transmitted (through friction) to these stiffeners causing a drop in compressive stress in the lower regions. For this reason, failure occurred near the top loading edge in the region of maximum compressive stress. It would seem that the lubricant helped to cause failure further away from the upper loaded edge.

Figure A-17 shows specimens 4 and 5. The lower (lighter colored) piece is specimen 4. Failure in this specimen was by shattering near the upper loaded edge. This thin sheet became warped during the rise to test temperature and it is very probable that the failure occurred in a region that was misaligned (due to the warping) even before the load was applied. Specimen 5 (darker colored) failed very gradually.

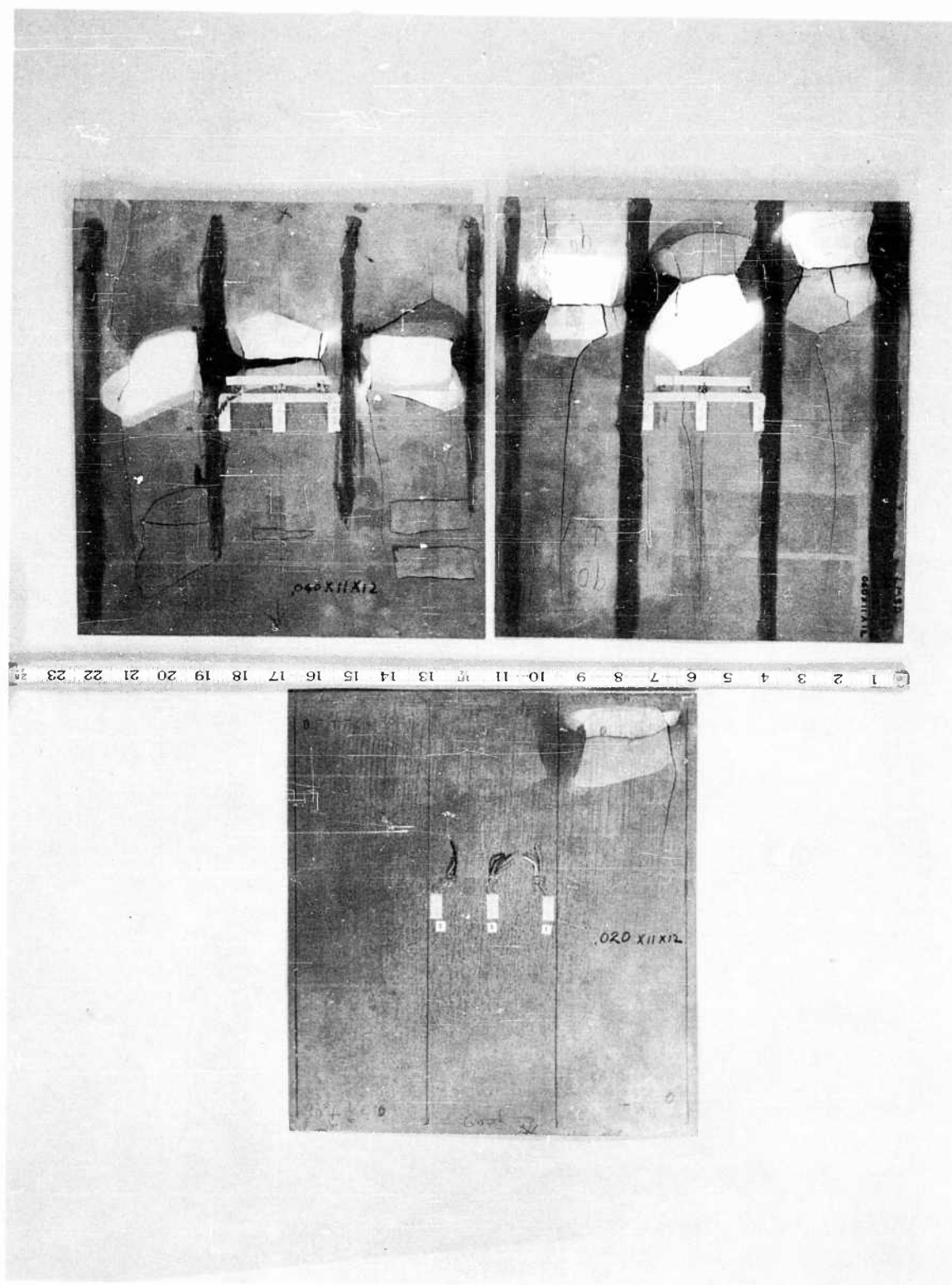


Fig. A-16 Room-Temperature Compression Panels After Test

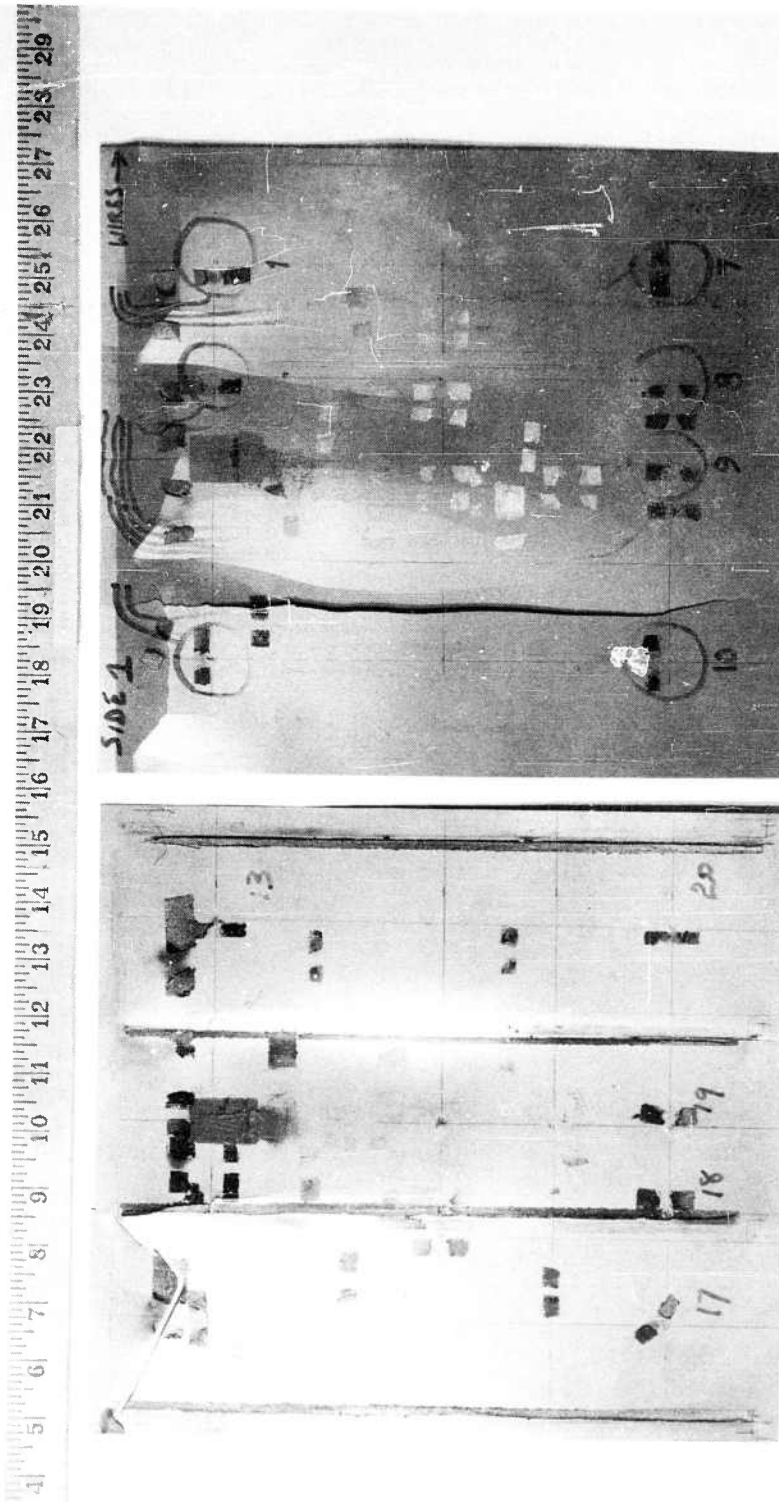


Fig. A-17 Elevated-Temperature Compression Panels After Test

A.3.2 Shear Panels

Two shapes of panels were tested, a 10-in. square and a 10-in. by 20-in. rectangle. Table A-9 gives basic information for five specimens tested (they are numbered 6 through 10 to avoid confusion with the compression-panel tests).

Two separate fixtures were designed for loading the two shapes of panels. These are shown in Figs. A-18 through A-21. For simplicity, Fig. A-18, an isometric sketch showing the assembly of the square test frame, has only 4 inconel bars on each side of the test panel. There was, in fact, one more set of 4 bars on each side of the panel so that the entire frame comprised 16 identical bars instead of the 8 shown in Fig. A-18.

For the rectangular frame, all details were identical except for the addition of 10 in. in length to 8 of the 16 inconel bars. The 1-in. spacing of 1/4-in. holes remained the same (Fig. A-21).

The edge bars were made of inconel because this material has an expansion coefficient fairly close to that of beryllium. The low yield stress of this material and the diminished cross-sectional area at the connecting pins made it necessary to have what would otherwise seem like an excessively heavy frame. The 3/4-in. dowel pins at the four corners were high-strength steel with a bearing yield point over 300,000 psi, and the 1/4-in. (NF-20 thread) bolts were corrosion-resistant steel with a yield point of 80,000 psi, and these were torqued to 75 in./lb. Holes for the bolts were located to ± 0.01 -in. accuracy, and were 0.016-in. oversize. No difficulty was experienced in assembly.

The yoke for connecting the frame to the testing machine was of mild steel and incorporated two dowel pins (similar to those in the frame) at right angles to each other so as to form a universal joint and insure axial loading of the frame (Fig. A-19).

The elongation of the loaded diagonal was measured in all tests. At room temperature, this was done with an extensometer fastened to the two loading pins (see Figs. A-20 and

Table A-9

SHEAR PANEL TESTS: BASIC INFORMATION

Test Data	Specimen Number				
	6	7	8	9	10
Sheet Dimensions (in.)	10 × 10	10 × 20	10 × 20	10 × 10	10 × 20
Nominal Thickness (in.)	0.02	0.02	0.01	0.04	0.04
Actual Thickness (in.)	0.022	0.023	0.010	0.039	0.039
Test Temperature (° F)	R. T.	R. T.	R. T.	825	805
Initial Buckling Load (lb)	2,000	2,000	500	7,500	8,500
Initial Buckling Stress (psi)	10,700	5,090	2,930	22,700	12,430
Maximum Load (lb)	6,050	6,250	3,740	10,700	19,800
Maximum Stress (psi)	32,400	15,900	21,900	32,400	29,800
Loading Rate (lb/min approx.)	1,500	2,000	1,200	2,000	3,000

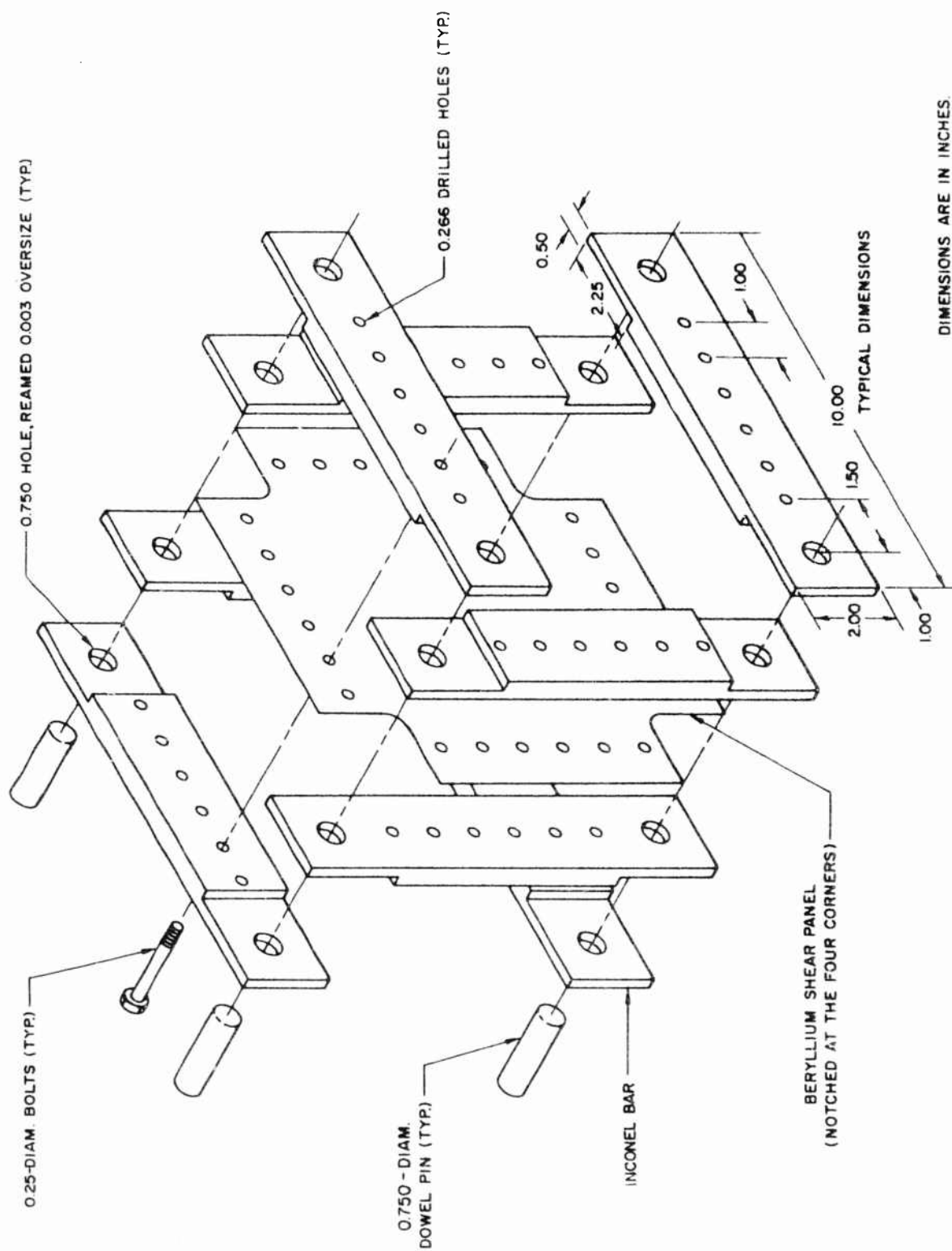


Fig. A-18 Shear Panel and Test Frame

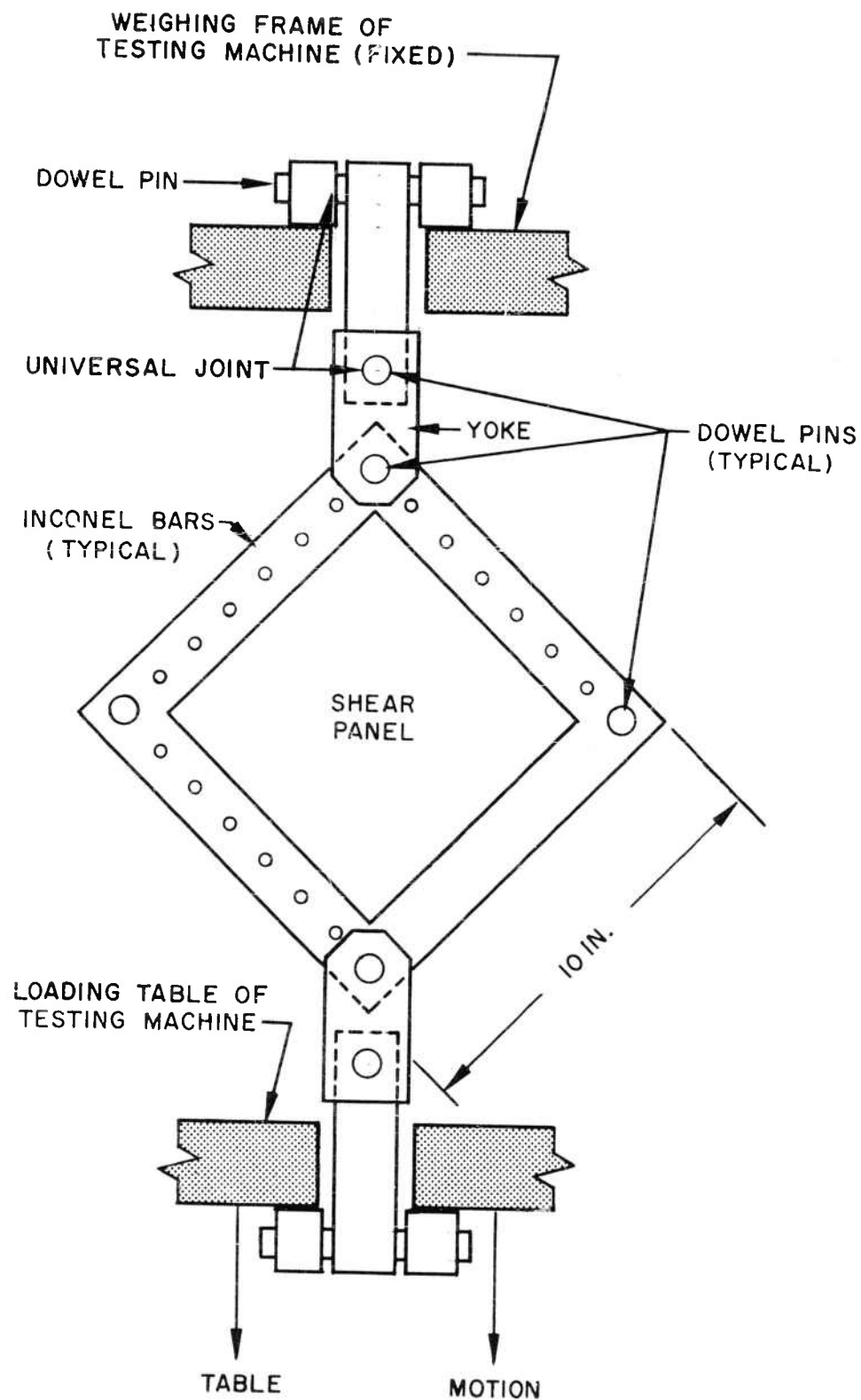


Fig. A-19 Square Panel and Method of Loading

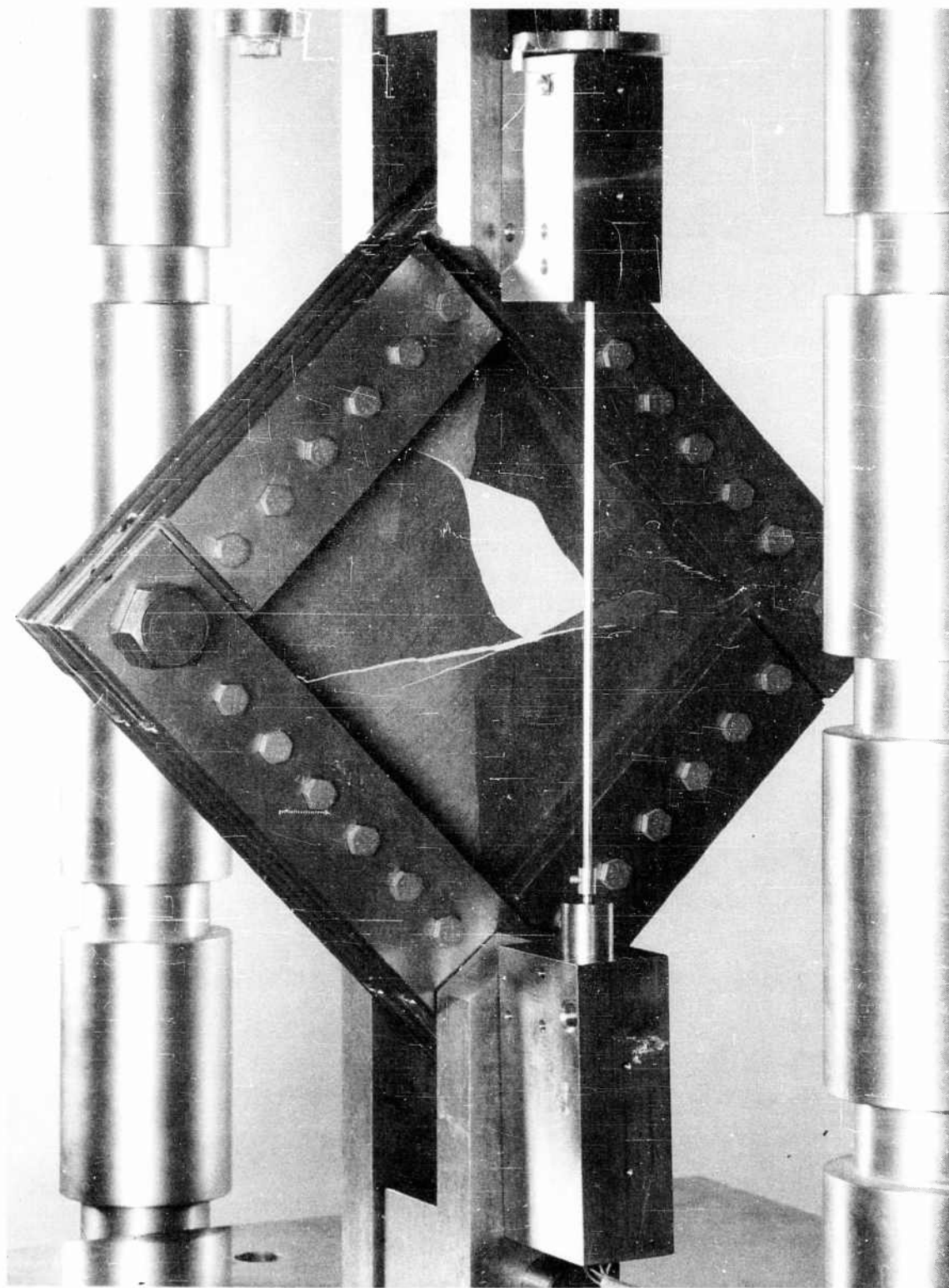


Fig. A-20 Shear Panel Specimen 6 After Test

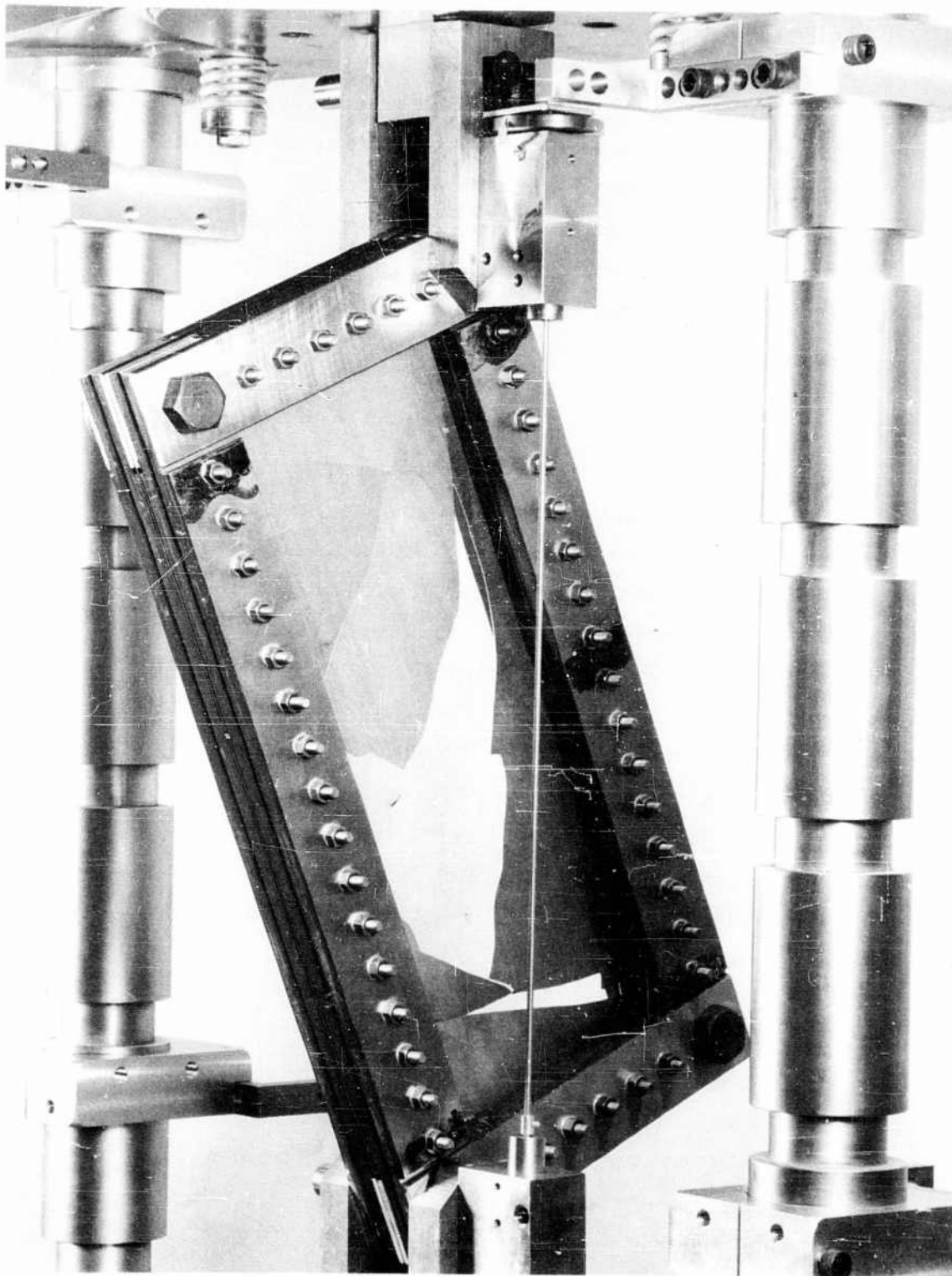


Fig. A-21 Shear Panel Specimen 7 After Test

A-21), and the transducer was a linearly variable differential transformer. A Sanborn preamplifier supplied the AC excitation, the phase-sensitive demodulation, and amplification. The system was found to have a deviation from linearity of less than 0.004 in. in a 0.25-in. range. The DC output of the Sanborn was connected to the X-axis of a Moseley X-Y plotter. The Y-axis of a Moseley was connected to the load-indicating potentiometer mentioned in subsection A.2.1. The plots of load versus elongation for the R.T. specimens are shown in Figs. A-22 through A-24. Although the R.T. specimens all failed suddenly by shattering, there were evidences of undulations (i.e., buckling patterns) in all cases. This is most conspicuous in Fig. A-20.

At elevated temperature, elongation of the diagonal was obtained by measuring the table motion of the testing machine. This introduced errors due to the elongation of the yoke (but partly compensated by the shortening of the test machine columns). Since no part of the loading system exceeded its yield point, the error was proportional to load, and it was evaluated at less than 0.003 in. for the maximum allowable load on the fixture (20,000 lb). This was preferred over the erratic drifting experienced with the differential transformer at elevated temperature.

The transducer measuring table motion was a flexible cantilever blade on which were mounted four strain gages wired to measure the bending of the blade as the table depressed its free end. The deviation from linearity of this device was found to be less than ± 0.003 in. over a range of 0.50 in. The strain-gage bridge was DC powered with 7.5 volts, and the output was connected directly to the X-axis of the X-Y plotter. The plots of load versus elongation for specimens 9 and 10 are shown in Figs. A-25 and A-26.

It was noticed in specimens 6 and 7 that cracking seemed to start at the notched corners, and since specimen 8 was a late addition to this series of tests, it was decided to cut the corners off diagonally to avoid a possible stress concentration in this zone. Figure A-27 is a photograph of specimen 8 after test. The cracks are approximately normal to the diagonal that was loaded.

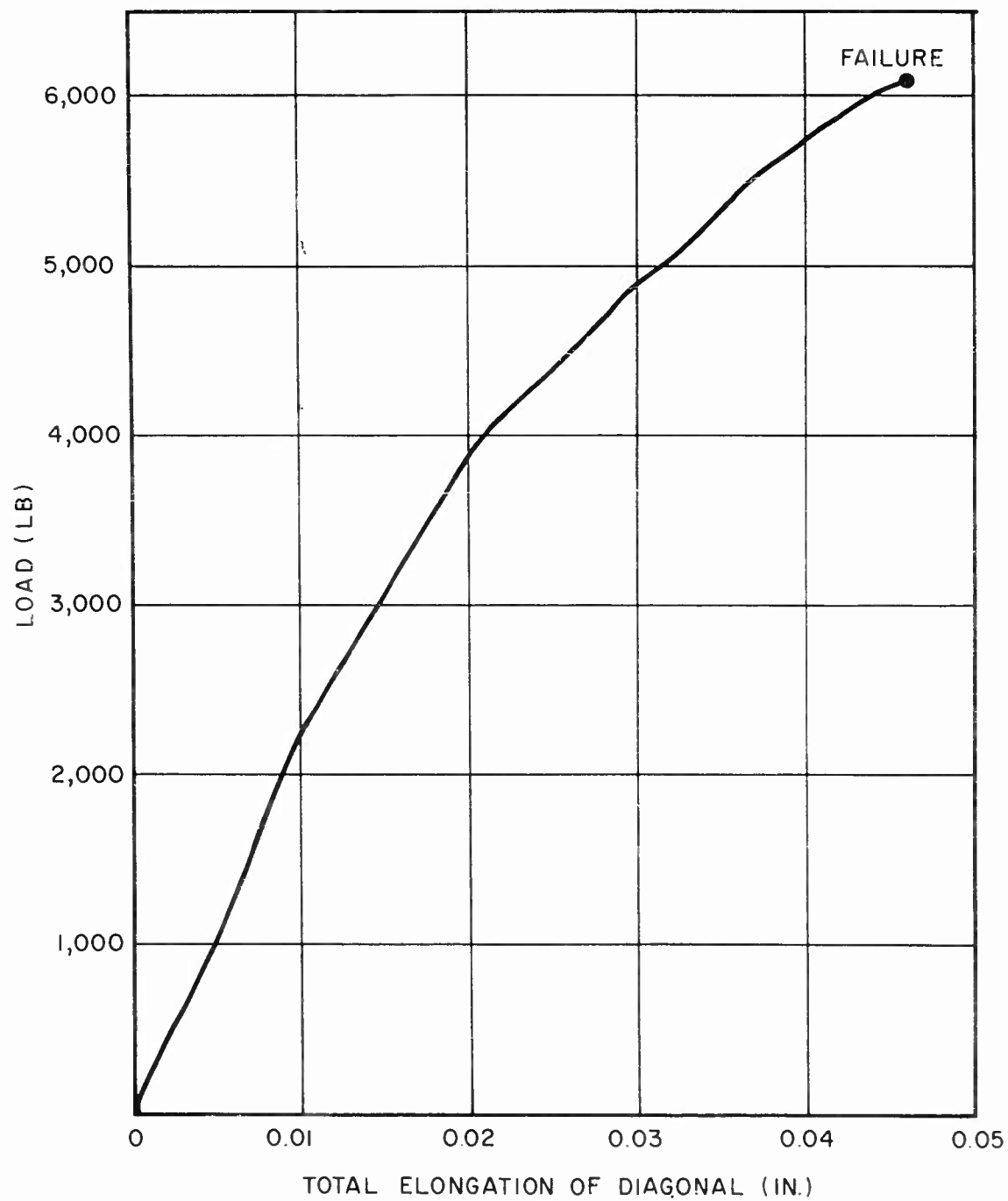


Fig. A-22 Shear Panel Specimen 6 Load Versus Elongation

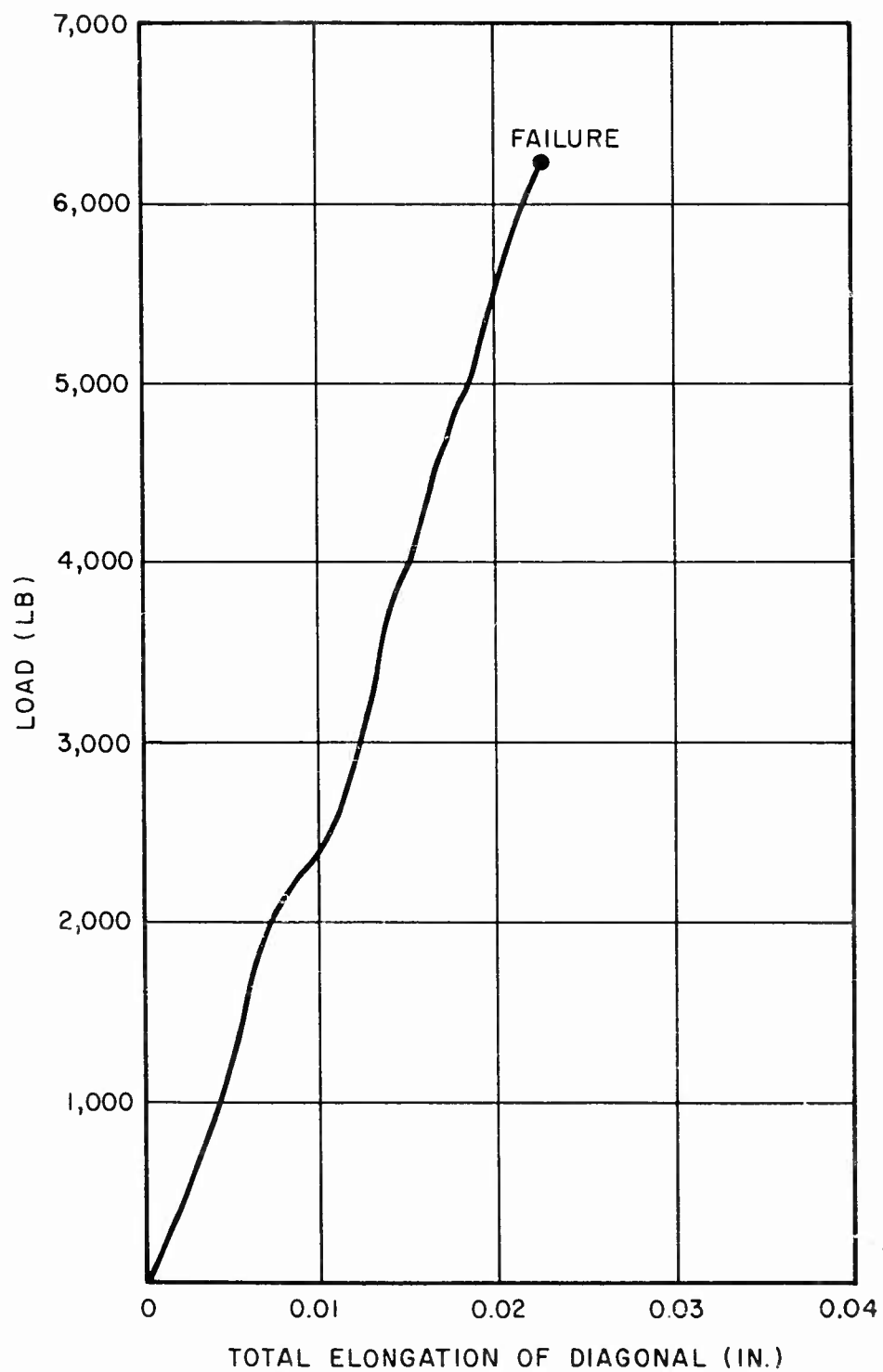


Fig. A-23 Load Elongation Curve, Shear Panel Specimen 7

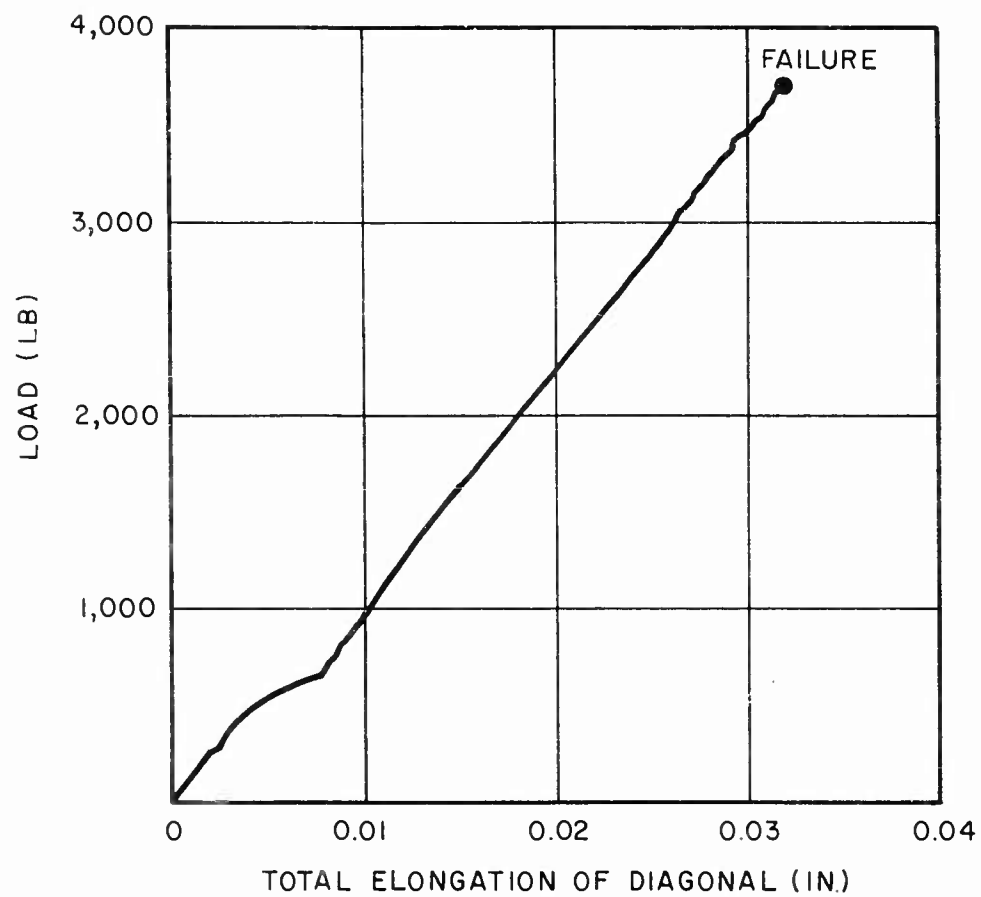


Fig. A-24 Shear Panel Specimen 8 Load Versus Elongation

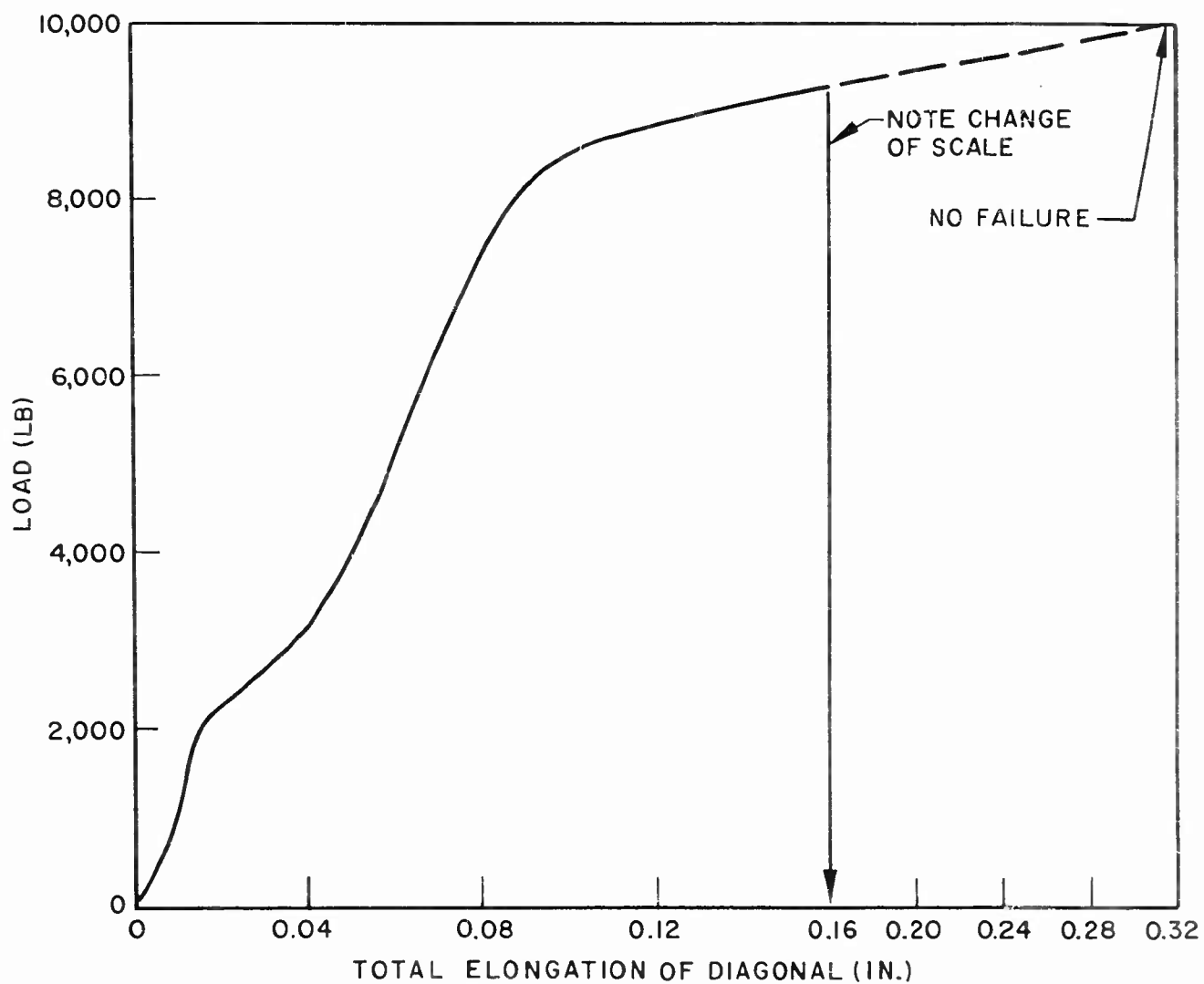


Fig. A-25 Load Elongation Curves, Shear Panel Specimen 9

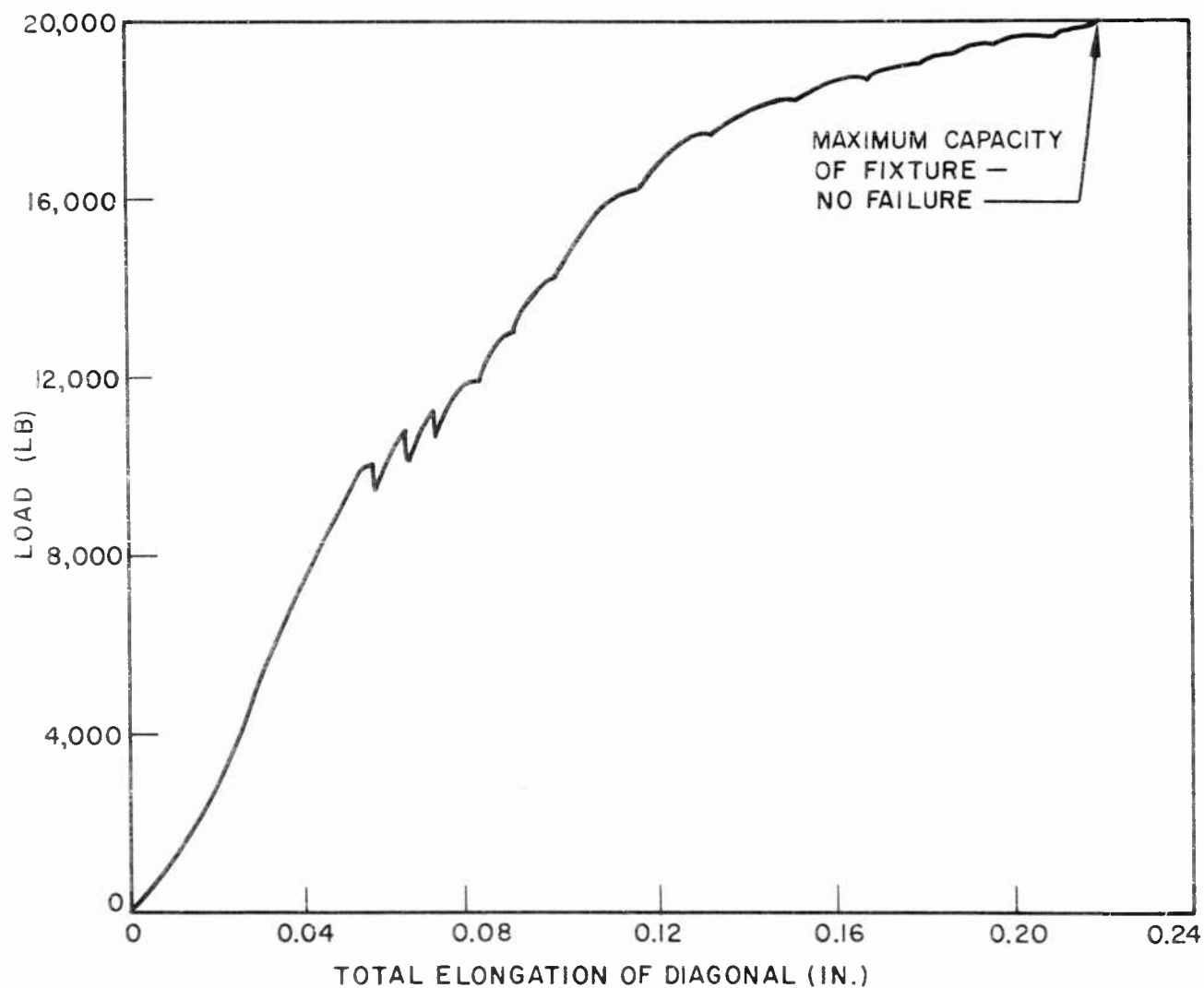


Fig. A-26 Shear Panel Specimen 10 Load Versus Elongation

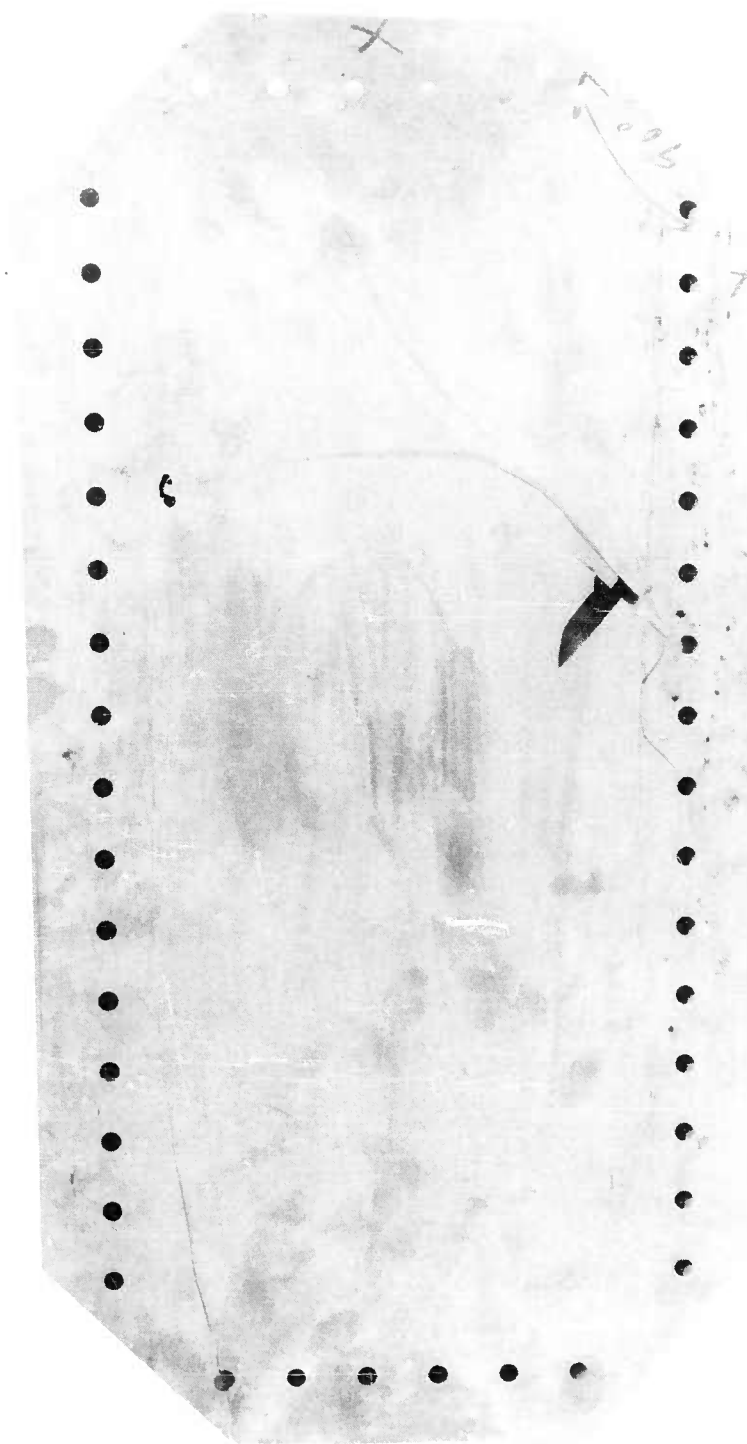


Fig. A-27 Shear Panel Specimen 8 After Test

The heating for specimen 10 was with twelve Research Incorporated reflectors (five 2,000-watt lamps per reflection - see subsection A. 2. 3). Figure A-28 shows six reflectors mounted on each of two frames, one on each side of the specimen. Two large screws at each reflector made it possible to tilt them in or out independently. This made it possible to adjust their relative proximities to the test panel and thereby compensate for nonuniform temperature caused by convection. Figure A-28 shows the lamps in their optimum positions (determined by several tests run on a dummy specimen). Note that the lower reflectors are closer to the specimen. Two smaller frames with 4 reflectors each and set at 45 deg were used on specimen 9. The spacing of the reflectors on all of the frames was 3 in. on centers.

Other precautions had to be taken to make the temperature more uniform. The frame, obviously a large heat sink, was painted with Aqua-dag (a colloidal solution of lamp-black) in order to increase its tendency to absorb heat. The test panel itself had to be shielded from the heat while the frame "caught up" to it. The shield was a three-layered sandwich of stainless-steel plates, each gold plated and spaced about 1/4-in. apart with spacer sleeves on the bolt connecting them. The final assembly for specimen 10 is shown in Fig. A-29.

Eighteen thermocouples, nine for each face, were installed on the panel for both specimens 9 and 10 and others were pinched between the panel and frame. The locations of these thermocouples are shown in Figs. A-30 and A-31, along with the average temperature at mid-test. The eighteen thermocouples on the panel were in back-to-back pairs, hence the term "average," which strictly speaking does not apply to the temperatures read on the four single thermocouples on the frame.

Specimens were brought to test temperature by slow heating for three hours, and allowed to soak at the test temperature for one hour. During the temperature rise, a tension of 100 to 400 lb was maintained on the specimen to keep the frame and yoke from displacing laterally due to thermal expansion. Loading was started immediately upon completion of the temperature survey. Specimen nine reached a maximum elongation of 0.42 in. at 10,700 lb (the curve in Fig. A-25 is not extended this far). This was close to the maximum elongation

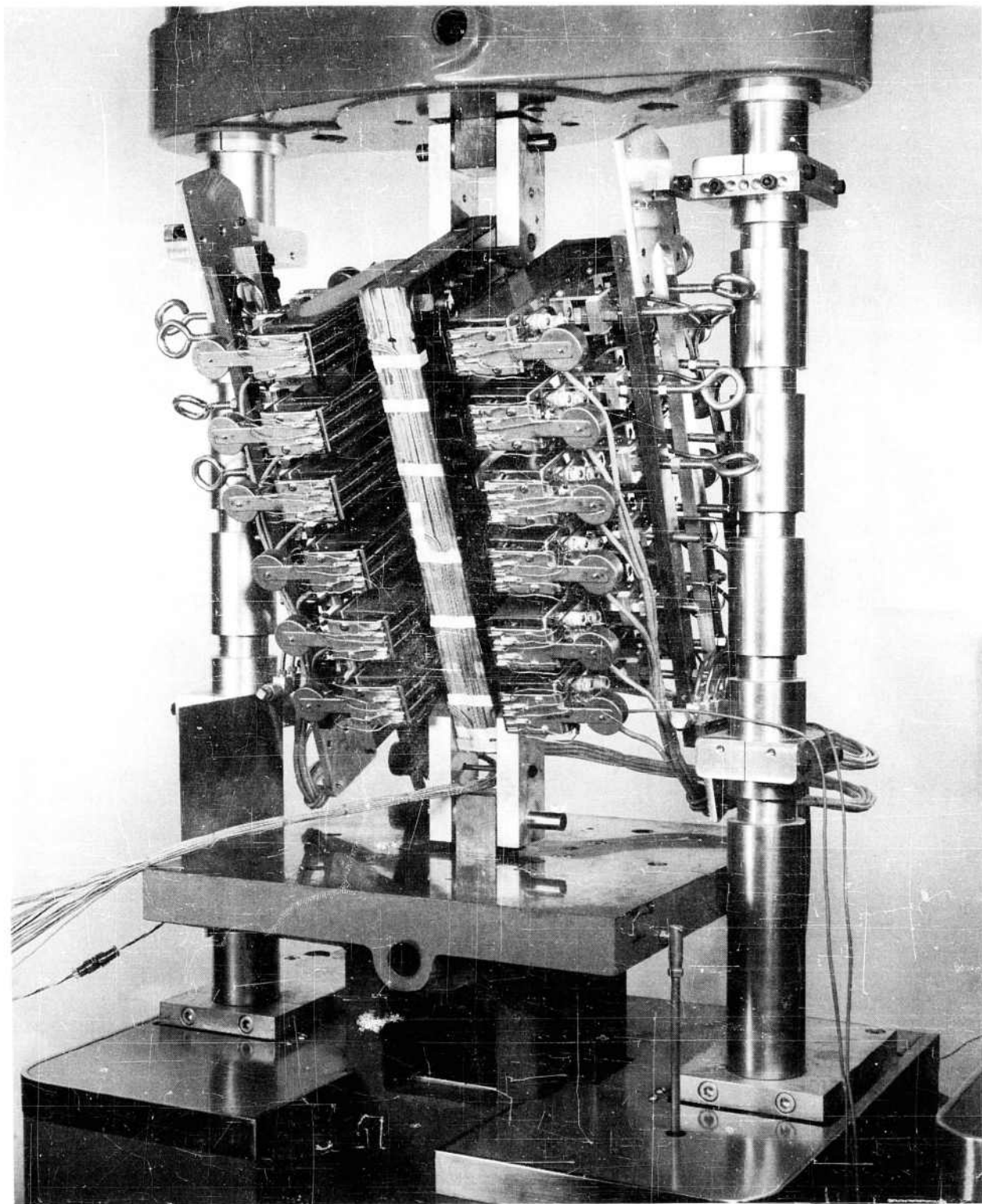


Fig. A-28 Shear Panel Test With Heat Lamps Installed

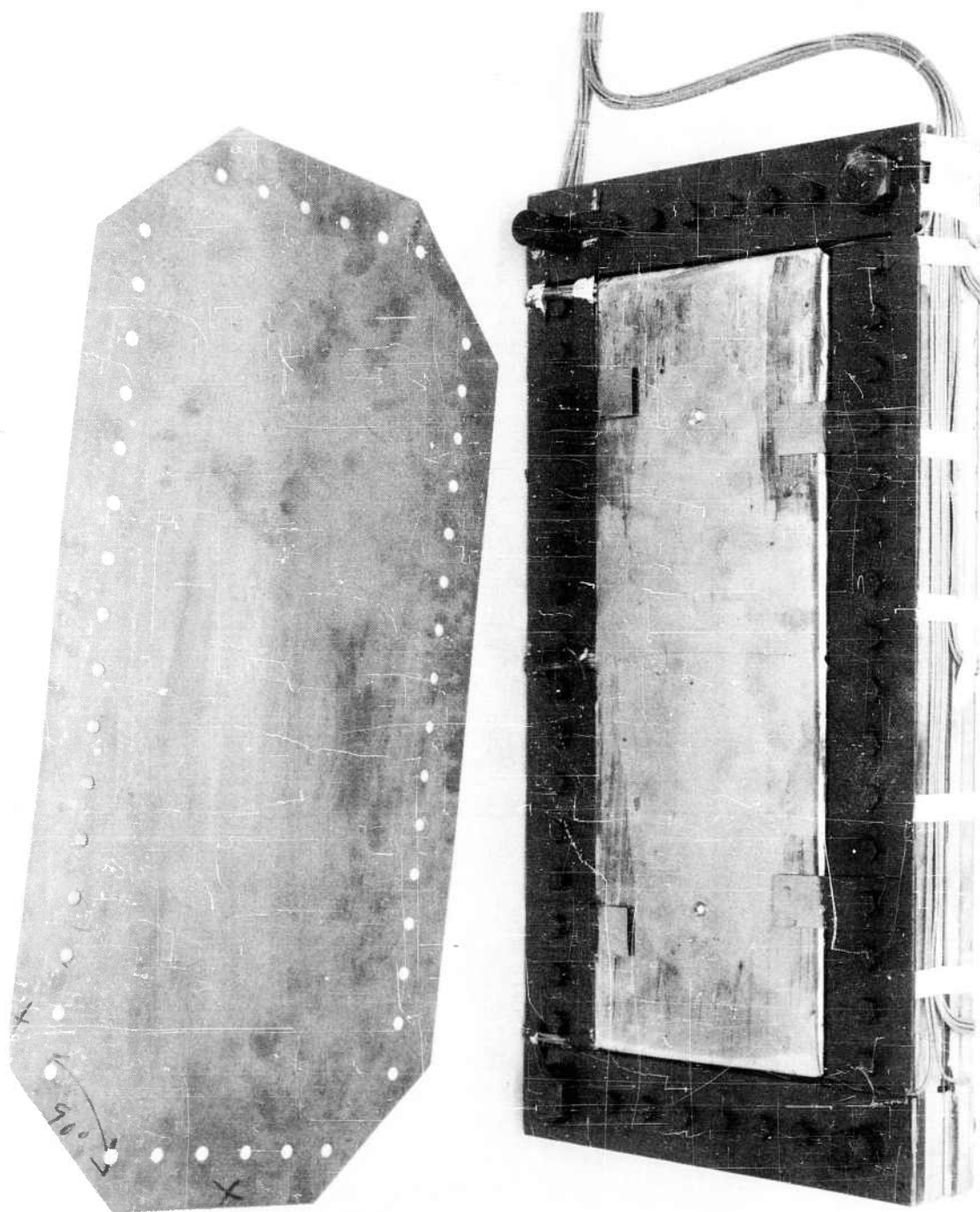


Fig. A-29 Shear Panel Specimen 10 With Heat Shield

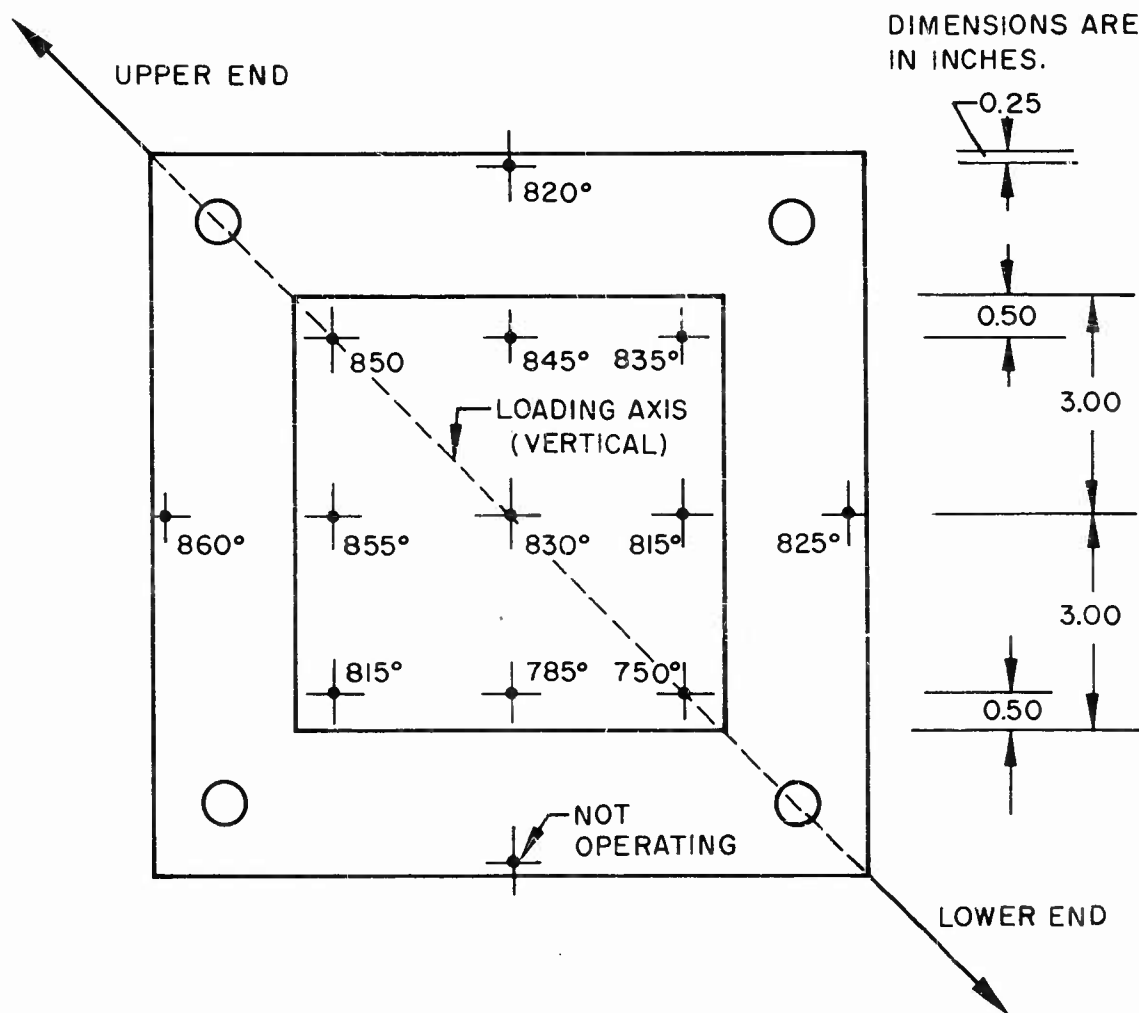


Fig. A-30 Average Temperatures (°F) at Midtest, Specimen 9

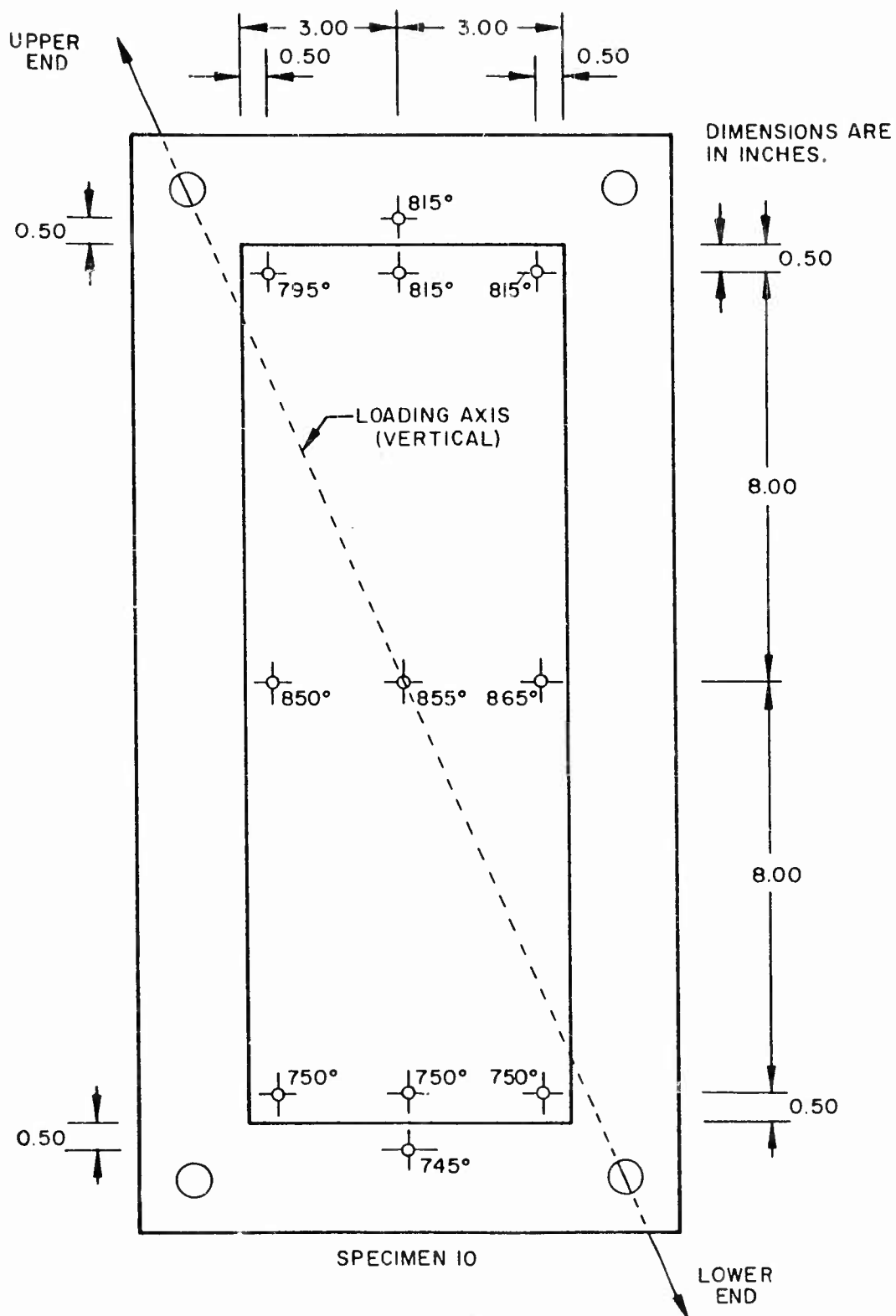


Fig. A-31 Average Temperatures (°F) at Midtest, Specimen 10

possible without damaging the interlocking joints of the frame, so the specimen was then unloaded and the heat was turned off after a second temperature survey was run. Upon return to zero load, the specimen had a permanent elongation of the diagonal of 0.30 in.

Specimen 10 reached 20,000 lb, the maximum design load of the fixture, and at this load the diagonal had elongated 0.22 in. Upon unloading, the permanent set was 0.14 in.

Neither specimen cracked under load or even after cooling. But upon loosening of the 1/4-in. bolts (at room temperature), specimen 10 became cracked (Fig. A-32), presumably because of an altered residual stress pattern. In the subsequent test of specimen 9, the 1/4-in. bolts were loosened immediately after unloading and before much cooling had taken place. The specimen was thus kept free of cracking (Fig. A-33).

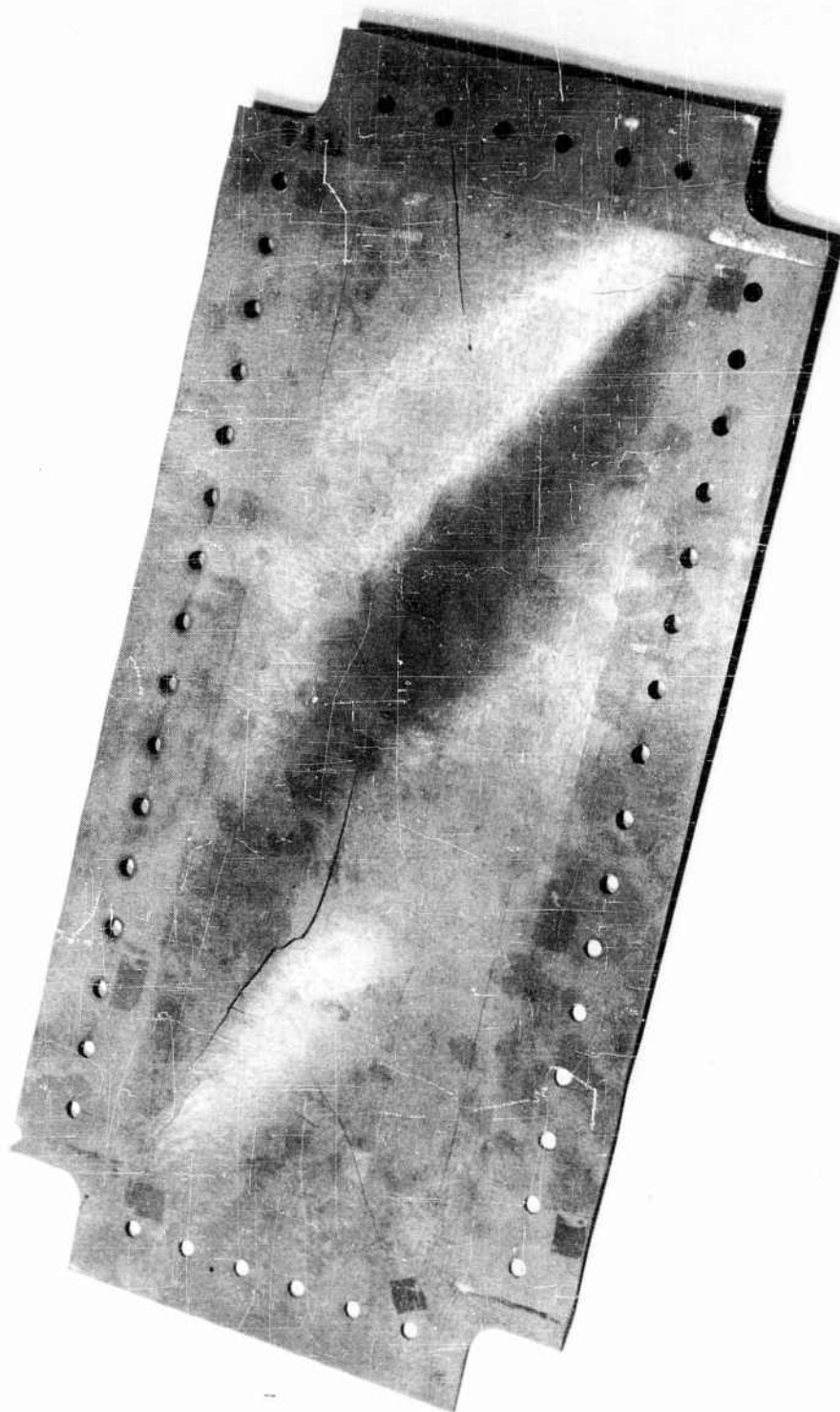


Fig. A-32 Shear Panel Specimen 10 After Test

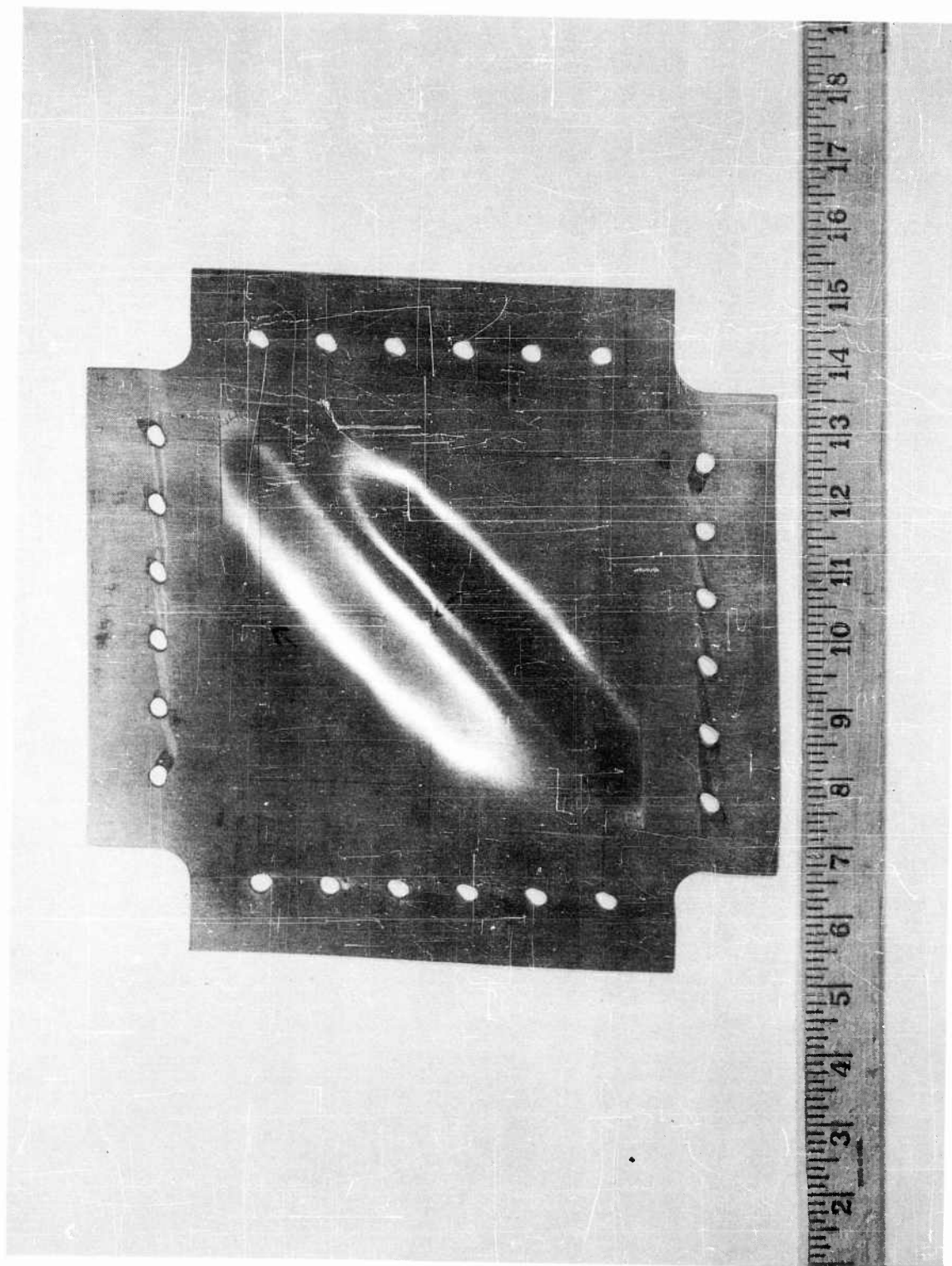


Fig. A-33 Shear Panel Specimen 9 After Test

A.3.3 Axially Loaded Monocoque Cylinders

Table A-10 summarizes the information on tests of five cylinders labelled specimens 11, 12, 13, 14, and 15.

The loading fixture consisted of three circular plates stacked and bolted together in pyramidal fashion so as to distribute the load from the 10-in. -diam. loading head of the universal testing machine to the 20-in. diameter of the largest specimens (Fig. A-34). These plates were machined flat and parallel to ± 0.005 in., and the loading head is flat and parallel to ± 0.001 in. If all conditions had combined to produce the worst situation, the two loading surfaces could have been out of parallel by as much as 0.03 in. They were, in fact, out by 0.01 in. This was absorbed by the bearing material that was used between the specimen and the loading surfaces. The bearing material varied with specimens and is given in Table A-10.

This bearing material also served to avoid stress concentrations due to lack of flatness of the cylinder edges or bearing surfaces.

The aluminum used was 3003-0 sheet, 0.063 in. thick. The copper was annealed QQ-C-504-2 bar, 3/8 in. thick, and the lead was pure lead plate 3/8 in. thick. At room temperature, the lead was found to be less successful than the aluminum. Being too soft, it caused any portion of the cylinder initially "out of true" to veer even more out of true as it cut a path through the lead. At elevated temperature, the aluminum was too soft and had the same problems as the lead at room temperature, but annealed copper proved very satisfactory at elevated temperature though not soft enough at room temperature. These remarks indicate comparative suitability, for even the less suitable materials worked fairly well. The ideal material should indent a little all around, since indenting indicates yielding of the bearing material, and yielding is followed by a plateau of stress on the stress-strain curve. This process is analogous to plastic hinges in limit design.

Table A-10

AXIALLY LOADED CYLINDERS: SUMMARY OF TEST INFORMATION

Test Data	Specimen Number				
	11	12	13	14	15
Diameter (in.)	8.00	8.00	10.00	20.00	20.00
Actual Thickness (in.)	0.042	0.041	0.040	0.020	0.021
Height (in.)	10.00	10.00	10.00	11.00	11.00
Test Temperature (° F)	R. T.	828	605	R. T.	870
Maximum Load (lb)	38,400	22,600	41,000	13,800	11,600
Stress at Maximum Load ^(a) (psi)	36,400	22,000	32,600	11,000	8,900
Number of Strain Gages	8	6	6	4	4
Bearing Material	Aluminum	Copper	Aluminum	Lead	Copper
Loading Rate (lb/min)	3,400	7,000	6,500	1,500	950

(a) Stress based on actual thickness.

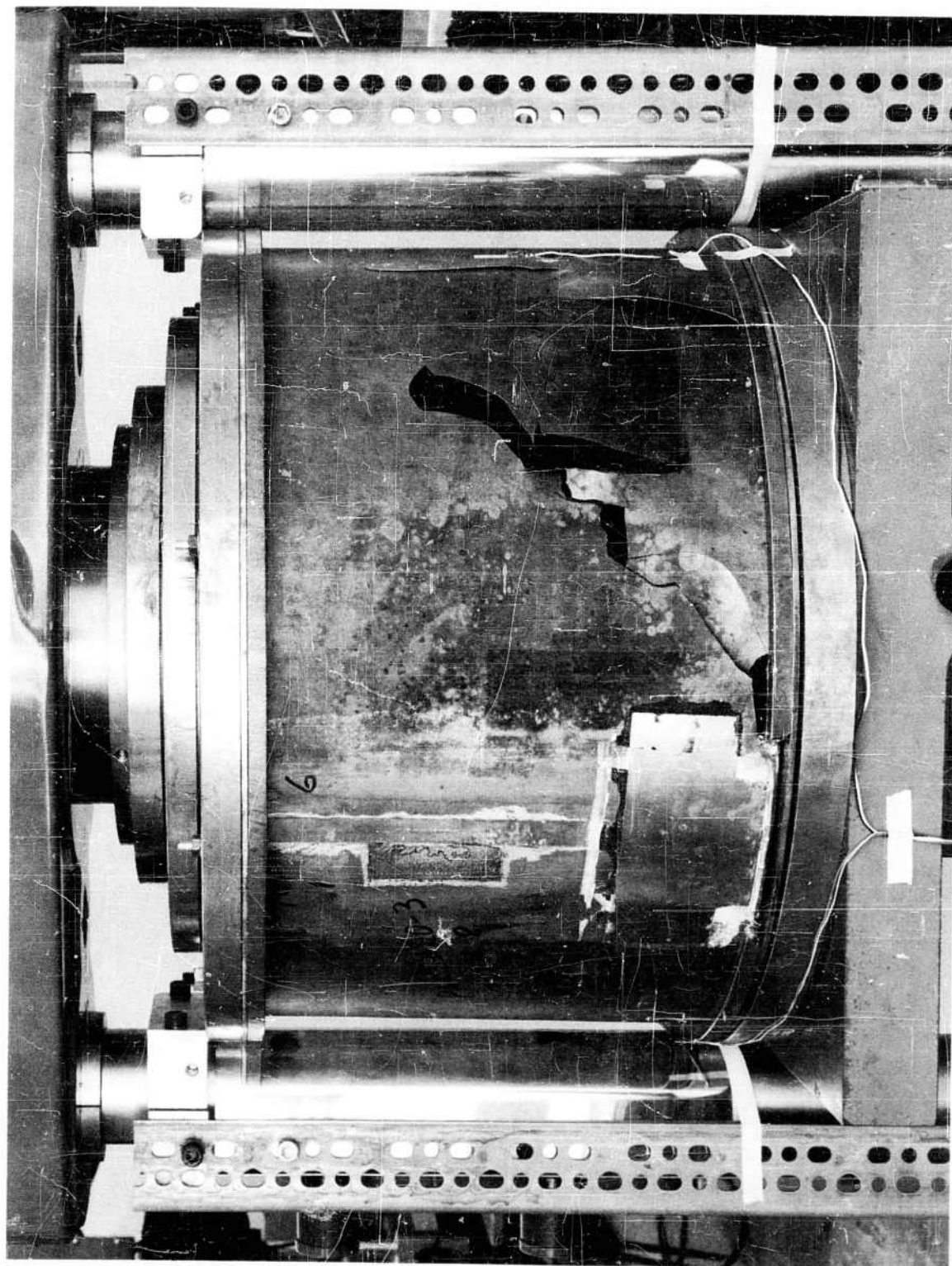


Fig. A-34 Cylinder-Loading Fixture and Specimen 14 After Test

The number of strain gages on each specimen varied, and this number is also indicated in Table A-10. In all cases, however, the gages were arranged in back-to-back pairs, odd numbered on the outside of the cylinder, even on the inside, and the pairs were distributed so as to be equidistant from each other on the cylinder's circumference. In all cases, strain gages were set with their axes parallel to the axis of revolution (which was the axis of load), and they were mounted at the cylinder's midheight. Figures A-35 through A-39 give strain-gage locations at these midplanes.

Tables A-11 through A-15 give strain-gage readings at various loads. These strains were not plotted because they proved to be of no value in identifying the onset of buckling. They do, however, give some indication of stress distribution prior to buckling. All strain readings are in microstrain and are compression unless followed by (T) for tension.

Specimens 12, 13, and 15 were heated in a cylindrical furnace. Figure A-40 shows a plan view of this furnace. Two semicircular reflectors made of 0.032-in. -thick Alzak (specially coated aluminum sheet) were fastened to the posts of the testing machine by brackets (not shown in Fig. A-40). Forty-eight lamps of 1,000-watt rating were arranged at intervals of 1.5 in. just inside the reflector. These had to be discontinued for two intervals at each post. The cylinder just described was closed at the top and bottom by the 21-in. -diam. loading plates and the small gap between the loading plate and the Alzak reflector was plugged with Fiberglas stuffing. The 48 lamps were wired in series and supplied with power by the system described in subsection A.2.3.

The lamps missing in the vicinity of the posts of the testing machine did cause a drop in temperature at these regions, and evaluation of this drop was made by selective placement of the thermocouples.

Figures A-37, A-38, and A-39 also show the location of thermocouples. These figures give the temperatures recorded at midtest. The test temperatures given in Table A-10

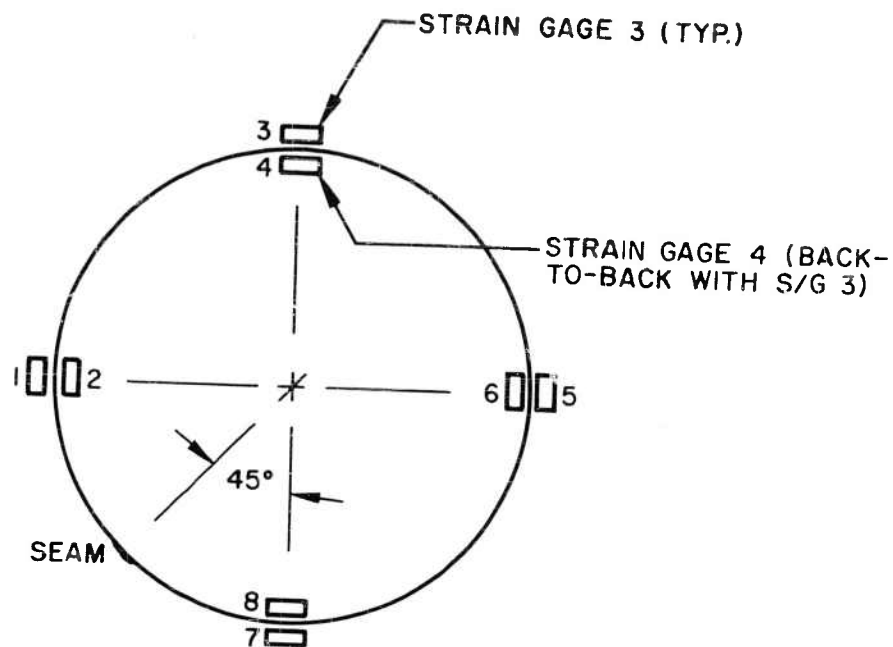


Fig. A-35 Strain-Gage Locations, Specimen 11

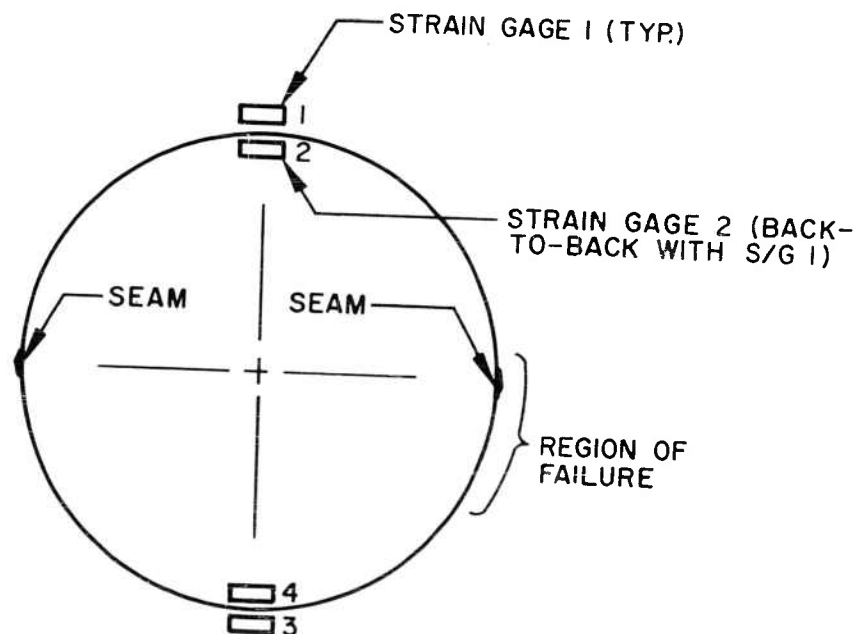


Fig. A-36 Strain-Gage Locations, Specimen 14

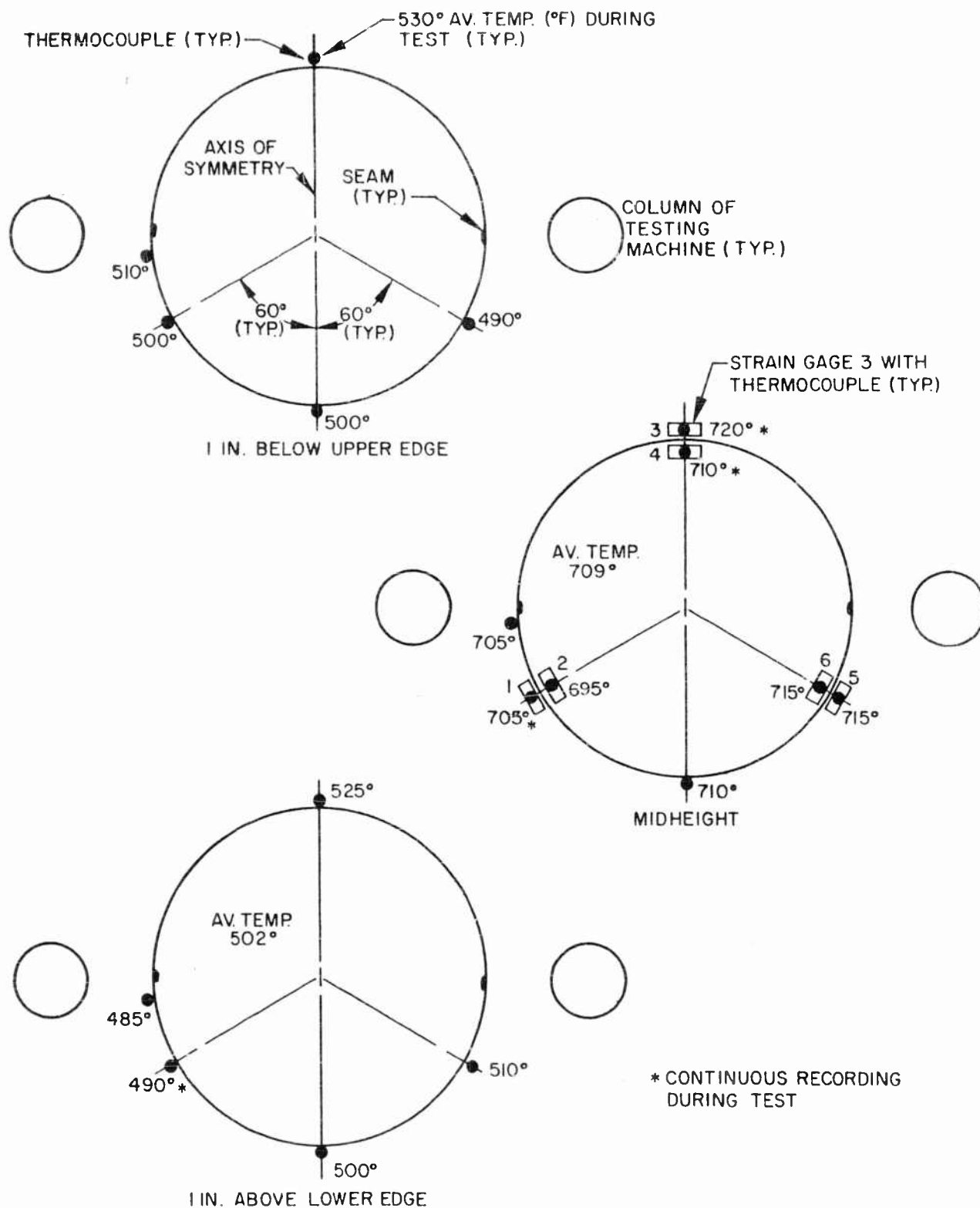


Fig. A-37 Specimen 13 Strain Gages, Thermocouples, and Temperatures Recorded

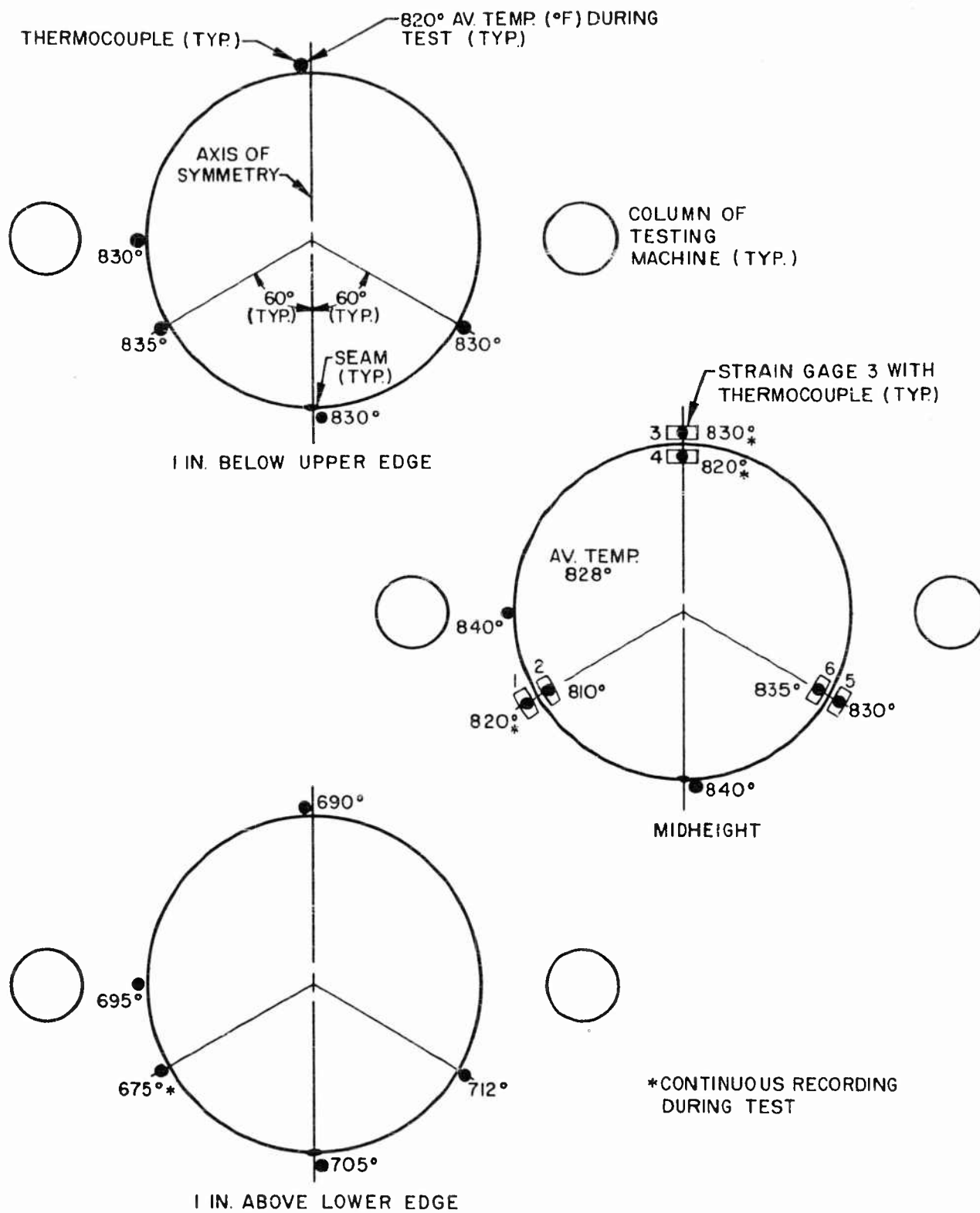


Fig. A-38 Specimen 12 Strain-Gage and Thermocouple Locations; Temperatures Recorded

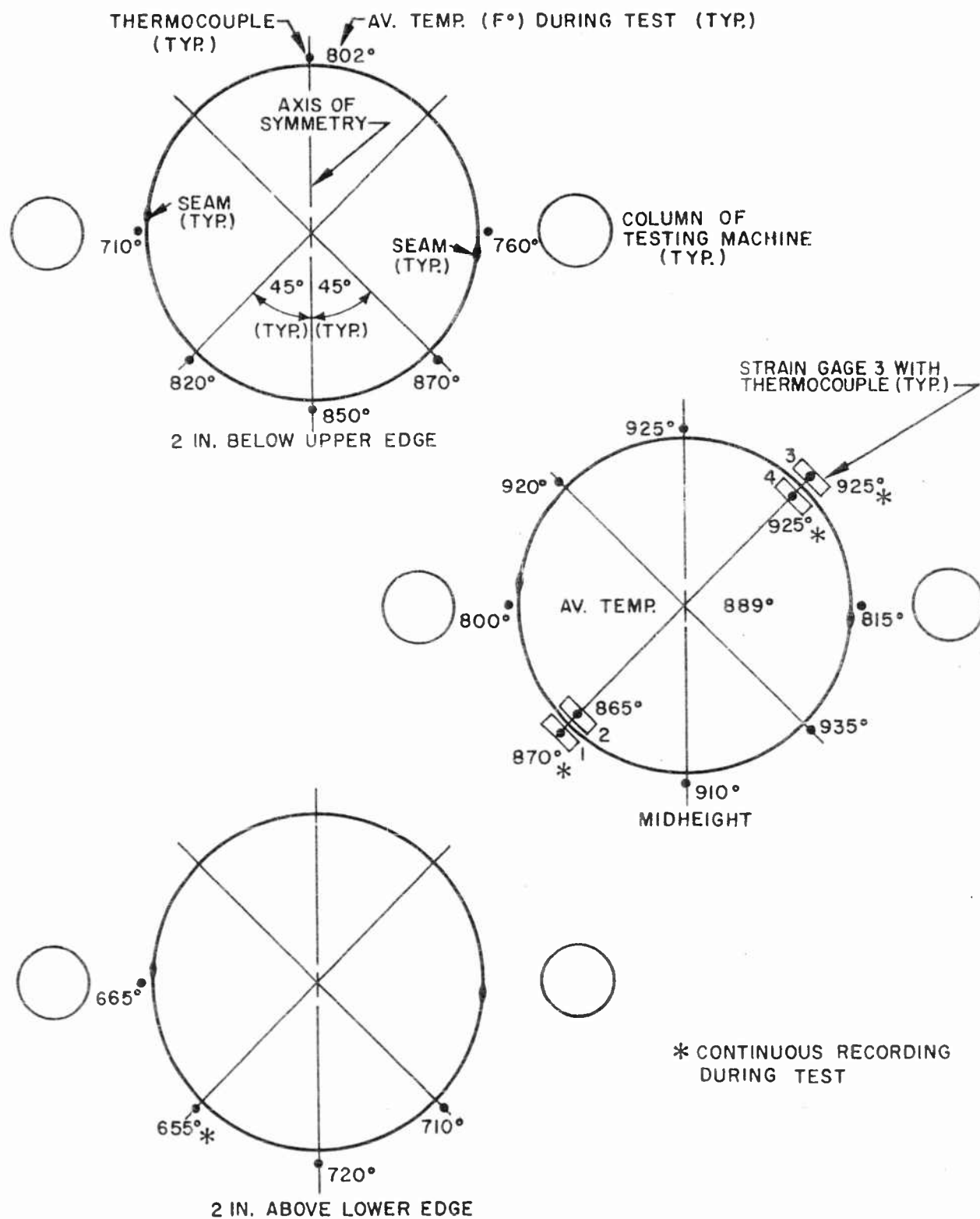


Fig. A-39 Strain-Gage and Thermocouple Locations, Specimen 15

Table A-11

SPECIMEN NO. 11 STRAIN-GAGE READINGS AT VARIOUS LOADS^(a)

Load (lb)	Strain-Gage Number							
	1	2	3	4	5	6	7	8
5,000	140	181	96	112	51	55	117	116
10,000	259	340	254	217	215	224	234	241
15,000	374	496	422	362	401	420	370	381
20,000	481	645	592	505	558	589	501	524
25,000	591	817	765	653	696	748	648	583
30,000	707	1,000	927	793	820	905	765	843
35,000	836	1,220	1,096	938	963	1,092	956	1,012
36,000	866	1,285	1,140	976	994	1,145	991	1,052
37,000	892	1,332	1,184	1,000	1,060	1,194	1,030	1,088
38,000	913	1,415	1,238	1,045	1,071	1,257	1,066	1,135
38,400	882	1,350	1,258	1,066	1,098	1,302	1,108	1,190

(a) All values in microstrain compression.

Table A-12

SPECIMEN NO. 12 STRAIN-GAGE READINGS AT VARIOUS LOADS^(a)

Load (lb)	Strain-Gage Number					
	1	2	3	4	5	6
3,000	95	140	95	36	9	71
6,000	290	308	169	125	23	134
9,000	308	452	243	211	27	263
12,000	446	615	338	336	36	378
15,000	679	839	486	520	82	93(T)
18,000	1,124	1,418	715	815	191	1,210(T)
21,000	2,086	1,980	1,170	1,505	422	1,660(T)
22,600	2,940	3,550	1,445	2,160	817	1,985(T)

(a) All values in microstrain compression unless followed by (T).

Table A-13

SPECIMEN NO. 13 STRAIN-GAGE READINGS AT VARIOUS LOADS^(a)

Load (lb)	Strain-Gage Number					
	1	2	3	4 ^(b)	5	6
4,000	57	50	100	—	5	9
8,000	80	95	213	—	45	58
12,000	123	154	309	—	131	161
16,000	178	227	397	—	216	268
20,000	241	322	468	—	288	375
24,000	317	418	535	—	364	474
28,000	407	522	598	—	423	572
32,000	487	613	660	—	477	639
36,000	572	704	732	—	535	715
39,000	634	767	828	—	585	769
40,000	620	808	878	—	598	805
41,000	681	826	999	—	630	845
39,000	643	749	1,087	—	590	809

(a) All values in microstrain compression.

(b) Strain-gage No. 4 inoperative.

Table A-14

SPECIMEN NO. 14 STRAIN-GAGE READINGS AT VARIOUS LOADS^(a)

Load (lb)	Strain-Gage Number			
	1	2	3	4
2,000	32	20	17(T)	19(T)
4,000	63	54	23	16
6,000	110	91	39	48
8,000	182	162	107	97
10,000	230	204	167	149
12,000	261	247	214	192
12,500	280	254	215	200
13,000	289	264	226	209
13,500	302	274	234	220
13,800	306	278	238	222
13,600	298	261	224	209

(a) All values in microstrain compression unless followed by (T).

Table A-15

SPECIMEN NO. 15 STRAIN-GAGE READINGS AT VARIOUS LOADS^(a)

Load (lb)	Strain-Gage Number			
	1	2	3	4
1,000	27	28	4	40(T)
2,000	54	53	15	43(T)
3,000	81	85	33	36(T)
4,000	128	121	63	18(T)
5,000	171	170	96	4(T)
6,000	217	218	107	7
7,000	264	266	151	47
8,000	322	322	206	97
9,000	388	379	275	169
10,000	461	453	351	244
11,000	570	538	443	328
11,500	655	609	502	388
11,600	717	616	513	396
11,600	19	—	487	370
11,000	352(T)	—	505	388

(a) All values in microstrain compression unless followed by (T).

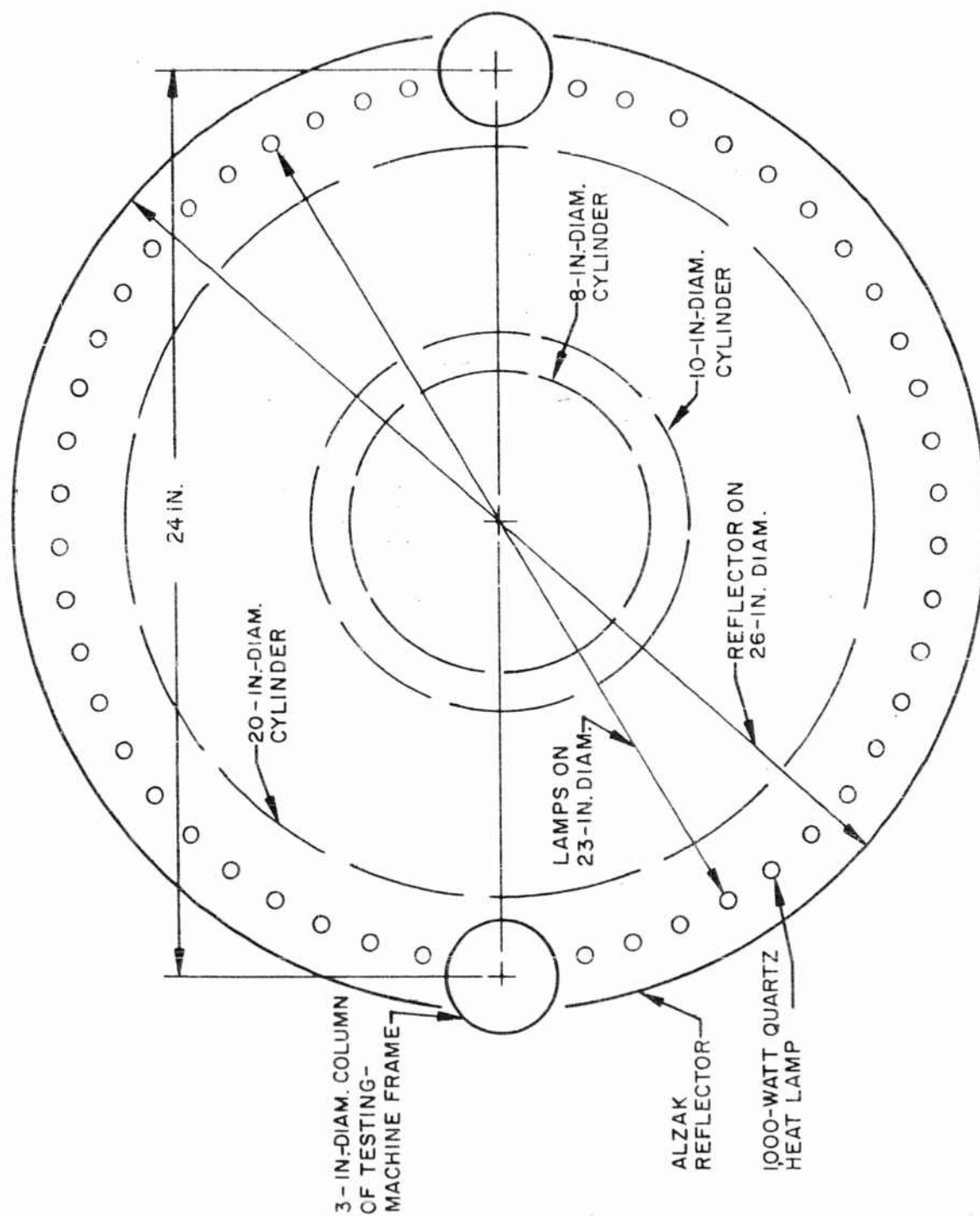


Fig. A-40 Furnace for Cylinder Tests - Plan View

are an estimate based on interpolations (except specimen 12 where failure occurred at midheight) of midtest temperature in the zone of failure. The accuracy of these test temperatures is subject to $\pm 25^{\circ}$ F.

At room temperature, failure of specimen 11 was sudden and complete. Failure of specimen 14 was by progressive cracking close to the lower edge and at a seam. It was felt that failure might have been premature due to the seam, so the specimen was unloaded and repaired in the failure zone by bonding two sheets of 0.02-in.-thick stainless steel (one each side) with epoxy resin. This patch is visible in Fig. A-34. Upon reloading, the specimen failed at a lower load than the previous time, and immediately adjacent to the repaired region. Cross-head motion was continued though the load did not increase. As a result, the cracking and buckling propagated to the extent shown in Fig. A-34.

Specimens 12, 13, and 15 were brought to test temperature by heating for one hour, and were then soaked at test temperature for one hour. Specimen 12 buckled gradually and cross-head motion was continued until cracking occurred. Figure A-41 shows specimen 12 on the left and specimen 11 on the right. Specimens 13 and 15 are shown in Figs. A-42 and A-43, respectively. Specimen 13 buckled gradually and sustained considerable table motion (at no increase in load) before reaching the cracked condition shown in Fig. A-42. Specimen 15 buckled suddenly and sustained some table motion at a continually decreasing load before reaching the heavily buckled condition shown in Fig. A-43. Notice also in this photograph the two copper-bearing rings which in this case had a circular groove 0.04 by 0.04 in. machined in them to hold the cylinder. These grooves were tried as a means of holding the very flexible cylinder in a true circle. It was observed that these 20-in.-diam. cylinders were so flexible that when they were pushed sideways (to align them on the loading surface), the friction between the cylinder and the surface was sufficient to keep them from returning (elastically) to their true circular shape (having been deformed by the lateral push). Sauereisen cement was used in this groove to fill the clearance space. This groove and cementing was used only on specimen 15.

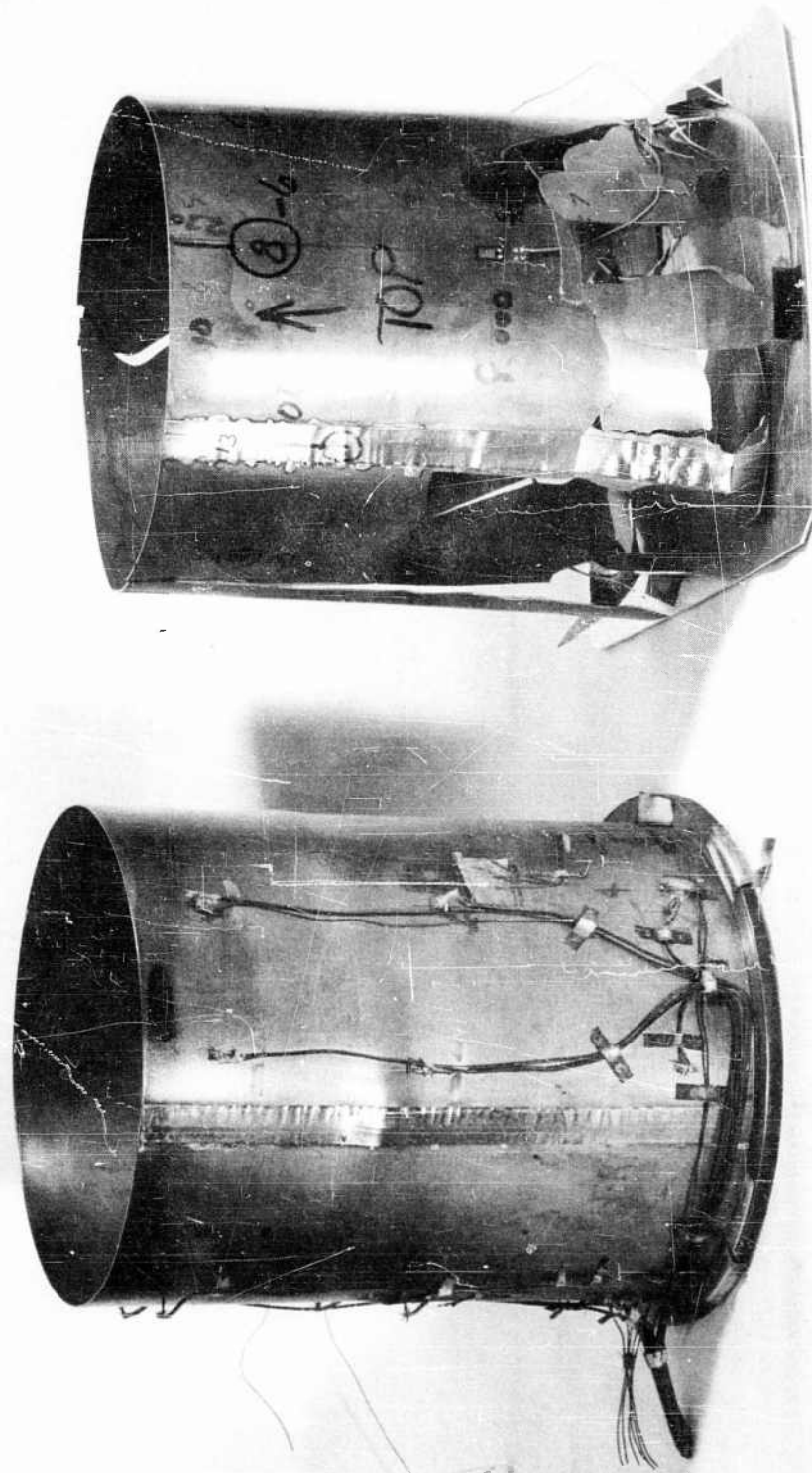


Fig. A-41 Specimens 11 (Right) and 12 (Left) After Test

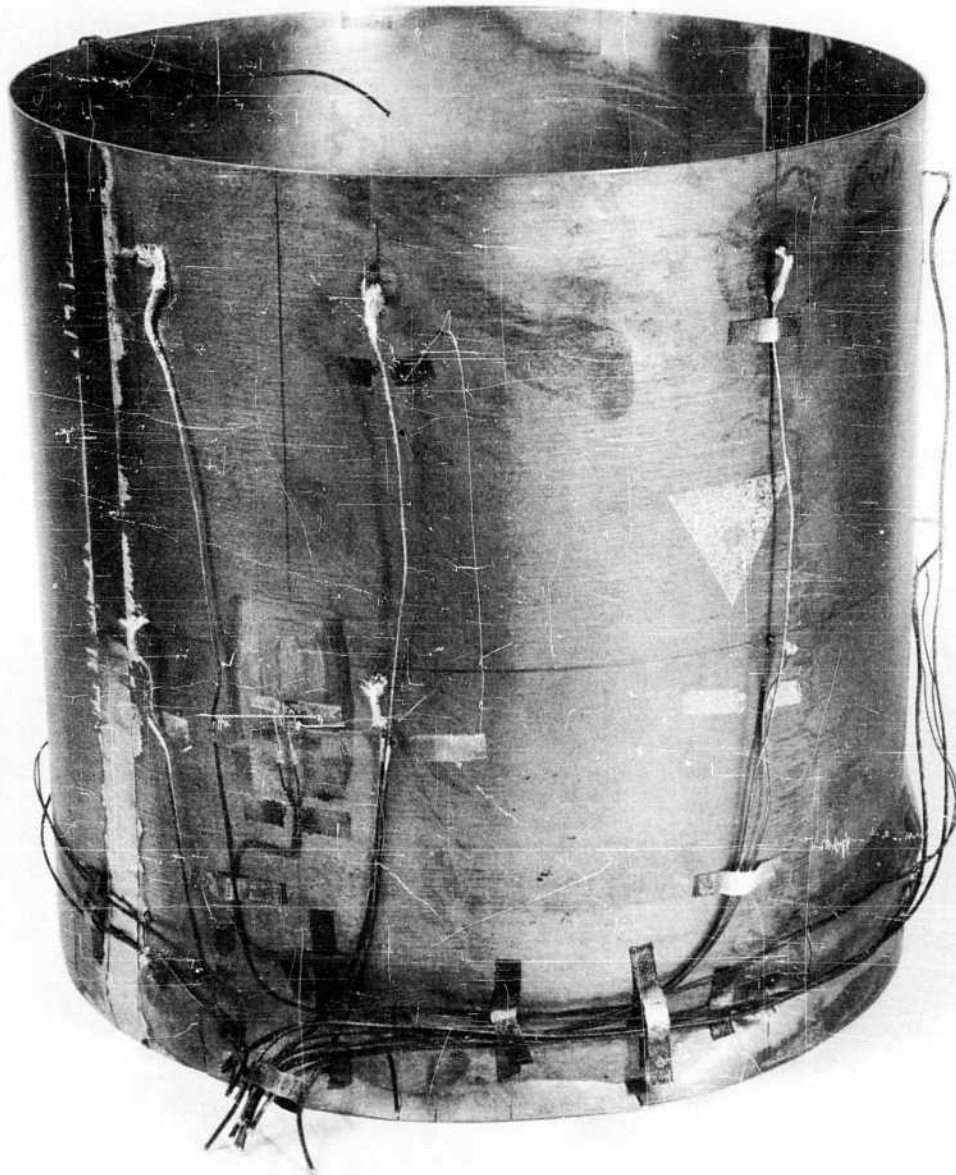


Fig. A-42 Specimen 13 After Test

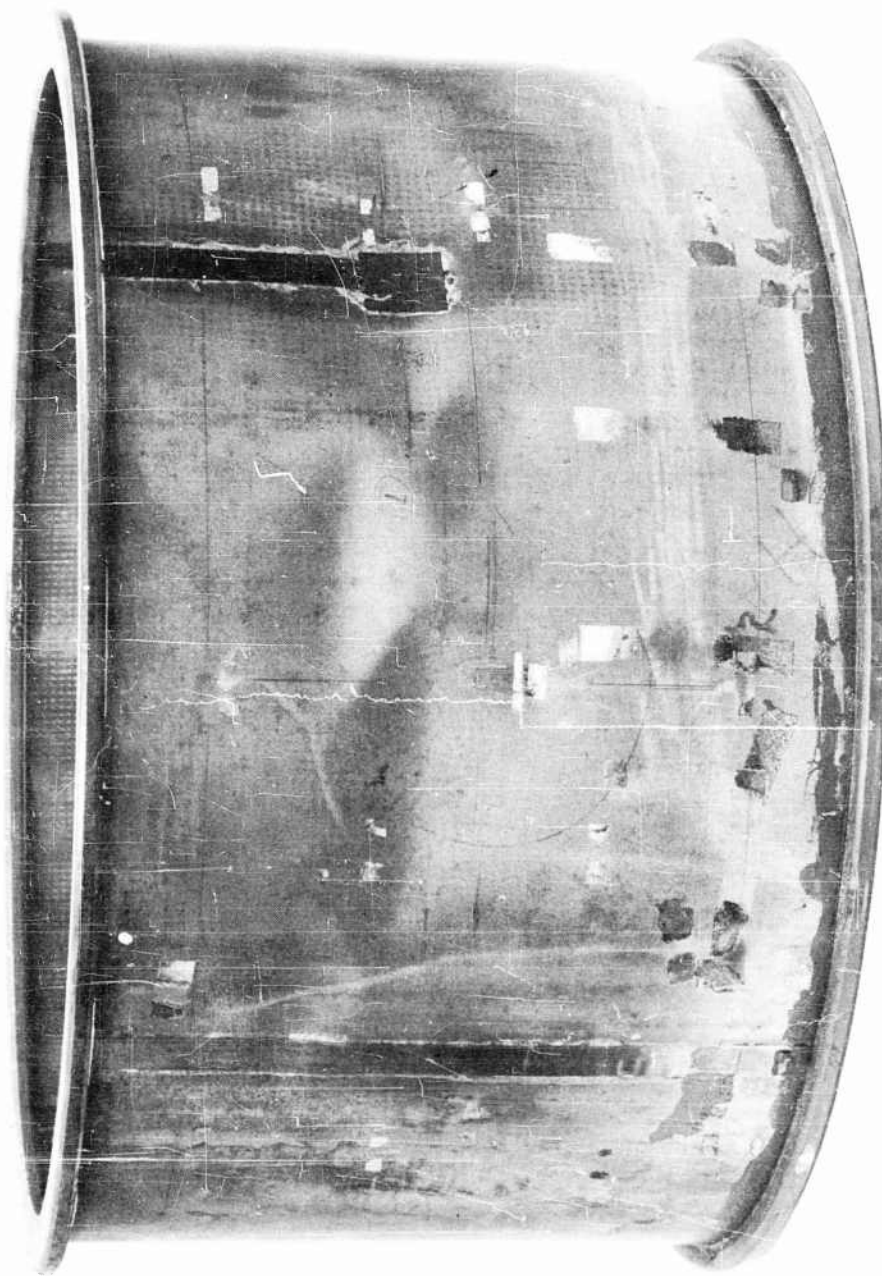


Fig. A-43 Specimen 15 After Test

A. 3. 4 Externally Pressurized Monocoque Cylinder Test

One cylinder (specimen 16), 20 in. in diameter, by 11 in. high, by 0.020 in. thick, was evacuated to create differential pressure.

Two aluminum plates, 3/8 in. thick and slightly larger in diameter than the test cylinder, had circular grooves machined on one face. These grooves were 20 in. in diameter (centerline) and were 0.18 in. deep and 0.18 in. wide. The grooves were filled with epoxy resin, and before the resin set, the cylinder was placed in the groove (and soft resin). Upon hardening of the resin, these two aluminum plates formed end-closure plates and provided substantial structural restraint for the cylinder. Clear span height of the cylinder after installation in the end plates was 10.65 in.

The pump used to evacuate the cylinder was a Cenco Hyvac. The cylinder failed after about 3 minutes of pumping at a pressure differential of 6.7 ± 0.3 psi.

Pressure was measured with a Statham pressure transducer (Model PO8TC, 0-15 psia). The 350-ohm bridge of the cell was DC powered at about 3 volts. The output of the bridge was connected directly to a sensitive galvanometer of the same type used in strain-gage recording, and the signal was recorded on the same optical oscillograph. The system was calibrated with a shunt resistor. The pressure equivalent of this shunt resistor had been previously determined by the Calibration and Standards Department. The failure was sudden. Figure A-44 shows the cylinder after test.

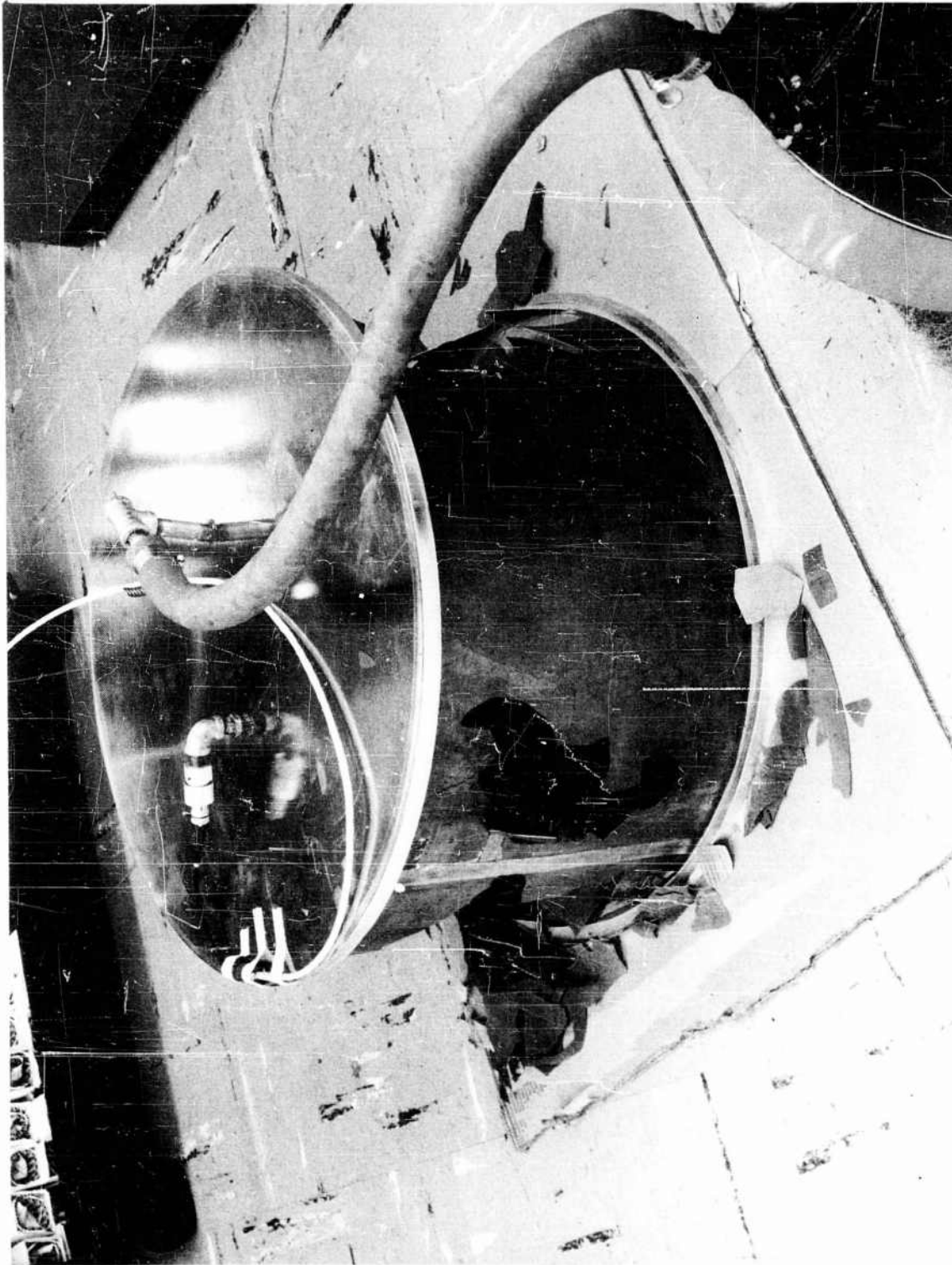


Fig. A-44 Evacuated Cylinder (Specimen 16) After Test

Appendix B

EXPERIMENTAL INVESTIGATION OF THE BIAXIAL STRENGTH
OF CROSS-ROLLED BERYLLIUM SHEET

B.1 INTRODUCTION

The biaxial stress-strain characteristics of cross-rolled beryllium sheet have been experimentally investigated at room and elevated temperatures. The results were analyzed in subsection 2.5. Descriptions of the tests, apparatus, and procedure are given here.

B.2 APPARATUS AND PROCEDURE

B.2.1 Specimens

The test specimens were obtained from the Brush Beryllium Company. They were processed as QMV block material and subsequently cross-rolled to the final nominal thickness of 0.102 in. The material was tested with the surface in the as-received condition, being machined only to nominal dimensions of 2.06 by 7.0 in. As fabricated, the specimens were slightly twisted, rather than flat.

B.2.2 Loading Apparatus

The loading apparatus is shown in Figs. B-1 and B-2; the arrangement of the loading jig and specimen is schematically shown in Fig. B-3, with pertinent dimensions. The specimen was tested as a beam subjected to four-point loading such that a constant moment was produced across its central portion. Self-alignment was induced in the loading jig, since it was pin-loaded at each end. A 600-lb Baldwin UC-1 load cell was used to weigh the load. Force was applied hydraulically by the Research Incorporated universal testing machine, in which all of these tests were performed. The load was programmed on a function generator, which is part of the automatic load-control system of the testing machine, as a straight-line ramp at a rate of approximately 220 lb/min. The load cell was calibrated prior to the test in conjunction with a Bristol Dynamaster load-versus-time recorder and a Moseley X-Y recorder. The error of the load record is assumed to be less than 1.0 percent, based on calibration with a secondary standard National Bureau of Standards calibration instrument, and taking into account the chart readability and the accuracy of the recorders.

The load procedure included a 25 to 50 lb preload on the specimen, which was used to ensure that self-alignment of the jig took place, and to remove all twist from the specimen prior to programming the load. This preload was, of course, part of the total recorded load.

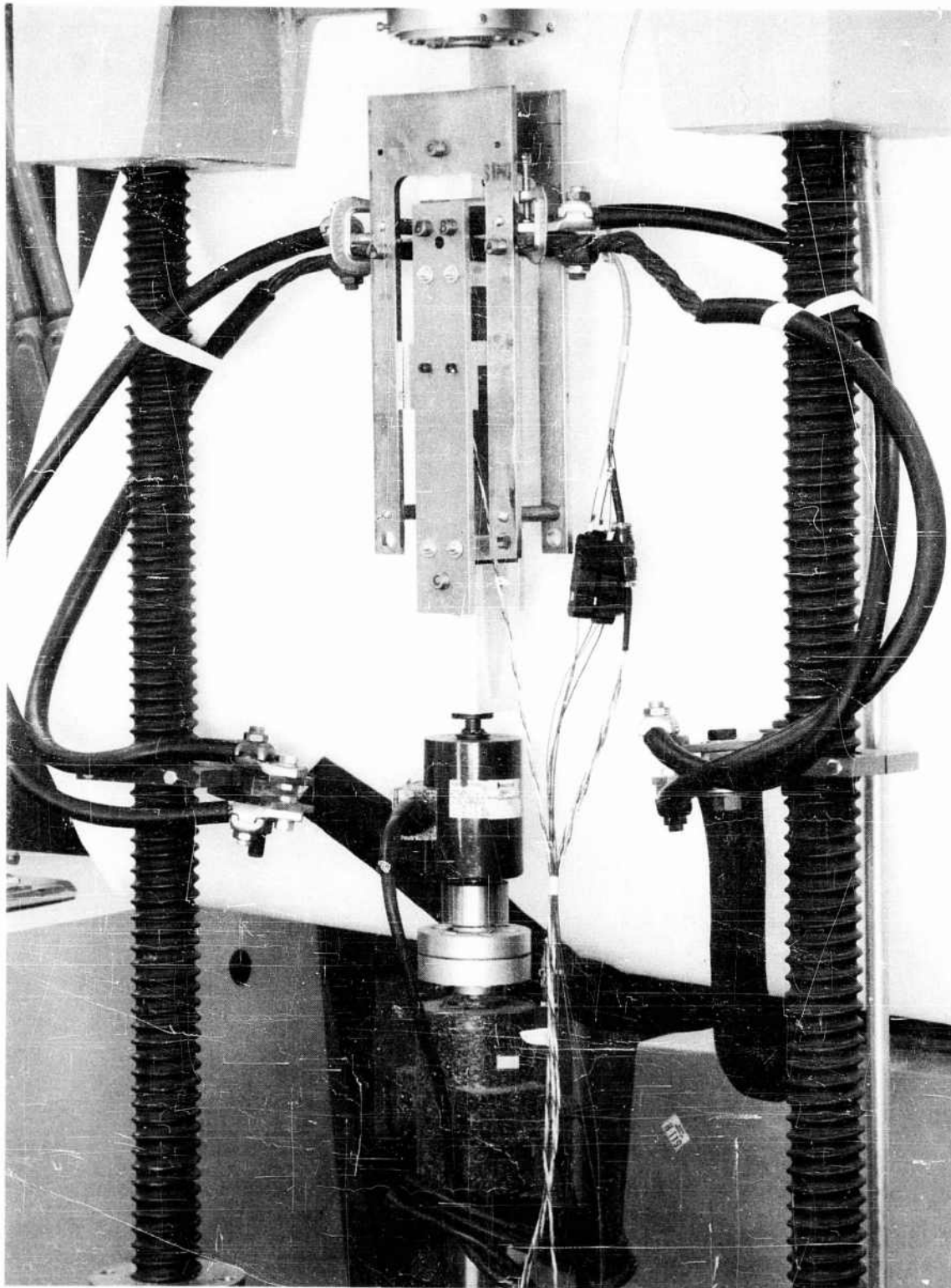


Fig. B-1 General Arrangement of Biaxial Stress Test for Elevated-Temperature Testing

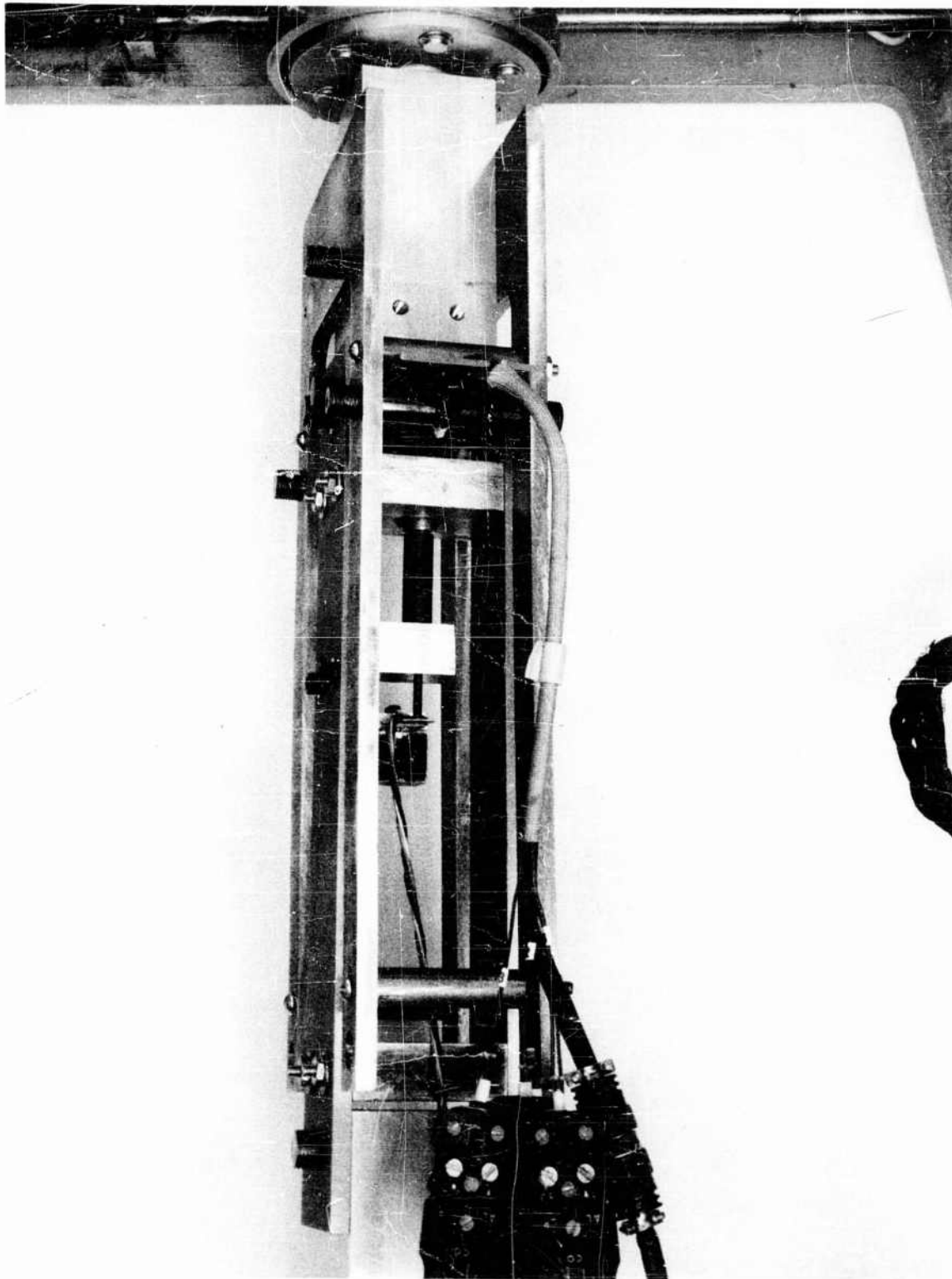


Fig. B-2 Details of Arrangement of Biaxial Stress Test Jig and Beam Deflectometer

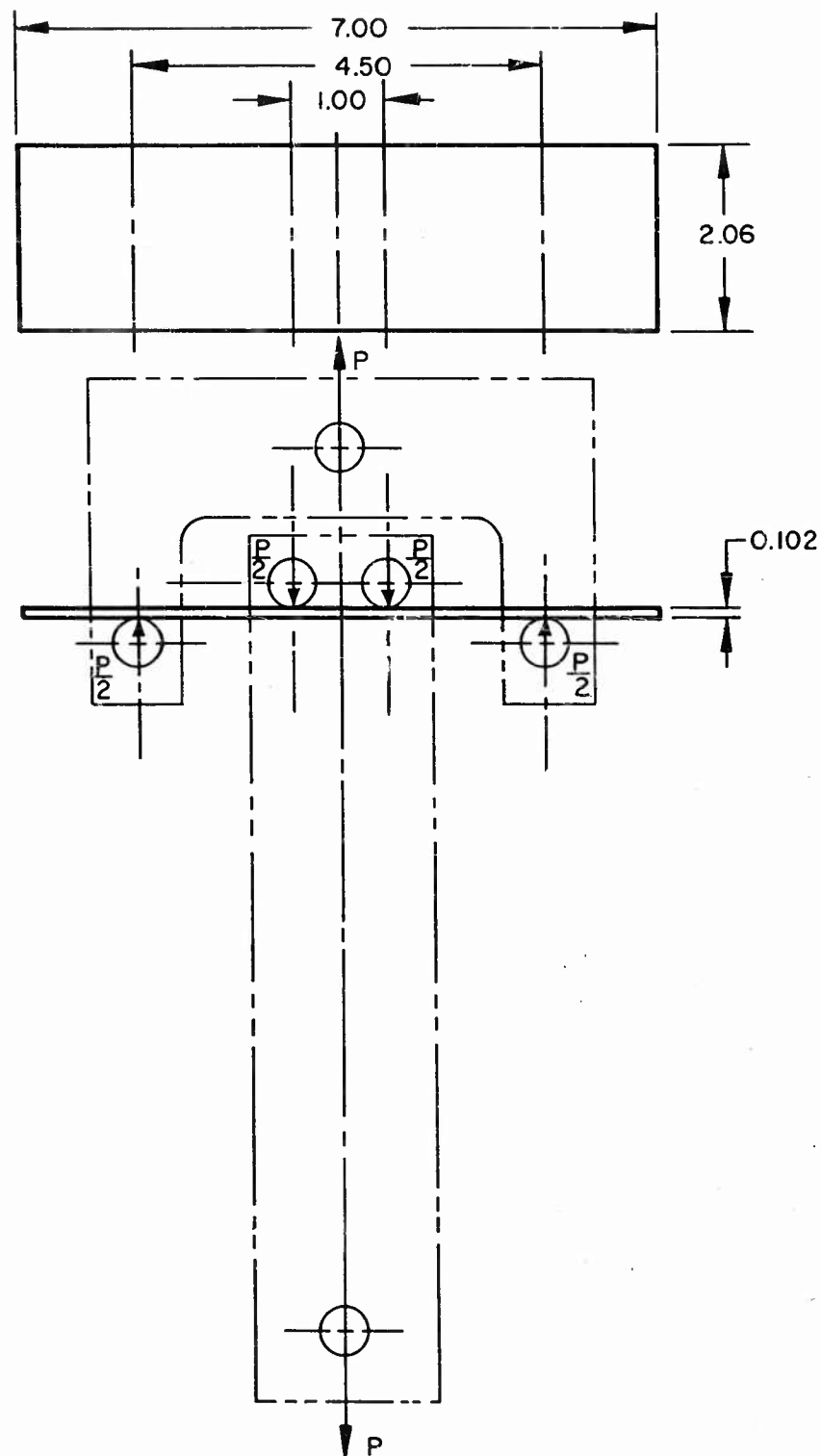


Fig. B-3 Schematic of Specimen Load Jig Used for Biaxial Stress Tests

B.2.3 Strain and Deflection Measurements

Tests were conducted at room temperature, at 400° F, and at 600° F. Surface strains were measured by means of SR-4 strain gages on both the top and the bottom surfaces of the beam. Two longitudinal gages were mounted back-to-back, and two transverse gages were mounted back-to-back. The transverse gages were offset from the mid-point between load points by approximately 0.250 in., but on the longitudinal centerline. The longitudinal gages were offset from the longitudinal centerline by approximately 0.250 in., but on the transverse centerline. This configuration can be seen in Fig. B-4, which shows the room-temperature specimen. Since longitudinal strains should be constant in this area, it was considered satisfactory to use this configuration, thereby permitting contact of the deflectometer at the exact center of the specimen.

For the room-temperature test, Baldwin-Lima-Hamilton A-7 gages were mounted with Dupont Duco cement. The accuracy of these gages is based on such items as accuracy or sensitivity of gage factor, errors due to lead wire resistance, temperature changes during loading if no temperature compensation is used, input voltage fluctuations during tests, signal amplification system errors, accuracy of known resistances of other legs of the bridge, and accuracy of calibrating resistance. Low strain levels are probably subject to greater errors because the signal requires higher amplifying ratios. It is believed that the error of the strain, as read at the recorder, was less than 5 percent.

The elevated-temperature tests were conducted using Baldwin-Lima-Hamilton free-filament strain gages, type 600-5B. These gages have a nominal resistance of 120 ohms and a gage factor of 2.2 at room temperature. A Chromel-Alumel thermocouple is installed as part of the gage but is not a means of temperature compensation. The gages were mounted with PBX Dry Mix, which is a ceramic type of cement recommended for this application. A curve of the change of gage factor with respect to temperature was supplied by the manufacturer of the gages, indicating a decrease of about 7 percent with increase of temperature to 600° F. Short Fiberglass-insulated Ni clad copper lead wire

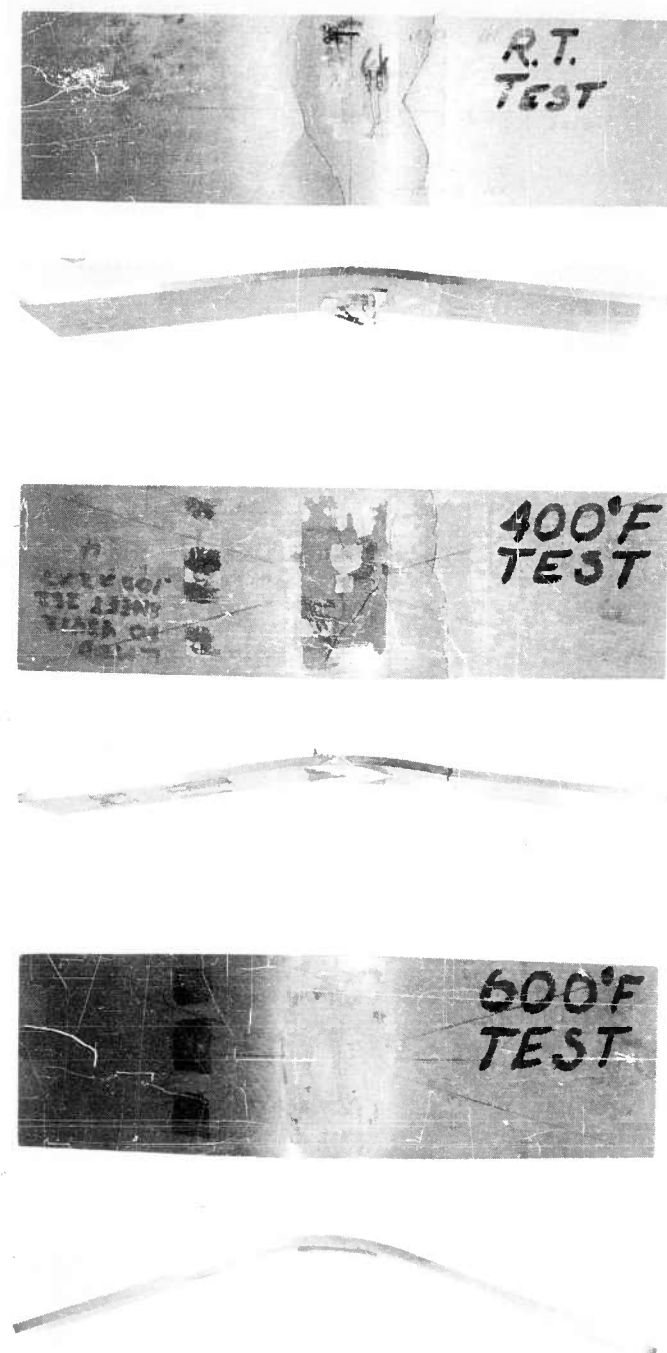


Fig. B-4 Biaxial Stress by Beam Bending of Cross-Rolled Beryllium Sheet at Room Temperature, 400°F, and 600°F

was used through the heat zone, beyond which standard shielded copper wire was used to connect to the bridge balance box and recorders. Errors in addition to those mentioned for the room-temperature gages are believed to have resulted in at least 7-percent probable error in strain recording.

Apparent strain due to temperature rise during heating was balanced out to effective zero strain after the test temperature was attained and stabilized, so that all strain recorded was the result of bending strains under load.

Deflection of the center of the specimen with respect to the central loading points was determined by a cantilever beam type of deflectometer. The deflectometer was rigidly attached to that part of the loading frame which carried the two central load pins. This frame was constructed so rigidly that strains between the deflectometer and the specimen contact point can be assumed to be negligible. The deflection of the cantilever beam was effected by means of a quartz-tipped transmission rod between the specimen and the beam. The quartz tip was used because of its low thermal conductivity and its small thermal expansion coefficient. The deflection of the beam was sensed by two pairs of SR-4 strain gages, type FA-12, mounted back-to-back on a 0.031-in.-thick steel blade, with all four gages wired into a bridge for measuring bending. This deflectometer was calibrated by means of a Daytronic micrometer type of calibrator, accurate to ± 0.0001 in., and recording on a Moseley X-Y plotter using a scale of 0.002-in. deflection per inch of chart. Taking all factors into consideration, the accuracy of the system is estimated to be within ± 0.0005 -in.

B.2.4 Heating of Specimens

The specimens were heated by self-resistant heating. The Research Incorporated universal testing machine includes a controller for heating which can be automatically controlled to a program or manually controlled. Since the time of heating was not important for this test, the specimen was heated by manual control. The power was furnished through a water-cooled 75 kva stepdown transformer, and battery cable leads were attached to the axials of the specimen, as can be seen in Fig. B-1.

B.2.5 Temperature Measurements

Chromel-Alumel thermocouples were installed on the elevated-temperature specimens as part of each strain gage. The outputs of these thermocouples were recorded on a Midwestern oscillographic recorder. Errors of ± 2 percent could occur in recorded temperatures.

A temperature gradient occurred in the central region from the midpoint of the specimen to the points of contact where load was applied. However, a constant bending stress condition existed in this region, so that strain at this stress was desired at the points where test temperature was achieved. The temperature at the various strain-gage locations varied very little, ranging from 400° to 412°F.

B.3 Summary of Test Results

The results of the room-temperature and the 400°F tests are shown in Table B-1. Because the strain data from the 600°F test are questionable when compared with calculated strain from the simple bending stress equation, these data are not shown. Figure B-4 shows the specimens that were tested at all three temperatures. It is interesting to note that there is little apparent difference in ductility, or permanent set, between the room-temperature and the 400°F test specimens. However, the specimen which was tested at 600°F did not fracture; it exhibited considerable ductility, and a fair degree of anticlastic bending occurred later in the test.

Table B-1
STRAIN AND DEFLECTION FOR BERYLLIUM BIAXIAL STRESS TESTS

Test Temp.	Load P	ϵ				Deflection δ	$\epsilon = 4\delta t$
		Bottom Transverse	Top Transverse	Bottom Long.	Top Long.		
°F	lb	%	%	%	%	in.	%
R. T.	74.0	0	0	0.042	0.039	0.00080	0.0326
	121.0	0	0	.081	.070	.00126	.514
	196.0	0	0	.110	.100	.00228	.0931
	304.5	0.0016	0.0040	.198	.175	.00396	.1615
	409.0	.0212	.0187	.340	.300	.00804	.3280
	447.0	—	—	.456	.400	.01122	.4580
	472.0	—	—	.552	.500	.01414	.5770
	483.0	—	—	.666	.617	.01600	.6530
400	82.0	0	No Data	.033	.017	.00070	.028
	88.0	0		.039	.026	.00076	.031
	119.5	0		.055	.040	.00100	.041
	153.0	0.002		.075	.061	.00138	.056
	226.5	.004		.111	.111	.00240	.098
	253.5	.005		.132	.124	.00280	.114
	270.5	.006		.140	.140	.00316	.129
	371.5	.010		.264	.304	.00640	.261
	420.0	.036		.472	.468	.01036	.423
	476.0	.084		.770	.697	.01782	.727

B.3.1 Room-Temperature Test Results

The strain data for each transverse and longitudinal strain gage used in the room-temperature tests are shown in Fig. B-5. It is seen that insignificant strains in the transverse direction resulted until at least 70 percent of the ultimate load was applied, indicating a small ratio for transverse strain over longitudinal strain. Figure B-6 shows the load versus deflection curve for the room-temperature test.

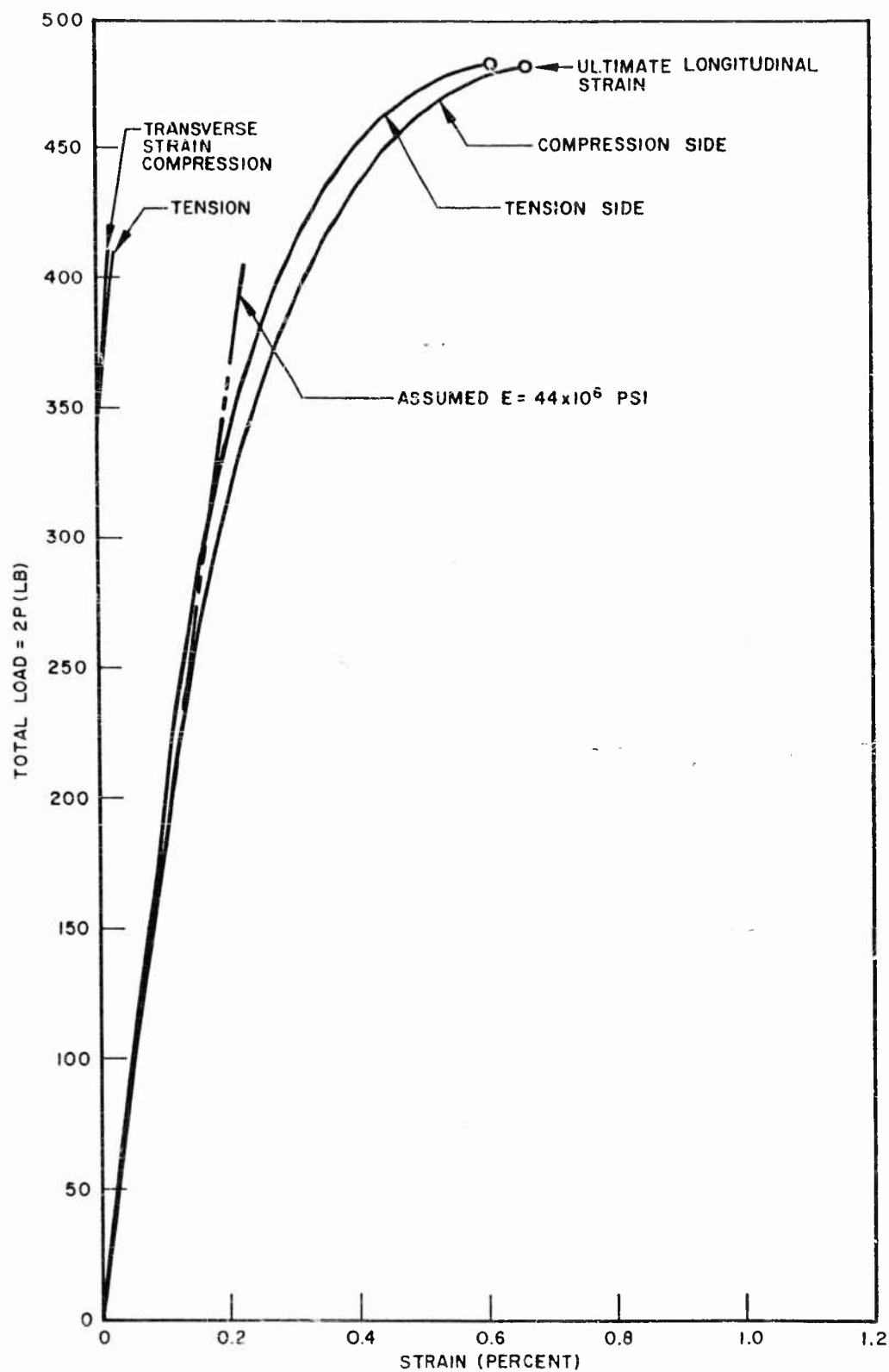


Fig. B-5 Surface Strains Due to Biaxial Stress of Cross-Rolled Beryllium Sheet at Room Temperature

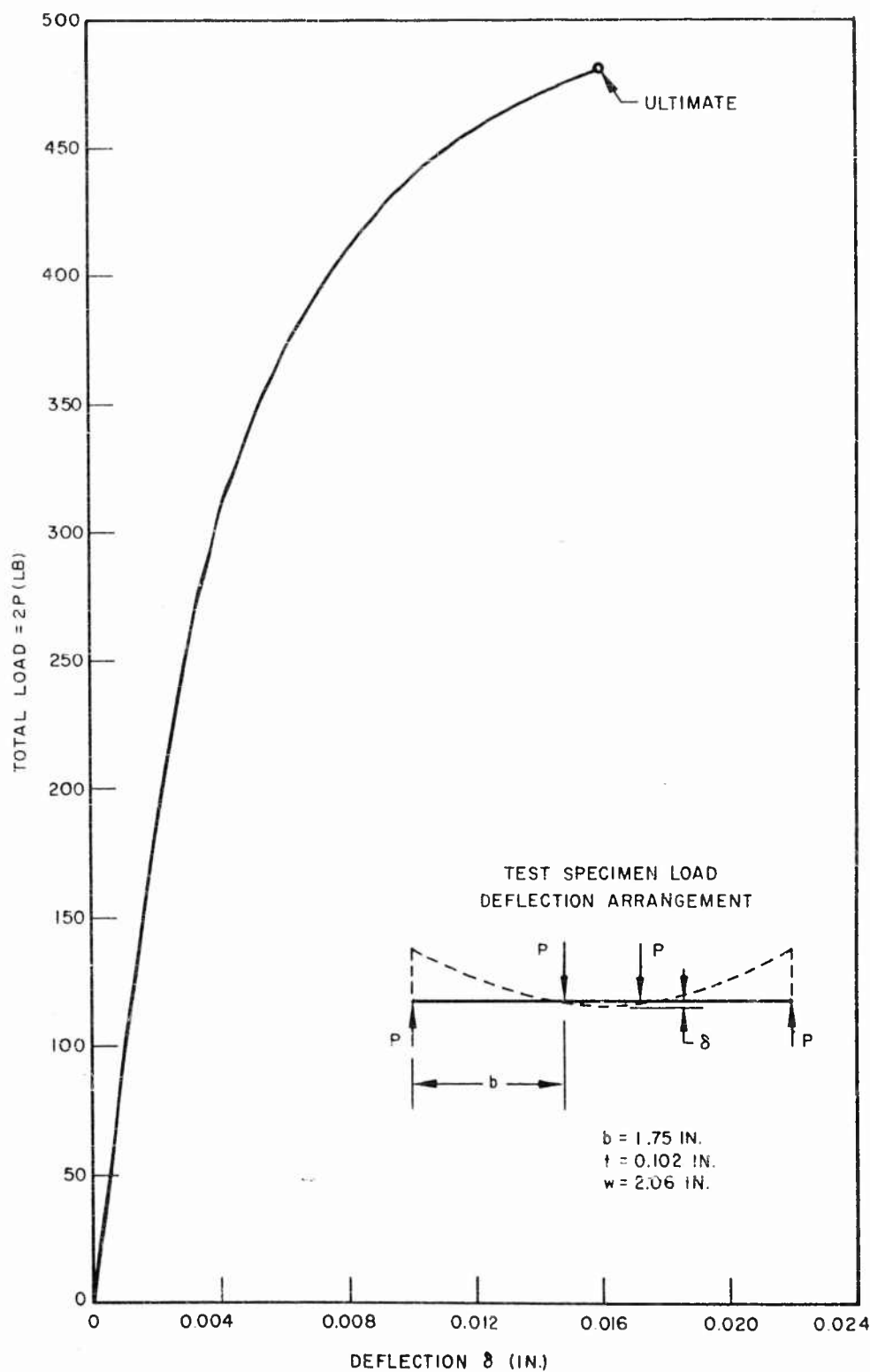


Fig. B-6 Beam Deflection for Biaxial Stress of Cross-Rolled Beryllium Sheet at Room Temperature

B.3.2 Elevated-Temperature Test Results

The results of the 400°F tests are shown graphically in Figs. B-7 and B-8. The former shows the strain data, and the latter shows the load versus deflection curve. Strain was measured in the longitudinal direction for both surfaces, but only the bottom transverse strain gage was operative for the transverse direction. Remarkable similarity was observed in the ultimate strengths of the room-temperature and the 400°F tests, and in the deflection and strain data.

Failure of instrumentation on the 600° F test prevented the presentation of the load-deflection and load-strain characteristics. However, the specimen was nominally the same as the room-temperature and 400° F specimens, and the ultimate load was measured to be 515 lb. As mentioned previously, the specimen did not fracture.

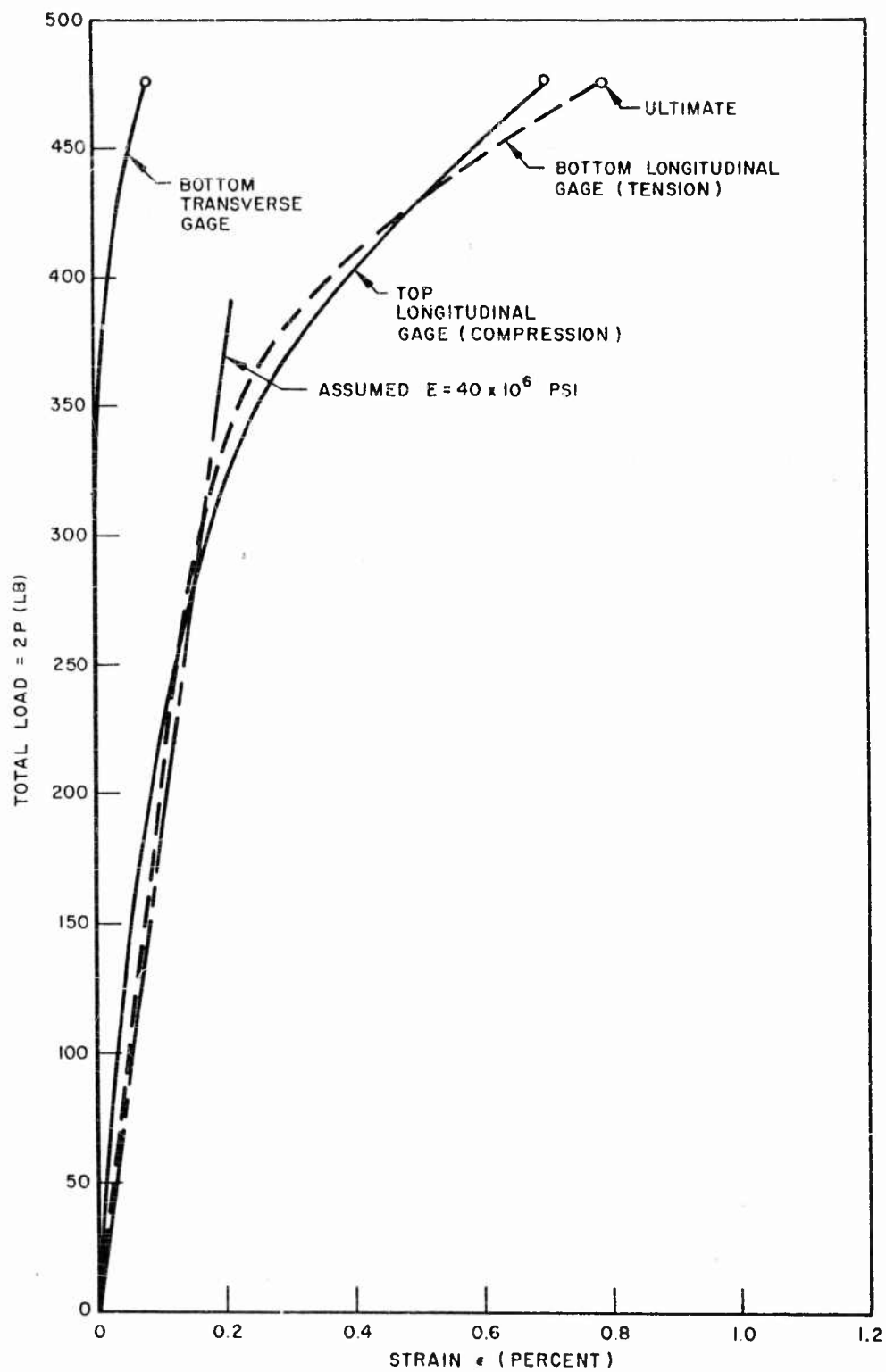


Fig. B-7 Surface Strains Due to Biaxial Stress of Cross-Rolled Beryllium Sheet at 400°F

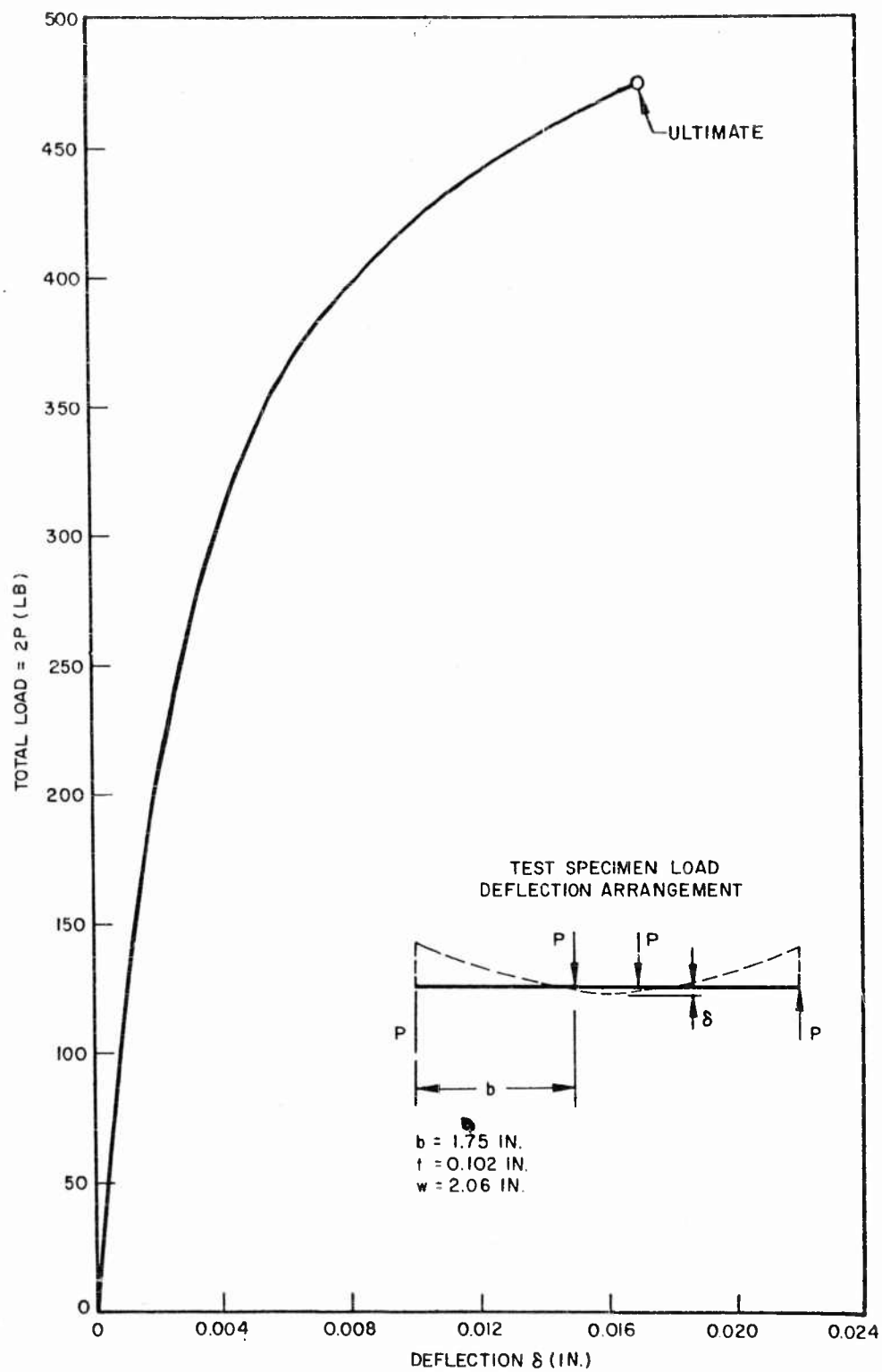


Fig. B-8 Beam Deflection for Biaxial Stress of Cross-Rolled Beryllium Sheet at 400°F

Appendix C

FABRICATION AND TESTING OF BERYLLIUM STRUCTURAL SANDWICHES

C.1 INTRODUCTION

As a part of this program, two beryllium sandwiches were constructed by the Solar Aircraft Company according to Lockheed specifications. The sandwiches and their end-loading attachments are shown in Figs. C-1 and C-2, and the cross-sectional geometries are shown in Fig. C-3. Although both sandwiches were subjected to structural tests (as discussed later in this appendix), the primary purpose of making the sandwiches was to determine the feasibility of constructing such complex structural components of beryllium.

The forming and brazing of the sandwiches was shown to be feasible, as demonstrated by the structural soundness of the sandwiches in the tests. However, it is emphasized that the successful fabrication was the result of significant developments in several stages of fabrication; namely, flattening, bending, choice of brazing alloy and technique, and tooling.

No previous mention of these sandwich tests has been made in this report because of the uncertainty of fabrication success until very late in the program, at which time most of this publication had been prepared. The information presented in this appendix is considered a valuable part of this program. In order to be made available to the aerospace industry, it is given independently here as Appendix C.

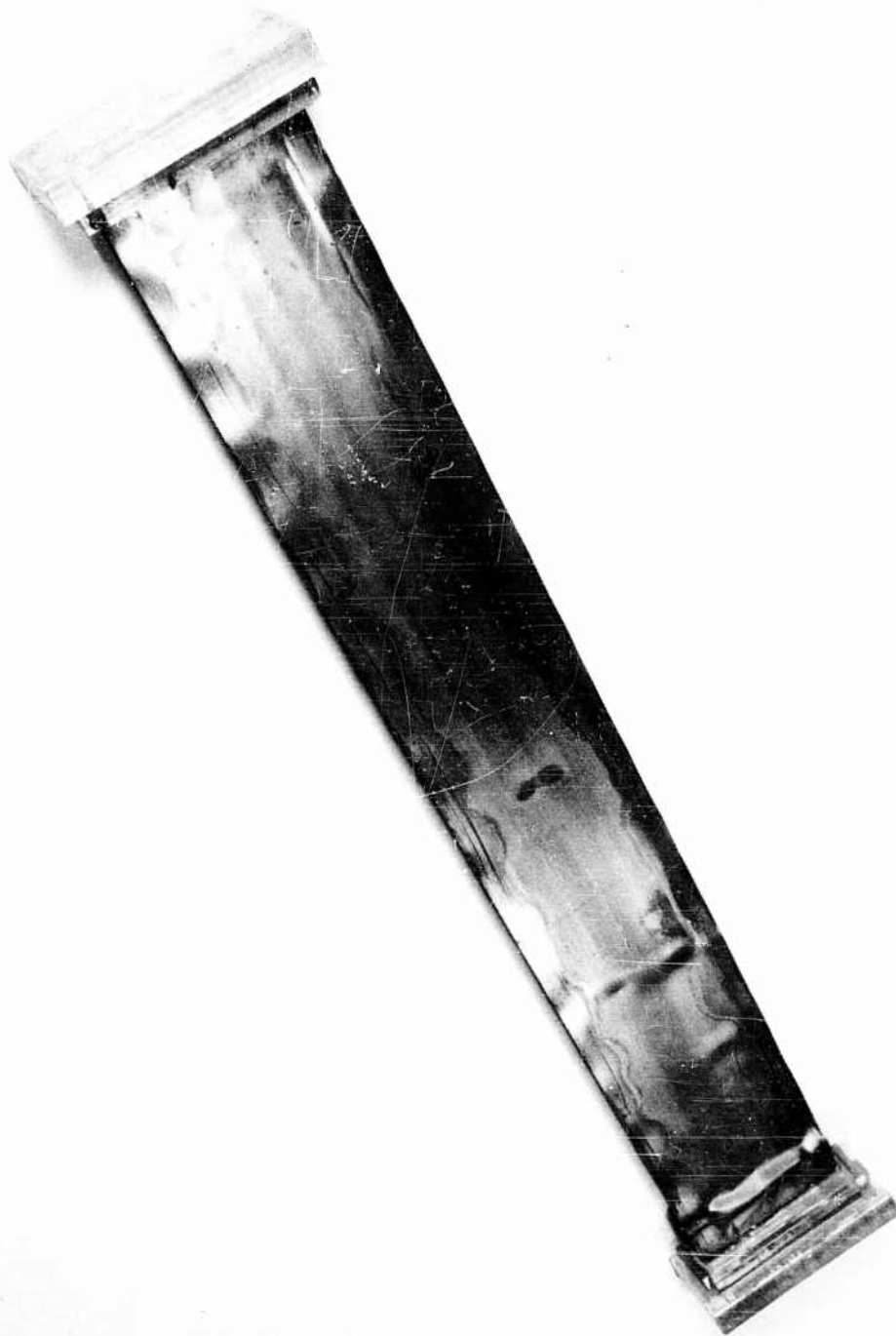
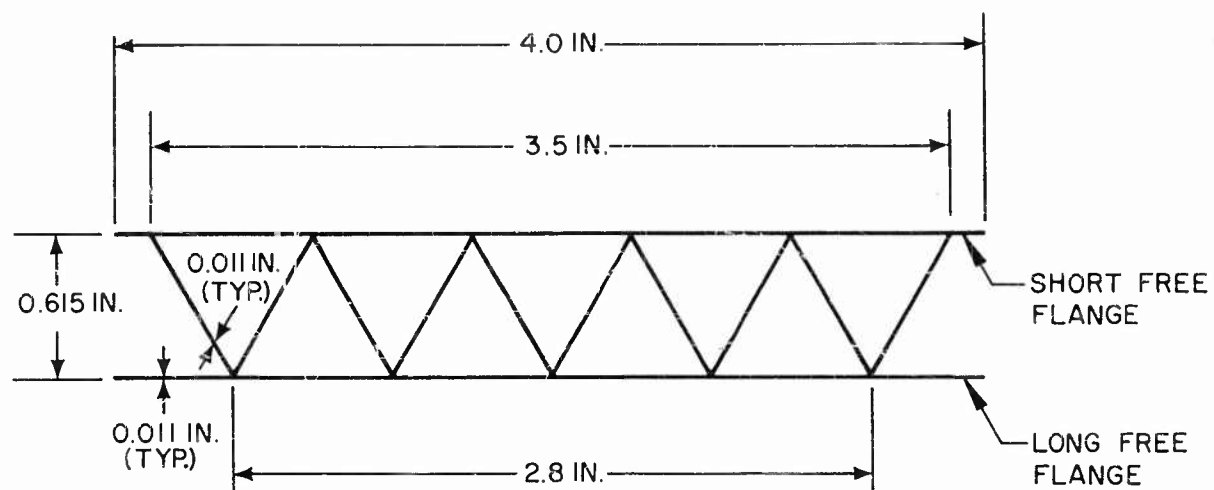


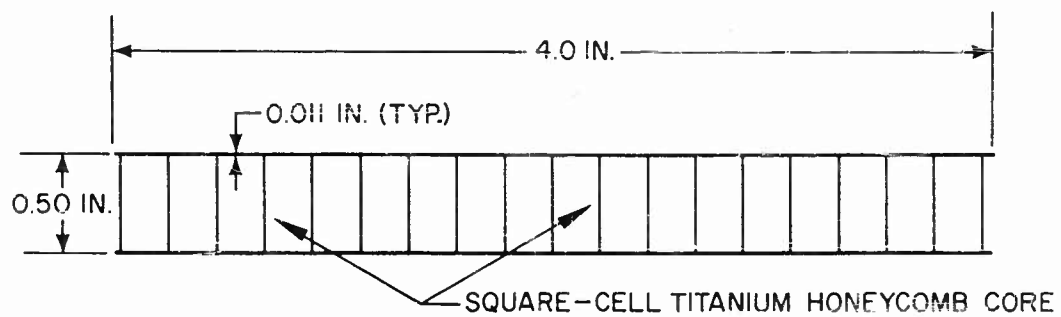
Fig. C-1 Beryllium Truss-Core Sandwich (After Test)



Fig. C-2 Beryllium Facings on Titanium-Core Honeycomb Sandwich
(After Test)



a. All-beryllium truss-core sandwich



b. Honeycomb sandwich with beryllium facings and titanium core

Fig. C-3 Cross Sections of Sandwiches

C.2 FABRICATION

Both of the sandwiches fabricated were nominally 30 in. long and had 0.011-in. -thick cross-rolled beryllium facing sheets. The truss-core configuration shown in Figs. C-1 and C-3 had beryllium core elements of the same thickness as the facings, while the honeycomb configuration shown in Figs. C-2 and C-3 had a titanium square-cell core of 0.0025 in. thickness and 0.38 in. width.

The truss-core sandwich was the more difficult of the two to fabricate, inasmuch as it was necessary to develop methods for flattening the wavy facing sheets and bending the core elements and to design special tooling for holding the elements while furnace-brazing them. In addition, it was necessary to choose a brazing alloy (50 Ag-15.5 Cu-15.5 Zn-16.0 Cd-3.0 Ni) and to develop a procedure for brazing both sandwiches, as discussed in Section 3. The titanium honeycomb sandwich was easier to fabricate, since neither flattening nor forming of the beryllium facings was required and tooling for brazing this type of sandwich had previously been developed.

Flattening of the facing sheets for the truss-core sandwich was accomplished by applying approximately 15-psi normal pressure to them while they were sandwiched between flat steel plates at 1500°F. The sheets were held in this condition for periods of 20 to 90 min, the shorter time being sufficient. When removed, no visible "oil cans" or waves existed, and the sheets were judged to be sufficiently flat for use in sandwich construction.

The core of the truss-core sandwich consisted of five pieces of beryllium bent into 60-deg V's. The radii of the V's were approximately three times their thickness. The bends were accomplished by slowly forming the pieces over 60-deg tools at temperatures between 1200° and 1400°F.

Details of the brazing fixture were not revealed; however, it consisted essentially of copper triangular bars that held the core elements in place during furnace brazing and were readily withdrawn after brazing.

Both sandwiches were well brazed and acceptably free of waviness. Visual inspection revealed no cracks. In summary, this part of the program showed that beryllium can be fabricated into either of the two types of flat structural sandwiches.

C.3 TESTING

The sandwiches shown in Figs. C-1 and C-2 were first tested by subjecting them to longitudinal compression. Their ends were loaded through 3/4-in.-thick magnesium bearing plates that were bonded to them by being cast in pools of epoxy resin about 1/2 in. deep. To insure uniform stresses, precautions were taken to set the panels perpendicular to the faces of the bearing plates. (See Fig. C-4.)

The sandwiches were compressed in a screw-driven universal testing machine of 50,000-lb capacity. The loading rate was approximately 500 lb/min on both specimens. As the load increased, but before visible failure occurred, occasional creaking noises were made by both specimens.

The truss-core sandwich panel reached a maximum compressive load of 3,680 lb or a stress of approximately 26,000 psi after having formed buckles in its elements. The precise value at which the local buckles began developing was not determined, but calculations show that the longer free flanges (Fig. C-3a) could have precipitated buckling at approximately 12,000 psi. Severe buckles were plastically set in the free flanges, as can be seen in Fig. C-1. Ultimate failure occurred by separation of the facings from the core, as is also shown in Fig. C-1. The test showed that rather severe local buckles may be sustained in the elements of the sandwich before either the sheet cracks or the twisting forces along the joints cause separation.

After the truss-core sandwich was tested in axial compression, a section of it that remained intact was subjected to a bending moment such that the short free flange (Fig. C-3) was the compression side. Buckles began appearing in the specimen in the pattern shown in Fig. C-5 at approximately 1,000 in.-lb or an extreme fiber stress of 29,000 psi. The buckles grew in amplitude until tensile fracture of the tension face occurred at approximately 1,230 in.-lb or 35,000 psi.

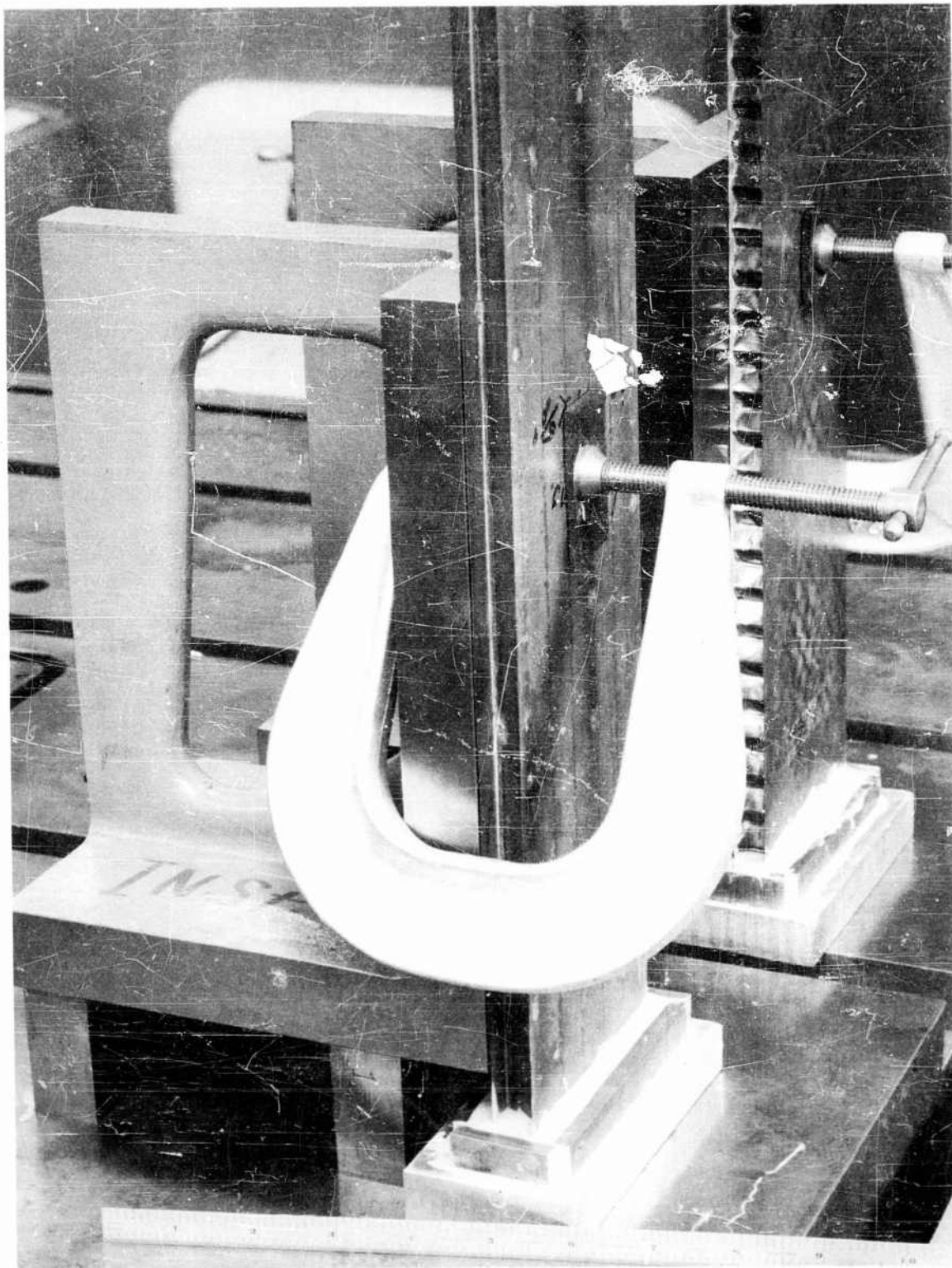


Fig. C-4 Tooling for Assuring That Panels Are Perpendicular to Bearing Plates



Fig. C-5 Failure of Truss-Core Sandwich Under Bending Loads

This test again illustrates that local buckling does not lead immediately to fracture of the sheet or the braze joints. The joints were therefore well brazed. It further illustrates that the beryllium facing sheets were being stressed into the plastic regime at buckling. Methods given for predicting buckling (Section 3) show that buckling should not have occurred before an extreme fiber stress of approximately 35,000 psi. The lower test buckling stress is probably the result of degradation of the mechanical properties of the sheet due to the severe temperatures during brazing. This effect is discussed in Section 3 for the axially loaded cylinders that were similarly brazed. Degradation of the mechanical properties of the facing sheets is further evidenced by the tensile fracture that occurred at only 35,000 psi.

Under axial loading, the honeycomb sandwich failed at 2,910 lb or a facing stress of approximately 33,000 psi (assuming that the core carries no load). Figure C-2 shows that buckling of the facing sheets into the cells of the honeycomb core precipitated fracture of the facing-to-core bond. Calculations show that the stress for this type of buckling is approximately 61,000 psi. Therefore, the material must have been stressed well into the plastic regime for the buckling to have occurred at 33,000 psi or below. However, since stress-strain curves were not determined for the facing sheets after they were subjected to the fabrication processes, this conclusion is not completely verified.

In an attempt to verify the conclusion, a portion of the honeycomb-core sandwich that remained intact was subjected to bending by loading it as a beam, as shown in Fig. C-6.

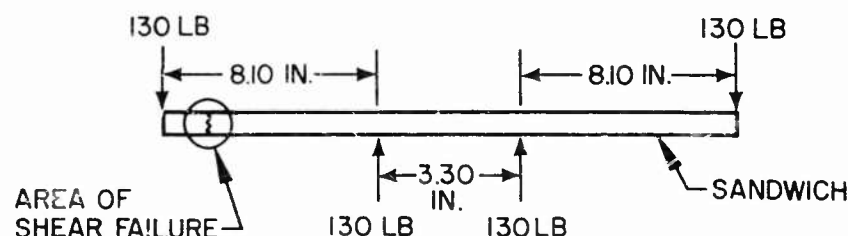


Fig. C-6 Beam Loading of Honeycomb Sandwich

Shear fracture of the sandwich occurred under a total shearing force of 130 lb. The failure load produced compression and tensile stresses of approximately 32,000 psi in the facing sheets, but no buckling was observed before the sandwich failed by shearing. The shearing stress in the braze joining the facings to the core is calculated as approximately 7,000 psi. This braze strength is considered to be satisfactory. It is noted that the shear fracture occurred close to the end force at the approximate position designated in Fig. C-6. It is concluded, therefore, that buckling did not precipitate the shear fracture, since it occurred in an area of low bending moment.

The following conclusions are drawn from the test results:

- Local instability can precipitate fracture of facing-to-core bonds, resulting in total failure of the sandwiches.
- After fabrication, the beryllium facing sheets had low proportional limits and strengths.
- The shear strength of the core-to-facing bond of the honeycomb-core sandwich is adequate.

USCOMM-DC-47064